INTERNATIONAL CONFERENCE

Mathematical Analysis and Applications in Science and Engineering

JUNE 20–22, 2024

ISEP · PORTO, PORTUGAL

Book of abstracts

ISEP P.PORTO

Editors:

Martin Golubitsky

Walter Lacarnobara

Carla M.A. Pinto

Lurdes Babo

Jorge Mendonça

Fernando Carvalho

Rui Rocha

ISBN: 978-989-35251-7-3

June 2024

Honorary Committee

Ravi P. Agarwal, USA

Linda Allen, USA

Jan Awrejcewicz, Poland

Carlos Braumann, Portugal

Marty Golubitsky, USA

Nicolae Herisanu, Romania

JA Tenreiro Machado, Portugal

Francesco Mainardi, Italy

Alain Le Méhauté, France

Raoul Nigmatullin, Russia

Lev Ostrovsky, USA

Jorge Nuno Silva, Portugal

Hari M. Srivastava, Canada

João Manuel R.S. Tavares, Portugal

James Yorke, USA

Chair of the Conference

Marty Golubitsky, USA

Co-Chairs

Walter Lacarbonara, Rome Sapienza University

Carla M. A. Pinto, Polytechnic of Porto

Chairs of the Scientific Committee

Stefano Boccaletti, Italy

Virginia Kyriakova, Bulgaria

Ruy M Ribeiro, Los Alamos, USA

Chairs of the Organizing Committee

António Vega Y De La Fuente, Portugal

Maria João Viamonte, Portugal

Co-Chairs of the Organizing Committee

Lurdes Babo, Portugal

Mário Cruz, Portugal

Jorge Mendonça, Portugal

Chairs of the Plenary Committee

Ana Paula Dias, Portugal

João Nuno Tavares, Portugal

Duarte Valério, Portugal

Chairs of the Special Sessions

Ricardo Queirós, Portugal

Helena Reis, Portugal

Chairs of the Publications Committee

Albert Luo, USA

Carla M. A. Pinto, Portugal

Ivanka Stamova, USA

Chairs of the Awarding Committee

Dumitru Baleanu, Turkey

Juan Carlos Cortés, Spain

Marty Golubitsky, USA

Walter Lacarbonara, Italy

Carla M.A. Pinto, Portugal

Chairs of the Sponsorship Committee

Roque Brandão, Portugal

Stefania Tomasiello, Estonia**Publicity Chairs**

Manuela Carvalho, Portugal

Jorge Mendonça, Portugal

Chairs of the Financial Committee

António Vega Y de La Fuente, Portugal

Francisco Silva, Portugal

Scientific Committee

Om P. Agarwal, USA

Praveen Agarwal, India

Obaid Algahtani, Saudi Arabia

Valerii Antonov, Russia

Iván Area, Spain

Omar Abu Arqub, Jordan

Lurdes Babo, Portugal

Jose Manoel Balthazar, Brazil

Roberto Barrio, Spain

Mustafa Bayram, Turkey

Konstantin Blyuss, United Kingdom

Stefano Boccaletti, Italy

Jorge Buescu, Portugal

Raul Campilho, Portugal

Chinmay Chakraborty, India

Joseph Páez Chávez, Ecuador

YangQuan Chen, USA

Dana Copot, Belgium

Michael Dellnitz, Germany

Ana Paula Dias, Portugal

Alberto D'Onofrio, Italy

Flávio Ferreira, Portugal

Stefano Galatolo, Italy

Alexandra Galhano, Portugal

Sílvio Gama, Portugal

Alireza K. Golmankhaneh, Iran

Tomas Götz, Germany

R. Hilfer, Germany

Clara Ionescu, Belgium

Maaita Jamal-Odysseas. Greece

Devendra Kumar, India

Yuliya Kyrychko, United Kingdom

Daniel Cao Labora, Spain

Stefano Lenci, Italy

Changpin Li, China

Rosana Rodriguez Lopez, Spain

Albert Luo, USA

Rachid Malti, France

António Marques, Portugal

Shaher Momani, Jordania

Cristina Muresan, Romania

Necati Ozdemir, Turkey

Marcello Pellicciari, Italy

Luís Miguel Pinho, Portugal

Alberto Adrego Pinto, Portugal

Igor Podlubny, Slovakia

Ioan-Lucian Popa, Romania

Carlos Ramos, Portugal

Julio C. Rebelo, France

Magda Rebelo, Portugal

Helena Reis, Portugal

Diogo Rodrigo Ribeiro, Portugal

José C. Sá, Portugal

Rita Sales, Brazil & Portugal

Gilberto Santos, Portugal

António Sartal, Spain

Aydin Seçer, Turkey

Stefan Siegmund, Germany

Francisco Silva, Portugal

Jaime Silva, Portugal

Jagdev Singh, India

A. Augusto Sousa, Portugal

Ivanka Stamova, USA

Nasser Sweilam, Egypt

Jian-Qiao Sun, USA

Hong Guan Sun, China

Stefania Tomasiello, Estonia

Delfim F.M. Torres, Portugal

Juan Trujillo, Spain

Duarte Valério, Portugal

Ezio Venturno, Italy

Dimitri Volchenkov, USA

Xiao-Jun Yang, China

Dia Zeidan, Jordan

Organizing Committee

Sandra Aires,Portugal

Luís Afonso, Portugal

Alcinda Barreiros, Portugal

Vítor Cardoso, Portugal

Fernando Carvalho, Portugal

Vítor Cunha, Portugal

Luís Pinto Ferreira, Portugal

Maria Hermínia Ferreira, Portugal

Nuno Miguel Ferreira, Portugal

Isabel Figueiredo, Portugal

Alexandra Gavina, Portugal

Gabriela Gonçalves, Portugal

Emanuel Guaraglia, Brasil

Maria da Graça Marcos, Portugal

João Matos, Portugal

Ana Cristina Meira, Portugal

Marisa Oliveira, Portugal

Arnaldo Pinto, Portugal

Isabel Pinto, Portugal

Gisela Ramadas, Portugal

Pedro Reis, Portugal

Rui Rocha, Portugal

António Varejão, Portugal

Secretary

Ana Costa, Portugal

ICMASC' 2024 is a joint organization by:

2024 Awards

CAREER AWARD

For extraordinary contributions in Nonlinear Dynamics

Professor Henk Broer – info

J.A. TENREIRO MACHADO AWARD

For breakthrough achievements in Fractional Calculus

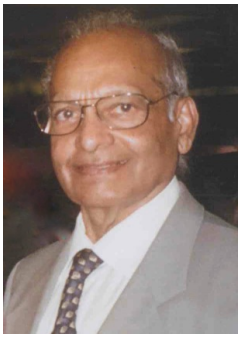

Professor Hari M. Srivastava – info

JAMES YORKE AWARD

For breakthrough achievements in Nonlinear Dynamics and Chaos

Professor Celso Grebogi – info

BEST STUDENT PAPER

For outstanding young scholars in Mathematical Analysis and Applications

Amani Rayene Ynineb, Ghent University, Belgium

Godwin Sani, Lodz University, Poland

BEST POSTER

For best poster presentation in Mathematical Analysis and Applications

Carla Pinto, P.Porto, Portugal

Lurdes Babo, P.Porto, Portugal

Jorge Mendonça, P.Porto, Portugal

Deolinda Rasteiro, P.Coimbra, Portugal

Cristina Caridade, P.Coimbra, Portugal

Grupetto Musical – Associação Cultural, Portugal

Nelida Crnjaric, University of Rijeka, Croatia

Ivan Drazic, University of Rijeka, Croatia

Plenary Talks

The Ohio State University, USA

Title: Quantifying approximate symmetries in biological systems

Abstract: What do leaves and human faces have in common? What about daisies and sea urchins? They possess bilateral and rotational symmetries! Symmetry is a fundamental feature of natural systems, and is often correlated with survival, fecundity, and evolvability. While symmetry is ubiquitous and often intuitively obvious, symmetry in biological organisms is rarely perfect, making it challenging to apply mathematical definitions of idealized symmetry. To address this challenge, we developed a flexible, entropy-based method for quantifying symmetry that requires very little user input. I will highlight some novel insights arising from applications of this measure, including evidence for convergent evolution in flowering plants, classification of biopolymer networks, and visualization of the emergence and loss of symmetries in pattern formation systems.

Bio: Dr. Adriana Dawes is a Professor at The Ohio State University, with a joint appointment in the Department of Mathematics and the Department of Molecular Genetics. Prof. Dawes' research tightly weaves experimental and theoretical approaches to better understand how biochemical, mechanical and geometric cellular features interact and regulate each other during development to give rise to a functional organism. Her research connects dynamics across multiple scales, using experimentally validated mathematical models to investigate force generation and large scale movement in the cell, and revealing how the structure of signaling networks interacts with genetic backgrounds to produce tissue-specific responses. Prof. Dawes is the recipient of an NSF CAREER award, and has also been funded by NIH and private foundations, including the Gordon and Betty Moore Foundation.

University of Liège, Belgium

Title: Breaking Indecision in Multiagent, Multioption Dynamics

Abstract: How does a group of agents break indecision when deciding about options with qualities that are hard to distinguish? Biological and artificial multiagent systems, from honeybees and bird flocks to bacteria, robots, and humans, often need to overcome indecision when choosing among options in situations in which the performance or even the survival of the group is at stake. Breaking indecision is also important because in a fully indecisive state, where agents are not biased toward any specific option, the agent group is maximally sensitive and prone to adapt to inputs and changes in its environment. Here, we develop a mathematical theory to study how decisions arise from the breaking of indecision. Our approach is grounded in both equivariant and network bifurcation theory. We model decision from indecision as synchrony-breaking in influence networks in which each node is the value assigned by an agent to an option. First, we show that three universal decision behaviors, namely, deadlock, consensus, and dissensus, are the generic outcomes of synchrony-breaking bifurcations from a fully synchronous state of indecision in influence networks. Second, we show that all deadlock and consensus value patterns and some dissensus value patterns are predicted by the symmetry of the influence networks. Third, we show that there are also many “exotic” dissensus value patterns. These patterns are predicted by network architecture but not by network symmetries through a new synchrony-breaking branching lemma. This is the first example of exotic solutions in an application. Numerical simulations of a novel influence network model illustrate our theoretical results.

Bio: Dr Alessio Franci received his Laurea Specialistica Degree in Theoretical Physics from the University of Pisa in 2008 and his PhD in Physics and Control Theory from the University of Paris Sud 11 in 2012. Between 2012 and 2015 he was a postdoctoral researcher at the University of Liege and at INRIA Lille and a long term visiting researcher at the University of Cambridge. Between 2015 and 2022 he was professor in the Math Department of the National Autonomous University of Mexico. Since 2023 he has been professor in the Department of Electrical Engineering and Computer Science of the University of Liege. His research is interdisciplinary but the central focus is on the control-theoretical and computational principles needed to understand and design biological and bio-inspired intelligent behaviors.

University of Porto, Portugal

Title: Network classification using ODE-equivalence

Abstract: It is known that non-isomorphic networks can generate the same space of admissible vector fields, once the cell phase spaces of the networks are identified in a suitable way. Those networks are called ODE-equivalent and previous results on network theory show that two networks are ODE-equivalent if and only if the two networks are linearly equivalent. In this talk we plan to show how to use ODE-equivalence to classify small excitatory-inhibitory networks. This is a joint work with M. Aguiar (Porto) and I. Stewart (Warwick, UK).

Bio: Dr Ana Paula Dias' current position is Associate professor at the Mathematics Department of the Sciences Faculty of the University of Porto, Portugal. Education. Ana Dias received her Ph.D. in Mathematics from the University of Warwick at United Kingdom in 1998 and was awarded a Habilitation in Mathematics from University of Porto, Portugal in 2007. Main research of interest. Impact of the network/hypernetwork at the dynamics and bifurcations of the associated coupled cell systems (dynamical systems with form consistent with the network/hypernetwork). Ana Dias is author of over 45 scientific papers in the area of Dynamical Systems. https://cmup.fc.up.pt/cmup/apdias/publications.html

University of Évora, Portugal

Title: General stochastic differential equation models for population growth and harvesting in random environments: Sustainability, optimization and impact of Allee effects

Joint work with: Clara Carlos and Nuno M. Brites

Abstract: We consider autonomous stochastic differential equation models, one without Allee effects and another with Allee effects, for the growth of a harvested population living in a randomly varying environment, even an environment with density-dependent noise intensities. These models are very general, satisfying only mild regularity assumptions and qualitative biologically driven assumptions, so that the conditions we obtain for population extinction and for the existence of a stochastic equilibrium are robust with respect to model choice. We use Itô calculus but will mention our results on its equivalence to Stratonovich calculus if one takes into account the different physical meaning of the average rates used. For both calculi and for both cases of absence and presence of Allee effects, we show that, if the per capita net growth rate (difference between the geometric average natural growth rate and the harvesting mortality rate) is positive when population size is very small, there is a stochastic equilibriumwith a stationary density. If, however, that rate is negative (overharvesting), the population becomes extinct. The results for Allee effects models are new and extend previous results of members of this team for non-harvested population models and for constant effort particular harvesting models. We then look at the case of constant harvesting effort and constant noise intensity for specific comparable models, namely the logistic (without Allee effects) and the logistic-like Allee effects models, including expressions for stationary densities and expected sustainable profits and yields. We assess the impact of Allee effects by comparing the two models and their optimal profits and yields for the Pacific halibut data.

Bio: Professor Carlos A. Braumann is Emeritus Professor at the Department of Mathematics of the University of Évora (Portugal), elected member of the International Statistical Institute, Honorary Member and 2019 Career Award holder of the Portuguese Statistical Society (SPE) and former President of ESMTB (European Society for Mathematical and Theoretical Biology) and of SPE. He is

working on stochastic differential equation models applied to biological phenomena occurring in randomly varying environments, area in which he recently authored a Wiley book.

Acknowledgements: C. A. Braumann (Departamento de Matemática, Escola de Ciências e Tecnologia, Universidade de Évora) and C. Carlos (Escola Superior de Tecnologia do Barreiro, Instituto Politécnico de Setúbal) are members of the Centro de Investigação em Matemática e Aplicações, Instituto de Investigação e Formação Avançada, Universidade de Évora, supported by the Fundação para a Ciência e a Tecnologia (FCT), Project UID/04674/2020, https://doi.org/10.54499/UIDB/04674/2020. N.M. Brites (ISEG/UL – Universidade de Lisboa, Department of Mathematics & REM – Research in Economics and Mathematics, CEMAPRE) was partially funded by FCT, Project CEMAPRE/REM – UIDB/05069/2020, through national funds.

University of Porto, Portugal

Title: On the dynamics of vector fields with univalued solutions

Abstract: We will discuss problems and recent results on the dynamics of differential equations / vector fields with univalued solutions. If time permits we will also discuss potential geometric applications.

Bio: Dr Helena Reis, Associate Professor with habilitation at Faculdade de Economia da Universidade do Porto; Director of CMUP (2023-); Editor-in-chief of Boletim da SPM (2023-) More information: https://www.fep.up.pt/docentes/hreis/

Paderborn University

Title: Glimpse of the Infinite – on the Approximation of the Dynamical Behavior for Delay and Partial Differential Equations

Abstract: Over the last decades so-called set-oriented numerical methods have been developed for the numerical analysis of finite-dimensional dynamical systems. The underlying idea is to approximate the dynamical objects of interest by outer coverings which are created via multilevel subdivision techniques in state space. These schemes have the flexibility to be applied to a variety of problems such as the numerical approximation of invariant manifolds, global attractors or corresponding invariant measures. Since these set-oriented techniques rely on partitions of the (finite-dimensional) state space it is not obvious how to extend them to the situation where the underlying dynamical system is infinite-dimensional. However, in this talk a novel numerical framework for the computation of finite dimensional dynamical objects for infinite dimensional dynamical systems will be presented. Within this framework the classical set-oriented numerical schemes mentioned above are extended to the infinite-dimensional context. The underlying idea is to utilize appropriate embedding techniques for the reconstruction of global attractors in a certain finite dimensional space. This approach will be illustrated by the computation of global attractors both for delay and for partial differential equations such as the Mackey-Glass equation or the Kuramoto-Sivashinsky equation.

Bio: Dr Michael Dellnitz is Chair of Applied Mathematics at Paderborn University, Chairman-Professor at Institut für Industriemathematik, Professor at Paderborn Center for Parallel Computing (PC2), Vorstand, Professor at Paderborn Institute for Scientific Computation (PaSCo). More information here: https://www.uni-paderborn.de/en/person/82

Institute of Complex Systems of the Italian CNR, Florence, Italy

Title: The transition to synchronization of networked systems

Abstract: With the only help of eigenvalues and eigenvectors of the graph's Laplacian matrix, we show that the transition to synchronization of a generic networked dynamical system can be entirely predicted and completely characterized.In particular, the transition is made of a well-defined sequence of events, each of which corresponds to either the nucleation of one(or several) cluster(s) of synchronized nodes or to the merging of multiple synchronized clusters into a single one.The network's nodes involved in each of such clusters can be exactly identified, and the value of the coupling strength at which such events are taking place (and therefore, the complete events' sequence) can be rigorously ascertained.We moreover clarify that the synchronized clusters are formed by those nodes which are indistinguishable at the eyes of any other network's vertex, and as such they receive the same dynamical input from the rest of the network.Therefore, such clusters are more general subsets of nodes than those defined by the graph's symmetry orbits, and at the same time more specific than those described by the network's equitable partitions.Finally, we present large scale simulations which show how accurate our predictions are in describing the synchronization transition of both synthetic and real-world large size networks, and we even report that the observed sequence of clusters is preserved in heterogeneous networks made of slightly non identical systems.

Bio: Professor Stefano Boccaletti received the PhD in Physics at the University of Florence on 1995, and a PhD honoris causa at the University Rey Juan Carlos of Madrid on 2015. He was Scientific Attache' of the Italian Embassy in Israel during the years 2007-2011 and 2014-2018. He is currently Director of Research at the Institute of Complex Systems of the Italian CNR, in Florence. His major scientific interests are i) pattern formation and competition in extended media, ii) control and synchronization of chaos, and iii) the structure and dynamics of complex networks. He is Editor in Chief of the Journal "Chaos, Solitons and Fractals" (Elsevier) from 2013, and member of the Academia Europaea since 2016. He was elected member of the Florence City Council from 1995 to 1999. Boccaletti has published 402 papers in peer-reviewed international Journals, which received more than 36,200 citations (Google Sholar). His h factor is 71 and his i-10 index is 232. With more than 12,300 citations, the monograph ¨Complex Networks: Structure and Dynamics¨, published by Boccaletti in Physics Reports on 2006 converted into the most quoted paper ever appeared in the Annals of that Journal.

University of Copenhagen, Denmark

Title: Estimation of time to a tipping point

Abstract: In recent years there has been an increasing awareness of the risks of collapse or tipping points in a wide variety of complex systems, ranging from human medical conditions, pandemics, ecosystems to climate, finance and society. They are characterized by variations on multiple spatial and temporal scales, leading to incomplete understanding or uncertainty in modelling of the dynamics. Even in systems where governing equations are known, such as the atmospheric flow, predictability is limited by the chaotic nature of the system and by the limited resolution in observations and computer simulations. In order to progress in analyzing these complex systems, assuming unresolved scales and chaotic dynamics beyond the horizon of prediction as being stochastic has proven itself efficient and successful. When complex systems undergo critical transitions by changing a control parameter through a critical value, a structural change in the dynamics happens, the previously statistically stable state ceases to exist and the system moves to a different statistically stable state. To establish under which conditions an early warning for tipping can be given, we consider a simple stochastic model, which can be considered a generic representative of many complex two state systems. We show howthis provides a robust statistical method for predicting the time of tipping. The method is used to give a warning of a forthcoming collapse of the Atlantic meridional overturning circulation.

References: Peter D. Ditlevsen and Susanne Ditlevsen (2023), Warning of a forthcoming collapse of the Atlantic meridional overturning circulation. Nat Commun 14, 4254

Bio: Professor Susanne Ditlevsen is professor of Statistics and Stochastic Models in Biology at Department of Mathematical Sciences at University of Copenhagen in Denmark. She has a Master in Mathematics from Universidad Nacional de Education a Distancia, Spain, and did her PhD in Biostatistics at university of Copenhagen. Her research interests are evolving around stochastic processes and their statistical inference, dynamical systems and biomathematics, with applications in ecology and neuroscience. She is vice-president and heading the section of Natural Sciences of the Danish Royal Academy of Sciences and Letters. She has published around 80 papers.

Sapienza University, Italy

Title: Nonlinear wave propagation in metamaterials

Abstract: Wave propagation and stopband behavior of 2D lattices hosting nonlinear resonators made of suspended piezoelectric membranes with a central mass are discussed. A generalized nonlinear version of the plane-wave expansion method is proposed to deliver the nonlinear wave propagation equations. The asymptotic treatment yielding the nonlinear dispersion functions is discussed. An exploration of the design process for semi-adaptively programmable metamaterials is offered, elucidating their potential for wave cloaking applications.

Bio: Walter Lacarbonara is a Professor of Nonlinear Dynamics at Sapienza University and Director of the Sapienza Center for Dynamics. During his graduate education he was awarded a MS in Structural Engineering (Sapienza University) and a MS in Engineering Mechanics (Virginia Tech, USA), and a PhD in Structural Engineering (Sapienza/Virginia Tech). His research interests cover nonlinear structural dynamics; dissipation in carbon nanotube/polymer nanocomposites; asymptotic techniques; nonlinear control of vibrations; experimental nonlinear dynamics; dynamic stability of structures. He is Editor in Chief of Nonlinear Dynamics, former Associate Editor for ASME Journal of Applied Mechanics, Journal of Vibration and Acoustics, Journal of Sound and Vibration. He served as Chair of the ASME Technical Committee on Multibody System and Nonlinear Dynamics, General co-Chair and technical program co-Chair of the ASME 2015 (Boston, USA) and 2013 (Portland, USA) IDETC Conferences. He has organized over 10 international symposia/conference sessions and, very recently, the First, Second, and Third International Nonlinear Dynamics Conferences (NODYCON, www.nodycon.org/2019, www.nodycon.org/2021, www.nodycon.org/2023). His research is supported by national and international sources (EOARD/AFOSR, NSF, European Commission, Italian Ministry of Science and Education). He has published over 250 papers and conference proceedings, 4 international patents (EU/USA/China), 24 book chapters, 6 co-edited Springer books and a single-authored book (Nonlinear Structural Mechanics, Springer, NY, https://link.springer.com/book/10.1007/978-1-4419-1276-3) for which he received the 2013 Texty Award nomination by Springer US.

Invited Talks

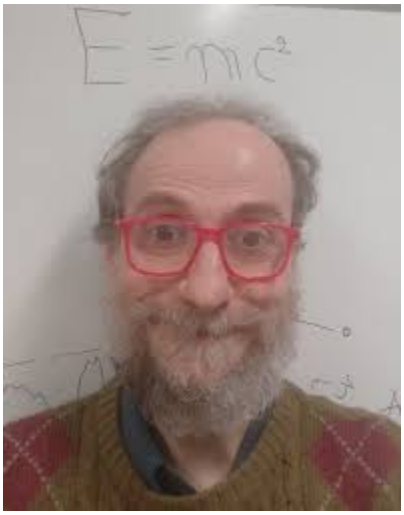

University of Trieste, Italy

Title: A spatiotemporoal random walk in Behavioral Epidemiology

Abstract: Human behavior, and in particular vaccine hesitancy, is a critical factor for the control of childhood infectious disease. Human decisions depends on information that is intrinsically non-local in space and in time. We show that under a series of important epidemiological assumption, the interplay between spatial and temporal nonlocality may induce a number of complex patterning and oscillations, including spatio-temporal chaos. Additionally we briefly illustrate a new simple algorithm for the computation of the Maximum Lyapunov Exponent of a chaotic system.

Bio: Dr Alberto d'Onofrio is senior researcher at the department of Mathematics and GEosciences of the University of Trieste (Italy) where he leads the "Computer Science for Complex Systems" laboratory. After a MSc in Control Engineering at Pisa University, he got a PhD i"Medical Computer Sciences" from Rome "La Sapienza" University in 2000. He has been postdoc (2000-2002), researcher (2003-2008) and Group Leader (2008-2013) in biomathematics at the European Institute of Oncology, Milan (Italy). Then from 2014 to 2020 he has been one of principal investigators at the "International Prévention Research Institute", Lyon (France). Alberto d'Onofrio research areas focus on theoretical and mathematical biophysics of complex biological systems. In particular he is a pioneer of Behavioral Epidemiology of Infectious Diseases, and he also works on modeling systems perturbed by bounded stochastic noises. He has published more than 120 papers in isi-indexed journals, 25 papers in books and proceedings, he has edited 5 books for Soringer-Nature group and 4 special issues of isi-indexed scientific journals. His H-index is 37 (WoS) and his Google scholar h index is 45. He is in the editorial boards of "Journal of Mathematical Biology"", of "Journal of Optimization: theory and Applications" and of "PLoS One". More info here: https://www.donofriolab.org/home

Ghent University, Belgium

Title: Measuring and Evaluating BMI Dependent Drug Dynamic Response in Anesthetised Patients

Abstract: In personalized medicine applications such as general anesthesia, an individualised pharmacokinetic (PK) model requires to move away from the classical assumption of homogeneous drug mixing in various tissue compartments in the body. However, the pharmacokinetic distributions are in fact following non-uniform distribution of uptake/clearance time constants for the drugs used to induce and maintain general anesthesia. This follows in the first instance from the tissue properties of muscle, fat, etc. These classical use of patient models assume to calculate these constants from population-based models as a function of age, gender, weight, height, lean body mass. Hitherto, there is no revision of these models for the incoming obesity problem in all adults as reported by WHO is expected to continually increase in coming decades, as co-morbidity correlated to increase of incidence in cardiovascular disease and type II diabetes. When these models are used in computer based optimization algorithms to find the best drug mixture for a personalized management of anesthesia, they do not suitably match the patient at hand. It follows that anomalous diffusion patterns affect the drug dynamic mixing and transforming to the effect site (further linked to its effect by PD pharmacodynamic models), and therefore affects the overall control system performance. As an example, a lean patient will have a faster and more homogeneous distribution of drug in the body than an obese patient. This presentation gives an overview on the opportunities to develop sensing techniques for a framework that will correlate BMI to fat volume in such PK models. There is an opportunity to employ fractional order models for anomalous diffusion characterization in drug accumulation and release dynamics. An experimental setup and data analysis from fat tissue samples is used to illustrate initial steps towards a theory that would offer a revision of the classic patient models.

Bio: Dr Clara Mihaela Ionescu is professor at Faculty of Engineering and Architecture, at Ghent University, Belgium since October 2016. She is a research-member of the laboratory of Dynamical Systems and Control. She holds a master degree is Automation and Applied Informatics in 2003 from Dunarea de Jos University of Galati, Romania, and a PhD degree in Biomedical Engineering from Ghent University in 2009. She was recipient of prestigious excellence scholarship for top-students going abroad from the Romanian Ministry of Research and Innovation during her master Studies at Ghent University in 2002. She was also recipient of prestigious excellent post-doctoral scholarship of Flemish Research Foundation, of Belgium for 6 years, from 2011 – 2017. She is an ERC Consolidator Grant fellow: AMICAS, Adaptive Multi-Drug Infusion Control System for General Anesthesia during Major Surgery.

Texas Tech University, USA

Title: Thermodynamic Insights into Network Dynamics: Statistical Mechanics Perspective

Abstract: Our study delves into the thermodynamic behaviors of extensive walks on non-random, connected graphs with potential random alterations and transportation noise. It employs statistical mechanics to gauge structural attributes crucial for network dynamics, revealing a Fermi–Dirac distribution of node fugacity in response to modifications. Notably, nodes with lower centrality are predisposed to future alterations. The analysis extends to finite graphs, emphasizing the applicability beyond random structures. This approach sheds light on complex network dynamics, especially in urban environments, elucidating the impacts of structural irregularities on mobility patterns. Ultimately, the research elucidates the statistical mechanics governing network evolution, crucial for understanding and optimizing complex systems.

Bio: Dr Dimitri Volchenkov is a Professor of Applied Mathematics and Statistics at the Texas Tech University (USA), former Chair Professor at the Artificial Intelligence Key Laboratory of Sichuan Province, School of Automation and Information Engineering, Sichuan University of Science and Engineering (China), former qualified professor in France and Germany, admitted as the TTU SIAM professor of the year 2021/2022, “Nationally recognized talent” of China (“1000 Talent Plan of China”), awarded by the G. Zaslavsky award in Nonlinear Science and Complexity (USA), Cheung Kong Scholarship (China), Alexander von Humboldt and Volkswagen Fellowships (Germany), NATO/OTAN and C.N.R.S Fellowships (France), George Soros Fellowship (USA), and Scientists Federal Awards (Russia).

University of Lisbon, Portugal

Title: Identifying fractional order transfer functions from frequency responses

Abstract: This paper explores simple methods to identify fractional order models from a frequency response. The models addressed are explicit and commensurate, with one or two pseudo-poles. Such identification methods complement Levy's identification method.

Bio: Dr Duarte Valério is Associate Professor at Instituto Superior Técnico — University of Lisbon, where he got his MSc (2001) and PhD (2005) in Mechanical Engineering, with theses on fractional control, i.e. on the use of fractional (non-integer) order derivatives in control. He has worked with fractional control and fractional dynamic systems, and their applications in several areas, ever since. He also researches in the fields of energy conversion (in particular, the control of Wave Energy Converters, that produce electricity from the energy of sea waves) and bioengineering applications (modelling and control of dynamic systems such as biological processes). He has co-authored over sixty papers in journals with impact factors, three books, over seventy papers in conference proceedings, and nine book chapters.

University Medical Center Utrecht in the Netherlands

Title: Targeted control of COVID-19 post-mass vaccination

Abstract: SARS-CoV-2 infection currently causes common cold- or flu-like illness in most individuals, but patients with chronic conditions still experience a higher chance of COVID-19 hospitalization and death. It is crucial to estimate COVID-19 burden in chronic patients and to determine how best to protect them from severe COVID-19. In this talk, I will present an assessment of the impact of post-pandemic vaccination strategies in chronic patients of different ages. The model population is stratified by age, risk due to chronic conditions, and immunity level before the start of a seasonal post-pandemic outbreak. For risk classification due to pre-existing chronic conditions, we compare different guidelines to stratify the population into three risk groups (low-, moderate-, and high-risk), i.e., the European classification by the European Centre for Disease Prevention and Control and national classifications by the public health institutes in individual European countries. We consider several strategies, namely vaccination of high-risk individuals, high- and moderate-risk individuals, individuals above 60 or 80 years old, and combinations of these strategies. I will discuss how best vaccination strategies differ depending on the metrics used for their evaluation: 1) maximum vaccination impact as quantified by the reduction in the number of hospitalizations due to vaccination; 2) maximum vaccination effectiveness as quantified by the number needed to vaccinate to prevent one hospitalization.

Bio: Dr Ganna Rozhnova is an Associate Professor in Infectious Disease Modeling at the University Medical Center Utrecht in the Netherlands. In addition, she holds an appointment as an Invited Associated Professor at the Faculty of Sciences of the University of Lisbon and a principal investigator at the BioISI—Biosystems & Integrative Sciences Institute in Lisbon, Portugal. Her research centers on the application of infectious disease modeling to answer questions and support evidence-based policymaking in public health. She is interested in understanding emergence, evolution and spatio-temporal dynamics of infectious diseases on different scales (e.g., host, hospital/school or population) and evaluating the impact of interventions on disease transmission. Her most recent research aims to address the prospects of HIV elimination, the impact of promising HIV cure strategies on HIV transmission, and (post-)pandemic dynamics of SARS-CoV-2. Other applications include influenza, CMV and childhood infections. More info here: https://www.umcutrecht.nl/en/research/researchers/rozhnova-g

International Hellenic University

Title: Investigating the dynamical behavior on systems with a positive maximal Lyapunov Characteristic Exponent near zero

Abstract: In this talk, we will try to answer the question: ” What is the dynamical behavior when the proposed system has a positive maximal Lyapunov Exponent” near to zero?”. To do so, we investigate many dynamical systems with the help of several numerical tools, such as Poincare sections and chaotic indices (SALI, FLI), and categorize the different dynamical behaviors.

Bio: Jamal-Odysseas Maaita is an Academic Fellow at the International Hellenic University physics department. His research interests are nonlinear dynamics, mechanical and electrical oscillations, dynamical systems theory, bifurcation theory,Hamiltonian mechanics, energy transfer in nonlinear oscillators, nonlinear electronic circuits, chaotic behavior, and Hidden attractors.He is an associate editor at “Discontinuity, Nonlinearity, and Complexity” and a member of the Greek Physicists Society and the Philosophy of Physics Society.

Universities of Colorado and North Carolina, USA

Title: Motion and concentration dynamics of small particles and plankton in fluid flows

Abstract: Advection and distribution of industrial impurities and biological organisms in the ocean and internal waters plays a crucial role in many ecological and biological situations. These processes have been studied for decades, but theoretical modeling of the action of currents and waves on micro-objects is limited. Even the basic equations for a particle motion in an inviscid fluid have been reconsidered several times up to the late 1980s. Here two classes of problems are outlined. The first is the complex dynamics of a particle with inertia in non-viscous fluid flows, studied both analytically and numerically. In general, the equations of such a motion are non-integrable, and we concentrate on the cases of axisymmetric flow (that is completely integrable) and a periodic cellular flow in which unbounded stochastic motions are possible. The second problem is the motion and redistribution of particles and plankton organisms under the action of currents and internal waves in the ocean. Particularly, the effect of solitary internal waves (internal solitons) which are sufficiently short to allow setting aside much slower processes such as diurnal changes of light and temperature, and internal tides. The cases of small Reynolds numbers Re when a passive particle moves with the fluid, and of large Re when its velocity can be smaller or larger than that of fluid, are considered. The dynamic of particles' concentration is also studied. Two models of vertical swimming juxtaposing with the transport by the current are considered. Specific calculations refer to the waves in a two-layer fluid and a stratified layer with a given buoyancy frequency. The results show that a wave affects the particles differently when they are initially distributed homogeneously, and when they occupy a thin layer as is rather common in the upper ocean. These results are in qualitative agreement with the available experimental data.

Bio: Prof. Lev Ostrovsky received a PhD degree and a Doctor of Science degree and the title of Full Professor in the Soviet Union. Until 1994 he was a Laboratory Head and Chief Scientist at the Institute of Applied Physics of Russian Acad., Sci. in Gorky (later Nizhny Novgorod). He also kept a part-time professorship at Gorky/Nizhny Novgorod University. From 1994 to 2016, he worked in the USA as a Senior Scientist at the University of Colorado in Boulder, then at NOAA Environmental Science Research Laboratory in Boulder. Now Lev Ostrovsky is affiliated with Universities of Colorado and North Carolina as Adjunct Professor. He also had numerous visiting positions and fellowships at universities and laboratories in the USA, Britain, France, Australia, Norway, China, and others. The scientific interests of Lev at different stages of his carrier included lasers and nonlinear optics,

biophysics, nonlinear and biomedical acoustics, fluid dynamics and oceanography, and general nonlinear wave theory. He is the author and co-author of 5 books, numerous book chapters and student's workbooks, over 300 papers, 11 Invention Certificates (Russian patents), and a registered Discovery. Under his supervision, 18 students obtained a PhD degree; 12 of them were then awarded the Doctor of Science degree. He has been a plenary and invited speaker and a member of program committees at numerous scientific meetings. Among the Lev's awards are the USSR State Prize, the Mandelstam Award of the Russian Academy of Sciences, Orson Andersen Distinguished Fellowship at Los Alamos National Laboratory, and the Lagrange Award of this Conference. He is a Fellow of the Acoustical Society of America, a member of American and European Geophysical Unions, and Russian Acoustical Society. He has been a Co-Editor of professional journals, including Chaos, Acoustical Physics, Atmospheric and Oceanic Physics, and Discontinuity, Nonlinearity, and Complexity (DNC). At present, he is an Honorary Editor of the journals Chaos and DNC.

Basque Center for Applied Mathematics (BCAM – Bilbao), Spain

Title: Within-host models unravelling the dynamics of dengue reinfections

Abstract: Caused by four serotypes, dengue fever is a major public health concern worldwide. Current modeling efforts have mostly focused on primary and heterologous secondary infections, assuming that lifelong immunity prevents reinfections by the same serotype. However, recent findings challenge this assumption, prompting a reevaluation of dengue immunity dynamics. In this study, we develop a within-host modeling framework to explore different scenarios of dengue infections. Unlike previous studies, we go beyond a deterministic framework, considering individual immunological variability. Both deterministic and stochastic models are calibrated using empirical data on viral load and antibody (IgM and IgG) concentrations for all dengue serotypes, incorporating confidence intervals derived from stochastic realizations. With good agreement between the mean of the stochastic realizations and the mean field solution for each model, our approach not only successfully captures primary and heterologous secondary infection dynamics facilitated by antibody-dependent enhancement (ADE) but also provides, for the first time, insights into homotypic reinfection dynamics. Our study discusses the relevance of homotypic reinfections in dengue transmission at the population level, highlighting potential implications for disease prevention and control strategies [1].

References

[1] Anam, V., Guerrero, B.V, Srivastav A.K., Stollenwerk, N., Aguiar, M. (2024). Within-host models unravelling the dynamics of dengue reinfections. Infectious Disease Modelling, 9(2), 458-473

Bio: Dr Maíra Aguiar is a mathematical epidemiologist working on infectious disease dynamics. With a multidisciplinary research profile, is trained in dynamical systems theory, stochastic processes, nonlinear dynamics, bifurcation analysis and biostatistics and her scientific interests addresses significant mathematical and fundamental questions in biology and medicine, with special focus on public health epidemiology modeling. Dr Aguiar is a former Marie Curie Fellow at Trento University, Italy. Since 2020, Dr. Aguiar is based at the Basque Center for Applied Mathematics (BCAM – Bilbao), Spain, where she leads the Mathematical and Theoretical Biology (MTB) group as an Ikerbasque & Ramon y Cajal Researcher. More info here: https://maira-aguiar.eu

Moscow State University of Civil Engineering, Russia

Title: Mathematical modeling of viscoelastic auxetic materials via fractional calculus

Abstract: In this talk I will examine the impact response of a viscoelastic auxetic plate with fractional viscosity, where the shear operator follows a fractional derivative model. Consequently, the auxetic's Poisson's ratio shifts from negative to positive over time. The mathematical model and numerical calculations based on asymptotic solutions confirm experimental results, showing improved indentation and impact resistance in auxetic materials.

Bio: Dr Marina Shitikova is a Soros Professor and Principal Researcher at the International Center of Dynamics of Solids and Structures at Voronezh State University of Architecture and Civil Engineering in Russia. She received her MEng in Civil Engineering in 1982, a PhD degree in Structural Mechanics in 1987 from Voronezh Civil Engineering Institute, a DSc degree in Solid Mechanics in 1995 from the Institute for Problems in Mechanics, Russian Academy of Sciences and full Professorship in 1995 from Voronezh State University of Architecture and Civil Engineering. Since 1994, she has been an Associate Member of the Acoustical Society of America, since 1995 she has been a Member of the EUROMECH, GAMM, the ASME International, and Russian Association “Women in Science and Education”. She has published more than 200 papers dealing with structural mechanics, vibrations, wave dynamics, acoustics, and fractional calculus viscoelasticity. In 1998 she was awarded the Russian President’s Fellowship for Outstanding Young Doctors of Sciences. She is a grantee of the International Foundation, DFG, DAAD, Fulbright Foundation, and Russian Foundation for Basic Research.

Los Alamos National Laboratory, USA

Title: Modeling Hepatitis Virus Infection in the Liver

Abstract: Mathematical models of viral replication and interactions with the host have been critical in developing a dynamical understanding of viral biology. At the same time, these models represent a paradigm in applying mathematics to medicine. Hepatitis B and hepatitis C viruses both infect the liver, but have very different life cycles. However, the principles of mathematical models and the models themselves are similar and applicable to both viruses. These models have helped us understand and quantify the effects of therapy against these infections, as well as the biology of the viruses. We have been studying infection directly in the liver, using a new technique based on single cell laser capture micro-dissection. This allows us to quantify the levels of infection in hepatocytes, the primary site of replication. The insights brought by these models tell us how fast the virus replicate, the effect on killing infected cells, the virus mutation rate and how to quantify the effect of novel therapies.

Bio: Dr Ruy M. Ribeiro got his Ph.D. in Mathematical Biology at the University of Oxford, UK. He then joined Los Alamos National Laboratory (LANL) in 2000, as a Postdoctoral Researcher, later becoming a staff scientist working on viral and immune system dynamics. His main research interests are the pathogenesis of infections, and the use of quantitative modeling tools to gain insight into viral and immune system dynamics. His work has always entailed close collaborations with experimental researchers to develop proper statistical and dynamic models to analyze experimental data. His modeling work spans multiple scales from the intracellular (eg. a model of the molecular details of HCV infection) to the epidemiological (including HIV and influenza epidemics). He was Professor of Statistics at the Medical School of the University of Lisbon, while on leave from LANL, between 2017 and 2020. Ruy Ribeiro has over 140 peer-reviewed papers in this area, and he is/was the PI of several research projects funded by the National Institutes of Health, the European Union, and the Department of Energy.

University of Pisa, Italy

Title: Weak and Not so weak Mean Field Coupling regime. Invariant Measures, Convergence to Equilibrium, Linear Response

Abstract: We describe a general approach to the theory of self consistent transfer operators. These operators have been introduced as tools for the study of the statistical properties of a large number of all to all interacting dynamical systems subjected to a mean field coupling. We consider a large class of self consistent transfer operators and prove general statements about existence of invariant measures, speed of convergence to equilibrium, statistical stability and linear response. We also consider the problem of finding the optimal coupling between maps in order to change the statistical properties of the system in a prescribed way.

Bio: Stefano Galatolo is Associate Professor at Dipartimento di Matematica, University of Pisa and director of Centro Interdipartimentale per lo Studio dei Sistemi Complessi. His research focuses on dynamical systems, its statistical behavior and computational methods. He is author of about 50 papers in these fields and currently editor of Chaos Solitons and Fractals and Journal of Fixed Point Theory and Applications. More info here: http://users.dma.unipi.it/galatolo/

University of Sevilha, Spain

Title: Approximating the dynamics of a stochastic PDE model by using colored noise

Abstract: The theory of Random Dynamical Systems is nowadays very well developed and provides an appropriate framework to describe the pathwise dynamics of a good number of interesting stochastic PDE models from applied sciences. The main idea is to transform the stochastic problem into a random one by performing some kind of transformation (also called conjugation) which allows us to use the deterministic techniques to analyze the long time behavior of the system. However, when the noise term in the stochastic model is not linear, such conjugation is not known yet when we are dealing with a stochastic partial differential equation. Recently, a new technique is being used to approximate the stochastic problem. The idea consists in replacing the standard white noise (usually the generalized derivative of a Wiener process) but the so-called colored noise, which is a stationary stochastic process (generally an Ornstein-Uhlenbeck process) and strongly related to the Wong-Zakai approximation to the white noise. In this talk, we will analyze a problem driven by colored noise and explain the advantages of Wong-Zakai approximations, and the limitations of this alternative as well.

Bio: Dr Tomás Caraballo is Professor at the Departamento de Ecuaciones Diferenciales y Análisis Numérico of the University of Sevilla, Spain. Professor Caraballo received his Ph.D. in Mathematical Sciences from the University of Sevilla in November 1998. His research interests include deterministic and stochastic dynamical systems and applications from the applied sciences. More specifically, he was worked on stochastic partial differential equations, models with delay and memory, impulsive systems, non-autonomous and random dynamical systems, nonlocal differential equations including those of fractional time, models from biology, epidemiology, physics, population dynamics, etc He has published more than 350 papers so far, which can be seen in the web. Link: https://personal.us.es/caraball/tcgpublic.html

“Aurel Vlaicu” University of Arad, Romania

Bio: Dr Valentina E. Balas is currently Full Professor in the Department of Automatics and Applied Software at the Faculty of Engineering, “Aurel Vlaicu” University of Arad, Romania. She holds a Ph.D. Cum Laude, in Applied Electronics and Telecommunications from Polytechnic University of Timisoara. Dr. Balas is author of more than 400 research papers in refereed journals and International Conferences. Her research interests are in Intelligent Systems, Fuzzy Control, Soft Computing, Smart Sensors, Information Fusion, Modeling and Simulation. She is the Editor-in Chief to International Journal of Advanced Intelligence Paradigms (IJAIP) and to International Journal of Computational Systems Engineering (IJCSysE), member in Editorial Board member of several national and international journals and is evaluator expert for national, international projects and PhD Thesis. Dr. Balas is the Head of Intelligent Systems Research Centre in Aurel Vlaicu University of Arad and Head of the Department of International Relations in the same university. She served as General Chair of the International Workshop Soft Computing and Applications (SOFA) in ten editions organized in the interval 2005-2022 and held in Romania and Hungary. Dr. Balas participated in many international conferences as Organizer, Honorary Chair, Session Chair, member in Steering, Advisory or International Program Committees and Keynote Speaker. Recently she was working in a national project with EU funding support: BioCell-NanoART = Novel Bio-inspired Cellular Nano-Architectures – For Digital Integrated Circuits, 3M Euro from National Authority for Scientific Research and Innovation. She is a member of European Society for Fuzzy Logic and Technology (EUSFLAT), member of Society for Industrial and Applied Mathematics (SIAM) and a Senior Member IEEE, member in Technical Committee – Fuzzy Systems (IEEE Computational Intelligence Society), chair of the Task Force 14 in Technical Committee – Emergent Technologies (IEEE CIS), member in Technical Committee – Soft Computing (IEEE SMCS). She is member in the Committee of IEEE Romania Section as Volunteers Training Coordinator and vice chair of IEEE Computational Intelligence Society Chapter – CIS 11. During the interval 2021-2022 she was a member of IEEE European Public Policy Committee Working Group on ICT. From May 2023 Dr. Balas is associate member of Romanian Academy of Scientists. Dr. Balas was past Vice President (awards) of IFSA – International Fuzzy Systems Association Council (2013-2015), is a Joint Secretary of the Governing Council of Forum for Interdisciplinary Mathematics (FIM), – A Multidisciplinary Academic Body, India. She is the recipient of the “Tudor Tanasescu” Prize from the Romanian Academy for contributions in the field of soft computing methods (2019) and “Stefan Odobleja” Prize from Romanian Academy of Scientists (2023).

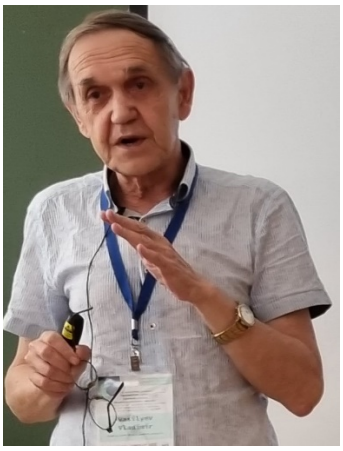

Belgorod State University, Russia

Title: Basic Problems in the Theory of Pseudo-Differential Equations

Abstract: A solvability problem for elliptic pseudo-differential equations in domains with a non-smooth boundary is studied. Digitization problem for these equations and certain problems related to a limit transform with a small parameter are considered also.

Bio: Professor Vladimir Vasilyev is Chair of Differential Equations, at Belgorod National Research University. More information: https://scholar.google.ru/citations?hl=en&user=NfV8TwkAAAAJ&view_op=list_works&sortby=pubdate and https://www.researchgate.net/profile/Vladimir-Vasilyev-2

Table of contents

International Conference on Mathematical Analysis and Applications in Science and Engineering ICMA²SC'24

ISEP **Porto-Portugal, June 20 - 22, 2024**

MATHEMATICAL MODELLING OF VECTOR-BORNE DISEASES

Urszula Skwara

Faculty of Mathematics, Informatics and Mechanics of the University of Warsaw, Poland

urszulaskwara@mimuw.edu.pl

Vector-borne diseases account for approximately 17% of all infectious diseases in the world and they cause about 700 000 deaths each year. Vector-borne diseases are transmitted by vectors including mosquitoes, ticks, and fleas. In our work we mainly focus on diseases transmitted by mosquitoes like dengue, zika and chikungunya. We extend a classical SISUV model [4] to a fractional-order system given by fractional-order differential equations [1]. This type of model better characterizes the virus transmission process as it involves memory and hereditary properties. We also consider a fractional version of SIRUV model [3]. We investigate asymptotic stability for both models and perform numerical simulations.

References

[1] Skwara U., Mozyrska D., Aguiar M., Stollenwerk N. , Dynamics of vector-borne diseases through the lens of systems incorporating fractional-order derivatives , *Chaos, Solitons and Fractals: the interdisciplinary journal of Nonlinear Science, and Nonequilibrium and Complex Phenomena* Volume 181, 2024, DOI: 10.1016/j.chaos.2024.114643

[2] Matigon D. Stability Results For Fractional Differential Equations With Applications To Control Processing *Compput Eng Syst Appl*, Vol.2, Citeseer, 1996, pp 963–968

[3] Rocha, F., Aguiar M, Souza M., Stollenwerk N. Time-scale separation and centre manifold analysis describing vector-borne disease dynamics, *International Journal of Computer Mathematics* , 2013, pp. 2105–2125, https://doi.org/10.1080/00207160.2013.783208

[4] Rocha, F., Mateus L., Skwara U. Aguiar M., Stollenwerk N., Understanding dengue fever dynamics: a study of seasonality in vector-borne disease models, *International Journal of Computer Mathematics* 2015, pp. 14051422 , https://doi.org/10.1080/00207160.2015.1050961

[5] WHO. www.who.int/news-room/fact-sheets/detail/vector-borne-diseases

International Conference on Mathematical Analysis and Applications in Science and Engineering ICMA²SC'24

ISEP **Porto-Portugal, June 20 - 22, 2024**

TARGETED CONTROL OF COVID-19 POST-MASS VACCINATION

Ilse Westerhof[1] **Annemarijn de Boer**[1] **Angela Lupattelli**[2]

Otilia Boldea[3] **Hedvig Marie Egeland Nordeng**[2] **Patricia Bruijning**[1]

Ganna Rozhnova[1,4,5,6*]

[1] Julius Centre for Health Sciences and Primary Care, University Medical Centre Utrecht, Utrecht University, Utrecht, The Netherlands

[2] Department of Pharmacy, University of Oslo, Oslo, Norway

[3] Department of Econometrics and OR, Tilburg School of Economics and Management, Tilburg University, Tilburg, The Netherlands

[4] Center for Complex Systems Studies (CCSS), Utrecht University, Utrecht, The Netherlands

[5] BioISI—Biosystems & Integrative Sciences Institute, Faculdade de Ciências, University of Lisbon, Lisbon, Portugal

[6] Faculdade de Ciências, University of Lisbon, Lisbon, Portugal

[1*]g.rozhnova@umcutrecht.nl

Abstract: SARS-CoV-2 infection currently causes common cold- or flu-like illness in most individuals, but patients with chronic conditions still experience a higher chance of COVID-19 hospitalization and death. It is crucial to estimate COVID-19 burden in chronic patients and to determine how best to protect them from severe COVID-19. In this talk, I will present an assessment of the impact of post-pandemic vaccination strategies in chronic patients of different ages. The model population is stratified by age, risk due to chronic conditions, and immunity level before the start of a seasonal post-pandemic outbreak. For risk classification due to pre-existing chronic conditions, we compare different guidelines to stratify the population into three risk groups (low-, moderate-, and high-risk), i.e., the European classification by the European Centre for Disease Prevention and Control and national classifications by the public health institutes in individual European countries. We consider several strategies, namely vaccination of high-risk individuals, high- and moderate-risk individuals, individuals above 60 or 80 years old, and combinations of these strategies. I will discuss how best vaccination strategies differ depending on the metrics used for their evaluation: 1) maximum vaccination impact as quantified by the reduction in the number of hospitalizations due to vaccination; 2) maximum vaccination effectiveness as quantified by the number needed to vaccinate to prevent one hospitalization.

keywords: infection dynamics; vaccination;

Acknowledgments

GR was supported by Fundação para a Ciência e a Tecnologia project 2022.01448.PTDC, DOI 10.54499/2022.01448.PTDC. This work was also supported by UIDB/04046/ 2020 (DOI: 10.54499/UIDB/04046/2020) and UIDP/04046/2020 (DOI: 10.54499/UIDP/04046/2020) Centre grants from the Fundação para a Ciência e a Tecnologia, Portugal (to BioISI). GR, IW, AdB, AL, OB, JB, FP, MSvdL, MK, and JvdW were supported by ZonMw project (10430362220002). GR, IW, AL, and PB were supported by the VERDI project (101045989), funded by the European Union. Views and opinions expressed are however those of the author(s) only and do not necessarily reflect those of the European Union or the Health and Digital Executive Agency. Neither the European Union nor the granting authority can be held responsible for them.

Mathematical modeling of IL-6 driven T lymphocyte cross-talk in the disease course and treatment of rheumatoid arthritis

Zviad Kalichava[1*] Kakhaber Odisharia[2] Vladimer Odisharia[2] Nona Janikashvili[3]

[1] N. Muskhelishvili Institute of Computational Mathematics, Tbilisi, Georgia
[2] Iv. Javakhishvili Tbilisi State University, Tbilisi, Georgia
[3] Tbilisi State Medical University, Tbilisi, Georgia
[1*] zviadi.kalichava@gmail.com

Abstract: Mathematical models of immune mediated disorders provide an analytic platform in which we can address specific questions concerning disease immune dynamics to dictate the choice of treatment. Rheumatoid arthritis is a systemic autoimmune disease characterized by the joint inflammation and the cartilage destruction. Autoreactive B lymphocytes represent the integral elements of the pathophysiology of rheumatoid arthritis. Immune balance between the effector and the regulatory T cell subsets guide the autoreactive B cell fate and play a cardinal role in disease severity. Using non-linear differential equations, we developed a novel mathematical model that describes the immunopathogenesis of rheumatoid arthritis [1, 2]. The model explores the functional dynamics of cartilage destruction during disease progression, in which a system of differential equations deciphers the interactions between autoreactive B lymphocytes and T helper cells. As the further task, we present here the refined model of the disease course in which the immunomodulatory effect of IL-6, - a molecule that drives the cross-talk of pro-inflammatory and regulatory subsets of T lymphocytes, is explained. IL-6 targeting is also taken into consideration in the disease treatment model, in which the modalities of treatment with methotrexate and tocilizumab in a separate or combined scheme are addressed. For such treatment model, the corresponding Cauchy problem is posed and its solution is found. In conclusion, we propose a novel mathematical model that best describes the readouts of the course and treatment outcomes of rheumatoid arthritis and, therefore, may take a rapid pace towards its implementation in biomedical and clinical research.

Keywords: non-linear differential equations, mathematical model, rheumatoid arthritis.

References:

[1] Odisharia K., Odisharia V., Tsereteli P., Janikashvili N. On the Mathematical Model of Drug Treatment of Rheumatoid Arthritis. Springer International Publishing, Mathematics, Informatics, and their Applications in Natural Sciences and Engineering, 10(2019),161-168.

[2] Tsereteli P., Odisharia V., Janikashvili N. Mathematical modeling of rheumatoid arthritis and its treatment. Computer Sciences and Telecomunications, 1(61)(2022),19-31.

International Conference on Mathematical Analysis and Applications in Science and Engineering
ICMA^{2}SC'24
ISEP Porto-Portugal, June 20 - 22, 2024

Mathematical modeling of high grade gliomas: Investigating the impact of hypoxic events on tumor growth dynamics through Lie symmetries

M.L. Gandarias[1⋆] M. Rosa[1,2] S. Chulián[1,2] A. Niño-López[1,2] Á. Martínez-Rubio[1,2]

[1] Departament of Mathematics, University of Cádiz, Cádiz,Spain
[2] Biomedical Research and Innovation Institute of Cádiz (INiBICA), Cádiz, Spain

[1⋆]marialuz.gandarias@uca.es

Abstract: We discuss the development and analysis of mathematical models for understanding the growth dynamics of high-grade gliomas, a type of deadly brain tumor. The models focus on the interplay between different cellular phenotypes, particularly in response to hypoxic (low oxygen) conditions. The study explores how hypoxic events may accelerate tumor growth and considers various scenarios of cellular behavior, aiming to provide insights into potential treatment strategies. The research uses mathematical techniques, including differential equations and symmetries, to derive exact analytical solutions and simulate different biological scenarios.

keywords: Lie symmetries; ordinary differential equations; gliomas.

MSC2020: 35Q92, 35K57, 92-08.

The authors are submitting this abstract to the Special Session number 10: Symmetries and Conservation Laws for Nonlinear Partial Differential Equations with Applications.

1 Introduction

Malignant gliomas are the most frequent and deadly type of brain tumors. Over the last years, complex mathematical models of cancerous growths have been developed increasingly, especially on solid tumors, in which growth primarily comes from cellular proliferation. High-grade gliomas are tumors of the glial cells, which are found in the brain and spinal cord. They are called *high-grade* because these tumors are fast-growing and they spread quickly through brain tissue, which makes them hard to treat. Median survival is generally less than one year from the time of diagnosis, and even in the most favorable situations, most patients die within two years [1].

Mathematical modeling is a powerful tool for analyzing biological problems. These models have the potential of becoming useful against cancer in three different ways: in personalized medicine, accessing unreachable scales and formulating novel hypothesis.

2 Results and discussion

In [2], the authors considered a reduced continuous model describing the evolution of high grade gliomas in response to hypoxic events through the interplay of different cellular phenotypes. This model was studied in order to show how hypoxic events may have a role on the acceleration of the growth speed of high grade gliomas. The authors considered two cellular phenotypes to describe this model: One of them is more migratory and a second one is more proliferative. Therefore, $u(t,x)$ denoted a proliferative (or normoxic) phenotype and $v(t,x)$ denoted a migratory (or hypoxic) phenotype. The authors assumed that the model is based on a pair of coupled Fisher-Kolmogorov equations (or diffusive Lotka-Volterra equations), including a coupling term accounting for the decay of hypoxic cells into the normoxic phenotype [2].

In this paper, the model considered has been generalized in the following manner: Here $u(t,x,y,z)$ denotes a proliferative (or normoxic) phenotype, and $v(t,x,y,z)$ denotes a migratory (or hypoxic) phenotype, where the force driving phenotype changes is the local oxygen pressure. We considered the independent variables t as the time and x,y,z as the 3-dimensional space. This model is based on a pair of diffusive Lotka-Volterra equations [3, 4, 5]), but including a coupling term accounting for the decay of hypoxic cells into the normoxic phenotype [2]. The generalized model is described by the equations

$$\begin{cases} F_1 \equiv u_t - d_1(u_{xx}+u_{yy}+u_{zz}) - \rho_1(1-u-v)u - g(v) = 0, \\ F_2 \equiv v_t - d_2(v_{xx}+v_{yy}+v_{zz}) - \rho_2(1-u-v)v + g(v) = 0, \end{cases} \tag{1}$$

where d_1 and d_2 are the diffusion coefficients for the proliferative and migratory phenotypes. These parameters satisfy $d_2 > d_1$, and ρ_1, ρ_2 are the proliferation rates for both phenotypes with $\rho_1 > \rho_2$. System 1 is then a generalization of the system considered in [2]. The function $g(v)$ corresponds to the migratory phenotype switch, changing from the proliferative type to a hypoxic one, where there is a lack of oxygen.

3 Conclusions and Future work

The search for exact solutions to nonlinear PDEs plays a fundamental role in the analysis of nonlinear physical phenomena. One of the most famous and established procedures for obtaining exact solutions of differential equations is the classical Lie method.

In this work, taking into account the classical symmetries admitted by the system [6, 7] we use the transformations groups to reduce the equations to ordinary differential equations. Then the work is focused on exact analytical solutions that present several relevant applications in the field of mathematical biology. Due to the interest in the phenotypic switch in normoxic and hypoxic cells [2], we focus on the simulation of such scenarios. In our case, we consider a linear and quadratic phenotypic switch and a limited decrease of hypoxic cells to track the interpretability of the parameters used.

Acknowledgments

The support of Junta de Andalucía group FQM-201 is gratefully acknowledged.

References

[1] Stupp, R., Mason, W. P., Van Den Bent, M. J., Weller, M., Fisher, B., Taphoorn, M. J., & Mirimanoff, R. O. Radiotherapy plus concomitant and adjuvant temozolomide for glioblastoma. New England journal of medicine, **352**(10) (2005), 987–996.

[2] Pardo, R., Martínez-González, A., Pérez-García, V. M. Nonlinear ghost waves accelerate the progression of high-grade brain tumors. Communications in Nonlinear Science and Numerical Simulation, **39** (2016), 360–380.

[3] Lotka AJ. Elements of Physical Biology. Williams and Wilkins, Baltimore, 1925.

[4] Volterra V. Variazioni e fluttuazioni del numero d'individui in specie animali conviventi. Memoria della Reale Accademia Nazionale dei Lincei 1926; 2:31-113.

[5] Hastings, A. Global stability in Lotka-Volterra systems with diffusion. Journal of Mathematical Biology 1978; 6:163-168

[6] Cherniha R & King JR. Lie symmetries of nonlinear multidimensional reaction-diffusion systems: I. Journal of Physics A: Mathematical and General 2000;33:267-282.

[7] Cherniha R, & King JR. Lie symmetries of nonlinear multidimensional reaction-diffusion systems: II. Journal of Physics A: Mathematical and General 2003;36:405-425.

[8] Ibragimov NH & Ibragimov NK. Elementary Lie Group Analysis and Ordinary Differential Equations. New York: Wiley;1999.

[9] Anco SC, Gandarias ML and Recio E. Conservation Laws, Symmetries, and Line Soliton Solutions of Generalized KP and Boussinesq Equations with p-Power Nonlinearities in Two Dimensions. Theoretical and Mathematical Physics 2018; 197:1393-1411.

[10] Olver P.J., Applications of Lie Groups to Differential Equations. Springer, Berlin, 1986.

International Conference on Mathematical Analysis and Applications in Science and Engineering
ICMA^{2}SC'24
ISEP Porto-Portugal, June 20 - 22, 2024

A MATHEMATICAL MODEL OF ACUTE LYMPHOBLASTIC LEUKEMIA DEVELOPMENT AND A FIRST PHASE OF TREATMENT

Ana Niño-López[1,2⋆] **Álvaro Martínez-Rubio**[1,2] **Salvador Chulián**[1,2]
Rocío Picón-González[1,2] **María Rosa**[1,2]

[1] Cádiz University , Spain
[2] Biomedical Research and Innovation Institute of Cadiz (INiBICA), Hospital Universitario Puerta del Mar, Cádiz, Spain

⋆ana.nino@uca.es

Abstract: At present, childhood leukemia patients survival accounts for the 80% of cases. This means that 20% of treatments are unsuccessful, therefore, it is definitely required to determinate different strategies to analyse patients data. Thus the importance to monitor the amount of leukemic cells to predict relapses in the first treatment phase. In this work we present results from our recently published article where a model of cells dynamics in bone marrow is proposed, taking into account the effect of the treatment. This model allows to observe how the risk of relapse is connected with some values in bone marrow in the first treatment phase. Furthermore, several parameters are related to treatment dynamics, therefore proposing a basis for future works regarding childhood ALL survival improvement.

keywords: Mathematical model; Leukemia; Cancer Treatment

MSC2020: 34A12; 92B05.

The authors are submitting this abstract to the Special Session number 10: Symmetries and Conservation Laws for Nonlinear Partial Differential Equations with Applications.

1 Introduction

Leukemia is a cancer originating in the bone marrow. Particularly, it arises from a disruption in hematopoiesis, the process in charge of blood cells production [5]. Depending on the affected cell, there are different types of leukemia. Acute Lymphoblastic Leukemia (ALL) is caused by cells with fast growth in the lymphoid branch, with special incidence in pediatric patients [6, 7].

Each type and subtype of leukemia has an associated protocol that specifies the therapeutic recommendations, and that varies from country to country [2]. In particular, SEHOP-PETHEMA-2013 protocol is used in Spain to treat pediatric patients with ALL. At present, mathematical models provide a wide variety of applications in medicine. Mathematical oncology is considered useful to understand and approach cells behavior. These works allow to study the healthy cells

development in bone marrow [3, 1] and simulate the appearance of a leukemic cell and its proliferation.

In this work, we focus on the simulation of leukemic cells dynamics when treatment is administered. In terms of mathematical analysis, we study how treatment affects to both leukemic and healthy cells develop. This will allow us to propose future works related to classify patients with higher risk of relapse and improve their treatments.

2 A mathematical model of treatment influence in a leukemic bone marrow

We base our study on previous works which presented mathematical models about the lymphoid branch dynamics cells [1], and other models about immunotherapy which described bone marrow behaviour [4] in other situations.

We present three cells populations depending on their maturation states: Pro-B (C_1), Pre-B (C_2) and Transition cells (C_3), and we included a Leukemic compartment (L):

$$\frac{dC_1}{dt} = c_0 + s\rho_1 C_1 - \alpha_1 C_1, \tag{1a}$$

$$\frac{dC_2}{dt} = s\rho_2 C_2 + \alpha_1 C_1 - \alpha_2 C_2, \tag{1b}$$

$$\frac{dC_3}{dt} = \alpha_2 C_2 - \alpha_3 C_3, \tag{1c}$$

$$\frac{dL}{dt} = s_L \rho_L L \left(1 - \frac{L}{L_{\max}}\right) - \gamma_L L. \tag{1d}$$

where ρ_1 and ρ_2 are the proliferation rates and α_1, α_2 and α_3 are transition rates. Depending on the stage where leukemia originates, $\rho_L = \rho_1$ if the first leukemic cell belongs to Pro-B compartment and if leukemia appears in Pre-B stage, $\rho_L = \rho_2$. Healthy cells are influenced by the total amount of cells in bone marrow while leukemic cells do not control their own proliferation, in consequence, signal is only generated by healthy cells. Being

$$s = \frac{1}{1 + k\left(L + \sum_{i=1}^{3} C_i\right)}, \qquad s_L = \frac{1}{1 + k\sum_{i=1}^{3} C_i}. \tag{2}$$

Now we model the treatment schedule from SEHOP-PETHEMA protocol, using in Spain for Standard Risk Patient, Figure 1.

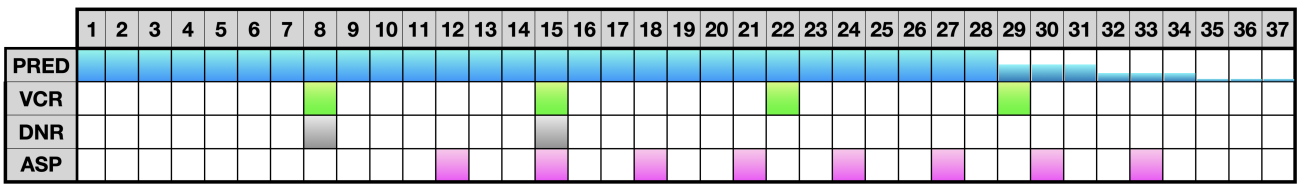

Figure 1: **Schedule for Induction I'A treatment for a Standard Risk Patient.** Data from SEHOP-PETHEMA protocol: Prednisone (PRED) is administered at $60mg/m^2/day$ for the first 28 days. Then, the dose is reduced. Vincristine (VCR): $1.5mg/day$ on days $8, 15, 22$ and 29. Daunorubicine (DNR): $30mg/m^2/day$ on days 8 and 15. Asparaginase (ASP): $10000U/m^2/day$ on days $12, 15, 18, 21, 24, 27, 30$ and 33.

We consider the treatment $\mu_j(t) = \mu_j$ as a function that describes the amount of drug j in the bone marrow at time t: Prednisone (μ_P), Vincristine (μ_V), Daunorubicin (μ_D) and Asparaginase (μ_A). Once the dose is administered, the drug has an exponential decrease associated with that medicine half-life. We then define $\mu_j : \mathbb{R}^+ \to \mathbb{R}^+$ as

$$\frac{d\mu_j}{dt} = -\lambda_j \mu_j, \tag{3}$$

with λ_j related to each drug j half-life τ_j measured in days $\lambda_j = \dfrac{\log(2)}{\tau_j}$.

Each drug j has a different dose q_j in several days $\mathcal{D}_j \subset \mathbb{N}$, as shown in Figure 1. We define the dose administered as $Q_j(t)$. We finally consider the total treatment function μ, as the weighted sum of all drugs with the weight δ_j which indicates the influence of drug j on the total effect of the treatment.

We obtain he mathematical model of treatment influence:

$$\frac{dC_1}{dt} = c_0 + s\rho_1 C_1 - \alpha_1 C_1 - \mu\rho_1 C_1, \tag{4a}$$

$$\frac{dC_2}{dt} = s\rho_2 C_2 + \alpha_1 C_1 - \alpha_2 C_2 - \mu\rho_2 C_2, \tag{4b}$$

$$\frac{dC_3}{dt} = \alpha_2 C_2 - \alpha_3 C_3, \tag{4c}$$

$$\frac{dL}{dt} = s_L \rho_L L \left(1 - \frac{L}{L_{\max}}\right) - \gamma_L L - \mu\rho_L L, \tag{4d}$$

$$\mu = \sum_{j \in J} \delta_j \left(\mu_j + Q_j\right), \tag{4e}$$

$$Q_j = \begin{cases} q_j & t \in \mathcal{D}_j, \\ \\ 0 & t \notin \mathcal{D}_j, \end{cases}, \tag{4f}$$

$$\frac{d\mu_j}{dt} = -\lambda_j \mu_j(t). \tag{4g}$$

3 Conclusions and Future work

Leukemia is the most frequently type of cancer in pediatric age. Even if its survival rate has increased in the recent years, about $15 - 20\%$ of treatments are unsuccessful, and patients relapse. For this reason, an analysis of leukemic cells behavior and its treatment. Our goal is to find patterns in bone marrow with drugs applied at the early stage of the disease. With this, it could be possible to predict relapses and improve current treatments.

We have reviewed a healthy bone marrow model, and included the assumption of the appearance of a leukemic cell. The Model (1) replicates the leukemic population growth. On the other hand, from the information collected in the SEHOP-PETHEMA-2013 protocol, we model the treatment behavior in the bone marrow when it is administered. A theoretical model of the bone marrow dynamics, Model (4), is presented to study, based on previous works along with new assumptions about leukemic cells behaviour and treatment.

In order to study parameters related to prednisone and vincristine, we have simulated Model (4) for different values of these parameters and a classifier have obtained.

Acknowledgments

This work has been partially supported by the Fundacióon Española para la Ciencia y la Tecnología (FECYT and University of CÃ¡diz, project UCA-PR214, Spain), the Asociación Pablo Ugarte (APU, Spain) and Junta de Andalucía (Spain) group FQM-201. This work was also funded by the Ministry of Science from Spain (grant number PID2022-140451OA-I00, project MATHPOH, Spain).

References

[1] Salvador Chulián, Alvaro Martínez-Rubio, Anna Marciniak-Czochra, Thomas Stiehl, Cristina Blázquez Goñi, Juan Francisco Rodríguez Gutiérrez, Manuel Ramirez Orellana, Ana Castillo Robleda, Víctor M. Pérez-García, and María Rosa. Dynamical properties of feedback signalling in b lymphopoiesis: A mathematical modelling approach. *Journal of Theoretical Biology*, 522:110685, 2021.

[2] Rachel A Egler, Sanjay P Ahuja, and Yousif Matloub. L-asparaginase in the treatment of patients with acute lymphoblastic leukemia. *Journal of pharmacology & pharmacotherapeutics*, 7(2):62, 2016.

[3] Anna Marciniak-Czochra, Thomas Stiehl, Anthony D. Ho, Willi Jäger, and Wolfgang Wagner. Modeling of asymmetric cell division in hematopoietic stem cells regulation of self-renewal is essential for efficient repopulation. *Stem cells and development*, 18(3):377–386, 2009.

[4] Álvaro Martínez-Rubio, Salvador Chulián, Cristina Blázquez Goñi, Manuel Ramírez Orellana, Antonio Pérez Martínez, Alfonso Navarro-Zapata, Cristina Ferreras, Victor M Pérez-García, and María Rosa. A mathematical description of the bone marrow dynamics during CAR T-cell therapy in B-cell childhood acute lymphoblastic leukemia. *International Journal of Molecular Sciences*, 22(12):6371, 2021.

[5] Stuart H. Orkin and Leonard I. Zon. Hematopoiesis: an evolving paradigm for stem cell biology. *Cell*, 132(4):631–644, 2008.

[6] Ching-Hon Pui, Dario Campana, and William E. Evans. Childhood acute lymphoblastic leukaemia–current status and future perspectives. *The lancet oncology*, 2(10):597–607, 2001.

[7] Ching-Hon Pui, Leslie L. Robison, and A. Thomas Look. Acute lymphoblastic leukaemia. *The Lancet*, (9617), 2008.

International Conference on Mathematical Analysis and Applications in Science and Engineering
ICMA^{2}SC'24
ISEP Porto-Portugal, June 20 - 22, 2024

Exponentially Varied Diffusivity with Gompertz Dynamics for Modeling Tumor Cells Proliferation

Jose Luis Diaz Palencia[1,2⋆]

[1] Department of Mathematics and its Education
Universidad a Distancia de Madrid, 28400 Madrid, Spain.
[2] Department of Information Technology, Escuela Politecnica Superior, Universidad San Pablo-CEU, CEU Universities, Campus Monteprincipe, Boadilla del Monte, Madrid 28668, Spain.

[1,2⋆]joseluis.diaz.p@udima.es or jose.diazpalencia@ceu.es

Abstract: This study involves using reaction-diffusion mathematical models, particularly the Gompertz dynamics along with spatially varied diffusivity, to analyze tumor cell behavior at different stages. It also examines the stability and uniqueness of solutions in weighted Sobolev spaces and explores solutions like travelling waves (dispersive and non-dispersive) and similarity solutions. When possible, these solutions have been validated with experimental tumor growth data.

keywords: Tumor Growth; Gompertz Model; Heterogeneous Diffusivity; Stability Analytis; Travelling Waves; Similarity Solutions

MSC2020: 35B35; 35C06; 35C07

1 Introduction

Reaction-diffusion models are important for predicting the spatiotemporal progression of tumors. A vital component of these models is the precise representation of cancer cell proliferation, a characteristic distinguishing cancer cells from normal ones. Traditional exponential growth models for cell proliferation are found inadequate for describing cancer progression beyond initial stages. More advanced models like Gompertzian and logistic growth, which include the concept of "carrying capacity" (the maximum sustainable cell population), provide better accuracy due to their additional adjustable parameters (for further details, see [1] and [2]). The form of the Gompertz growth is generally given as $R(u) = ru \ln\left(\frac{K}{u}\right)$, where r is the maximum growth rate of the tumor cells, K is the carrying capacity of the environment and u the cells population. In addition, it is very relevant to model the spread of tumor cell through adequate diffusivity mechanisms that consider the particular microenvionments (see [3]), and this shall be based in experimental data as provided in [4] (and particularly the modelling of normoxic cells which are those with an advanced capacity for proliferation given their adequate levels of oxygen). Considering the Grades 2 and 3 of glioma (Figure 2 of [4]) we propose a diffusivity of the form: $D_i(x) = d_i \exp(-\lambda_i x)$, where $i = 2, 3$ represent the Grades 2 and 3, d_i represents the diffusivity at the tumor center, and λ_i is the decay rate. For Grade 4 of glioma (Figure 2 of [4]) the proposed diffusivity is assessed as $D_4(x) = g_4 \exp(-\gamma(x - x_0)^2)$, where $\exp(-\gamma(x - x_0)^2)$ adds a Gaussian peak at x_0 to model increased diffusivity and g_4, γ, x_0 are parameters.

Based on the these principles, we consider a PDE of the form

$$\frac{\partial u}{\partial t} = \nabla \cdot (D_j(x)\nabla u) + R(u), \tag{1}$$

where $j = 2, 3, 4$ for each Grade of tumor, $u(x,t)$ represents the normoxic tumor cell density at position $x \in \Omega \subset \mathbb{R}^d$, $d = 2, 3$ and time $t \in (0, T)$. The initial distribution of normoxic tumor cells is $u(x,0) = u_0(x) \in L^2(\Omega)$, where Ω represents the spatial domain of the organic tissue. We consider Neumann boundary conditions $\frac{\partial u}{\partial \mathbf{n}}\Big|_{\partial\Omega} = 0$, where $\mathbf{n}$ is the outward normal vector on the smooth boundary $\partial\Omega$. To accommodate these spatial variations in the diffusivity within a functional framework, we employ a weighted Sobolev space $W^{k,p}_\omega(\Omega)$ with weight $\omega(x) = \exp(\gamma(x - x_0)^2)$, so that the weighted Sobolev space is $W^{k,p}_\omega(\Omega) = \left\{u \in L^p_\omega(\Omega) : \frac{\partial^\alpha u}{\partial x^\alpha} \in L^p_\omega(\Omega), \forall |\alpha| \le k\right\}$, where α is a multi-index representing the order of derivatives. For Eq. (1), we set $k = 2$ for second-order spatial derivatives in the diffusivity terms and $p = 2$ for the L^2-space, leading to the space $W^{2,2}_\omega(\Omega)$. This space is apt for formulating weak solutions to Eq. (1) and captures the non-uniform tumor microenvironment through spatially varying diffusivity for different tumor grades.

2 Results and discussion

Theorem: *(Uniqueness of Weak Solution) Consider the reaction-diffusion equation in a bounded domain Ω given by*

$$\int_\Omega \frac{\partial u}{\partial t}\phi \, dx = -\int_\Omega D(x)\nabla u \cdot \nabla \phi \, dx + \int_\Omega R(u)\phi \, dx \quad \forall \phi \in W^{k,p}_\omega(\Omega), \tag{2}$$

where $D(x)$ is the diffusivity function satisfying $0 < D_{min} \le D(x) \le D_{max} < \infty$ for $x \in \Omega$ (note that we omit the sub-index j in D_j for simplicity), and $R(u) = ru\ln\left(\frac{K}{u}\right)$ is the reaction term. Then, there exists a unique weak solution $u \in W^{k,p}_\omega(\Omega)$.

To introduce a short version of the proof, we establish the boundedness and coercivity of the bilinear form associated with the diffusion term and the Lipschitz continuity of the nonlinear term $R(u)$. The bilinear form is $B(u,\phi) = \int_\Omega D(x)\nabla u \cdot \nabla \phi \, dx$, for $u, \phi \in W^{k,p}_\omega(\Omega)$. We assume that $D(x)$ is bounded above in Ω by a constant $D_{\max}$. Then $|B(u,\phi)| \le D_{\max}\|\nabla u\|_{L^2(\Omega)}\|\nabla\phi\|_{L^2(\Omega)}$, where this last term follows from the Cauchy-Schwarz inequality. To establish coercivity, we assume that $D(x)$ is bounded below by a positive constant $D_{\min}$: $B(u,u) \ge D_{\min}\int_\Omega |\nabla u|^2 \, dx = D_{\min}\|\nabla u\|^2_{L^2(\Omega)}$. The nonlinear term $R(u) = ru\ln\left(\frac{K}{u}\right)$ satisfies Lipschitz continuity: Let M be the upper bound of $|R'(u)|$ on a compact subset of Ω. Then, by the mean value theorem for all $u, v \in W^{k,p}_\omega(\Omega)$ and for almost every $x \in \Omega$, there exists ξ between $u(x)$ and $v(x)$ such that: $|R(u(x)) - R(v(x))| = |R'(\xi)||u(x) - v(x)| \le M|u(x) - v(x)|$. Although, we have provided some results concerning the L^2 space, recovering the space $W^{k,p}_\omega(\Omega)$ follows from the application of Sobolev embedding theorems (refer to [5, 6]). By the application of the Lax-Milgram theorem, we conclude that there exists a unique $u \in W^{k,p}_\omega(\Omega)$ satisfying the weak formulation. The time weak continuity follows simply by considering the expression $\lim_{h\to 0}\int_\Omega \frac{u(t+h)-u(t)}{h}\phi(t)\,dt + \int_\Omega u(t)\frac{\partial\phi}{\partial t}(t)\,dt = 0$.

Now, we focus on the stability of solutions and the effectiveness of clinical treatments. For this, consider the concentration of stationary cells in a tumor, denoted as u_s that can resist to therapies in time. A steady-state solution is given by $0 = \nabla \cdot (D(x)\nabla u) + ru\ln\left(\frac{K}{u}\right)$, with Neumann boundary condition. Consider a small perturbation around the steady-state solution denoted by $\epsilon\eta(x,t)$, where ϵ is a small parameter and $\eta(x,t)$ is the perturbation. Then $u(x,t) = u_s(x) + \epsilon\eta(x,t)$. Substitute the perturbed solution and linearize around $u_s(x)$ neglecting higher-order terms of ϵ to have: $\nabla \cdot (D(x)\nabla\epsilon\eta)$. The reaction term linearizes using a first-order Taylor

expansion: $ru_s \ln\left(\frac{K}{u_s}\right) + r\epsilon\eta \ln\left(\frac{K}{u_s}\right) - \frac{r\epsilon\eta}{u_s}$. Combining these, we get the linearized PDE for $\eta(x,t)$: $\eta_t = \nabla \cdot (D(x)\nabla\eta) + r\eta \ln\left(\frac{K}{u_s}\right) - \frac{r\eta}{u_s}$. This linearized equation is analyzed for stability considering solutions of the form $\eta(x,t) = \phi(x)e^{\sigma t}$, where σ is the growth rate related with the effectiveness clinical treatment and $\phi(x)$ is a smooth function with $0 < \nabla\phi \ll 1$. The sign of σ determine the stability of the steady-state solution $u_s(x)$ and the efficiency of clinical treatment. If $\mathrm{Re}(\sigma) < 0$ for all perturbations, $u_s(x)$ is stable and time decreasing. This means that the beginning of clinical treatment is effective. If $\mathrm{Re}(\sigma) > 0$ for any perturbation, u_s is unstable and time increasing. In this case, the stationary cells are reactive making the clinical treatment less effective. Substituting into the linearized equation yields: $\phi(x)\sigma e^{\sigma t} = \nabla \cdot \big(D(x)\nabla(\phi(x)e^{\sigma t})\big) + r\phi(x)e^{\sigma t} \ln\left(\frac{K}{u_s}\right) - \frac{r\phi(x)e^{\sigma t}}{u_s}$. Considering that $\nabla\phi \ll 1$ so that the diffusive terms are small, we have: $\sigma \approx r \ln\left(\frac{K}{u_s}\right) - \frac{r}{u_s}$. In this approximation, the behavior of the solution is primarily governed by the reaction term. The sign of σ depends on the balance of these two terms. If the positive contribution from the logarithmic term outweighs the negative term, σ will be positive, indicating instability. If the negative term dominates, σ will be negative, indicating stability.

Our intention now is to search for travelling waves solutions for Grades 2 and 3 of normoxic cells (Figure 2 in [4]). Then, $u(\mathbf{x},t) = f(z)$ where $z = \mathbf{x}\cdot\mathbf{b} - ct \in \mathbb{R}$, being $\mathbf{b}$ the direction of propagation and c is the wave speed. For the sake of simplicity, we will assume that $\mathbf{x}\cdot\mathbf{b} = x$. This transformation turns the original PDE (1) into an ODE in terms of the travelling wave variable z: $-c\frac{df}{dz} = \frac{d}{dz}\left(d_i \exp(-\lambda_i(z+ct))\frac{df}{dz}\right) + rf\ln\left(\frac{K}{f}\right)$. For tumor Grades 2 and 3, as indicated in Figure 2 of [4], the normoxic tumor cell density remains relatively constant with distance, implying that local growth dynamics (like Gompertzian growth) are more influential than diffusion. Therefore, in these tumor grades, the proliferation zone is primarily governed by the reaction term. Then, $\frac{df}{f\ln\left(\frac{K}{f}\right)} = -\frac{r}{c}dz$. Using a substitution for the left-hand side: $\int \frac{-Ke^{-y}dy}{Ke^{-y}y} = \int \frac{-dy}{y} = -\ln|y| + C_1$, where $y = \ln\left(\frac{K}{f}\right)$. Operating with standard means, we have that $f(z) = \frac{K}{\exp\left(\exp\left(C_1 + \frac{r}{c}z - C_2\right)\right)}$. After applying Neumann condition, we have that $f(z) \approx \frac{K}{\exp\left(\exp\left(C_1+\frac{r}{c}z\right)\right)}$. Based on this expression, we carry out a data fitting process with the Grade 2 of normoxic cells as indicated in Figure 2 of [4]. Making an optimization based on the minimization of the squared errors, the estimated values for the parameters are: $K \approx 0.240$; $C_1 \approx -2.374$; $r \approx 0.216$; $c \approx 0.345$. We repeat the same calibration process for the Grade 3 of normoxic cells that are indicated in Figure 2 of [4]. In this case, the values for the involved constants are: $K \approx 0.615$; $C_1 \approx -1.410$; $r \approx 0.3985$; $c \approx 59.594$.

Now, we aim at applying the Tanh-method to obtain dispersive travelling waves. For this: $u = A\tanh(z)$, where $z = \mathbf{x}\cdot\mathbf{b} - ct \in \mathbb{R}$, with $\mathbf{b}$ representing the unit direction of wave propagation and c denoting the wave speed that in general is given as $c(x,t)$. Upon substitution and assuming that $z = x - ct$ is small: $-c(1-z^2) \approx rz\ln\left(\frac{K}{z}\right)$. Since we are considering small values of z, we have $c \approx rz\ln z \approx -rz$. Hence, recovering the original variables, we have the following value for $c(x,t) \approx \frac{rx}{rt-1}$. We remark that in a complex environment various factors contribute to non-uniform proliferation of cells as expressed by a spatially and time varied travelling wave speed $c(x,t)$.

Now, we search for solutions in case of grade 4 of cancer growth, we consider that main driver is given by the diffusion of cells which is predominant over the reaction term. We make use of the travelling wave ansazt, this is $u(\mathbf{x},t) = f(z)$ where $z = \mathbf{x}\cdot\mathbf{b} - ct \in \mathbb{R}$, then: $-cf(z) = (g_4 \exp(-\gamma(z+ct-x_0)^2))\frac{df}{dz} + C$. where C is assumed to be null for simplification purposes. This last equation can be solved by separating variables and integrating, so that upon recovering the original variables, we get that: $f(x-ct) = \exp\left(\int \frac{-c}{g_4}\exp(-\gamma(x-x_0)^2)dx\right)$. To assess the specific values of the involved constants, we use again the data obtained from Grade 4 of normoxic cells

as plotted in Figure 2 of [4]. After applying optimization and fitting techniques, we obtain the following values for the involved constants and t value: $c = 0.62$; $g_4 \approx 1.73$; $\gamma \approx 2.43$; $t \approx -0.2431$. Such a negative value for the time variable is not actually a physical burden as travelling waves are equivalent up to translations.

Eventually, we seek a similarity solution of the form $u(x,t) = U(\xi)$ with the similarity variable $\xi = \frac{x-x_0(t)}{t^\alpha}$. Substituting these into the PDE, assuming $x_0 = x_0(t)$ and $x_0' = \frac{dx_0}{dt}$, the equation becomes: $-\alpha\xi t^{-\alpha-1}U'(\xi) - x_0' t^{-\alpha}U'(\xi) = \frac{d}{dx}\left(g_4 \exp(-\gamma(x-x_0)^2))U'(\xi)\right)$. Considering $x = \xi t^\alpha + x_0$, and differentiating the right side with respect to x, we find $-\alpha\xi t^{-1}U'(\xi) - x_0'U'(\xi) = t^\alpha \frac{d}{d\xi}\left(g_4 \exp(-\gamma(\xi t^\alpha)^2))U'(\xi)\right)$. This equation can be simplified by recognizing that the term involving x_0' represents the movement of the peak in diffusivity, which could be related to a constant travelling speed c if x_0 is linear in t. Then we arrive to: $(\xi - c)U'(\xi) = g_4 \exp(-\gamma\xi^2)U''(\xi) - 2g_4\gamma\xi \exp(-\gamma\xi^2)U'(\xi)$. The resolution of this equation is complex, requiring simplifications based on biological realities. Specifically, we posit that the second term on the right-hand side is negligible compared to the first. This is due to the minimal global slope of the Grade 4 curve in Figure 2 of [4]. Near the diffusivity peak, where ξ is small, the linear and exponential terms further diminish the second term's impact, emphasizing the diffusion term's dominance. Thus, we simplify the expression as: $(\xi - c)U'(\xi) = g_4 \exp(-\gamma\xi^2)U''(\xi)$. By separating variables an integrating both sides with respect to ξ: $\ln|U'(\xi)| = \int \frac{\xi - c}{g_4 \exp(-\gamma\xi^2)} d\xi$. After evaluating the integral, we can solve for $U(\xi)$: $U'(\xi) = \exp\left(\int \frac{\xi - c}{g_4 \exp(-\gamma\xi^2)} d\xi\right)$, $U(\xi) = \int U'(\xi) d\xi$. Aligning similarity solutions with data from [4] is challenging, but the observed time-varying peak of normoxic cells, assumed to move at speed c, due to factors like vascular tissue formation and nutrient availability, remains of high interest.

3 Conclusions and Future work

This analysis has permitted to model tumor growth using Gompertz dynamics and spatially varied diffusivity, examining solution regularity, stability, and traveling waves in different cancer grades and microenvironments. We have correlated the solutions with real data from the field presented in [4]. As future research topic, it would be of interest to continue correlating the obtained solutions with other forms of cancer growth.

References

[1] Laird, A. K., *Dynamics of Tumor Growth*, British Journal of Cancer, **18**(3) (1964), 490, *doi:10.1038/bjc.1964.55.*

[2] Norton, L., *A Gompertzian Model of Human-Breast Cancer Growth*, Cancer Research, **48**(24) (1988), 7067-7071.

[3] Gatenby, R. A., Gawlinski, E. T., *A Reaction-Diffusion Model of Cancer Invasion*, Cancer Research, **56**(24) (1996), 5745-5753.

[4] Swanson, K. R., Rockne, R. C., Claridge, J., Chaplain, M. A., Alvord, E. C. Jr., Anderson, A. R., *Quantifying the role of angiogenesis in malignant progression of gliomas: in silico modeling integrates imaging and histology*, Cancer Research, **71**(24) (2011), 7366-7375, *doi:10.1158/0008-5472.CAN-11-1399.*

[5] Brezis, H., *Functional Analysis, Sobolev Spaces and Partial Differential Equations*, Springer (2011).

[6] Adams, R. A., Fournier, J. J. F., *Sobolev Spaces* (2nd ed.), Academic Press (2003).

International Conference on Mathematical Analysis and Applications in Science and Engineering
ICMA^{2}SC'24
ISEP Porto-Portugal, June 20 - 22, 2024

Leveraging Physics-Informed Neural Networks for Immunotherapy Models in Cancer

José Alberto Rodrigues[1]

[1] CIMA and Department of Mathematics of
ISEL-Higher Institute of Engineering of Lisbon,
Rua Conselheiro Emídio Navarro, 1,
1959-007 Lisbon, Portugal

[1]jose.rodrigues@isel.pt

Abstract: Mathematical modeling plays a pivotal role in understanding complex biological systems, particularly in the realm of cancer immunotherapy. With this work, we propose leveraging Physics-Informed Neural Networks (PINNs) as a powerful tool for modeling immunotherapy dynamics within cancer contexts. PINNs offer distinct advantages in solving both differential equations describing biological processes and in addressing inverse problems to obtain models from data sets. This paper explores the application of PINNs in these two contexts and discusses their potential to enhance our understanding of immunotherapy dynamics in cancer treatment.

keywords: physics-informed neural networks (PINNs); differential equation ; loss function; activation function; deep learning; cancer cells; immunotherapy.

MSC2020: 92-08,92-10.

1 Introduction

Physics-Informed Neural Networks (PINNs) are a groundbreaking tool that leverages the power of machine learning to solve forward and inverse problems governed by partial differential equations (PDEs) and ordinary differential equations (ODEs). By embedding the underlying physical laws directly into the neural network, PINNs ensure that the solutions adhere to the governing equations, providing accurate and efficient problem-solving capabilities.

In this work, we demonstrate the application of PINNs to determine parameters for a mathematical model of cancer growth. This model encapsulates the complex interactions between normal cells, tumor cells, and immune cells. By using PINNs, we can accurately infer critical parameters and predict the system's behavior under various conditions, offering valuable insights into the dynamics of cancer progression and potential therapeutic strategies. This approach not only enhances our understanding of cancer biology but also exemplifies the versatility and robustness of PINNs in tackling challenging biomedical problems.

2 Mathematical Model of Cancer Growth

In this study, we consider two mathematical models to describe the interactions among three cell populations: normal cells (N), tumor cells (T), and immune cells (I). The first model is a simplified version that captures the essential dynamics, while the second model is a more detailed one derived from existing literature [Alharbi(2020)]. This comparative analysis aims to demonstrate the versatility of Physics-Informed Neural Networks (PINNs) in solving both forward and inverse problems for different levels of model complexity.

2.1 First Model

The simplified model focuses on the basic interactions between normal cells, tumor cells, and immune cells, represented by the following system of ordinary differential equations (ODEs):

$$\frac{dN}{dt} = r_N N \left(1 - \frac{N+T}{K_N}\right) - d_N N, \tag{1}$$

$$\frac{dT}{dt} = r_T T \left(1 - \frac{N+T}{K_T}\right) - d_T T - kIT, \tag{2}$$

$$\frac{dI}{dt} = s_I - d_I I + pIT - qI. \tag{3}$$

Here, r_N and r_T are the growth rates of normal and tumor cells, K_N and K_T are the carrying capacities, d_N, d_T, and d_I are the death rates, k is the rate at which immune cells kill tumor cells, s_I is the source term for immune cells, p is the proliferation rate of immune cells in response to tumor cells, and q is the rate of immune cells dying due to interactions with tumor cells.

2.2 Second Model

We now present another model introduced in [Alharbi(2020)], which includes different biological factors and interactions.

$$\frac{dN}{dt} = rN\Big(1 - \beta_1 N\Big) - \eta NI - \gamma NT, \tag{4}$$

$$\frac{dT}{dt} = \alpha_1 T\Big(1 - \alpha_2 T\Big) + \beta_2 NT - \alpha_3 TI, \tag{5}$$

$$\frac{dI}{dt} = \sigma - \delta I + \frac{\rho NI}{m+N} + \frac{\rho_1 TI}{m_1+T} - \mu NI - \mu_1 TI \tag{6}$$

3 Physics-Informed Neural Networks (PINNs)

PINNs leverage neural networks to approximate the solutions of ODEs/PDEs while enforcing the physical laws described by these equations. A PINN consists of a neural network $\hat{\boldsymbol{u}}(t, \boldsymbol{\theta})$, where $\boldsymbol{\theta}$ represents the trainable parameters of the neural network to obtain the solution $\hat{\boldsymbol{u}}$. The network is trained to minimize a loss function that incorporates both the data and the governing equations.

3.1 Network Architecture

The neural network for our problem will have one input (time t) and three outputs corresponding to the cell populations $N(t)$, $T(t)$, and $I(t)$. The network can be defined with multiple hidden layers and activation functions such as Tanh or ReLU.

3.2 Loss Function

The loss function for training the PINN combines the data loss and the physics-informed loss:

$$\mathcal{L} = \mathcal{L}_{\text{data}} + \mathcal{L}_{\text{physics}}, \tag{7}$$

where

$$\mathcal{L}_{\text{data}} = \frac{1}{N}\sum_{i=1}^{N}\left[(\hat{N}(t_i) - N_i)^2 + (\hat{T}(t_i) - T_i)^2 + (\hat{I}(t_i) - I_i)^2\right], \tag{8}$$

and

$$\mathcal{L}_{\text{physics}} = \frac{1}{N}\sum_{i=1}^{N}\left[\left(\frac{d\hat{N}}{dt} - f_N(\hat{N},\hat{T},\hat{I})\right)^2 + \left(\frac{d\hat{T}}{dt} - f_T(\hat{N},\hat{T},\hat{I})\right)^2 + \left(\frac{d\hat{I}}{dt} - f_I(\hat{N},\hat{T},\hat{I})\right)^2\right]. \tag{9}$$

Here, $\hat{N}(t)$, $\hat{T}(t)$, and $\hat{I}(t)$ are the outputs of the neural network, and f_N, f_T, f_I are the right-hand sides of the ODEs for each of the mathematical models (1)-(3) and (4)-(6), respectively.

4 Numerical Results

With PINNs, we can either obtain the parameters from the data and select the best corresponding model, or, if the parameters are known, solve the problem numerically.

4.1 The Inverse Problem

We begin by consedering the extracted data from [Alharbi(2020)], both PINN models are trained to accurately capture the dynamics of the cell populations. To train the PINN, we initialize the neural network parameters and the ODE parameters for both mathematical models. The training process involves minimizing the loss function (7) using optimization algorithms such as Adam followed by L-BFGS for fine-tuning.

After training, the neural network will provide continuous approximations for $N(t)$, $T(t)$, and $I(t)$. The learned parameters can be validated against experimental data or used for further analysis.

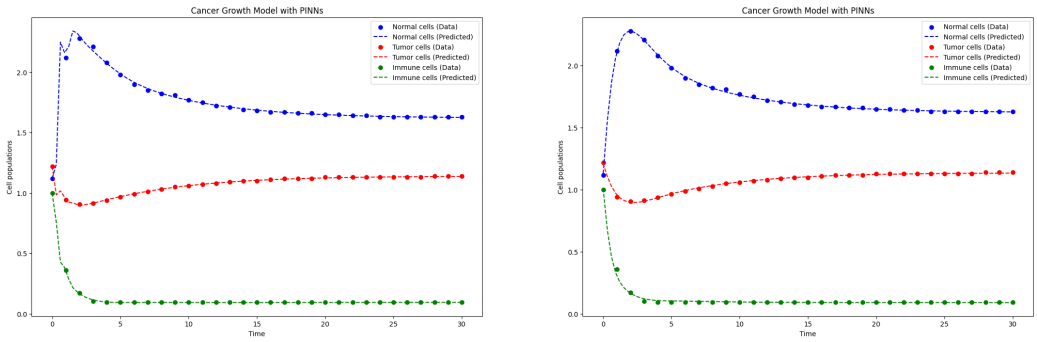

(a) First model: $\mathcal{L} = 2.4 \times 10^{-4}$ (b) Second model: $\mathcal{L} = 7.05 \times 10^{-4}$

Figure 1: Comparison of the fit results to the data for the two models.

A comparison of the fit results to the data for the two models at Figure 1 reveals that both demonstrate a reasonable approximation of the observed values after 2×10^4 epochs.

4.2 Numerical Solution with PINNs

Here we will consider the previously determined parameters to solve the problems formulated by each of the models, minimizing the associated $\mathcal{L}_{\text{physics}}$ function. We will compare it with the classical fourth-order Runge-Kutta method.

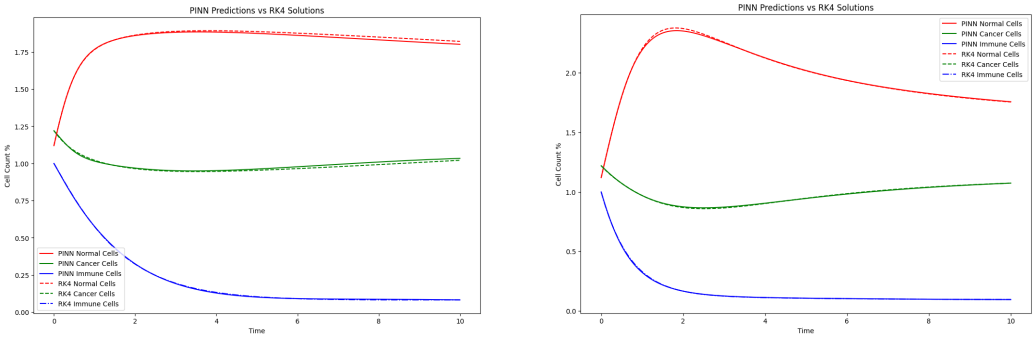

(a) First model: $\mathcal{L}_{\text{physics}} = 3.61 \times 10^{-4}$ (b) Second model: $\mathcal{L}_{\text{physics}} = 2.02 \times 10^{-4}$

Figure 2: Comparison of PINN resolution with RK4 for each model.

In Figure 2, we present the comparison of the numerical resolution for both models using 2×10^3 epochs with the RK4 method. Increasing the dataset size would lead to a higher match between Figure 2 and Figure 1 for both cases (a) and (b).

5 Conclusion

PINNs provide a robust framework for integrating data and physical laws to determine parameters in complex biological systems. By enforcing the ODE constraints within the neural network training process, we can obtain accurate and physically consistent parameter estimates for both cancer growth model. Also, the PINNs method demonstrates good performance compared to classical methods.

Acknowledgments

This research was partially sponsored with national funds through the Fundação Nacional para a Ciência e Tecnologia, Portugal-FCT, under projects UIDB/04674/2020 (CIMA).

DOI: https://doi.org/10.54499/UIDB/04674/2020

References

[Alharbi(2020)] Alharbi, S.A.; Rambely, A.S. A New ODE-Based Model for Tumor Cells and Immune System Competition.*Mathematics***2020**, *8*, 1285.

[Chen(2023)] Chen, Q.; Ye, Q.; Zhang, W. Li, H.; Zheng, X. TGM-Nets: A deep learning framework for enhanced forecasting of tumor growth by integrating imaging and modeling. *Engineering Applications of Artificial Intelligence* **2023**, *126*, 106867.

[Kamyab(2022)] Kamyab, S.; Azimifar, Z.; Sabzi, R.; Fieguth, P. Deep learning methods for inverse problems. *PeerJ Comput Sci.* **2022** *May 2;8:e951.*

[Rodrigues(2024)] Rodrigues, J.A. Using Physics-Informed Neural Networks (PINNs) for Tumor Cell Growth Modeling. *Mathematics* **2024**, 12, 1195.

Lockdown Optimal Strategy for a Pandemic desease spread

Chakib Jerry[1⋆] **Amine Bernoussi**[2]

[1] Moulay Ismail University,Faculty of Law, Economics and Social Sciences, Morocco
[2] Ibn Tofail University, Faculty of Sciences, Morocco

[1⋆]c.jerry@umi.ac.ma

Abstract: Most integrated models of pandemic deseases have been developed under the assumption that the policy-sensitive reproduction number is certain, specially those deseases who need quaranteen or lockdownn to control the spread. The decision to exit from the lockdown, in Covid or Malaria crisis, has been made in most countries without knowing the reproduction number that would prevail after the deconfinement. In this paper, we explore the role of uncertainty and learning on the optimal dynamic lockdown policy. We limit the analysis to suppression strategies. In the absence of uncertainty, the optimal confinement policy is to impose a constant rate of lockdown until the suppression of the virus in the population. We show that introducing uncertainty about the reproduction number of deconfined people reduces the optimal initial rate of confinement.

keywords: Optimal Control; Lockdown; reproduction number.

MSC2020: 49-XX; 34-XX; 92-XX.

References

[1] A. Abta, A. Kaddar, H. T. Alaou, Global stability for delay SIR and SEIR epidemic models with saturated incidence rates, Electronic Journal of Differential Equations, **23** (2012), 1–13.

[2] K. Hattaf, A. A. Lashari, Y. Louartassi, N. Yousfi; A delayed SIR epidemic model with a generalized incidence rate , Electronic Journal of Qualitative Theory of Differential Equations, **3** (2013), 1–9.

[3] A. Bernoussi, S. Elkhaiar, C. Jerry; Stability Analysis of an SEIRS Epidemic Model with Relapse, Immune and General Incidence Rates, Journal of Applied Nonlinear Dynamics, **11**(1) (2022), 217–231.

International Conference on Mathematical Analysis and Applications in Science and Engineering
ICMA^{2}SC'24
ISEP Porto-Portugal, June 20 - 22, 2024

Application of Random Differential Equations in Compartmental Models for Oral Drug Administration

Vicente J. Bevia[1] **Juan-Carlos Cortés**[1] **Cristina Luisovna Pérez**[1⋆] **Rafael-Jacinto Villanueva**[1]

[1] Universitat Politècnica de València, Spain

[1⋆]cperdiu@upv.edu.es

Abstract: In this work, we apply a compartmental model formulated via Random Differential Equations to synthetic data of multiple-dose drug administration. The synthetic data is simulated with noise in order to evaluate whether the random model captures this variability in the data. This investigation seeks to explain the model's potential applicability in real-world pharmacokinetic studies.

keywords: mathematical modelling; random differential equations; pharmacokinetic.

MSC2020: 34F05; 92-10.

1 Introduction

Differential equations are powerful tools for mathematically modeling physical phenomena, enabling us to approximate the rate of change of processes even when their underlying mechanics remain incompletely understood. Despite their basic form, both ordinary and partial linear differential equations prove highly effective in encapsulating real-world dynamics, finding applications across diverse scientific domains. These include studies on chemical reactions [1], electrical networks [2], and drug absorption by organs [3], among others.

Integrating data to construct accurate models becomes imperative, enabling us to tailor equations to specific observed phenomena sensibly. However, data inherently carries a degree of uncertainty due to measurement errors and the device's limitations. Moreover, the intrinsic uncertainty in modeling arises from the intricate nature of real-life processes, some of which may remain beyond complete comprehension. Consequently, adopting random models to handle such uncertainty presents a compelling alternative to deterministic approaches, promising more realistic outcomes. Random Differential Equations (RDEs), as a means of introducing randomness into differential equations, involve treating certain parameters as random variables, thereby rendering the solutions as stochastic processes [4, Ch. 5].

This study utilizes a system of linear ordinary differential equations supplemented with source terms featuring discontinuities, applicable to real-world scenarios. To illustrate our approach, we generate synthetic data and apply our model. The choice of synthetic data over real data allows us to introduce randomness into the model and assess the extent to which the randomized

model captures the uncertainties inherent in the synthetic dataset. We simulate synthetic data representing medication concentrations in both the gut (G_i) and blood (B_i) over at the i^{th} hour, with $i \in 1, \ldots, 40$ since the initial dose following the guidelines from [5]. We set the absorption coefficient to 0.1 and the elimination coefficient to 0.05. The generation of synthetic data proceeds as outlined below:

$$\begin{aligned} G_0 &= 100 + \epsilon_0^G, \\ G_i &= \begin{cases} G_{i-1} - 0.1G_{i-1} + 10 + \epsilon_i^G, & \text{if} \quad \text{mod } (t, 12) = 0, \\ G_{i-1} - 0.1G_{i-1} + \epsilon_i^G, & \text{otherwise}, \end{cases} \\ B_0 &= 0 + \epsilon_0^B, \quad B_i = B_{i-1} - 0.05B_{i-1} + 0.1G_{i-1} + \epsilon_i^B, \end{aligned} \tag{1}$$

with, $\epsilon_i^G \sim N(0, 0.05 \cdot G_i)$ and $\epsilon_i^B \sim N(0, 0.05 \cdot B_i + 0.01)$.

2 Results and discussion

To model the process of oral drug administration, we employ a system of random differential equations with explicit solutions (y_1, y_2), representing the concentrations in the gut and bloodstream, respectively. These solutions incorporate jumps that model oral drug intake, and we adjust their parameters using synthetic data generated by applying the *NonlinearModelFit* (NLM) function within *Mathematica*. As depicted in Figure 1, the solutions with parameters estimated via NLM closely align with the data, indicating a good fit of the constructed model.

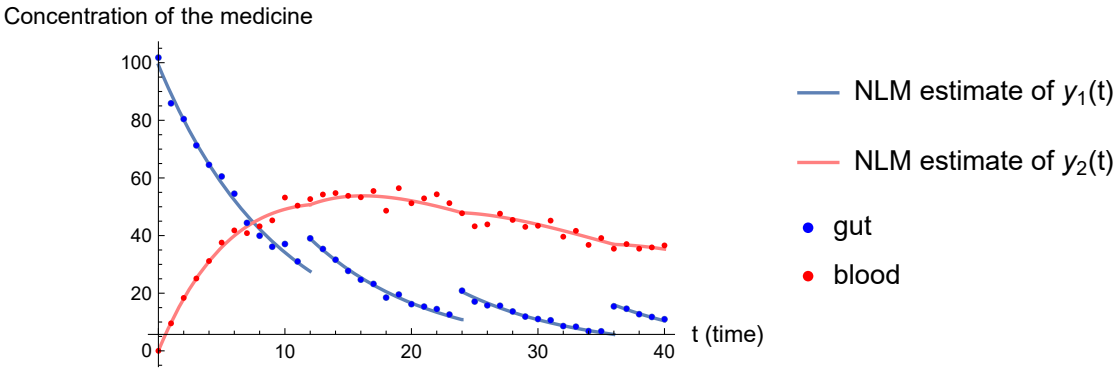

Figure 1: Synthetic data as described in (1) and fitted functions.

We then proceed to randomize the model and consider some model parameters to be continuous random variables defined on a common complete probability space $(\Omega, \mathcal{F}_\Omega, \mathbb{P})$. We choose to model them as truncated normal distributions and adjust the hyper-parameters of each corresponding distribution to the synthetic data.

The results are depicted in Figures 2 and 3. These graphical representations show that nearly all synthetically generated data points for drug concentrations in the gut and blood fall within the 95% probabilistic intervals (PI). Additionally, it is observable that as the concentration in the gut decreases, the 95%-PI narrows. This trend stems from the inherent nature of the error embedded in the synthetic data. It is crucial to note that the error is modeled as independent Gaussian random variables with a variance proportional to the concentration. Hence, it is logical for this variance to decrease as the magnitude of the concentration diminishes. In the case of the blood concentration data, we see that we start from an almost certain initial condition of no concentration in the blood before the first dose; hence, here, the 95% PI is quite narrow. The PI then gets wider as multiple doses of the drugs are administered orally. As expected,

we observe a delay between the times (in hours) when the drugs are taken $\{12\,\mathrm{h}, 24\,\mathrm{h}, 36\,\mathrm{h}\}$ and the rise of the drug's concentration in the blood. There are also no sudden jumps in the drug's concentration in the blood as in the gut.

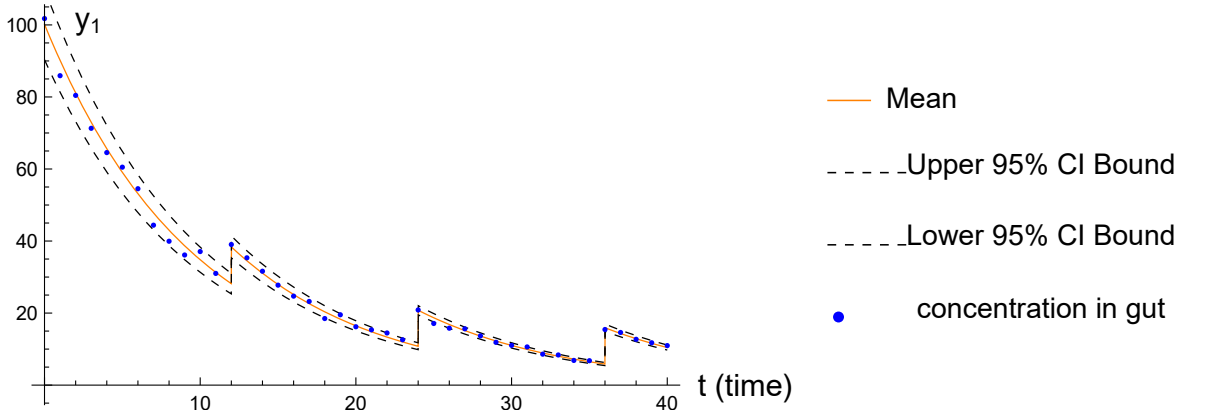

Figure 2: Mean and 95%-PI of $y_1(t)$ and synthetic data points of drug concentration in the gut generated as described in (1) (blue points) for times $t \in \{0, 1, \ldots, 40\}$.

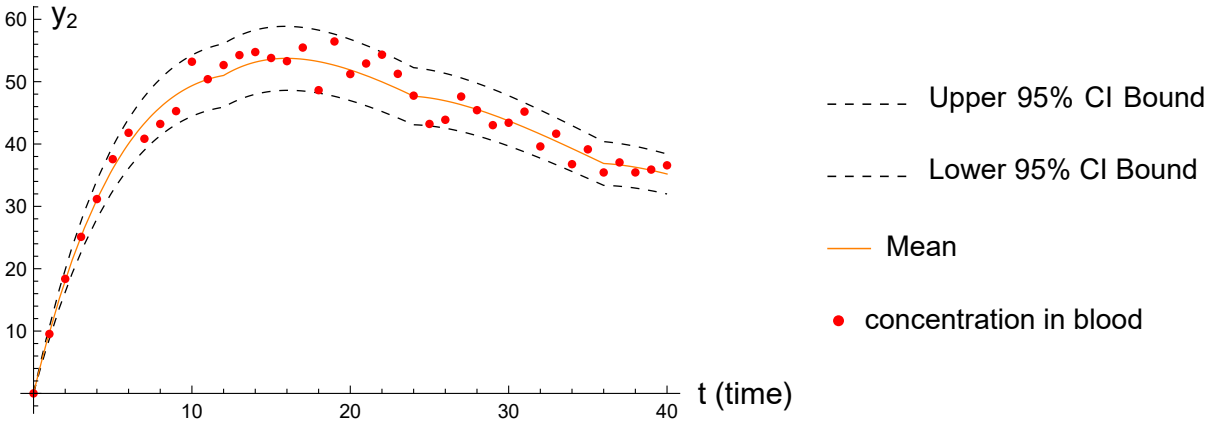

Figure 3: Mean and 95%-PI of $y_2(t)$ and synthetic data points of drug concentration in the blood generated as described in (1) (red points) for times $t \in \{0, 1, \ldots, 40\}$.

3 Conclusions and Future work

We have utilized RDEs to address a practical challenge involving uncertainties in synthetic data from multiple-dose drug intake, specifically focusing on gut and blood concentrations through time. Via this approach, we successfully captured the mean behavior of the data, providing valuable insights into the dynamics of drug absorption and distribution within the body. This enabled us to not only understand the underlying processes more comprehensively but also to quantify the inherent uncertainty present in the noisy dataset, thereby enhancing our confidence in the model's predictive capabilities.

Our future work aims to expand the model's scope by incorporating the concentration of medication in urine. By doing so, we seek to gain a deeper understanding of the complete journey of the drug through the body, including its eventual elimination from the system. This extension

will enrich our understanding of pharmacokinetics and offer practical insights into optimizing drug dosage regimens and minimizing potential adverse effects.

Acknowledgments

This work has been supported by the Spanish Agencia Estatal de Investigación grant PID2020-115270GB-I00. Cristina Luisovna Pérez has been supported by an FPU21/02343 grant (Formación de Profesorado Universitario 2021) from the Ministerio de Universidades. Vicente Bevia acknowledges the doctorate scholarship granted by Programa de Ayudas de Investigación y Desarrollo (PAID), Universitat Politècnica de València (UPV).

References

[1] G. Scholz and F. Scholz, *First-order differential equations in chemistry*, *ChemTexts*, vol. 1, pp. 1–12, 2015, Springer. https://doi.org/10.1007/s40828-014-0001-x

[2] Y.-D. Save, H. Narayanan, and S.-B. Patkar, *Solution of Partial Differential Equations by electrical analogy*, *Journal of Computational Science*, vol. 2, no. 1, pp. 18–30, 2011, ISSN: 1877-7503, doi: https://doi.org/10.1016/j.jocs.2010.12.006.

[3] K. Kubota, F. Dey, S.-A. Matar, and E.H. Twizell, *A repeated-dose model of percutaneous drug absorption*, *Applied Mathematical Modelling*, vol. 26, no. 4, pp. 529–544, 2002, ISSN: 0307-904X, doi: 10.1016/s0307-904x(01)00068-3.

[4] T.-T. Soong, *Random Differential Equations in Science and Engineering*, Academic Press, 1973, ISBN: 9780080956121, doi: https://doi.org/10.1016/S0076-5392(08)60151-4.

[5] J. Chamberlain, *The use of spreadsheets for pharmacokinetic simulations*, *The Scientific World Journal*, vol. 3, pp. 265–278, 2003, Publisher: Hindawi, doi: https://doi.org/10.1100%2Ftsw.2003.02.

International Conference on Mathematical Analysis and Applications in Science and Engineering
ICMA^{2}SC'24
ISEP Porto-Portugal, June 20 - 22, 2024

A probabilistic approach to determine the best chemotherapy strategy to delay breast tumor relapse

Clara Burgos[1⋆] Juan Carlos Cortés[1] Sergio. Díez-Domingo[2]
Elena López-Navarro[1] Jose Villanueva-Tarazona[1]
Rafael Jacinto Villanueva[1]

[1] Instituto Universitario de Matemática Multidisciplinar.
Universitat Politécnica de Valéncia. Valencia, Spain
[2] Radiation Physics Service, Hospital Clínico Universitario de Valencia. Valencia, Spain

[1⋆]clabursi@upv.es

Abstract: In this work, we propose a mathematical approach to describe breast tumor growth, incorporating the inherent randomness of the problem. Consequently, we aim to determine the optimal chemotherapy strategy to delay tumor relapse as effectively as possible. It is widely acknowledged that biological processes are influenced by randomness, while data obtained from electronic devices may contain machine errors. The model we propose for describing breast tumor growth involves a differential equation, wherein the input parameters defining the equations are treated as random variables rather than deterministic values. It is important to note that the differential equation used to model breast tumor growth includes discontinuous terms, referred to as jumps, to represent the administration of chemotherapy. We will compute the probability distribution (PDF) of the solution to the differential equation and adjust the random input parameters to ensure that the PDF of the solution aligns with the available random data.

keywords: Breast Cancer growth Description; Chemotherapy administration Modelling; Uncertainty Quantification

MSC2020: 37H10; 49K45; 62P10; 93A30.

1 Introduction

Breast cancer is one of the most common types of malignant tumors in the female population. Among a 30% of all cancers are in the breast. This study focuses on studying the growth of type HER2 since it used to be the most aggressive. In the literature, there are different mathematical models describing tumor growth, but to the best of our knowledge, only a few contributions considering chemotherapy treatments and tumor resection have been found. On the other hand, it is well known the existence of random factors which may affect tumor growth. Describing this randomness may result in a better modeling of tumor evolution. In this work, we will consider that the proposed model is affected by randomness. We will consider that the parameters which defines the model are random variables instead deterministic values.

2 Methods

In this study, a novel tool has been designed to describe breast tumor growth, considering the inherent randomness associated with the complex factors that determine the dynamics of this class of malignant tumors. The proposed tool includes chemotherapy administrations and tumor resection. The growth model is described by a differential equation with discontinuous terms. These discontinuous terms models the time instants when chemotherapy is administered. The model we propose is given by

$$\left.\begin{aligned} T'(t) &= KT(t) - BT(t)\sum_{i=1}^{N} e^{-A(t-t_i)}H(t-t_i), \\ T(0) &= \hat{t}_0. \end{aligned}\right\}$$

where K denotes tumor growth, B the rate at which chemotherapy kills tumor cells and A rate of chemotherapy clearance in human body. A probabilistic technique has been developed to obtain probabilistic distributions of model parameters according to data that have uncertainty. The times $\{t_i\}_{i=0}^{N}$ describe the time instants where chemotherapy had been administered. The sum represents the effect of chemotherapy in human body.

We can observe the model is given by a linear equations system, so we can obtain its solution

$$T(t) = T_0 \exp\left(Kt + \frac{B}{A}\sum_{i=1}^{N}\left(e^{-A(t-t_i)} - 1\right)H(t-t_i)\right).$$

The technique we propose based on a combination of different computational and probabilistic techniques: random variable transformation method is applied to obtain the first probability density function of the model solution; the principle of maximum entropy is numerically used to assign reliable probabilistic distributions to random parameters; optimization algorithms have been applied to fit the random model to the probabilistic distributions assigned to data. The advantage of this tool is that it can be customized for each patient to obtain individualized tumor growth predictions.

3 Results and discussion

The proposed tool has been applied to two different patients. In view of the results obtained for both patients, the developed tool fits with a high level of accuracy to the available random data. Different chemotherapy administrations have been simulated to establish the best strategy to delay tumor relapse. Results are in agreement with the extant literature in such a way that there is a delay in the relapse when more chemotherapy cycles are administered. However, doctors must evaluate the toxicity of the treatment. The proposed tool can provide further details about chemotherapy concentration in the body and, consequently, the negative effects of different chemotherapy strategies.

4 Conclusions

The proposed tool describes breast tumor growth considering the uncertainty of data. Moreover, it can be personalized to each patient. This tool allows us to simulate different chemotherapy strategies and choose the best one for a patient. The proposed tool can also obtain chemotherapy concentration in the body and its toxicity. All these results and simulations are given by means

of probabilistic quantities in order to account for the uncertainties present in the evolution of the breast tumor.

Acknowledgments

This work has been supported by

- This work has been supported by the grant PID2020-115270GB–I00 funded by MCIN/AEI/10.13039/501100011033.
- The posdoctoral grant from Universitat PolitÃ¨cnica de Valencia *Margarita Salas* funded by the Spanish Ministry of Universities and Next-Generation, EU.
- Ayuda a Primeros Proyectos de Investigación (PAID-06-22) from Vicerrectorado de Investigación de la Universitat Politécnica de Valéncia (UPV).

References

[1] T. L. Jackson, P. D. Senter, and J. D. Murray, *Development and validation of a mathematical model to describe anti-cancer prodrug activation by antibody-enzyme conjugates*, Computational and Mathematical Methods in Medicine, vol 2, no 38953, pp. 93-103, April 1999.

[2] T. L. Jackson, H. M. Byrne, *A mathematical model to study the effects of drug resistance and vasculature on the response of solid tumors to chemotherapy*, Mathematical Biosciences, vol. 164, no. 1, pp. 17-38, November 1999.

International Conference on Mathematical Analysis and Applications in Science and Engineering
ICMA^{2}SC'24
ISEP Porto-Portugal, June 20 - 22, 2024

MODELLING NONLINEAR SYSTEMS FOR DRUG ADMINISTRATION VIA KOOPMAN OPERATOR

Paul A. Pintea[1⋆] **Eva H. Dulf**[2]

[1,2] Technical University of Cluj-Napoca, Romania

[1⋆]Paul.Pintea@aut.utcluj.ro, [2]Eva.Dulf@aut.utcluj.ro

Abstract: The collaboration between control engineers and clinicians offers a number of promising opportunities, with potential for broad applications. Advances in the field have made closed-loop drug delivery a popular option. One of the key issues in this process is the development of appropriate mathematical models that can help us understand and control the distribution of drug delivery in the human body. The current study proposes a novel approach to reconstruct the dynamics of nonlinear compartmental models that are commonly utilised in medical administration. The method employs the Koopman Operator, known for its linear nature, which facilitates the analysis of complex systems that exhibit nonlinear behaviour. By using this operator, the study aims to overcome the limitations of conventional techniques that are often cumbersome and computationally expensive. The proposed methodology has the potential to enhance our understanding of the underlying mechanisms governing the dynamics of complex systems and can have significant implications for the healthcare industry.

keywords: koopman; modelling; physiological models.

MSC2020: 49-XX; 34-XX; 92-XX.

1 Introduction

The diffusion of drug concentration between two main compartments of the body can be represented through a general model as seen in (1). An example of usage, but not limited to, is the insulin-glucose system.

$$(\Sigma_m): \begin{cases} \dot{x}_1(t) &= -k_{11}x_1(t) + k_{12}x_2(t) + n \cdot x_1(t) \cdot x_2(t) \\ \dot{x}_2(t) &= k_{21}x_1(t) - k_{22}x_2(t) + u(t) \end{cases} \tag{1}$$

where $x_1, x_2[mg/dL]$ are concentrations of a substance found in two interacting compartments, $u(t)$[mU/L] is an infusion rate of medicine. It is easy to spot the nonlinearity in the mode and that this is not a very complex model however, it is the choice to show the proof of concept for Koopman Linearization. Considering continuous-time dynamics for the nonlinear system from (1) given in general form as an autonomous system $\dot{\mathbf{x}}(t) = f(\mathbf{x}(t)), \ \mathbf{x}(t) \in \mathbb{R}^n$ for which $f : \mathcal{A}_x \to \mathbb{R}^n$ is a Lipschitz function, $\mathcal{A}_x \subset \mathbb{R}^n$ is the smooth manifold of admissible states, and

$t \in \mathbb{R}_+$ is the continuous time over which the states flow. The manifold $\mathcal{A}_{\mathbf{x}} \subset \mathbb{R}^n$ is equipped with a Lipschitz flow functional $\mathbf{F}^t : \mathcal{A}_{\mathbf{x}} \to \mathcal{A}_{\mathbf{x}}$ defined as:

$$\mathbf{F}^t = \mathbf{x}_0 + \int_{t_0}^{t_0+t} f(\mathbf{x}(\tau))d\tau. \tag{2}$$

This map dictates the flow of the states from the initial conditions $\mathbf{x}(t_0) \equiv \mathbf{x}_0$ over $t_0 + t$ time steps. For the general form of the system (1) a scalar function $h : \mathcal{A}_{\mathbf{x}} \to \mathbb{R}$ is attached, this will be referred to as an *observable* and $\mathcal{F} \subset \mathcal{C}^1$ is the Banach space of observables. A *Koopman Operator* $\mathcal{K}_{\mathbf{F}} : \mathcal{F} \to \mathcal{F}$ engulfs how the observables flow in time over the manifold $\mathcal{A}_{\mathbf{x}}$ in the same manner as the flow map $\mathbf{F}^t$. Assuming the existence of a finite-dimension Koopman invariant subspace $\mathcal{F}_m \subset D_{\mathcal{G}_{\mathcal{K}}}$ and $\Psi^\top = \begin{pmatrix} \psi_1 & \cdots & \psi_m \end{pmatrix}$ is the set of observables which form a basis for $\mathcal{F}_m$, with $\mathcal{K}^t_{\mathbf{F}} = \mathbf{G}^\top \in \mathbb{R}^{m \times m}$ where $\mathbf{G}$ is the matrix representation of the Koopman Operator, the dynamics from (1) with the associated flow map (2) can be linearly described by a lifted system in a finite manner in following relation form: $\dot{\Psi}(\mathbf{x}) = \mathcal{K}^t_{\mathbf{F}}\Psi(\mathbf{x})$. A proposed condition for the existence of a finite-dimension Koopman Operator is $\nabla_{\mathbf{x}}\Psi \cdot f(\mathbf{x}) \in \text{Span}\{\Psi\}$. The easiest manner in which this condition is met is to choose the observables which are also eigenfunctions. This paper proposes the following coordinate change for the system from (1) with its Koopman Operator:

$$\mathbf{z} = \Theta(\mathbf{x}) = \begin{pmatrix} \theta_1(\mathbf{x}) \\ \theta_2(\mathbf{x}) \\ \hline \theta_3(\mathbf{x}) \end{pmatrix} = \begin{pmatrix} x_1 \\ x_2 \\ \hline x_1 \cdot x_2 \end{pmatrix}; \quad \mathcal{K}^t_{\mathbf{F}} = \left(\begin{array}{c|c} A_{2\times 2} & \Xi_{2\times 1} \\ \hline \Gamma_{1\times 2} & \Lambda_{1\times 1} \end{array}\right) = \left(\begin{array}{cc|c} -k_{11} & k_{12} & -n^{-1} \\ k_{21} & -k_{22} & 0 \\ \hline k_{11} & k_{22} & -n \end{array}\right), \tag{3}$$

The resulting system can be projected onto the perspective output using a bordered output matrix $\overline{\Upsilon} \in \mathbb{R}^{m \times m}$.

$$(\Sigma_{\mathcal{K}}) : \begin{cases} \dot{\mathbf{z}} = \overline{\Upsilon} \cdot \mathcal{K}^t_{\mathbf{F}} \cdot \mathbf{z} + \overline{B} \cdot u; \\ y = \psi(\Theta(\mathbf{x})) = \overline{C} \cdot \mathbf{z}, \end{cases} \tag{4}$$

where $\overline{B} = \begin{bmatrix} B & 0_{1\times\mu} \end{bmatrix}^\top$, $\overline{C} = \begin{bmatrix} C & 0_{1\times\mu} \end{bmatrix}$ with $B = \begin{bmatrix} 0 & 1 \end{bmatrix}^\top$ the input matrix from (1) and $C = \begin{bmatrix} 1 & 0 \end{bmatrix}$ an output matrix.

2 Results and discussion

The choice in the parameters values from (1) is the following $k_{11} = 10.1; k_{12} = 2.1; k_{21} = 4.1; k_{22} = 12.1; n = 5.1$. For the purposes of the current paper and without the loss of generality, the vector trajectories of the systems from (1) and (4) will be compared assuming no input $u(t) \equiv 0$ and non-zero initial conditions. In order to arrive at objective results a simulation was made for each system with the same initial conditions, and the phase space was constructed.

In Figure (1a) the phase portrait of the Koopman system can be observed if the projection matrix is constructed as follows: $\overline{\Upsilon} = \text{diag}(1, 1, 0)$ the trajectory of the states for each initial condition can be projected onto $x_1 - x_2$ plane. By overlaying the nonlinear phase space of the system with the aforementioned projection, it can be observed that the trajectories are highly similar. This indicates that the Koopman linear system is an effective approximation of the dynamics and behaviour of the initial system. This can be observed in Figure (1b) where the phase space of the nonlinear system (1) is overplayed with the projection of the Koopman system as previously mentioned. It is also worth mentioning that this method has its drawbacks, for instance, it might be affected if the nonlinear system has a limit cycle, as this can not be incorporated by nature into any linear approximation.

The construction of the matrix operator $\mathcal{K}^t_{\mathbf{F}}$ needs to be made with educated decisions about the system given that as of now there is no theory regarding the matrix components.

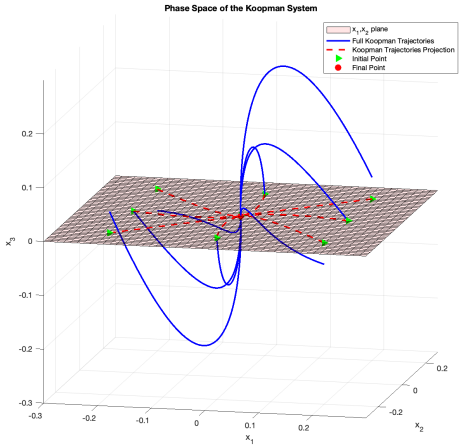

(a) 3D Phase Space Of Koopman System from different initial conditions and the projection plan of the trajectories

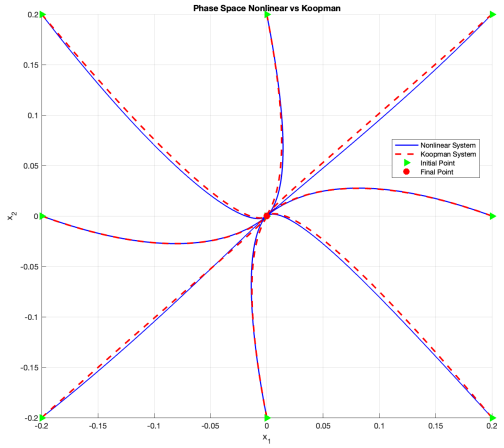

(b) 2D Phase Space of the Nonlinear System compared with the projected trajectory of the Koopman System

3 Conclusions and Future work

It is presented a method of linearization for a specific class of systems via the Koopman Operator. This is presented as a coordinate transformation into some higher-dimensional manifold for which the projection of the state trajectories onto the plane formed by the initial states has almost the same evolution as the initial system. This results in the system being linearized. Future work might provide the theory regarding the Koopman Linearization for a larger variety of systems.

Acknowledgments

This work was financed by a grant of the Romanian Ministry of Research, Innovation and Digitization, PNRR-III- C9-2022-I8, grant number 760068/23.05.2023.

References

[1] R.N. Bergman,Y.Z. Ider, C.R. Bowden,C. Cobelli, Quantitative estimation of insulin sensitivity, *American Journal of Physiology-Endocrinology And Metabolism*, pp. 667–677, 1979.

[2] I.Abraham, G.De La Torre, T.D.Murphey, *Model-based control using Koopman operators*, arXiv preprint arXiv:1709.01568, 2017.

[3] L.C.Iacob, R.Toth, M.Schoukens, *Koopman form of nonlinear systems with inputs*, Automatica, 162, p.111525, 2024.

[4] P. Bevanda, S. Sosnowski, S. Hirche, Koopman operator dynamical models: Learning, analysis and control, *Annual Reviews in Control*, 52, pp.197-212, 2021.

OPTIMIZING IMMUNOTHERAPIES FOR IMPROVED CANCER TREATMENT

Anne M. Talkington[1*] **Anthony J. Kearsley**[1]

[1] National Institute of Standards and Technology, United States

[1*]anne.talkington@nist.gov

Special Session #2: Mathematical Modeling of Biological Systems

Abstract: Despite decades of promising leads, a disparity remains between preclinical results and success rates of clinical trials for cancer therapies. This disparity arises from complexity in all levels, or scales, of the drug's intended trajectory, from interference with delivery to inefficiency in targeting. We can define models across scales of organ systems and cellular dynamics to investigate the desirable properties of an ideal drug. Here we address the question of efficiency in an immune checkpoint blockade system. When an immune cell interacts with an antigen presenting cell, the process triggers a cellular state transition dependent on the stimulating or exhausting nature of the interaction. Immune checkpoint blockade, in turn, seeks to disrupt unfavorable, or exhausting, interactions in the tumor immune system[1, 2]. By perturbing blockade efficiency, we can optimize a drug's dosage and receptor binding affinity leading to improved immune cell state balance. We demonstrate a novel dynamical system for optimizing immunotherapeutic strategies and present predictions for target blockade efficiency. We then discuss an agent-based model system, representing interactions of cancer cells, T cells, and standard-of-care treatments designed to block inhibitory receptors, as a means of testing blockade efficiency under different binding affinities and dosing conditions. With the added cellular-level intuition and spatial dynamics, we can account for how the system responds to changes in blockade efficiency, and test various means of achieving the desired efficiency. Together, these complementary models promise a solution to the optimal control problem of maximizing the success rate of immune checkpoint inhibition.

keywords: Dynamical systems; immunotherapy; cancer

MSC2020: 92-10; 37N25; 34C60.

References

[1] Drew M. Pardoll, The blockade of immune checkpoints in cancer immunotherapy, Nature Reviews Cancer, **12** (2012), 252-264.

[2] Julian A. Marin-Acevedo et al., Next generation of immune checkpoint therapy in cancer: new developments and challenges, Journal of Hematology & Oncology, **11**(39) (2018).

The dynamics of vaccination strategies depending on the perceived vaccination-infection morbidity risks

José Martins[1⋆] **Alberto Pinto**[2]

[1] LIAAD-INESC TEC, Portugal
[2] School of Technology and Management, Polytechnic of Leiria, Portugal
[3] Faculty of Sciences, University of Porto, Portugal

[1⋆]jmmartins@ipleiria.pt

Abstract: Special Session 12 - Dynamical Systems, Games and Applications
In [1], Martins and Pinto introduced the evolutionary vaccination dynamics of the population vaccination strategy for the basic reinfection SIRI model. In this work, we add the dynamics of the relative morbidity risk, which compares the morbidity risk of the vaccine with the morbidity risk of the disease. Using the epidemiological SIRI model, that considers both reinfection and temporary immunity, we study the evolution of the homogeneous population vaccination strategy when the individuals vaccination strategies and the relative morbidity risks evolve over time.

keywords: Game theory; SIRI model; vaccination; reinfection.

MSC2020: 91A12; 91A40; 92B05.

Acknowledgments

This work is financed by National Funds through the Portuguese funding agency, FCT - Fundação para a Ciência e a Tecnologia, within project LA/P/0063/2020. DOI 10.54499/LA/P/0063/2020

References

[1] J. Martins, A. Pinto, Bistability of Evolutionary Stable Vaccination Strategies in the Reinfection SIRI Model, Bulletin of Mathematical Biology, **79**(4) (2017), 853–883.

International Conference on Mathematical Analysis and Applications in Science and Engineering ICMA²SC'24

ISEP **Porto-Portugal, June 20 - 22, 2024**

POPULATION DYNAMICS IN THE CONTEXT OF THE INFLUENCE OF COVID-19

Nicolae Herisanu[1,2*] **Bogdan Marinca**[1] **Vasile Marinca**[1,2]

[1] University Politehnica Timisoara, Romania
[2] Romanian Academy Branch of Timisoara, Romania

[1*]nicolae.herisanu@upt.ro

Abstract: The first objective of this research is to find an approximate analytical solution for the model of Susceptible-Exposed symptomatically infected-Asymptomatically infected or Hospitalized and Recovered group (SEIAHR). The mathematical model depending on six nonlinear differential equations is presented for a complex problem. Nonlinear equations are studied with the help of Optimal Auxiliary Functions Method which is a very powerful tool to solve a nonlinear problem. The new proposed approach is based on the presence of some auxiliary functions, the involvement of the convergence-control parameters, the original construction of the initial approximation and first iteration and large freedom to select the methodology for determining the optimal values of the convergence-control parameters. The second objective is related to the stability of the model. The local stability is carried out to the disease free and endemic equilibrium points. The Hopf and saddle-node bifurcation are studied, and Routh-Hurwitz criterion is adopted. For global stability, the Lyapunov function and LaSalle's invariance principle are used.

keywords: Novel coronavirus; Pandemic SEIAHR model; Lyapunov function

MSC2020: 92C60; 34D23; 34G20.

1 Introduction

The appearance of the Middle East Respiratory Syndrome Coronavirus in 2012 (MERS-CoV) and of the new virus: Severe Acute Respiratory Syndrome Coronavirus 2 (SARS-CoV-2) led to considerable turmoil all around the world. After the spread of the novel coronavirus out of Wuhan, Hubei Province of China, the evolution of the epidemic worldwide shows some differences in many other countries. Infections diseases are a leading cause of death worldwide and can spread directly or indirectly peer to peer, or from animals and birds to humans.

In our study we found an approximate analytical solution for the mathematical model with six nonlinear differential equations of Susceptible-Exposed-symptomatically-infected-Asymptomatically -infected-isolated or Hospitalized and Recovered group (SEIAHR). For this aim we consider an

original and very efficient procedure: Optimal Auxiliary Functions Method (OAFM) which assures a high efficiency by means of some auxiliary functions and of the optimal convergence-control parameters. Our technique does not suppose the presence of small or large parameters in the governing equation or in the boundary/initial conditions. We have a large freedom to choose the auxiliary functions and the number of parameters. These optimal convergence-control parameters can be determined by rigorous mathematical procedures. Our method is effective, and easy to apply. The local stability of the proposed model is studied using Routh-Hurwitz criteria. The Hopf and saddle node bifurcation are studied for the disease free and endemic equilibrium points in the space with two parameters. Also, the global stability is carried out by means of Lyapunov function for the disease-free equilibrium point and then for the endemic equilibrium point. By means of La Salle's invariance principle we show that these equilibrium points are global asymptotically stable.

The total population is divided into the following six categories: Susceptible (S), Exposed (E), Infected (I), Asymptomatic (A), Hospitalized (H) and Recovered (R) when no vaccine is available. The governing nonlinear differential equations are:

$$\begin{aligned}
\dot{S} &= a - \frac{a_1(a_2 I + A)S}{N} - a_8 S \\
\dot{E} &= \frac{a_1(a_2 I + A)S}{N} - (a_4 + a_8)E \\
\dot{I} &= (I - a_3)a_4 E - (a_5 + a_6 + a_8)I \\
\dot{A} &= a_3 a_4 E + (a_7 + a_8 + a_{10})A \\
\dot{H} &= a_5 I + a_{10} A - (a_8 + a_9 + a_{11})H \\
\dot{R} &= a_6 I + a_7 A + (a_9 + a_{11})H - a_8 R
\end{aligned} \tag{1}$$

where the dot denotes differentiation with respect to time and N = S+ E + I + A + H + R . The parameters a_i $i = \overline{1,n}$ are positive and well-defined.

For every component equation from (1) are established the linear and nonlinear operators, in which the linear operators do not necessarily coincide entirely with the linear part of the governing equation.

To prove the accuracy of our procedure, a numerical example is considered. The approximate solutions are graphically compared with the corresponding numerical integration of Eq.(1). We obtain that the approximate solutions are nearly identical with the numerical solutions.

2 Results and discussion

We study equilibrium, local and global stability, because it is known that a slight disturbance or change in the system can influence equilibrium points. Based on Eq.(1), the equilibrium points are obtained from the equations:

$$\frac{dS}{dt} = 0, \frac{dE}{dt} = 0, \frac{dI}{dt} = 0, \frac{dA}{dt} = 0, \frac{dH}{dt} = 0, \frac{dR}{dt} = 0 \tag{9}$$

After some manipulations, the disease-free equilibrium point and the endemic equilibrium point are, respectively:

$$P_{1e}\left(\frac{a}{a_8}, 0,0,0,0,0\right) \tag{10}$$

$$P_{2e}(\overline{S}, \overline{E}, \overline{I}, \overline{A}, \overline{R}) \tag{11}$$

where $\overline{S}, \overline{E}, \overline{I}, \overline{A}, \overline{R}$ are known.

If f_i, $i = \overline{1,6}$ are the functions which appear in the right side of Eq.(1), then the Jacobian matrix at equilibrium points (10) and (11) is

$$J(P_{ke}) = \left(\frac{\partial f_i}{\partial \theta}\right), \quad \theta \in \{S, E, I, A, H, R\}, \quad k = 1,2 \tag{12}$$

The characteristic equation corresponding to the equilibrium point P_{1e} and P_{2e} are respectively

$$(\lambda + a_8)^2(\lambda + a_8 + a_9 + a_{11})(\lambda^3 + \Pi_1\lambda^2 + \Pi_2\lambda + \Pi_3) = 0 \tag{13}$$

$$(\lambda + a_8)(\lambda + a_8 + a_9 + a_{11})(\lambda^4 + \mathrm{X}_1\lambda^3 + \mathrm{X}_2\lambda^2 + \mathrm{X}_3\lambda + \mathrm{X}_4) = 0 \tag{14}$$

where Π_i, i=1,2,3 and X_j, j=1,2,3,4 are known from Eqs.(10) and (11).

For the disease-free equilibrium point and for endemic equilibrium point are established the borderline of Hopf bifurcation, the boundary of the saddle-node bifurcation and the domain of asymptotically stable in the parameter space (a_1,a_2).

Finally, we study the global stability of the two equilibrium points by means of Lyapunov function and La Salle's invariance principle.

For the disease-free equilibrium point P_{1e}, the Lyapunov function is

$$L(t) = \frac{1}{2}[S(t) - \frac{a}{a_8} + E(t) + I(t) + A(t) + H(t) + R(t)]^2 \quad (15)$$

Using the equation

$$\dot{N}(t) = a - a_8 N(t), \quad N(0) = S_0 \quad (16)$$

whose solution becomes

$$N(t) = \frac{a}{a_8} + \left(S_0 - \frac{a}{a_8}\right) e^{-a_8 t} \quad (17)$$

the derivative of the Lyapunov function is

$$\dot{L}(t) = -a_8(N - S_0)^2 \quad (18)$$

such that the disease-free equilibrium point P_{1e} is global asymptotically stable.

For the endemic equilibrium point, the Lyapunov function is defined as

$$L(t) = S(t) - \bar{S} + E(t) - \bar{E} + I(t) - \bar{I} + A(t) - \bar{A} + H(t) - \bar{H} + R(t) - \bar{R} \quad (19)$$

where $\bar{S}, \bar{E}, \bar{I}, \bar{A}, \bar{R}$ are known from Eq.(11).

In this case, the derivative of the Lyapunov function is

$$\dot{L}(t) = -a_8(N - \bar{N}) < 0 \quad (20)$$

where $\bar{N} = \bar{S} + \bar{E} + \bar{I} + \bar{A} + \bar{R}$. It follows that $\dot{L}(t)$ is negative and $\dot{L}(t) = 0$ only if $N = \bar{N}$ or equivalent:

$$S(t) = \bar{S}, E(t) = \bar{E}, I(t) = \bar{I}, A(t) = \bar{A}, H(t) = \bar{H}, R(t) = \bar{R} \quad (21)$$

It is clear that the endemic equilibrium point P_{2e} is global asymptotically stable.

3 Conclusions and Future work

The mathematical model of SEIAHR is presented. The system of six nonlinear differential equations is solved with a high accuracy by means of OAFM. The main novelties of our technique are the presence of the auxiliary functions and the convergence-control parameters. It should be emphasized that we do not need the presence of small or large parameters. The local stability is carried out for the disease-free and endemic equilibrium points varying two parameters. The Hopf, saddle-node bifurcation and domain of asymptotically stable are studied. Global stability is analyzed by Lyapunov function and La Salle's invariance principle.

In future works should be established the influence of the vaccination in our model and the reproduction number for quantify the transmissibility of the COVID-19.

References

[1] C.T. Deressa, Y.D. Musa, G.F. Deressa, Optimal control and sensitivity for transmission dynamics of coronavirus, Results in Physics, **19** (2020), 103642.

[2] X.P.Li, A. Bayati, A. Zeh, A rigorous study of fractional order COVID-19 model via ABC derivations, Results in Physics, **29** (2021), 104737.

[3] B. Marinca, V. Marinca, C. Bogdan, Dynamics of SEIR epidemic model by optimal auxiliary functions method, Chaos, Solitons and Fractals, **147** (2021), 110949.

International Conference on Mathematical Analysis and Applications in Science and Engineering
ICMA^{2}SC'24
ISEP Porto-Portugal, June 20 - 22, 2024

POTENTIAL IMPACT OF A DEMONSTRATION ON COVID-19 CONTAGION: AN APPLICATION OF A METHOD

Conceição Leal[1,2⋆] **Leonel Morgado**[1,2] **Teresa A. Oliveira**[1,2]

[1] Universidade Aberta, Portugal
[2] CEAUL, FCUL, Portugal
[3] INESC TEC, Portugal

[1,2⋆]conceicao.leal2010@gmail.com

Abstract: There is evidence that some outdoor events may have contributed to the spread of COVID-19. We updated an empirical methodology based on regression modeling and hypothesis testing to analyze the potential impact of a demonstration that took place in Lisbon, within the scope of the 'Black Lives Matter' context, on the contagion pattern in the region where this event occurred. We find that in the post-impact period there was no acceleration in the number of cases in the region, unlike in a prior event in the region. The proportion of counties where there was a potential impact of the event is not statistically significant. This result demonstrates that not all outdoor events contributed to the spread of COVID-19 and exemplifies how to apply the selected empirical methodology.

keywords: Time series segmentation; Modeling COVID-19 data; Geographic heterogeneous impacts.

MSC2020: 49-XX; 34-XX; 92-XX.

1 Introduction

The COVID-19 coronavirus disease is characterized by a high level of human-to-human transmission hazard. Some outdoor events played an important role in the spread of COVID-19 [1]. A retrospective analysis of the change in the incidence rate of COVID-19 during the two weeks after outdoor mass gatherings in low-incidence US counties revealed a mean increase of 1.5 times [4]. To analyze the potential impact of large-scale public events, in an earlier work [3], we implemented an empirical analysis based on regression modeling and hypothesis testing for two periods: before the potential impacts of the event are reported (pre-impact) and after potential impacts have been reported (post-impact). We use this approach to analyze the potential impact in COVID-19 contagion of the demonstration of thousands of people in Lisbon, joining the "Black Lives Matter" movement, on June 6, 2020. We first observed that there was no acceleration in contagion in the region where the event took place (Lisbon Metropolitan Area – AML) after it was held (Fig 1b) similarly to what happened in the rest of the country. This is in contrast to what was seen in the May 1*st* event studied in the previous study [3] (Fig. 1a). Then, we analyzed whether this pattern of no acceleration of contagion was geographically homogeneous across the AML counties.

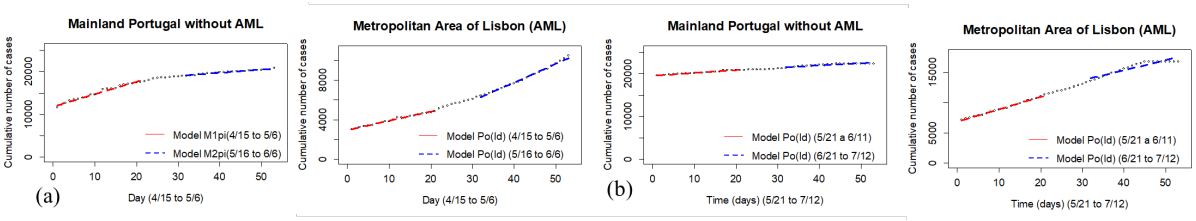

Figure 1: Number of cumulative cases: Portugal & Lisbon region (AML, Portuguese-language acronym): (a) May 1*st* event; (b) "Black Lives Matter" event

2 Results and discussion

2.1 Data

Data on the cumulative number of COVID-19 cases in Portuguese counties come from the daily situation reports issued from May 21 to July 12, 2020, by the National Health Directorate. Data were collected daily by the authors, directly from official reports and from the online repository of the "Data Science for Social Good Portugal" community, which extracted these data daily and made them publicly available (*https://github.com/dssg-pt/covid19pt-data*). Following the method presented in an earlier work [3], the analysis was implemented using R software tools and applied to data matching two timeframes: an S1 period where possible event contagion had not yet been reported (pre-impact) and an S3 period where any such contagion would expectably have been reported (post-impact). In the intermediate period S2, any event-related contagion reporting would be developing and we ignore it because, to detect if an impact occurred, it is not relevant to detect its ongoing development, only its existence after the impact is complete.

2.2 Times series segmentation

To define the S1, S2, and S3 periods from publicly available data, previous work [3] estimated the reporting delay using the country-level data (i.e., nationally) on new daily cases per symptom emergence date, via graphical measuring of the only data source: bar charts in public daily reports. This was done from April 17 to May 9, 2020, and later confirmed by a public statement of the National Health Directorate (ibid.).

To estimate the number of days, X, until the number of reported cases stabilised on day t, we used a Shewhart Control Chart targeting the zero daily variation of the reported daily number. We took the value 4.1 for the reporting delay [3]. Combining the expectation that less than 2.5% of infected people will show symptoms within 2.2 days after infection [3] and the average reporting delay of 4.1 days, an extremely small number of cases of infection on June 6, 2020 will have been reported until June 12. So, the first segment (S1) refers to the period from May 21 to June 11. By Lauer et al., [2], 97.5% of cases will show symptoms within 11.5 days after infection. So, the intermediate period, in which any contagions that occurred during the event will be reported, runs from June 12 to June 20. This period corresponds to the second segment (S2). S3 corresponds to the period from June 21 to July 12, 2020.

2.3 Models

For the S1 and S3 periods under analysis, we defined Poisson regression models, with Identity (model 1) and Log link functions, adjusted to $S1 \cup S3$ data, for the Lisbon region, for the rest of the country (Fig. 1), and for individual counties in the AML (Lisbon) region (Fig. 2). In the

models, we considered the interaction between time and a dummy variable that identifies the periods S1 and S3, to test the β homogeneity coefficient between periods S1 and S3.

$$\begin{aligned} &Po(Id): \quad g(E(NCases)) = \beta_0 + \beta_1 t + \beta_2 \text{Dummy} + \gamma(\text{Dummy} \times t) \\ &g(E(NCases)) = E(NCases) \quad \text{(Identity link function)} \\ &NCases \sim Po(g(E(NCases))) \end{aligned} \tag{1}$$

t is the time, in days, between May 21 and July 12, 2020, $g()$ designates the link function and $E()$ is the expected value.

2.4 Testing homogeneity of regression coefficients - some results

In the methodology, we systematically used one-way ANCOVA to test the homogeneity of coefficients in the S1 and S3 periods for the $Po(Id)$ and $Po(Log)$ models. When the homogeneity hypothesis was rejected, we employed graphical visualisation to determine the nature of the differences and used the Likelihood Ratio test to statistically assess whether the rate of change in the number of COVID-19 cases decreased from S1 to S3.

Counties where the hypothesis of homogeneity of variation rates was not rejected for $Po(Id)$ (i.e., the hypothesis of maintaining the growth pattern after the event was not rejected), and counties where this hypothesis was rejected but graphical visualisation and the Likelihood Ratio test did not indicate an acceleration of case growth from S1 to S3, even suggesting a reduction, were included in the group of counties for which the growth pattern of cases did not accelerate from S1 to S3.

For other counties, we tested the homogeneity of the $Po(Log)$ model coefficients. Subsequently:

- Counties where the homogeneity of $Po(Log)$ model coefficients was also rejected were placed in the group of counties which exhibited case growth acceleration from the S1 to the S3 period.

- For counties where there was an acceleration in the case growth rate from S1 to S3 (the hypothesis of homogeneity of $Po(Id)$ coefficients was rejected), but where the hypothesis of coefficient homogeneity for $Po(Log)$ was not rejected, it can be inferred that such exponential growth had already been occurring in S1, and that the growth rate could already be accelerating exponentially. Thus, it is expected that the exponential model will continue to be the best fit for S3.

  Using the AIC criterion, we can check which model better fits each period. If $Po(Log)$ fits better to S3, then there was no acceleration; if $Po(Log)$ fits better to S1 and $Po(Id)$ fits S3 better, we extend the S1 period by one month earlier to evaluate which model fits each period best. If both are linear ($Po(Id)$), then it is assumed that the growth pattern has changed. If Po(Id) has the best fit for S1 and Po(Log) has the best fit for S3, then we assume that the growth pattern has not changed from one period to the other.

Based on the results obtained, it is found that for all counties in the AML, from period S1 (May 21 to June 11) to period S3 (June 21 to July 12), there is no statistical evidence of an increase in the growth rate of the cumulative number of COVID-19 cases. In all counties, either the null hypothesis of homogeneity of growth rates in the two periods was not rejected, or it was rejected in favour of the alternative hypothesis of a decrease in this rate.

Therefore, based on the implemented methodology, it is concluded that there is no statistical evidence to support that the "Black Lives Matter" demonstration had an effect on the spread of COVID-19 in the AML, contrary to what was observed in the May 1st demonstration ([3])

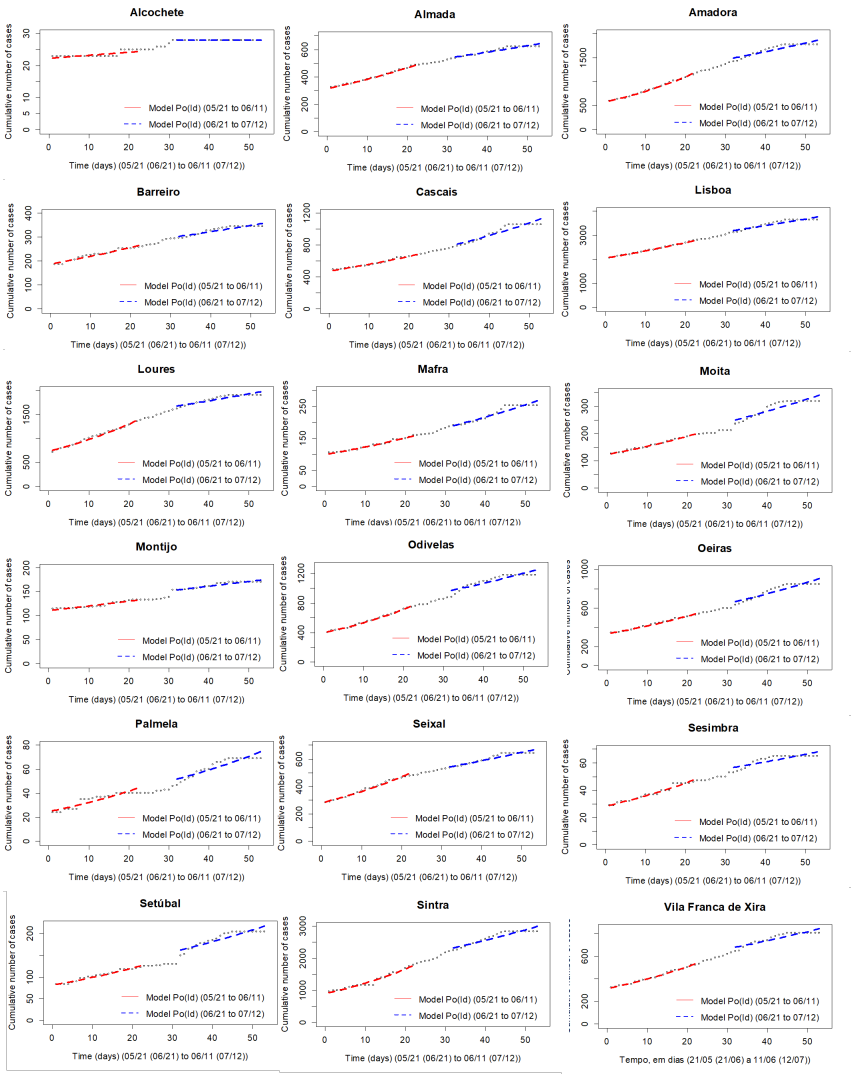

Figure 2: Poisson regression model with *Identity* link function, adjusted to S1 and S3 and observed data.

References

[1] Kucharski, A. J., Russell, T. W., Diamond, C., Liu, Y., Edmunds, J., Funk, S., ... Flasche, S. (2020). Early dynamics of transmission and control of COVID-19: a mathematical modelling study. The lancet infectious diseases, 20(5), 553-558.

[2] Lauer, S. A., Grantz, K. H., Bi, Q., Jones, F. K., Zheng, Q., Meredith, H. R., ... Lessler, J. (2020). The incubation period of coronavirus disease 2019 (COVID-19) from publicly reported confirmed cases: estimation and application. Annals of internal medicine, 172(9), 577-582.

[3] Leal, C., Morgado, L., Oliveira, T. A. (2023). Mathematical and Statistical Modelling for Assessing COVID-19 Superspreader Contagion: Analysis of Geographical Heterogeneous Impacts from Public Events. Mathematics, 11(5), 1156.

[4] Miron, O., Yu, K. H., Wilf-Miron, R., Davidovitch, N. (2020). COVID-19 infections following outdoor mass gatherings in low incidence areas: retrospective cohort study. medRxiv, 2020-10.

International Conference on Mathematical Analysis and Applications in Science and Engineering
ICMA^{2}SC'24
ISEP Porto-Portugal, June 20 - 22, 2024

Relative risk of COVID-19 contagion in Mozambique

Teresa A. Oliveira[1,2⋆] **M. Filomena Teodoro**[3,4] **Élio Taero**[5]

[1] Departamento C&T, Universidade Aberta, Lisboa, Portugal
[2] CEAUL, Universidade Lisboa, Lisboa, Portugal
[3] CEMAT, Center for Computational and Stochastic Mathematics, Instituto Superior Técnico, 1048-001 Lisboa, Portugal
[4] CINAV, Center of Naval Research, Naval Academy, Instituto Universitário Militar, Portuguese Navy, 2810-001 Almada, Portugal
[5] Instituto Superior Politécnico de Tete, Moçambique

⋆Teresa.Oliveira@uab.pt

Abstract: COVID-19 is a viral disease with significant impacts on the public health of a country, with emphasis on health systems, due to its rapid spread. To understand its form of transmission and analyze the spatial distribution of COVID-19 cases, a set of mathematical and statistical models which are applied in the modeling of infectious diseases are described, as well as several useful methods and techniques for risk assessment in epidemiology. In the present manuscript it is evaluated and estimated the risk of COVID-19 contagion in Mozambique.
The ICAR, BYM, BYM2 and Leroux models, which were formulated based on the hierarchical Bayesian structure, were proposed to capture the spatial dependence between neighboring regions, allowing an estimation and more accurate prediction of relative risk. These models were adjusted using the package R-INLA and selected using the Deviation Information and Watanabe-Akaike criteria in addition to the Marginal Pseudo-Likelihood Logarithm criteria and graphical visualization.
Tests to detect clusters of the disease were also applied in this work. Upon concluding this project, it became clear that in comparative terms the region Southern Mozambique presented a high relative risk of COVID-19 contagion, with emphasis on the City of Maputo, which presented a very high value.

keywords: covid-19; R-INLA; disease mapping; hierarchical Bayesian models; statistical modeling.

MSC2020: 62C10; 62A09; 91B05.

1 Introduction

Efforts have been made by the scientific community to study the pandemic and its impact on the lives of citizens and the economy of countries and, in particular, in research in epidemiology, with a view to understanding the relationship between some risk factors associated with the disease. As an example, refer to [1, 2, 3, 4, 5, 6, 7, 8, 9, 10]. Given these antecedents, which motivated the authors to carry out this work and embark on this area of knowledge, in order to contribute to the Mozambican scientific community, with elements of spatial epidemiology based on modeling, in this case in particular statistical modeling, involving spatial models with

the hierarchical Bayesian approach, taking into account disease mapping. The choice of disease mapping associated with hierarchical Bayesian models (HBM) is an area to be explored extensively in Mozambique, as not much epidemiological studies carried out in the case of COVID-19 are published for studies. This scenario led the author of the thesis [11] to embark on filling the gap found in this area.

Summarizing, the main focus of the present work was to have comprehensive analysis that allowed an assessment of the relative risk for COVID-19 cases in Mozambique, adopting as objective to analyze the risk of COVID-19 contagion in Mozambique using HBM and mapping of illness.

HBM are part of models made up of several levels. The adoption of these levels means that different sources of variations are captured or rather, in these models, each level responds to different sources of variations, thus being able to contribute to improving the quality of parameter estimates. These models are ideal for developing spatially structured models [12].

A HBM, in its structure, represents a statistical model composed of three levels. At each level it is represented by a model, and these models are, respectively, applied to represent the data, the process and the parameters. The models adopted at each level are specified to deal with the three sources of uncertainty that are associated with the data, the process and the parameters [13]. For example, for the case of disease mapping, the HBM is applied to the case of area data (aggregated data) and, in the first component, the model for the data can be the Poisson model, as we know the counts or rates that are the characteristics of the epidemiological data (as they are non-negative data) suit this model, in the second component, the model for the process, which will describe the relative risk (it could be mortality or contagion, or another necessary) can be a model consisting of two random effects (spatially structured and spatially unstructured) and the risk given with a logarithmic link function, due to the choice of the Poisson model in the previous level. And if the spatially structured and spatially unstructured components are adopted, these will represent the BYM that it is addressed in [11] and in the third component, the model for the parameters, which can be adopted gamma, normal, uniform and other distributions. The choice of distribution in this third component is related to the chosen HBM, for more details on this choice see the texts by [14] and [15].

2 Results and Final Remarks

In figure 1 we find of the hierarchy map of the Provinces of Mozambique based on the risk of COVID-19 contagion.

Mozambique shows a growing COVID-19 contagion trend as that moves from the North to the South of the country. The two highest levels of categorization of risk, namely Severo and Alto, is made up of the provinces in the southern region of country, while the provinces of the central region except Zambézia (listed in the fourth level) are included in the third level of risk categorization and the provinces in the northern region, except Niassa (listed in the third level), are listed in the fourth level of categorization of the risk. Therefore, the most energetic actions of health authorities must focus on for the city and province of Maputo. At the peak of the disease, it was in this region that more restrictive measures were effectively taken to combat COVID-19 (mandatory home call at night).

Acknowledgments

The first author was supported by Portuguese funds *The Portuguese Foundation for Science and Technology* (FCT), through the project `UIDB/Multi/00006/2020`.

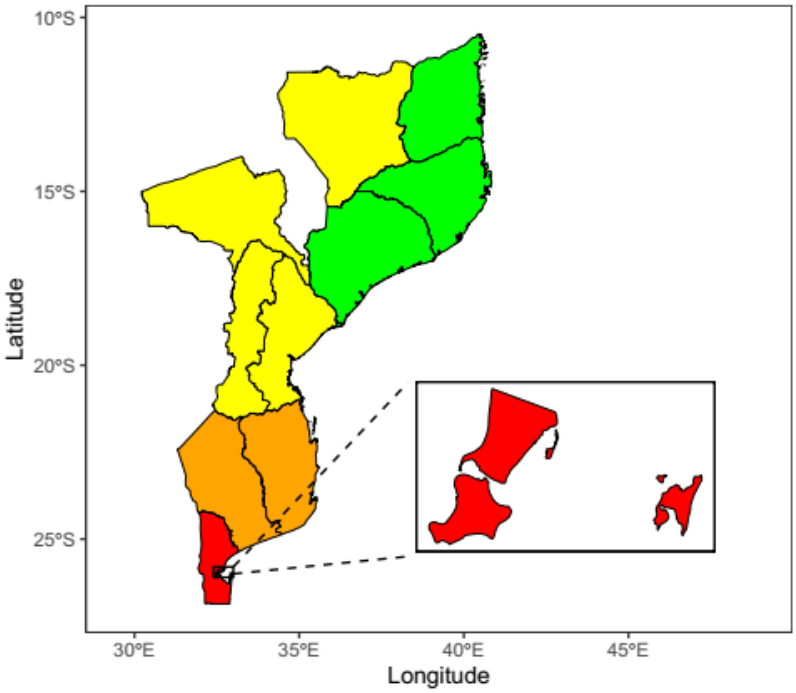

Figure 1: Hierarchy of the Mozambique Provinces. Legend: Red: severe risk, Orange: high risk, Yellow: moderate risk, Green: low risk. Source:[11].

The second author was supported by Portuguese funds *The Portuguese Foundation for Science and Technology* (FCT), through the *Center for Computational and Stochastic Mathematics* (CEMAT), University of Lisbon, Portugal, project `UIDB/Multi/04621/2020`, DOI: `(https://doi.org/10.54499/UIDB/04621/2020)` and through the *Center of Naval Research* (CINAV), Naval Academy, Portugal.

References

[1] J. Wang, K. Tang, K. Feng, W. Lv, and et al., High temperature and high humidity reduce the transmission of covid-19, (2020). Available at `SSRN,3551767:2020b`.

[2] B. Z. Diop, M. Ngom, C. P. Biyong, and J. N. P. Biyong, The relatively young and rural population may limit the spread and severity of covid-19 in africa: a modelling study, BMJ global health, **5**(5) (2020), e002699.

[3] P. J. Rosenthal, J. G. Breman, A. A. Djimde, C. C. John, and et al., Covid-19: shining the light on africa. The American journal of tropical medicine and hygiene, **102**(6) (2020), 1145.

[4] J. N. Nkengasong and W. Mankoula, Looming threat of Covid-19 infection in Africa: act collectively, and fast, The Lancet, **395**(10227) (2020), 841–842.

[5] H. F. Martins and R. Hansine, Análise epidemiológica e demográfica da covid-19 em África. Anais Do Instituto de Higiene e Medicina Tropical, **19**(2020), 7–42.

[6] E. M. Cambaza, G. C. Viegas, and et al., Potential impact of temperature and atmospheric pressure on the number of cases of covid-19 in Mozambique, southern Africa, Journal of Public Health and Epidemiology, **12**(3) (2020), 246–260.

[7] C. Boakye-Agyemang and S. Oka, The african region reinforces preparedness for novel coronavirus. World Health Organization, (2020). https://www.afro.who.int/news/african-region-reinforcespreparedness-novel-coronavirus. Accessed at April 18th 2023.

[8] J. W. Cabore, H. C. Karamagi, H. Kipruto, J. A. Asamani, and et al., The potential effects of widespread community transmission of sars-cov-2 infection in the world health organization African region: a predictive model, BMJ global health, **5**(5) (2020), e002647.

[9] A. E. Chongo, A. R. Sineque, O. Augusto, J. Sumbana, and et al., Covid-19 reproduction rate: relevance in the Mozambican context, Revista CientÃfica da UEM: Série Ciências Biomédicas e Saúde Pública, (2020).

[10] M. F. Teodoro, T. Oliveira and É. Taero, Covid-19 infection and risk analysis: a short introduction. Biometrics & Biostatistics International Journal, **12**(4) (2023), 121–125.

[11] Élio Taero, Análise e Avaliação do Risco de Contágio da COVID-19 em Moçambique. PhD Thesis in Applied Mathematics and Modelation. Advisers: Teresa A. Oliveira and M. Filomena Teodoro, Universidade Aberta. Lisboa. Portugal. (Under evaluation)

[12] R. S. Bivand, E. J. Pebesma, V. Gómez-Rubio, *Applied spatial data analysis with R*, 2nd edition. New York: Springer (2013). DOI:https://doi.org/10.1007/978-1-4614-7618-4

[13] R. P. Haining, G. Li, *Modelling Spatial and Spatial-Temporal Data: A Bayesian Approach*. New York: Chapman and Hall/CRC (2020). DOI:https://doi.org/10.1201/9780429088933

[14] M. Blangiardo and M. Cameletti, *Spatial and spatio-temporal Bayesian models with R-INLA*. Chichester, West Sussex, UK: John Wiley & Sons (2015). DOI:https://doi.org/10.1002/9781118950203

[15] A. B. Lawson, *Bayesian disease mapping: hierarchical modeling in spatial epidemiology,*3rd editionn. New York: Chapman and Hall/CRC (2018). DOI:https://doi.org/10.1201/9781351271769

International Conference on Mathematical Analysis and Applications in Science and Engineering
ICMA^{2}SC'24
ISEP Porto-Portugal, June 20 - 22, 2024

EXPLORING FORMS OF DISAGGREGATING COVID-19 DATA: AN EXAMPLE

Conceição Leal[1,2⋆] **Teresa A. Oliveira**[1,2] **Amitava Mukherjee**[3]
Amílcar Oliveira[1,2]

[1] Universidade Aberta, Portugal
[2] CEAUL, FCUL, Portugal
[3] XLRI-Xavier School of Management, India

[1⋆]conceicao.leal2010@gmail.com

Abstract: COVID-19 data provided by Portuguese public health authorities lack consistency in periodicity and metrics. To facilitate time series analysis, we transformed those data to achieve homogeneous periodicity and metrics. We present one method we used and assess the potential introduced bias and its impact on spatial distribution models of COVID-19 in Portugal, using spatial and non-spatial models. Comparing models fitted with transformed data to those with observed data for two specific days, we found no clear evidence of a worse fit for the disaggregated data.

keywords: Times Series Disaggregation; Modelling COVID-19 data; Model fit.

MSC2020: 49-XX; 34-XX; 92-XX.

1 Introduction

The SARS-CoV-2 virus, which causes COVID-19, was a significant public health threat. Spatial epidemiology can elucidate the disease's distribution and spread due to its varying incidence rates across locations, leading to uneven impacts. The dynamics of the disease feature a lag between exposure and detection, with asymptomatic transmission affecting public health responses. Given human-to-human transmission of the virus and the influence of atmospheric conditions on human behavior, this study incorporates meteorological variables (temperature, humidity, and rainfall) in modelling daily COVID-19 cases.

Portuguese public health authorities' COVID-19 data are inconsistent in periodicity and metrics. From March 24, 2020, to March 24, 2021, we transformed the data, potentially introducing bias. We evaluate if such bias affects geographic risk distribution maps of COVID-19. We modelled daily COVID-19 cases in Mainland Portugal, considering spatial data and meteorological factors, to capture pandemic evolution. Weather data, from IPMA, included maximum and minimum temperatures, humidity, and rainfall with a 7-day lag. Using Latent Gaussian Models via the R-INLA package, we estimated daily cases in 278 counties, analysing data from June 1, 2020 and March 24, 2021, to assess the transformation's impact on model accuracy.

The best model for 1st June 2020, using observed daily data, included only unstructured spatial effects. For 24th March 2021, using transformed data, the best-fitting model also included only unstructured spatial effects. Minimum temperature was significant on 24th March 2021, and minimum humidity on 1st June 2020.

2 Results and discussion

2.1 A Latent Gaussian Model (LGM)

Suppose y_{it} the number of cumulative daily cases of COVID-19 in county i of mainland Portugal (i=1,2,...,278) on day t (t=1,2,...,142), modelled as:

$$y_{it} \sim Poisson(\mu_{it} E_i) \tag{1}$$

with link function

$$\eta_{it} = ln(\mu_{it}) \tag{2}$$

defining Latent Gaussian Field as $x = (\eta, \alpha, f, \beta)$. Since η, α, f and β are random variables, they require parameters. Suppose *f(i)* is a parameter for y_i and Ψ is a parameter for x, then we can build a hierarchical structure for this.

In the first stage, we used a latent Gaussian model as follows.

$$\eta_{it} = ln(\mu_{it}) = \alpha + \sum_{k=1}^{m} \beta_i x_i^k + \sum_{j=1}^{c} P\left(x_{it-lag}^j\right) + s_i + \nu_i + \gamma_t + \varepsilon_t, i = 1, ...n \quad \text{and} \quad t = 1, .., T \tag{3}$$

where μ_{it} represents the mean or relative risk; α represents the intercept term (overall mean or risk); $s_i = f_1(i)$ represents spatially structured residuals in county i; $\nu_i = f_2(i)$ represents spatially unstructured residuals in county i; $\gamma_i = f_3(t)$ represents temporally structured residuals in period t; $\varepsilon_t = f_4(t)$ represents temporally unstructured residuals in period t; $\beta_i x_i^i$ represents linear effects of jth covariate in county i; $P\left(x_{it-lag}^j\right)$ represents a polynomial that allows establishing a non-linear relationship between temporally-lagged covariates, X_{it-lag} and μ_{it}.

In the second stage, we considered spatial structure with two distributions as follows:

1. s_i spatially-structured effect on county i with an intrinsic conditional autoregressive (iCAR) structure (BYM model [1])

$$s_i | s_(j \neq i) \sim Normal\left(\frac{1}{N_i}\sum_{j=1}^{n} w_{ij} s_j; \frac{\sigma_s^2}{N_i}\right) \tag{4}$$

   where N_i is the number of neighbours that county i has and w_{ij} is the element (i, j) of the row-standardised matrix W of dimension $n \times n$ that represents the neighbourhood matrix for the counties: $w_{ij} = \frac{1}{N_i}$ if counties i and j are neighbours, otherwise $w_{ij} = 0$ and σ_s^2 represents the variance of the spatially-structured effect.

2. ν_i spatially-unstructured effect over the counties, an independent and identically distributed Gaussian prior is considered

$$\nu_i \sim Normal\left(0; \sigma_\nu^2\right) \tag{5}$$

   where σ_ν^2 represents the variance of the spatially-unstructured effect of the model.

3. γ_t temporally-structured effect was modelled through a second-order random walk

$$\gamma_t | \gamma_{t-1}, \gamma_{t-2} \sim Normal\left(2\gamma_{t-1} + \gamma_{t-2}; \sigma_\gamma^2\right) \tag{6}$$

   where σ_γ^2 represents the variance component.

4. ε_t temporally-unstructured effect, an independent and identically distributed Gaussian prior is considered

$$\varepsilon_t \sim Normal\left(0; \varepsilon^2\right) \tag{7}$$

$E_i = \sum_j f_j P_{ij}$ where f_i is the incidence of cases in the age group j for the whole population of the country and P_{ij} the population in county corresponding to age group j ([2]) represents the expected number of cases and $ln(E_i)$ is used as the offset term of the linear predictor.

Furthermore, in the third stage, we defined the hyperparameter as follows:

$$\Psi = \left(\sigma_s^2; \sigma_\nu^2\right) \tag{8}$$

Informative prior for the hyperparameter are specified by INLA's (R-INLA package) default:

$$\sigma_s^2 \sim Gamma^{-1}(1; 0.0005) \text{ and } \sigma_\nu^2 \sim Gamma^{-1}(1; 0.0005) \tag{9}$$

The neighbourhood matrix W for the counties is defined by

$$w_{ij} = \begin{cases} \frac{1}{N_i}, & \text{counties } i \text{ and } j \text{ are neighbours (a common geographical border)} \\ 0, & otherwise \end{cases}$$

2.2 COVID-19 data and IPMA data

The analysis focused on the counties of mainland Portugal (i.e., excluding Azores and Madeira islands), a contiguous study area. COVID-19 data were sourced from the online repository "Data Science for Social Good Portugal" (https://github.com/dssg-pt/covid19pt-data).

The study period spans from 24 March 2020 to 24 March 2021. The health authorities' data were inconsistent in metrics throughout this period. From 24 March to 4 July 2020, daily cumulative cases were reported; from 14 July to 26 October 2020, cumulative cases were reported weekly. From 11 November 2020, data were published weekly as cumulative incidence per fortnight (14 days) per 100k inhabitants, calculated using the population estimates from 31 December 2019 by the National Statistics Institute (as noted in the DGS Situation Reports from 16 November 2020). Since fortnightly reports are weekly, the first week of each fortnight overlaps with the last week of the previous fortnight, preventing direct calculation of new daily or weekly cases.

We explored various methods of disaggregating data to address this inconsistency. For the data from 11th November 2020 to 24th March 2021, in one of the methods, we assumed a uniform distribution of new cases across each 14-day period, U(0,14). To estimate the daily number of new cases in each overlapping interval, we calculated the average of the estimated daily new cases from the uniform distribution of one fortnight with those from the next fortnight.

Given x_{di} the number of new cases on day d in each week i, with $d = 1, 2, \ldots, 7$ and $i = 1, 2, \ldots, 21$, starting from November 4, 2020; a_{dj} the number of new daily cases in day d of the first week of each fortnight j, estimated by the uniform distribution $U(0, 14)$ and $a_{(d+7)(i-1)}$ the number of new daily cases in day d of the second week of each fortnight $j-1$, estimated by the uniform distribution U(0,14)(Fig. 1), then:

$$x_{di} = \frac{a_{(d+7)(j-1)} + a_{dj}}{2} \tag{10}$$

for $i = 1, \ldots, 20$ and $d = 1, 2, ..., 7$.

y_i are new cases obtained by adding the number x_{di} of cases between two reporting days.

Covariates were max. and min. temperature, max. and min. humidity and maximum rainfall, (IPMA data). Per the literature on incubation time of COVID-19, the parameter Lag was varied from Lag=2 to Lag=14 days. We used 7-days lag.

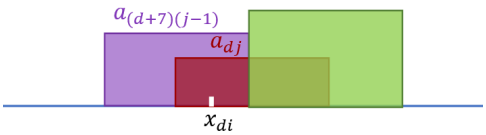

Figure 1: Estimation of the number of COVID-19 cases from the 14-day incidence

Using Integrated Nested Laplace Approximation (INLA)[3], we fitted: fixed effects model; unstructured spatial effects model; a BYM [3] (structured and unstructured) spatial effects model (iCAR) with weather covariates (7-days lag), to data for June 1, 2020 (non-transformed) and March 24, 2021 (transformed). We selected best-fitting models using DIC and WAIC criteria.

MODEL	DIC		WAIC	
	2020/6/1	2021/3/24	2020/6/1	2020/3/24
Fixed effects	403.78	946.55	3.86e+18	972.66
Fixed effects + spatially-structured(+)unstructured effects	260.78	756.72	5.68e+22	756.72
Fixed effects + spatially-unstructured effects (iCar)	258.76	434.41	6.38e+16	423.98

Table 1: Comparative table of models

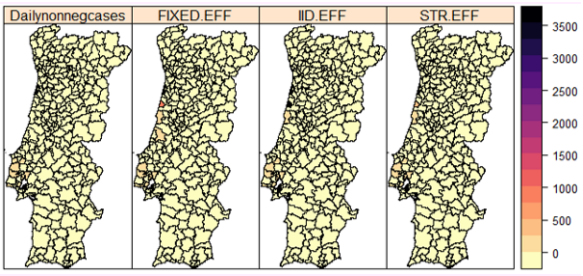

(a) June 1, 2020: observed daily number of cases; estimated daily number of cases by the three models

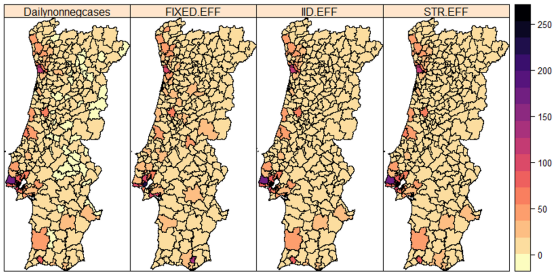

(b) March 24, 2021: observed daily number of cases; estimated daily number of cases by the three models

Figure 2: Comparison of observed and estimated daily number of cases

In both cases the unstructured spatial effects model (iCAR) better captures the distribution of the epidemic across the counties of Portugal. DIC criterium supports this conclusion.

The maps of Figure 2 shows the daily cumulative number of cases observed for June 1st, 2020 and for March 24th, 2021, and the daily cumulative number of cases predicted by the models that considers all covariates and 7-days lag. Observing the maps, we can conclude that models with spatial effects fitted with observed data and with transformed data well reflect the spatial distribution of the number of observed cases, without clear evidence of a worse fit to the transformed data.

References

[1] Besag, J., York, J., Mollié, A. (1991). Bayesian image restoration, with two applications in spatial statistics. Annals of the institute of statistical mathematics, 43, 1-20.

[2] Briz-Redón, Á., Serrano-Aroca, Á. (2020). A spatio-temporal analysis for exploring the effect of temperature on COVID-19 early evolution in Spain. Science of the total environment, 728, 138811.

[3] Rue, H., Martino, S., Chopin, N. (2009). Approximate Bayesian inference for latent Gaussian models by using integrated nested Laplace approximations. Journal of the Royal Statistical Society Series B: Statistical Methodology, 71(2), 319-392.

International Conference on Mathematical Analysis and Applications in Science and Engineering ICMA²SC'24

ISEP Porto-Portugal, June 20 - 22, 2024

Mathematical Model for the Dynamics of COVID-19 Pandemic Incorporating Isolation and Non-Linear Recovery Rate

N. I. Akinwande[1], T. T. Ashezua[4], S. A. Somma[1], N. O. Abdurrahman[1], F. A. Oguntolu[1], O. M. Adetutu[3], R. I. Gweryina[4], R. O. Olayiwola[1], T. P. Adajime[5], F. A. Kuta[2], S. Abdulrahman[6], A. I. Enagi[1], G. A. Bolarin[1], M. D. Shehu[1] and A. Usman[3]

[1]Department of Mathematics, Federal University of Technology, Minna, Nigeria.
[2]Department of Microbiology, Federal University of Technology, Minna, Nigeria.
[3]Department of Statistics, Federal University of Technology, Minna, Nigeria.
[4]Department of Mathematics, Joseph Sarwuan Tarka University Makurdi, Nigeria.
[5]Department of Epidemiology and Community Health, Benue State University, Makurdi, Nigeria.
[6]Department of Mathematics, Federal University Birnin-Kebbi, Nigeria.

Abstract

COVID-19 has in recent times created a major health concern in both developed and developing parts of the world. In this wise, there is every need to theoretically explore ways that will provide some insights into curtailing the spread of the disease in the population. In this paper, we present a population model for COVID-19 pandemic incorporating isolation and nonlinear recovery rate. The reproduction number was obtained using the next generation method. The disease-free equilibrium (DFE) of the model (1) was found to be locally and globally asymptotically stable whenever the associated reproduction number is less than unity. Results from the sensitivity analysis of the model, using the reproduction number, R_C show that the top parameters that largely drive the dynamics of COVID-19 in the population are COVID-19 transmission rate and the proportion of individuals progressing to the class of reported symptomatic infectious individuals. Numerical simulations of the model shows that increasing the recovery rate of infected patients in the population will lead to an initial decrease in the number of hospitalized patients before subsequent increase. The reason for this could be attributed to the number of unreported symptomatic infectious individuals who are progressing to reported symptomatic infectious stage of infection for immediate isolation.

Keywords: COVID-19, reproduction number, isolation, stability, nonlinear recovery rate

The effect of migration in predator-prey differetial systems

Érika Diz-Pita [1⋆] **M. Victoria Otero-Espinar**[1]

[1] Universidad de Santiago de Compostela, Spain

[1⋆] erikadiz.pita@usc.es

Abstract: Migrations occur in a large number of species in nature, which is why it is interesting to include this phenomenon in the modeling of predator-prey systems. There are some works in the literature where this phenomenon has been studied, but they are quite simple and do not include the possibility of migration can affect both species simultaneously. We have made some progress in the study of in the study of predator-prey systems with immigration in both species, and we present here the results obtained.

keywords: predator-prey; immigration; global dynamics.

MSC2020: 37-N25; 37-C15X; 92-D25.

1 Introduction

Population dynamics is a cornerstone of biomathematical research, with a long history of inquiry into the factors governing population change. Predator-prey models have been a particular focus, generating a big number of works in the literature. However, real-world systems exhibit complexities that need further mathematical investigation, as they can significantly influence population dynamics. In [2], we try to give a state-of-art review of recent predator-prey models which include different realistic characteristics, among which are migrations. We compare the qualitative results obtained for different models, particularly regarding the singular points, local and global stability and the existence of limit cycles.

Motivated by the analyzed works, we want to carry out a study of the global dynamics of predator-prey systems with immigration in both species, as this has not been studied in depth. The fact of studying global dynamics provides knowledge that is not limited to to local behavior, because through a compactification, we will be able to know the behavior at infinity. We take a constant immigration rate, as it is done in many of the works in the literature, because it is reasonable from a biological point of view. Then we consider the general systems

$$\dot{x} = rx - \frac{ax^{1+\alpha}y}{1+hx^{1+\alpha}} + c_1, \qquad \dot{y} = \frac{bx^{1+\alpha}y}{1+hx^{1+\alpha}} - ny + c_2, \tag{1}$$

where all the parameters are real and positive and have the following biological meaning: r represents the growth rate of prey; n is the death rate of predator; a is the rate of predation; b is the conversion rate of eaten prey into new predators; h and α are the functional response coefficients; and c_1 and c_2 are the immigration rates of prey and predator, respectively.

In [1] we have carried out the study of the case with $\alpha = h = 0$, which corresponds with a Holling type I functional response, and in [3] we deal with the case $\alpha = 0$, $h \neq 0$, which corresponds with a Holling type II functional response

In the following sections we will discuss the results obtained so far, as well as the pending work for the future.

2 Results

Let consider the case with Holling type I functional response, i.e., the system

$$\dot{x} = rx - axy + c_1, \qquad \dot{y} = bxy - ny + c_2. \tag{2}$$

Our main result is the proof that the global phase portrait of system (2), in the positive quadrant of the Poincaré disc is one of the following:

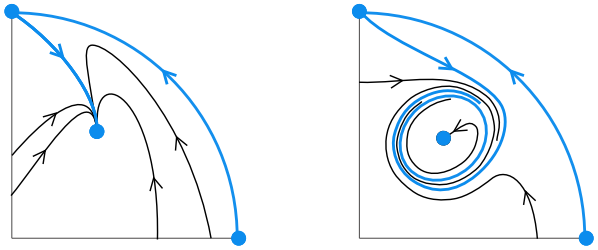

Figure 1: Global phase portraits of system (1) with $\alpha = h = 0$ in the positive quadrant of the Poincaré disk.

The importance of this result is that it allows us to determine that for any value of the parameters, the behavior will follow one of these two schemes, and therefore we can conclude that two scenarios can occur: either there is a coexistence point that is globally asymptotically stable, or there is a region of asymptotic stability for that singular point, delimited by a limit cycle, that is attactor on the outside, so that for initial conditions outside it, the behavior would tend to be oscillatory.

We begin by proving that system (2) has exactly one positive singular point

$$P = \left(\frac{-bc_1 - ac_2 + nr + R}{2br}, \frac{bc_1 + ac_2 + nr + R}{2an} \right),$$

and that this point is a stable focus if $((n + r)(bc_1 + ac_2) + (n - r)(nr + R))^2 < 16n^2r^2R$, and a stable node if $((n + r)(bc_1 + ac_2) + (n - r)(nr + R))^2 > 16n^2r^2R$.

Hereunder, we introduce the Poincaré compactification of system (2), as this technique allows us to study the dynamics near the infinity. We use the local charts of the sphere to calculate the expression of the compactification.

In chart U_1 there are two singular points: the origin and the point $(-b/a, 0)$, but as this second point is not on the positive quadrant of the Poincaré disk, we can omit its study. The origin is a semi-hyperbolic singular point, and applying the classification results in [4], we get to determine that it is a saddle-node.

Studying the flow over the horizontal axes we have that $\dot{v} \mid_{v=0} = 0$ and $\dot{u} \mid_{v=0} = au^2 + bu$. Then, in a neighborhood of the origin there are four possibilities for the position and orientation of the different sectors, but studying the flow over the vertical axis, we have that $\dot{u} \mid_{u=0} = c_2v^2 > 0$ and $\dot{v} \mid_{u=0} = -v^2(c_1v+r)$, and this is only compatible with one of the configurations, which is the one given in Figure 2(a).

The origin of U_2 is also a semi-hyperbolic saddle-node, but in this case, analyzing the flow over the axes we conclude that the orientation and position of the different sectors is as shown in Figure 2(b).

So far we have not been able to give an analytical proof of the existence of a limit cycle. The results of our numerical simulations suggest the possibility of a limit cycle existing under certain conditions.

In Figure 3, we include the solutions of system (2), with parameters $r = a = b = n = 0.2$, $c_1 = 0.3$, and $c_2 = 0.18$. In this case, the solutions tend to the equilibrium point of the coexistence.

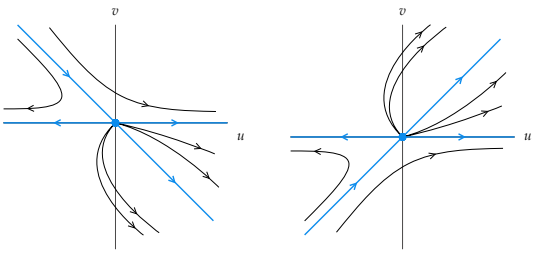

(a) (b)

Figure 2: Configurations for the saddle-node in the origin of system (2) in U_1 and U_2.

In Figure 4, the values of the parameters are $r = 50$, $a = 2553/524288$, $c_1 = 5$, $b = 5/2147483$, $n = 1000/1024$ and $c_2 = 1$, and the solutions show an oscillatory behavior that could represent that of an orbit approaching the limit cycle.

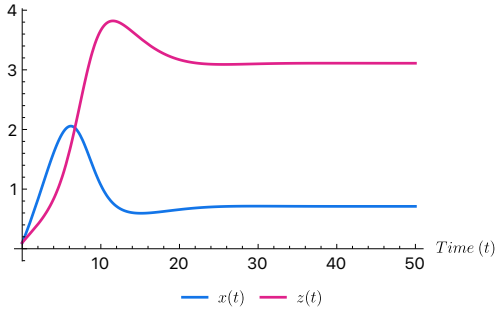

Figure 3: Solutions of system (1) with parameters $r = 50$, $a = 2553/524288$, $c_1 = 5$, $b = 5/2147483$, $n = 1000/1024$, and $c_2 = 1$ and initial conditions $x(0) = y(0) = 0.1$.

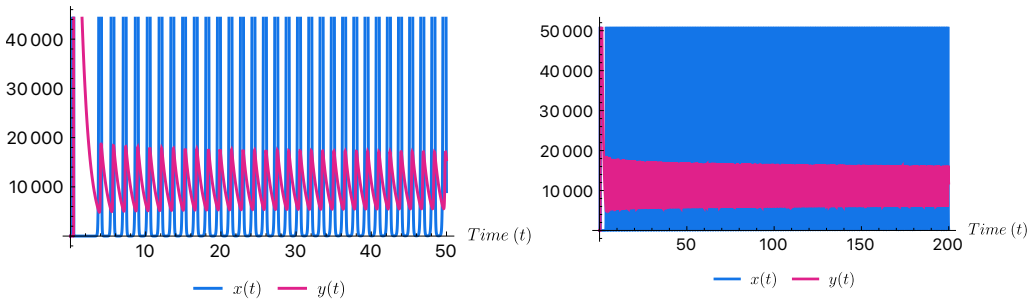

(a) Solutions computed for time $t \in [0, 50]$.

(b) Solutions computed for time $t \in [0, 200]$.

Figure 4: Solutions of system (1) with parameters $r = a = b = n = 0.2$, $c_1 = 0.3$, and $c_2 = 0.18$, and initial conditions $x(0) = y(0) = 0.1$.

Finally we determine the global phase portraits. We know that there exists always one positive singular point, and it is a stable node or a stable focus, which are topologically equivalent.

At the infinity, the origin of U_1 has the phase portrait in Figure 2(a), and we have that there are orbits that enter into the positive quadrant from each point of the axis $u = 0$, except from the origin. The origin of U_2 has the phase portrait in Figure 2(b). There exists a separatrix in the positive quadrant which leaves from this infinity singular point generating two sectors. Between the separatrix and the infinity there are orbits which leave all from the singular point, and between the separatrix and the $u = 0$ axis, there are orbits that enter the positive quadrant of the Poincaré disk from each one of the points of the $u = 0$ axis.

With this information we can obtain two global phase portraits. If there is no limit cycle, all trajectories go to the positive singular point, which will then be globally asymptotically stable. If a limit cycle exists, it is an attractor on the outside and a repulsor on the inside: the orbits starting at the region inside the limit cycle, go to the positive singular point when t tends to infinity; the separatrix and the orbits entering the positive quadrant from the points on the $u = 0$ and $v = 0$ axes, go to the limit cycle when t tends to infinity.

The case with Holling type II functional response corresponds with the system

$$\dot{x} = rx - \frac{axy}{1+hx} + c_1, \qquad \dot{y} = \frac{bxy}{1+hx} - ny + c_2. \tag{3}$$

In this case we have considered some variable changes in order to get an equivalent polynomial differential system. Then we have also studied its global dynamics, which has turned out to be much more complex. There can be up to three positive equilibria, and they have a much richer dynamic. The same occurs when we study the dynamics at the infinity, where the system has up to 3 singular points in the positive quadrant of the Poincaré disk.

3 Conclusions and ongoing work

We believe that this work represents an advance in the study of the influence of migration on predator-prey systems, and in particular, we consider that there are two aspects of special relevance: we are considering that migration affects the two species, which is not covered in most works in the literature, and we are making a study of the global dynamics through a compactification, which makes it possible to understand the behavior at infinity.

For the future we would like to complete these works, achieving, for example the analytical prove the existence of the limit cycle.

We believe that these works help one to conclude on the effects and importance of migrations in the evolution of predator-prey systems.

Acknowledgments

The authors are partially supported by the Ministerio de Ciencia e Innovación, Agencia Estatal de Investigación (Spain), grant PID2020-115155GB-I00 and the Consellería de Educación, Universidade e Formación Profesional (Xunta de Galicia), grant ED431C 2023/31 with FEDER funds.

References

[1] É. Diz-Pita, Global dynamics of a predator-prey system with immigration in both species, Electronic Research Archive, **32**(2) (2024), 762–778.

[2] É. Diz-Pita, M. V. Otero-Espinar, Predator-prey models: a review on some recent advances, Mathematics, **9** (2021), 1783.

[3] É. Diz-Pita, M. V. Otero-Espinar, A Holling-Type II predator-prey model with immigration in both species, *Preprint*.

[4] F. Dumortier, J. Llibre and J. C. Artés, Qualitative theory of planar differential systems, UniversiText, Springer-Verlag, New York, 2006.

An Optimal Control Problem for a Predator-Prey Model with Strong and Weak Preys

Paulo Rebelo[1⋆] **Silvério Rosa**[2]

[1,2] Universidade da Beira Interior, Portugal

[1⋆]rebelo@ubi.pt

Abstract: The aim of this work is to study an optimal control problem for a non-autonomous model with a predator and two prey species, one strong and the other weak. The resulting model incorporates a weak Allee effect in the strong prey, seasonal breeding in both prey, and an extra-food supply that depends upon both prey. Existence, uniqueness, uniformly boundedness of solutions, and extinction scenario for predators are proved. An optimal control problem related to predator biomass is formulated. The existence and uniqueness (over the whole time interval) of optimal solutions are established. Simulation results show the usefulness and efficacy of the proposed control measures to manage the predator biomass.

keywords: Predator-Prey, Optimal Control, Allee Effect.

MSC2020: 49J15; 34H05 ; 92B05.

Acknowledgments

This research was funded by Fundação para a Ciência e a Tecnologia (FCT, the Portuguese Foundation for Science and Technology) through Centro de Mateática e Aplicações da UBI (CMUBI), Grant Number UIDB/00212/2020 (Paulo Rebelo), and Instituto de Telecomunicações (IT), Grant Number UIDB/50008/2020 (Silvério Rosa).

References

[1] Soovoojeet Jana, Abhijit Ghorai, Srabani Guria, and T.K. Kar. Global dynamics of a predator, weaker prey and stronger prey system. *Applied Mathematics and Computation*, 250:235–248, 2015.

[2] L.S. Pontryagin. *Mathematical Theory of Optimal Processes*. Classics of Soviet Mathematics. Taylor & Francis, 1987.

[3] Wendell Fleming and Raymond Rishel. *Deterministic and Stochastic Optimal Control*. Number 1 in Applications of Mathematics. Springer-Verlag, first edition edition, 1975.

[4] Holly Gaff and Elsa Schaefer. Optimal control applied to vaccination and treatment strategies for various epidemiological models. *Mathematical biosciences and engineering: MBE*, 6(3):469–492, 2009.

[5] Wolfgang Hackbusch. A numerical method for solving parabolic equations with opposite orientations. *Computing*, 20:229–240, 08 1978.

[6] S. Lenhart and J. Workman. *Optimal Control Applied to Biological Models*. Mathematical and Computational Biology. New York: Chapman and Hall/CRC, 2007.

[7] Joaquim Mateus, Paulo Rebelo, Silvério Rosa, Cesar Silva, and Delfim F. M. Torres. Optimal control of non-autonomous seirs models with vaccination and treatment. *Discrete & Continuous Dynamical Systems - S*, 11(06):1179–1199, 2018.

International Conference on Mathematical Analysis and Applications in Science and Engineering ICMA²SC'24

ISEP Porto-Portugal, June 20 - 22, 2024

A Marcus formulation of the stochastic population dynamics of nuisance algae population

Hidekazu Yoshioka[1*] **Kunihiko Hamagami**[2]

[1] Japan Advanced Institute of Science and Technology Japan
[2] Iwate University, Japan
[1*]yoshih@jaist.ac.jp

Abstract: Sediment replenishment has been considered as an effective environmental restoration scheme to suppress bloom of nuisance benthic algae on riverbed. We develop a simple jump-driven stochastic differential equation of the algae population dynamics such that the population possibly decreases during sediment-laden flood events as random jumps. Its jump term is based on hydraulic experimental results and is understood in a Marcus sense. We show that the sediment replenishment, even if it is fully implemented, will suppress the algae population but not be able to exterminate it.

keywords: Marcus formulation; algae detachment; power decay

MSC2020: 37-H10; 37-H30; 65-C05

1 Introduction

Stochastic differential equations (SDEs) are indispensable mathematical tools for analyzing random dynamical systems in the real world [1]. They have been widely used in the ecological modeling where the main state variables are populations of biological organisms [2]. Unresolved parts of the population dynamics, which would be extremely complicated to fully describe, have effectively been modelled as noise terms so that the resulting SDE becomes concise as well as tractable.

In this study, we focus on bloom of nuisance filamentous green algae on riverbed in regulated rivers (**Photo 1**). This has been an environmental problem especially in dam-downstream river reaches where physical disturbances to suppress the algae bloom, such as the supply of sand and gravel particles from the upstream river reach, are absent. The sediment replenishment is an environmental restoration project that artificially supplies sand and gravel to the river reach encountering the problem.

The authors have been experimentally studying removal efficiency of the benthic algae by the sand and gravel supply mimicking sediment replenishment. We found that the algae population decays only at a power function of time that is slower than an exponential one [3]. However, this point has not been considered in modeling the sediment supply so far.

Below, we formulate a jump-driven stochastic differential equation (SDE) of the algae population dynamics considering its growth as well as the removal by sediment supply. The population decay is modelled as a jump term in the Marcus sense [4] based on our experimental results. We then argue that the solution to the SDE never becomes extinct with probability 1, and hence the algae population cannot be exterminated by the sediment supply but only suppressed. We also provide computational results by Monte Carlo simulation.

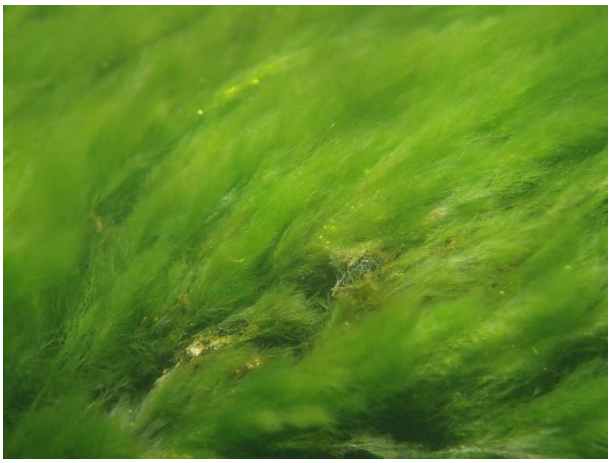

Photo 1. Filamentous green algae on riverbed: taken by Hidekazu Yoshioka on August 11, 2020.

2 Mathematical model

The SDE proposed in this study, which is defined on a suitable complete probability space as in the conventional studies [1], is given as follows:

$$\underset{\text{Increment}}{\mathrm{d}X_t} = \underbrace{g\left(X_t\right)\mathrm{d}t}_{\text{Continuous growth}} - \underbrace{f\left(z_t, X_{t-}\right)\circ \mathrm{d}N_t}_{\text{Jump decrease during flood}},\ t>0 \tag{1}$$

subject to an initial condition $X_0 \in \Omega := [0,1]$. Here, $t \geq 0$ is time, $X = \left(X_t\right)_{t\geq 0}$ is a stochastic process representing the covering ratio by the alga population ($X_t = 1$ if the riverbed is fully covered by the algae and $X_t = 0$ if they are absent, and is intermediate otherwise), $g : \Omega \to \mathbb{R}$ is the drift coefficient, $f : [0,+\infty) \times \Omega \to [0,+\infty)$ is the jump size of the population, $N = \left(N_t\right)_{t\geq 0}$ is a compound Poisson process with the intensity parameter $\lambda > 0$ and the probability density function $p : [0,+\infty) \to [0,+\infty)$ of flood duration, and z_t is the duration of the flood occurred at time t. Clearly, we must have $\int_0^{+\infty} p\left(z\right)\mathrm{d}z = 1$. For simplicity, we can assume that p is a Gamma distribution. The jump term in Eq. (1) is understood in a Marcus sense [4] (see Eq. (4) in the next page). Here, we assume that the supply of sand and gravel particles is abundant so that there will be no sediment starvation.

For the coefficient g, we assume the following generalized logistic model that is common in ecological modeling:

$$g\left(X_t\right) = \underset{\text{Exponential growth}}{rX_t} \times \underbrace{\left(1 - X_t^{\alpha}\right)}_{\text{Growth supression}} \tag{2}$$

with the intrinsic growth rate $r > 0$ and shape parameter $\alpha > 0$. The other coefficient f is the unique element in our model that is specified as follows based on the experimental

study (Yoshioka et al. [3]):

$$f\left(z_t, X_{t-}\right) = \frac{X_{t-}}{\left(1 + X_{t-}^{1/a} b z_t\right)^a} \tag{3}$$

so that the population changes at each jump time τ, the time of flood, as follows [4]:

$$X_\tau - X_{\tau-} = -\left(X_{\tau-} - \frac{X_{\tau-}}{\left(1 + X_{\tau-}^{1/a} b z_t\right)^a} \right) \Rightarrow X_\tau = \frac{X_{\tau-}}{\left(1 + X_{\tau-}^{1/a} b z_t\right)^a}. \tag{4}$$

Here, $a, b > 0$ are parameters to be calibrated. The coefficients f in Eq. (3) were motivated from the hydraulic experimental results in Yoshioka et al. [3] that the decrease of the algae cover on a gravel surface in an artificial flood event is modelled as

$$x_t = \frac{1}{\left(1 + bt\right)^a}, \; t > 0 \text{ with the initial condition } x_0 = 1, \tag{5}$$

where we experimentally inferred that $a \in (0,1]$. We therefore found a power decay of the population. Notice that the following nonlinear and autonomous ordinary differential equation is satisfied by $x = \left(x_t\right)_{t \geq 0}$ of Eq. (5):

$$\frac{\mathrm{d}x_t}{\mathrm{d}t} = -ab x_t^{1+\frac{1}{a}} \text{ for } t > 0, \text{ leading to } x_t = \frac{x_s}{\left(1 + x_s^{1/a} b\left(t - s\right)\right)^a} \text{ for } t \geq s \geq 0. \tag{6}$$

Comparing the last equations between Eqs. (4) and (6), the jump term in (1) represents the power-type population decay during flood events, which can be physically justified if the flood duration is significantly shorter than that of the timescale of the population growth on average. Typically, we will have the growth rate $r = O\left(10^{-2}\right)$ to $O\left(10^{-1}\right)$ (day) and the flood duration of $z_t = O\left(10^{-1}\right)$ (day) to $O\left(10^{0}\right)$ (day).

3 Main result and computation

The following proposition is the main result of this study.

Proposition 1. *Assume that* $X_0 \in (0,1)$, $a \in (0,1]$, *and* $\alpha = a^{-1} \geq 1$. *Then, the SDE (1) admits a path-wise unique càdlàg solution* $X = \left(X_t\right)_{t \geq 0}$ *satisfying* $X_t = Y_t^{-a}$, *where* $Y = \left(Y_t\right)_{t \geq 0}$ *is given by the positive process*

$$Y_t = 1 - e^{-\frac{r}{a}t} + X_0^{-\frac{1}{a}} e^{-\frac{r}{a}t} + b\int_0^t e^{-\frac{r}{a}(t-s)} \mathrm{d}N_s, \; t \geq 0 \text{ and } Y_0 = X_0^{-\frac{1}{a}}. \tag{7}$$

Moreover, the solution X_t *and its expectation are positive with probability 1 for* $t > 0$.

Eq. (7) is an Ornstein–Uhlenbeck process solving a linear SDE. The proof of **Proposition 1** is based on a regularization of the coefficients f, g to apply the theorem [Theorem 4.76 of 1] along with a contradiction argument that any solutions to Eq. (1) are valued in Ω.

Proposition 1 has the three significant consequences. The first one is that it proves the unique existence of a nonlinear SDE. The second one is that it gives an explicit solution formula of a nonlinear SDE. The third one is that it implies the positivity of the

solution and its expectation, the latter being strictly positive, which implies that the algae population cannot be exterminated by a sediment replenishment project even if it completely avoids sediment starvation. The last one is due to the power-type decay of the algae population found through in our experiments.

We computed sample paths of the SDE (1) based on Monte Carlo simulation that discretizes the equation in a time-explicit way as shown in **Fig. 1**, demonstrating that the bounded sample paths are simulated successfully.

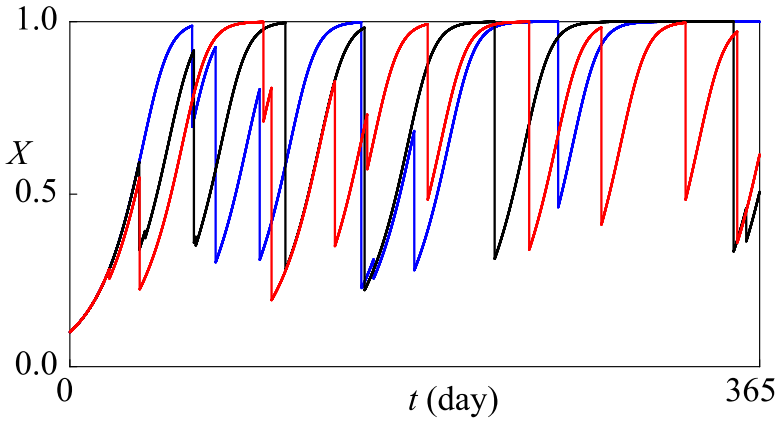

Fig 1. Sample paths generated by Monte Carlo simulation. Distinct colors represent different paths. Parameter values were determined from experimental and public data.

4 Summary and perspectives

We proposed an SDE of the algae population dynamics and discussed its key properties. We also conducted Monte Carlo simulation to compute sample paths of the SDE. The next step of this study will be to incorporate a model of a sediment replenishment project to the proposed SDE so that the supply of sand and gravel can be coupled with the algae population dynamics, which is undergoing by the authors. The coupled model will give a pessimistic result than that in this study because the former should assume that the sediment does not exists at each flood event; hence, there will be some missing shot of algae removal with a nonzero probability. More detailed analysis results will be discussed at the conference talk and full paper version.

Acknowledgments

This study was supported by the JSPS research grant 22K14441.

References

[1] Capasso V, Bakstein, D. Introduction to Continuous-Time Stochastic Processes. Birkhäuser, Cham, 2021.

[2] Pimentel C.E.H, Rodriguez P.M., Valencia L.A. A note on a stage-specific predator–prey stochastic model. Physica A: Statistical Mechanics and its Applications, 553 (2020), 124575.

[3] Yoshioka H., Yoshioka Y., Hamagami K. Subexponential memory of water environmental variables through the superstatistics. Proceedings of The 55th ISCIE International Symposium on Stochastic Systems Theory and Its Applications (SSS '23), (2024). Accepted on February 1, 2024.

[4] Chechkin A., Pavlyukevich I. Marcus versus Stratonovich for systems with jump noise, Journal of Physics A: Mathematical and Theoretical, **47**(34) (2014), 342001.

International Conference on Mathematical Analysis and Applications in Science and Engineering
ICMA^{2}SC'24
ISEP Porto-Portugal, June 20 - 22, 2024

Modeling social media growth using an extension of the random classical logistic equation

Juan Carlos Cortés[1] **Ana Navarro-Quiles**[2] **Sorina Madalina Sferle**[1⋆]

[1] Instituto Universitario de Matemática Multidisciplinar, Universitat Politècnica de València, Spain
[2] Departamento de Estadística e Investigación Operativa, Universitat de València, Spain

[1⋆]smsferle@doctor.upv.es

Abstract: We undertake a probabilistic analysis of an extension of the classical logistic model by considering all its parameters as continuous random variables with a joint probability density function estimated through Bayesian sampling techniques. Given the stochastic nature of the solution, we will derive its first probability density function using the random variable transformation technique, thus obtaining a comprehensive probabilistic description of the model. We then apply our theoretical findings to model the growth of social networks using real-world data.

keywords: growth model; sigmoidal function; logistic equation; inflection point; random differential equation; uncertainty quantification; first probability density function.

MSC2020: 34-F05

1 Introduction

Studying growth processes is crucial for understanding the evolution of systems over time and predicting their future behavior. Growth processes are omnipresent in nature and man-made systems, encompassing phenomena such as population growth, economic expansion, technological innovation, and biological processes. Mathematical models play a fundamental role in describing and analyzing growth processes, providing a quantitative framework for understanding their dynamics. In this work, we will focus on those whose solutions capture sigmoidal-type growth patterns, i.e., those that follow an S-shaped curve, in which the growth starts slowly, accelerates, and then levels off as the system approaches its carrying capacity. Differential equations, including well-known models like the Verhulst, Gompertz and Richards, are frequently employed to characterize such growth processes. Our interest focuses on the study of an extension of the classical logistic model, referred to as the hyper-logistic model proposed by Turner [1], that is formulated via the following differential equation

$$\begin{cases} y'(t) = \frac{b}{K} y(t)^{1-p} (K - y(t))^{1+p}, \\ y(t_0) = y_0, \end{cases} \tag{1}$$

where $y = y(t)$ represents the quantity of interest at time t; $y_0 > 0$ is the initial quantity at the initial time $t_0 \geq 0$; $y'(t)$ is the rate of change of y with respect to time t; $b > 0$ and $K > 0$ are the growth rate and the carrying capacity of the system, respectively, with $\frac{b}{K}$ being the proportionality constant; and $0 < p < 1$ is the shape parameter.

While the logistic equation provides a simple framework for modeling population growth constrained by a carrying capacity, the hyper-logistic equation offers greater flexibility by introducing the parameter p. This allows for describing more complex growth dynamics, accommodating variations in growth rate or the shape of the S-curve, thereby capturing a wider range of growth patterns and behaviors. The equation proposed in (1) overcomes another drawback of the Verhulst model, in which the inflection point is fixed at half of the carrying capacity, i.e, $y_{Inf} = K/2$, a condition that could be very restrictive when modeling some real-world phenomena. The hyper-logistic equation offers more flexibility in locating the inflection point as it depends on p, namely, $y_{Inf} = \frac{K(1-p)}{2}$.

It is important to note that growth is a multifaceted process influenced by many external factors that often are unpredictable, time-varying, and interact in intricate ways, contributing to adding uncertainty to the model. To account for real-world conditions' variability and provide a more realistic representation of the growth scenario, we will consider the model parameters as random variables. Consequently, equation (1) becomes a random differential equation, rendering its solution a stochastic process,

$$y(t,\omega) = K(\omega) - \frac{K(\omega)}{1 + \left(p(\omega)b(\omega)(t-t_0) + \left(\frac{K(\omega)}{y_0(\omega)} - 1\right)^{-p(\omega)} \right)^{\frac{1}{p(\omega)}}}, \tag{2}$$

where $b(\omega), K(\omega), p(\omega)$ and $y_0(\omega)$ are continuous random variables defined on a common complete probability space $(\Omega, \mathcal{F}_\Omega, \mathbb{P})$ with a known joint probability density function (PDF), say $f_0(b, K, p, y_0)$. Here, $\omega \in \Omega$ stands for an outcome.

The aim of the present work is to provide a comprehensive probabilistic characterization of the stochastic solution at every time point. This can be done by means of the computation of the main statistics of the solution, such as the mean, variance, probabilistic intervals, etc. This key probabilistic information can be determined through the 1-PDF of the solution.

2 Results and discussion

The Random Variable Transformation (RVT) technique [2] has been applied to obtain the following expression of the 1-PDF for the solution (2)

$$f_1(y,t) = \int_{\mathbb{R}^4} f_0\left(\frac{\left(\frac{K}{y} - 1\right)^{-p} - \left(\frac{K}{y_0} - 1\right)^{-p}}{p(t-t_0)}, K, p, y_0 \right) \frac{K}{y^2(t-t_0)} \left(\frac{K}{y} - 1\right)^{-p-1} dy_0\, dp\, dK. \tag{3}$$

This same technique can be employed to determine the PDF of the inflection point, given its significant importance.

To illustrate the usefulness of the theoretical results, we apply them to real-world data. As the proliferation of social networking platforms in recent years has revolutionized the way we communicate, interact, and consume information, we will study digital growth, especially in the realm of social media, and see how the hyper-logistic random differential equation can be used to model it. The data used in this study can be found in [3], where there are statistics on the number of users of different social networks in recent years. Specifically, we have taken the data from Instagram and WhatsApp.

To effectively apply the theoretical findings in practice, it is necessary to accurately define the joint PDF to encapsulate data uncertainty. Several approaches address this goal, but here, we will apply Bayesian techniques. The PDF f_0 herein corresponds to the posterior distribution

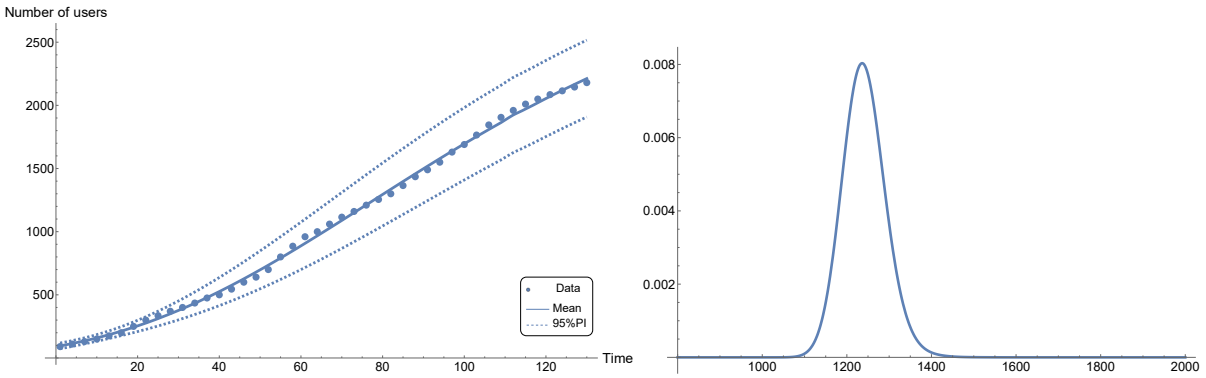

Figure 1: Left side: Probabilistic fit to the Instagram data (dots), consisting of the expectation (solid line) and 95% PI's (dashed lines) of the 1-PDF (3) associated of the solution (2). **Remark:** The time span covers the years from 2013 to 2023. User counts have been recorded quarterly for each year, whereby months are represented on the abscissa axis. Right side: PDF of the inflection point.

obtained via Bayes' theorem. This, in turn, is estimated using the Gibbs sampling algorithm, a component of Markov Chain Monte Carlo methods [4]. Considering the positivity and boundedness of the parameters, together with our knowledge from the literature, we have chosen a Normal distribution for the likelihood function and non-informative distributions for the prior distributions of the model parameters.

After deducing the joint PDF, $f_0(b, K, p, y_0)$, of the model parameters, we proceed to calculate the 1-PDF, $f_1(y, t)$, of the solution of the hyper-logistic model. This enables us to establish a probabilistic fit for the data, encompassing the mean and 95% probabilistic intervals (PI's). The outcomes related to the Instagram social network are depicted in the left segment of Figure 1, while those pertaining to WhatsApp are showcased in the left segment of Figure 2.

We observe distinct behaviors between the two social networks. Instagram is still booming, indicative of its position within phase two of the sigmoidal curve, associated with exponential growth. This aligns with the PI's and the mean of the PDF of the inflection point (right segment of Figure 1), estimated at 1300 users (in millions), roughly corresponding to the year 2020 coinciding with the pandemic. Consequently, Instagram has not yet entered the third phase, characterized by users approaching the platform's carrying capacity and a subsequent decline in growth rate due to factors like market saturation or limited user interest.

Conversely, WhatsApp's trajectory appears to align with all three phases of the sigmoidal curve, currently situated in the third phase of stabilization. This observation is consistent with the findings derived from both the PI's and the mean of the PDF of the inflection point (right segment of Figure 2), which stands at 1000 users (in millions), corresponding to the year 2017.

Nevertheless, our model adeptly captures trends in growth.

3 Conclusions and Future work

We have explored a random growth model from a probabilistic perspective, analyzing the 1-PDF of its stochastic solution under mild assumptions. This investigation considers the inputs as random variables with a joint probability density function estimated using Bayesian techniques. The obtained results have been applied to the specific context of social network growth utilizing real-world data.

The generalization of the proposed growth model is part of our future work.

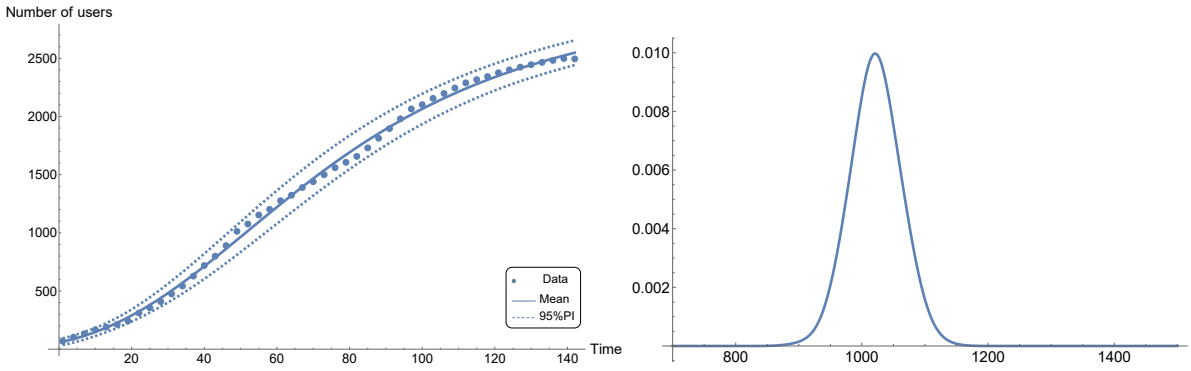

Figure 2: Left side: Probabilistic fit to the WhatsApp data (dots), consisting of the expectation (solid line) and 95% PI's (dashed lines) of the 1-PDF (3) associated of the solution (2). **Remark:** The time span covers the years from 2012 to 2023. User counts have been recorded quarterly for each year, whereby months are represented on the abscissa axis. Right side: PDF of the inflection point.

Acknowledgments

This work has been supported by the Spanish grant PID2020-115270GB- I00 granted by MCIN/AEI/10.13039/501100011033. S.M. Sferle has been suported by the grant PRE2021-101090 granted by MCIN/AEI/10.13039/501100011033 and by FSE+.

References

[1] M. E. J. Turner, E. L. J. Bradley, K. A. Kirk, K. M. Pruitt, A theory of growth, Mathematical Biosciences, **29** (1976), 367–373.

[2] T. T. Soong, *Random Differential Equations in Science and Engineering*. New York: Academic Press, 1973.

[3] Business of Apps, https://www.businessofapps.com/. Accessed May 15, 2024.

[4] R. Smith, *Uncertainty Quantification: Theory, Implementation, and Applications*. New York: SIAM, 2014.

International Conference on Mathematical Analysis and Applications in Science and Engineering
ICMA^{2}SC'24

ISEP **Porto-Portugal, June 20 - 22, 2024**

A stochastic analysis of the hepatitis B virus model

Abdallah Alsammani

Jacksonville University, Jacksonville, FL32211, USA

aalsamm@ju.edu

Abstract: This study investigates the stochastic dynamics of hepatitis B virus (HBV) infection using a newly proposed stochastic model. Unlike deterministic models that do not capture the inherent randomness and fluctuations in biological processes, our stochastic model offers a more realistic representation of HBV infection dynamics. It includes random variability, accounting for changes in viral and cellular populations and uncertainties in parameters such as infection rates and immune responses. We investigate the existence, uniqueness, and positivity of solutions for the proposed model, followed by a detailed stability analysis. We provide the necessary and sufficient conditions for local and global stability, offering more profound insights into the infection dynamics. Additionally, we use numerical simulations to support our theoretical findings. The results provide a solid tool to understand the complex behavior of HBV dynamics, significantly contributing to the ongoing efforts for more effective HBV control and prevention strategies.

keywords: Stochastic dynamics, HBV, stability in probability, Euler-Maruyama, Milstein.

MSC2020: 49-XX; 34-XX; 92-XX.

Note: I am submitting this abstract to Special Session 6.

1 Introduction

Hepatitis B is a severe viral infection affecting the liver, leading to acute and chronic conditions. The virus is commonly transmitted through pregnancy, contact with infected blood or body fluids, and unsafe injections. In 2019, approximately 296 million people lived with chronic hepatitis B, with 1.5 million new infections and an estimated 820,000 deaths, primarily from liver-related complications. Effective vaccines are available that offer essential prevention [10]. Mathematical modeling extensively enriches our understanding of HBV infection dynamics and the effects of antiviral therapies. The model, based on ordinary differential equations (ODEs), reflect the intricate interactions between the virus and the host immune response [7, 8, 1, 3].

Deterministic models provide pivotal insights into HBV's pathogen and therapeutic impacts but neglect the inherent randomness intrinsic to biological processes [5]. Stochastic models offer a nuanced and accurate representation of HBV dynamics by embedding random variability into the equations, capturing fluctuations in viral and cellular populations and parameter uncertainty [9].

This research presents a mathematical analysis of a stochastic HBV infection dynamics model, discussing the solution's existence, uniqueness, and positivity. Stability analysis provides necessary and sufficient conditions for stability in probability. Numerical simulations substantiate the theoretical findings, offering robust tools for understanding HBV dynamics.

2 The Model

We employ a modified stochastic version of a deterministic model representing HBV infection dynamics [2].

The stochastic model introduces noise to each equation to capture inherent biological variability:

$$\begin{aligned} dx(t) &= (\Lambda - \mu_1 x - (1-\eta)\beta xz + qy)dt + \sigma_1 x dW_1(t), \\ dy(t) &= ((1-\eta)\beta xz - \mu_2 y - qy)dt + \sigma_2 y dW_2(t), \\ dz(t) &= ((1-\epsilon)py - \mu_3 z)dt + \sigma_3 z dW_3(t). \end{aligned} \tag{1}$$

Here, $W_1(t)$, $W_2(t)$, and $W_3(t)$ are standard Wiener processes, and σ_1, σ_2, and σ_3 are noise coefficients controlling stochastic fluctuations.

3 Results and Discussion

3.1 Existence, Uniqueness, and Positivity of the Solution

We rigorously prove the solution's existence, uniqueness, and positivity for the stochastic model (1). The coefficients adhere to local Lipschitz continuity and linear growth conditions, ensuring a unique solution that remains positive for all time [4].

3.2 Stability Analysis

Stability analysis identifies the conditions under which the model remains stable in probability. The stability of the trivial solution is established under certain conditions, with necessary and sufficient conditions provided [6]. The stability of components representing infected cells and free viruses is also investigated, demonstrating exponential stability under specific conditions.

3.3 Numerical Simulations

Numerical simulations were conducted using the Euler-Maruyama and Milstein methods. The Euler-Maruyama method, known for its simplicity and first-order convergence, and the Milstein method, with second-order convergence, validated the theoretical results and demonstrated the stochastic model's practical applicability.

4 Conclusion

This paper presents a refined stochastic model for HBV infection dynamics, capturing biological processes' inherent variability and randomness. The analysis ensures the solution's existence, uniqueness, and positivity. Stability analysis delineates the necessary and sufficient conditions for stability in probability. Numerical simulations validate the theoretical results and demonstrate the model's practical applicability. This research advances our understanding of HBV infection dynamics and aids in developing effective control and prevention strategies.

Conflicts of Interest

The author declares no conflicts of interest regarding the publication of this study.

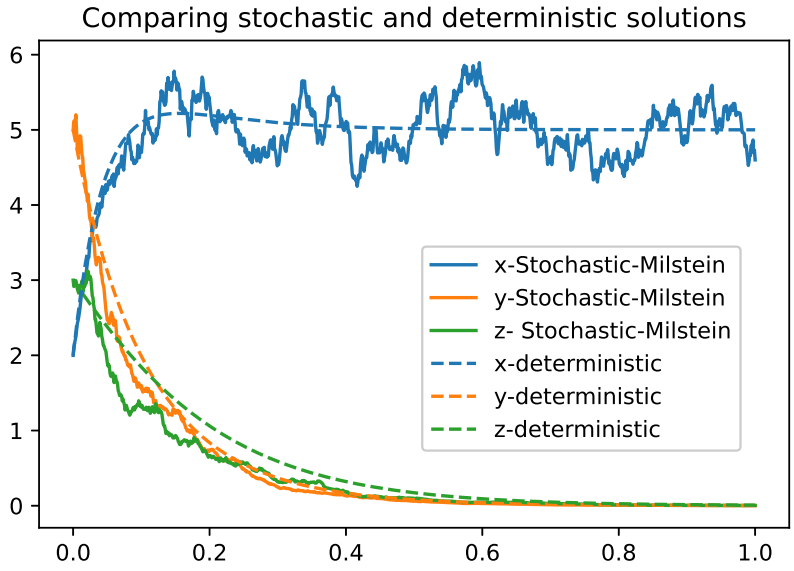

Figure 1: Comparison of the stochastic (Milstein) and deterministic solutions.

References

[1] I. Abdulrashid, A. Alsammani, and X. Han. Stability analysis of chemotherapy model with delays. *Discrete and Continuous Dynamical Systems Series B*, 24, 2019.

[2] Abdallah Alsammani. Mathematical analysis of autonomous and nonautonomous hepatitis b virus transmission models. In *Computational Science and Its Applications – ICCSA 2023 Workshops*, pages 327–343. Springer Nature Switzerland, 2023.

[3] Abdallah Alhadi Mahadi Alsammani. *Dynamical Behavior of Nonautonomous and Stochastic HBV Infection Model*. PhD thesis, Auburn University, 2020.

[4] R. Z. Has'minskii. *Stochastic Stability of Differential Equations*. Sijthoff Noordhoff, Alphen aan den Rijn, The Netherlands, 1980.

[5] Alun L Lloyd. Realistic distributions of infectious periods in epidemic models: Changing patterns of persistence and dynamics. *Theoretical Population Biology*, 60(1):59–71, 2001.

[6] X. Mao. *Stochastic Differential Equations and Applications*. Horwood Publishing Limited, 2 edition, 2007.

[7] Martin A Nowak et al. Viral dynamics of primary viremia and antiretroviral therapy in simian immunodeficiency virus infection. *Journal of virology*, 70(10):6735–6741, 1996.

[8] Alan S Perelson and Patrick W Nelson. Modelling viral and immune system dynamics. *Nature Reviews Immunology*, 2(1):28–36, 2002.

[9] Andre S Ribeiro. Effects of stochastic population dynamics on the quantification of gene expression. *Physical Review E*, 71(1):011912, 2005.

[10] World Health Organization. Hepatitis b, 2023. Accessed: 2023-07-23.

International Conference on Mathematical Analysis and Applications in Science and Engineering
ICMA^{2}SC'24
ISEP Porto-Portugal, June 20 - 22, 2024

Assessing the Symmetry of Contralateral Periodontal Lesions Using Statistical Methods

Pereira J. A.[1,4,5⋆] **Luzia Mendes**[5] **Anuj Mubayi**[2] **Davide Carvalho**[3] **Teresa Oliveira**[1,4]

[1] Universidade Aberta, Portugal,
[2] Illinois State University, USA
[3] Faculty of Medicine Universidade of Porto, Portugal
[4] Center of Statistics and Applications of Universidade de Lisboa
[5] Faculty of Dental Medicine of University of Porto, Portugal

⋆up241045@up.pt

Abstract: Periodontal disease is a prevalent condition that can lead to significant oral health issues if left untreated. One aspect of periodontal health that has garnered interest is the symmetry of periodontal lesions between contralateral sites. Symmetry in this context can provide insights into the uniformity of disease progression and provide information for contralateral inference. Previous studies have often assumed symmetry in periodontal lesions, but few have rigorously tested this assumption using robust statistical methods. This study aims to assess the symmetry of contralateral periodontal lesions using data from the National Health and Nutrition Examination Survey (NHANES) 2011-2012. By comparing the probabilistic distributions of periodontal variables from contralateral sites, this research seeks to provide a detailed understanding of periodontal lesions symmetry.

keywords: periodontal disease; symmetry; statistical analysis.

MSC2020: 49-XX; 34-XX; 92-XX.

1 Introduction

Periodontal disease is a prevalent condition that can lead to significant oral health issues if left untreated. One aspect of periodontal health that has garnered interest is the symmetry of periodontal lesions between contralateral sites in the mouth. Symmetry in this context can provide insights into the uniformity of disease progression. Previous studies have often assumed symmetry in periodontal lesions, but few have rigorously tested this assumption using robust statistical methods. This study aims to assess the symmetry of contralateral periodontal lesions using data from the National Health and Nutrition Examination Survey (NHANES) 2011-2012. By comparing the probabilistic distributions of periodontal variables from contralateral sites, this research seeks to provide a detailed understanding of the extent to which periodontal lesions are symmetric.

2 Materials and Methods

The data for this study were obtained from the National Health and Nutrition Examination Survey (NHANES) 2011-2012. NHANES is a program of studies designed to assess the health and nutritional status of adults and children in the United States. It combines interviews and physical examinations, providing a comprehensive dataset for various health-related research.

The study population includes individuals aged 30 and above who participated in the NHANES 2011-2012 cycle and had complete periodontal examinations. Exclusion criteria included individuals with missing data for key periodontal variables .

Periodontal examinations were conducted by trained dental professionals and included measurements of pocket probing depth (PPD) at six sites per tooth (mesio vestibular (MV), vestibular (V), distovestibular(DV) , mesiolingual (ML), lingual (L), distolingual (DL)). For this study, data from upper right (11) and left (21) central incisors were analyzed.

2.1 Statistical Analysis

Comparison of Probability Density Functions (PDFs) Probability density functions for PPD were estimated for each contralateral site using kernel density estimation. The kernel density estimator $\hat{f}(x)$ for a dataset $X = \{x_1, x_2, \ldots, x_n\}$ is given by:

$$\hat{f}(x) = \frac{1}{nh} \sum_{i=1}^{n} K\left(\frac{x - x_i}{h}\right)$$

where K is the kernel function (e.g., Gaussian kernel) and h is the bandwidth parameter. The estimated PDFs were plotted for visual inspection of symmetry. Divergence measures, such as Kullback-Leibler divergence, were calculated to quantify differences between the PDFs.

Kolmogorov-Smirnov (K-S) Test The K-S test was used to compare the empirical distribution functions of periodontal variables from contralateral sites. The K-S statistic D is defined as:

$$D = \sup_x |F_n(x) - G_n(x)|$$

where $F_n(x)$ and $G_n(x)$ are the empirical distribution functions of the two samples. The test provides a p-value indicating whether the distributions are significantly different.

Generalized Additive Models for Location, Scale, and Shape (GAMLSS) GAMLSS models were fitted to the data, with periodontal variables as the response and the side (left or right) as a factor. The GAMLSS framework allows modeling not only the mean (μ) but also other parameters such as the variance (σ), skewness (ν), and kurtosis (τ) of the distribution. The general form of a GAMLSS model is:

$$Y_i \sim \text{Distribution}(\mu_i, \sigma_i, \nu_i, \tau_i)$$

$$g(\mu_i) = \eta_{\mu,i} = \mathbf{X}_{\mu,i}\boldsymbol{\beta}_\mu$$

where $g(\cdot)$ is a link function, $\mathbf{X}_{\mu,i}$ is the design matrix for the mean, and $\boldsymbol{\beta}_\mu$ are the regression coefficients. The null model (excluding the side factor) was compared with the side model using Akaike Information Criterion (AIC) and Bayesian Information Criterion (BIC). A likelihood ratio test was conducted to assess the significance of the side effect. The test statistic Λ is given by:

$$\Lambda = -2(\log L_{\text{null}} - \log L_{\text{side}})$$

where L_{null} and L_{side} are the likelihoods of the null and side models, respectively. This statistic follows a chi-squared distribution with degrees of freedom equal to the difference in the number of parameters between the models. K-fold cross-validation was performed to evaluate the predictive performance of both models, ensuring that the inclusion of the side factor improves the model's robustness. The data was split into k subsets, and the model was trained on $k-1$ subsets while the remaining subset was used for validation. This process was repeated k times.

3 Results and discussion

Site	Stats	Teeth		Test Results		K-S	SM	Bhat.	Corr.
		11	21	Stats	p			Coef.	Coef.
DV	Mean	1.40	1.42	t = -0.738	0.461	D = 0.007	0.85	1.000	0.58
	Median	1	1	W = 3589510	0.638		1		
	Variance	0.685	0.761	F = 0.266	0.606	p = 1	0.042		
V	Mean	0.868	0.928	t = -2.936	**3.34e-03**	D = 0.028	0.86	0.999	0.64
	Median	1	1	W = 3474941	**3.02e-03**		1		
	Variance	0.538	0.578	F = 0.065	0.799	p = 0.247	0.047		
MV	Mean	1.31	1.41	t = -4.6212	**3.91e-06**	D = 0.079	0.89	0.997	0.66
	Median	1	1	W = 3354774	**5.33e-09**		1		
	Variance	0.639	0.702	F = 18.218	**2.00e-05**	p = **9.96e-08**	0.036		
DL	Mean	1.48	1.56	t = -3.513	**4.47e-04**	D = 0.050	0.85	0.998	0.62
	Median	1	1	W = 3258241	**2.35e-04**		1		
	Variance	0.729	0.807	F = 11.600	**6.65e-04**	p = **3.18e-03**	0.041		
L	Mean	1.14	1.16	t = -0.925	0.355	D = 0.013	0.86	0.999	0.65
	Median	1	1	W = 3591491	0.267		1		
	Variance	0.731	0.726	F = 0.230	0.647	p = 0.9772	0.046		
ML	Mean	1.73	1.81	t = -3.242	**1.20e-03**	D = 0.055	0.89	0.998	0.73
	Median	2	2	W = 3405239	**5.38e-05**		1		
	Variance	0.826	0.779	F = 7.425	**6.45e-03**	p = **5.21e-04**	0.032		

Abreviatures: 11 – Upper right central incisor; 21 – Upper left central incisor; Stats – Statistics; p – p-value; Statts – Tests statistics; K-S – Kolmogorov-Smirnov test; SM – Symmetry measure; Bhat. Coef.– Bhattacharyya coefficient; Corr. Coef. – Pearson Correlation coefficient

Table 1: Summary of statistical tests comparing central incisors 11 and 21 PPD means, medians and variances across six dental sites; distances between distributions.

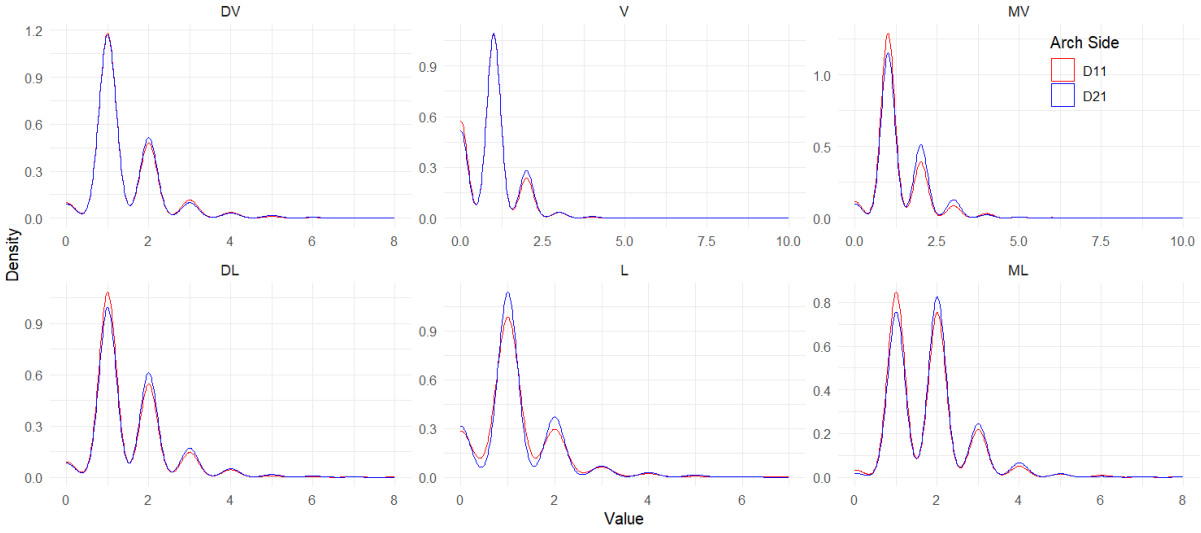

Figure 1: Kernel density plots to compare probability densities of 11 and 21 PPD by site

From the analysis of PPD at DV, V, MV, DL, L, and ML of 11 and 21) (Table 1) significant findings were observed in the DV sites, the comparison of means showed no significant difference (t = -0.738, p = 0.461), and the K-S test, together with the kernel density plots confirmed this with a D-value of 0.007 (p = 1.00) and overlaping curves. Conversely, significant differences

were noted in the V sites, where both the mean difference (t = -2.936, p = 3.34e-03) and the K-S test (D = 0.028, p = 0.247) and discordant kernel density plots, suggested asymmetry. The GAMLSS model for the V sites further indicated a significant side effect, with a notable reduction in AIC and an LRT p-value of 0.03.

Further, the MV sites exhibited significant asymmetry, with the mean PPD significantly different between 11 and 21 (t = -4.621, p = 3.91e-06). The K-S test also highlighted a significant difference (D = 0.079, p = 9.96e-08). The GAMLSS analysis for these sites supported the presence of asymmetry, as indicated by a significant LRT with a p-value of 9.59e-06. Similar patterns were observed in the DL sites, where significant differences were found in mean PPD (t = -3.513, p = 4.47e-04) and the K-S test (D = 0.050, p = 3.18e-03). In contrast, the L sites showed no significant differences (t = -0.925, p = 0.355; D = 0.013, p = 0.977), indicating symmetry at these sites. Cross-validation metrics, including RMSE and MAE, consistently supported these findings, with significant differences noted in the V, MV, and D-L sites but not in the L sites.

Conclusion

The analysis of PPD across six periodontal sites of the upper central incisors (11 and 21) reveals asymmetry in specific sites. Significant differences were observed in the V, MV, and DL sites, indicating that periodontal signals varies between these contralateral sites. However, no significant differences were found in the L sites, suggesting symmetry at these points. Further research should explore the new approachs of symmetry evaluation. The presented symmetry assessment relies on hypothesis testing, which assumes that any observed symmetry falls within a defined confidence interval, allowing for a margin of error. This approach ensures that minor deviations from perfect symmetry are accounted for and are not mistakenly interpreted as significant asymmetry.

4 Conclusions and Future Work

The analyses provide strong evidence of asymmetry in contralateral periodontal lesions but do not quantify the degree of symmetry. Future work should focus on quantifying symmetry to extract valuable information for contralateral inference and improve clinical assessments.

References

[1] Centers for Disease Control and Prevention (CDC). National Center for Health Statistics (NCHS). National Health and Nutrition Examination Survey Data. Hyattsville, MD: U.S. Department of Health and Human Services, Centers for Disease Control and Prevention, 2011-2012. Available from: https://www.cdc.gov/nchs/nhanes/index.htm

[2] Massey, F. J., The Kolmogorov-Smirnov Test for Goodness of Fit, Journal of the American Statistical Association, **46**(253) (1951), 68–78.

[3] Baelum, V., Luan, W. M., Chen, X., Fejerskov, O., Predictors of tooth loss over 10 years in adult and elderly Chinese, Community Dentistry and Oral Epidemiology, **23**(4) (1997), 192–199.

[4] Rigby, R. A., Stasinopoulos, D. M., Generalized Additive Models for Location, Scale and Shape (GAMLSS) in R, Journal of Statistical Software, **23**(7) (2007), 1–46.

International Conference on Mathematical Analysis and Applications in Science and Engineering
ICMA^{2}SC'24
ISEP Porto-Portugal, June 20 - 22, 2024

Quantifying Symmetry in Periodontal Disease: A Novel Measure for Clinical and Epidemiological Applications

Pereira J. A.[1,4,5⋆] **Luzia Mendes**[5] **Anuj Mubayi**[2] **Davide Carvalho**[3] **Teresa Oliveira**[1,4]

[1] Universidade Aberta, Portugal,
[2] Illinois State University, USA
[3] Faculty of Medicine Universidade of Porto, Portugal
[4] Center of Statistics and Applications of Universidade de Lisboa
[5] Faculty of Dental Medicine of University of Porto, Portugal

⋆up241045@up.pt

Abstract: Symmetry quantification in periodontal disease is crucial for understanding disease progression and facilitating population-based studies, especially with incomplete data. This study introduces a novel measure for symmetry assessment using a decay-type exponential function. Designed to maximize spatial predictability and align with clinical perceptions of symmetry, this measure demonstrated high efficacy. An evaluation involving periodontists showed a strong correlation (0.96) between clinical assessments and the symmetry scores generated by the measure. Additionally, the measure enhanced predictive models, outperforming simpler models in terms of RMSE, MAE, and R^2 values. Future research should validate this measure across diverse populations and explore its broader applications

keywords: symmetry quantification; periodontal disease; predictive modeling

MSC2020: 49-XX; 34-XX; 92-XX.

1 Introduction

From an epidemiological perspective, symmetry quantification facilitates the estimation of population disease parameters, especially when data is incomplete. This is evident in studies designed with half-mouth evaluations. Clinically, the significance of symmetry is underscored by the notion that asymmetric values of periodontal disease indicators might be influenced by asymmetric factors that affect both the onset and the progression of disease.

In the realm of fuzzy symmetry, when examining periodontal structures, it becomes imperative to quantify the symmetry between distinct entities. For this purpose, consider two values, A and A', each representing specific attributes or measurements of contralateral sites taken on the same scale. This means that both A and A' are quantified using the same units and methodology, allowing for direct comparison or estimation between the two.

2 Proposed Measure

To create a measure that captures similarity information, maximizes spatial predictability, and mimics the clinician's perception of symmetry grade, we introduce a decay-type exponential function with the form:

$$SM(A, A', \alpha, \beta) = e^{-\frac{|A-A'|}{\alpha+\beta\frac{A+A'}{2}}} \quad (1)$$

Where: - α is a scaling parameter. - β is the association parameter between A and A' (its contralateral counterpart).

2.1 Parameter α

Alpha (α) acts as a scaling factor that helps control the steepness of the exponential decay in the function. The α adjusts the sensitivity of the SM function to absolute differences between A and A'; a smaller α makes the function more sensitive. The default values of α are set to 1, 0.1, and 0.01 according to the scale of A, when A and A' are integers, decimals, or centesimals, respectively.

When A and A' are integers, the potential differences between A and A' are larger in absolute terms compared to when A and A' range from 0 to 0.9 on a decimal scale. Consequently, α needs to be adjusted to maintain a function response similar to what was observed with larger integer values. α must be reduced to increase the function's sensitivity to these smaller differences. This feature allows for the comparison of symmetry grades between pairs A and A' measured on different scales.

2.2 Parameter β

Making the parameter β equal to the correlation coefficient between A and A', we are effectively stating that the higher the correlation, the more predictable the behavior of one site based on the other. This fits well with the goal of using symmetry grading for prediction, as highly correlated contralateral sites will have similar characteristics and responses.

In this application of SM, β is always positive, as there is no biological justification for it to be negative. This positivity is crucial because it ensures that the function emphasizes similarity rather than dissimilarity in the grading of periodontal lesions between sites. Positive values of β reduce the denominator in the SM function for pairs of sites with higher correlation, thereby diminishing the impact of absolute differences $|A-A'|$ and highlighting their inherent similarity. The use of β as a correlation coefficient in the context of symmetry grading for periodontal lesions leverages statistical relationships to enhance contralateral spatial predictivity. Additionally, directionality of the difference was incorporated into the function by creating SM_dir, which involves multiplying SM by γ, a parameter that takes values of -1 and $+1$.

2.3 Empirical Results

Evaluation of SM Function in Clinical Setup To evaluate the effectiveness of the SM function in capturing the clinical magnitude of symmetry, a study was conducted involving ten experienced periodontists. These experts were asked to score twenty pairs of pocket probing depth (PPD) values on a scale from zero to ten. The results of this expert assessment were then compared to the symmetry scores generated by the SM function for the same pairs of values. The analysis revealed a high correlation coefficient of 0.96, indicating a strong agreement between the periodontists' evaluations and the SM function's outputs.

Evaluation of SM Function in Contralateral Prediction To evaluate the importance of $SM\_dir11.Site$ for contralateral prediction, two gradient boosting machine (GBM) models were fitted using the National Health and Nutrition Examination Survey (NHANES) 2011-2012 data and evaluated. The first model, GBM1, included both the values of PPD for the modeled *site*, each one of the six sites per tooth: Disto-Vestiblular (DV), Vestibular (V), Mesio-Vestibular (MV), Disto-Lingual (DL), Lingual (L) and Mesio-Lingual (ML) of the upper right central incisor ($11Site$) and the mean directional SM ($SM\_dir11.Site$) as predictors. The second model, GBM2, included only the PPD of the modeled *Site* ($11.Site$) as a predictor.

Table 1: Performance Metrics for GBM Models Including Right Side Values ($Site1$) and Directional SM (GBM1) and only Right Side Values ($Site2$) (GBM2)

	GBM models											
Metric	**DV1**	**DV2**	**V1**	**V2**	**MV1**	**MV2**	**DL1**	**DL2**	**L1**	**L2**	**ML1**	**ML2**
RMSE	0.167	0.760	0.230	0.653	0.210	0.682	0.252	0.740	0.220	0.705	0.350	0.685
MAE	0.037	0.484	0.049	0.416	0.037	0.457	0.064	0.535	0.055	0.468	0.086	0.465
MSE	0.028	0.578	0.053	0.427	0.044	0.466	0.063	0.547	0.049	0.497	0.122	0.469
R^2	0.969	0.357	0.930	0.375	0.954	0.502	0.932	0.417	0.943	0.417	0.871	0.506
Adj. R^2	0.967	0.322	0.927	0.340	0.951	0.474	0.928	0.385	0.940	0.385	0.864	0.479
Exp. Var.	0.969	0.356	0.923	0.375	0.951	0.493	0.932	0.415	0.943	0.416	0.871	0.505

Abreviatures: RMSE – Root Mean Squared Error, MAE – Mean Absolute Error, MSE – Mean Squared Error, R^2 – R-squared, Adj. R^2 – Adjusted R^2, Exp. Var. – Explained Variance, DV – Disto-Vestiblular, V – Vestibular, MV – Mesio-Vestibular, DL – Disto-Lingual, L – Lingual, ML – Mesio-Lingual *sites* of the upper right central incisor ($11Site$), $SM\_dir11.Site$ – Mean directional SM

Table 2: Variable Importance in GBM1 Models per Site of Upper Central Incisors

Variable	**DV1**	**V1**	**MV1**	**DL1**	**L1**	**ML1**
SM_dir11.Site	69.554	61.598	54.865	64.871	66.539	47.927
Site	30.446	38.402	45.135	35.130	33.461	52.073

The performance of both models was assessed on a hold-out test set using Root Mean Squared Error (RMSE), Mean Absolute Error (MAE), Mean Squared Error (MSE), R-squared (R^2), Adjusted R^2 (Adj. R^2) and Explained Variance (Exp. Var.) as evaluation metrics across multiple sites for the two GBM models by site GBM1 (DV1, V1, MV1, DL1, L1 and ML1) and GBM2 (DV2, V2, MV2, DL21, L2 and ML2).

For site DV, GBM1 (which incorporated both $11DV$ and $SM\_dir11.DV$) achieved an RMSE of 0.167, an MAE of 0.037, an MSE of 0.028, and an R^2 of 0.969, significantly outperforming GBM2, which had an RMSE of 0.760, an MAE of 0.484, an MSE of 0.578, and an R^2 of 0.357. Similar results where found for the other five sites, as can be observed in table 1

The trend observed in the performance metrics across all sites indicates that GBM1, which includes the additional predictor $DM\_dir11.Site$, consistently outperforms GBM2. This is evident from the lower RMSE and MAE values and higher R^2 values for GBM1, suggesting a better fit to the test data.

Table 2 shows the relative importance of the predictors in the GBM1 models for different sites of the central incisors. The mean directional SM ($DM\_dir11.Site$) had a higher importance than the site value alone in most cases, highlighting its significant contribution to the improved performance of GBM1. For example, the importance of $SM\_dir11.DV$ was highest for site DV1 (69.554) compared to the DV PPD *site* value alone (30.446). Similar trends are seen across other sites, emphasizing the value of including directional SM as a predictor.

3 Conclusions and Future Work

The proposed measure for symmetry quantification in periodontal disease offers a robust framework for both clinical and epidemiological applications. By adjusting α and β, this measure can be tailored to different scales and correlation levels, enhancing its utility in various contexts. Future research should focus on validating this measure in larger and more diverse populations and exploring its application in other fields.

References

[1] Friedman, J. H., Greedy function approximation: a gradient boosting machine, Annals of Statistics, **29**(5) (2001), 1189–1232.

[2] Filev, D. P., Yager, R. R., Fuzzy Sets and Applications: Selected Papers by L.A. Zadeh, John Wiley & Sons, 1987.

[3] Kaufmann, A., Introduction to the Theory of Fuzzy Subsets, Volume 1: Fundamental Theoretical Elements, Academic Press, 1975.

[4] Centers for Disease Control and Prevention (CDC). National Center for Health Statistics (NCHS). National Health and Nutrition Examination Survey Data. Hyattsville, MD: U.S. Department of Health and Human Services, Centers for Disease Control and Prevention, 2011-2012. Available from: https://www.cdc.gov/nchs/nhanes/index.htm

International Conference on Mathematical Analysis and Applications in Science and Engineering
ICMA^{2}SC'24
ISEP Porto-Portugal, June 20 - 22, 2024

Disentangling High-Order Cardiorespiratory Interactions in Postural Stress

Helder Pinto[1⋆] **Yuri Antonacci**[2] **Michal Javorka**[3] **Luca Faes**[2]
Ana Paula Rocha[1]

[1] CMUP, Departamento de Matemática, Faculdade de Ciências, Universidade do Porto, Portugal
[2] Department of Engineering of University of Palermo, Italy
[3] Department of Physiology, Jessenius Faculty of Medicine, Comenius University of Bratislava, Slovakia

[1⋆]helder.pinto@fc.up.pt

Abstract: Mutual Information Rate (MIR) serves as one of the main tools for quantifying the dynamic coupling between two processes within a network, particularly for the analysis of cardiorespiratory interactions. However, it can vary significantly in its conditioned calculation due to high-order dependencies among system processes. In this study, a novel approach is proposed: searching multiplets of variables that maximize or minimize dynamic coupling. This approach breaks down the maximal MIR into unique, redundant, and synergistic components, allowing the assessment of high-order effects relative importance compared to dyadic effects. The applicability of the proposed framework in that characterization is demonstrated using experimental data of heart period and respiratory time series in healthy subjects during rest and postural stress.

keywords: Information Theory; Mutual Information Rate; High-Order Interactions

MSC2020: 60G10; 60B10; 94A17.

1 Introduction

In the framework of Information Theory several measures have been proposed for the study on cardio-respiratory interactions. Among them, the Mutual Information Rate (MIR) has been showed to be a very promising tool for assessing the dynamic interdependence between pairs of physiological systems [1]. However, the traditional representation of pairwise interactions is not appropriate to provide a complete description of complex interactions occurring in physiological networks. In recent years, the growing interest in high-order interactions [2, 3] has led to an increased emphasis on understanding the emergent properties of these complex relationships. These properties are evident in high-order behaviors in data, surpassing conventional dyadic descriptions. In this study, using partial conditioning in multivariate data sets [4], we decomposed the maximum dynamical coupling between two processes into unique, redundant, and synergistic MIR components. This framework was then applied to analyze physiological time series data on the effects of postural stress on cardiovascular and respiratory variability.

2 Materials and Methods

2.1 Data Acquisition and Time Series Extraction

The analysis relies on a database previously used for the study of cardiovascular and cardiorespiratory interactions (for details on data acquisition and protocol see e.g [2]). From the acquired signals five variability time series were extracted: RR intervals (RR), Systolic Arterial Pressure (SAP), Diastolic Arterial Pressure (DAP), Mean Arterial Pressure (MAP) and Respiration (RESP). The time series were extracted from a group of 127 healthy subjects monitored in the resting supine position (REST), and in the upright position (UP) induced through passive head-up tilt. The study was approved by the local Ethical Committee. The analysis was performed on 300-point artifact-free, weak-sense stationary segments from each subject and condition and the time series were normalized to zero mean and unit variance before the analysis.

2.2 Conditioning Approach for the Assessment of High Order Interactions

Consider two ergodic stationary stochastic processes X and Y with zero mean. Denote by X_n and Y_n the current states of both processes, and let $X_n^q = [X_{n-1}, \ldots, X_{n-q}]$ and $Y_n^q = [Y_{n-1}, \ldots, Y_{n-q}]$ represent the past states, where q sets the history length. The degree of association is quantified by the pairwise MIR [1]

$$I_p = I_{X;Y} = \lim_{q \to \infty} \frac{1}{q} I\left(X_n^q; Y_n^q\right), \tag{1}$$

where $I(\cdot;\cdot)$ denotes Mutual Information (MI). Suppose that N other processes $\mathbf{Z} = \{Z_1, \ldots, Z_n\}$ are simultaneously measured. Define $I_k = I_{X;Y|\mathbf{Z}_k}$, the conditional MIR (cMIR), where $\mathbf{Z}_k$ is an element of the powerset of $\{Z_1, Z_2, \ldots, Z_n\}$. Additionally, denoting as $\mathbf{Z}_m$ the subset of processes in $\mathbf{Z}$ which minimizes I_k, and $I_m = I_{X;Y|\mathbf{Z}_m}$ the corresponding value of the cMIR. Similarly, $\mathbf{Z}_M$ represents the subset of processes in $\mathbf{Z}$ that maximizes I_k, with the corresponding value of the cMIR denoted as $I_M = I_{X;Y|\mathbf{Z}_M}$. The reduction on MIR is associated with redundancy (R), $R = I_p - I_m$. Conversely, synergistic information (S) represents the increase in MIR resulting from adding variables to the conditioning set, $S = I_M - I_p$, while unique information (U) shared between X and Y corresponds to I_m. Accordingly, the following decomposition holds, $I_M = U + R + S$. Exhaustive search of subsets $\mathbf{Z}_m$ and $\mathbf{Z}_M$ is impractical for large n. Instead, we use a greedy strategy with a surrogate-based stopping criterion [4]. For estimating MIR and cMIR, a parametric approach based on Vector AutoRegressive (VAR) models is employed [1].

3 Results and Discussion

In this work, the network {RR, SAP, DAP, MAP, RESP} was considered. To analyze cardiorespiratory interactions, we set X = RR, Y = RESP, and the vector $\mathbf{Z}$ composed by the remaining processes. Fig.1 depicts distributions of I_M, U, R, and S during REST and UP. Differences between the two conditions were assessed using the Wilcoxon test for paired data. I_M decreases with the postural stress suggesting reduced coupling between RR and RESP, reflecting the weakening of RSA during tilt [2]. No statistically significant differences in U were reported between REST and UP. Moreover, in both conditions, the estimated values are very low, indicating that RESP and RR do not share a large amount of unique information. Both R and S, decrease significantly with postural stress, with a predominance of redundancy over synergy in both physiological conditions, corroborating previous studies [2].

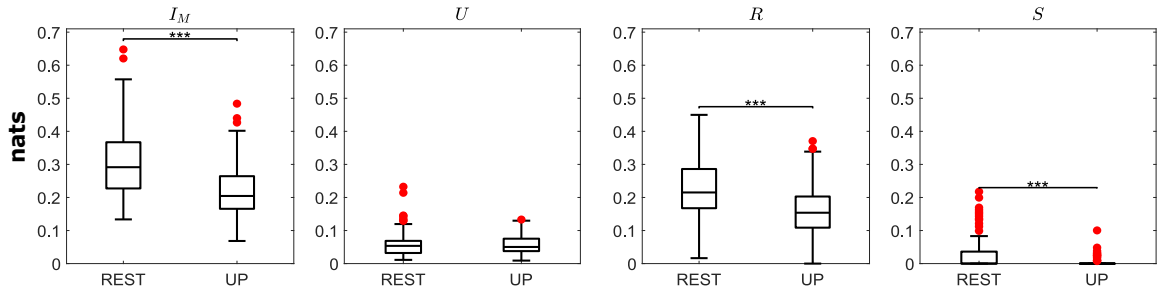

Figure 1: Boxplot distributions of I_M, U, R and S (expressed in natural units, *nats*) computed during REST and UP. Statistical analysis using Wilcoxon test for paired data: *, $p < 0.05$, **, $p < 0.01$, ***, $p < 0.001$.

4 Conclusions and Future Work

This study introduces a novel approach utilizing MIR to differentiate dyadic dependence from polyadic effects in cardiorespiratory interactions. The observed decrease in maximal MIR between RESP and RR confirms the dampening of RSA during postural stress. Our findings suggest that cardiorespiratory interactions are mainly mediated by redundancy, underscoring the need to analyze polyadic interactions. This framework could help to quantify the emergence of higher-order behaviors in brain-heart interactions in the future.

Acknowledgments

H.P and A.P.R were supported by CMUP, member of LASI, funded by national funds through FCT under projects UIDB/00144/2020 and UIDP/00144/2020. H.P. thanks FCT for the Ph.D. Grant 2022.11423.BD. L.F. and Y.A is supported by the Sicilian Micronanotech Research And Innovation Center (SAMOTHRACE, MUR, PNRR-M4C2, ECS_00000022), spoke 3 - University of Palermo "S2-COMMs - Micro and Nanotechnologies for Smart & Sustainable Communities.

References

[1] Gorana Mijatovic, Laura Sparacino, Yuri Antonacci, Michal Javorka, Daniele Marinazzo, Sebastiano Stramaglia, and Luca Faes. Assessing high-order links in cardiovascular and respiratory networks via static and dynamic information measures. *IEEE Open Journal of Engineering in Medicine and Biology*, pages 1–13, 2024.

[2] Hélder Pinto, Riccardo Pernice, Maria Eduarda Silva, Michal Javorka, Luca Faes, and Ana Paula Rocha. Multiscale partial information decomposition of dynamic processes with short and long-range correlations: theory and application to cardiovascular control. *Physiological Measurement*, 43, 8 2022.

[3] Fernando E Rosas, Pedro AM Mediano, Andrea I Luppi, Thomas F Varley, Joseph T Lizier, Sebastiano Stramaglia, Henrik J Jensen, and Daniele Marinazzo. Disentangling high-order mechanisms and high-order behaviours in complex systems. *Nature Physics*, 18(5):476–477, 2022.

[4] Sebastiano Stramaglia, Luca Faes, Jesus M. Cortes, and Daniele Marinazzo. Disentangling high order effects in the transfer entropy. arXiv:2402.03229, 2024.

International Conference on Mathematical Analysis and Applications in Science and Engineering
ICMA^{2}SC'24
ISEP Porto-Portugal, June 20 - 22, 2024

Cotinine: Exploring the Impact of Smoking Habits on Periodontal Disease

João Onofre[1,a)], Luzia Mendes[1], Pereira J.A.[1,2]

[1] Faculty of Dental Medicine of University of Porto, Portugal,
[a)] up201907471@edu.fmd.up.pt
[3] Centro de Estatística Aplicações da Universidade de Lisboa, Portugal

Abstract

1 Introduction

Smoking is a recognized risk factor for the onset and exacerbation of periodontal disease. Researches into the relationship between tobacco use and periodontal health began in the 20th century, highlighting tobacco's significant impact on the initiation, progression, and severity of periodontal disorders. Smoking is the principal behavioral risk factor for periodontitis, impacting its prevalence, extent, and severity.

Cotinine, an alkaloid found in tobacco and the primary active metabolite of nicotine, serves as a biomarker to measure tobacco smoke exposure, with a minimal amount being excreted through the kidneys. Cotinine provides a more precise measure of nicotine intake than self-reported smoking habits due to its detectability in blood, saliva, or urine. The extended half-life of cotinine, ranging from 15 to 20 hours—contrasted with nicotine's shorter half-life of approximately 2 hours—establishes it as a reliable biochemical marker for assessing nicotine consumption.

Periodontitis is defined as a chronic multifactorial inflammatory disease associated with a dysbiotic biofilm and characterized by the progressive destruction of the tooth-supporting apparatus. The periodontal apparatus, comprising the gingiva, cementum, periodontal ligament, and alveolar bone, plays a critical role in maintaining dental stability within the oral cavity. The pathogenesis of periodontitis is initiated by gingivitis, a condition characterized by localized gingival inflammation due to dental biofilms. Without clinical intervention, this preliminary inflammatory phase can evolve into chronic periodontitis. This advancement is marked by the emergence of profound periodontal pockets, a critical indicator of progressed periodontal disease, potentially leading to tooth loss. The pathophysiological framework of this progression is characterized by the intricate interaction between the pathogenic biofilm and the host's immune response, perpetuating a chronic inflammatory state that amplifies the systemic inflammatory burden.

The GAMLSS framework is a flexible approach for modeling a wide variety of distributions for the response variable. Unlike traditional linear models, GAMLSS allows for the simultaneous modeling of location, scale, and shape parameters, providing a comprehensive understanding of the data's distribution. This flexibility is particularly useful for handling non-normal data and accommodating heteroscedasticity and skewness in the response variable. GAMLSS supports a wide range of distributions, enabling the selection of the most appropriate distribution for the data. The model allows for the separate modeling of location (mean), scale (variance), and shape (skewness and kurtosis) parameters, offering a detailed characterization of the data. GAMLSS incorporates smooth functions of explanatory variables, which can capture non-linear relationships effectively and provides robust diagnostic tools for model checking and validation, ensuring the reliability of the model's inferences. In this study, the GAMLSS model was used to analyze the behavior of the dependent variable PPDmax in relation to serum cotinine levels, gender, and smoking habits. The flexibility of GAMLSS allowed for the accommodation of the skewed distribution of PPDmax and the inclusion of covariates affecting different aspects of the distribution.

CART is a non-parametric decision tree learning technique that can be used for both classification and regression tasks. The method builds a tree by recursively splitting the data into subsets based on the values of the predictor variables, aiming to create homogenous groups with respect to the response variable. It handles non-linear relationships between predictors and the response variable without requiring transformations or pre-specification of the functional form. The model naturally identifies interactions between variables, as splits are based on the combined effect of predictors. CART provides measures of variable importance, indicating the relative contribution of each predictor to the model. The resulting tree structure is easy to interpret and visualize, showing the decision rules used to split the data. In this study, the CART model was used to analyze the impact of smoking habits on periodontal health, particularly on PPDmean and CALmean. The ability of CART to capture non-linear interactions and provide clear variable importance measures was crucial for understanding the complex relationships in the data.

2 AIM

The study aimed to determine if the maximum probing pocket depth (PPDmax) and the Clinical Attachment Loss (CAL) are associated with serum cotinine levels, age, gender, and smoking habits.

3 Materials and Methods

Data from the National Health and Nutrition Examination Survey was analyzed using GAMLSS and CART models within the R software. The variables considered in this study were maximum probing pocket depth (PPDmax); mean

probing pocket (PPDmean); maximum clinical attachment level (CALmax); mean clinical attachment level (CALmean), serum cotinine levels, age, gender, and smoking habits.

4 Results

The sample consisted of 835 males (62.4%) and 504 females (37.6%), indicating a significant gender imbalance. The mean age was 52.68 years, with a standard deviation of 14.15 years. Periodontal variables included PPDmean, PPDmax, CALmean, and CALmax. Descriptive statistics provided insights into the central tendencies and distributions within the sample.

The clinical attachment loss variables, CALmean and CALmax, exhibited means of 1.99 mm and 4.91 mm, respectively, with significant skewness and kurtosis, indicating a wide range of attachment loss severity within the sample. Cotinine levels, a biomarker for tobacco exposure, showed substantial variation, with a mean of 108.14 ng/mL. The duration of smoking had a mean of 34.90 years, further emphasizing the long-term tobacco exposure in this population.

Comparing the two models GAMLSS models for PPDmax (Table 3 and Table 5), the model with age as a factor presented a lower AIC (3715.331) compared to the model with smoking habits as a variable (AIC = 3744.620), suggesting that age is a more significant predictor for PPDmax than smoking habits when considering model complexity. The model with age also showed lower RMSE (1.543) and MAE (1.190) values compared to the model with smoking habits (RMSE = 1.574, MAE = 1.218), further demonstrating that the model with age provides more accurate predictions. Additionally, the model with age as a predictor had a higher R^2 (0.084) compared to the other model ($R^2 = 0.046$). The higher R^2 value for the age model indicates that it explains a greater proportion of the variance in PPDmax, highlighting age as a more substantial factor in predicting periodontal probing depth.

In the GAMLSS model for CALmax (Table 13), cotinine levels ($\beta = 3.2 \times 10^{-3}$; p-value $= 1.72 \times 10^{-13}$) suggested a positive relationship between cotinine levels and CALmax, indicating that higher cotinine levels are associated with increased clinical attachment loss. Female gender ($\beta = -0.967$; p-value = ¡ 2×10^{-16}) was associated with lower CALmax compared to males, suggesting gender differences in periodontal health. Age ($\beta = 0.0541$; p-value = ¡ 2×10^{-6}) indicated that CALmax increases with age, implying that older individuals tend to have higher clinical attachment loss.

The analysis of smoking habits ($\beta = 2.6 \times 10^{-3}$; p-value $= 1.48 \times 10^{-7}$) indicated a significant positive relationship between smoking and CALmax. This suggests that smoking contributes to increased clinical attachment loss. However, this was not observed in the PPDmax model, highlighting the need for further investigation into the differential impact of smoking on various periodontal health measures.

The CART model analysis demonstrated that the primary split is based on cotinine levels, underscoring its significance in predicting PPDmean. Gender

and smoking duration were also significant predictors.

The choice of the CART model over the GAMLSS model for analyzing the impact of smoking habits on periodontal health is justified by CART's capacity to handle non-linear relationships and interactions more effectively.

The CART model provides a clearer interpretation of variable importance and reveals critical insights into the influence of cotinine, gender, and smoking duration on PPDmean.

5 Conclusions

The results suggest that cotinine is associated with the severity of periodontal disease, being linked to increased values of PPDmax and CALmax. The GAMLSS models demonstrated a significant relationship between cotinine and both PPDmax and CALmax, which remained robust even after the inclusion of additional predictors such as age, gender, and smoking habits. Furthermore, the CART models indicated that cotinine is the most important factor influencing the severity of periodontal disease compared to age, gender, and smoking habits. These findings can help patients understand the detrimental effects of tobacco use on periodontal health.

Keywords: Serum cotinine levels, Probing pocket depth, Clinical Attachment Level, GAMLSS model, CART model

International Conference on Mathematical Analysis and Applications in Science and Engineering ICMA²SC'24

ISEP **Porto-Portugal, June 20 - 22, 2024**

RELATION BETWEEN ZONA PELLUCIDA SHEAR STRESS AND DIFFERENT SPERM DISTRIBUTION IN THE CONTEXT OF THE CONTACT STRESS THEORY

Andjelka Hedrih[1*] **Katica (Stevanovic) Hedrih**[1] **Đorđe Jovanović**[1]

[1] Mathematical Institute of Serbian Academy of Sciences and Arts, Belgrade, Serbia

[1*] handjelka@mi.sanu.ac.rs

Abstract: The paper presents the results of research into possible scenarios of sperm penetration through the zona pellucida (ZP) due to deformation work caused by the deformation of the ZP in the radial direction and, additionally, in the tangential plane by parts of the transmitted kinetic energy of the sperm impact on the ZP. The results of the numerical experiment were analyzed, and a number of conclusions were drawn based on the hypothesis of the highest normal stress or the hypothesis of the highest shear stress, in which ZP damage or crack progression in the ZP occurs, allowing spermatozoa to penetrate through the ZP to the oocyte.

keywords: shear stress; sperm distribution; contact stress theory

MSC2020: 74M-15; 74B-10; 92-10

1 Introduction

There are different theories regarding sperm penetration mechanism trough zona

pellucida (ZP) of the oocyte, such as: biochemical receptor recognition, maximum normal stress [1] and oscillations of relaxation [2]. However, the very mechanism of sperm penetration still remains elusive. Pleasure that sperm generates upon the ZP depends of sperm mass m_k, velocity and contact surface. The experiments with probing the mechanical properties of ZP shows that the more you press ZP, the more it resists [3]. This indicates that the maximum contact pressure is not the optimal strategy for ZP penetration. In numerical simulations of non-linear sperm-oocyte frictional contact [2], the authors suggested that the possible mechanism of sperm penetration could be oscillations of relaxation, which is in concordance with experiments [4], which show that sperm creates an oblique path through ZP.
Starting from the hypotheses that shear stress is an important element in sperm penetration mechanism contact stress theory and collision theory, [5] are used to study the relation between different sperm distribution on the oocyte surface and shear stress that is generated on different areas of the oocyte surface -zona pelucida (ZP). In the model, the oocyte surface was divided into 10 equal segments. The following assumptions of the model are will now be stated. The main assumption is that the kinetic energy of each sperm is transformed into potential energy of deformation of local area of the ZP surface. Stress and strain in the ZP are related to the initial sperm arrangement. Ratio between progressive and non-progressive sperm cells that interact with an oocyte in the in vitro conditions is embedded in the numerical simulation. To study the effect of sperm impact on ZP shear stress three different configurations of sperm cells distribution were used: equal number of sperm cell to each segment; different number of sperm cells to oocyte surface segments but symmetrical arrangement and different number of sperm cells to oocyte surface segments but asymmetrical arrangement.

2 Results and discussion

We assume that each sperm cell has two component velocities in the contact with the oocyte surface: in radial direction $\vec{v}_{r,k}, k = 1,2,3\ldots,N$, and in tangent plane regarding the contact point with oocyte surface $\vec{v}_{T,k}, k = 1,2,3\ldots,N$. Taking into account referent surface contact area S and different restitution coefficients $k_{res,k}$ for each sperm the deformation work caused by ZP radial deformation for each surface segment of the oocyte is equal to kinetic energy of impact radial component velocity of sperm and we can write the following relation in the form:

$$\mathbf{A}_{\mathbf{def},r} = S\delta\frac{\sigma^2}{2\mathbf{E}} = \left[\sum_{k=1}^{k=N_1}\frac{1}{2}m_k\left(v_{r,k}\right)^2 + \sum_{k=N_1}^{k=N}\frac{1}{2}m_k\left(\left(1-k_{res.k}\right)v_{r,k}\right)^2\right] \quad (1)$$

The ZP deformation work caused by ZP deformation in tangent plane for each surface segment of the oocyte is equal to kinetic energy of impact tangential component velocity of each sperm and the relation follows in the form:

$$A = S\delta\frac{\tau^2}{2G} = \left[\sum_{k=1}^{k=N_1}\frac{1}{2}m_k(v)^2 + \sum_{k=N_1}^{k=N}\frac{1}{2}m_k\left((1-k_{\mathrm{res}.k})v\right)^2\right] \quad (2)$$

where σ is normal stress, τ is shear stress, S-contact surface area, E-Young modulus, G-shear modulus, δ is ZP thickness, $k_{res,k}$ is coefficient of restitution and can have values [0;1]. Three different configurations of sperm cells distribution were used: equal number of sperm cell to each segment; different number of sperm cells to oocyte surface segments but symmetrical arrangement and different number of sperm cells to oocyte surface segments but asymmetrical arrangement. Deformation work caused by ZP radial deformation and ZP deformation in tangent plain of the same segment are calculated

with the data of sperm count and sperm velocities taken from WHO using a numerical simulation, which simulates sperm cell penetration on the oocyte surface.
The duration of simulated time lasts 120 seconds, in intervals of 1s. Each second of sperm cell penetration is simulated in the following manner. Firstly, each sperm is assigned a cell group using the roulette wheel method. This method is comprised of selecting one of n given options, where the chances of selecting an option are not equal. The following cell groups are considered: progressive, which have a speed of 4.9E-6 m/s and 32 percent chance of occurrence; non-progressive, which have a speed of 80.7E-6 m/s and 8 percent chance of occurrence, and non-motive, which have a speed of 0 m/s and 60 percent chance of occurrence. Once the cell group is determined, the point of penetration on the sphere is selected in a random manner. Deformation works that is a result of ZP radial deformation and deformation in tangent plane for each surface segment are calculated.
Then, this process is repeated for 2.3E7 times, which represents the number of sperm cells which try to penetrate the oocyte each second.

3 Conclusions and Future work

For different sperm distribution configuration deformation work of ZP radial deformation and ZP deformation in tangent plain have different values. Segments with minimum and segments with maximum values of shear stress of ZP are identified for the defined initial conditions.
Our future work will be to identify potential "weak spot" in ZP segment based on the values of normal and shear stresses for defined initial conditions.

Acknowledgments

We are grateful to the financial support from Ministry of Science, Technological Development and Innovation of Republic of Serbia trough Mathematical Institute of Serbian Academy of Sciences and Arts.

References

[1] Pavel Kozlovsky, Amit Gefen, The relative contributions of propulsive forces and receptor–ligand binding forces during early contact between spermatozoa and zona pellucida of oocytes, Journal of Theoretical Biology, **7**(294) (2012), 139-43.

[2] Andjelka Hedrih, Milan Banić, The effect of friction and impact angle on the spermatozoa–oocyte local contact dynamics Journal of Theoretical Biology **393** (2016), 32-42.

[3] Massimiliano Papi, Roberto Brunelli, Lakamy Sylla, Tiziana Parasassi, Maurizio Monaci, Giuseppe Maulucci, Mauro Missori, Giuseppe Arcovito, Fulvio Ursini, Marco De Spirito, Mechanical properties of zona pellucida hardening, Eurropean Biophysics Journal, **39**(6) (2010), 987-92.

[4] Michael J Bedford Why do penetrating sperm create an oblique path in the zona pellucida, Reproduction. 131 (2006), 23–25.

[5] K. R. Hedrih (Stevanović), *Izabrana poglavlja Teorije elastičnosti (Selected chapters of Theory of Elasticity), (in Serbian),* proširena i dopunjeno. Nis: Mašinski fakultet u Nišu, 1988. http://elibrary.matf.bg.ac.rs/handle/123456789/3766

International Conference on Mathematical Analysis and Applications in Science and Engineering ICMA²SC'24

ISEP **Porto-Portugal, June 20 - 22, 2024**

CROSS-CORRELATION OF LOWER LIMB SAGITTAL JOINT ANGULAR KINEMATICS FOR COORDINATION ASSESSEMENT

Carlos Rodrigues[1,2*] **Miguel Correia**[1,2] **João Abrantes**[3]

Marco Rodrigues[4] **Jurandir Nadal**[5]

[1] INESC TEC, Portugal
[2] FEUP, Portugal
[3] ULHT, Portugal
[4] UFPE, Brazil
[5] UFRJ, Brazil

[1*] carlos.b.rodrigues@inesctec.pt

Abstract: This study presents and applies normalized cross-correlation of entire time series from lower limb sagittal joint angular kinematics to assess intra-joint coordination during long, short and no countermovement (CM) with muscle stretch-shortening cycle (SSC) on standard maximum vertical jump. Applied metrics allowed the detection of lower-limb intra-joint coordination differences on maximum cross-correlation time delay based on entire time series of kinematic bio-signal at each CM condition, SSC and joint.

keywords: cross-correlation; time delay; coordination

MSC2020: 62M10; 62H20; 92C10.

1 Introduction

Human movement performance strongly depends on four levels of integration, starting with neuromuscular control of the muscle motor unit, the sum of the twitches from all the motor units at the level of the tendon, the musculoskeletal integration at each joint of the force and force moments of the passive and active structures crossing each joint and the synergy of multiple joints towards a common goal [1]. At the principal of equal simplicity, Bernstein [2] postulated that the central nervous system (CNS) must exert control at the joints or at the synergy level since it would be incredibly complex to separately control each muscle [1,2]. Muscle stretch-shortening cycle (SSC) corresponds to an anticipation muscle stretch before muscle contraction to produce more efficient submaximal and powerful maximal action than it would be achieved in the absence of muscle stretch [3]. Despite at lower limbs, muscle SSC can be observed at gait and run,

its isolated assessment is performed at standard maximum vertical jump (MVJ) with long countermovement (CM) and SSC on countermovement jump (CMJ), and short CM and SSC on drop jump (DJ) for comparison with no CM and SSC at squat jump (SJ) [4]. In order to assess joint coordination, sagittal lower limb joint angular phase-plane has been applied at long, short and no CM [5], as well as cross-correlation of lower limb joint angular kinematic for inter-joint coordination assessment during impulse phase on standard MVJ [6], with an open issue on sagittal intra-joint angular kinematic coordination. For this reason, we present and applied a cross-correlation analysis of lower limb sagittal joint angular kinematic for coordination assessment of the joint angles, angular velocities and angular accelerations at the hip, the knee and the ankle during standard MVJ with long, short and no CM comparison.

2 Data and Methodology

3D cartesian coordinates of anatomical selected joint marks were obtained from direct linear transformation (DLT) of 2D images from two cameras acquisitions at 100 Hz on anterior and posterior position at sagittal plane. Lower limb sagittal joint angles, angular velocities and angular accelerations were obtained from inverse kinematics using 3D cartesian coordinates of selected anatomical joint marks. Normalized cross-correlations of the lower limb sagittal joint angles (θ), angular velocities (ω), and angular accelerations (α) during the impulse phases at standard MVJ were implemented using MATLAB R2017a (MathWorks Inc., Massachusetts, USA). Time delay (τ) of the normalized maximum cross-correlations (*CCr max*) between the lower limb sagittal joint angular kinematic time series θ, ω and α were then compared among joints and standard MVJ at 5% significance for the mean (μ) and standard deviation (σ) of each subject best trial of 3 CMJ, 3 DJ and 3 SJ on a total of 54 repetitions for a sample of six male subjects with (21.5 ± 1.4) years, (76.7 ± 9.3) kg mass and (1.79 ± 0.06) m height.

3 Results and discussion

The hip presented at CMJ, DJ and SJ, with long, short and no CM, higher time delay τ of the maximum cross correlation *CCr max* between the sagittal joint angles θ and the corresponding joint angular velocities ω in relation to the knee and the ankle joints, as presented on Table 1 with reduced statistical significative differences (p<0.05) Table 2, pointing to longer τ of the hip joint angular velocity ω to produce its effect at the hip joint angle θ when compared to the knee and the ankle, regardless of the long, short and no CM condition, allowing this effect to be associated to the hip, and the knee, ankle joints intrinsic factors.

Table 1: Mean (μ) and standard deviation (σ) of the maximum cross-correlation time delay τ (s).

τ (s)	CMJ			DJ			SJ		
μ (σ)	Hip	Knee	Ankle	Hip	Knee	Ankle	Hip	Knee	Ankle
(θ, ω)	0.024 (0.023)	0.006 (0.013)	0.000 (0.000)	0.054 (0.064)	0.006 (0.009)	0.004 (0.005)	0.008 (0.013)	0.000 (0.000)	0.000 (0.000)
(ω, α)	0.168 (0.049)	0.038 (0.008)	0.028 (0.008)	0.046 (0.030)	0.048 (0.008)	0.030 (0.000)	0.095 (0.063)	0.030 (0.011)	0.025 (0.012)
(θ, α)	0.180 (0.092)	0.040 (0.020)	0.028 (0.013)	0.070 (0.024)	0.038 (0.024)	0.036 (0.011)	0.100 (0.072)	0.027 (0.016)	0.022 (0.012)

As regards to the time delay of *CCr max* between the sagittal joint angular velocities ω and the corresponding joint angular accelerations α, CMJ and SJ presented higher τ at

the hip than the knee both higher than the ankle, whereas DJ presented higher $\tau(\omega, \alpha)$ at the knee than the hip and the ankle, as presented on Table 1, with statistical significative differences presented at Table 2, thus pointing to different behavior of $\tau(\omega, \alpha)$ on short CM at DJ in relation to long and no CM on CMJ and SJ.

Table 2: Mean difference ($\Delta\mu$) and significance (p) of the time delay difference $\tau_i - \tau_j$ (s).

$\tau_i - \tau_j$ (s)	CMJ			DJ			SJ		
$\Delta\mu$ (p)	H-K	H-A	K-A	H-K	H-A	K-A	H-K	H-A	K-A
(θ, ω)	0.018 (0.085)	0.024 (0.040)	0.000 (0.187)	0.048 (0.085)	0.050 (0.079)	0.002 (0.341)	0.008 (0.093)	0.008 (0.093)	0.000 (0.500)
(ω, α)	0.130 ($<10^{-3}$)	0.140 ($<10^{-3}$)	0.010 (0.048)	-0.002 (0.446)	0.016 (0.153)	0.018 (0.004)	0.065 (0.016)	0.070 (0.011)	0.005 (0.237)
(θ, α)	0.140 (0.005)	0.152 (0.003)	0.012 (0.147)	0.032 (0.035)	0.034 (0.011)	0.002 (0.435)	0.073 (0.027)	0.078 (0.022)	0.005 (0.278)

Finally, the time delay of the maximum cross-correlation *CCr max* between the sagittal joint angles θ and the corresponding joint angular accelerations α presented a systematic behavior at long, short and no CM as presented on Table 1 and statistical significative differences (p<0.05) at Table 2, with longer $\tau(\theta, \alpha)$ at the hip in relation to the knee, both higher than the ankle on CMJ, DJ and SJ, pointing to longer time delay for the hip joint acceleration to reflect at corresponding hip joint angle than the knee and the ankle, regardless the CM condition.

4 Conclusions and Future work

Selected metric of time-delay from normalized maximum cross-correlation conduced to detection of shared and specific features at lower limb intra-joint coordination on each CM condition, namely at the effect of the time integration of each joint sagittal angular acceleration on the corresponding joint angular velocity and the time integration of the sagittal joint angular velocity on the corresponding sagittal joint angular displacement. Additionally, time delay of maximum cross-correlation presents as an adequate approach for coordination assessment of high-dimensional and strongly correlated kinematic bio-signal with temporal lag based on entire time series, while avoiding single point subjective analysis.

References

[1] D.A. Winter, *Biomechanics and motor control of human movement*, 4th ed. New Jersey: John Wiley & Sons, Inc., 2009.

[2] N.A. Bernstein, *The coordination and regulation of movements*. Oxford, UK: Pergamon Press, 1967.

[3] D. Knudson, *Fundamentals of biomechanics*. New York: Springer, 2007.

[4] P.V. Komi, *Strength and power in sport*. Oxford, UK: Blackwell Science Ltd, 2003.

[5] C. Rodrigues, M. Correia, J. Abrantes, M. Rodrigues, J. Nadal, Sagittal Lower Limb Joint Angular Phase-Plane Analysis at Long, Short and No-Countermovement, 2023 IEEE 7th Portuguese Meeting on Bioengineering (ENBENG), 167–170.

[6] C. Rodrigues, M. Correia, J. Abrantes, M. Rodrigues, J. Nadal, Cross-Correlation of Lower Limb Joint Angular Kinematic Signal for Coordination Assessment During Impulse Phase on Standard Maximum Vertical Jump, Proceedings of the 10th Congress of the Portuguese Society of Biomechanics. CNB 2023, Lecture Notes in Bioengineering. Cham: Springer, 2023, 908–916.

International Conference on Mathematical Analysis and Applications in Science and Engineering
ICMA^{2}SC'24
ISEP Porto-Portugal, June 20 - 22, 2024

Application of geometric methods to the calibration of a SIRS model for the RSV in infants

S. Blanes[1] **J. C. Cortés**[1] **N. Kopylov**[1⋆] **R.-J. Villanueva**[1]

[1] Universitat Politècnica de València, Spain

[1⋆]nikop1@upv.es

Abstract: We consider a SIRS model for the dynamics of the RSV infection. Using positivity- and mass-preservivg integrators and derivative-free optimization methods, we demonstrate a robust procedure to fit the model to the infant hospitalization data to predict the load of the healthcare system.

keywords: dynamic transmission model; compartmental model; respiratory syncytial virus infection; positivity-preserving integrators; derivative-free optimization

MSC2020: 49J52; 92D30.

1 Introduction

The respiratory syncytial virus (RSV) is a highly contagious RNA virus that infects nearly all children by age two, causing a spectrum of symptoms from mild colds to severe respiratory issues, with a significant impact on pediatric hospitalizations. RSV is a common cause of bronchiolitis in young children and can lead to pneumonia, respiratory failure, and even death [10, 24] The RSV can potential long-term neurological consequences [18].

Recent advances in RSV vaccine development have been significant, with the approval of the world's first RSV vaccines for adults. Additionally, a candidate maternal RSV vaccine has been evaluated, demonstrating efficacy in protecting infants [3, 25, 27, 19, 11, 23, 6, 17, 12]. Nonetheless, there is still no widely available vaccine for infants, making prevention through hygiene practices and isolation crucial [7, 21, 4].

Various [15] mathematical models have been employed for epidemiological modeling of RSV that highlight the importance of such models in decision-making for prevention and vaccination programs. To estimate disease burden and assess the impact of vaccination in different age groups, deterministic compartmental transmission models and machine learning models were used [26, 22, 28, 22, 13, 8, 20, 14]. Other models were used extract parameter values by fitting the model to *in vivo* data [2, 9].

2 Results and discussion

We consider the group of children under 1 year old, who are predominantly affected by the RSV, and use weekly data on hospitalizations of children [1] to estimate the fraction s of infected

children that would be hospitalized. We build our model under the following assumption and simplifications: population does not change significantly in one respiratory virus season (for several reasons: mortality is negligible, birth data updated annually); there is no difference between primary and secondary infections; there are no maternal antibodies.

$$\dot{S}(t) = -\beta(t)\frac{SI}{N} + \gamma R,$$
$$\dot{I}(t) = \beta(t)\frac{SI}{N} - \nu I$$
$$\dot{R}(t) = \nu I - \gamma R,$$

where $S(t)$, $I(t)$, $R(t)$ are the proportion of susceptible, infected, and recovered, correspondingly; $\beta(t) = b_0\,(1 + b_1\cos(\varphi + 2\pi t b_2))$ time-dependent disease transmission parameter, reflecting the seasonality of RSV; $1/\gamma$ is the average immunity duration; $1/\nu$ is the average recovery time. Particle swarm optimization is used to fit the parameters to the data.

Under the assumptions made, $S(t) + I(t) + R(t) = 1$, and each variable is non-negative at any given moment. This fact calls for the utilization of integrators that preserve mass and positivity (which belong to the wide family of geometric methods) [5], effectively preventing the occurrence of non-physical numerical solutions when the system exhibits stiff or highly oscillatory behavior. As a result, this approach helps in reducing computational time during model fitting. A similar strategy has been implemented in other (stochastic) SIVS epidemic models, addressing challenges related to negative outcomes in epidemic modeling [16].

To fit the model for the hospitalization count, we solve the ODE system with various sets of its parameters and the factor s to find one that minimizes the fitting error. Commencing on the 1$^{\text{st}}$ of September, a low number of children are expected to be infected and recovered, as approximately five to six months have elapsed since the conclusion of the RSV season in March. The majority of the population is anticipated to be susceptible.

3 Conclusions and Future work

We have applied geometric integrators to ensure a robust fitting procedure of compartmental epidemiological model to the data to predict the load of the health system.

It would be possible to generalize the model through introducing uncertainty (either by converting to random ODE or to a stochastic ODE). Additionally, the population change should be taken into account (flow and seasonal changes). Obviously, this will require numerical integration schemes that preserve only the positivity of the solution. Moreover, it would be favorable to get an insight into the modeling and the prediction of the infection peaks that may overload the healthcare system. Furthermore, given the recent development of the vaccines, we aim at investigating how vaccination campaigns may lower the number of hospitalization.

Acknowledgments

This work has been funded by Ministerio de Ciencia e Innovacion (Spain) through project PID2020-115270GB-I00, PID2022-136585NB-C21, MCIN/AEI/10.13039/ 501100011033/FEDER, UE, and also by Generalitat Valenciana (Spain) through project CIAICO/2021/180.

References

[1] A multivariate age-structured stochastic model with immunization strategies to describe bronchiolitis dynamics. `rotapp.shinyapps.io`.

[2] L. Acedo et al. "Mathematical modelling of respiratory syncytial virus (RSV): vaccination strategies and budget applications". In: *Epidemiol. Infect.* 138.6 (Dec. 2009), pp. 853–860. ISSN: 1469-4409. DOI: 10/c8k7hx.

[3] L. Anderson et al. "Strategic priorities for respiratory syncytial virus (RSV) vaccine development". In: *Vaccine* 31 (Apr. 2013), B209–B215. ISSN: 0264-410X. DOI: 10/f4wqc6.

[4] E. Baraldi et al. "RSV disease in infants and young children: Can we see a brighter future?" In: *Human Vaccines and Immunotherapeutics* 18.4 (June 2022). ISSN: 2164-554X. DOI: 10/gtt5rs.

[5] S. Blanes, A. Iserles, and S. Macnamara. "Positivity-preserving methods for ordinary differential equations". In: *ESAIM: Mathematical Modelling and Numerical Analysis* 56.6 (Aug. 2022), pp. 1843–1870. ISSN: 2804-7214. DOI: 10/gtt7bm.

[6] V. Cimica et al. "Novel Respiratory Syncytial Virus-Like Particle Vaccine Composed of the Postfusion and Prefusion Conformations of the F Glycoprotein". In: *Clin. Vaccine Immunol.* 23.6 (June 2016). Ed. by M. F. Pasetti, pp. 451–459. ISSN: 1556-679X. DOI: 10/f8q2b2.

[7] S. Esposito et al. "RSV Prevention in All Infants: Which Is the Most Preferable Strategy?" In: *Front. Immunol.* 13 (Apr. 2022). ISSN: 1664-3224. DOI: 10/grtjnb.

[8] J. A. Galvis et al. "Modeling the transmission and vaccination strategy for porcine reproductive and respiratory syndrome virus". In: (May 2020). DOI: 10/gtt5rr.

[9] G. González-Parra and H. M. Dobrovolny. "Assessing Uncertainty in A2 Respiratory Syncytial Virus Viral Dynamics". In: *Comput. Math. Method. M.* 2015 (2015), pp. 1–9. ISSN: 1748-6718. DOI: 10/gccgsm.

[10] L. He et al. "Efficacy and safety of interferon on neonates with respiratory syncytial virus pneumonia". In: *Exp. Ther. Med.* 20.6 (Oct. 2020), pp. 1–1. ISSN: 1792-1015. DOI: 10/gs8wwc.

[11] E. Jordan et al. "Reduced Respiratory Syncytial Virus Load, Symptoms, and Infections: A Human Challenge Trial of MVA-BN-RSV Vaccine". In: *The Journal of Infectious Diseases* 228.8 (Apr. 2023), pp. 999–1011. ISSN: 1537-6613. DOI: 10/gtt5rq.

[12] M. Koltai et al. "Estimating the cost-effectiveness of maternal vaccination and monoclonal antibodies for respiratory syncytial virus in Kenya and South Africa". In: *BMC Med.* 21.1 (Mar. 2023). ISSN: 1741-7015. DOI: 10/gtt5rn.

[13] I. K. Kombe et al. "Integrating epidemiological and genetic data with different sampling intensities into a dynamic model of respiratory syncytial virus transmission". In: *Sci. Rep.* 11.1 (Jan. 2021). ISSN: 2045-2322. DOI: 10/gtt5rm.

[14] F. Krauer et al. "Estimating RSV seasonality from pandemic disruptions: a modelling study". In: (June 2022). DOI: 10/gtt5rk.

[15] J. C. Lang. "Use of mathematical modelling to assess respiratory syncytial virus epidemiology and interventions: a literature review". In: *J. Math. Biol.* 84.4 (Feb. 2022). ISSN: 1432-1416. DOI: 10/gtt5rj.

[16] W. Li and Q. Zhang. "Construction of positivity-preserving numerical method for stochastic SIVS epidemic model". In: *Adv. Differ. Equ.* 2019.1 (Jan. 2019). ISSN: 1687-1847. DOI: 10/gtt7bn.

[17] S. Mahmud et al. "Cost-effectiveness of pharmaceutical strategies to prevent respiratory syncytial virus disease in young children: a decision-support model for use in low-income and middle-income countries". In: *BMC Med.* 21.1 (Apr. 2023). ISSN: 1741-7015. DOI: 10/gtt5rg.

[18] R. Matteo et al. "Respiratory Syncytial Virus: An Uncommon Cause of Febrile Seizures Results from a Systematic Review and Meta-Analysis". In: *Pediatric Reports* 14.4 (Nov. 2022), pp. 464–478. ISSN: 2036-7503. DOI: 10/gtt5rf.

[19] A. Mejias et al. "Respiratory Syncytial Virus Vaccines: Are We Making Progress?" In: *Pediatr. Infect. Dis. J.* 38.10 (Oct. 2019), e266–e269. ISSN: 0891-3668. DOI: 10/gtt5rd.

[20] H. C. Moore et al. "Modelling the Seasonal Epidemics of Respiratory Syncytial Virus in Young Children". In: *PLoS ONE* 9.6 (June 2014). Ed. by R. J. Sugrue, e100422. ISSN: 1932-6203. DOI: 10/f6dx7p.

[21] G. Rainisch et al. "Estimating the impact of multiple immunization products on medically-attended respiratory syncytial virus (RSV) infections in infants". In: *Vaccine* 38.2 (Jan. 2020), pp. 251–257. ISSN: 0264-410X. DOI: 10/gtt5rb.

[22] R. Sungchasit, I.-M. Tang, and P. Pongsumpun. "Mathematical Modeling: Global Stability Analysis of Super Spreading Transmission of Respiratory Syncytial Virus (RSV) Disease". In: *Computation* 10.7 (July 2022), p. 120. ISSN: 2079-3197. DOI: 10/gtt5q9.

[23] G. Taylor et al. "Efficacy of a virus-vectored vaccine against human and bovine respiratory syncytial virus infections". In: *Sci. Transl. Med.* 7.300 (Aug. 2015). ISSN: 1946-6242. DOI: 10/f725jx.

[24] L. Toivonen et al. "Respiratory syncytial virus infections in children 0–24 months of age in the community". In: *J. Infection* 80.1 (Jan. 2020), pp. 69–75. ISSN: 0163-4453. DOI: 10/gtt5q8.

[25] M. Treskova et al. "Assessment of the Effects of Active Immunisation against Respiratory Syncytial Virus (RSV) using Decision-Analytic Models: A Systematic Review with a Focus on Vaccination Strategies, Modelling Methods and Input Data". In: *PharmacoEcon.* 39.3 (Jan. 2021), pp. 287–315. ISSN: 1179-2027. DOI: 10/gtt5q7.

[26] T. Van Effelterre et al. "Modeling Respiratory Syncytial Virus Adult Vaccination in the United States With a Dynamic Transmission Model". In: *Clin. Infect. Dis.* 77.3 (Mar. 2023), pp. 480–489. ISSN: 1537-6591. DOI: 10/gtt5q6.

[27] P. Venkatesan. "First RSV vaccine approvals". In: *The Lancet Microbe* 4.8 (Aug. 2023), e577. ISSN: 2666-5247. DOI: 10/gtt5q5.

[28] Y. Wei et al. "Progress and Perspective of Transmission Dynamics Models in Prevention and Control of Infectious Diseases". In: *Progress in China Epidemiology*. Springer Nature Singapore, 2022, pp. 419–435. ISBN: 9789811921995. DOI: 10/gtt5q4.

International Conference on Mathematical Analysis and Applications in Science and Engineering
ICMA^{2}SC'24
ISEP Porto-Portugal, June 20 - 22, 2024

Bi-cooperative Games: A Bi-dimensional Perspective

Mekdad Slime[1⋆] **Mohammed El Kamli**[2] **Abdellah Ould Khal**[1]

[1] Laboratory of Mathematical, Statistics and Application.
Faculty of Sciences - Mohammed V University in Rabat, B.P. 1014 - Rabat, Morocco.
[2] Laboratory of Economic Analysis and Modelling (LEAM). Faculty of Sciences, Economic, Juridical and Social - Souissi, Mohammed V University in Rabat. B.P. 1014 - Rabat, Morocco.

[1⋆]mekdad_slime@um5.ac.ma

Abstract: Cooperative game theory is a specialized field within game theory that explores how individuals can collaborate to achieve mutually beneficial outcomes. Over time, researchers have expanded this concept to encompass higher dimensions, offering new perspectives. In 2000, J. M. Bilbao et al. [1] introduced the notion of bi-cooperative games, which represents a broader extension of traditional cooperative games. Unlike the conventional approach of utilizing functions defined from 2^N to $\mathbf{R}$, bi-cooperative games introduce a distinctive viewpoint by employing functions defined from 3^N to $\mathbf{R}$. This departure enables a more nuanced analysis, considering ordered pairs (S, T) of disjoint coalitions, where members of $S \subset N$ contribute positively, members of $T \subset N$ contribute negatively, and the remaining players do not participate. In 2024, M. Slime et al. [2] further expanded cooperative games, focusing on scenarios where players choose actions from the cartesian product of two sets. They extended the scope of cooperative games by utilizing functions defined from 2^N to $\mathbf{R}$, to a bi-dimensional cooperative game framework with functions defined from $2^{N\times N'}$ to $\mathbf{R}$. Building upon these developments, our paper contributes to the advancement of bi-cooperative games by extending their application to the cartesian product $N \times N'$. This extension introduces a new layer of complexity, capturing interactions not only within a single set N, but also between two sets N and N'. The functions are now defined from $3^{N\times N'}$ to $\mathbf{R}$, reflecting the expanded range of possibilities and scenarios.

keywords: game theory; cooperative games; bi-cooperative games; bi-submodular games; bi-supermodular games.

MSC2020: 91Axx; 91A12; 91Bxx.

References

[1] Bilbao, J. M., Fernandez, J. R., Losada, A. J., Lebrón, E., Bicooperative games, Cooperative games on combinatorial structures. Kluwer Acad, Publ (2000), 131–295.

[2] Slime, M., El Kamli, M., Ould Khal, A., Analyzing Cooperative Game Theory Solutions: Core and Shapley Value in Cartesian Product of Two Sets, Frontiers in Applied Mathematics and Statistics **10** (2024), 1332352.

International Conference on Mathematical Analysis and Applications in Science and Engineering ICMA²SC'24

ISEP **Porto-Portugal, June 20 - 22, 2024**

Convolutional Neural Networks for Automated Classification of Childhood Leukemia Cells: A Machine Learning Method for Differentiating Between Normal and Abnormal Cells in Microscopic Images

OLUWASEUN OLUMIDE OKUNDALAYE [1]✉, NECATI ÖZDEMIR [2]

[1]Adekunle Ajasin University, Akungba-Akoko, Department of Mathematical Sciences, Faculty of Science, Ondo State, Nigeria

[2]Balikesir University, Department of Mathematics, Faculty of Science and Art, Balikesir, Turkey.

Emails:okundalaye.oluwaseun@aaua.edu.ng, nozdemir@balikesir.edu.tr

Abstract: Approximately 25% of pediatric cancer cases are acute lymphoblastic leukemia (ALL), making it the most common kind of childhood cancer. In order to differentiate abnormal leukemic blasts from normal cells, this work aims to develop a machine-learning model for classifying normal and abnormal (leukaemia) cells in microscopic images. An experienced oncologist has annotated the ground truth labels on 15,135 segmented cell images from 118 patients in the collection.

Although staining noise and illumination problems were mostly fixed during acquisition, the images nonetheless indicate real-world samples. The classification task is a substantial problem because immature leukemic blasts and normal cells share certain physical similarities. To help with ALL diagnoses and treatments, the suggested model seeks to distinguish between these two classifications with accuracy. We used a suitable machine learning algorithm (Convolutional Neural Network CNN) to train the dataset. The efficacy of the model in classification is evaluated using performance evaluation metrics, including accuracy, precision, recall, and F1-score. By developing automated diagnostic methods for childhood leukemia, this research could enhance the precision and effectiveness of diagnosis and treatment planning. Lastly, this model's effective use could completely transform the area of pediatric cancer by providing specialists with a strong tool to improve patient outcomes and care.

keywords: Pediatric cancer, acute lymphoblastic leukemia (ALL), machine learning, convolutional neural network (CNN), image classification, automated diagnosis, childhood cancer.

International Conference on Mathematical Analysis and Applications in Science and Engineering
ICMA^{2}SC'24
ISEP Porto-Portugal, June 20 - 22, 2024

Nonlinear Neural Dynamics of Language Processing: A Recurrence Quantification Analysis of EEG in Dyslexia

Ignacio Rodríguez-Rodríguez[1⋆] J. Ignacio Mateo-Trujillo[1] Marco A. Formoso[1] Nicolás J. Gallego-Molina[1] Andrés Ortiz[1] Juan Luis Luque[2]

[1] Communications Engineering Department, University of Málaga 29004 Málaga, Spain
[2] Department of Developmental and Educational Psychology, University of Málaga 29004 Málaga, Spain

[1⋆]ignacio.rodriguez@ic.uma.es

Abstract: This study investigates the application of chaos theory and Recurrence Quantification Analysis (RQA) to EEG signals in skilled and dyslexic readers. By quantifying the nonlinear dynamics of brain activity, we aim to identify differences in the complexity and predictability of neural oscillations associated with language processing. Our results demonstrate that the recurrence plot of individuals with dyslexia exhibits higher recurrence rate, determinism, and entropy compared to control subjects. These findings suggest that brain activity around T7 (AUC 0.726), crucial for phonological processing in the dorsal route of language processing, is more repetitive, predictable, and less flexible in dyslexia. The observed patterns align with the Hickok and Poeppel's dual-route model of language processing and support the hypothesis that dyslexia involves disruptions in the neural mechanisms underlying phonological processing and auditory-motor integration.

keywords: Dyslexia; Machine Learning; Recurrence Quantification Analysis; Chaos Theory.

MSC2020: 49-XX; 34-XX; 92-XX.

1 Introduction

Chaos theory has emerged as a powerful framework for understanding complex systems, including the intricate processes of the human brain. By applying the principles of nonlinear dynamics to electroencephalography (EEG) signals, researchers have gained valuable insights into the underlying neural processes that govern cognitive functions [1]. In the realm of language processing and reading disorders, chaos theory has proven particularly useful in unraveling the complexities of dyslexia, a neurodevelopmental disorder characterized by difficulties in accurate and fluent word recognition, poor spelling, and decoding abilities. By utilizing Recurrence Quantification Analysis (RQA) to quantify the nonlinear dynamics of brain activity, researchers have identified key differences in the complexity and predictability of neural oscillations between skilled and dyslexic readers. This approach aligns with findings by Giraud, Poeppel and Goswami, who

identified synchronization deficits between sensory inputs and primary auditory areas, suggesting a broader impact on network connectivity and dynamics crucial for language processing. These insights, underscore the potential of RQA not only to detect these deficits but also to deepen our understanding of their implications for the neural mechanisms underlying dyslexia, thus highlighting the interplay between micro-level neuronal behavior and macro-level cognitive functions in reading impairments.

2 Results and discussion

2.1 Data acquisition and preprocessing

The University of Málaga's Leeduca Study Group conducted a study with 97 participants, including 67 skilled readers and 30 dyslexic readers, aged 88-100 months. They were exposed to a 4.8 Hz modulated auditory stimulus for 5 minutes to investigate synchronicity patterns. EEG signals were recorded using a Brainvision actiCHamp Plus with 32 active electrodes at 500 Hz. All participants were right-handed native Spanish speakers without hearing impairment and with normal or corrected-to-normal vision.

EEG signals were preprocessed using ICA and segment elimination to remove artifacts. Channels were referenced to Cz and filtered using a band-pass FIR filter to extract Theta frequency information, avoiding phase distortion. A two-way zero-phase lag band-pass FIR Least-Squares filter was employed, along with low-pass filtering (80 Hz threshold) and a 50 Hz notch filter.

2.2 Phase Space Reconstruction and Recurrence Quantification Analysis (RQA)

The phase states of the different channels will be reconstructed using the Takens' theorem, after preprocessing and filtering the signals to the theta frequency band (4-8 Hz), coherent with the stimulus. Takens' theorem texto states that it is possible to reconstruct the phase space of a dynamical system from a single time series by creating a set of delayed copies of the original time series, forming a new higher-dimensional space (e.g., Figure 1). This reconstructed phase space preserves the essential dynamics of the original system, allowing for the analysis of its properties [3].

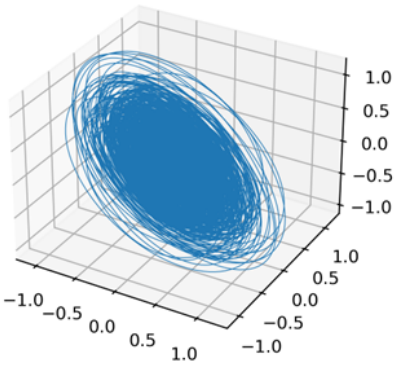

Figure 1: Phase Space reconstruction of EEG signal

Once the phase space reconstructions have been performed, a Recurrence Quantification Analysis (RQA) will be conducted using Recurrence Plots (RP). RQA is a nonlinear data analysis method that quantifies the recurrence behavior of dynamical systems, providing insights into their complexity and predictability. Recurrence Plots are two-dimensional graphical representations of the recurrence matrix, which captures the times at which the system's trajectory returns to a previous state. From these RPs, several characteristics will be extracted to characterize the system's behavior:

- Recurrence Rate (RR): The percentage of recurrence points in the RP.
- Determinism (DET): The percentage of recurrence points forming diagonal lines.
- Divergence (DIV): The system's divergence or chaoticity.
- Laminarity (LAM): The percentage of recurrence points forming vertical lines, indicating the presence of laminar states or intermittency.
- Trapping Time (TT): The average time the system remains in a laminar state.

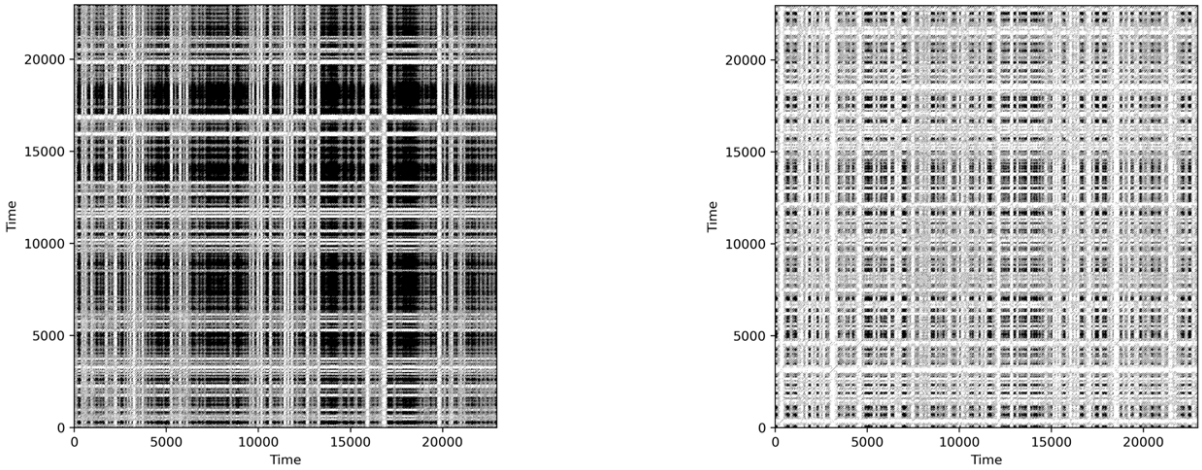

Figure 2: Recurrence Plot T7 electrode. Left, patient with dyslexia. Right, control group

- Average Diagonal Line Length (L), Longest Diagonal Line (Lmax), Longest Vertical Line (Vmax), Longest White Vertical Line (WVLmax) and Average White Vertical Line Length (WVLM): The lengths of the lines in the RP, represent the time the system stays in a laminar / non-laminar state.
- Entropy of Diagonal Lines (ENTR), Entropy of Vertical Lines (VENTR) and Entropy of White Vertical Lines (WVENTR): The entropy of the lines length distribution, representing the average time the system remains in a non-laminar state.

These RQA measures will provide a characterization of the system's dynamics, enabling the identification of differences between skilled and dyslexic readers in their EEG signal complexity and predictability. In the context of RQA applied to EEG from the T7 electrode (Figure 2), it is coherent that the recurrence plot (RP) of an individual with dyslexia shows a higher recurrence rate (RR), determinism (DET), entropy of diagonal lines (ENT), entropy of vertical lines (ENTR_vert), and entropy of white lines (ENTR_white) compared to a control subject. These results suggest that brain activity in the area around T7, relevant for language processing, is more repetitive, predictable, and less flexible in dyslexia, but at the same time presents greater variability in the duration of recurrent states, laminar states, and in the transition times between states. This combination of increased recurrence and variability could reflect a less efficient, stable, and adaptable brain dynamics for language processing in dyslexia. Visually, these patterns would manifest in the RP of an individual with dyslexia as a generally darker tone, with more "squares" or recurrence blocks of variable sizes, and greater variability in the space between these blocks, compared to the RP of a control subject.

2.3 Machine Learning classification

The feature selection method employed in this study is the MRMR (Minimum Redundancy Maximum Relevance) algorithm, which combines the SULOV (Searching for Uncorrelated List of Variables) method and Recursive XGBoost. This approach ensures low redundancy and high relevance in the selected features. The results from the Gradient Boosting classifier indicate a maximum performance at electrode T7 with an AUC of 0.726 (Figure 4), alongside commendable performances above 0.7 at electrodes C3 and CP1 (Figure 3). Interpreting these findings within the framework of Hickok and Poeppel's dual-route model of language processing [2], particularly the dorsal route, offers insightful implications. The electrode T7, positioned over the superior temporal area of the left hemisphere, is integral to phonological processing and speech production, (dorsal route), and our result aligns with the hypothesis that dyslexia involves disruptions

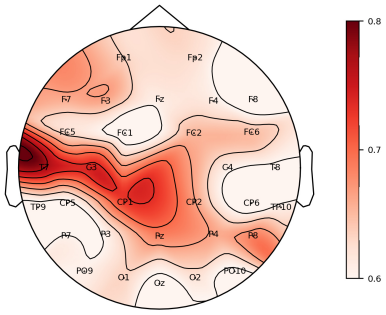

Figure 3: AUC distribution in topoplot

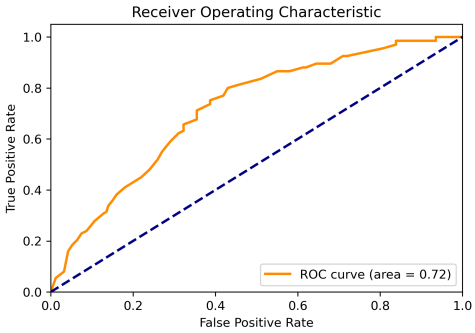

Figure 4: . ROC curve electrode T7

in the neural mechanisms underlying phonological processing and the integration of sensory speech inputs with motor outputs. Furthermore, the noteworthy performances at C3 and CP1, which are associated with motor functions and somatosensory feedback in the left hemisphere, respectively, support the notion of atypical lateralization in dyslexics. These electrodes' involvement underscores the potential deficiencies in integrating auditory-motor mappings.

3 Conclusions and Future work

This study demonstrates the potential of RQA in uncovering distinct EEG patterns associated with dyslexia, consistent with the dual-route framework. Further research involving diverse stimuli scenarios, combined with feature importance ranking, will deepen our understanding of the neural dynamics underlying dyslexia and contribute to developing targeted interventions.

Acknowledgments

This publication is part of the project PID2022-137461NB-C32 funded by MICIU/AEI/10.13039/501100011033 and by ERDF/EU. I.R.-R. funded by Plan Andaluz de Investigación, Desarrollo e Innovación (PAIDI), Junta de Andalucía. Marco A. Formoso grant PRE2019-087350 funded by MICIU/AEI/10.13039 /501100011033 by "ESF Investing in your future".

References

[1] Iwona Gruszczyńska, Romuald Mosdorf, Piotr Sobaniec, Milena Żochowska-Sobaniec, and Marta Borowska. Epilepsy identification based on eeg signal using rqa method. *Advances in medical sciences*, 64(1):58–64, 2019.

[2] Gregory Hickok and David Poeppel. Neural basis of speech perception. *Handbook of clinical neurology*, 129:149–160, 2015.

[3] Simranjit Kaur, Sukhwinder Singh, Priti Arun, Damanjeet Kaur, and Manoj Bajaj. Phase space reconstruction of eeg signals for classification of adhd and control adults. *Clinical EEG and neuroscience*, 51(2):102–113, 2020.

International Conference on Mathematical Analysis and Applications in Science and Engineering
ICMA^{2}SC'24
ISEP Porto-Portugal, June 20 - 22, 2024

A Trust Region Algorithm for Modeling BMI Related Risk in Anesthesia

Amani R. Ynineb[1⋆] Erhan Yumuk[1] Ghada Ben Othman[1] Hamed Farbakhsh[1] Dana Copot[1] Robin De Keyser[1] Samir Ladaci[2] Clara M. Ionescu[1]

[1] Ghent University, Belgium, [2] National Polytechnic School, Algeria,

[1⋆]amani.ynineb@ugent.be

Abstract: Obesity lies at the very baseline of comorbidities challenging surgery outcomes and patient recovery times. This paper introduces a theoretical framework for modelling drug diffusion in fat tissues, addressing a significant gap in conventional pharmacokinetic models for non-lean patients in long-term anesthesia. The research uses the trust region algorithm to approximate the risk of drug trapping in fat cells, correlating the Body Mass Index (BMI) with the ratio of porosity to permeability in fat tissues. Through performance analysis and iterative modeling, an optimal approximation is identified, offering significant insights into drug behavior for different BMI type. This novel methodology promises to enhance drug dosing strategies in long-term general anesthesia for obese patients, moving towards more personalized and effective closed-loop control.

keywords: Pharmacokinetics; Trust Region Algorithm; Long-term general anesthesia.

MSC2020: 49-11; 34-04; 92-10.

1 Introduction

Obesity significantly increases the risk of various health complications [1] and poses challenges for surgical outcomes and patient recovery time. This is particularly evident in long-term general anesthesia procedures, which are essential in specific critical situations to stabilize patients following traumatic events [2]. In addition, there is a parallel increase in the number of obese patients admitted to intensive care units, corresponding to the global rise in obesity rates [3]. In such extreme situations, the standard compartmental models, which are used to characterize the time constants of drug distribution within the body, are no longer valid and need to take into consideration drug diffusion patterns.

Fat cells, or adipocytes, have a semi-permeable cell membrane that selectively controls the passage of molecules. This permeability is crucial for the dynamic processes of molecular diffusion. Adipose tissue's cells encompass various types of fat cells whose properties depend on their type or the period of time it has been formed. Similarly to geological materials such as clay, sand, gravel, and stones, there is a degree of porosity and degree of permeability of water through these kinds of substrates. The stages of fat tissue and their properties can vary depending on body mass index (BMI). In individuals with a lower BMI, brown fat, known for its thermogenic properties, is potentially more prevalent whereas white adipose tissues are less present. In this

case, the balance of interstitial liquid and inner permeability are nominal and can facilitate the molecular binding in-out of the cell, thereby abiding to a normal diffusion pattern as best described by Fick's laws of diffusion. Most of our fat is white fat and serves as an energy storage depot. Higher BMI individuals tend to accumulate more white fat. In such cases, molecular diffusion exhibits anomalous behavior at the meso- and micro-scales within the complex lattice matrices that make up the structure of fat tissue, impacting their properties [4].

As adipose tissue accumulates and transforms into white fat cells, it aggregates and sticks together, growing in number and size [5]. This leads to significant changes in the dynamics of drug diffusion within the tissue. The increased volume and porosity resulting from fat deposition allow for a greater capacity to transfer drug molecules, but simultaneously, the time constant for uptake/release may slow down. With continued fat accumulation, the fat cells develop an inflammatory response, leading to fibrosis of the cells and further impaired diffusion [6]. This inflammatory environment not only hinders the diffusion of drugs and reduces angiogenesis in tissue reconstruction but also contributes to the entrapment of interstitial liquid [7]. In extreme cases, the porosity pattern becomes mixed whereas the permeability is much impaired, resembling geological composite layers where gravel is mixed with sand and fine sediment, thereby obstructing water flow. These complex changes in the properties of fat tissue reflect the intricate challenges in drug delivery within the context of obesity.

Modelling the real-world problems is a challenge in contemporary scientific research [8]. Given the previous definitions, this work aims to model the relationship between the BMI, porosity of fat tissue, and permeability of drug molecules in order to model the risk of drug trapping in the adipose for patients undergoing long-term general anesthesia. Using the Trust-Region algorithm in Matlab, nonlinear approximations are introduced and then compared using performance measures. These results are also contrasted with a linear approximation obtained through the linear least square method. The resulting model would be the next step to enhance the pharmacokinetic model. Creating a framework towards specialized medicine and implementing the fractional order impedance models [9].

2 Results and discussion

The results are shown in Figure 2, Table 1, and Table 2 where 70% of data is taken for identification and 30% for validation. The trust region algorithm used in sine-based approximations significantly outperforms the linear least squares method used in the 4th-order polynomial regression. Trust region is effective because it iteratively improves the fit by considering both the direction and the step size that should be taken in the parameter space, thus providing a more nuanced approach to minimizing errors compared to the linear least squares method which may be more rigid and less adaptive to the complex nature of the data. In addition, increasing the number of sine terms in the models results in significant improvements across all performance measures. This suggests that more sine terms can capture the variability and complexity of the dataset more effectively, leading to a more accurate and reliable fit. However, while the 6-sine model performs best on these metrics, it may be prone to overfitting.

Table 1: Performance measures of the approximations for goodness of identification (70% of data), goodness of validation (30% of data) and global fit (100% of data)

	Goodness of Identification			Goodness of validation		Global Fit	
Approximation	SSE	R-square	RMSE	SSE	RMSE	NRMSE	Fit
3 sine	0.8468	0.9356	0.2552	0.4823	0.1736	0.0600	94.0005
4 sine	0.3499	0.9734	0.1871	1.0360	0.2545	0.0613	93.8737
6 sine	0.0070	0.9995	0.0418	0.0357	0.0472	0.0108	98.9246
4th order regression	3.9939	0.6965	0.4847	1.7784	0.3334	0.1502	84.9756

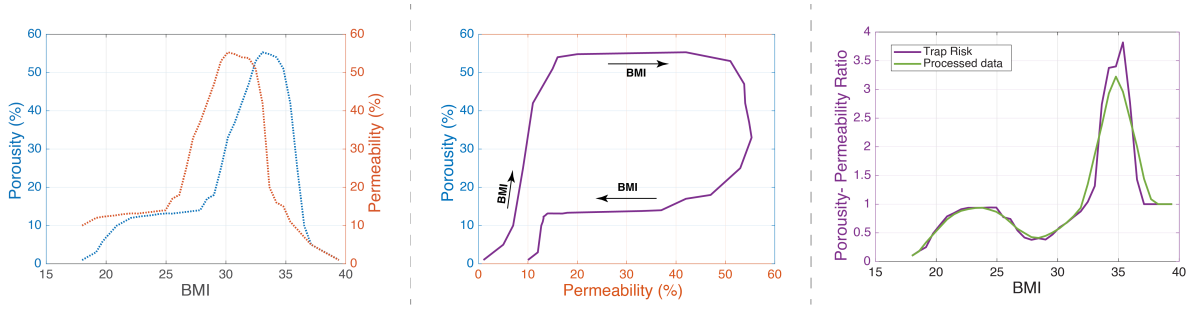

Figure 1: Relation between porosity of fat tissue and permeability of drug molecules to body mass index (Left). Relation between porosity of fat tissue and permeability of drug molecules. Arrows indicate the evolution of BMI from normal to morbidly obese (Middle), Relation between relative ratio of porosity to permeability against BMI from normal to morbidly obese (Left)

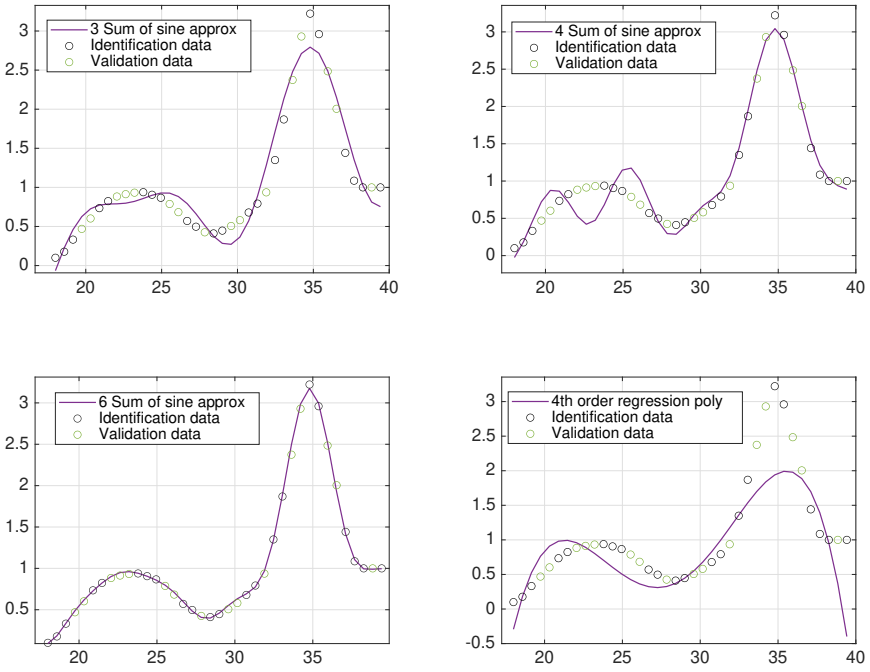

Figure 2: Comparison between different degrees of nonlinear approximation (Top Figures and Bottom Left Figure) and a linear approximation (Bottom Right) for the trap risk model. x-axes are the BMI, y-Axes are the Fat Trap risk

Table 2: Approximation Results

Type of approximation	Results
3 sine	$Risk = 27.4472 \cdot sin(0.0033 \cdot BMI - 0.0570) + 0.8002 \cdot sin(0.5390 \cdot BMI - 4.2180)$ $+0.4815 \cdot sin(0.7595 \cdot BMI - 6.2212)$
4 sine	$Risk = 22.0610 \cdot sin(0.0041 \cdot BMI - 0.0708) + 0.7952 \cdot sin(0.5379 \cdot BMI - 3.9841)$ $+0.6032 \cdot sin(0.7129 \cdot BMI - 4.8350) + 0.2605 \cdot sin(1.3344 \cdot BMI + 5.5266)$
6 sine	$Risk = 1.5323 \cdot sin(0.1068 \cdot BMI - 1.8903) + 0.7569 \cdot sin(0.3100 \cdot BMI + 2.4903)$ $+0.8676 \cdot sin(0.6957 \cdot BMI - 2.9134) + 0.1462 \cdot sin(1.4868 \cdot BMI - 0.5250)$ $+0.6010 \cdot sin(0.8387 \cdot BMI + 2.8708) + 0.2260 \cdot sin(1.3274 \cdot BMI - 6.1737)$
4th order regression	$Risk = -0.000436 \cdot BMI^4 + 0.0489 \cdot BMI^3 - 2.012 \cdot BMI^2 + 36.01 \cdot BMI - 236$

3 Conclusions and Future work

This paper introduces a novel approach for approximating the risk of drug trapping in fat molecules, a significant factor in general anesthesia. The findings indicate that the risk of drug trapping increases in patients with a higher BMI index. Future work can investigate the integration of fractional order calculus in a pharmacokinetic model with an augmented compartment representing the risk of drug trapping. Creating a parallel between the fractional-order impedance model of a real fat sample and the approximation made from theory.

Acknowledgments

This work was funded in part by the European Research Council (ERC) Consolidator Grant AMICAS, grant agreement No. 101043225. Funded by the European Union. Views and opinions expressed are however those of the author(s) only and do not necessarily reflect those of the European Union or the European Research Council Executive Agency. Neither the European Union nor the granting authority can be held responsible for them.
D. Copot acknowledges the support of Flanders Research Foundation, Postdoc grant 12X6819N.

References

[1] M. Ri, S. Aikou and Y. Seto, Obesity as a surgical risk factor, Annals of gastroenterological surgery **2**(1) (2018), 13–21.

[2] J. Hahn and O. T. Inan, Physiological closed-loop control in critical care: opportunities for innovations, Progress in Biomedical Engineering, **4**(3) (2022), 033001.

[3] J. L. Pepin, J. F. Timsit, R. Tamisier, J. C. Borel, P. Levy and S. Jaber, Prevention and care of respiratory failure in obese patients, Lancet Respiratory Medicine, **4**(5) (2016), 407-418.

[4] M. Palombo, A. Barbetta, C. Cametti, G. Favero and S. Capuani, Transient anomalous diffusion MRI measurement discriminates porous polymeric matrices characterized by different sub-microstructures and fractal dimension, **8**(2) (2022).

[5] M.K. DeBari and R. D. Abbott, Adipose tissue fibrosis: mechanisms, models and importance, LInt J Mol Sci, **21**(17) (2020), 6030.

[6] X. Huang, W. Zhou and D. Deng, Effective diffusion in fibrous porous media: a comparison study between lattice Boltzmann and pore network modelling methods, Materials (Basel), **14**(4)(2021), 756.

[7] A. Samourides, L. Browning, V. Hearnden and B. Chen, The effect of porous structure on the cell proliferation, tissue ingrowth and angiogenic properties of poly(glycerol sebacate urethane) scaffolds, Mat Sci and Eng:C, **108** (2020), 110384.

[8] C. Pinto, Nonlinear Dynamics and Complexity - Mathematical Modelling of Real-World Problems, (2022).

[9] D. Copot and C.M. Ionescu, Tailored pharmacokinetic model to predict drug trapping in long-term anesthesia, Journal of Advanced Research, **32** (2021), 27–36.

International Conference on Mathematical Analysis and Applications in Science and Engineering
ICMA^{2}SC'24
ISEP Porto-Portugal, June 20 - 22, 2024

Generation of Virtual Children for testing a Recommendation System for Interventions with Children with Dyslexia

J. Ignacio Mateo-Trujillo[1⋆] Ignacio Rodríguez-Rodríguez[1]
Diego Castillo-Barnes[1] Andrés Ortiz[1] Juan Luis Luque[2]

[1] Communications Engineering Department,
University of Málaga 29004 Málaga, Spain
[2] Department of Developmental and Educational Psychology,
University of Málaga 29004 Málaga, Spain

⋆nachomateo912@uma.es

Abstract: The LEEDUCA project has developed a recommendation system to generate intervention sessions tailored to children with dyslexia. Due to the limitations in obtaining real data for preliminary testing, the generation of in silico data, referred to as "virtual children," has been implemented. This approach allows for the simulation of a wide range of profiles and response patterns, enabling comprehensive testing of the system before its implementation with real users. The behavior of virtual readers is modeled using logistic curves, which reflect the natural evolution of users in a system that suggests words ordered by difficulty over time. By introducing variations to the model based on the coefficients that define the logistic curve, response sequences with different difficulty levels and learning rates can be simulated. To evaluate the stability of the system, multiple variations are generated from a given virtual child, creating a shadow of possible sequences. The generation of virtual children using logistic curves and the controlled introduction of variations in their responses provide a robust framework for testing the recommendation system, ensuring its reliability and adaptability to the individual needs of children with dyslexia.

keywords: data modelling; data simulation; logistic model; recommendation system.

MSC2020: 49-XX; 34-XX; 92-XX.

1 Introduction

Within the framework of the LEEDUCA project (https://leeduca.es/), a Recommendation System has been developed to generate intervention sessions tailored to children with dyslexia. During these sessions, batches of 100 consecutive words and pseudo-words generated according to phonological rules from an AI generator module are serially suggested, with an intrinsic difficulty assigned by a machine learning system and validated by a team of psychologists. The main objective is to adapt the difficulty of the recommended words to the child's performance throughout multiple interventions. Before implementing the system with real users, comprehensive testing is crucial to ensure its effectiveness and reliability. However, given that the recommendation system is intended for children, there are limitations in the availability of real

data for preliminary testing. For this reason, the generation of in silico data, referred to as "virtual children," has been chosen to simulate a wide range of profiles and response patterns [3]. In addition to overcoming data scarcity, the purpose of multiple system testing is to evaluate the error in recommendations and the stability of the system under different levels of input variability.

2 Results and discussion

2.1 Generation of the model from empirical data

Using data collected from similar intervention projects and validated by the team of psychologists, the behavior of diverse profiles of virtual children has been modeled using logistic curves. These curves reflect the natural evolution of users in a system of suggestions ordered by difficulty over time. The logistic function, also known as the S-shaped curve, is a mathematical tool widely used in various fields, such as population growth, disease propagation, and diffusion in social networks. This function constitutes a refinement of the exponential model and allows for a more realistic description of the growth of a magnitude, taking into account limiting factors [2]. In general, it is observed that the user tends to answer correctly at a rapid pace until reaching their difficulty limit, at which point they stagnate during that intervention. This behavior is captured by the logistic curve, which exhibits a rapid initial growth followed by a gradual leveling offas the user approaches their maximum performance level. Readers at risk of dyslexia show poorer performance from the beginning of literacy (assumed to be the first stage); and persistently show difficulties in learning and generalising conversion rules and automating them, resulting in slow progress, with numerous setbacks, and finally not reaching the same levels as their peers (gap). These profiles can be simulated by manipulating the parameters of the logistic curve. The versatility of the logistic curve lies in its ability to generate models by adjusting different parameters, such as the initial difficulty, the final difficulty the virtual children reach, the time they remain in the initial and final phases, and the learning speed, represented by the slope of the curve. By manipulating these parameters, it is possible to create profiles of virtual children with diverse characteristics and learning rhythms, simulating a wide range of potential users and their responses to the intervention system.

2.2 Variations to the model

Once the fit of the logistic curve to the empirical data has been verified, it is possible to introduce variations to the model based on the coefficients that define the curve. In this way, response sequences that reach higher difficulty or present a faster learning rate can be simulated without the need for specific empirical data for those scenarios. The logistic model is defined by equation 1.

$$f(x) = \frac{L}{1 + e^{-\frac{k}{x - x_0}}} \tag{1}$$

Where: L: Max difficult achieved.$x_0 = \frac{n_1+n_2}{2}$: Midpoint of the curve. $n = 100$: Total number of words. n_1: Start of the rise. n_2: Stabilization point. k: Rate of change. By adjusting these parameters, sequences of in silico simulated data can be generated that follow a specific curve (Figure 1). This flexibility allows for the exploration of a wide range of possible user behaviors and the evaluation of the system's performance under different conditions.

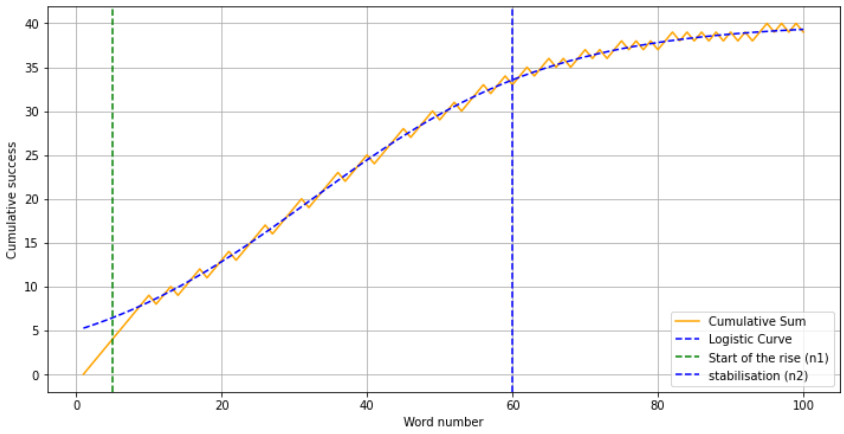

Figure 1: Construction of a virtual child.

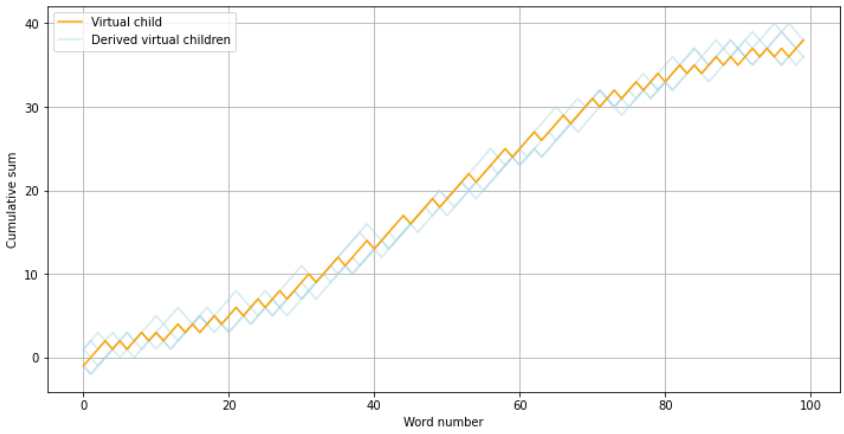

Figure 2: Derived virtual children.

2.3 Derived children

To evaluate the stability of the system, multiple variations are generated from a given virtual child, which deviate from the basic data sequence until reaching a specific dispersion, generating a shadow of sequences whose median is the basic sequence and share the same logistic model (Figure 2). The process of creating variations involves applying a percentage of variance to the base virtual child, resulting in derived virtual children that exhibit random variations in their interactions with the system while maintaining the same overall learning trajectory. The dispersion of the difficulties recommended by the system can be observed, and it can be evaluated whether the output dispersions are contained and proportional to the input dispersions.

This evaluation is performed by analyzing the relationship between the variance introduced in the inputs (the responses of the virtual children, Figure 3) and the variance observed in the outputs (the difficulty levels proposed by the system, Figure 4). If, for a given level of input variance, the output variance does not exhibit erratic behavior or exceeds a reasonable range, it can be concluded that the system is stable and robust. A stable system should be capable of adapting to individual variations among users without compromising its ability to provide coherent and personalized recommendations [1]. The creation of virtual children using logistic curves and the generation of random variations from base profiles constitute fundamental tools to overcome the challenges of cold start and data scarcity in the development of an intervention system for children with reading difficulties. These techniques allow for the simulation of a wide

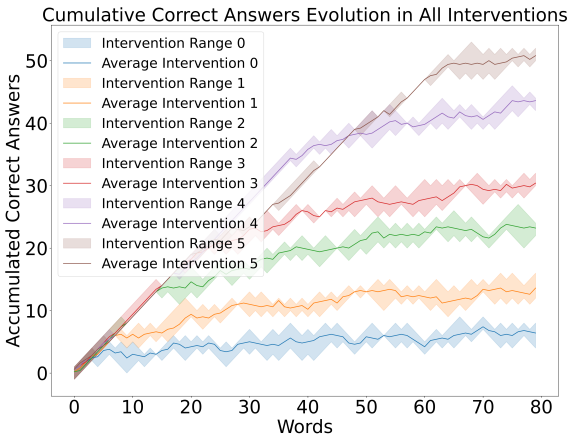

Figure 3: Behaviour of virtual children.

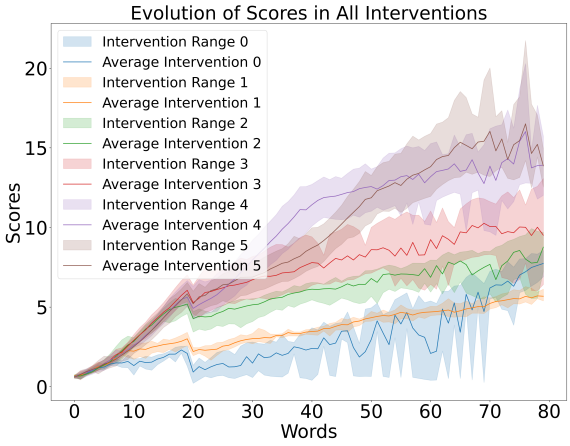

Figure 4: Scores achieved by virtual children.

range of potential users, the evaluation of system robustness, and the assurance of its reliability.

3 Conclusions and Future work

The generation of virtual children through logistic curves and the controlled introduction of variations in their responses enable comprehensive testing of the recommendation system developed in the LEEDUCA project. This approach not only addresses the limitations arising from the scarcity of real data but also enables the evaluation of stability and error in recommendations under different levels of input variability. Collaboration with a team of psychologists to obtain realistic profiles and the ability to adjust the parameters of the logistic curves provide great flexibility to the testing process, allowing for the coverage of different scenarios and ensuring that the system is prepared to adapt to the individual needs of each child with dyslexia.

Acknowledgments

This publication is part of the TED2021-132261B-I00 project funded by MICIU/AEI/10.13039/501100011033 and by European Union NextGenerationEU/PRTR, as well as the PID2022-137461NB-C32 project, funded by MICIU/AEI/10.13039/501100011033 and by ERDF/EU. I.R.-R. funded by Plan Andaluz de Investigación, Desarrollo e Innovación (PAIDI), Junta de Andalucía. Work by D.C.B. is part of the grant FJC2021-048082-I funded by MICIU/AEI/10.13039/501100011033 and by European Union NextGenerationEU/PRTR

References

[1] Gediminas Adomavicius and Jingjing Zhang. Stability of recommendation algorithms. *ACM Transactions on Information Systems (TOIS)*, 30(4):1–31, 2012.

[2] Scott W Menard. *Logistic regression: From introductory to advanced concepts and applications*. Sage, 2010.

[3] Swaraj Samant and Sandeep Prabhu. Studying human behavior, perception, and cognition to controlled stimulus in a virtual environment. In *2022 International Interdisciplinary Humanitarian Conference for Sustainability (IIHC)*, pages 80–86. IEEE, 2022.

International Conference on Mathematical Analysis and Applications in Science and Engineering
ICMA^{2}SC'24
ISEP Porto-Portugal, June 20 - 22, 2024

Improving Acute Lymphoblastic Leukemia Relapse Prediction with Machine Learning Biomarkers

Rocío Picón-González[1⋆] Salvador Chulián[1] Álvaro Martínez-Rubio[1] Ana Niño-López[1] María Rosa[1]

[1]Biomedical Research and Innovation Institute of Cádiz (INIBICA)
Puerta del Mar University Hospital; Universidad de Cádiz

[1⋆]rocio.picon@uca.es, salvador.chulian@uca.es, alvaro.martinezrubio@uca.es, ana.nino@uca.es, maria.rosa@uca.es

Abstract: Machine learning (ML) techniques are increasingly being used in different areas, providing new ways to analyze complex data. In the field of healthcare, ML can offer promising possibilities to improve diagnostic accuracy and treatment effectiveness, thereby enhancing outcomes for patients. This study explores the integration of ML methodologies with mathematical methods like Topological Data Analysis (TDA), using clinical data obtained through flow cytometry to differentiate between relapse and non-relapse cases in Acute Lymphoblastic Leukemia (ALL). The data analysis involves 188 patients, with approximately 20% of them experiencing relapses. For classification, Random Forests (RF) were used, and imbalances in the number of patients were addressed through cross-validation and oversampling techniques.

keywords: Acute lymphoblastic leukemia (ALL); Topology; Machine Learning.

MSC2020: 92-B05; 55-U99.

1 Introduction

In the field of healthcare, machine learning (ML) holds considerable potential for improving key aspects such as diagnostic accuracy, therapeutic efficacy, and patient outcomes. This potential is particularly relevant in the context of malignant hematologic diseases, among which acute lymphoblastic leukemia (ALL) stands out as the most common childhood cancer. It is estimated that around 20% of children diagnosed with ALL experience relapses, which are much more dangerous than the initial disease.

In this scenario, our goal is to predict relapse at the time of diagnosis, which would allow us to adjust treatment more precisely and adopt preventive measures to avoid it. To achieve this purpose, we employ ML techniques that analyze clinical data and specific biomarkers, leveraging the capacity of these tools to identify complex patterns in large datasets. By foreseeing the likelihood of relapse from the onset of treatment, we can personalize the medical care of each patient, thereby improving both their prognosis and quality of life.

2 Results and discussion

This study was based on a comprehensive analysis of a dataset that included information from 188 patients, of which approximately 20 % experienced relapses in ALL. By employing advanced machine learning techniques, specifically using classifiers such as Random Forests (RF), we were able to distinguish between relapse and non-relapse cases in ALL at the moment of early diagnosis. This approach allowed us to identify specific biomarkers that contributed to improving the accuracy of our predictions.

To address discrepancies in the sample size among patient groups, we implemented sophisticated strategies such as oversampling. This tactic enabled us to balance the representation of minority classes, ensuring that our classification model was not biased toward the majority class and therefore generated more reliable and accurate predictions.

Additionally, to prevent overfitting of the model caused by oversampling, we applied cross-validation techniques. This approach allowed us to assess the generalization capability of the model by dividing the data into multiple subsets for iterative training and testing, ensuring that our model was robust and capable of making accurate predictions on unseen data.

These combined efforts resulted in the creation of a classification model with good metrics, representing an important step towards improving the clinical management and personalized treatment of this disease.

3 Conclusions and Future work

In summary, this study highlights the potential of ML in analyzing data related to ALL and other malignant hematological diseases. The ability to differentiate between relapse and non-relapse cases using specific biomarkers underscores the utility of ML in understanding disease progression and developing personalized treatments.

The findings of this study suggest that ML can play a crucial role in improving the clinical management and prognosis of ALL. By predicting the likelihood of relapse from the outset of treatment, it becomes possible to tailor medical care for each patient, thereby enhancing both their prognosis and quality of life.

Furthermore, by addressing discrepancies in sample sizes among patient groups through advanced techniques such as oversampling and cross-validation, we have been able to create a robust and accurate classification model.

In conclusion, these findings suggest that ML has the potential to transform the management and prognosis of hematological diseases, ultimately leading to better outcomes for patients in the future.

Acknowledgments

This work has been partially supported by the Fundacióon Española para la Ciencia y la Tecnología (FECYT and University of Cádiz, project UCA-PR214, Spain), the Asociación Pablo Ugarte (APU, Spain) and Junta de Andalucía (Spain) group FQM-201. This work was also funded by the Ministry of Science from Spain (grant number PID2022-140451OA-I00, project MATHPOH, Spain).

References

[1] S. Chulián. A. Martínez-Rubio, V.M. Pérez-García, M. Rosa, C. Blázquez Goñi, J.F. Rodríguez Gutiérrez, L- Hermosín-Ramos, A. Molinos Quintana, T. Caballero Velázquez, M. Ramírez-Orellana, A. Castillo Robleda, J.L. Fernández-Martínez, (2020) *High-dimensional analysis of single-cell flow cytometry data predicts relapse in childhood acute lymphoblastic*. Cancers, **13**(1), 17.

[2] S. Chulián, B.J. Stolz, A. Martínez-Rubio, C. Blázquez Goñi, J.F. Rodríguez Gutiérrez, T. Caballero Velázquez, A. Molinos Quintana, M. Ramírez-Orellana, A. Castillo Robleda, J.L. Fuster Soler, A. Minguela Puras, M.V. Martínez Sánchez, M. Rosa, V.M. Pérez-García, H.M. Byrne, (2023) *The shape of cancer relapse: Topological data analysis predicts recurrence un paediatric acute lymphoblastic leukaemia*. PLOS Computational Biology, **19**(8), e1011329.

International Conference on Mathematical Analysis and Applications in Science and Engineering
ICMA^{2}SC'24
ISEP Porto-Portugal, June 20 - 22, 2024

Exact solutions and conservation laws of a one-dimensional PDE model for a blood vessel

S.C. Anco[1] **T.M. Garrido**[2] **A.P. Márquez**[2] **M.L. Gandarias**[2]

[1]Department of Mathematics and Statistics
Brock University, St Catharines Canada
[2]Department of Mathematics
University of Cadiz, Puerto Real, Spain

Abstract: Two aspects of a widely used 1D model of blood flow in a single blood vessel are studied by symmetry analysis, where the variables in the model are the blood pressure and the cross-section area of the blood vessel. As one main result, all travelling wave solutions are found by explicit quadrature of the model. Solutions of interest include shock waves and sharp wave-front pulses for the pressure and the blood flow. Another main result is that three new conservation laws describing generalized momentum and generalized axial and volumetric energies are derived for inviscid flows. For viscous flows, these conservation laws get replaced by conservation balance equations which contain a dissipative term proportional to the friction coefficient in the model.

keywords: travelling wave; conservation law; blood flow; 1D model

MSC2020: 35B06;35C07;37K06;35Q92;92C30

1 Introduction

One-dimensional (1D) models of blood flow in human blood vessels have been widely used in clinical applications and are effective for understanding averaged features of blood flow locally, such as velocity, volume flux, and pressure. For non-branching blood vessels, a common 1D model is described as a cylindrical tube whose radius varies as a function of time t and axial distance x, in which the blood is an incompressible fluid governed by the Navier-Stokes equations averaged over cross-sections of the tube. A derivation and discussion of biological and physical features can be found in Ref. [1, 2, 3].

The variables in this model consist of the cross-section area A, the volume flux Q of blood flow, the mean pressure P, and the mean blood velocity $\bar{u} = Q/A$, while the blood density is taken to be constant. A and Q satisfy a system of two coupled partial differential equations (PDEs) [4]

$$A_t + Q_x = 0, \quad Q_t + \alpha(Q^2/A)_x + \rho_0^{-1} A P_x + kQ/A = 0 \tag{1}$$

where $\alpha \geq 1$ is a momentum correction coefficient (determined by the axial velocity profile), $k \geq 0$ is the friction coefficient (proportional to the viscosity). Here $\rho_0 > 0$ is the blood density, which is constant.

The system (1) is closed by specifying a relation for the pressure in terms of the cross-section area (called a "tube law") [5]. A simple widely-used relation is that the pressure change across the vessel wall

$$P - P_{\text{ext.}} = \beta f(A/A_0) \tag{2}$$

is proportional to the change in radius of the vessel, $f = \sqrt{A/A_0} - 1$, where $\beta > 0$ is a constant, and $P_{\text{ext.}}$ is the external pressure caused by the tissue surrounding the blood vessel, which will be assumed to be constant. In absence of external pressure, the area is constant $A = A_0$. Substitution of the pressure-area relation (2) into the PDEs (1) yields the closed system

$$A_t + Q_x = 0, \quad Q_t + \alpha(Q^2/A)_x + \beta_0(A/A_0)f'(A/A_0)A_x + kQ/A = 0 \tag{3}$$

where $\beta_0 = \beta/\rho_0 > 0$. In terms of Q and A, the mean blood flow velocity is $\bar{u} = Q/A$.

2 Conservation laws

Firstly, the PDE (3) for A itself is a continuity equation. Integration of A over any portion $x_1 \le x \le x_2$ of a blood vessel gives the total volume of blood in that portion:

$$V = \int_{x_1}^{x_2} A\,dx. \tag{4}$$

This quantity satisfies the conservation law

$$\tfrac{d}{dt}V = -Q\big|_{x_1}^{x_2} \tag{5}$$

stating that the rate of change in blood volume is balanced by the net change in blood flow through the end points $x = x_1$ and $x = x_2$. It holds for both inviscid and viscous flows.

In the inviscid case, $k = 0$, the PDE for Q is a continuity equation. It gives the net (mean) blood flux

$$\bar{Q} = \tfrac{1}{L}\int_{x_1}^{x_2} Q\,dx, \quad L = x_2 - x_1 \tag{6}$$

which satisfies the conservation law

$$\tfrac{d}{dt}\bar{Q} = -\tfrac{1}{L}\big(\alpha Q^2/A + \beta_0\big(Af(A/A_0) - F(A)\big)\big)\big|_{x_1}^{x_2} = -\tfrac{2}{L}\rho_0^{-1}\bar{P}A\big|_{x_1}^{x_2} \tag{7}$$

with $F(A) = \int_{A_0}^{A} f(A/A_0)\,dA$, where $\bar{P} = \frac{1}{2}\alpha\rho_0\bar{u}^2 + \frac{1}{2}\big(P(A) - \beta A^{-1}F(A) - P_{\text{ext.}}\big)$ is the analog of mechanical pressure in fluid dynamics. Thus, the rate of change in the net blood flux is proportional to the difference in the mechanical force $\bar{P}A$ on the cross-sections at each end.

There are two conserved energies

$$E^{\pm} = \int_{x_1}^{x_2} \big(\tfrac{1}{2}\rho_0 Q^2/A^{r_\pm} + \beta J(A; r_\pm)\big)\,dx \tag{8}$$

which satisfy the conservation laws

$$\tfrac{d}{dt}E^{\pm} = -\big(\tfrac{4\alpha - r_\pm}{6}\rho_0 Q^3/A^{r_\pm+1} + \beta Q H(A; r_\pm)\big)\big|_{x_1}^{x_2}. \tag{9}$$

Here $J(A;r) = AH(A;r) + (r-2)\int_{A_0}^{A} H(A;r)\,dA$ and $H(A;r) = \int_{A_0}^{A} A^{-r}f(A/A_0)\,dA$, with $r^2 - (4\alpha - 1)r + 2\alpha = 0$. The roots $r_\pm = 2\alpha - \frac{1}{2} \pm 2\sqrt{\alpha(\alpha-1) + \frac{1}{16}}$ are real and satisfy $r_+ \ge 2$, $1 \ge r_- > \frac{1}{2}$ since $\alpha \ge 1$. When $\alpha = 1$, the energy integrals (8) become

$$E^- = \rho_0\int_{x_1}^{x_2} (\tfrac{1}{2}\bar{u}^2 + \beta_0 J^-(A))A\,dx = E \quad \text{and} \quad E^+ = \rho_0\int_{x_1}^{x_2} (\tfrac{1}{2}\bar{u}^2 + \beta_0 J^+(A))\,dx \tag{10}$$

in terms of $J^-(A) = J(A; r_-) = \int_0^1 f(\lambda A/A_0)\, d\lambda$ and $J^+(A) = J(A; r_+) = A\int_{A_0}^A A^{-2} f(A/A_0)\, dA$ after simplifications, where $r_- = 1$, $r_+ = 2$. The quantity E^- is the volumetric energy of the blood flow, while the other quantity E^+ is the axial energy.

In addition, a conserved momentum-like quantity is given by

$$M = \rho_0 \int_{x_1}^{x_2} Q/A^{2\alpha-1}\, dx = \rho_0 \int_{x_1}^{x_2} \bar{u}/A^{2(\alpha-1)}\, dx \tag{11}$$

satisfying

$$\tfrac{d}{dt} M = -\big(\tfrac{1}{2}\rho_0 Q^2/A^{2\alpha} + \beta G(A;\alpha)\big)\big|_{x_1}^{x_2} - k\int_{x_1}^{x_2} Q/A^{2\alpha}\, dx, \tag{12}$$

where $G(A;\alpha) = A^{2(1-\alpha)} f(A/A_0) + 2(\alpha-1)\int_{A_0}^A A^{1-2\alpha} f(A/A_0)\, dA$. When $\alpha = 1$, this integral (11) reduces to $M = \rho_0 \int_{x_1}^{x_2} \bar{u}\, dx$ which is the ordinary momentum of the blood flow.

For viscous blood flow, the preceding four conservation laws (7), (9), (12) are replaced by corresponding balance equations:

$$\tfrac{d}{dt}\bar{Q} = -\tfrac{2}{L}\rho_0^{-1}\bar{P}A\big|_{x_1}^{x_2} - k\bar{U} \tag{13}$$

where $\bar{U} = \frac{1}{L}\int_{x_1}^{x_2} \bar{u}\, dx$ is mean velocity;

$$\tfrac{d}{dt} E^{\pm} = -\big(\tfrac{4\alpha - r_\pm}{6}\rho_0 Q^3/A^{r_\pm+1} + \beta Q H(A; r_\pm)\big)\big|_{x_1}^{x_2} - k\int_{x_1}^{x_2} Q^2/A^{r_\pm+1}\, dx \tag{14}$$

and

$$\tfrac{d}{dt} M = -\big(\tfrac{1}{2}\rho_0 Q^2/A^{2\alpha} + \beta G(A;\alpha)\big)\big|_{x_1}^{x_2} - k\int_{x_1}^{x_2} Q/A^{2\alpha}\, dx. \tag{15}$$

Note that the righthand side of each equation contains a dissipative integral term.

3 Travelling waves

The blood flow system (1) possesses travelling waves

$$A = A(\xi), \quad Q = Q(\xi), \quad \xi = x - ct \tag{16}$$

where c is the wave speed. These solutions arise from group-invariance with respect to the translation symmetry $(t, x) \to (t + \epsilon, x + c\epsilon)$, with group parameter ϵ.

Substitution of expressions (16) into the PDS (1) yields the travelling wave ODEs

$$-cA' + Q' = 0, \quad -cQ' + \alpha(Q^2/A)' + \beta_0(A/A_0)f'(A/A_0)A' + kQ/A = 0. \tag{17}$$

The first ODE gives $Q = c(A - C)$ in terms of A, where C is an integration constant, and then the second ODE becomes a nonlinear separable equation for A

$$A' = \frac{\kappa(A-C)A}{\sigma - \gamma A^2 - (\beta_0/A_0)A^3 f'(A/A_0)}, \tag{18}$$

with

$$\gamma = (\alpha-1)c^2 \geq 0, \quad \sigma = C^2\alpha c^2 > 0, \quad \kappa = kc \neq 0. \tag{19}$$

Note that the physical parameters are given in terms of κ, σ, γ by the relations

$$\alpha = \sigma/(\sigma - \gamma C^2), \quad c = \pm\sqrt{\sigma - \gamma C^2}/(\sqrt{2}C), \quad k = \pm\kappa C/(\sqrt{2}\sqrt{\sigma - \gamma C^2}). \tag{20}$$

For the pressure-area relation (2), the ODE (19) has an explicit solution

$$C = 0: \quad \tfrac{2}{3}\mu A^{3/2} + \gamma A = \kappa(\xi_0 - \xi); \tag{21}$$

$$C < 0: \quad 2\mu|C|^{3/2} \arctan\left(\sqrt{A}/\sqrt{|C|}\right) - (\sigma/|C|)\ln(A) - (\gamma|C| - \sigma/|C|)\ln(A + |C|) \tag{22}$$
$$+ \tfrac{2}{3}\mu A^{3/2} + \gamma A - 2\mu|C|\sqrt{A} = \kappa(\xi_0 - \xi);$$

$$C > 0: \quad \mu C^{3/2} \ln\left(|\sqrt{C} - \sqrt{A}|/(\sqrt{C} + \sqrt{A})\right) + (\sigma/C)\ln(A) + (\gamma C - \sigma/C)\ln(|C - A|) \tag{23}$$
$$+ \tfrac{2}{3}\mu A^{3/2} + \gamma A + 2\mu C\sqrt{A} = \kappa(\xi_0 - \xi).$$

A variety of interesting behaviours are exhibited by these solutions
- pressure shocks;
- blood flow shocks;
- sharp wave-front pulses in pressure and blood flow;
- flows in which the blood vessel is expanding or constricting.

Detailed features and physical interpretation are discussed in Ref. [6].

References

[1] A. Quarteroni, L. Formaggia, Mathematical modelling and numerical simulation of the cardiovascular system. In: Computational Models for the Human Body (ed. N. Ayache), Handbook of Numerical Analysis Vol. 12, 2004, 3–127.

[2] J. Britton, Y. Xing, Well-balanced discontinuous Galerkin methods for the one-dimensional blood flow through arteries model with man-at-eternal-rest and living-man equilibria, Comput. Fluids 203 (2020), 104493.

[3] G. V. Krivovichev, Comparison of inviscid and viscid one-dimensional models of blood flow in arteries, Appl. Math. Comput. 418 (2022), 126856.

[4] A.C. Barnard, W.A. Hunt, W.P. Timlake, E. Varley, A theory of fluid flow in compliant tubes, Biophys. J. 6(6) (1966), 717–724.

[5] Y.V Vassilevski, V.Y. Salamatova, S.S. Simakov, On the elasticity of blood vessels in one-dimensional problems of hemodynamics, Comput. Math. Math. Phys. 55(9) (2015), 1567–1578.

[6] S.C. Anco, T.M. Garrido, A.P. Márquez, M.L. Gandarias, Exact solutions and conservation laws of a system of 1D partial differential equations for blood flow, Chaos, Solitons and Fractals 170 (2023), 113360.

International Conference on Mathematical Analysis and Applications in Science and Engineering
ICMA²SC'24
ISEP Porto-Portugal, June 20 - 22, 2024

Performance Evaluation Metrics for Automatic Liver Segmentation on Medical Imaging Scans

Stephanie Batista[1⋆] **Miguel Couceiro**[1,2,3,4] **Ricardo Filipe**[5]
Paulo Rachinhas[6] **Jorge Isidoro**[6] **Inês Domingues**[1,7]

[1] Polytechnic Institute of Coimbra, Coimbra Institute of Engineering,
Rua Pedro Nunes - Quinta da Nora, 3030-199 Coimbra, Portugal
[2] Institute of Applied Research (i2A), Portugal
[3] Laboratory for High Performance Computing (LaCED), Portugal
[4] Laboratory of Instrumentation and Experimental Particle Physics (LIP-Coimbra),
Rua Larga da Universidade de Coimbra, 3004-516 Coimbra, Portugal
[5] Altice Labs, S.A, Portugal
[6] Coimbra Hospital and University Center, Portugal
[7] IPO Porto Research Center (CI-IPOP): Medical Physics,
Radiobiology & Radiation Protection Research Group, Portugal

[1⋆]stephanieabn@gmail.com

Abstract: Liver segmentation in medical imaging scans is fundamental for the diagnosis and treatment planning of liver-related pathologies. It aids in identifying and characterizing diseases, providing accurate recognition of affected organs and tissues. Despite its significance, achieving precise segmentation is a major challenge due to the presence of artifacts and the different densities of soft tissues and neighboring organs. Given the inherent difficulty associated with the subjectivity regarding the validation and acceptance of manual segmentation by clinicians, this work emphasizes the importance of quantitative metrics to complement the subjective assessment for automatic liver segmentation outcome.

keywords: Medical Imaging; Liver; Automatic Liver Segmentation; Evaluation Metrics.

1 Introduction

The evolution of medical imaging represents a hallmark of technological advancement in healthcare, revolutionizing diagnostic practices from invasive to non-invasive methods, thus enhancing patient comfort and healthcare standards [1]. Beyond diagnosis, medical imaging plays a crucial role in treatment planning and follow-up care, signifying a dedication to improving patient well-being across the continuum of medical intervention. Stemming from the pioneering efforts of figures like Marie Curie [2], medical imaging modalities such as CT, PET, SPECT, and MRI continue to expand treatment options and elevate the standard of care.

One significant advancement in this field is the progress made in organ segmentation, particularly with liver segmentation [3]. This is crucial for monitoring the health of the digestive system and treat pathologies related to liver. Despite obstacles such as artifacts and the close proximity of tissues, automatic techniques have seen substantial improvements [4, 5]. However, consistent evaluation metrics for these techniques remain lacking, hindering comparative analysis of their evolution and effectiveness [6].

2 Segmentation Evaluation Metrics

There are two main types of metrics, region-based and contour-based metrics. **Region-based metrics** assess the correctness of the area covered by segmentation, regardless of border precision. These include Accuracy, Dice Similarity Coefficient (DSC), Precision, and Volume Overlap Error (VOE). **Contour-based metrics** measure the correctness of boundary delineations. These include Average Symmetric Surface Distance (ASSD) and Mean Symmetric Surface Distance (MSSD). Figures 1 and 2 illustrate the calculation of these metrics, with True Positives (TP) in green, True negatives (TN) in blue, False negatives (FN) in red, False positives (FP) in orange.

Figure 1: Illustration of Image Segmentation results: (a) Original image; (b) Ground truth segmentation; (c) Automatic segmentation; (d) Classification outcomes.

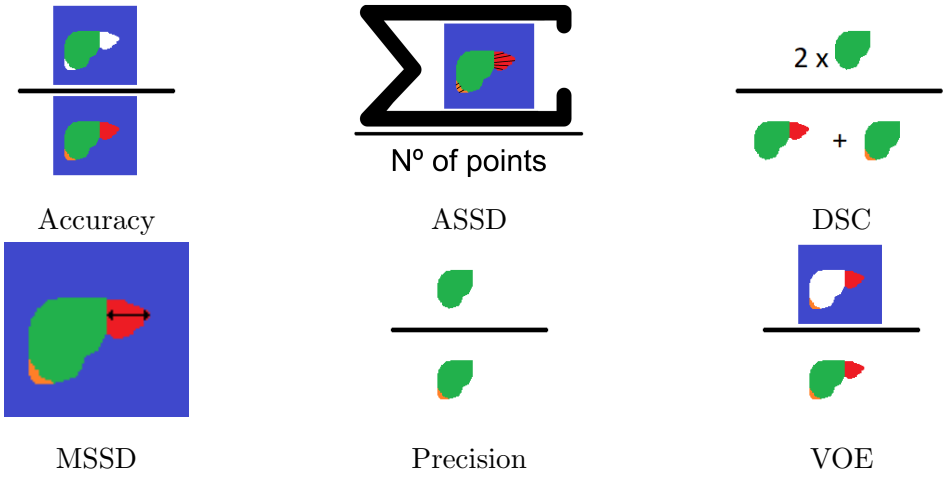

Figure 2: Illustration of metrics calculation.

Research on liver segmentation in medical imaging demonstrates promise, yet the lack of consistent evaluation metrics is often overlooked [7, 8]. A literature review conducted previously [6] selected studies dated between 2014 and 2024, focusing on fully automatic liver segmentation techniques. As a result, the most commonly used metrics in these studies were the ones shown in Figure 3.

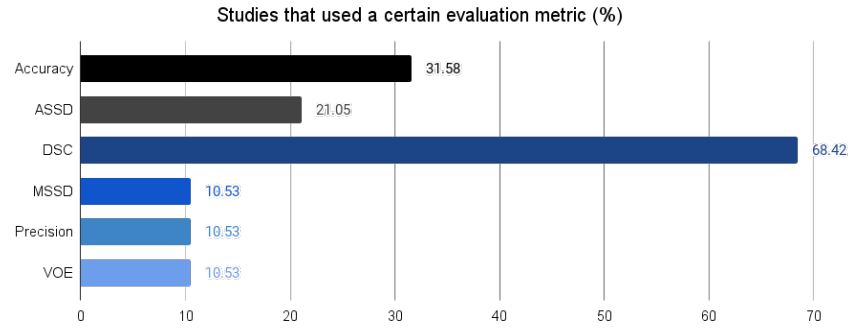

Figure 3: Distribution of the metrics used in the selected studies.

Table 1 presents an overview of the metrics, along with their main advantages and shortcomings.

Table 1: Summary of the main evaluation metrics used by automatic liver segmentation studies.

Metric	**Definition**	**Main Advantages**	**Main Disadvantages**
Accuracy	Measures the proportion of correctly identified voxels (both liver and non-liver), including TPs and true negatives, to the total number of voxels.	-Provides a comprehensive overview of the segmentation performance. -Easy to calculate and interpret.	-May be misleading in datasets with a large imbalance between liver and non-liver voxels. -Does not specifically focus on liver tissue accuracy.
ASSD	Calculates the average distance between corresponding points on the surfaces of the segmented liver region and the ground truth, in both directions.	-Offers a detailed assessment of boundary accuracy. -Highlights discrepancies in the segmentation's surface alignment.	-More complex to compute and interpret compared to overlap-based metrics. -Can be influenced by outliers or extreme values.
DSC	Measures the overlap between the segmented liver region and the ground truth, calculated as the size of the intersection divided by the summed size of the two regions.	-Provides a clear, straightforward measure. -Easy to interpret and widely used in medical imaging.	-Might not fully capture small discrepancies in boundary delineation. -Can be overly optimistic in cases of large overlap but poor boundary alignment.
MSSD	Determines the maximum distance between any point on the segmented liver surface and the nearest point on the ground truth surface, and vice versa.	-Identifies the worst-case scenario in segmentation discrepancies. -Useful for assessing the reliability of segmentation in critical areas.	-Focused on the maximum error, potentially overlooking overall segmentation quality. -Can be overly punitive for generally accurate segmentations with minor outliers.
Precision	Assesses the proportion of voxels correctly identified as liver tissue out of all voxels classified as liver by the algorithm.	-Highlights the algorithm's ability to avoid over-segmentation.	-Does not account for missed liver tissue (FNs). -It may only identify very clear cases of liver boundaries and ignore the more ambiguous cases.
VOE	Quantifies the volumetric discrepancy between the segmented liver region and the ground truth as the percentage of non-overlapping volume to union volume.	-Directly related to clinical relevance, reflecting the actual volume error. -Intuitive and easy to understand.	-Can be sensitive to the size of the liver, with larger livers potentially showing more significant absolute errors.

The results presented indicate that DSC, Accuracy, and ASSD stand out as the most frequently employed metrics in liver segmentation evaluations. Despite some studies validating the effectiveness of these metrics in tackling common challenges such as under-segmentation and over-segmentation, there remains an evident need for the adoption of standardized metrics in the field. We advocate for the use of at least one metric within each type of evaluation metric (region and contour). The introduction of such standards would greatly advance segmentation studies by underscoring key aspects, enabling straightforward comparisons across various methods, and significantly improving the reliability and effectiveness of automated liver segmentation in medical imaging.

3 Conclusions and Future Work

Non-invasive imaging techniques have vast potential to transform patient care, emphasizing the need for consistent metrics in automatic liver segmentation. By developing unified, quantitative standards, the accuracy, reliability, and comparability of segmentation methods can be significantly enhanced. This will not only aid clinicians but also steer advancements toward more effective and user-friendly solutions.

Standardizing evaluation metrics is essential for progressing liver segmentation technology. Clear metrics will enable better comparisons, foster innovation, and improve the development and validation of new methods. This will directly benefit clinical practices by improving diagnostics and treatment planning.

It is crucial to align technological developments with clinical needs to incorporate automatic liver segmentation into routine medical care. This alignment will improve diagnoses and help customize treatments for liver diseases, enhancing patient outcomes.

References

[1] Friebe, M; Illanes, A, Advancements in Medical Imaging and Image-Guided Procedures: A Potential-Or Rather Likely-Paradigm Shift in Diagnosis and Therapy: Understand Disruption and Take Advantage of It!, Appl. Sci., **13** (2023), 9218.

[2] American Institute of Physics, Marie Curie - War Duty (1914-1919), n.d. Retrieved March 24, 2024 from https://history.aip.org/exhibits/curie/war1.htm

[3] Torres, A, Segmentação de imagens médicas visando a construção de modelos médicos, Instituto Politécnico de Bragança, Escola Superior de Tecnologia e Gestão, 2012.

[4] Trefts, E; Gannon, M; Wasserman, D, Primer - The liver, Current Biology Magazine, 2017.

[5] Francque, S, The liver and the cardiovascular system: Two of a kind?, J Am Heart Assoc, **10**(8) (2021).

[6] Niño, SB; Bernardino, J; Domingues, I, Algorithms for Liver Segmentation in Computed Tomography Scans: A Historical Perspective, Sensors, **24** (2024), 1752.

[7] Crum, WR; Camara, O; Hill, DL, Generalized overlap measures for evaluation and validation in medical image analysis, IEEE Trans Med Imaging, **25**(11) (2006), 1451-1461. PMID: 17117774.

[8] Bilic, P; Christ, P; Li, HB; Vorontsov, E; Ben-Cohen, A; Kaissis, G; Szeskin, A; Jacobs, The Liver Tumor Segmentation Benchmark (LiTS), Medical Image Analysis, **84** (2023), 102680, ISSN 1361-8415.

International Conference on Mathematical Analysis and Applications in Science and Engineering ICMA²SC'24

ISEP **Porto-Portugal, June 20 - 22, 2024**

Mathematical modeling and numerical analysis of "Car abandonment" during tsunami evacuation

Sayu Arai[1*] **Hidekazu Yoshioka**[1]

[1] Japan Advanced Institute of Science and Technology Japan

[1*]s2310006@jaist.ac.jp

Abstract: Evacuation on foot has long been common during tsunami disaster. The situation has completely changed in Japan at the 2011 Tohoku earthquake that triggered a massive tsunami during which many people used cars. Evacuation by car has many risks, such as traffic congestion and liquefaction, both possibly reduce survival rate of evacuees. In this study, we investigate the "car abandonment," which is an evacuation strategy where evacuees of tsunami move either on foot or by car, and those by car has an option to abandon it during their evacuation. We mathematically formulate the movement of evacuees as an initial-boundary value problem of a system of 1-D nonlinear hyperbolic equations that governs evacuees' spatio-temporal densities. We discretize the system using a time-explicit and upwind conservative finite difference method. We present demonstrative computational results of our mathematical model, and finally discuss limitations and future perspectives of our research.

keywords: Tsunami disaster; car abatement; nonlinear hyperbolic system

MSC2020: 35-L04; 65-M06; 76-A30

1 Introduction

We should get away from the shoreline as quickly as possible when tsunami hits. It has been reported that 57% of evacuees used cars in the 2011 Tohoku earthquake that triggered a massive tsunami. The upper about 30 % of the reasons they evacuated by cars were "they use cars on a daily basis" and "they thought they would not be able to evacuate on time" [1]. One may be able to move faster than on foot by using a car; however, there are several risks that reduce survival rate of evacuees. Such examples include but are not limited to "traffic congestion," "liquefaction," and "cracks in the ground." Sekiya [2] noted that it is necessary to "design a car-oriented town where people can evacuate and move safely" and "install a road shoulder and parking lot to abandon cars". However, such options have not been investigated well to the best of our knowledge.

Based on this research background, we investigate "car abandonment" (**Fig. 1**), which is an evacuation strategy where evacuees of tsunami move either on foot by car, or those by car has a way to abandon it during their evacuation. We propose to formulate this new evacuation strategy based on an initial-boundary value problem of a system of

two 1-D nonlinear hyperbolic equations that governs evacuees' movement dynamics on foot and by cars. The model can be distinguished from the existing ones for traffic modelling that do not assume switching modes of transportation. Our ultimate research goal is to clarify how the car abandonment improve the survival of evacuees, but here we present demonstrative computational examples based on a time-explicit finite difference method to get insights into studies in the future.

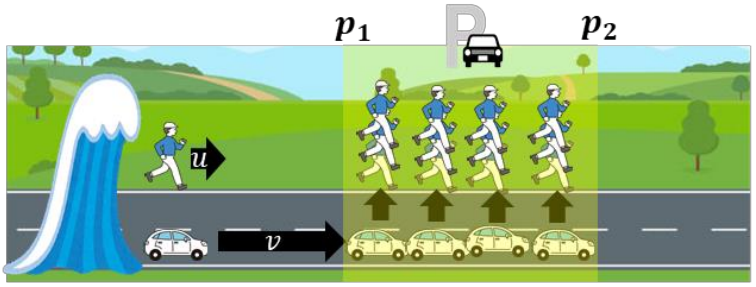

Figure 1. Conceptual image of the "car abandonment."

2 Mathematical model and computation

We propose a mathematical model to formulate "car abandonment" in a hypothesized 1-D road where a tsunami is coming from the left, and evacuees move toward right (**Fig.1**). The load is identified as the interval $\Omega=(0,L)$ with the length L. We assume that the road is divided into the three parts, which are the transition region where evacuees using cars can abandon their cars and transit to those on foot, which is $A=(p_1,p_2)\subset\Omega$ in **Fig. 1**, and the two regions where car abandonment is not allowed. We formulate the evacuees' dynamics by hyperbolic equations as shown below where t is time.

Pedestrian (evacuees on foot)

$$\frac{\partial}{\partial t}f_1(t,x)+\frac{\partial}{\partial x}\left(uf_1(t,x)\right)=p\lambda f_2(t,x) \text{ for } t>0 \text{ and } x\in A, \tag{1}$$

$$\frac{\partial}{\partial t}f_1(t,x)+\frac{\partial}{\partial x}\left(uf_1(t,x)\right)=0 \text{ for } t>0 \text{ and } x\in\Omega-A \tag{2}$$

Car (evacuees by cars)

$$\frac{\partial}{\partial t}f_2(t,x)+\frac{\partial}{\partial x}\left(v_{\max}\left(1-\frac{f_2(t,x)}{f_{2,\max}}\right)f_2(t,x)\right)=-\lambda f_2(t,x) \text{ for } t>0 \text{ and } x\in A, \tag{3}$$

$$\frac{\partial}{\partial t}f_2(t,x)+\frac{\partial}{\partial x}\left(v_{\max}\left(1-\frac{f_2(t,x)}{f_{2,\max}}\right)f_2(t,x)\right)=0 \text{ for } t>0 \text{ and } x\in\Omega-A. \tag{4}$$

Here, $f_1(t,x)$ is the unit-length pedestrian density at time t and location x, $f_2(t,x)$ is that of cars, $u>0$ is the moving speed of pedestrian, $v_{\max}>0$ is the maximum speed of cars, $f_{2,\max}>0$ is the maximum car density, $\lambda>0$ is the switching rate from Car to Pedestrian, and $p>0$ is the average number of evacuees in one car. This model assumes that evacuees of Car is possibly faster than those of Pedestrian if the car density f_2 is not large; otherwise, there may be a situation where $v_{\max}\left(1-f_2/f_{2,\max}\right)<u$. In such a situation, some evacuees by cars would be motivated to abandon their cars and then continue to

evacuate on foot. The system (1)-(4) is equipped with some initial condition, no-flux and free-outflow boundary conditions at $x = 0$ and $x = L$, respectively.

We discretized the system (1)-(4) using a conservative finite difference method based on a classical upwind discretization. The road with the length of 20 (km) was discretized into 3,000 cells, and we used 6,000 time steps with the increment 1/6,000 (hour). We assumed that Car's (normalized) initial distribution is a Gaussian distribution with mean 3 (km) and variance 1 (km^2), and that of Pedestrian with mean 8 (km) and variance 1 (km^2). The parameter values were set as follows: u is 8 (km/h), $v_{\max}$ is 40 (km/h), $f_{2,\max}$ is 120 (car/km), λ is 3 (1/hour), and p is 3 (people/car). **Fig. 2** show that a part of Car switches to Pedestrian in the transition region, and both Pedestrian and Car densities form traveling waves, the latter involving a shock while the former does not possibly due to the drift nonlinearity of the latter. The car abandonment seems to better work when the density of Car is smaller and is more elongated.

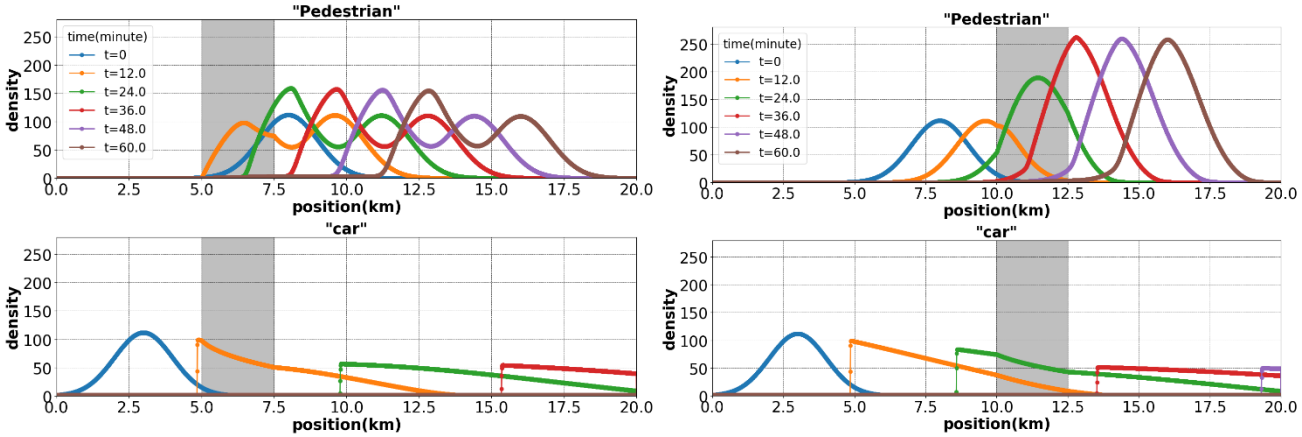

Figure 2. Computational results with different transition regions.

3 Conclusion

We proposed a model for evacuees' dynamics considering the "car abandonment" based on a system of nonlinear conservation laws and presented demonstrative computational results. In the future, we will improve accuracy of the finite difference method using a TVD technique [3]. We will also incorporate Tsunami movement in the model in a way that evacuees touched by tsunami do not survive. Then, we will try to optimize the transition region A to maximize the total number of successful evacuees.

References

[1] Cabinet Office (Disaster Management), Survey on Evacuation from Earthquake and Tsunami during the Great East Japan Earthquake: Major Survey Results, Cabinet Office, Government of Japan. Disaster Management Information page, 2012. In Japanese. Accessed March 12, 2024. Available at: https://www.bousai.go.jp/jishin/tsunami/hinan/pdf/20121221_chousa1_1.pdf.

[2] Sekiya N. The problems of disaster prevention measures in Japan in terms of tsunami evacuation after the Great East Japan Earthquake. Journal of JSCE, F6 (Safety Problem), 68(2) (2012), l_1–l_11. (In Japanese with English Abstract).

[3] Castro M. et al. High order finite volume schemes based on reconstruction of states for solving hyperbolic systems with nonconservative products, applications to shallow-water systems. Mathematics of Computation, 75 (2006), 1103–1134.

International Conference on Mathematical Analysis and Applications in Science and Engineering ICMA²SC'24

ISEP **Porto-Portugal, June 20 - 22, 2024**

MATHEMATICAL MODEL OPTIMIZATION TO ADDRESS PALLET LOADING ISSUES IN THE AUTOMOTIVE INDUSTRY.

Rita C. M. Sales-Contini[1,2*], Naiara P. V. Sebbe[1], Ana B. M. Machado[1], Francisco J. G. Silva[1,3], Isabel M. Pinto[1]

[1]CIDEM, ISEP, Polytechnic of Porto, Portugal

[2]Technological College of São José dos Campos, Centro Paula Souza, Brazil

[3]Associate Laboratory for Energy, Transports and Aerospace (LAETA-INEGI), Portugal

[1,2*]rcmsc@isep.ipp.pt

Abstract: Within enterprises, supply chain management and logistics are crucial areas of concentration. As a result of their commercial obligations and the need to adhere to product delivery time and batch amount requirements, different businesses usually experience an increase in additional and needless transport expenses due to planning gaps, which has a negative economic impact. Therefore, this objective was to alter an optimisation model to maximise businesses' frequent shipments. A car component manufacturer was selected to validate the model, which enabled to evaluate the tool's advantages and disadvantages by applying it to a real-world case study. It was found that many companies exports most of its goods but most of the pallets exported are not fully optimised, costing excessive amounts for expedited shipping. Two mathematical optimisation methods were applied to the problem to maximise both the customer's and the company's present reality about the arrangement of boxes per pallet. Using the new tool, it was easy to calculate those five pallets, matching the customer's needs and configure them properly to ensure that the pallet is supplied in its entirety, and should be sent to them each week.

keywords: optimization; transport management program; pallets loading problem.

ICMASC2024: 96

1 Introduction

Mathematical programming models, of which optimisation models are a subset, enable the determination of the conditions under which a particular objective can be maximised or minimised, given the presence of a set of constraints. As a result, the issue at hand is one of linear programming, which is the most basic kind of problem and forms the core of operational research [1]. Furthermore, the practical aspect of linear programming contributes to its widespread implementation [2], as it enables the acquisition of findings that, when combined with qualitative data and subjective evaluations, may be implemented realistically.

Pallet optimisation problems, which are connected to the real-world issue our work will tackle, are one example of how operational research has been applied in the literature. Beasley [3] used the "Tree search procedure" method to conduct heuristic research on the exact cut in two dimensions. The necessity to cut raw materials to precise specifications to minimise material waste gave rise to this

study. After conducting numerical experiments in which it reduced waste by 100% in some cases, the author concluded that his optimisation model could handle average problems for non-guillotined cutting, with an average of 60% throughout all tests. A straightforward and efficient heuristic was provided by Morabito et al. [4] to address the issue of packing the most boxes possible on a pallet without overlapping, considering MPL (Manufacturer's Pallet Loading). The authors found the best solution in 99.9% of the over 20,000 situations they examined using this process. Likewise, Letchford et al. [5] examined the top bounds for the Pallet Loading Problem (PLP). It was found that two limits predominate over all others: one derived from the linear programming relaxation of a packing formulation and the other from a Nelissen limit, with the latter nearly always being optimal.
Due to the broad nature of this field, numerous works in supply chain and logistics have been published. On the other hand, a large body of literature exists about mathematical modelling and pallet optimization, many of which are challenging to implement in businesses where time is of the essence to meet their contractual obligations to their clients, businesses must incur additional and needless costs due to the issue of urgent transit. This kind of expense has a significant economic impact as it accounts for about 33% of all transportation costs, thus, this activity is a result of the necessity to examine the transportation that the company is examining to cut expenses and arrange its shipment schedule. An example of the characterisation of current transport, which took place in an automotive component's producer between weeks 22 and 39 of 2023, was taken into consideration to evaluate the established model. This included determining the occupancy of the pallets and optimising their use.

2 Results and discussion

The efficiency of transport and storage activities, as well as the expenses associated with packing and handling, are known to be directly impacted by the geometric properties of the items and the packaging units employed in their distribution. Pallets sent via regular transport can be optimised to reduce the cost of urgent transit. A mathematical optimisation model was created in this way to maximise the arrangement of packages per pallet and client. Two important firm initiatives were evaluated to assess the concept: A1 and B1. For every reference, these projects include detailed packing instructions. Pallets and nine different kinds of packages were thus employed to deliver the goods to the client.
Shipments delivered to customer 14701 from the A1 product—the most difficult in terms of diversity of packages and number of orders—were utilized to optimize pallets, save costs, and provide improved efficiency. Moreover, Gunes Erdogan of the University of Bath created the "CLP Spreadsheet Solver," an open-source program for expressing, resolving, and displaying the outcomes of CLPs (Container Loading Problems).
The customer's weekly order was optimized to use just two types of pallets in a single shipment. For this project, the company now uses six distinct types of pallets; the main discrepancies are linked to height, which the optimization model corrects. Thus, information about the kinds of pallets that are available, and the weekly demand that corresponds to each box are shown in Table 1. It should be mentioned that to maximize the volume of the pallets, a maximum height of 1200 mm was taken into consideration for the pallets acceptable by the chosen customer.

Table 1. Pallets and package types employed in the mathematical model.

Pallet designation	Available pallets dimensions ($\boldsymbol{l} \times \boldsymbol{w} \times \boldsymbol{h}$) [mm]	Package designation	Available package dimensions ($\boldsymbol{l} \times \boldsymbol{w} \times \boldsymbol{h}$) [mm]	Weekly search
Pallet 1	800x600x1200	Box A or Item type 1	400x300x120	24
Pallet 2	1200x800x1200	Box B or Item type 2	800x400x150	19
		Box C or Item type 3	600x400x150	20
		Box D or Item type 4	800x600x245	18
		Box F or Item type 5	1200x190x200	12

The "CLP Spreadsheet Solver" tool's solution indicated that four pallets of type 2 and one pallet of type 1 were required. Table 2 allows to see how the products are distributed among the chosen pallets.

Table 2. A solution from "CLP Spreadsheet Solver" for matching pallets with appropriate packages.

Pallets´ Quantity	Pallet designation	Package designation	Packages´ Quantity
1	Pallet 1	Package A	23
		Package C	4
2	Pallet 2	Package B	3
		Package D	8
1	Pallet 2	Package C	14
		Package E	12

1	Pallet 2	Package A	1
		Package B	13
		Package C	2
		Package D	2

The distribution of packages across all configurations, as calculated by the "CLP Spreadsheet Solver" program, is depicted in Figure 3. Figure 3.b) depicts the distribution of packages on the type 2 pallet, where this configuration is used twice and is referred to as configuration 1. Figure 3.a) shows the distribution of packages on the type 1 pallet, which is used only once. Figure 3.d) depicts configuration 3 of the pallet type 2, while Figure 3.c) displays the distribution of products on the type 2 pallet identified as configuration 2. As a result, to solve the issue, client 14701 must receive five pallets every week that are appropriate for their needs. The software therefore counts the products that must be sent, maximizing the amount of goods on a pallet to reduce the number of pallets required for shipment.

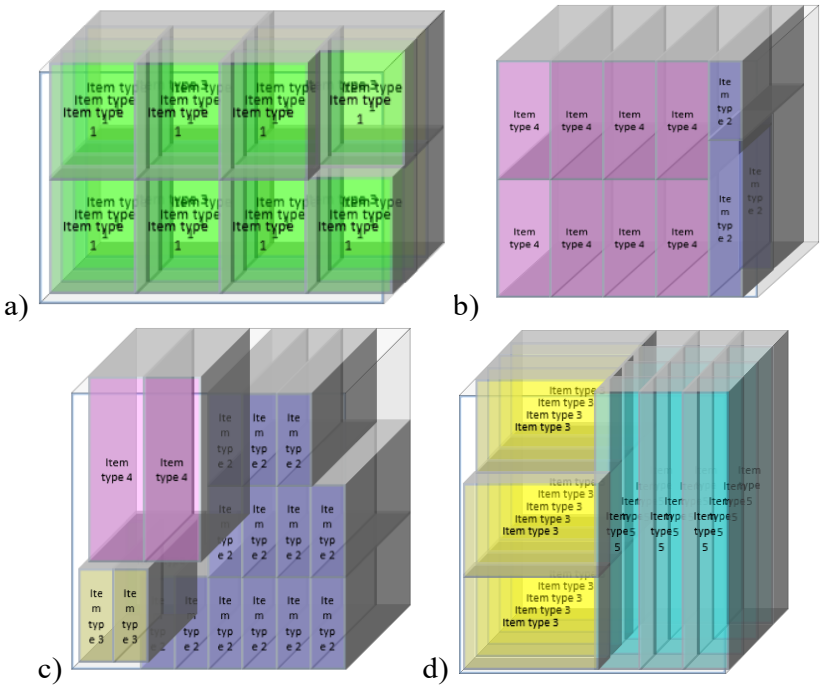

Figure 3. a) Singular configuration for type 1 pallet; b) Configuration 1 of pallet 2; c) Configuration 2 of pallet 2, and d) Configuration 3 of pallet 2.

The results show that, with appropriate programming and models that allow the work to be systematised, logistical operations can be optimised, leading to significant financial savings, without requiring any additional work on the part of the company that, in this case, assembles the pallets. In this case, an automotive components manufacturer. The field of logistics and supply chain faces significant challenges when it comes to reducing waste as much as possible, not only for economic reasons, which are crucial for the company's ability to survive economically but also for environmental reasons, since less transport means less emissions, which is better for the environment [6]. Since packaging affects how commodities are bundled and arranged for later transportation, a great deal of research has been done in this field. Nearly all these studies use mathematical optimization models of various levels of complexity, using a model that could virtualize the logistic and operational costs as well as the transportation and disposal impact of reusable and recyclable plastic containers. Nevertheless, the model presented by the current work is more desirable than the one previously presented because it is simpler.

Some optimization models, which are typically run in two stages, are highly complex. To select the suppliers with the best performance, Resat and Unsal [7] first applied the Analytic Hierarchy Process (AHP). After that, they used a mixed-integer linear multi-objective mathematical model to optimize the supply chain, with cost, time, and social factors being the main factors of concern. The goal of Vitale et al.'s study [8] was to maximize raw material flow within the wood pellet sector. This was accomplished by using a typical decomposition technique, which involved first planning routes and then calculating the products´ flows and raw materials to solve the optimization problem. Studies meant to maximize pallet and container occupancy, however, have not received much attention. Robotic container loading was explored by Jiao et al. [9], although there were some limitations, including load balance, orientations, stability, and multi-drop, in addition to limits on robot position and pallet

continuity. The solution is far more complicated than the one developed by the present work, considering the limitations the algorithm would have to work around.

3 Conclusions and Future Work

By adhering to the work's objectives and utilizing a case study that was provided by an external organization, it was feasible to describe the company's current mode of transportation and illustrate issues that arise from insufficient pallet loading. It was discovered that most of the company's goods are exported, and most pallets are shipped partially, which adds exorbitant and needless expenses to the business. The goal of this study was to identify a low-cost, easy-to-implement, and adaptable solution to this issue, as it affects a few small and medium-sized businesses, to increase their competitiveness when it comes to the prices of external logistics. In this situation, it was also feasible to create mathematical models that would enable the corporation to optimize the number of pallets transported, making better use of the available space for each shipment. It was confirmed that five pallets must be supplied each week to meet the needs of the customer in various configurations that permit the pallets to be sent full, with the use of the "CLP Spreadsheet Solver" program. The limitations applied in this study are typical of many issues that Small and Medium-Sized Businesses need to deal with and can be promptly modified to meet requirements. It is suggested that future research enhance the mathematical models to consider the features of the vehicles being utilized and analyse the necessity for urgent transportation, which raises the company's freight expenses.

Acknowledgements

The authors thank the School of Engineering, Polytechnic of Porto and FicoCables Lda for the infrastructure offered for the development of this project.

References

[1] Ramalhete, M.; Guerreiro, J.; Magalhães, A. Programação Linear I; McGrawHill: Lisboa, Portugal, 1995.
[2] Hill, M.M.; dos Santos, M.M. Investigação Operacional—Programação Linear, 3rd ed.; Edições Sílabo: Lisboa, Portugal, 2015.
[3] Beasley, J.E. An Exact Two-Dimensional Non-Guillotine Cutting Tree Search Procedure. Oper. Res., **33** (1985), 49–64.
[4] Morabito, R.; Morales, S. A Simple and Effective Recursive Procedure for the Manufacturer's Pallet Loading Problem. J. Oper. Res. Soc., **49** (1998), 819–828.
[5] Letchford, A.N.; Amaral, A. Analysis of Upper Bounds for the Pallet Loading Problem. Eur. J. Oper. Res., **132** (2001), 582–593.
[6] Ronzoni, M.; Accorsi, R.; Guidani, B.; Manzini, R. Economic and Environmental Optimization of Packaging Containers Choice in Food Catering Supply Chain. Transp. Res. Procedia, **67** (2022), 163–171.
[7] Resat, H.G.; Unsal, B. A Novel Multi-Objective Optimization Approach for Sustainable Supply Chain: A Case Study in Packaging Industry. Sustain. Prod. Consum., **20** (2019), 29–39.
[8] Vitale, I.; Dondo, R.G.; González, M.; Cóccola, M.E. Modelling and Optimization of Material Flows in the Wood Pellet Supply Chain. Appl. Energy, **313** (2022), 118776.
[9] Jiao, G.; Huang, M.; Song, Y.; Li, H.; Wang, X. Container Loading Problem Based on Robotic Loader System: An Optimization Approach. Expert Syst. Appl., **236** (2024), 121222.

International Conference on Mathematical Analysis and Applications in Science and Engineering
ICMA^{2}SC'24
ISEP Porto-Portugal, June 20 - 22, 2024

Queue Management Analysis in Single-Server Manufacturing System with Working Breakdowns, Vacations, and Retrial Policy

Shalini Sharma[1⋆]

[1] Department of Mathematics, Central University of Jammu, Samba, Jammu & Kashmir, India-181143

[1⋆]shalini.math@cujammu.ac.in

Abstract: This investigation focuses on conducting a queue management analysis for failed machines within a manufacturing system featuring a single server, incorporating elements such as server vacations, breakdown occurrences, and the discouragement behavior exhibited by the failed machines. Initially, the system will commence with a server vacation period, followed by transitioning into normal operational states characterized by server activity, including both normal busy periods and instances of working breakdowns. During the vacation period, breakdown period, and normal busy period, the failed machines exhibit balking behavior, whereas reneging behavior is observed during the normal busy periods. A retrial orbit materializes as failed machines arrive during the server's working breakdown period electing to enter the retrial orbit instead of promptly joining the queue. In this study, to solve steady-state probabilities, the matrix-analytic method is utilized as well as develop various performance metrics that measure the system's efficacy. On the basis of system performance metrics, a cost function is constructed. Further, we optimized the cost function using a Genetic Algorithm (GA).

keywords: Retrial; Server vacation; Server working breakdown; Matrix-analytic method; Cost-optimization.

MSC2020: 60K25; 90B22; 68M20.

1 Introduction

This study focuses on queue management of failed machines in manufacturing handled by a single server experiencing breakdowns and taking vacations. Failed machines may balk due to slow service or long wait times, or renege after joining the queue but leaving due to delays, as first studied by Haight [1, 2]. Additionally, some machines exhibit retrial behavior and the retrial machining system may be unreliable or experience a breakdown due to the server's unreliability as examined by Aissani [5] and Chen [6]. Queueing systems with server vacations, introduced by Levy and Yechiali [7], are applicable in various domains. Several studies have addressed machine repair issues with a server's vacation policy (Jain et al.[8]; Meena et al.[9]).
In this study a manufacturing system handling a queue of K machines, repaired by an unreliable server that takes vacations. Failures occur according to a Poisson process with rate λ and are served on a first-come, first-served (FCFS) basis. An incoming failed machine joins the queue with probability γ_n if it encounters n or more machines in the system; otherwise, it balks with

probability $1-\gamma_n$. Specifically, $\gamma_0 = 1$ (always joins if no machines are in the system), γ for $1 \leq n \leq K-1$, and $\gamma_K = 0$ (will not join if the system already has K machines).

Machines can exhibit reneging behavior during normal busy state of the server, with an exponential rate of ϕ. In the working breakdown state, incoming failed machines form a retrial orbit, reattempting service in a normal busy state. If the server is busy, the machine returns to the orbit, continuing until service is received. The retrial time is exponentially distributed with rate $n\eta$, where n is the orbit size, and this process also operates on an FCFS basis. The server transitions from vacation to a normal busy state at an exponential rate θ and provides full service at rate μ. It may experience working breakdowns and repairs with exponential rates α and β, respectively, providing service at a slower rate μ_1 during breakdowns. The balking behavior is observed in all states (vacation, normal busy, and working breakdown), with the state-dependent arrival rate of failed machines given by:

$$\lambda_n = \begin{cases} \lambda\gamma_n, & \text{for } n = 0, 1, \ldots, K-1, \\ 0, & \text{otherwise.} \end{cases}$$

2 Results and discussion

This section includes figures with numerical illustrations to support our concept and approach. We optimized the cost function using a genetic algorithm with default parameters: $K = 25$, $\lambda = 0.5$, $\mu = 3$, $\mu_1 = 2$, $\eta = 0.5$, $\alpha = 0.5$, $\beta = 0.8$, $\gamma = 0.5$, $\phi = 0.5$, and $\theta = 0.5$.
Figure 2 illustrates that as λ increases, the system's throughput (T_P), expected waiting time (W_T), probability of a busy server (P_B), and expected number of failed machines (E_S) all increase, especially with higher values of θ, α, and K. Figure 3 shows that as μ increases, T_P and the probability of an idle server (P_I) increase, with the maximum effect seen at higher β and lower K, while E_S and W_T decrease, with a smaller decrement at higher ϕ and lower γ.

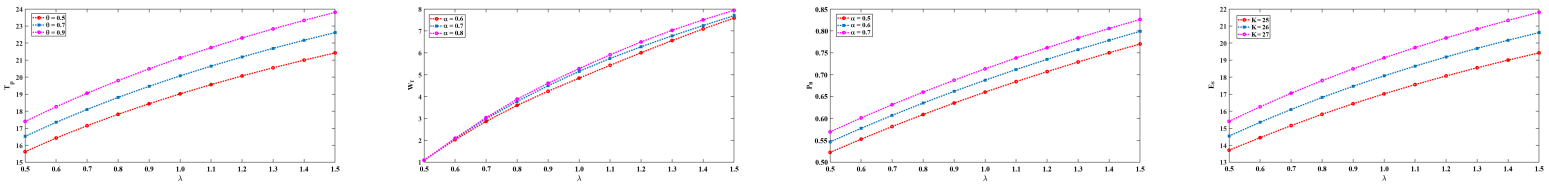

(a) (b) (c) (d)

Figure 1: Effect of λ on: (a) T_P with different θ; (b) W_T with different α; (c) P_B with different α; (d) E_S with different K.

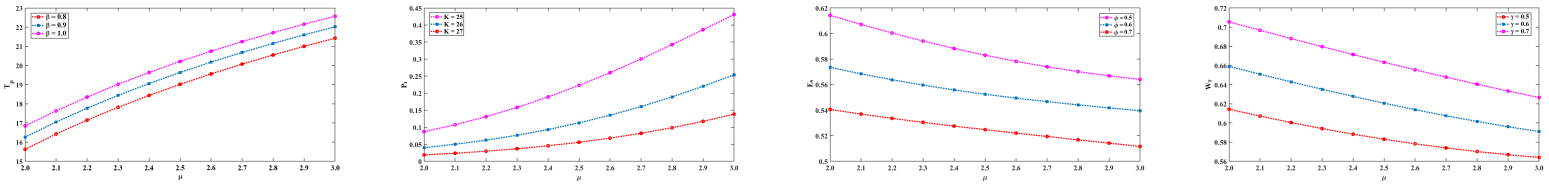

(a) (b) (c) (d)

Figure 2: Effect of μ on: (a) T_P with different β; (b) P_I with different K; (c) E_S with different ϕ; (d) W_T with different γ.

We optimized the expected cost function using a genetic algorithm (GA) with two continuous decision variables, μ_1 and μ. The convexity region for μ_1 is [2, 5] and for μ is [4, 7], with cost

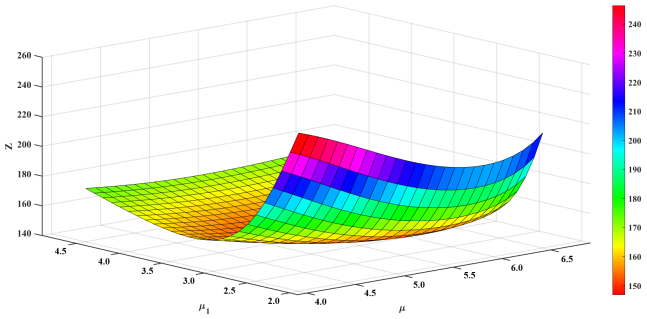

Figure 3: Convexity behavoir of decision variables on an expected cost function.

components $C_1 = 100$, $C_2 = 200$, $C_3 = 300$, $C_4 = 100$, $C_5 = 300$, and $C_6 = 150$. GA parameters were set to a population size of 25, generation count $g_n = 25$, crossover factor $P_{cr} = 0.8$, and mutation factor $P_{mt} = 0.01$. The goal was to minimize the expected cost function as shown in Figure 3.

Table 1 shows that μ_1^* and μ^* increase with λ due to higher arrival rates causing overcrowding, which requires a higher service rate to reduce waiting costs and improve server utilization. Table 2 indicates that as θ increases, μ_1^* decreases while μ^* increases, correlating with higher average vacation rates and a greater likelihood of the server being accessible and occupied. Table 3 demonstrates that increasing α results in a higher μ_1^* and a lower μ^*. Table 4 shows that increasing β leads to higher values for both μ_1^* and μ^*, suggesting that higher α and β can increase the estimated optimal service rate μ_1^*.

Table 1: Effect of λ on μ_1^*, μ^*, and Z.

Cases	λ	μ_1^*	μ^*	Z_{GA}
1	0.5	4.87240	6.50000	190.43557
2	0.6	4.91465	6.50845	190.47380
3	0.7	4.91605	6.54502	190.77606
4	0.8	4.95610	6.55194	190.80233

Table 2: Effect of θ on μ_1^*, μ^*, and Z.

Cases	θ	μ_1^*	μ^*	Z_{GA}
1	0.8	4.96332	6.50000	189.72576
2	0.9	4.83991	6.50294	189.44489
3	1.0	4.77714	6.51570	189.20203
4	1.1	4.67876	6.52638	188.00700

Table 3: Effect of α on μ_1^*, μ^*, and Z.

Cases	α	μ_1^*	μ^*	Z_{GA}
1	0.5	4.82873	6.553584	190.07189
2	0.6	4.91067	6.531125	190.01770
3	0.7	4.92097	6.529775	189.53609
4	0.8	4.95093	6.518052	189.40189

Furthermore, the data presented in Tables 1-4 indicate the following: (i) The value of Z increases as λ and β increase. (ii) The value of Z decreases as α and θ increase. The aforementioned

Table 4: Effect of β on μ_B^*, μ_V^*, and Z.

Cases	β	μ_1^*	μ^*	Z_{GA}
1	1.0	4.75328	6.50000	190.28416
2	1.1	4.91210	6.50506	190.28576
3	1.2	4.94870	6.51066	190.28584
4	1.3	4.96260	6.53630	190.28590

findings provide a point of reference for manufacturing service system administrators.

3 Conclusions and Future work

This work aims to manage the queue of failed machines in a manufacturing system with server breakdowns and vacations, considering behaviors like reneging, balking, and retrials. We developed steady-state solutions using the matrix analytic method and examined various performance metrics. The expected cost function was optimized using a genetic algorithm (GA) to find the optimal decision variables at the lowest cost.
Future Scope: Incorporate heterogeneous unreliable repairmen, integrate feedback mechanisms, implement retention of reneged machines, conduct transient analysis, etc.

References

[1] Haight F. A., Queueing with balking, Biometrika, **44(3/4)** (1957), 360–369.

[2] Haight F. A., Queueing with reneging, Metrika, **2** (1959), 186–197.

[3] Ammar S. I., T. Jiang, Q. Ye, Transient analysis of impatient customers in an M/M/1 disasters queue in random environment, Engineering Computations, **37(6)** (2020), 1945–1965.

[4] Bouchentouf A. A., M. Boualem, L. Yahiaoui, H. Ahmad, A multi-station unreliable machine model with working vacation policy and customers impatience, Quality Technology & Quantitative Management, **19(6)** (2022), 766–796.

[5] Aissani A., A retrial queue with redundancy and unreliable server, Queueing systems, **17** (1994), 431–449.

[6] Chen W. L., System reliability analysis of retrial machine repair systems with warm standbys and a single server of working breakdown and recovery policy, Systems Engineering, **21(1)** (2018), 59–69.

[7] Levy Y., U. Yechiali, Utilization of idle time in an M/G/1 queueing system, Management Science, **22(2)** (1975), 202–211.

[8] Jain, M., R. K. Meena, P. Kumar, Maintainability of redundant machining system with vacation, imperfect recovery and reboot delay, Arabian Journal of Science and Engineering, **45** (2020), 2145–2161.

[9] Meena, R.K., M. Jain, S. S. Sanga, A. Assad, Fuzzy modeling and harmony search optimization for machining system with general repair, standby support and vacation, Applied Mathematics and Computation, **361** (2019), 858–873.

Features Extraction Over the Years in International Logistics Performance Index

Aldina Correia[1] **Diogo Ribeiro**[3]

[1] CIICESI, ESTG, Instituto Politécnico do Porto, Portugal
[2] MySense, United Kingdom

[1]aic@estg.ipp.pt, [2]diogo.ribeiro@mysense.ai

Abstract: The Logistics Performance Index (LPI) assesses global logistical performance by measuring factors such as the quality of commercial and transport infrastructure, the ease of customs procedures and the efficiency of customs clearance, among other aspects that influence the transnational flow of goods. To identify the variables that most contribute to the countries' logistical performance, techniques for selecting or extracting key indicators can be used. In both cases, the aim is to retain the indicators that maximise the variance extracted from the original data. In [1], to ensure that the extracted characteristics were relevant and informative in relation to the 2023 Logistics Performance Index indicators, extraction techniques were used, in particular Exploratory Factor Analysis (EFA), using PCA in the JASP software. The present study considers LPI indicators over several years, being therefore a longitudinal approach, using the software R. This analysis is based on the values of the LPI indicators in the years 2007, 2010, 2012, 2014, 2016, 2018 and 2023. As the EFA carried out in [1] allowed the identification of a single factor, in this work a Principal Component Analysis (PCA) was carried out over the available years, considering one component. Our results confirm the LPI as a longitudinal latent variable, characterised by its indicators, which demonstrate remarkable internal consistency. This consistency underpins the reliability of the LPI for assessing global logistics performance. Recognised as a valuable measure of logistics efficiency, LPI serves as a practical tool in business and politics, guiding strategic decision-making and improving the operational cost-benefit ratio and competitiveness of organisations.

keywords: Logistics Performance, LPI, Logistics Decision-Making, Feature Aggregation, Principal Component Analysis, Longitudinal

MSC2020: 62Hxx; 62H25; 62Pxx.

Acknowledgments

This work has been supported by national funds through FCT - FundaÃ§Ã£o para a CiÃªncia e Tecnologia through project UIDB/04728/2020.

References

[1] *Correia, A. and Mendes D., International Logistics Performance Feature Extraction Insights and Portugal's Global Positioning, Proceedings of International Conference Innovation In Engineering, São Miguel Island, Azores, Portugal.* Springer, 2024.

International Conference on Mathematical Analysis and Applications in Science and Engineering ICMA²SC'24

ISEP Porto-Portugal, June 20 - 22, 2024

Railway Wagons Anomaly Prediction Using TinyML

Ricardo Pereira[1] **Pedro Ribeiro**[2] **António Sousa**[1] **Jorge Mendonça**[1] **Veríssimo Lima**[1] **Fernando Carvalho**[1*]

[1] ISEP – P.Porto, Portugal
[2] Evoleo Technologies Lda, Portugal

[1*]fjc@isep.ipp.pt

Abstract: The anomalies detected in the wheels of railway wagons can cause significant damage to the railway tracks and pose risks to people and their property. To prevent these risks, this work, dedicated to Evoleo Technologies Lda, aims to develop an anomaly detector based on Machine Learning (ML) that monitors the operational state of the wheels and distinguishes three distinct classes of anomalies: wheel wear, axle breakage, or the presence of both simultaneously. For this purpose, a mechanical prototype was implemented, on which disturbances simulating the anomalies are induced.
The ML model was trained and validated/tested using a dataset collected from the mechanical prototype. The training phase of the model was carried out on the Edge Impulse development platform, which simplifies the deployment of the model on edge computing devices, where resources are usually limited. It also determines which features best describe and discriminate the four classes used and provides the trained model as a library for various edge computing devices, with particular interest in Arduino.
The dataset is based on the acceleration values that determine the existence of movement along the coordinate axes of the three-dimensional plane. To this end, the hardware architecture uses two Arduino edge computing devices: the first, with an integrated accelerometer, reads the accelerations at a frequency of 100 Hz; the second receives the data, processes the entire classification procedure, and informs the user of the presence or absence of anomalies in the wagon wheels.
Finally, in the testing phase, the detector was thoroughly tested based on two experiments: one that considers samples similar to those observed during the training phase, and another that considers samples representing the initial state of anomalies that were not trained.

keywords: Arduino; Edge Impulse; Features; Machine Learning; Railcar Anomaly; TinyML.

1 Introduction

Predictive maintenance has become a crucial element in asset management within the industrial sector. It is anticipated that inadequate maintenance strategies can reduce production capacity by 5% to 20% [1]. In contrast, the application of predictive maintenance techniques can increase equipment availability by 5% to 15% and reduce maintenance costs by 18% to 25% [2]. Currently, predictive maintenance is already implemented in the railway industry [3-4], where it is expected to save approximately €7.5 billion annually on a global scale. This benefit stems from the use of edge computing, where data is processed at or near the source of generation [5]. TinyML combines machine learning techniques tailored for edge computing, enabling the execution of simplified algorithms on low-power yet highly efficient systems.
Various platforms and libraries are available for implementation in TinyML, such as TensorFlow Lite, Edge Impulse and PyTorch, among others [6]. Specifically, Edge

Impulse, which emerged in 2019, simplifies the creation and deployment of ML models, following the cyclical process illustrated in Fig. 1a) [7].

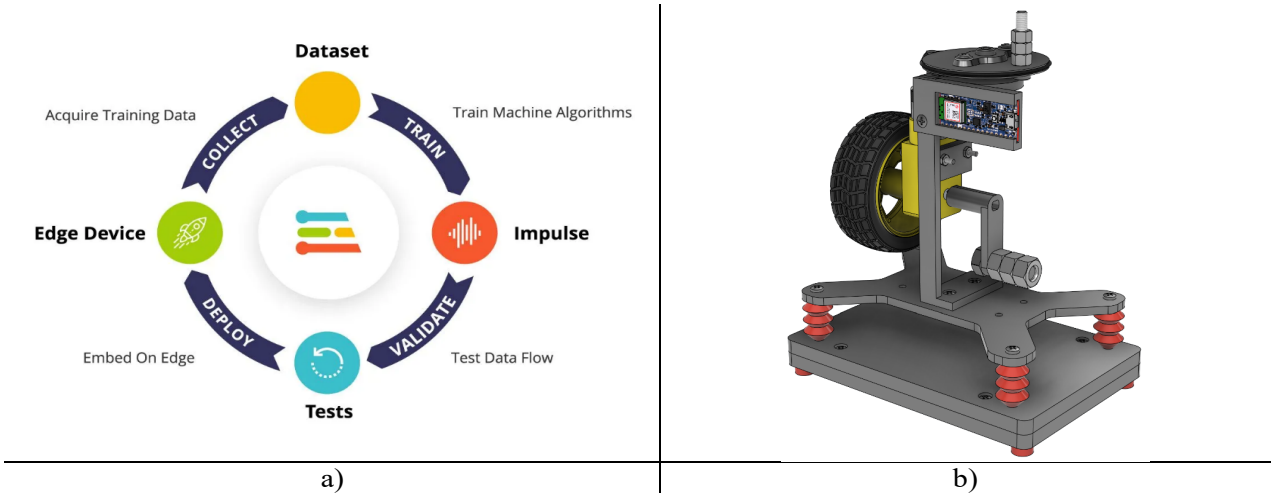

Fig.1 – Operational cycle of the Edge Impulse development platform in a) and the mechanical prototype developed in b).

Fig. 1b) presents the developed mechanical prototype, which simulates the wheelset of a railway wagon coupled to a DC motor. Various disturbances are induced on the prototype to simulate different anomalies. For classification purposes, four different classes are considered based on the labels: "ON", where the motor runs freely without anomalies; "Side_Unb", an anomaly caused by a lateral rod attached to the motor shaft with a bolt and three metal nuts, simulating breaks in the horizontal support axle of the wheelset; "Top_Unb", a pulley that creates imbalance on the vertical axis using too a bolt and three metal nuts, simulating wheel wear; and "Top&Side_Unb", which combines both previous anomalies simultaneously, as shown in Fig. 1b). The Fig. 1b) also shows the attachment of the Arduino Nano 33 BLE Sence Rev2 to the prototype structure, which includes an integrated accelerometer. The idea is to measure acceleration values along the main axes of the three-dimensional space, resulting from the propagation of vibrations through the mechanical prototype structure, which indicates the presence of movement. This movement may or may not be anomalous, but it is relevant for classification.

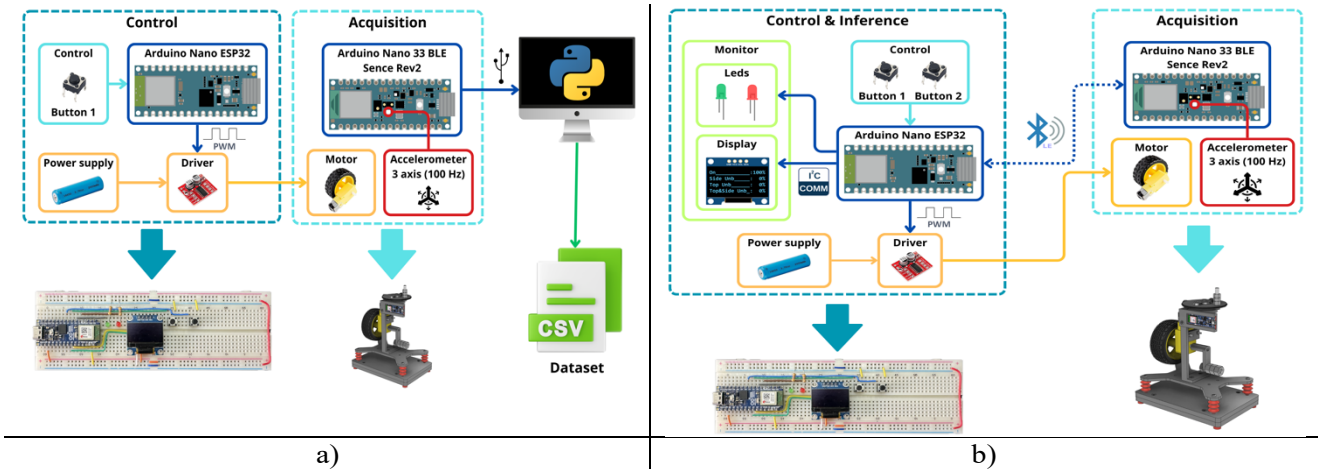

Fig. 2 – Hardware architecture dedicated to training dataset acquisition for input into the Edge Impulse platform in a) and hardware architecture dedicated to testing new samples using the Arduino in b).

The mechanical prototype was developed based on two different hardware architectures. The architecture presented in Fig. 2a) is dedicated to training dataset acquisition. For this purpose, the Arduino Nano ESP32 is used to control the motor speed via a PWM signal. To train the ML model, acceleration samples are acquired by the Arduino Nano 33 BLE Sence Rev2 at a frequency of 100 Hz and saved in an Excel file using a Python script. The

"ON" class is represented by 12 minutes of samples, which corresponds to 40% of the data, while each of the remaining three classes is represented by 6 minutes of samples, which corresponds to 60% of the data. The samples are then uploaded to the Edge Impulse platform, where it was observed that 1-second samples contain all the essential characteristics that describe each class. From 2-second sample subsets and a 1-second sliding window with 0.2-second shifts, six samples of 1-second each are obtained, allowing the dataset to be expanded. Therefore, each sample of 1-second contains the three-dimensional coordinates of 100 acceleration points.
The feedforward neural network associated with the ML model has two hidden layers containing 20 and 10 neurons, respectively, and is trained on 80% of the observed samples, while the remaining 20% are used for validation. It should be noted that the Edge Impulse platform automatically determines the features that best describe the samples and classifies them into their respective classes, using, among other possibilities, time-domain and frequency-domain statistics. The spectral density analysis, which represents the energy as a function of frequency for each axis, shows distinct absolute maximum values for each class. Thus, the 111 most relevant features indicated by the platform were used, determined in the frequency domain from the FFT, include, among others: "accZ Spectral Power 3.91 - 5.47 Hz", "accX RMS", "accZ Spectral Power 7.03 - 8.59 Hz", etc.
So, training is configured by setting the number of epochs and the learning rate.
After the validation phase, the ML model is exported from the Edge Impulse platform as a library dedicated to an edge computing device, in this case, the Arduino.
The architecture presented in Fig. 2b) represents the prototype in which the ML model is integrated into the Arduino software. For controlled simulation purposes, the samples to be classified are currently requested individually via a push button, with the probability values for each class displayed on the screen. Additionally, LEDs indicate the identification of the "ON" class by lighting up a green LED; otherwise, one of the three anomalous classes is indicated by lighting up a red LED.

2 Results and discussion

During the training phase of the neural network associated with the ML model, six empirical experiments were realized, using different numbers of epochs (1, 5, and 10) combined with different learning rates (0.0001 and 0.0005), and measuring both training and validation accuracies. The best accuracies obtained were 99.80% for training and 99.82% for validation, using a learning rate of 0.0005 over 10 epochs. The results presented indicate that the model is not overfitted, and thus can be considered well-configured.
The algorithm assumes that a sample belongs to a given class with a probability of 0.6; otherwise, it is considered to belong to an additional uncertainty class. Thus, the ML model testing phase is based on two experiments that classify 80 samples, 20 from each class, under the following conditions: 1) "Side_Unb" and "Top_Unb" are perturbed under conditions similar to those observed during the training phase, i.e., with a bolt and three nuts, Fig. 1b); 2) "Side_Unb" and "Top_Unb" are perturbed with a bolt and one nut, simulating the anomaly in its hypothetical initial state.
Fig. 3 presents the results based on the confusion matrix. For experiment 1), the accuracy is 98.75%, with only one sample misclassified, Fig. 3a). In experiment 2, the accuracy is 90.00%, with three misclassified samples and five cases of uncertainty, Fig. 3b).

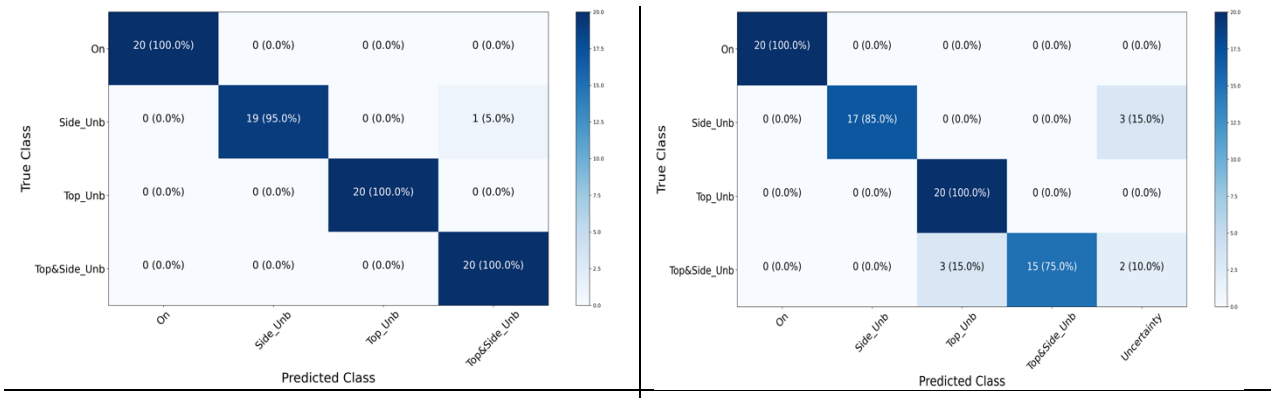

a) b)

Fig. 3 – Confusion matrix, considering that "Side_Unb" and "Top_Unb" are perturbed by the coupling of: three nuts and a bolt in a); one nut and a bolt in b).

3 Conclusions and Future work

The positive results achieved in this project enable Evoleo Technologies Lda to have the foundational hardware and software necessary for implementing an anomaly detector for railway wagons, with algorithmic inference presenting low response latency. It is also concluded, with particular interest to the company, that the Edge Impulse platform is a tool with great potential for implementing ML-based models, allowing for the export of libraries dedicated to a wide range of edge computing devices.

As future work, the following needs to be highlighted: collecting real data for model training; replacing accuracy metrics by sensitivity and specificity metrics; and implementing this model on other devices used by Evoleo Technologies Lda, including the Nordic Thingy:91 and Nordic Thingy:52.

References

[1] C. Coleman, S. Damofaran, and E. Deuel, *Predictive maintenance and the smart factory*. Deloitte, 2017.

[2] S. Bradbury, B. Carpizo, M. Gentzel, D. Horah, and J. Thibert, *Digitally enabled reliability: Beyond predictive maintenance*. McKinsey & Company, Oct. 2018.

[3] R. Prytz, *Machine learning methods for vehicle predictive maintenance using off-board and on-board data*, no. 9, Halmstad University, 2014.

[4] S. Stern, A. Behrendt, E. Eisenschmidt, S. Reimig, L. Schirmers, and I. Schwerdt, *The Rail Sector's Changing Maintenance Game*, 2017.

[5] M. Satyanarayanan, *The emergence of edge computing*. Computer (Long Beach Calif), vol. 50, no. 1, 2017.

[6] N. Schizas, A. Karras, C. Karras, S. Sioutas, *TinyML for Ultra-Low Power AI and Large Scale IoT Deployments: A Systematic Review*. Future Internet, vol. 14, no. 12, 2022.

[7] Edge Impulse, *The Leading edge AI platform*. [Online]. Available: https://edgeimpulse.com/. [Accessed: Mar. 20, 2024].

International Conference on Mathematical Analysis and Applications in Science and Engineering
ICMA^{2}SC'24
ISEP Porto-Portugal, June 20 - 22, 2024

Portuguese Service Electricity Continuity Indicators: Quality Service Evaluation

Marina A. Andrade[1⋆] **M. Filomena Teodoro**[2]

[1] ISCTE, University Institute of Lisbon, and
ISTAR - Information Sciences, Technologies and Architecture Research Center, Portugal
[2] CINAV, Center of Naval Research, and Portuguese Naval Academy, Military Universitary Institute, and CEMAT - Center for Computational and Stochastic Mathematics, IST, Portugal

[1⋆]marina.andrade@iscte-iul.pt

Abstract: Supply disturbances could be detrimental to some customers, such as in some industries, where these types of disruptions can represent a serious cost. Productivity and competitiveness in manufacturing and service industries increasingly depend on the quality of electricity supply and are also dependent on the good efficiency of continuity indicators. After initially monitoring its indicators in 2001, Portugal introduced a continuity of supply incentive regime in 2003. Since the introduction of the regime, indicators have consistently improved over the years, which pressures a constant improvement of the service related to client satisfaction. Recently, the frequency and duration of continuity service indicators were considered by the authors to study the quality of service in Portugal's mainland in the period of 2014 up to 2022 where a two–way analysis of variance (ANOVA) was performed aiming to evaluate the existence of differences between two factors: quality service regulation (QSR) zones and municipality code. The results pointed to the need to seek a more accurate analysis for each of the variables that represent continuity indicators. As a continuation of the previous work, and with such purpose, the authors transformed the already considered variables so they could get adequate validation during the residuals analysis. Suitable results were obtained and discussed. Service continuity, as measured by the frequency and duration of electricity supply interruptions, stands as a key determinant of service quality in electric utilities. Ensuring high service continuity not only upholds customer trust but also aligns with governmental regulations. The repercussions of frequent or prolonged outages are multifaceted, ranging from inconvenience to customers to diminished productivity in commercial and industrial sectors, and even potential public safety risks. The insights met from this study offer a fresh perspective on interpreting the dataset, suggesting both vertical and horizontal interpretations. Vertically, the QSR zone factor offers a broad nationwide view, while horizontally, the municipality code factor allows for nuanced exploration within specific QSR zones. Future research could explore a deeper understanding of the interplay between these factors and explore innovative strategies to further improve service continuity in the electric utility sector.

keywords: electricity continuity service; Interruption Frequency Index; Interruption Duration Index; two–way ANOVA.

MSC2020: 62-06; 62-08; 62-11.

Acknowledgments

The first author, this work was partially supported by Fundação para a Ciência e a Tecnologia, I.P. (FCT) [ISTAR Projects: UIDB/04466/2020 and UIDP/04466/2020]. The second was supported by Portuguese funds through the Center of Naval Research (CINAV), Naval Academy, Portugal and The Portuguese Foundation for Science and Technology (FCT), through the Center for Computational and Stochastic Mathematics (CEMAT), University of Lisbon, Portugal, project UIDB/Multi/04621/2020, DOI: (https://doi.org/10.54499/UIDB/04621/2020).

References

[1] Bewick, V., Cheek, L., Ball, J.: Statistics review 9: Analysis of variance. Critical Care **7**, 451-459 (2004)

[2] Montgomery, D. C.: Design and Analysis of Experiments. 5th ed. John Wiley & Sons Inc, New York (2001)

[3] Morgado, L. and Teodoro, M. F. and Perdocoulis, T.: Manual de Métodos Estatísticos em Ciências. Universidade de Trás os Montes e Alto Douro (UTAD, Vila Real). Série Didáctica Ciências Aplicadas, 400, ISBN 978-972-669-018-2, (2010)

[4] Regulação da Energia — Legislação Essencial. Entidade Reguladora dos Serviços Energéticos (2024)

[5] Seltman, H.J.: Experimental Design and Analysis. Available online: https://www.stat.cmu.edu/∼hseltman/309/Book/Book.pdf

[6] scheffé, H.A.: The Analysis of Variance. Willey, New York (1959)

[7] Andrade, M. A. and Teodoro, M. F.: Portuguese Service Electricity Continuity Indicators: municipality code and quality service zones evaluation – 2014 to 2022. In: Gervasi, O., et al. Computational Science and Its Applications – ICCSA 2024 Workshops. ICCSA 2024. Lecture Notes in Computer Science. To appear

[8] 7th Benchmarking Report on the Quality of Electricity and Gas Supply. Council of European Energy regulators (CEER) and the Energy Community Regulatory Board (ECRB) (2022)

International Conference on Mathematical Analysis and Applications in Science and Engineering
ICMA^{2}SC'24
ISEP Porto-Portugal, June 20 - 22, 2024

Energy Efficiency of Machine Learning Frameworks in Cloud Computing: TensorFlow vs. PyTorch

Sergio Aquino-Britez[1⋆] Pablo García-Sánchez[1] Andrés Ortiz[2] Diego Aquino-Britez[1]

[1] Department of Computer Engineering, Automation and Robotics, University of Granada, 18014, Granada, Spain
[2] Department of Communications Engineering, University of Málaga, 29004, Málaga, Spain

[1⋆]sergioaquino@correo.ugr.es

Abstract: Nowadays, joint implementations of Machine Learning (ML) algorithms and Cloud Computing (CC) are widespread due to their capacity to address and solve a wide range of problems. Similarly, energy efficiency and green computing is currently receiving special attention due to environmental sustainability with a main focus on the mitigation of greenhouse gas emissions. In this context, ML architectures are increasingly demanding more electrical power every day for their training process due to the growing complexity of these architectures. Several factors can affect energy consumption during the training process of ML models, such as the programming language, available hardware, and even the architecture itself. Therefore, it is important to identify which aspects can be optimized to achieve energy-efficient algorithms. In this research, a comparative analysis of energy consumption is conducted between two different frameworks (TensorFlow and PyTorch), the most widely used frameworks to implement ML algorithms. The comparison was done using Google Colab and training classical Convolutional Neural Networks (CNN) on this platform. In addition, the measurement of energy consumption has been performed using a Python library called Codecarbon. The preliminary results obtained in this work indicate lower energy consumption with the TensorFlow framework when training shallow CNN's.

keywords: energy-efficient; machine learning frameworks; green computing; Codecarbon.

MSC2020: 49-XX; 34-XX; 92-XX.

1 Introduction

In recent years, Cloud Computing (CC) and the energy efficiency of algorithms have gained significant importance. Cloud computing offers various services, including Platform as a Service (PaaS), which provides tools and services to facilitate the creation, testing, and deployment of applications, while keeping their underlying infrastructure hidden from the user. On the other hand, the development of energy-efficient algorithms is a trending topic of great interest aimed at reducing costs and promoting environmental sustainability. In this way, there is currently a vast amount of effort being made to achieve these objectives [1, 2].

In this context, the utilization of PaaS during the lifecycle of Machine Learning (ML) algorithms is widespread. In particular, Google Colab [3] (GC) is one of the most adopted PaaS platform

by the scientific community and AI practitioners. Currently, GC easily provides the necessary computational resources (CPU, GPU, RAM, and other devices.) and software libraries for ML algorithms, including two of the most widely used ML frameworks: TensorFlow and PyTorch.

Despite the advantages offered by the PaaS, precisely determining energy consumption during algorithm executions is not an easy task, mainly due to the infeasibility of accessing infrastructure details. This limitation is due to permission restrictions for accessing as administrators and executing the necessary commands to register energy consumption data [4].

In this work, the intention is to conduct an evaluation to determine the energy efficiency of ML frameworks (TensorFlow and PyTorch) using Google Colab Pro (GCP). Therefore, in order to perform the comparison between the different ML frameworks, a classical CNN known as AlexNet [6] has been implemented for each of them. In addition, the dataset used during the training phase corresponds to the MNIST [7].

Finally, CNN operations rely on GPUs for parallel execution, enhancing task efficiency. GPUs are responsible for 70% of energy consumption during the CNN training phase [4]. Therefore, the execution of experiments conducted on the platform includes the utilization of different NVIDIA GPUs available on GCP: Tesla T4 (T4), A100-SXM4-40GB (A100), Tesla V100-SXM2-16GB (V100), and L4. Additionally, energy consumption during CNN training was measured using the Codecarbon library [5] as it offers the highest precision according to Bouza et al. in [4].

2 Results and discussion

The experiments measured the energy consumption, execution time, and CO_2_eq emissions of AlexNet training across different frameworks. Energy consumption and CO_2_eq emissions were measured using CodeCarbon, based on the following definitions.

1. **Energy Consumption (kWh):**

$$\text{Energy Consumption (kWh)} = \text{Power (kW)} \times \text{Time (h)} \tag{1}$$

2. **CO_2 Emissions (CO_2_eq):**

$$CO_2\_eq = \text{Energy Consumption (kWh)} \times \text{Emission Factor (kg } CO_2\text{/kWh)} \tag{2}$$

The emission factor varies based on energy source. CodeCarbon estimates the emission factor based on geographical location and the energy mix of the corresponding electrical grid.

Table 1 provides detailed information on the conducted experiments and the achieved results.

Table 1: Summary by ML Framework and GPU

ML Framework	GPU	Exec.	Energy Consumed (kWh)		Duration (minutes)		Emissions (kg CO_2)	
			Avg.	Std. Dev.	Avg.	Std. Dev.	Avg.	Std. Dev.
PyTorch	A100	15	0.00587	0.00006	2.21803	0.01953	0.00267	0.00074
	T4	15	0.00652	0.00005	3.45019	0.02791	0.00253	0.00002
	V100	15	0.00693	0.00022	2.71463	0.07182	0.00168	0.00049
	L4	**15**	**0.00459**	**0.00002**	**2.28285**	**0.00764**	**0.00100**	**0.00001**
TensorFlow	A100	15	0.00241	0.00006	0.58171	0.02825	0.00118	0.00003
	T4	15	0.00440	0.00004	2.39710	0.00226	0.00061	0.00001
	V100	15	0.00390	0.00020	1.40491	0.01117	0.00147	0.00014
	L4	**15**	**0.00234**	**0.00001**	**1.13923**	**0.00231**	**0.00082**	**0.00001**

Note: The bold rows highlight the best performing GPU for each ML framework.

Additionally, Alexnet training was performed for 10 epochs on GCP using each available GPU. To ensure accuracy, 15 executions were conducted.

In Figure 1, the average energy consumption of CNN shows that TensorFlow generally consumes less energy than PyTorch across the same GPU models. Notably, the L4 GPU exhibits the lowest energy consumption within both frameworks, establishing it as the most energy-efficient option for operating CNN's. In addition, it has been determined that there are significant differences in the average energy consumption among different frameworks, which suggests that the framework influences energy consumption.

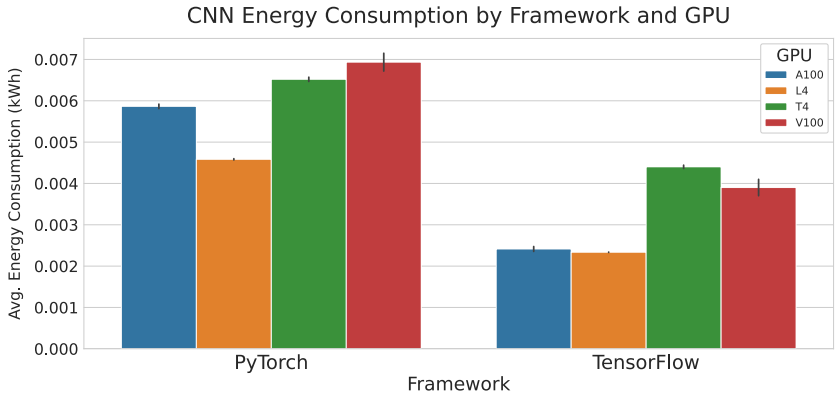

Figure 1: Comparative Analysis: Energy Consumption of CNN's in TensorFlow and PyTorch on GPU Models.

Figure 2 shows the average CO_2 emissions (kg) generated by training AlexNet using PyTorch and TensorFlow on A100, L4, T4, and V100 GPUs. PyTorch generally produces higher emissions than TensorFlow for the same GPUs, with the V100 GPU showing the highest emissions in Tensorflow. The L4 GPU has the lowest emissions in Pytorch. The error bars indicate greater variability in PyTorch emissions for the A100 and V100 GPUs.

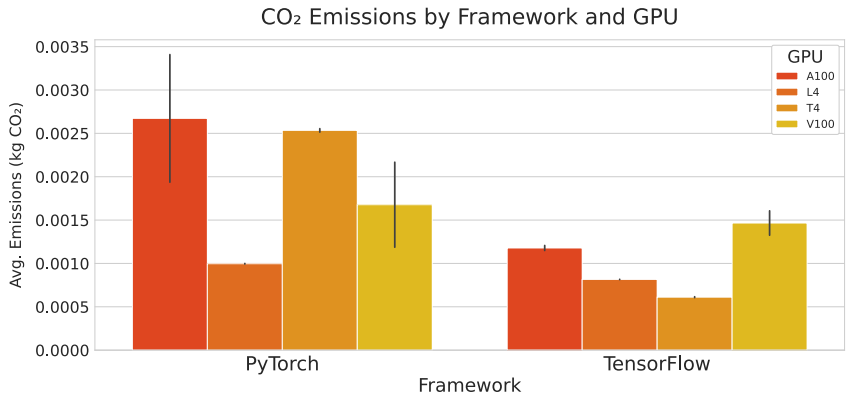

Figure 2: Comparative Analysis: CO_2 emissions of CNN's in TensorFlow and PyTorch on GPU Models.

3 Conclusions and Future work

Finally, the preliminary results indicate that TensorFlow is more energy-efficient and has lower CO_2 emissions than PyTorch when training shallow CNN's on Google Colab Pro. TensorFlow consistently consumed less energy, with the L4 GPU being the most efficient. Similar studies on

local platforms support these findings. These insights are essential for optimizing deep learning training to reduce environmental impact and operational costs.

Future work will involve evaluations of the energy consumption and efficiency of multiple frameworks and GPUs using various ML algorithms. Additional cloud platforms will be explored to better understand energy performance in different settings. This research will guide hardware and software choices in machine learning projects, considering both processing power and environmental impact.

Acknowledgments

This research is part of the PID2022-137461NB-C32, PID2023-147409NB-C21 and PID2020-115570GB-C22 projects, funded by the MICIU/AEI/10.13039/501100011033 and by ERDF/EU as well as TIC251-G-FEDER project, funded by ERDF/EU.

References

[1] Juan José Escobar, Francisco Rodríguez, Beatriz Prieto, Dragi Kimovski, Andrés Ortiz, Miguel Damas, A distributed and energy-efficient KNN for EEG classification with a dynamic money-saving policy in heterogeneous clusters, *Computing*, **105**(11) (2023), 2487–2510

[2] Antonio F. Díaz, Beatriz Prieto, Juan José Escobar, Thomas Lampert, Vampire: A smart energy meter for synchronous monitoring in a distributed computer system, *Journal of Parallel and Distributed Computing*, **184** (2024), 104794

[3] Ekaba Bisong, Google Colaboratory, in *Building Machine Learning and Deep Learning Models on Google Cloud Platform: A Comprehensive Guide for Beginners*, Apress, Berkeley, CA, 2019

[4] Lucía Bouza, Aurélie Bugeau, Loïc Lannelongue, How do we estimate carbon footprint when training deep learning models? A guide and review, *Environmental Research Communications*, **5**(11) (2023).

[5] Victor Schmidt, Kamal Goyal, Aditya Joshi, Boris Feld, Liam Conell, Nikolas Laskaris, Doug Blank, Jonathan Wilson, Sorelle Friedler, Sasha Luccioni, CodeCarbon: Estimate and Track Carbon Emissions from Machine Learning Computing, 2021, Available at: `https://github.com/mlco2/codecarbon`, Accessed: 2022-04-19.

[6] Alex Krizhevsky, Ilya Sutskever, Geoffrey E. Hinton, Imagenet classification with deep convolutional neural networks, *Advances in Neural Information Processing Systems*, **25** (2012).

[7] Li Deng, The MNIST database of handwritten digit images for machine learning research, *IEEE Signal Processing Magazine*, **29**(6) (2012), 141–142.

International Conference on Mathematical Analysis and Applications in Science and Engineering
ICMA^{2}SC'24
ISEP Porto-Portugal, June 20 - 22, 2024

A shear flow problem for compressible micropolar real gas

Ivan Dražić[1⋆] **Nelida Črnjarić**[1] **Valentino Marković**[1]

[1] University of Rijeka, Faculty of Engineering, Croatia

[1⋆]ivan.drazic@uniri.hr

Abstract: In this paper we analyse the micropolar, viscous, polytropic and thermally conductive real gas, assuming the generalised form of the pressure function in the sense that pressure is the affine function of temperature and the power function of mass density. The unsteady shear flow between two parallel, solid and thermally insulated horizontal plates is considered, with the upper plate moving irrotationally. We assume that in a Cartesian coordinate system (x, y, z) the solution of the corresponding problem depends only on the variable x. Using the above thermodynamic and constitutive assumptions, we derive the model on the basis of balance laws, first in the Eulerian and then in the Lagrangian description. We obtain a model consisting of eight partial differential equations of parabolic type with inhomogeneous boundary conditions. Using the Faedo-Galerkin method and homogenising the boundary conditions, we derive an approximate system which we use to obtain a numerical solution for the given problem.

keywords: micropolar fluid; real fluid; shear flow.

MSC2020: 35Q35; 76A05; 76N15.

1 Introduction

In this paper we analyze the micropolar, viscous, polytropic and thermally conductive real gas, assuming the generalized form of the pressure function in the sense that pressure is the affine function of temperature and the power function of mass density. The unsteady shear flow between two parallel, solid and thermally insulated horizontal plates is considered, with the upper plate moving irrotationally. Such a model was introduced in the case of an ideal compressible micropolar fluid [1]. For the problem of real fluids in the context of micropolarity, we refer to [2].

We assume that in a Cartesian coordinate system x, y and z, solutions of the corresponding problem depend only on x. Using the above thermodynamic and constitutive assumptions, we derive the model on the basis of equilibrium laws in the Lagrangian description as follows:

$$\partial_t \rho + L^{-1}\rho^2 \partial_x u = 0, \tag{1}$$

$$\partial_t u = -L^{-1}R\partial_x(\rho^p \theta) + L^{-2}(\lambda + 2\mu)\partial_x(\rho\, \partial_x u), \tag{2}$$

$$\partial_t \mathbf{u} = L^{-2}(\mu + \mu_r)\partial_x(\rho\, \partial_x \mathbf{u}) + 2L^{-1}\mu_r \nabla \times \mathbf{w}, \tag{3}$$

$$j_I \partial_t w = L^{-2}(c_0 + 2c_d)\partial_x(\rho\, \partial_x w) - 4\mu_r \frac{w}{\rho}, \tag{4}$$

$$j_I \partial_t \mathbf{w} = L^{-2}(c_d + c_a)\partial_x(\rho\, \partial_x \mathbf{w}) - \frac{4\mu_r}{\rho}\mathbf{w} + 2L^{-1}\mu_r \nabla \times \mathbf{u}, \tag{5}$$

$$\begin{aligned} c_v \partial_t \theta = L^{-2} k_\theta \partial_x(\rho \partial_x \theta) - L^{-1} R \rho^p \theta \partial_x u + L^{-2}(\lambda + 2\mu)\rho(\partial_x u)^2 \\ + L^{-2}(\mu + \mu_r)\rho|\partial_x \mathbf{u}|^2 + 4\mu_r \frac{w^2}{\rho} + 4\mu_r \frac{|\mathbf{w}|^2}{\rho} - 4L^{-1}\mu_r(\nabla \times \mathbf{u}) \cdot \mathbf{w} + \\ L^{-2}(c_0 + 2c_d)\rho(\partial_x w)^2 + L^{-2}(c_d + c_a)\rho|\partial_x \mathbf{w}|^2, \end{aligned} \tag{6}$$

for $(x,t) \in]0,1[\times]0,T[$,

$$\rho(x,0) = \rho_0(x), \quad \theta(x,0) = \theta_0(x), \tag{7}$$

$$u(x,0) = u_0(x), \quad \mathbf{u}(x,0) = (0, v_{20}, v_{30})(x), \tag{8}$$

$$w(x,0) = w_0(x), \quad \mathbf{w}(x,0) = (0, \omega_{20}, \omega_{30})(x), \tag{9}$$

for $x \in [0,1]$,

$$u(0,t) = u(1,t) = 0, \tag{10}$$

$$\mathbf{u}(0,t) = \mathbf{0}, \quad \mathbf{u}(1,t) = \mathbf{a}(t) = (0, a_1(t), a_2(t)), \tag{11}$$

$$w(0,t) = w(1,t) = 0, \tag{12}$$

$$\mathbf{w}(0,t) = \mathbf{w}(1,t) = \mathbf{0}, \tag{13}$$

$$\partial_x \theta(0,t) = \partial_x \theta(1,t) = 0, \tag{14}$$

for $t \in [0,T]$, where we denote

$$\mathbf{u} = (0, v_2, v_3), \quad \mathbf{w} = (0, \omega_2, \omega_3). \tag{15}$$

Here ρ, (u, v_2, v_3), $(\omega, \omega_2, \omega_3)$, and θ are respectively mass density, velocity, microrotation velocity, and absolute temperature. The positive constant j_I is microinertia density, λ and μ are coefficients of viscosity, and μ_r, c_0, c_d and c_a are coefficients of microviscosity. By the constant k_θ ($k_\theta \geq 0$) we denote the heat conduction coefficient. The dimensionless constant $p \geq 1$ is called pressure exponent, the positive constant R is the generalized gas constant and the positive constant c_v denotes the specific heat at a constant volume.

2 Results and discussion

Using the Faedo-Galerkin method and homogenizing the boundary conditions, we derive an approximate system that we use to obtain a numerical solution for the given problem and analyze few numerical examples.

We consider first the numerical solutions to the problem defined with the following initial functions:

$$\rho_0(x) = 1, \tag{16}$$

$$u_0(x) = \sin(\pi x), \quad \mathbf{u}_0(x) = \sin(\pi x)(0,1,1), \tag{17}$$

$$w_0(x) = \sin(2\pi x), \quad \mathbf{w}_0(x) = \sin(2\pi x)(0,1,1), \tag{18}$$

$$\theta_0(x) = 2 + \cos(\pi x). \tag{19}$$

Non-homogeneous boundary condition (11) are defined by the function

$$\mathbf{a}(t) = 0.5 \sin(\pi t)(0,1,1). \tag{20}$$

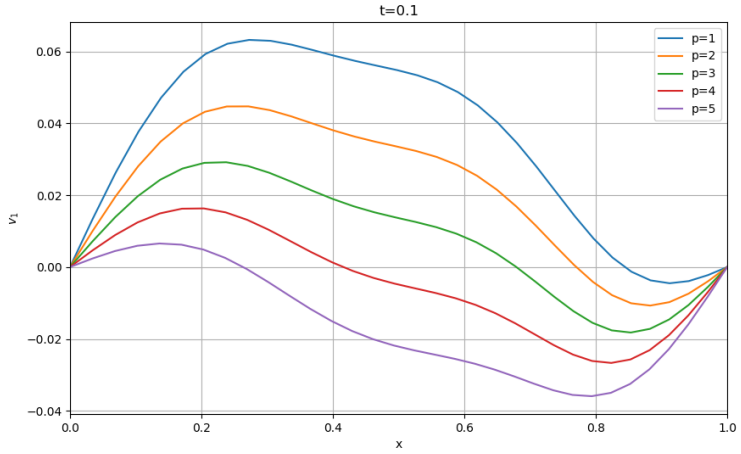

Figure 1: Numerical approximations at $t = 0.1$ for velocity

Other parameters of the system are set to: $L = 1$, $c_d = c_0 = c_v = 1$ $R = 1$ $j_I = 1$, $c_a = 0$, $\lambda = -2$, $\mu_r = 1$, $\mu = 3$, $k_\theta = 0.024$.

The main goal of the numerical experiment is to investigate the influence of the parameter p on the behavior of the solution. For example, the influence of that parameter on the velocity u is shown in the following figure.

3 Conclusions and Future work

In this work we have constructed an approximate system of ordinary differential equations which we have used to obtained a numerical solution for the described model. Using this approximate system, we conducted a series of numerical experiments in which we showed that the introduction of the pressure exponent has a significant impact on the corresponding solution. The obtained approximate system will also be the basis for further mathematical analysis of the model, in particular for the proof of local existence.

Acknowledgments

All authors of this work are supported by the University of Rijeka, Croatia under the project Mathematical modeling of micropolar fluid and numerical spectral analysis using data-driven algorithms (uniri-iskusni-prirod-23-184).

References

[1] Ivan Dražić, Črnjarić Nelida, Simčić Loredana, A shear flow problem for compressible viscous micropolar fluid: derivation of the model and numerical solution, Mathematics and Computers in Simulation 162 (2019), 249-267.

[2] Angela Bašić-Šiško, Ivan Dražić, Simčić Loredana, One-dimensional model and numerical solution to the viscous and heat-conducting micropolar real gas flow with homogeneous boundary conditions, Mathematics and Computers in Simulation, 195 (2022), 71-81

International Conference on Mathematical Analysis and Applications in Science and Engineering
ICMA^{2}SC'24
ISEP Porto-Portugal, June 20 - 22, 2024

Insights into the European Innovation Scoreboard: Intelligent Features Selection with R

Aldina Correia[1⋆] **Diogo Ribeiro**[2] **M. Fimonena Teodoro**[3,4]

[1] CIICESI, ESTG, Instituto Politécnico do Porto, Portugal
[2] MySense, United Kingdom
[3] CINAV, Center of Naval Research, Naval Academy,
Military Universitary Institute, Portugal
[4] CEMAT, Center for Computational and Stochastic Mathematics,
Instituto Superior Técnico, Lisboa University, Portugal

[1⋆]aic@estg.ipp.pt, [2]diogo.ribeiro@mysense.ai, [3,4]maria.teodoro@tecnico.ulisboa.pt

Abstract: This study examines the robust correlation structure between European Innovation Scoreboard (EIS) dimensions over time. The European Innovation Scoreboard (EIS) provides a comparative assessment of the Research and Innovation performance of EU Member States, other European countries, and regional neighbours. It helps countries assess the relative strengths and weaknesses of their national innovation systems and identify challenges that they need to address [1]. The EIS aims to measure the performance of countries' national innovation systems and includes several indicators that capture different dimensions of innovation, such as research and development, business activities and economic effects. Our work investigates the existence of latent variables, which are not directly observed, but rather inferred from observed variables, with the aim of discovering patterns and relationships underlying the data. The data used comprises the EIS dimensions over the years. The focus is to identify correlations between them, using an intelligent methodology for selecting variables/dimensions. This methodology involves statistical and machine learning techniques to analyse EIS data and is based on principal component analysis and factor analysis, and has been implemented in R software.

keywords: Intelligent features selection; EIS; Innovation

MSC2020: 62Hxx; 62H25; 62Pxx.

Acknowledgments

This work has been supported by national funds through FCT - Fundação para a Ciência e Tecnologia through project UIDB/04728/2020.

References

[1] H. Hollanders. A critical assessment of the european innovation scoreboard. in handbook of innovation indicators and measurement. Technical report, Edward Elgar Publishing, 2023.

International Conference on Mathematical Analysis and Applications in Science and Engineering
ICMA^{2}SC'24
ISEP Porto-Portugal, June 20 - 22, 2024

Saving public goods

Alberto Pinto[1,2⋆] **Elvio Accinelli**[3] **Atefeh Afsar**[2] **Filipe Martins**[2]
José Martins[1,4] **Bruno M. P. M. Oliveira**[1,2] **Jorge Oviedo**[5]
Luis Quintas[5]

[1] LIAAD-INESC TEC, Portugal
[2] University of Porto, Portugal
[3] Universidad Autónoma de San Luis Potosí México
[4] School of Technology and Management, Polytechnic of Leiria, Portugal
[5] Universidad Nacional de San Luis, Argentina

[1⋆]aapinto@fc.up.pt

Abstract: Special Session 12 - Dynamical Systems, Games and Applications
Baliga and Maskin introduced a model of contributions for the provisions of public goods such as contributions for the reduction of air pollution. For an extended version of their model, we consider the formation of stable coalitions which are absorbing states of a bargaining Markov chain, where agents join/leave coalitions according to their cooperation/free-riding incentives. Following Baliga and Maskin, we consider heterogeneous agents with quasi-linear utilities of the form $u_j(r_j; r) = \theta_j r^\alpha - r_j$, where r is the aggregate contribution ($r = 1/2$ in Baliga and Maskin) and the exponent α is the elasticity of the gross utility. We show that there is a stable high coalition consisting of the set of agents most preferring/valuing the public good. The increase of the parameter α increases the size of the stable high coalition that changes from a single member (called the competitive coalition as appears in Baliga and Maskin's paper) to the grand coalition involving all agents. However, the utility of members of the stable coalition can be very small when compared to the utility of the free-riders, rendering the formation of stable coalitions difficult. We show that the coalition folk theorem holds, meaning that member heterogeneity will tend to favor the formation of smaller stable coalitions. We show that the formation of stable coalitions is subject to the paradox of cooperation, since even when the stable coalitions is large and free-riders have not very low preferences for the public good, the utility of the stable coalition may still be low when compared to the full cooperation scenario of the grand coalition. However, the paradox does not hold when the free-riders have a very low preference for the public good, which also facilitates the spontaneous formation of stable coalitions, or when there are no free-riders and the grand coalition is stable.

keywords: public and common goods; free-riding; coalitions; Barrett's paradox.

MSC2020: 91A12; 91A40.

International Conference on Mathematical Analysis and Applications in Science and Engineering
ICMA^{2}SC'24
ISEP Porto-Portugal, June 20 - 22, 2024

Strategic Integration of Risk Analysis in Robotics: exploring synergies

Teresa A. Oliveira[1,2⋆] **M. Filomena Teodoro**[3,4]

[1] Departamento C&T, Universidade Aberta, Lisboa, Portugal
[2] CEAUL, Universidade Lisboa, Lisboa, Portugal
[3] CEMAT, Center for Computational and Stochastic Mathematics, Instituto Superior Técnico, 1048-001 Lisboa, Portugal
[4] CINAV, Center of Naval Research, Naval Academy, Instituto Universitário Militar, Portuguese Navy, 2810-001 Almada, Portugal

⋆Teresa.Oliveira@uab.pt

Abstract: Special session 6 − Computational Mathematics, Computational Statistics and Applications.

Risk analysis and robotics have become closely intertwined fields that are reshaping the ways in which organizations assess and manage potential hazards. The intersection of both areas promote futuristic approaches in what concerns to risk mitigation and contingency planning with strong impact in diverse areas such as business, industry, medicine and social sciences.
By leveraging AI-driven models and predictive analytics, robotics technologies enable organizations to enhance their risk assessment capabilities. The advent of automated risk management systems (ARMS) and robotic process automation (RPA) has streamlined risk analysis processes and, in other hand empowered organizations to respond swiftly and to make data-driven decisions with higher confidence. Nonetheless, the convergence of risk analysis and robotics poses complex legal and compliance challenges that demand careful attention and proactive measures to act effectively. Looking ahead, the horizon for risk analysis and robotics holds significant opportunities for innovation and growth, paving the way for enhanced risk management practices and improved organizational resilience.
This article delves into the intricate synergy between risk analysis and robotics, showcasing the advances, the eventual hurdles, and future potential of this transformative partnership.

keywords: risk analysis; robotics; integration; AI.

MSC2020:

International Conference on Mathematical Analysis and Applications in Science and Engineering ICMA²SC'24

ISEP **Porto-Portugal, June 20 - 22, 2024**

Exploratory data analysis, regression analysis, and supervised machine learning for predicting Infant Mortality in Pakistan

Mansoor Shaukat Khan[1] **Hijab Fatima**[1] **Shumaila Javeed**[1*] **Dumitru Baleanu**[2]

[1] COMSATS University Islamabad, Pakistan

[2] Lebanese American University, Beruit, Lebnan

[2*] Shumaila_javeed@comsats.edu.pk

Abstract: In this research paper, we embark on a comprehensive examination of infant mortality in Pakistan using data from the 2017-18 Pakistan Demographic Health Survey. Our study encompasses three primary components: Exploratory Data Analysis, Regression Analysis, and the application of Supervised Machine Learning Techniques. We harness various demographic and health-related data to construct predictive models for infant mortality, emphasizing a well-rounded approach to the analysis. Our findings underscore the superior performance of machine learning algorithms, including Random Forest, Support Vector Machines, Logistic Regression Models, and Decision Trees, in accurately predicting infant mortality rates when contrasted with conventional statistical methods. The results not only provide valuable insights for policymakers in Pakistan, aiding in the development of more effective interventions but also highlight the pivotal role of technology in improving health outcomes. This research advocates for further exploration in this critical domain, fostering advancements in public health and infant mortality reduction in Pakistan.

keywords: Artificial Intelligence; Regression; Epidemiology

MSC2020: 68T20; 62J05; 92D30.

References

[1] Ritu Agarwal, Michelle Dugas, Guodong Gao, PK Kannan. Emerging technologies and analytics for a new era of value-centered marketing in healthcare. Journal of the Academy of Marketing Science, 48 (2020), 9-23.

[2] Sohail Agha, The determinants of infant mortality in Pakistan, Social science & medicine, 51(2000),199-208.

[3] Fikrewold H Bitew, Samuel H Nyarko, Lloyd Potter, Corey S Sparks. Machine learning approach for predicting under-five mortality determinants in Ethiopia: evidence from the 2016 Ethiopian demographic and health survey, Genus, 76(2020), 1-16.

[4] William M Callaghan, Marian F MacDorman, Sonja A Rasmussen, Cheng Qin, and Eve M Lackritz. The contribution of preterm birth to infant mortality rates in the United States, Pediatrics, 118(2006),1566–1573.

[5] Paulo JG Lisboa, A review of evidence of health benefit from artificial neural networks in medical intervention. Neural networks, 15(2002), 11-39.

International Conference on Mathematical Analysis and Applications in Science and Engineering
ICMA^{2}SC'24
ISEP Porto-Portugal, June 20 - 22, 2024

Operational Efficiency of Larzac Engines using Statistical Methods: An Approach to Risk Analysis and Risk Management

M. Filomena Teodoro[1,2⋆] **Teresa A. Oliveira**[3,4]

[1] CEMAT, Center for Computational and Stochastic Mathematics, Instituto Superior Técnico, 1048-001 Lisboa, Portugal
[2] CINAV, Center of Naval Research, Naval Academy, Instituto Universitário Militar, Portuguese Navy, 2810-001 Almada, Portugal
[3] Departamento C&T, Universidade Aberta, Lisboa, Portugal
[4] CEAUL, Universidade Lisboa, Lisboa, Portugal

⋆mteodoro64@gmail.com

Abstract: Special session 6 − Computational Mathematics, Computational Statistics and Applications.

This work proposes an integrated approach to optimize the operational efficiency of Larzac engines. Statistical methods will be used to explore and analyze data, and also to identify potential hazards, allowing for the development of tailored strategies to mitigate risks and enhance the performance of the engines, by identifying and rectifying deviations in performance. This research was initiated in response to reports of diminished propulsive output in certain Larzac engines that resulted in operational immobilization. Thus, based on real data obtained from a test bench, the current study centers on gathering and analyzing statistical data related to engine operations and configuration in order to discern recurring patterns. While the available data set was limited in scope, several potential root causes of the issue were identified. The findings presented herein have also contributed towards the development of a diagnostic framework. Scrutinizing the measured parameters and comparing them against established operational norms and trends, the data analysis has facilitated the identification of certain anomalies, thereby enabling to set recommendations on proactive maintenance measures for their prevention. The study also provided valuable insights to the field of engine optimization and risk management.

keywords: Larzac engine; risk; operational efficiency.

MSC2020:

International Conference on Mathematical Analysis and Applications in Science and Engineering
ICMA^{2}SC'24
ISEP Porto-Portugal, June 20 - 22, 2024

Generalized hypergeometric representation of 2-orthogonal polynomial eigenfunctions of a third-order differential operator

Teresa A. Mesquita[1⋆]

[1] Escola Superior de Tecnologia e Gestão, Instituto Politécnico de Viana do Castelo, Portugal, & Centro de Matemática da Universidade do Porto, Portugal

[1⋆] teresa.mesquita@fc.up.pt

Abstract: Special Session # 11: Orthogonal Polynomials, Special Functions and their Applications.
In the recent works [7, 8], the author presents the polynomial functions that are eigenfunctions of a given differential operator defined by parametrized polynomial coefficients. Assuming that such polynomial sets are 2-orthogonal, the corresponding recurrence coefficients are described in terms of each differential operator, and also, the obtained polynomial sequences are proved to be Hahn-classical.
We now analyse the generalized hypergeometric representation for these polynomial sequences, reviewing relevant references on the subject of d-orthogonality in connection with the generalized hypergeometric polynomials. Some illustrative examples are given.

keywords: d-orthogonal polynomials; differential operators; polynomial eigenfunctions, generalized hypergeometric polynomials.

MSC2020: 42C05 ; 33C45 ; 68W30 ; 33-04 ; 34L10 .

1 Introduction

Bochner's characterization of the classical orthogonal polynomial sequences [1], establishes those families as polynomial eigenfunctions of a second-order differential equation that can be written in the form [2]:

$$a_2(x)y'' + a_1(x)y' + a_0(x)y + \lambda y = 0\,,$$

where $a_2(x)$, $a_1(x)$, $a_0(x)$ are polynomials of degrees at most 2,1, and 0, respectively, and $\lambda \neq 0$.

The analogous problem with respect to the 2-orthogonal polynomial sequences was dealt in [7, 8] with the help of technical relations, like Proposition 1 below, fulfilled by the general differential operator J defined on the vector space of polynomials with coefficients in $\mathbb{C}$, as in (1) where D is the standard derivative operator [4, 6]:

$$J = \sum_{n\geq 0} \frac{a_n(x)}{n!} D^n, \quad \deg a_n \leq n, \quad n \geq 0\,, \tag{1}$$

with

$$a_\nu(x) = \sum_{i=0}^{\nu} a_i^{[\nu]} x^i = a_0^{[\nu]} + a_1^{[\nu]} x + a_2^{[\nu]} x^2 + \cdots + a_\nu^{[\nu]} x^n\,.$$

Proposition 1 *[7] Given an operator J defined by (1), and taking into account the definition of the operator $J^{(m)}$, $m \geq 0$:*

$$J^{(m)} = \sum_{n\geq 0} \frac{a_{n+m}(x)}{n!} D^n \,, \tag{2}$$

the following identities hold.

$$J^{(i)}\left(xp(x)\right) = J^{(i+1)}\left(p(x)\right) + xJ^{(i)}\left(p(x)\right) \,, \;\; i = 0, 1, 2, \ldots . \tag{3}$$

The d-orthogonal polynomial sets are known to fulfil a recurrence relation of order $d+1$ [5], and therefore, a (monic) 2-orthogonal polynomial sequence is uniquely defined by three numerical sequences $\{\beta_n\}_{n\geq 0}$, $\{\alpha_{n+1}\}_{n\geq 0}$ and $\{\gamma_{n+1}\}_{n\geq 0}$, called the recurrence coefficients, so that:

$$P_{n+3}(x) = (x-\beta_{n+2})P_{n+2}(x) - \alpha_{n+2}P_{n+1}(x) - \gamma_{n+1}P_n(x), \tag{4}$$

$$P_0(x) = 1, \;\; P_1(x) = x - \beta_0, \;\; P_2(x) = (x-\beta_1)P_1(x) - \alpha_1 \,, \;\; \gamma_{n+1} \neq 0 \,, \;\; n \geq 0. \tag{5}$$

The content of Proposition 1 allowed the development of a symbolic approach to the problem of finding the (normalized) 2-orthogonal polynomial sequences $\{P_n(x)\}_{n\geq 0}$ that fulfil the following differential identity

$$\left(a_0(x)I + a_1(x)D + \frac{a_2(x)}{2}D^2 + \frac{a_3(x)}{3!}D^3\right)\left(P_n(x)\right) = \lambda_n^{[0]}P_n(x) \,, \quad \lambda_n^{[0]} \neq 0 \,, \tag{6}$$

$$\text{with } \lambda_n^{[0]} = a_0^{[0]} + \binom{n}{1}a_1^{[1]} + \binom{n}{2}a_2^{[2]} + \binom{n}{3}a_3^{[3]} \,, \; n \geq 0 \,, \text{ and } \deg\left(a_\nu(x)\right) \leq \nu \,.$$

As an example of application of this method, we recall next a 2-orthogonal polynomial set constituted by polynomial eigenfunctions of a third order operator J.

Theorem 2 *[7, 8] Let us consider a (monic) 2-orthogonal polynomial sequence $\{P_n\}_{n\geq 0}$ fulfilling*

$$J\left(P_n(x)\right) = \lambda_n^{[0]}P_n(x)$$

where J is defined by (6), with a[illegible]

Then the polynomial $a_3(x)$ has [illegible]e coefficients of the sequence $\{P_n\}_{n\geq 0}$ are the following

$$\beta_n = -\frac{a_2^{[3]}}{2a_1^{[1]}}(n-1)n - \tag{7}$$

$$\alpha_n = \frac{n(n-1)}{12(a_1^{[1]})^2}\left(-3a_1^{[1]}a_1^{[3]} \cdot \qquad\qquad \right)\Big) \,, \; n \geq 1 \,, \tag{8}$$

$$\gamma_n = -\frac{1}{216(a_1^{[1]})^3}n(n+1)\left(36(a_1^{[1]})^2a_0^{[2]} - 6a_1^{[1]}\left(6a_0^{[1]}a_1^{[2]} + (n-1)^2a_1^{[3]}a_2^{[3]}\right)\right. \tag{9}$$

$$\left. + a_2^{[3]}\left(6a_0^{[1]} + (n-1)na_2^{[3]}\right)\left(6a_0^{[1]} + (n-1)(n-2)a_2^{[3]}\right)\right) \,, \; n \geq 1 \,,$$

provided that $\gamma_n \neq 0, \;\; n \geq 1$.

Recalling the Pochhammer symbol or shifted factorial:

$$(a)_0 = 1 \,, \;\; (a)_n = a(a+1)(a+2)\cdots(a+n-1) \,, \;\; n \geq 1 \,,$$

and assuming that none of the parameters $b_1, b_2, \ldots, b_q$ is a nonpositive integer, the generalized hypergeometric function is defined by [9]

$$ {}_pF_q\left(\begin{matrix} a_1, \ldots, a_p \\ b_1, \ldots, b_q \end{matrix}; z\right) = \sum_{k=0}^{\infty} \frac{(a_1)_k \cdots (a_p)_k}{(b_1)_k \cdots (b_q)_k} \frac{z^k}{k!}. $$

Considering $D = \frac{\mathrm{d}}{\mathrm{d}x}$ and $\vartheta = x\frac{\mathrm{d}}{\mathrm{d}x}$, the function

$$ w = {}_pF_q\left(\begin{matrix} a_1, \ldots, a_p \\ b_1, \ldots, b_q \end{matrix}; x\right) = {}_pF_q\left(a_1, \ldots, a_p\,;\, b_1, \ldots, b_q\,; x\right) $$

fulfils the generalized hypergeometric differential equation

$$ \left(\vartheta(\vartheta + b_1 - 1)\cdots(\vartheta + b_q - 1) - x(\vartheta + a_1)\cdots(\vartheta + a_p)\right) w = 0. $$

In the work [3], we may follow a clear description of d-orthogonal polynomials that may be expressed using the generalized hypergeometric function.

In the following, we present examples of such representations regarding the polynomial sets obtained in [7, 8].

2 Results and discussion

From the work of Y. Ben Cheikh and K. Douak [3] and references therein, we know that the sequence $y_n(x) = l_n^{(\sigma_1,\sigma_2)}(x) = {}_1F_2\left(-n\,;\sigma_1+1, \sigma_2+1\,;\,x\right)$, $n \geq 0$, is a 2-orthogonal polynomial sequence that fulfils the generalized hypergeometric differential equation

$$ \left(x\left(\vartheta - n\right) - \vartheta\left(\vartheta + \sigma_1\right)\left(\vartheta + \sigma_2\right)\right) y_n(x) = 0\,, $$

where $\vartheta = xD$. We can also define the corresponding monic polynomial sequence

$$ \tilde{y}_n(x) = \tilde{l}_n^{(\sigma_1,\sigma_2)}(x) = (-1)^n \left(\sigma_1 + 1\right)_n \left(\sigma_2 + 1\right)_n \; l_n^{(\sigma_1,\sigma_2)}(x)\,,\; n \geq 0\,, $$

indicating that it fulfils

$$ \Big(\left(x - 1 - \sigma_1 - \sigma_2 - \sigma_1\sigma_2\right) D - \left(3 + \sigma_1 + \sigma_2\right) xD^2 - x^2D^3\Big)\tilde{y}_n(x) = n\tilde{y}_n(x)\;,\; n \geq 0\,. $$

Example 1 *Let us consider an operator J as in* (6) *with the following polynomial coefficients:*

$$ a_1(x) = x + 2 + \sigma_1(3 + \sigma_1)\;,\; a_2(x) = 0\;,\; a_3(x) = -6x^2\;\;. $$

Then, the corresponding (monic) 2-orthogonal polynomial eigenfunctions $\{P_n(x)\}_{n\geq 0}$ constitute a sequence defined by the recurrence coefficients [7]:

$$ \beta_n = -2 - 3n + 3n^2 - 3\sigma_1 - (\sigma_1)^2\,,\; n \geq 0\,, \tag{10} $$

$$ \alpha_n = 3n(n-1)(n - 3 - \sigma_1)(n + \sigma_1)\,,\; n \geq 1\,, \tag{11} $$

$$ \gamma_n = n(n+1)(n - 3 - \sigma_1)(n - 2 - \sigma_1)(n + \sigma_1)(n + 1 + \sigma_1)\,,\; n \geq 1. \tag{12} $$

Furthermore, $P_n(x) = (-1)^n \left(\sigma_1 + 1\right)_n \left(-\sigma_1 - 2\right)_n \; {}_1F_2\left(-n\,;\sigma_1+1, -\sigma_1-2\,;\,x\right)$, $n \geq 0$, where $\sigma_1 + 1$ and $-\sigma_1 - 2$ are not nonpositive integers.

Example 2 *Let us consider an operator J as in* (6) *with the following polynomial coefficients:*

$$a_1(x) = x - 6\ ,\ a_2(x) = -12x\ ,\ a_3(x) = -6x^2\ \ .$$

Then, the corresponding (monic) 2-orthogonal polynomial eigenfunctions $\{P_n(x)\}_{n\geq 0}$ constitute a sequence defined by the recurrence coefficients [8]:

$$\beta_n = 3(n+1)(n+2)\,,\ n \geq 0\,, \tag{13}$$

$$\alpha_n = 3n(n+1)^2(n+2)\,,\ n \geq 1\,, \tag{14}$$

$$\gamma_n = n(n+1)^2(n+2)^2(n+3)\,,\ n \geq 1. \tag{15}$$

Furthermore, $P_n(x) = (-1)^n\,(\sigma_1+1)_n\,(\sigma_2+1)_n\ {}_1F_2\,(-n\,;\sigma_1+1,\sigma_2+1\,;\,x)$, $n \geq 0$, with $\sigma_1 = 1$ and $\sigma_2 = 2$.

The use of an affine transformation will allow the modification of some parameters of J. Thus considering the corresponding affine transformations of ${}_1F_2\,(-n\,;\sigma_1+1,\sigma_2+1\,;\,x)$, we can develop further generalized hypergeometric representations of sequences of 2-orthogonal polynomial eigenfunctions.

Acknowledgments

The author T. A. Mesquita was partially supported by CMUP, which is financed by national funds through FCT-Fundação para a Ciência e a Tecnologia, I.P., under the project with reference UIDB/00144/2020.

References

[1] S. Bochner, *Über Sturm-Liouvillesche Polynomsysteme*, Math. Zeit. vol. 29 (1929), pp. 730-736.

[2] T. S. Chihara, *An Introduction to Orthogonal Polynomials*, Gordon and Breach, New York, 1978.

[3] Y. Ben Cheikh, K. Douak, *A generalized hypergeometric d-orthogonal polynomial set*, C. R. Acad. Sci. Paris, Sér. I, Math. 331, No.5, (2000) 349-354.

[4] P. Maroni, *New results about orthogonality preserving maps*, J. Korean Math. Soc. 42, No.2 (2005), 243-254.

[5] P. Maroni, *L'orthogonalité et les récurrences de polynômes d'ordre supérieur à deux* , Ann. Fac. Sci. Toulouse, Math. (5) 10, No. 1 (1989), 105-139.

[6] T. A. Mesquita and P. Maroni , *Around operators not increasing the degree of polynomials*, Integral Transforms Spec. Funct. 30, No.5 (2019), 383-399.

[7] T. A. Mesquita, *Symbolic Approach to 2-Orthogonal Polynomial Solutions of a Third Order Differential Equation*, Math. Comput. Sci. 16 (2022), No.1, Paper No.6, 21 pp.

[8] T. A. Mesquita, *On a general family of 2-orthogonal polynomial eigenfunctions of a third order differential equation via symbolic computation*, in press.

[9] NIST Digital Library of Mathematical Functions. https://dlmf.nist.gov/, Release 1.2.0 of 2024-03-15. F. W. J. Olver, A. B. Olde Daalhuis, D. W. Lozier, B. I. Schneider, R. F. Boisvert, C. W. Clark, B. R. Miller, B. V. Saunders, H. S. Cohl, and M. A. McClain, eds.

International Conference on Mathematical Analysis and Applications in Science and Engineering
ICMA^{2}SC'24
ISEP Porto-Portugal, June 20 - 22, 2024

Quadratic Decomposition of the normalized derivatives of the Classical Orthogonal Polynomials - revisited

Ângela Macedo*

* UTAD, Portugal
Polo CMAT-UTAD

*amacedo@utad.pt

Abstract: Special Session #11 - Orthogonal Polynomials, Special Functions and their applications In this work we will present Quadratic Decomposition (QD) of the monic derivatives of the Classical Orthogonal Polynomials using the symbolic implementation presented in [3].

keywords: quadratic decomposition, orthogonal polynomials, classical orthogonal polynomials, symbolic computations.

MSC2020: 33C45 - 42C05

Acknowledgments

This research was partially financed by FCT (Fundação para a Ciência e a Tecnologia) within the Projects UIDB/00013/2020 and UIDP/00013/2020.

Centro de Matemática, Univ. do Minho - Polo CMAT-UTAD.

References

[1] T. S. Chihara, *An Introduction to Orthogonal Polynomials*, Gordon and Breach, New York, NY, 1978.

[2] Â. Macedo and P. Maroni, General quadratic decomposition, J. Differ. Equ. Appl. **16 (11)** (2010), 1309-1329.

[3] Â. Macedo, T.A. Mesquita and Z. da Rocha, Symbolic Approach to the General Quadratic Polynomial Decomposition. Math.Comput.Sci. **12**, 151-172 (2018).

[4] P. Maroni, Sur la decomposition quadratique d'une suite de polynômes orthogonaux. I, Riv. Mat. Pura ed Apl. **(6)** (1990), 19-53.

[5] P. Maroni, Une théorie algébrique des polynômes orthogonaux. Application aux polynômes orthogonaux semi-classiques, in *Orthogonal Polynomials and their Applications*, C. Brezinski, L. Gori and A. Ronveaux, eds., IMACS Annals on Computing and Applied Mathematics **9** (1991), 95-130 .

[6] P. Maroni, Sur la décomposition quadratique d'une suite de polynômes orthogonaux II, Port. Math. **50 (3)** (1993), 305-329 .

International Conference on Mathematical Analysis and Applications in Science and Engineering
ICMA^{2}SC'24
ISEP Porto-Portugal, June 20 - 22, 2024

Sturm's Comparison Theorem for Classical Discrete Orthogonal Polynomials

Alexandre Suzuki[1]

[1] University of Coimbra, Portugal

[1]asuzuki@uc.pt

Abstract: Special Session #11 - Orthogonal Polynomials, Special Functions and their Applications. In an earlier work [Castillo et al., J. Math. Phys., 61 (2020) 103505], it was established, from a hypergeometric-type difference equation, tractable sufficient conditions for the monotonicity with respect to a real parameter of zeros of classical discrete orthogonal polynomials on linear, quadratic, q-linear, and q-quadratic grids. In this work, we continue with the study of zeros of these polynomials by giving a comparison theorem of Sturm type. As an application, we analyze in a simple way some relations between the zeros of certain classical discrete orthogonal polynomials.

keywords: classical discrete orthogonal polynomials; difference equations; zeros.

MSC2020: 30C15, 05A30, 33C45, 33D15

1 Introduction

In a companion paper (see [1]), we give new tractable sufficient conditions for the monotonicity with respect to a real parameter of zeros of classical orthogonal polynomials (COP) on linear, quadratic, q-linear and q-quadratic grids. However, these results do not allow us to compare the zeros of the elements of two different sequences of COP. For this purpose we need a "comparison theorem" of Sturm type for difference equations. In [4, Corollary 1], Lun and Rafaeli used a comparison theorem of Sturm type to obtain inequalities between the zeros of solutions of two differential equations. As we will see, this result can be extended to difference equations and be used to obtain relations between the generalized zeros of two COP. The following results as well as their proofs can be found with more details in [7].

2 Preliminary results

As in [1], our starting point is the hypergeometric-type difference equation introduced by Nikiforov and Uvarov in [5, (5)]:

$$a(s)\frac{\Delta}{\Delta x(s-1/2)}\left(\frac{\nabla y(x(s))}{\nabla x(s)}\right)+b(s)\frac{\Delta y(x(s))}{\Delta x(s)}+c\,y(x(s))=0, \tag{2.1}$$

where $x(s)$ defines a class of grids with, generally nonuniform, step $\Delta x(s)=x(s+1)-x(s)$, $\nabla x(s)=x(s)-x(s-1)$, the functions a and b are polynomials of degree at most 2 and 1 in

x, respectively, and c is a constant. In what follows, we assume that x is a real-valued function defined on an interval of the real line. For similar purposes, in [1, (2.1)], we rewrite (2.1) in the following useful way:

$$A(s)y(x(s-1)) + B(s)y(x(s+1)) + C(s)y(x(s)) = 0, \tag{2.2}$$

where

$$A(s) = \frac{a(s)}{\nabla x(s)\Delta x(s-1/2)}, \quad B(s) = \frac{a(s) + b(s)\Delta x(s-1/2)}{\Delta x(s)\Delta x(s-1/2)}, \quad C(s) = c - B(s) - A(s). \tag{2.3}$$

For our purposes, we use another difference equation obtained from (2.2), as done by Porter in [6]. Fix $\mathrm{a} \in \mathbb{R}$ and $N \in \{3, 4, \dots\}$. Denote $s_i = \mathrm{a} + i$ $(i = 0, 1, \dots, N-1)$, $S = \{s_0, s_1, \dots, s_{N-1}\}$ and $S' = S \setminus \{s_0, s_{N-1}\}$. Assume $A(s)B(s) \neq 0$ for each $s \in S'$. Setting $y = u\,v$ on S, v being the new unknown function and u so that v satisfy a difference equation of the form

$$\Delta\nabla v(x(s)) + \lambda(s)\, v(x(s)) = 0 \tag{2.4}$$

on S, we obtain the difference equation

$$v(x(s+1)) + v(x(s-1)) + G(s)v(x(s)) = 0, \tag{2.5}$$

where

$$G(s_k) = \begin{cases} \dfrac{u(x(\mathrm{a}))}{u(x(\mathrm{a}+1))}\dfrac{C(s_k)}{B(s_k)}\displaystyle\prod_{j=1}^{k/2}\frac{A(s_{2j-1})B(s_{2j})}{A(s_{2j})B(s_{2j-1})}, & k \text{ even}, \\ \dfrac{u(x(\mathrm{a}+1))}{u(x(\mathrm{a}))}\dfrac{C(s_k)}{A(s_k)}\displaystyle\prod_{j=1}^{(k-1)/2}\frac{A(s_{2j})B(s_{2j-1})}{A(s_{2j-1})B(s_{2j})}, & k \text{ odd}, \end{cases} \tag{2.6}$$

with the initial conditions that $v(x(\mathrm{a})) \neq 0$ is arbitrarily chosen and

$$v(x(\mathrm{a}+1)) = -\frac{C(\mathrm{a})}{B(\mathrm{a})}\frac{u(x(\mathrm{a}))}{u(x(\mathrm{a}+1))}v(x(\mathrm{a})), \qquad B(\mathrm{a}) \neq 0.$$

Definition 1 (Node of a function) *Let v be a real function defined on S. Assume that v changes its sign on the interval $(x(s'-1), x(s')]$ $(s' \in S \setminus \{s_0\})$. The point of intersection of the x-axis with the line segment with endpoints $(x(s'-1), v(x(s'-1)))$ and $(x(s'), v(x(s')))$ is called a node of v.*

Definition 2 (Generalized zero of a function) *We say that a function f has a generalized zero at $x(s')$ $(s' \in S \setminus \{s_0\})$ if either $f(x(s')) = 0$ or $f(x(s'-1))f(x(s')) < 0$.*

Under certain conditions (see [7, Section 2]), the generalized zeros of a solution of (2.1) and (2.5) coincide. Consequently, we may use (2.5) to obtain information about the generalized zeros of a solution of (2.1).

3 Main result

The next result is an analogue of [4, Corollary 1] for difference equations and it is our main result.

Theorem 1 *Let v_1 and v_2 be nontrivial solutions of*

$$v_1(x(s+1)) + v_1(x(s-1)) + G_1(s)v_1(x(s)) = 0, \tag{3.7}$$

$$v_2(x(s+1)) + v_2(x(s-1)) + G_2(s)v_2(x(s)) = 0, \tag{3.8}$$

on S, with n and m nodes on $(x(\mathrm{a}), x(\mathrm{a}+N))$, respectively. Denote the generalized zeros of v_1 and v_2 by $x_1 < \cdots < x_n$ and $X_1 < \cdots < X_m$, respectively. If $m \leq n$ and there exists $j \in \{2, \ldots, N\}$ such that $G_2(s) < G_1(s)$ for each $s \in S'_j$ and $G_1(s) < G_2(s)$ for each $s \in S \setminus S_j$, and

$$v_1(x(\mathrm{a}))v_2(x(\mathrm{a})) > 0,$$

$$v_1(x(\mathrm{a}+N))v_2(x(\mathrm{a}+N)) > 0,$$

$$v_1(x(\mathrm{a}))v_2(x(\mathrm{a}+1)) - v_1(x(\mathrm{a}+1))v_2(x(\mathrm{a})) > 0,$$

$$v_1(x(\mathrm{a}+N-1))v_2(x(\mathrm{a}+N)) - v_1(x(\mathrm{a}+N))v_2(x(\mathrm{a}+N-1)) > 0,$$

then $x_k \leq X_k$ for each $k = 1, \ldots, m$.

Remark 1 *In order to use Theorem 1 to compare all the zeros of two COP, we may choose any $N \in \{3, 4, \ldots\}$ such that all these zeros are on $(x(\mathrm{a}), x(\mathrm{a}+N))$ to verify if the conditions are satisfied.*

4 Applications

As an example, we consider two COP on the linear grid $x(s) = s$.

The *Meixner polynomials* (see [2, Section 9.10]),

$$y(s) = M_n^{(\gamma,\mu)}(s) = {}_2F_1\left(\begin{matrix} -n, & -s \\ & \gamma \end{matrix}\middle|\, 1 - \frac{1}{\mu}\right)$$

($n = 1, 2, \ldots; 0 < \mu < 1, \gamma > 0$), satisfy the difference equation (2.2) with $A(s;\gamma,\mu) = s$, $B(s;\gamma,\mu) = \mu(s+\gamma)$ and $C(s;\gamma,\mu) = n(1-\mu) - s - (s+\gamma)\mu$. Note that $A(s;\gamma,\mu)B(s;\gamma,\mu) > 0$ for each $s \in \{1, 2, \ldots\}$.

The *Charlier polynomials* (see [2, Section 9.14]),

$$y(s) = C_n^{(\alpha)}(s) = {}_2F_0\left(\begin{matrix} -n, & -s \\ & - \end{matrix}\middle|\, -\frac{1}{\alpha}\right)$$

($n = 1, 2, \ldots; \alpha > 0$), satisfy the difference equation (2.2) with $A(s;\alpha) = s$, $B(s;\alpha) = \alpha$ and $C(s;\alpha) = n - s - \alpha$. Note that $A(s;\alpha)B(s;\alpha) > 0$ for each $s \in \{1, 2, \ldots\}$.

Denote the comparison functions of $M_n^{(\gamma,\mu)}$ and $C_n^{(\alpha)}$ by F_M and F_C, respectively. As an example, consider $n = 10$. Set $\alpha = 10$, $\gamma = 100$ and $\mu = 1/10$. In this case,

$$C_{10}^{(10)}(0)M_{10}^{(100,1/10)}(1) - M_{10}^{(100,1/10)}(0)C_{10}^{(10)}(1) > 0,$$

$$C_{10}^{(10)}(0)M_{10}^{(100,1/10)}(0) > 0,$$

and $F_C(s) > F_M(s)$ for $s = 1, 2, \ldots, 29$ and $F_C(s) < F_M(s)$ for $s = 30, 31, \ldots, 38$. Since all the zeros of $M_{10}^{(100,1/10)}(s)$ are on $(0, 40)$ (see [3, Theorem 7]), we only need to verify what happens on that interval. Moreover,

$$C_{10}^{(10)}(39)M_{10}^{(100,1/10)}(40) - M_{10}^{(100,1/10)}(39)C_{10}^{(10)}(40) > 0,$$

$$M_{10}^{(100,1/10)}(40)C_{10}^{(10)}(40) > 0.$$

Therefore, by Theorem 1, we have $\lceil x_k \rceil \leq \lceil X_k \rceil$ for each $k = 1, \ldots, 10$, where $x_1 < \cdots < x_{10}$ are the zeros of $C_{10}^{(10)}(s)$ and $X_1 < \cdots < X_{10}$ are the zeros of $M_{10}^{(100,1/10)}(s)$ (see Figure 1).

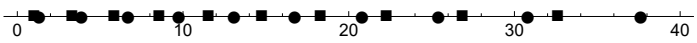

Figure 1: Zeros of $C_{10}^{(10)}(s)$ and $M_{10}^{(100,1/10)}(s)$ (■ and •, respectively)

Acknowledgments

The author is supported by the FCT grant 2021.05089.BD and partially supported by the Centre for Mathematics of the University of Coimbra - UIDB/00324/2020, funded by the Portuguese Government through FCT/ MCTES.

References

[1] K. Castillo, F. R. Rafaeli and A. Suzuki. Stieltjes' theorem for classical discrete orthogonal polynomials. *J. Math. Phys.*. **61** pp. 103505 (2020)

[2] R. Koekoek, P. Leskyand and R. Swarttouw. Hypergeometric orthogonal polynomials and their q-analogues. Springer-Verlag, Berlin (2010)

[3] I. Krasikov and A. Zarkh. On zeros of discrete orthogonal polynomials. *J. Approx. Theory.* **156** pp. 121-141 (2009)

[4] Y. Lun and and F. R. Rafaeli. Inequalities for zeros of Jacobi polynomials via Sturm's theorem: Gautschi's conjectures. *Numer. Algorithms.* **67**, 549-563 (2014)

[5] A. Nikiforov and V. Uvarov. Классические ортогональные полиномы дискретной переменной на неравномерных сетках (Russian) [Classical orthogonal polynomials of a discrete variable]. Preprint 17, Keldysh Inst. Appl. Math. (1983)

[6] M. Porter. On the roots of functions connected by a linear recurrent relation of the second order. *Ann. Of Math.*. **3** pp. 55-70

[7] A. Suzuki. Sturm's Comparison Theorem for Classical Discrete Orthogonal Polynomials. *Results Math.*. **79**, Paper No. 153 (2024)

International Conference on Mathematical Analysis and Applications in Science and Engineering
ICMA^{2}SC'24
ISEP Porto-Portugal, June 20 - 22, 2024

Brauer and Geršgorin locations of zeros of perturbed Chebyshev polynomials of the second kind by translation

Zélia da ROCHA[1⋆]

[1] University of Porto, Portugal

[1⋆]mrdioh@fc.up.pt

Abstract: Orthogonal Polynomials, Special Functions, and their Applications (Special Session N. 11).
We consider some perturbed Chebyshev polynomials of the second kind obtained by modifying by translation one of its recurrence coefficients at an arbitrary order. By applying Brauer and Geršgorin theorems to Jacobi matrices associated with such perturbed sequences we obtain some locations of their zeros and a refined location of one extremal zero [1].

keywords: Perturbed Chebyshev polynomials; zeros; Jacobi matrices; Gersgorin circle theorems; *Mathematica*®.

MSC2020: 33C45, 33D45, 42C05, 65F15, 65F50.

Acknowledgments

The author was partially supported by CMUP, a member of LASI, which is financed by national funds through FCT – Fundação para a Ciência e a Tecnologia, I.P., under the projects with reference UIDB/00144/2020 and UIDP/00144/2020.

References

[1] Z. da Rocha, Brauer and Geršgorin locations of zeros of perturbed Chebyshev polynomials of the second kind by translation, accepted for publication as chapter 13 of the volume of *Coimbra Mathematical Texts* dedicated to *José Carlos Petronilho*, Springer, 2024.

International Conference on Mathematical Analysis and Applications in Science and Engineering
ICMA^{2}SC'24
ISEP Porto-Portugal, June 20 - 22, 2024

From basic Fourier to basic Fourier-Bessel expansions

José Luis Cardoso*

* UTAD, Portugal
Polo CMAT-UTAD

*jluis@utad.pt

Abstract: Orthogonal Polynomials, Special Functions and their Applications (Special Session N. 11).

We introduce the concepts that underlie the Fourier expansions in terms of the q-analogues of the classical exponential and trigonometric functions, and also in terms of a q-analogue of the classical Bessel function.

keywords: Fourier expansions; Hahn-Exton q-Bessel function; Third Jackson q-Bessel function.

MSC2020: 42-C-10; 33-D-15.

Acknowledgments

This research was partially financed by FCT (Fundação para a Ciência e a Tecnologia) within the Projects UIDB/00013/2020 and UIDP/00013/2020.
Centro de Matemática, Univ. do Minho - Polo CMAT-UTAD.

References

[1] L. D. Abreu, J. Bustoz, J. L. Cardoso, The roots of The Third Jackson $q-$Bessel Function, Intern. J. Math. Math. Sci., **2003**(67) (2003), 4241–4248.

[2] J. Bustoz and J. L. Cardoso, Basic Analog of Fourier Series on a $q-$Linear Grid, J. Approx. Theory, **112** (2001), 134–157.

[3] J. L. Cardoso, Basic Fourier series on a $q-$linear grid: convergence theorems, J. Math. Anal. Appl., **323** (2006), 313–330.

[4] J. L. Cardoso, Basic Fourier series: convergence on and outside the $q-$linear grid, J. Fourier Anal. Appl., **17**(1) (2011), 96–114.

[5] J. L. Cardoso, J. Petronilho, Variations around Jackson's quantum operator, Methods Appl. Anal., **22**(4) (2015), 343–358.

[6] J. L. Cardoso, A few properties of the Third Jackson q-Bessel Function, Analysis Mathematica, **42**(4) (2016), 323–337.

[7] J. L. Cardoso, On basic Fourier-Bessel expansions, SIGMA, **14**(035) (2018), 13 pages.

[8] L. D. Abreu, R. Álvarez-Nodarse, J. L. Cardoso, Uniform convergence of basic Fourier-Bessel series on a q-linear grid, Ramanujan J, **49** (2019), 421–449.

International Conference on Mathematical Analysis and Applications in Science and Engineering
ICMA^{2}SC'24
ISEP Porto-Portugal, June 20 - 22, 2024

An exactly solvable system via the Nikiforov-Uvarov method: the Rosen-Morse potential. Applications to φ^{2p+2} field theory

G. Gordillo-Núñez[1⋆] **R. Álvarez-Nodarse**[2] **Niurka R. Quintero**[3]

[1]Universidade de Coimbra, Portugal
[2]Universidad de Sevilla, Spain
[3]Universidad de Sevilla, Spain

[1⋆]up202310693@up.pt

Abstract: *Orthogonal Polynomials, Special Functions and their Applications. Special Session #11.* We determine exact solutions of the time-independent Schrödinger equation for the Rosen-Morse type potential by using the Nikiforov-Uvarov method. This method allows us to write the eigenfunctions of the Schrödinger equation as the product of two simpler functions in a constructive way. The resolution of this problem is used to show that the kinks of the non-linear Klein-Gordon equation with φ^{2p+2} type potentials are stable. We also derive the orthogonality and completeness relations satisfied by the set of eigenfunctions, which are useful in the description of the dynamics of kinks under perturbations or interacting with antikinks.

keywords: Special functions; Nikiforov-Uvarov method; Stability of nonlinear waves.

MSC2020: 81Q05; 35Q51; 33C45.

1 Introduction

One-dimensional non-linear Klein-Gordon potentials, $U(\varphi)$, with multiple vacuum states support topological solitary waves and solitons, such as in the sine-Gordon potential. These waves solve the nonlinear Klein-Gordon equation (NKGE)

$$\varphi_{tt} - \varphi_{xx} + U'(\varphi) = 0,$$

where subscripts t and x denote partial derivatives with respect to time and space, respectively, and the prime denotes the derivative of the potential $U(\varphi)$ with respect to the field φ. In particular, kinks are topological waves connecting two minima of the potential solving NKGE and satisfying

$$\lim_{x\to+\infty} \varphi(x,t) = \lim_{x\to-\infty} \varphi(x,t) + \theta Q,$$

where $\theta \in \mathbb{R}^+ \setminus \{0\}$ and $Q \in \mathbb{Z}$ is the topological charge, typically $Q = \pm 1$ for kink and antikink solutions.

NKGE for various potentials $U(\varphi)$ and their associated kinks has numerous applications, such as in explaining continuous second-order phase transitions in Ginzburg-Landau theory or as

mobile domain walls in φ^4 type potentials. This makes the study of their stability crucial for observability in real systems. For instance, for sine-Gordon and φ^4 kinks, stability is analyzed using a Sturm-Liouville problem equivalent to the Schrödinger equation for a symmetric Pöschl-Teller potential. Its spectrum, consisting of a discrete and a continuous part, indicates that these kinks are stable as every eigenvalues are non-negative. In addition, knowing the spectrum is not only important for determining the stability of non-linear waves: in the presence of an internal mode, loss of integrability and inelastic collisions of solitary waves are predicted.

In Higher Order Field theories such as φ^6, φ^8 and so on, the Sturm-Liouville problem associated to the stability of their kinks is equivalent to the Schrödinger equation for the non-symmetric Rosen-Morse potential. Thus, our aim in [1] is to solve this potential by means of the so-called Nikiforov-Uvarov method which roughly consists of writing the eigenfunctions in terms of two simpler functions in a constructive way. In this way, we are ultimately able to answer the question about the existence of internal modes and its dependence on p in φ^{2p+2} type models raised by Saxena, Christov and Khare in [2].

2 Results and Discussion

The (time-independent) Schrödinger equation with the Rosen-Morse type potential (SERM) is given by

$$\left[\frac{d^2}{dz^2} - v(z) + \varepsilon\right]\psi(z) = 0,\ v(z) = v_0\cosh^2\mu\left[\tanh(z) + \tanh\mu\right]^2,\ z \in \mathbb{R}$$

where $\varepsilon \in \mathbb{R}$ is the eigenenergy and v_0, $\mu \in \mathbb{R}^+ \setminus \{0\}$. We identify three regions based on the asymptotic values of the potential $v_\pm = \lim_{z\to\pm\infty} v(z) = v_0 e^{\pm 2\mu}$ where $0 < v_- < v_+$. We define the regions as follows:

R1 For $\varepsilon \in (0, v_-)$ we distinguish the region of the so-called bound states, where the particle would be classically confined in a finite region of space and the eigenvalue problem should have a non-trivial function, $\psi(z)$, satisfying that $\psi(z) \in L^2(\mathbb{R})$, this is, the space of square-integrable functions in $\mathbb{R}$.

R2 For $\varepsilon \in (v_-, v_+)$ we distinguish the region of the so-called reflecting states: where the particle could (classically) reach $-\infty$ but not $+\infty$ and square-integrability condition on its eigenfunction could be dropped and substituted by $\psi(z) \in L^\infty(\mathbb{R})$, this is, the space of bounded functions on $\mathbb{R}$.

R3 For $\varepsilon \in (v_+, \infty)$ we distinguish the last region of the so-called free states: where the particle could reach any point in the one-dimensional space and its eigenfunction only need to be bounded, i.e., $\psi(z) \in L^\infty(\mathbb{R})$.

Before applying the NU method, we transform SERM by setting $u = -\tanh z$. Dividing the resulting equation by $(1-u^2)^2$ gives a generalized hypergeometric equation (GHE)

$$\psi''(u) + \frac{\widetilde{\tau}(u)}{\sigma(u)}\psi'(u) + \frac{\widetilde{\sigma}(u)}{\sigma^2(u)}\psi(u) = 0, \quad u \in (-1,1),$$

where $\widetilde{\tau}(u) = -2u$, $\sigma(u) = 1-u^2$, and $\widetilde{\sigma}(u) = \varepsilon - v_0\cosh^2\mu(u-\tanh\mu)^2$. The NU method seeks a solution of the form $\psi(u) = \phi(u)y(u)$ with $\phi(u)$ chosen in a constructive way such that $y(u)$ solves a simpler hypergeometric differential equation (HDE). In particular, for

$$\phi(u;\varepsilon) = (1-u)^{\frac{\varkappa_-(\varepsilon)}{2}}(1+u)^{\frac{\varkappa_+(\varepsilon)}{2}},\ \varkappa_+(\varepsilon) = \sqrt{v_+ - \varepsilon},\ \varkappa_-(\varepsilon) = \sqrt{v_- - \varepsilon},$$

$y(u;\varepsilon)$ solves a Jacobi's HDE given by

$$\left(1-u^2\right)y''(u)+2\left[a(\varepsilon)-(b(\varepsilon)+1)\,u\right]y'(u)+(k(\varepsilon)-b(\varepsilon))\,y(u)=0,$$

where $u\in(-1,1)$ and $k(\varepsilon)$, $a(\varepsilon)$, and $b(\varepsilon)$, are given by

$$k(\varepsilon)=\frac{\varepsilon+v_0}{2}-\frac{\varkappa_+(\varepsilon)\varkappa_-(\varepsilon)}{2},\quad a(\varepsilon)=\frac{\varkappa_+(\varepsilon)-\varkappa_-(\varepsilon)}{2},\quad b(\varepsilon)=\frac{\varkappa_+(\varepsilon)+\varkappa_-(\varepsilon)}{2},$$

respectively. In addition, it is useful to transform previous Jacobi's HDE into a Gauss's HDE by setting $u=-1+2s$. In this way, we obtain

$$s(1-s)y''(s)+\big[-2(b(\varepsilon)+1)s+b(\varepsilon)+a(\varepsilon)+1\big]y'(s)+(k(\varepsilon)-b(\varepsilon))y(s)=0,$$

where $s\in(0,1)$ whose associated parameters are

$$\alpha(\varepsilon)=b(\varepsilon)+\frac{1}{2}-\sqrt{v_0\cosh^2\mu+\frac{1}{4}},\quad \beta(\varepsilon)=b(\varepsilon)+\frac{1}{2}+\sqrt{v_0\cosh^2\mu+\frac{1}{4}},$$
$$\gamma(\varepsilon)=a(\varepsilon)+b(\varepsilon)+1.$$

Considering these simplifications together with the extra conditions imposed to the eigenfunction in each of the regions R1, R2 and R3, we are able to characterize the spectrum of SERM.

For region R1, we obtain the following result.

Theorem 1 *The nontrivial bound states of SERM for Region R1, (ε_n,ψ_n), are given by*

$$\psi_n(z)\propto\frac{e^{-a_n z}}{(e^z-e^{-z})^{b_n}}P_n^{(b_n-a_n,b_n+a_n)}\left(-\tanh z\right),$$

and their corresponding eigenvalues $\varepsilon_n\in(0,v_-)$ fulfill the equation

$$k_n-b_n=n(n+2b_n+1),\quad n\in\mathbb{N}\cup\{0\},$$

which has solutions for a finite number of integers n; being $a_n\coloneqq a(\varepsilon_n)$, $b_n\coloneqq b(\varepsilon_n)$ and $k_n\coloneqq k(\varepsilon_n)$. Here, $P_n^{(b_n-a_n,b_n+a_n)}(x)$ stands for the classical Jacobi polynomials.

Theorem 2 *The nontrivial scattering states for Region R2 and R3, $(\varepsilon,\psi_\varepsilon)$, read*

$$\psi_\varepsilon(z)\propto\psi_1(z;\varepsilon),\quad \varepsilon\in(v_-,v_+),$$
$$\psi_\varepsilon(z)\propto\psi_1(z;\varepsilon)+C\psi_2(z;\varepsilon),\quad C\in\mathbb{C},\quad \varepsilon\in(v_+,\infty),$$

where $\psi_1(z;\varepsilon)$ and $\psi_2(z;\varepsilon)$ are given, respectively, by

$$\psi_1(z;\varepsilon)=\frac{\operatorname{sech}^{b(\varepsilon)}z}{e^{a(\varepsilon)z}}F\left(\alpha(\varepsilon),\beta(\varepsilon),\gamma(\varepsilon);\frac{1-\tanh z}{2}\right),$$
$$\psi_2(z;\varepsilon)=\frac{e^{b(\varepsilon)z}}{\operatorname{sech}^{a(\varepsilon)}z}F\left(\alpha(\varepsilon)-\gamma(\varepsilon)+1,\beta(\varepsilon)-\gamma(\varepsilon)+1,2-\gamma(\varepsilon);\frac{1-\tanh z}{2}\right),$$

being $F(\alpha,\beta,\gamma;s)$ the Gauss's hypergeometric function.

Finally, we are able to precisely obtain the limits of each component of the spectrum.

Theorem 3 *Concerning $\varepsilon=v_\pm$ and the continuous spectrum Σ,*

1. *$v_+\in\Sigma$ and its scattering state is written in the form*

$$\psi_{v_+}(z)\propto\psi_1(z;v_+),$$

2. *$v_-\in\Sigma$ if and only if $\alpha(v_-)=-l$ for some $l=0,1,2,\ldots$ In that case, its scattering state, $\psi_{v_-}(z)$, reduces to*

$$\psi_{v_-}(z)\propto e^{-a(v_-)z}\operatorname{sech}^{a(v_-)z}(z)P_l^{(0,2a(v_-))}\left(-\tanh z\right),$$

being $a(v_-)=\frac{1}{2}\sqrt{v_+-v_-}$ but it is never square-integrable.

Kink stability of φ^{2p+2} field theory

The static kink solution, $\varphi_p^{st}(x)$, of NKGE for the potential

$$U(\varphi) = \frac{\varphi^2(\varphi^p - 2\varphi_1)^2}{4p^2},$$

where $p \in \mathbb{N}, (p \geq 2)$, and $\varphi_1 > 0$, is given by

$$\varphi_p^{st}(x) = \varphi_1^{1/p}\left(1 + \tanh\left[\frac{\varphi_1 x}{\sqrt{2}}\right]\right)^{1/p}.$$

The moving soliton can be obtained from $\varphi_p^{st}(x)$ by using the Lorentz transformation. The Lorentz invariance also allows the kink (antikink) stability analysis to be reduced to considering a perturbation $\Psi(x,t) = (c_1 e^{i\omega t} + c_2 e^{-i\omega t})\,\psi(x)$ around the static wave. Therefore, NKGE is linearized around its static solution. As a consequence, $\psi(z)$ verifies the following Sturm-Liouville problem (SL)

$$\left[\frac{d^2}{dz^2} + \Lambda^2 - V(z)\right]\psi(z) = 0,$$

where $z = \varphi_1 x/\sqrt{2}$, $\Lambda^2 = 2(\omega^2 - \omega_{ph}^2)/\varphi_1^2$, being

$$\omega_{ph}^2 = \min\left\{\lim_{x\to-\infty} U''[\varphi^{st}(x)], \lim_{x\to+\infty} U''[\varphi^{st}(x)]\right\} = \frac{2\varphi_1^2}{p^2},$$

and the function $V(z) = 2\,(U''[\varphi^{st}(z)] - \omega_{ph}^2)/\varphi_1^2$ satisfies that

$$V(z) = -\frac{3(p+1)}{p^2} + \frac{2(p^2-1)}{p^2}\tanh(z) + \frac{(2p+1)(p+1)}{p^2}\tanh^2(z),$$

which is the well-known Rosen-Morse potential. Previous SL can be transformed into SERM by denoting

$$v_0 = \frac{3(p+1)(p+2)}{p(2p+1)},\ \tanh\mu = \frac{p-1}{2p+1},\ \varepsilon = \Lambda^2 + \frac{v_0(p+2)}{3p},$$

and by translating the potential. Therefore, it can be shown that $v_- = (p+2)^2(p+1)/(p^2(2p+1))$, $v_+ = 9(p+1)/(2p+1)$, and $\Lambda^2(\varepsilon) \equiv \varepsilon - v_-$. It is straightforward to verify that, here, the condition $v_0 > e^{2\mu}\tanh\mu$ is satisfied for all values of p.

Now, from Theorems 1, 2 and 3, it can be found that that there always is only one bound state, and the solution for the bound regions is given by parameters $n = 0$, $a_0 = (p-1)/p$, $b_0 = (p+1)/p$, $\varepsilon_0 = (p+5)/(2p+1)$, and the corresponding eigenfunction

$$\psi_0(z) = \mathcal{N}_0 e^{-(p-1)z/p}\,\mathrm{sech}^{(p+1)/p}(z).$$

Notice that, in this case, $\Lambda^2(\varepsilon_0) = -4/p^2$, implying that $\omega(\varepsilon_0) = 0$. This frequency corresponds to the well-known Goldstone mode meaning $\psi_0(z) \propto d\varphi_p^{st}/dz$.

In addition, the state $\varepsilon = v_-$ does not belong to the continuum. Hence, $\varepsilon \in (v_-, v_+]$ and $\varepsilon \in (v_+, +\infty)$ define the associated R2 and R3 regions, respectively; and theirs corresponding eigenfunctions can be obtained in a similar way as shown in the previous examples. In this way, $\omega(\varepsilon)$ associated to the continuous spectrum, $\Sigma = (v_-, \infty)$, given that $\Lambda^2(\varepsilon) > \Lambda^2(v_-) = 0$, satisfy that

$$\omega^2(\varepsilon) > \omega_{ph}^2 = \frac{2\varphi_1^2}{p^2} > 0,$$

meaning the kinks are stable for every value of $p \geq 2$, $p \in \mathbb{N}$.

3 Conclusions

This work investigates the solutions $(\varepsilon, \psi(z))$ of the time-independent Schrödinger equation for the Rosen-Morse type potential. The equation is transformed into a generalized hypergeometric equation (GHE) using the variable change $u = -\tanh(z)$. By applying the Nikiforov-Uvarov method, the solution is expressed as $\psi(u) = \phi(u)y(u)$, where $y(u)$ satisfies a simpler GHE. To achieve this, $\phi(u)$ is chosen to satisfy a first-order linear differential equation for a convenient $\pi(u)$, determined after identifying the coefficients and polynomials related to the hypergeometric differential equation (HDE).

The Rosen-Morse potential is asymmetric, leading to three regions of eigenenergies ε determined by the potential's asymptotic values $v_{\pm} = v_0 e^{\pm 2\mu}$. The main results are stated in two theorems, characterizing the discrete and continuous spectra. Theorem 1 deals with the discrete spectrum, providing n_b bound states $\psi_n(z)$ for $\varepsilon_n \in (0, v_-)$. Theorem 2 addresses the continuous spectrum, where eigenfunctions $\psi_\varepsilon(z)$ are bounded and never square-integrable. For $\varepsilon \in (v_-, v_+)$, only one eigenfunction is bounded, while for $\varepsilon \in (v_+, \infty)$, both linearly independent solutions satisfy the boundedness condition.

Finally, the stability of static kinks $\varphi_p^{st}(x)$ of the non-linear Klein-Gordon equations with φ^{2p+2} $(p \geq 2)$ potentials is also justified. For every $p \geq 2$, the corresponding Sturm-Liouville problem has only one bound state, the Goldstone mode, indicating no internal modes. This answers a question posed by Saxena, Christov, and Khare in [2]. The continuous spectrum is defined as $\omega \in (\omega_{ph}, +\infty)$, with an exception for $p = 1$ where the Pöschl-Teller potential arises.

References

[1] G. Gordillo-Núñez, R. Alvarez-Nodarse and N.R. Quintero The complete solution of the Schrödinger equation with the Rosen-Morse type potential via the Nikiforov-Uvarov method *Physica D*, 458:134008, 2024.

[2] A. Saxena, I. C. Christov, and A. Khare. Higher-Order Field Theories: ϕ^6, ϕ^8 and Beyond. In Panayotis G. Kevrekidis and Jesús Cuevas-Maraver, editors, *A Dynamical Perspective on the ϕ^4 Model: Past, Present and Future*, pages 253–279. Springer International Publishing, Cham, 2019.

International Conference on Mathematical Analysis and Applications in Science and Engineering ICMA^{2}SC'24

ISEP **Porto-Portugal, June 20 - 22, 2024**

Solution of systems of integro-differential equations based on the Lanczos' Tau method

José A.O. Matos[1,2⋆] **Paulo B. Vasconcelos**[1,2] **José M.A. Matos**[1,3]

[1] CMUP, Departamento de Matemática, Faculdade de Ciências, Universidade do Porto, Rua do Campo Alegre s/n, 4169–007 Porto (Portugal)
[2] FEP, University of Porto, Portugal
[3] ISEP, Portugal

[2⋆]jamatos@fep.up.pt

Abstract: The Spectral Tau method, first introduced by Lanczos in the 1930s, is a technique to produce polynomial approximation solutions of linear differential problems with polynomial coefficients. This method has been expanded to solve a wider range of mathematical problems, including those with functional coefficients, nonlinear differential equations, and integro-differential equations.
Tautoolbox is a software package available in Matlab/Octave and Python versions that took inspiration from Lanczos' Tau method to generate polynomial approximations for these problems. Specifically, it implements the polynomial solutions using orthogonal families of polynomials.
One of the main objectives of Tautoolbox is to provide a user-friendly notation for expressing these problems. The software handles all the necessary internal computations to solve these problems. This work explores the challenges associated with extending the Tautoolbox to solve systems of integro-differential equations. The implementation supports both the solution to be described as (i) a polynomial over the integration domain and (ii) to break the integration domain in a partition where the solution comes as a piecewise polynomial defined over that mesh/partition.

keywords: Orthogonal polynomials; Differential Equations.

MSC2020: 33C45; 34-04.

Acknowledgments

The authors were partially supported by CMUP, member of LASI, which is financed by national funds through FCT – Fundação para a Ciência e a Tecnologia, I.P., under the projects with reference UIDB/00144/2020 and UIDP/00144/2020.

Numerical study of a partial differential equation with nonstandard growth conditions

Rui M. P. Almeida[1] **José C. M. Duque**[1] **Jorge Ferreira**[2]
Willian S. Panni[1⋆]

[1] Mathematics and Applications Center, University of Beira Interior, Portugal
[2] Department of Exact Sciences, Federal Fluminense University, Brazil

⋆willian.panni@ubi.pt

Abstract: In this talk, we investigate a partial differential equation with nonstandard growth conditions involving the p-biharmonic operator. Using a change of variable, we transform the fourth-order nonlinear parabolic problem into a system of two second-order differential equations. Applying Brouwer's fixed point theorem we prove the existence of the discrete solution. The uniqueness and a priori estimates of the discrete solution are demonstrated using classic Functional Analysis techniques. Additionally, we study the order of convergence in space and time considering a one-dimensional spatial domain. Finally, using the finite element method with Lagrange basis, we implement the computational code in Matlab software and present some examples to illustrate and validate the theory.

keywords: p-biharmonic operator; nonstandard growth conditions; nonlinear parabolic equation; discrete solution; numerical simulations.

MSC2020: 35A01; 35A02; 35K55; 65M12; 65M60.

References

[1] S. Antontsev and S. Shmarev. *Evolution PDEs with nonstandard growth conditions*, volume 4 of *Atlantis Studies in Differential Equations*. Atlantis Press, Paris, 2015.

[2] A. Chaoui and M. Djaghout. Galerkin mixed finite element method for parabolic p-biharmonic equation with memory term. *SeMA J.*, pages 1–15, 2023.

[3] T. Cömert and E. Pişkin. Global existence and decay of solutions for p-biharmonic parabolic equation with logarithmic nonlinearity. *Open J. Math. Anal.*, 6(1):39–47, 2022.

[4] C. Liu and P. Li. A parabolic p-biharmonic equation with logarithmic nonlinearity. *Politehn. Univ. Bucharest Sci. Bull. Ser. A Appl. Math. Phys.*, 81(1):35–48, 2019.

International Conference on Mathematical Analysis and Applications in Science and Engineering
ICMA^{2}SC'24
ISEP Porto-Portugal, June 20 - 22, 2024

Numerical simulations of compressible micropolar fluid flow between moving parallel plates

Nelida Črnjarić[1⋆] Ivan Dražić[2]

[1,2] Faculty of Engineering, University of Rijeka, Croatia

[1⋆]nelida.crnjaric@riteh.uniri.hr

Abstract: In this paper, numerical simulations of a compressible micropolar fluid flow between moving parallel plates are presented. The fluid is characterized as viscous and thermally conductive with polytropic thermodynamic properties. The considered shear flow is unsteady and takes place between two solid and thermally isolated horizontal plates moving irrotationally. The mathematical model is three-dimensional, but the variables depend on only one spatial variable. It is formulated in the Lagrangian description. Various numerical simulations are conducted to investigate the model's behavior on problems with non-homogeneous boundary conditions. The numerical approximations are performed using the finite difference scheme and the Faedo-Galerkin method. The finite difference method offers advantages over the Faedo-Galerkin method as it implements non-homogeneous boundary conditions directly and its computational complexity is less demanding. Comparisons of the obtained results show good agreement between the two approaches.

keywords: compressible micropolar fluid; parallel plates; numerical simulations; finite difference approximations; Faedo-Galerkin method.

MSC2020: 35Q35; 76M25; 76N99.

1 Introduction

Micropolar fluid theory extends classical fluid mechanics by incorporating the microstructure and microrotation of fluid particles. Here we study of a shear flow problem between two moving parallel plates. The mathematical model consists of the conservation laws for mass, momentum, momentum moment and energy and includes the constitutive equations for micropolar continuum, Fourier's law, and the assumption that the fluid is perfect and polytropic. By focusing on a scenario in which all variables depend on a single spatial variable, the study in [1] simplifies the three-dimensional model into a more tractable form expressed in Lagrangian coordinates as

$$\partial_t \rho + L^{-1}\rho^2 \partial_y u = 0, \tag{1}$$

$$\partial_t u = -L^{-1} R \partial_y(\rho\theta) + L^{-2}(\lambda + 2\mu)\partial_y(\rho\, \partial_y u), \tag{2}$$

$$\partial_t \mathbf{u} = L^{-2}(\mu + \mu_r)\partial_y(\rho\, \partial_y \mathbf{u}) + 2L^{-1}\mu_r \nabla \times \mathbf{w}, \tag{3}$$

$$j_I \partial_t w = L^{-2}(c_0 + 2c_d)\partial_y(\rho\, \partial_y \omega_1) - 4\mu_r \rho^{-1} w, \tag{4}$$

$$j_I \partial_t \mathbf{w} = L^{-2}(c_d + c_a)\partial_y(\rho\, \partial_y \mathbf{w}) - 4\mu_r \rho^{-1}\mathbf{w} + 2L^{-1}\mu_r \nabla \times \mathbf{u}, \tag{5}$$

$$\begin{aligned} c_v \partial_t \theta = {} & L^{-2} k_\theta \partial_y(\rho \partial_y \theta) - L^{-1} R\rho\theta \partial_y u + L^{-2}(\lambda + 2\mu)\rho(\partial_y u)^2 + L^{-2}(\mu + \mu_r)\rho|\partial_y \mathbf{u}|^2 + 4\mu_r \rho^{-1} w^2 \\ & + 4\mu_r \rho^{-1}|\mathbf{w}|^2 - 4L^{-1}\mu_r(\nabla \times \mathbf{u}) \cdot \mathbf{w} + L^{-2}(c_0 + 2c_d)\rho(\partial_y w)^2 + L^{-2}(c_d + c_a)\rho|\partial_y \mathbf{w}|^2, \end{aligned} \tag{6}$$

for $(y,t) \in]0,1[\times]0,T[$. Here ρ, $\mathbf{v} = (u, v_2, v_3)$, $\boldsymbol{\omega} = (w, \omega_2, \omega_3)$, and θ are mass density, velocity, microrotation velocity, and absolute temperature, respectively. The notation $\mathbf{u} = (0, v_2, v_3)$, $\mathbf{w} = (0, \omega_2, \omega_3)$ is used here. j_I, λ, μ, μ_r, c_0, c_d, c_a, k_θ, c_v and R are physical constants that should satisfy some physical constraints. To formulate the specific type of the flow, the initial and boundary conditions should be added to the system (1)-(6). We assume that both plates can move irrotationally. Their motion, written in Eulerian coordinates, is defined with the following boundary conditions for the velocity vector $\mathbf{v}$:

$$\mathbf{v}(h_L(t),t) = \mathbf{v}_L(t) = (u_L(t), v_{2L}(t), v_{3L}(t)), \qquad \mathbf{v}(h_R(t),t) = \mathbf{v}_R(t) = (u_R(t), v_{2R}(t), v_{3R}(t)), \tag{7}$$

where $h_L(t) = \int_0^t u_L(\tau)d\tau$ and $h_R(t) = h + \int_0^t u_R(\tau)d\tau$ denote smoothly moving domain boundaries. Since the system (1)-(6) is given in normalized mass Lagrangian coordinates, the moving domain boundaries become fixed and the spatial domain is equal to $[0,1]$, so that the boundary conditions for the velocity becomes: $\mathbf{v}(0,t) = (u_L(t), v_{2L}(t), v_{3L}(t))$ and $\mathbf{v}(1,t) = (u_R(t), v_{2R}(t), v_{3R}(t))$. We assume homogeneous boundary conditions for the microrotation field and the heat flux, i.e. $\boldsymbol{\omega}(0,t) = \boldsymbol{\omega}(1,t) = \mathbf{0}, \quad \partial_y\theta(0,t) = \partial_y\theta(1,t) = 0.$

For initial conditions we take $\rho(x,0) = \rho_0(x), \theta(x,0) = \theta_0(x)$, $\mathbf{v}(x,0) = (u_0(x), v_{20}(x), v_{30}(x))$, and $\boldsymbol{\omega}(x,0) = (w_0(x), \omega_{20}(x), \omega_{30}(x))$, where the functions on the right-hand sides are smooth. The variable y of the mass Lagrangian coordinate system is defined by $y = L^{-1}\eta(\xi)$, where $\eta(\xi) = \int_0^\xi \rho_0(s)ds$ and $L = \eta(h)$, and (ξ,t) denotes the Lagrangian coordinates, which are related to the Eulerian coordinates by

$$x(\xi,t) = x_0(\xi) + \int_0^t u(x(\xi,\tau),\tau)\,d\tau, \quad x_0(\xi) = \xi = \eta^{-1}(Ly).$$

By integrating (1) over $[0,1]\times[0,t]$, and using boundary conditions for u, one obtains

$$\int_0^1 \frac{dy}{\rho(y,t)} = \int_0^1 \frac{dy}{\rho_0(x)} + \frac{1}{L}\int_0^t (u_R(\tau) - u_L(\tau))d\tau = A(t). \tag{8}$$

To define problem appropriately, we assume that there exists a constant $\delta > 0$ such that $A(t) \geq \delta$ for $t \in [0,T\rangle$. We expect that if this condition is satisfied, and if the initial and boundary functions are smooth enough, there exists the generalized solution of our problem. We are interested here in the numerical simulations of the flow modeled by the described model.

2 Results and discussion

Finite difference scheme. We propose here the finite difference scheme based on the semi-discrete approach. It uses a uniform staggered grid for spatial discretization. The staggered grid points are denoted by $y_k = kh$, $k \in \{0,1,\ldots,N\}$ and $y_j = jh$, $j \in \left\{\frac{1}{2},\ldots,N-\frac{1}{2}\right\}$, where $h = \frac{1}{N}$. We construct the following time dependent functions

$$\rho_j(t), \theta_j(t), u_k(t), \mathbf{u}_k(t), w_k(t), \mathbf{w}_k(t), \quad j = \tfrac{1}{2},\ldots,N-\tfrac{1}{2}, \quad k = 0,1,\ldots,N, \tag{9}$$

which represent a discrete approximation to the solution at the corresponding grid points. These functions are determined as the solution of the ordinary differential equation system obtained by introducing the spatial discretization into the system (1)-(6) in which the partial derivatives are approximated by $\partial_y g(y_l,t) \approx \frac{g_{l+\frac{1}{2}} - g_{l-\frac{1}{2}}}{h}$, for $l = j$ or $l = k$.

Faedo-Galerkin method. Faedo-Galerkin method is applied to this system in a similar way as in [2]. The method consists of two steps: the first is the transformation of the variables to homogenize the boundary conditions, and the second is the application of the Faedo-Galerkin method to the system in the new variables. The approximate solutions are constructed in the form of trigonometric polynomials. The coefficients of these polynomials are obtained as the

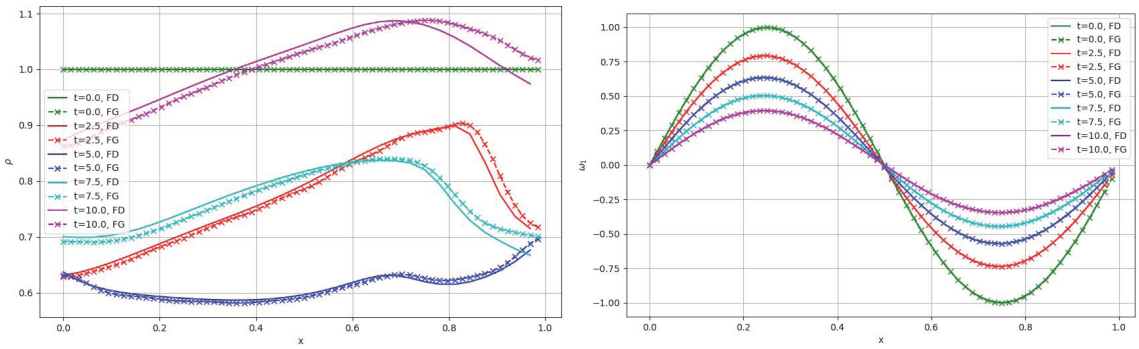

Figure 1: The comparison of the results obtained by finite-difference scheme and Faedo-Galerkin method.

solution of an ordinary differential equation system obtained in accordance to the Faedo-Galerkin method.

In both numerical approaches the solutions of the obtained ordinary differential equations systems are calculated using the third order strongly stable explicit Runge-Kutta method.

Numerical example. We consider the problem defined with the following initial functions:

$$\rho_0(x) = 1, \quad \mathbf{v}_0(x) = \sin(\pi x)(1,1,1), \boldsymbol{\omega}_0(x) = \sin(2\pi x)(1,1,1), \quad \theta_0(x) = 2 + \cos(\pi x).$$

Non-homogeneous boundary conditions modeling moving plates are defined by

$$\mathbf{v}_L(t) = -0.5\sin(\pi t)(1,0,0), \quad \mathbf{v}_R(t) = 0.5\sin(\pi t)(1,1,1).$$

For the initial domain we take $h = 1$. The other parameters of the system are set to: $L = 1$, $c_d = c_0 = c_v = 10^{-3}$, $R = 1$, $j_I = 1$, $c_a = 0$, $\lambda = -2 \cdot 10^{-3}$, $\mu_r = 10^{-3}$, $\mu = 3 \cdot 10^{-3}$, $k_\theta = 0.024$.

3 Conclusions and Future work

Both the finite difference scheme and Faedo-Galerkin method effectively model compressible micropolar fluid flow between moving plates, with good agreement between them. The simulations provided insights into the dynamics of the fluid flow and the influence of the initial and boundary conditions. In future work we will investigate more complex boundary conditions and extend the model to the real gas flow.

Acknowledgments

This work was supported by the University of Rijeka, Croatia under the project uniri-iskusni-prirod-23-184.

References

[1] Nelida Črnjarić-Žic, Ivan Dražić, Loredana Simčić, A shear flow problem for compressible viscous micropolar fluid: Derivation of the model and numerical solution, Mathematics and Computers in Simulation **162** (2019), 249-267.

[2] Nermina Mujaković, Non-homogeneous boundary value problem for one-dimensional compressible viscous micropolar fluid model: a local existence theorem, Annali di Universita di Ferrara, **53** (2007), 361–379.

International Conference on Mathematical Analysis and Applications in Science and Engineering
ICMA^{2}SC'24
ISEP Porto-Portugal, June 20 - 22, 2024

CD-FEM solutions of fourth-order nonlinear models for the confinement of fluid flows

N. D. Lopes [1,2,⋆] **H. B. de Oliveira**[3,4]

[1]ISEL – Instituto Politécnico de Lisboa, Lisboa, Portugal
[2] CEMAT-Ciências – Universidade de Lisboa, Lisboa, Portugal
[3] FCT – Universidade do Algarve, Faro, Portugal
[4] CMAFcIO –Universidade de Lisboa Lisboa, Portugal

⋆nuno.lopes@isel.pt

Abstract: In this work, we present a Continuous/Discontinuous Finite Element Method (CD-FEM) with interior penalty terms to solve nonlinear fourth-order problems arising in the analysis of fluid flow confinement. Specifically, we consider stationary flows governed by stream-function formulations of the Stokes or Navier-Stokes equations. Here, our focus lies on the numerical solutions obtained through the CD-FEM scheme. To show the applicability and robustness of the numerical model, we present several test cases. Additionally, we illustrate the effect of the nonlinear term in these systems, which is given by a feedback forces field associated with the confinement property of the fluid flow. Finally, we provide some numerical tests showcasing the extension of this numerical scheme to the stream-function formulation of the transient Navier-Stokes model.

keywords: 2d Navier-Stokes; CD-FEM; Feedback forces.

MSC2020: 35Q35; 65N30; 76M10.

1 Introduction

Given a bounded domain $\Omega := (0, K) \times (0, L)$ of $\mathbb{R}^2$, where L and K are positive constants, let us consider the following problem arising from the Navier-Stokes equations with a feedback forces field written in a stream-function formulation:

$$\nu\Delta^2\psi + \psi_x\Delta\psi_y - \psi_y\Delta\psi_x = \delta\left(|\psi_y|^{\sigma-2}\psi_y\right)_y \qquad \text{in} \quad \Omega, \tag{1.1}$$

$$\psi = f_* \quad \text{and} \quad \frac{\partial\psi}{\partial\mathbf{n}} = g_* \quad \text{on} \quad \overline{\Gamma}^*, \tag{1.2}$$

$$\psi = 0 \quad \text{and} \quad \frac{\partial\psi}{\partial\mathbf{n}} = 0 \quad \text{on} \quad \overline{\Gamma}^0, \tag{1.3}$$

where the stream-function is denoted by ψ, $\Delta^2\psi$ accounts for the bi-Laplacian of ψ, $\frac{\partial\psi}{\partial\mathbf{n}}$ is the normal derivative of ψ, with $\mathbf{n} = (n_1, n_2)$ standing for the outward unit normal to the boundary $\partial\Omega$ of the domain Ω, which in turn is decomposed into the following two disjoint subsets

$$\overline{\Gamma}^* := \{(x, y) \in [0, K] \times [0, L] : x = 0\},\ \overline{\Gamma}^0 := \{(x, y) \in (0, K] \times [0, L] : y = 0 \vee y = L \vee x = K\}. \tag{1.4}$$

Moreover, the feedback forces field, written in terms of the stream function, reads as

$$\mathbf{f}(\mathbf{x}, \psi_y, -\psi_x) = -\delta \left(|\psi_y|^{\sigma-2} \psi_y, 0 \right). \tag{1.5}$$

where $\delta > 0$ is a constant that accounts for the intensity of the forces field, and $\sigma > 1$ is another constant that characterizes the flow.

Data f_* and g_*, given in (1.2), can be written in terms of the prescribed velocity of the fluid flow (u_*, v_*) at the strip entrance $x = 0$ as follows $f_*(y) = \int_0^y u_*(s)\,\mathrm{d}s, \quad g_*(y) = v_*(y), \quad y \in (0, L)$, and are assumed to satisfy the compatibility conditions $f_*(0) = f_*(L) = g_*(0) = g_*(L) = 0$.

Note that the Stokes problem arises when the terms $\psi_x \Delta\psi_y - \psi_y \Delta\psi_x$ in (1.1) are disregarded. A detailed study of these numerical problems can be found in Oliveira and Lopes [1] and [2], where the existence and uniqueness of weak solutions for the associated continuous and discrete problems, as well as the consistency, stability and convergence of the numerical method, are rigorously proven.

The aim of the present work is to study the numerical solution of the boundary-value problem (1.1)-(1.3) by using the the Continuous/Discontinuous Finite Element Method.

2 Results and discussion

With respect to the Continuous/Discontinuous Finite Element Method (CD-FEM), introduced in [3] and used in our work for the numerical study, it has been widely used over the last 20 years, especially to numerically study higher order PDEs. It is worth mentioning that the main feature of this method is the weak enforcement of continuity of first and higher-order derivatives through stabilization terms on interior boundaries. Further developments of this method, were subsequently carried out by many authors, among whom [4, 5, 6].

Several test cases were considered in order to show the applicability and robustness of the numerical method. Here, we use a test case to illustrate the effects related to the advection and feedback forces field (see [7]). We stress that in order to approximate the exact solution ψ^h of the discrete nonlinear problem, we have used a Picard-type iterative method. This iterative procedure is stopped when the relative error (calculated in the $L^2(\Omega)$, $H^1(\Omega)$ and $l^\infty(\Omega)$ norms) between two consecutive approximations reaches a certain threshold value $\varepsilon > 0$.

In this framework, let us consider the following problem:

$$\Delta^2 \psi + \frac{1}{\nu} \left(\psi_x \Delta\psi_y - \psi_y \Delta\psi_x \right) - \frac{\delta}{\nu} \left(|\psi_y|^{\sigma-2} \psi_y \right)_y = 0 \qquad \text{in} \quad \Omega := (0,4) \times (0,1), \tag{2.1}$$

$$\psi = 0 \quad \text{and} \quad \frac{\partial \psi}{\partial \mathbf{n}} = 0 \qquad \text{on } y = 0,\ y = 1 \text{ and on } x = 4, \tag{2.2}$$

$$\psi = 0 \quad \text{and} \quad \frac{\partial \psi}{\partial \mathbf{n}} = -100\pi e^{4 - \frac{8}{1-(-2y+1)^4}} \qquad \text{on } x = 0 \quad \text{for } y \in (0,1). \tag{2.3}$$

The computational domain is discretized using a symmetric triangular mesh with 200 and 50 equally spaced intervals along the x-axis and y-axis parallel boundaries, respectively.

For this experiment, the exponent of nonlinearity σ and the magnitude δ of the feedback forces field are fixed at $\sigma = 1.5$ and $\delta = 1$, respectively. On the other hand, we vary the values for the kinematics viscosity ν. In Fig. 1 one can see the numerical solutions ψ_ν^h for the given test problem for $\nu^{-1} \in \{1, 15\}$. As can be observed from these figures, decreasing the value of the kinematics viscosity produces two effects on the behavior of the solutions: it makes the solution asymmetric around the horizontal line with $y = 0.5$, pulling the maximum of the solution towards the x-axis (see Fig. 1); it accentuates the decay of the solution along the x-axis (see Fig. 1).

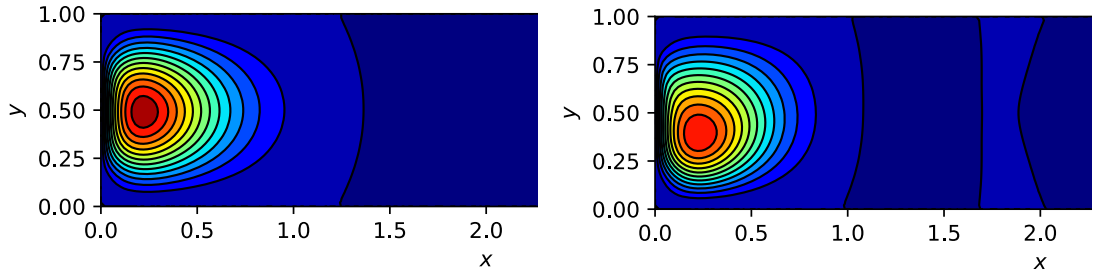

Figure 1: Contour plots of ψ_ν^h with $\sigma = 1.5$ and $\delta = 1.0$ for $\nu = 1$(left) and $\nu = \frac{1}{15}$ (right)

.

Finally, we show the damping of the solutions by decreasing the value of the exponent of the feedback forces field σ. We start by comparing the numerical solutions of (2.1)–(2.3) for different values of σ. More specifically, in what follows we consider $\sigma \in \{1.1, 1.75\}$. On the other hand, the kinematics viscosity and the intensity of the feedback forces field are assumed to be fixed: $\nu = 10^{-1}$ and $\delta = 4$. Here, we denote these numerical solutions by ψ_σ^h. In Fig. 2 we show of the contour lines for the solutions ψ_σ^h with values of σ decreasing from 1.75 to 1.1. We can observe the damping effect occurring as the parameter σ decreases. This effect is visually demonstrated through contour plots of the solutions, wherein decreasing values of σ consistently shift the isovalues of the solutions toward the y-axis.

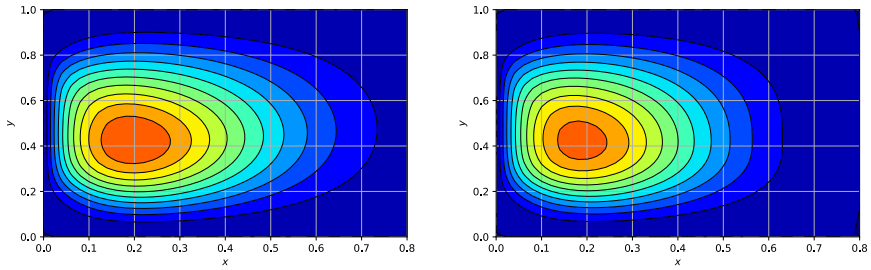

Figure 2: Contour plots of ψ_σ^h with $x \in (0, 0.8)$ for $\sigma \in \{1.1, 1.75\}$.

3 Conclusions and future work

This work is part of a project we developed to study, both from an analytical and numerical point of view, the 2d Navier-Stokes equations with feedback forces fields that are able to confine the fluid. In the first two outputs [1, 2] of this project, we have studied the Stokes and Navier-Stokes versions of the problem (1.1)-(1.3) with respect to the existence and uniqueness of weak solutions for both continuous and discrete problems, and we have shown analytically the consistency, stability and convergence of the proposed numerical method. Additionally, the proposed numerical scheme has shown robustness in addressing these challenges.

Finally, it should be mentioned that the transient version of the Navier-Stokes problem is still open. We are currently working on the extension of the numerical method to handle the transient problem. Initial results suggest that this numerical scheme is very promising. In Fig.: 3 one can see the initial condition and the solution ψ^h after 50 time steps for the transient problem with a time dependent Dirichlet boundary condition imposed at the strip entrance. Our next goal will be to tackle the confinement property.

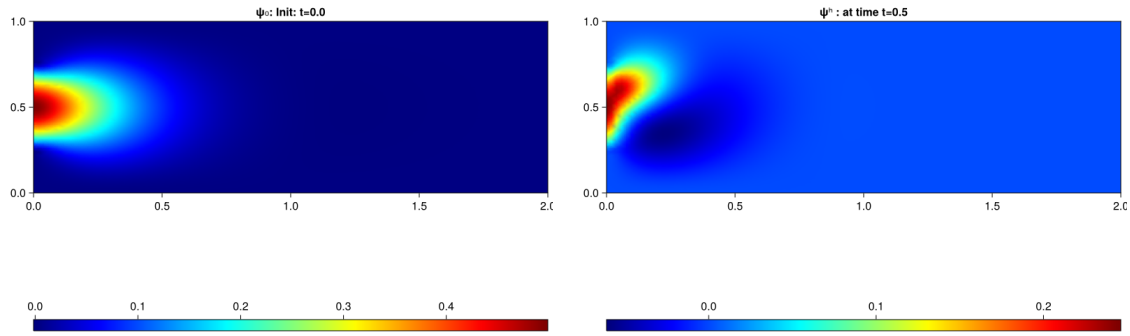

Figure 3: Contour plots of $\psi^h_{\sigma=1.5}$ at two different time steps.

Acknowledgments

The first author has been partially supported by `https://doi.org/10.54499/UIDB/04621/2020`. The second author has been partially supported by `https://doi.org/10.54499/UIDB/04561/2020`.

References

[1] N. D. Lopes and H. B. de Oliveira, Continuous/discontinuous Galerkin approximations for a fourth-order nonlinear problem, Computers & Mathematics with Applications, **97** (2021), 122–152.

[2] H. B. de Oliveira and N. D. Lopes, Continuous/discontinuous finite element approximation of a 2d Navier-Stokes problem arising in fluid confinement. To appear in International Journal of Numerical Analysis and Modeling, **21**, (2024).

[3] G. Engel, K. Garikipati, T.J.R. Hughes, M.G. Larson, L. Mazzei and R.L. Taylor. Continuous/discontinuous finite element approximations of fourth-order elliptic problems in structural and continuum mechanics with applications to thin beams and plates, and strain gradient elasticity. *Comput. Methods Appl. Mech. Engrg.* **191** (2002), no. 34, 3669–3750.

[4] S.C. Brenner, T. Gudi and L.-Y. Sung. An a posteriori error estimator for a quadratic C^0-interior penalty method for the biharmonic problem. *IMA J. Numer. Anal.* **30** (2010), no. 3, 777–798.

[5] D.A. Di Pietro and A. Ern. *Mathematical aspects of discontinuous Galerkin methods.* Springer, Heidelberg, 2012.

[6] N.D. Lopes, P.J.S. Pereira and L. Trabucho. A numerical analysis of a class of generalized Boussinesq-type equations using continuous/discontinuous FEM. *Int. J. Numer. Meth. Fluids*, **69** (2012), 1186–1218.

[7] S.N. Antontsev, J.I. Diaz and H.B. de Oliveira. Stopping a viscous fluid by a feedback dissipative field: II. The stationary Navier-Stokes problem. *Rend. Mat. Acc. Lincei s. 9* **15** (2004), 257–461.

International Conference on Mathematical Analysis and Applications in Science and Engineering ICMA²SC'24

ISEP **Porto-Portugal, June 20 - 22, 2024**

DETECTION OF ANOMALIES/OUTLIERS IN TIMES SERIES IN THE STOCK MARKET

Vítor Cardoso[1*]

[1] Superior Institute of Engineering of Porto, Portugal

Abstract: Collecting a large amount of data over time generates time series, making it important to study anomalies/outliers that may be errors or events of interest.

This article aims to improve the detection of anomalies/outliers in time series, identifying errors that allow data cleaning or identifying changes in the time series that can identify events of interest.

Two different techniques for detecting outliers in time series are implemented according to the input data type (univariate or multivariate time series), the type of outlier (point outliers, subsequence outliers or an entire outlier time series), the nature of the method (univariate or multivariate method) and model-based methods (estimation or prediction models), with the aim of comparing their performances to see which one is more efficient in detecting outliers in time series.

The data is processed and analyzed, comparing and discussing the results obtained.

Finally, the main conclusions of the work are drawn and perspectives for future work are presented to improve even better the detection of anomalies/outliers in time series.

keywords: Outlier detection, time series analysis, Median model, MAD model,

ARIMA model

MSC2020: 62-08

1 Introduction

The advances in technology have enabled the collection of a vast quantity of data over time in a multitude of fields, including finance, cybersecurity, health monitoring and machine learning, among others. The accumulation of such a substantial amount of data over an extended period of time generates time series, which necessitates the examination of anomalies or outliers that may be errors or events of interest. Outlier detection is the process of identifying points in the data that are markedly distinct from the majority of other data points [1].

This work aims to enhance the identification of anomalies/outliers in time series, thereby enabling the detection of errors that facilitate data cleansing or the identification of changes in the time series that can indicate the occurrence of events of interest.

Two distinct methodologies for identifying outliers in time series have been developed, contingent upon

the nature of the input data (univariate or multivariate time series), the type of outlier (point outliers, subsequence outliers or an entire outlier time series), the character of the method (univariate or multivariate method) and model-based methods (estimation or prediction models) [1]. The objective is to evaluate the efficacy of these approaches in detecting outliers in time series, with a view to identifying the most effective method.
In the Results and Discussion section, the Median time series modelling method and the Median Absolute Deviation (MAD) estimate method are presented and implemented. The data is processed and analysed, with comparisons and discussions of the results obtained.
In the final section, the main conclusions of the work are drawn, along with perspectives for future work to further enhance the detection of anomalies/outliers in time series.

2 Results and discussion

A. DATA
The dataset represents a historical record of stock market activity extracted from Yahoo Finance, spanning a five-year period. The dataset comprises daily records of stock performance metrics for the 500 largest companies based on market capitalization [2].
However, this study focused on the volume of AAPL shares traded in the period between 9 July and 6 August 2020. This was a period of significant turbulence for the company in question and there is a strong possibility of detecting outliers, as can be seen in Figure 1 below.

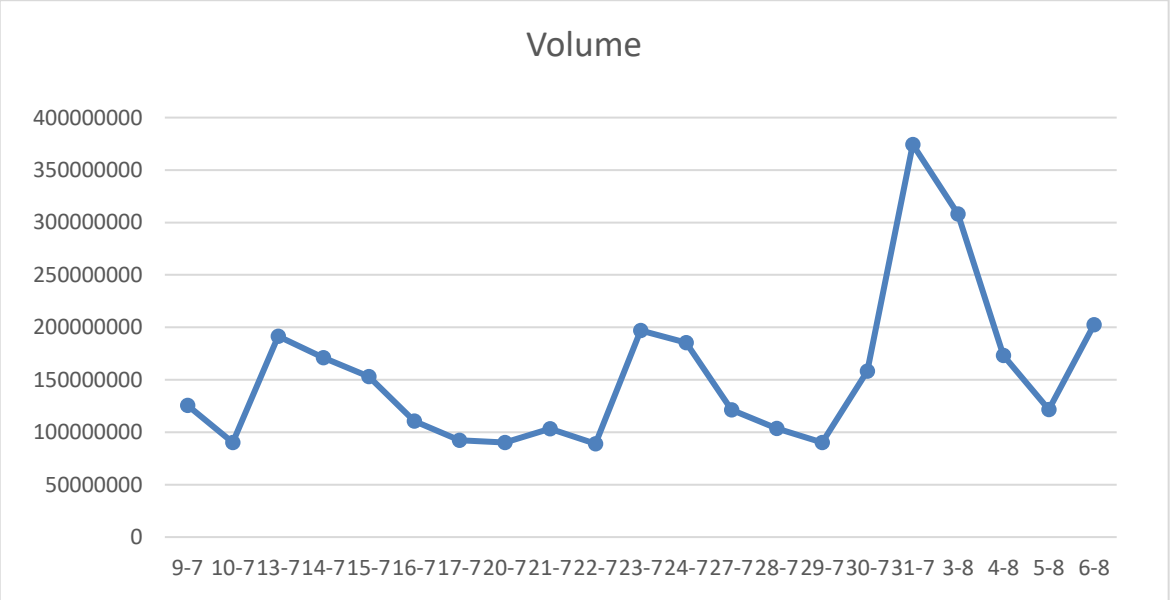

Figure 1 - Time series of the volume of shares traded by AAPL between 9th July and 6th August.

The efficacy of outlier detection techniques for time series data is contingent upon the input type of data, the specific type of outlier, the nature of the method and model-based methods to be applied.
The input data may be univariate or multivariate, but in this case, it is univariate. This is because $X = \{X_t\}_{t \in T}$ is an ordered set of observations with real values, where each observation is recorded at a given time $t \in T \subseteq \mathbb{Z}^+$ [1].
The outlier type may be a single point, a contiguous subsequence or an entire time series. In this instance, the outlier is a point, as it stands out anomalously when compared to the other values in the time series (global outlier) or its neighboring points (local outlier).
The method may be univariate or multivariate in nature. In this instance, the method is univariate, as it considers a single time-dependent variable.
In a univariate time series, a point in time t is considered an outlier if the distance to its expected value

is greater than a predefined threshold τ: $|x_t - \hat{x}_t| > \tau$. (1)
, where x_t is an observed point and $\hat{x}_t$ is its expected value [1].
The outlier detection methods based on the strategy described in equation (1) are referred to as model-based methods. If the estimated value, $\hat{x}_t$, is derived from observations preceding and following the observed value, x_t, then the technique is referred to as an estimation-based method. Conversely, if the estimated value, $\hat{x}_t$, is derived only from observations preceding the observed value, x_t, then the technique is referred to as a prediction-based method.

B. Methodology

In this study, the data is univariate, the outlier point is also univariate and the method is also univariate. The simplest estimation models, using basic statistical measures, are the Median model [3] or the Median Absolute Deviation (MAD) model [4], which are used to obtain the expected value $\hat{x}_t$.
Median and MAD models are often used for robust statistics, particularly for detecting outliers in time series data, which is the case in this study and are both implemented with the R programme.
The Median model detects outliers by comparing each point to the median of the dataset $Me(x_t)$ and predefining $\tau = 3$ as the threshold for detecting outliers, since the most commonly used value [3]. Points that are significantly different from the median are considered outliers, in other words, the points that fulfil the following inequality: $|x_t - Me(x_t)| > \tau$. (2)
Thus, the outliers are the points that are outside the window defined by the threshold.
The Median model presented is a simple model based on the Median estimation model presented in [3].
The MAD model is a robust measure of dispersion, calculated as the median of the absolute deviations from the median, the MAD value, using R's mad function with the constant equal to unity, considering that the data has a normal distribution. It's predefined $\tau = 3 * MAD$ as threshold for detecting outliers, since the most commonly used value [4]. Points that are significantly different from the median are considered outliers, in other words, the points that fulfil the following inequality: $|x_t - Me(x_t)| > \tau$. (3)
Thus, the outliers are the points that are outside the window defined by the threshold. The MAD model presented is a simple model based on the MAD estimation model presented in [4].
Note both models presented can also be defined taking only past observations into account, using the prediction model.

C. RESULTS

The output from the Median model algorithm is that the median value is 125642800 and that all observations are outliers, except the first observation.
On the other hand, the output from the MAD model is the same median, as expected, the MAD value is 35324800, the threshold for outlier detection is 105974400 and identifies only the 17th and 18th observations as outliers, 374336800 and 308151200, respectively.

D. DISCUSSION

It is evident that the MAD model is demonstrably more efficacious than the Median model in the detection of outliers. It is noteworthy that the MAD model may be applied to data exhibiting a non-normal distribution.
By modifying the default values of the thresholds, it is possible to create a Median model with a reduced number of outliers and a MAD model with a greater number of outliers. This would be a worthwhile area for further investigation, with a focus on analysing the sensitivity (the proportion of actual positive cases that are correctly identified by the model) and specificity (the proportion of actual negative cases

that are correctly identified by the model) of the two models under consideration [4].
It would also be beneficial to compare the MAD model with other methods based on estimation and prediction models.

3 Conclusions and Future work

The study concluded that the MAD estimation model is significantly more efficient than the Median model. Further research would be beneficial by comparing the MAD model with the autoregressive integrated moving average (ARIMA) time series model. This is because the ARIMA model is also a univariate method and an estimation model. It would also be interesting to compare it with other estimation and forecasting models. It is also possible to use other variables in addition to the volume of shares, either individually or collectively, in relation to AAPL or other companies, over a range of time periods, including the full five-year period.

References

[1] Ane Blásquez-García, Angel Conde, Usue Mori, Jose A. Lozano, A Review on Outlier/Anomaly Detection in Time Series Data, *ACM Comput. Surv.* **54** (3) (2021), article 56, 33 pages.

[2] Massive Yahoo Finance Dataset, Yahoo Finance, from https://www.kaggle.com/datasets/iveeaten3223times/massive-yahoo-finance-dataset?resource=download

[3] S. Basu and M. Meckesheimer. 2007. Automatic outlier detection for time series: An application to sensor data. Knowl.Info. Syst. 11, 2 (2007), 137–154.

[4] Saeed Mehrang, Elina Helander, Misha Pavel, Angela Chieh and Ilkka Korhonen, Outlier Detection in Weight Time Series of Connected Scales, International Conference on Bioinformatics and Biomedicine, IEEE, 1489–1496.

International Conference on Mathematical Analysis and Applications in Science and Engineering
ICMA^{2}SC'24
ISEP Porto-Portugal, June 20 - 22, 2024

Mathematical modeling of crime data with stochastic differential equations

Julia Calatayud[1⋆]

[1] Departament de Matemàtiques, Universitat Jaume I, Castellón, Spain

[1⋆]calatayj@uji.es

Abstract: Criminality is a serious problem for any region, which risks its economy, security and quality of life. Mathematical criminology is a current field of research which uses mathematical methods for understanding and predicting the incidence of crime. In this work, we show models based on stochastic differential equations to fit crime data, both temporal and spatial, in Spain and in the city of Valencia. We present some results of our recent papers https://doi.org/10.1007/s00477-022-02369-x and https://doi.org/10.1080/00207160.2024.2302840.

keywords: criminality; data fitting; differential equation; stochastic noise

MSC2020: 34F05; 34C60; 91D10

1 Introduction

There are many works on statistical modeling of crime. There are also works on mathematical modeling of crime, based on high-dimensional ordinary differential equations and partial differential equations [1, 2]. However, although useful for analyzing and simulating system dynamics, these mathematical models are not usually amenable to fitting real crime data, due to the complexities involved in the formulations.

We only found three works on differential equations with real-data fitting: Manchester [3], Cape Town [4], and Los Angeles and Houston [5]. We then decided to investigate differential equation-based models for crime, focusing on real-data fitting. The main objective was the spatio-temporal modeling of crime records. We started with usual models from mathematical epidemiology, considering interactions in crime [6]. But we did not find a good way to calibrate parameters in general. Hence we moved to stochastic differential equations, based on quantitative-finance methodologies. We focus on [7, 8].

2 Compartmental models

The population is divided into offender and non-offender individuals. An offender is defined as a person who commits an illegal act that should require attention by authorities (for instance, with a fine, community services, or lack of liberty). At a certain time instant, offenders may or may not be in prison. The latter situation may occur when the person has not yet been caught

by the police, he/she is waiting for trial or decisions but out of jail, or he/she has been found guilty and is serving sentence but not with penalty of deprivation of liberty.

The compartmental model is

$$\begin{cases} \frac{\mathrm{d}S}{\mathrm{d}t} = \lambda - \beta SL + rP + a_1 L - \mu S, \\ \frac{\mathrm{d}L}{\mathrm{d}t} = \beta SL - a_1 L - a_2 L - \mu L, \\ \frac{\mathrm{d}P}{\mathrm{d}t} = a_2 L - rP - \mu P, \end{cases} \tag{1}$$

where $S(t)$ is the amount of susceptible individuals, $L(t)$ is the amount of offenders in liberty, and $P(t)$ is the amount of offenders in prison, at instant $t \geq 0$. The total population $N = S + L + P$ is constant. The total number of individuals convinced by an offender is given by the basic reproduction number,

$$\mathcal{R}_0 = \frac{\beta N}{a_1 + a_2 + \mu}. \tag{2}$$

A result is the following:

- If $\mathcal{R}_0 \leq 1$, then the CFE is globally asymptotically stable.
- If $\mathcal{R}_0 > 1$, then the CEE is globally asymptotically stable.

It indicates that if $\mathcal{R}_0 \leq 1$, then criminality is eradicated at long term. Although our proposed model is an idealization of the complex process of criminality, it demonstrates how suitable policies that manipulate the parameters (i.e. the transitions between states) eventually affect the proportion of criminally active people in the population. When $\mathcal{R}_0 > 1$, criminality is not descending and concrete policies should be implemented.

In Spain, with real data on imprisonment, the basic reproduction number is $\mathcal{R}_0 = 0.998$. Since it is less than 1, one concludes that, if things remain the same and the parameters keep time invariant, criminality will become extinct in the future. However, $\mathcal{R}_0$ is actually near the threshold 1, so any variation of the parameters may make it greater than 1 and make criminality endemic. There should be control policies to ensure that $\mathcal{R}_0$ does not grow and, even better, reduces.

The sensitivity index of a parameter λ is

$$\Gamma_\lambda = \frac{\partial \mathcal{R}_0}{\partial \lambda} \times \lambda.$$

In Spain, the sensitivity indices are

$$\Gamma_\beta = 0.998, \quad \Gamma_{a_1} = -0.247, \quad \Gamma_{a_2} = -0.751.$$

Thus, the most important parameter to control is the force of influence, followed by the transitions from L to P and from L to S.

To account for the unexplained variability of the data and obtain probabilistic intervals, a random error is incorporated into the model. This random error is a Gaussian white noise with bounded homogeneous variance. Nonlinear regression is employed as a generalization of linear regression. A 95% confidence interval for $\mathcal{R}_0$ is $[0.968, 1.030]$. See the details in [7].

3 Stochastic models of Itô type

The reader is referred to [8]. Our dataset contains information about reported criminal events in the city of Valencia (Spain) for ten complete years, from 2010 to 2020. We have a total of 90247 events communicated to the 112-emergency phone, split into *aggression* (55610 cases), *stealing*

(25342 cases), *woman alarm* (454 cases) and *others* (8841 cases). Each incident is located in Valencia by its latitude and longitude position. We assign a zip code (a patch) to each latitude-longitude location, among the 26 codes existing in Valencia, from 46001 until 46026. This procedure gives 26 time series, along eleven years.

The proposed model of Itô stochastic differential equations, for $n = 26$, is

$$\mathrm{d}x_{1,t} = \mu_1 x_{1,t}\,\mathrm{d}t + \sigma_1 x_{1,t}\,\mathrm{d}B_{1,t}, \quad \ldots, \quad \mathrm{d}x_{n,t} = \mu_n x_{n,t}\,\mathrm{d}t + \sigma_n x_{n,t}\,\mathrm{d}B_{n,t}.$$

The Brownian motions satisfy $\mathrm{corr}[B_{i,t}, B_{j,t}] = \rho_{ij} \in [-1, 1]$. The construction is as follows: given the correlation matrix $\mathrm{A} = (\rho_{ij})_{i,j}$ and given auxiliary independent Brownian motions $\tilde{B}_{1,t} = B_{1,t}$, $\tilde{B}_{2,t}, \ldots, \tilde{B}_{n,t}$, just define

$$\begin{pmatrix} B_{1,t} \\ \vdots \\ B_{n,t} \end{pmatrix} = \mathrm{L} \begin{pmatrix} \tilde{B}_{1,t} \\ \vdots \\ \tilde{B}_{n,t} \end{pmatrix},$$

where L is a lower-triangular matrix and $\mathrm{A} = \mathrm{LL}^\top$ is the Cholesky decomposition of A. A relevant property is $\mathrm{corr}[\mathrm{d}x_{i,t}, \mathrm{d}x_{j,t} | x_{i,t}, x_{j,t}] = \rho_{ij}$.

The key role of correlation: It measures how similar the increasing and decreasing patterns of crime incidence around the expected value are between zip codes. In practice, knowledge of spatial correlations permits reallocating police personnel, given an unexpected escalation of criminal activity in a specific district. The proposed methodology may be applied to fit whole trend time series, obtain the correlations between the zip codes, and forecast incidences at short term.

References

[1] D. McMillon, C.P. Simon, J. Morenoff, Modeling the underlying dynamics of the spread of crime, PLoS ONE **9**(4) (2014), e88923.

[2] M. Short, A. Bertozzi, P. Brantingham, Nonlinear patterns in urban crime: Hotspots, bifurcations, and suppression, SIAM Journal on Applied Dynamical Systems, **9**(2) (2010), 462–483.

[3] A.A. Lacey, M.N. Tsardakas, A mathematical model of serious and minor criminal activity, European Journal of Applied Mathematics, **27**(3) (2016), 403–421.

[4] K.A. Jane White, E. Campillo-Funollet, F. Nyabadza, D. Cusseddu, C. Kasumo, N.M. Imbusi, V. Ogesa Juma, A.J. Meir, T. Marijani, Towards understanding crime dynamics in a heterogeneous environment: A mathematical approach, Journal of Interdisciplinary Mathematics, **24**(8) (2021), 2139–2159.

[5] Y. Cao, K. Dong, B. Siercke, M. Wilber, Final Report: Crime Modeling, UCLA, LA, USA, 9th August 2013.

[6] F. Brauer, P. Driessche, J. Wu, *Mathematical Epidemiology*. Berlin Heidelberg: Springer-Verlag, 2008.

[7] J. Calatayud, M. Jornet, J. Mateu, A dynamical mathematical model for crime evolution based on a compartmental system with interactions, International Journal of Computer Mathematics (2024), https://doi.org/10.1080/00207160.2024.2302840.

[8] J. Calatayud, M. Jornet, J. Mateu, Spatio-temporal stochastic differential equations for crime incidence modeling, Stochastic Environmental Research and Risk Assessment, **37** (2023), 1839–1854.

International Conference on Mathematical Analysis and Applications in Science and Engineering
ICMA^{2}SC'24
ISEP Porto-Portugal, June 20 - 22, 2024

Probabilistic analysis of a simply supported beam with random parameters

J.-C. Cortés[1] **G. Falsone**[2] **R. Laudani**[2] **E. López-Navarro**[1⋆] **M.-D. Roselló**[1]

[1] Instituto Universitario de Matemática Multidisciplinar,
Universitat Politècnica de València, València, Spain
[2] Dipartimento di Ingegneria,
Università degli Studi di Messina, Italy

⋆ellona1@doctor.upv.es

Abstract: This paper adopts a probabilistic approach to analyze the deflection, bending moment, and shear force of a simply supported beam. By randomizing the classical governing fourth-order differential equation with boundary conditions, we aim to gain a more comprehensive understanding of these mechanical properties. The stochastic analysis is conducted using the Probabilistic Transformation Method to calculate the first probability density function of the aforementioned quantities of interest.

keywords: Probabilistic Transformation Method; Statically determinate beams; Statically indeterminate beams; Probability density function; Deflection; Bending moment; Shear Force.

This abstract is included in **Special Session #9: Modeling with Differential and Difference Equations with Uncertainties.**

1 Introduction

In this contribution, we consider an Euler-Bernoulli beam, which is represented by the following linear fourth-order differential equation [1]

$$\frac{\mathrm{d}^4 u(x)}{\mathrm{d}\, x^4} = \frac{1}{EI} q(x), \quad 0 < x < l, \tag{1}$$

where $u = u(x)$ represents the static deflection of the beam of length l at the spatial position x on the beam. The product EI is the flexural rigidity, where E stands for the Young's modulus and I denotes the moment of inertia. Finally, $q(x)$ represents the load distribution over the beam. In this contribution we will consider that $q(x)$ is a single load placed at a random position, that is, $q(x) = F_0 R_{-1}(x - X_f)$, where F_0 is a random variable representing the intensity of the load, [1] $R_{-1}(x - X_f) = \delta(x - X_f)$ is the Dirac delta function and X_f is the random variable that represents the position of the load over the beam. These random variables are defined in a common

[1] $R_{-1}(\cdot)$ is the most common generalized function. In this work, we will use the linear and cubic ramp functions, that is,

$$R_n(x - X_f) = \begin{cases} 0, & \text{if} \quad x < X_f, \\ \frac{1}{n!}(x - X_f)^n, & \text{if} \quad x > X_f, \end{cases} \tag{2}$$

for $n = 1, 3$, respectively.

complete probability space $(\Omega, \mathcal{F}_\Omega, \mathbb{P})$. In Mechanical Engineering, incorporating randomness into loads and their positions is essential. This approach reflects real-world variability, ensuring that designs are robust and capable of withstanding unpredictable conditions effectively.

To be precise, we will study a simply supported beam that is characterized by the following boundary conditions $u(0) = 0$, $u(l) = 0$, $u''(0) = 0$ and $u''(l) = 0$. The simply supported beam is a structural element supported at both ends with no resistance to rotation. They can be found in building construction, where they can create floor and roof structures, and support heavy loads. Fig. 1 shows a graphical representation of this case. The main goal will be to obtain the first probability density function (1-PDF) of the deflection, the shear force, and the bending moment via the Probabilistic Transformation Method (PTM) [2].

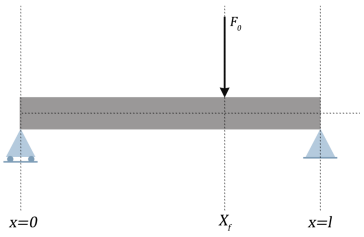

Figure 1: Simply supported beam with the random load positioned arbitrarily.

2 Results and discussion

First, we begin by establishing the necessary components to obtain the 1-PDF, two domains, $D_+ = \{\omega \in \Omega : x < X_f(\omega)\}$ and $D_- = \{\omega \in \Omega : x > X_f(\omega)\}$ and the two complementary events $P_1 = \mathbb{P}_{X_f}[D_+] = \int_{\max(a,x)}^{\max(b,x)} p_{X_f}(x_f)\,\mathrm{d}\,x_f$, and $P_2 = [D_-] = \int_{\min(a,x)}^{\min(b,x)} p_{X_f}(x_f)\,\mathrm{d}\,x_f$, where $P_1 + P_2 = 1$. Here, $p_{X_f}(x_f)$ denotes the PDF of X_f.

Solving model (1) with the corresponding boundary conditions, gives the deflection of a simply supported beam

$$u(x) = \frac{F_0}{EI}\left(R_3(x - X_f) - \frac{1}{6l}(l - X_f)x^3 - \frac{1}{6l}(l - X_f)^3 x + \frac{l}{6}(l - X_f)x\right). \tag{3}$$

After applying the PTM, and considering the definition of $R_3(\cdot)$ and the expressions D_+, D_-, P_1 and P_2, previously defined, one can obtain the PDF of the deflection:

$$\begin{aligned} p_{u(x)}(u) =& P_1 \int_{\mathcal{D}(D_+)} p_{F_0}\left(uEI\left(-\frac{1}{6l}(l - x_f)x^3 - \frac{1}{6l}(l - x_f)^3 x + \frac{l}{6}(l - x_f)x\right)^{-1}\right) \\ & \cdot p_{X_f}(x_f)\left|EI\left(-\frac{1}{6l}(l - x_f)x^3 - \frac{1}{6l}(l - x_f)^3 x + \frac{l}{6}(l - x_f)x\right)^{-1}\right| \mathrm{d}\,x_f \\ & + P_2 \int_{\mathcal{D}(D_-)} p_{F_0}\left(uEI\left(\frac{1}{6}(x - x_f)^3 - \frac{1}{6l}(l - x_f)x^3 - \frac{1}{6l}(l - x_f)^3 x + \frac{l}{6}(l - x_f)x\right)^{-1}\right) \\ & \cdot p_{X_f}(x_f)\left|EI\left(\frac{1}{6}(x - x_f)^3 - \frac{1}{6l}(l - x_f)x^3 - \frac{1}{6l}(l - x_f)^3 x + \frac{l}{6}(l - x_f)x\right)^{-1}\right| \mathrm{d}\,x_f. \end{aligned} \tag{4}$$

It is easy to check that he bending moment is given by

$$M(x) = -EIu''(x) = F_0\left(\frac{1}{l}(l - X_f)x - R_1(x - X_f)\right). \tag{5}$$

Then, applying the PTM, taking into account the definition of $R_1(\cdot)$ and the probabilities P_1 and P_2, one can obtain after some calculations that the 1-PDF

$$p_{M(x)}(m) = P_1 \int_{\mathcal{D}(D_+)} p_{F_0}\left(\frac{ml}{x(l-x_f)}\right) p_{X_f}(x_f) \left|\frac{l}{x(l-x_f)}\right| \mathrm{d}\, x_f \tag{6}$$

$$+ P_2 \int_{\mathcal{D}(D_-)} p_{F_0}\left(\frac{m}{x_f(1-x/l)}\right) p_{X_f}(x_f) \left|\frac{1}{x_f(1-x/l)}\right| \mathrm{d}\, x_f. \tag{7}$$

It can be checked that the shear force can be explicitly expressed as

$$T(x) = -EIu'''(x) = F_0\left(\frac{1}{l}(l - X_f) - R_0(x - X_f)\right) \tag{8}$$

Utilizing the PTM, it can be seen that the PDF of the shear force is given by

$$p_{T(x)}(t) = P_1 \int_{\mathcal{D}(D_+)} p_{F_0}\left(\frac{tl}{l-x_f}\right) p_{X_f}(x_f) \left|\frac{l}{l-x_f}\right| \mathrm{d}\, x_f \tag{9}$$

$$+ P_2 \int_{\mathcal{D}(D_-)} p_{F_0}\left(\frac{-lt}{x_f}\right) p_{X_f}(x_f) \left|\frac{-l}{x_f}\right| \mathrm{d}\, x_f. \tag{10}$$

Example 1 *For the deterministic parameters, we have considered a beam of length* $l = 10\,\mathrm{m}$, *with material properties:* $E = 25 \cdot 10^9\,\mathrm{N/m^2}$, *Young's modulus, and* $I = 1.35 \cdot 10^{-3}\,\mathrm{m^4}$, *the moment of inertia. And for the random parameters, we have considered that the intensity of the load follows a normal distribution with mean* $\mu_{F_0} = 500 \cdot 10^3\,\mathrm{N}$ *and standard deviation* $\sigma_{F_0} = 0.25 \cdot \mu_{F_0}\,\mathrm{N}$, *then* $F_0 \sim \mathrm{N}(\mu_{F_0}, \sigma_{F_0})$. *For the random position, we also have taken a normal distribution with mean* $\mu_{X_f} = 6\,\mathrm{m}$ *and standard deviation* $\sigma_{X_f} = 0.25 \cdot \mu_{X_f}\,\mathrm{m}$, *then* $X_f \sim$ *mathrmN*$_{\mathcal{T}}(\mu_{X_f}, \sigma_{X_f})$, *where* $\mathcal{T} = [0, l]$.

Figures 2a, 3a and 4a show, in color red, the mean (solid line) obtained by means of the 1-PDF and confidence intervals (dotted lines) constructed through the mean plus/minus 2 standard deviations. In color blue, we show the deterministic results for the deflection, bending moment, and shear force, respectively. Figures 2b, 3b, and 4b show the 1-PDF of the three mechanical characteristics of the beam. We can observe in all of them, that the variance increases in the middle of the beam, approximately.

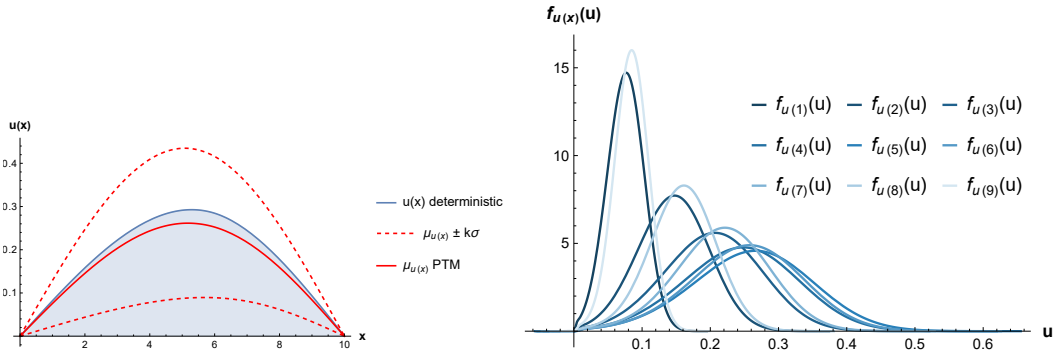

(a) (b)

Figure 2: Deflection.

3 Conclusions and Future work

In this contribution, we have studied a fundamental model from a probabilistic approach to describe the deflection of a simply supported beam under the influence of a randomly positioned

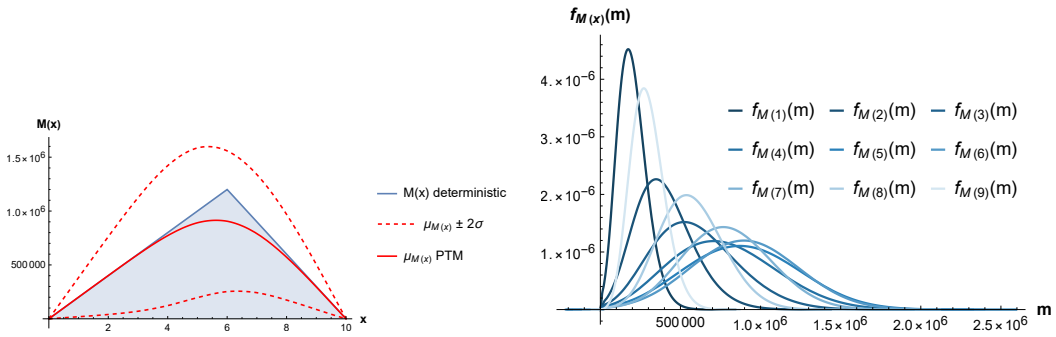

(a) (b)

Figure 3: Bending moment.

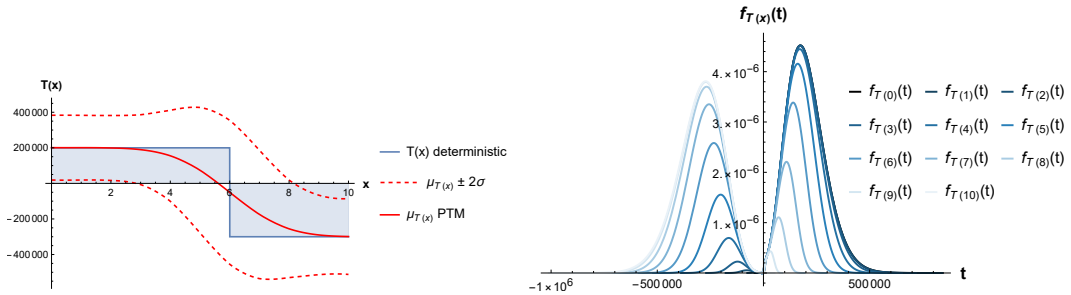

(a) (b)

Figure 4: Shear force.

load. We have obtained the first probability density function of the deflection, the bending moment, and the shear force of the beam, providing a numerical example. In future works, we are going to consider the load a delta-correlated process given by $q(x) = \sum_{i=1}^{N(x)} F_i R_{-1}(x - X_i)$, where $N(x)$ denotes a Poisson counting process. In this setting, we will apply the theoretical findings to different types of beams.

Acknowledgments

This work has been supported by the grant PID2020-115270GB-I00 funded by MCIN/AEI/10.13039/501100011033, the grant AICO/2021/302 (Generalitat Valenciana), and the Ferran Sunyer i Balaguer foundation (Borses FSB 2023).

References

[1] A. Öchsner, *Classical Beam Theories of Structural Mechanics*. Springer, 2021.

[2] T. Soong, *Random Differential Equations in Science and Engineering*. New York: Academic Press, 1973.

International Conference on Mathematical Analysis and Applications in Science and Engineering
ICMA^{2}SC'24
ISEP Porto-Portugal, June 20 - 22, 2024

A PSO-Based Calibration Method to Estimate Random Model Parameters Distribution in Antibiotic Resistance Dynamics

Carlos Andreu-Vilarroig[1⋆] **Juan Carlos Cortés**[1]
Rafael-Jacinto Villanueva[1]

[1] Instituto de Matemática Multidisciplinar, Universitat Politècnica de València, Valencia, Spain

[1⋆]caranvi1@upv.es

Abstract: In this work, we propose a method to empirically estimate the joint probability density function of the parameters of a random model of the antibiotic resistance dynamics of a microorganism. The main idea is to calibrate the model using the Particle Swarm Optimization evolutionary algorithm, and subsequently select a subset of PSO evaluations that equidistributively represent the parameter search space and that whose solutions better fit the data, taking into account their randomness. As a case study, we have calibrated the model with available data series on the resistance proportion of colistin-resistant *Acinetobacter baumannii* in the Valencian Community, Spain, during the 2012-2020 period. The results show how our method allows us to generate a multivariate distribution for the random model parameters which does not respond to any a priori prefixed family of probability distributions, and whose samples adequately fit the data and capture their uncertainty.

keywords: Antibiotic resistance; Antibiotic consumption; Mathematical modelling; Particle Swarm Optimization; PDF estimation.

MSC2020: 68W50; 92D30; 37H10.

1 Introduction

Antibiotic resistance is one of the most concerning public health threats in recent years [5]. The emergence of resistance to new antibiotic drugs, which has been particularly fast in recent years, has been mainly linked to the non-rational consumption of antibiotics [3]. In addition, the inherently random nature of the biological process and the method of collecting and recording data add a certain randomness to the dynamics of the process. In this context, although it has been little applied, mathematical modelling with uncertainty can be particularly useful to describe and predict the antibiotic resistance dynamics over time.

A random model describing the dynamics of the antibiotic resistance proportion $p(t)$ considering antibiotic consumption [1] is given by equation

$$p(t,\omega) = \frac{e^{\tau(\omega)A(t)-\Delta\kappa(\omega)t+\theta_0(\omega)}}{e^{\tau(\omega)A(t)-\Delta\kappa(\omega)t+\theta_0(\omega)}+1} \in (0,1),\ \omega \in \Omega, \tag{1}$$

where $\tau(\omega)$, $\Delta\kappa(\omega)$ and $\theta_0(\omega)$ are the random model parameters (random variables) defined on a common complete probability space $(\Omega, \mathcal{F}_\Omega, \mathbb{P})$, and where $A(t) = \int_0^\infty a(s)ds \in \mathbb{R}^+$ is the cumulative antibiotic consumption function over time, i.e., $A(t) = \int_0^\infty a(s)ds$, where $a(t)$ is the antibiotic consumption at time t. This equation is derived from a model describing the competition between two strains of an infectious microorganism – sensitive and resistant to the antibiotic – and where $p(t)$ is the proportion of resistant population over the total population. As can be seen from equation, antibiotic consumption kills sensitive strains at a τ rate and causes resistant strains to predominate, increasing resistance proportion. Also, in the absence of antibiotic, the fitness difference between strains $\Delta\kappa$ gives a competitive advantage to the sensitive strain, causing a resistance proportion decay. A more detailed explanation of the model can be found in [4, 1].

In this work, we propose a method of estimating an empirical joint probability density function (joint PDF) of the random vector of model parameters $(\tau, \Delta\kappa, \theta_0) \sim f(\tau, \Delta\kappa, \theta_0)$ that best explains a real-world scenario and fully characterises the random model. As our reference, we have the data series on monthly colistin-resistant *Acinetobacter baumannii* proportions $\{p_{t_i}\}_{i=0}^n$ in 2012-2020 period in Valencian Community, Spain, and the colistin consumption data series $\{a_{t_i}\}_{i=0}^n$ in Spain for the same period. As the consumption data present a linear increasing trend, the antibiotic consumption function $a(t)$ has been estimated by fitting a linear regression model to the data.

For the model parameters calibration, the Particle Swarm Optimisation algorithm (PSO) was applied, taking as particles the parameters vectors $(\tau, \Delta\kappa, \theta_0)$, and as the fitness function the sum of squared errors (SEE) between resistance proportions of the model $p(t_i; \tau, \Delta\kappa, \theta_0)$ and that of the data series p_{t_i}. After the PSO execution, all evaluations of the algorithm were sorted according to their error. To select a subset of solutions that equally represents all regions of the parameter search space explored by the PSO, a k-means on the log fitness function was applied, and a similar number of solutions was taken from each cluster. Finally, from this error-ordered set of n solutions, the $2, 3, \ldots, n$ first solutions have been successively selected, its standard deviation and 95% confidence interval have been computed for all times t_i, and two objectives have been evaluated for each subset [2, 1]: *(i)* the inside-outside error, which is the sum of the distances between the points of the resistance proportion data series that fall outside the confidence interval and their nearest confidence interval (if a point falls inside the confidence interval, its distance is 0), and *(ii)* the standard deviation error, which is the sum of all the standard deviations for all times t_i. Note that, the more points the confidence interval of the solution set captures, the smaller the inside-outside error. Likewise, the standard deviation tends to increase with the number of simulations.

With both objectives, a Pareto front is finally established, and the knee point, which represents the k first solutions, is chosen. With these k first solutions, a representative distribution of model parameter vectors $(\tau, \Delta\kappa, \theta_0)$ is available, from which an empirical joint PDF can be estimated using a kernel density function.

2 Results and discussion

The PSO calibration performed 899 970 evaluations. The global best was for the parameter set $(\tau, \Delta\kappa, \theta_0)^* = (0.01, 0.43, -3.27)$, with a SEE of 0.0990. Clustering with k-means detected that the optimal number of clusters/regions of distinct minima was 4 (following the elbow method), and that the smallest cluster with less solutions – the one with the worst error – contained 46 solutions, while the second worst cluster had 550. To give a greater variety of solutions, the mean between the two smaller clusters sizes, 280 solutions, was taken from each cluster (except from the smallest, which could only take 46 solutions), giving a subset of $n = 1400$ representative

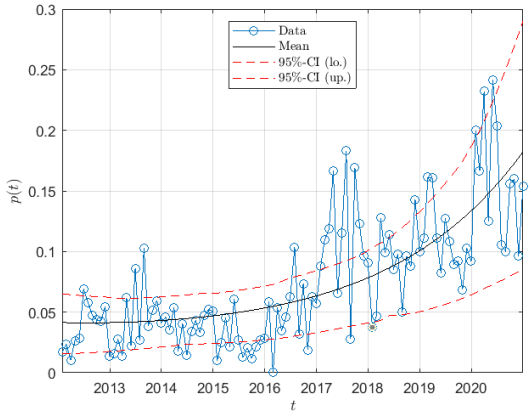

(a) Mean and 95% confidence interval of the selected $k = 650$ solutions vs. data series

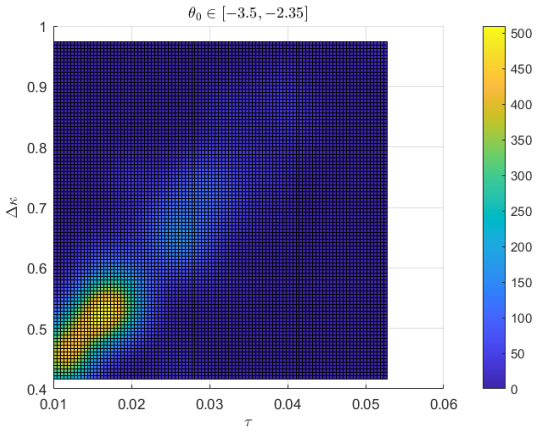

(b) Empirical joint PDF $f(\tau, \Delta\kappa, \theta_0)$ (kernel density estimation) of the model parameters for $\theta_0 \in [-3.5, 2.35]$.

solutions of all the parameters search space, ordered by their error. After calculating the inside-outside error and standard deviation objective functions for each subsets of $2, 3, \ldots, n$ solutions, the knee point of the Pareto front was taken at $k = 650$ solutions.

Figure 1a shows the mean and 95% confidence interval of the 650 selected model simulations against the resistance proportion data series. Here we can see how well the mean fits the data, and how the 95% confidence interval captures the randomness of the data. Additionally, Figure 1b shows the empirical joint PDF (computed by kernel density estimation) of the model parameters τ and $\Delta\kappa$, for $\theta_0 \in [-3.5, -2.35]$ interval, where most of the selected solutions are found. From the joint PDF it is clear that the values of τ and $\Delta\kappa$ parameters are highly correlated, as expected: given the data series, if τ takes larger values, $\Delta\kappa$ will have to take larger values, in order to compensate for excess of antibiotic resistance growth generated by a higher τ and maintain a good fit with the data.

3 Conclusions and future work

In this work, we have successfully calibrated and found an empirical joint PDF of the parameters of a random antibiotic resistance model, taking into account antibiotic consumption. The main advantage of this method is that it is not necessary to assume any family of PDF of the parameters a priori. This is especially relevant when the parameters are correlated, and the PDF shapes do not follow classical distributions. On the other hand, its main limitation is that the estimation of the joint PDF will strongly depend on the parameter regions that the PSO optimization algorithm has explored. Therefore, to achieve a more robust joint PDF estimation, it is recommended to do several calibrations with the PSO, initializing the particles in different regions of the parameters search space.

Acknowledgments

This work has been supported by the grant PID2020-115270GB–I00 funded by MCIN/AEI/10.13039/501100011033.

References

[1] Juan A Aledo, Carlos Andreu-Vilarroig, Juan-Carlos Cortés, Juan C Orengo, and Rafael-Jacinto Villanueva. A random mathematical model to describe the antibiotic resistance depending on the antibiotic consumption: the acinetobacter baumannii colistin-resistant case in valencia, spain. *International Journal of Computer Mathematics*, pages 1–18, 2024.

[2] C. Andreu-Vilarroig, J. Ceberio, J.-C. Cortés, F. Fernández de Vega, J.-I. Hidalgo, and R.-J. Villanueva. Evolutionary approach to model calibration with uncertainty: an application to breast cancer growth model. *Proceedings of the Genetic and Evolutionary Computation Conference Companion*, pages 1895–1901, 2022.

[3] B.G. Bell, F. Schellevis, E. Stobberingh, H. Goossens, and M. Pringle. A systematic review and meta-analysis of the effects of antibiotic consumption on antibiotic resistance. *BMC Infectious Diseases*, 14(1):1–25, 2014.

[4] M. Sundqvist. Reversibility of antibiotic resistance. *Upsala Journal of Medical Sciences*, 119(2):142–148, 2014.

[5] World Health Organization (WHO). Antimicrobial resistance. `https://www.who.int/news-room/fact-sheets/detail/antimicrobial-resistance`, 2020. [Accessed: 21/07/2022].

International Conference on Mathematical Analysis and Applications in Science and Engineering
ICMA^{2}SC'24
ISEP Porto-Portugal, June 20 - 22, 2024

SGD method for the simultaneous controllability of a parameter-dependent finite dimensional linear model

U. Biccari[2] **A. Navarro-Quiles**[1⋆] **E. Zuazua**[2,3]

[1] Department of Statistics and Operational Research, Universitat de Valencia, Dr. Moliner 50, 46100, Burjassot
[2] Chair of Computational Mathematics, Fundacion Deusto, Avenida de las Universidades 24, 48007 Bilbao, Basque Country, Spain
[3] Chair for Dynamics, Control, Machine Learning and Numerics, Alexander von Humboldt-Professorship, Department of Mathematics, Friedrich-Alexander-Universitat Erlangen-Nurnberg, Erlangen 91058, Germany

[2⋆]ana.navarro@uv.es

Abstract: We apply the classical Stochastic Gradient Descent for the simultaneous control of a parameter-dependent finite dimensional lineal model. We address the challenge of computing simultaneous controls by minimizing a cost functional. This functional is defined as the sum of individual costs associated with each realization of the system. We compare the performances of this stochastic approach, in terms of their computational complexity, with the classical Gradient Descent algorithm, and we discuss the advantages and disadvantages of each methodology. In agreement with well-established results in the machine learning context, we show how the SGD can significantly reduce the computational burden when treating control problems depending on a large amount of parameters. This is corroborated by numerical experiments.

keywords: Parameter-dependent systems; simultaneous control; stochastic optimization

MSC2020: 34H05, 49J15, 49M29, 90C15, 93E20

1 Introduction

In this work, we investigate the use of stochastic optimization methods for the simultaneous control of parameter-dependent systems. Our focus is on the classical Stochastic Gradient Descent (SGD) method.

SGD method is a stochastic variant of the Gradient Descent (GD) optimization technique. Instead of using the full dataset to compute the gradient of f, SGD approximates the minimum of f by employing a gradient-based methodology that uses an estimate obtained from a randomly selected batch of a few components of the dataset. Thus, it is an iterative method for optimizing functions that are expressed as a sum of different observations within a dataset:

$$\begin{aligned} \widehat{u} &= \min_{u\in\mathbb{R}^N} f(u) \\ f(u) &:= \frac{1}{n}\sum_{i=1}^{n} f_i(u). \end{aligned} \tag{1}$$

This approach was originally proposed in 1951, in the seminal work of Robbins and Monro [1]. But, it has recently received renewed attention, especially in the Machine Learning and Big Data communities. In this work we will make use of it in the context of parameter-dependent optimal control problems. In particular, for the computation of simultaneous controls, in which one is interested on controlling all states simultaneously.

In many real-life applications, models that depend on various parameters are used to describe physical phenomena with diverse realizations. The computation of simultaneous controls typically involves conducting numerous simulations of the dynamics under consideration, across a wide range of parameters. With each new parameter configuration, a distinct equation must be solved, leading to a computationally demanding task, particularly when dealing with parameter sets of considerable size.

For this reason, many analytical and computational techniques have been developed in the past years in order to speed up the simulation of parameterized optimal control problems. Among others, we can mention Proper Orthogonal Decomposition (see, e.g., [2]) or other more general Reduced Basis approaches ([3]).

2 Results and discussion

In this study, we will examine the concept of simultaneous control, which involves designing a single control function capable of guiding all the diverse realizations of a given parameter-dependent system towards a predetermined final target.

In particular, we will consider the parameter-dependent finite-dimensional linear model

$$\begin{cases} x'_\nu(t) = \mathbf{A}_\nu x_\nu(t) + \mathbf{B}u(t), \quad 0 < t < T, \\ x_\nu(0) = x^0, \end{cases} \tag{2}$$

in which $x_\nu(t) \in L^2(0,T;\mathbb{R}^N)$, $N \geq 1$, denotes the state, the $N \times N$ matrix $\mathbf{A}_\nu$ describes the dynamics, and the function $u(t) \in L^2(0,T;\mathbb{R}^M)$, $1 \leq M \leq N$, is the M-component control acting on the system through the $N \times M$ matrix $\mathbf{B}$.

All along this paper, $\nu \in \{\nu_1, \nu_2, \ldots, \nu_{|\mathcal{K}|}\} =: \mathcal{K}$, where $|\mathcal{K}|$ denotes the cardinality of $\mathcal{K}$, is a random parameter following a probability law μ, with $(\mathcal{K}, \mathcal{F}, \mu)$ the corresponding complete probability space. Moreover, the initial datum x^0 is assumed to be independent of ν.

The aim of simultaneous control is to find a unique *parameter-independent* control u such that, at time $T > 0$, the corresponding solution x_ν of (2) satisfies

$$x_\nu(T) = x^T, \quad \nu \in \mathcal{K} \quad \mu - \text{a. e.} \tag{3}$$

for some desired final target $x^T \in \mathbb{R}^N$.

Our objective is to compute simultaneous controls by minimizing a cost functional, which is constructed by minimizing the distance between the solution of system (2) and the desired final target x^T.

We compare the computational complexity of the SGD with traditional optimization techniques such as the GD algorithm, highlighting the strengths and weaknesses of each.

3 Conclusions and Future work

Consistent with findings in the machine learning field, our study demonstrates that SGD algorithm can significantly reduce computational burdens for control problems with a large number

of parameters. These findings are validated through numerical experiments. This is so because, although the GD algorithm is expected to have exponential convergence, in practical applications this rate may dramatically deteriorate as a consequence of the bad conditioning of the problem one aims to solve. We conclude our discussion by proposing some avenues for future research that are relevant to the topics covered in this contribution.

1. *Comparison with the greedy methodology.* In the context of the control of parameter-dependent linear equations, in the recent years several authors proposed the employment of the so-called *greedy methodology*, [4]. This approach aims to approximate the dynamics and controls by identifying the most meaningful realizations of the parameters. In certain situations, it showed up to be a very efficient way to largely reduce the overall computational complexity. Therefore, a comparison of the greedy and stochastic approaches applied to parameter-dependent models, with the final aim of clearly determine in which situation one technique is preferable with respect to the other, becomes a very relevant issue.

2. *Simultaneous controllability of PDE models.* The study in this contribution is focused on the scenario of simultaneous controllability of finite-dimensional ODE systems. It would be interesting to extend our analysis to the infinite-dimensional PDE context. This, however, may be a cumbersome task. As a matter of fact, in the PDE setting, simultaneous controllability is a quite delicate issue because of the appearance of peculiar phenomena which are not detected at the ODE level.

Acknowledgments

This project has received funding from the European Research Council (ERC) under the European Union's Horizon 2020 research and innovation programme (Grant Agreement No: 694126-DyCon). The work of U.B. and E.Z. is partially supported by the Grant PID2020-112617GB-C22 KILEARN of MINECO (Spain) and the Elkartek Grant KK-2020/00091 CONVADP of the Basque Government. E.Z. has been funded by the Alexander von HumboldtProfessorship program, the ModConFlex Marie Curie Action, HORIZON-MSCA-2021-DN-01, the COST Action MAT-DYN-NET, the Transregio 154 Project "Mathematical Modelling, Simulation and Optimization Using the Example of Gas Networks" of the DFG, grants PID2020-112617GB-C22 and TED2021-131390B-I00 of MINECO (Spain), and by the Madrid Goverment - UAM Agreement for the Excellence of the University Research Staff in the context of the V PRICIT (Regional Programme of Research and Technological Innovation). The work of A.N.Q. has been supported by the Spanish grant PID2020-115270GB-I00 granted by MCIN/AEI/10.13039/501100011033.

References

[1] H. Robbins, S. Monro, A stochastic approximation method, The Annals of Mathematical Statistics, **22** (1951), 400–407.

[2] K. Ito, S.S. Ravindran, A reduced basis method for control problems governed by PDEs, Control and estimation of distributed parameter systems, Springer (1998), 153–168.

[3] K. Ito, S.S. Ravindran, Reduced basis method for optimal control of unsteady viscous flows, International Journal of Computational Fluid Dynamics, **15** (2001), 97–113.

[4] M. Lazar, E. Zuazua, Greedy controllability of finite dimensional lineal systems, Automatica, **74** (2016), 327–340.

International Conference on Mathematical Analysis and Applications in Science and Engineering
ICMA^{2}SC'24
ISEP Porto-Portugal, June 20 - 22, 2024

Uncertainty study in a 0-D SCR Model for NOx Emissions

Marcos Llamazares López[1⋆] **José Ponce Hernando**[2] **Juan-Carlos Cortés**[1]
Rafael-Jacinto Villanueva[1] **Carlos Guardiola García**[2]

[1] I.U. de Matemática Multidisciplinar, UPV València, Spain
[2] Departamento de Máquinas y Motores Térmicos, UPV València, Spain

[1⋆]marllalo@upvnet.upv.es

Abstract: Selective Catalytic Reduction (SCR) systems are integral in reducing nitrogen oxides (NOx) emissions from diesel engines, achieved by injecting a urea-based reductant agent into the exhaust stream. In this study, extensive experimental data from real engine tests is utilized to calibrate a 0-Dimensional model of the SCR system, encompassing its physical and chemical behavior. The model is characterized by equations governing NH3 and NOx concentrations, with parameters optimized using a Particle Swarm Optimization (PSO) algorithm. Due to the model's complexity and experimental uncertainties, a statistical approach is proposed, yielding mean values with Confidence Intervals (CIs) to capture experimental variability. Notably, the model outputs NOx emissions as time series data, with confidence bands encompassing approximately 90% of the experimental data. Future work will focus on maintaining consistent parameter sets across experiments for improved model calibration efficacy.

keywords: SCR; PSO; Uncertainty.

MSC2020: 49-XX; 34-XX; 92-XX.

1 Introduction

Selective Catalytic Reduction (SCR) [1] system is a technology used to reduce nitrogen oxides (NO_x) emissions from diesel engines. It involves injecting a urea-based reductant agent into the exhaust stream, which reacts with NO_x over a catalyst to convert it into nitrogen (N_2) and water (H_2O), two harmless substances.

In this work, experimental data from hundreds of experiments conducted in a real engine is utilized in order to calibrate a 0-Dimensional model [2] of the SCR system. This model includes the physical and chemical behavior of the SCR and presents the following differential equations [3]

$$\frac{\mathrm{d}C_{\mathrm{NH_3}}}{\mathrm{d}t} = \Omega \cdot \Omega_A \cdot (r_{\mathrm{a}} - r_{\mathrm{d}}) + SV \cdot (C_{\mathrm{NH_3,us}} - C_{\mathrm{NH_3}}), \tag{1}$$

$$\frac{\mathrm{d}C_{\mathrm{NO}}}{\mathrm{d}t} = \Omega \cdot \Omega_A \cdot (r_{\mathrm{std}} - r_{\mathrm{fst}}) + SV \cdot (C_{\mathrm{NO,us}} - C_{\mathrm{NO}}), \tag{2}$$

$$\frac{\mathrm{d}C_{\mathrm{NO_2}}}{\mathrm{d}t} = \Omega \cdot \Omega_A \cdot (r_{\mathrm{fst}} - r_{\mathrm{slw}}) + SV \cdot (C_{\mathrm{NO_2,us}} - C_{\mathrm{NO_2}}), \tag{3}$$

where Ω (mg) is the ammonia (NH_3) accumulation capacity in the SCR, $\Omega_A \in [0, 1]$ is the ageing factor of the SCR, C_X (ppm) are the output concentrations of the chemical species, and $C_{X,\mathrm{us}}$ the upstream concentrations, for $X = \mathrm{NH_3}$, NO, $\mathrm{NO_2}$. SV (m/s) is the spatial velocity of the gasses flowing through the SCR and follows the equation

$$SV = \frac{4\pi R \cdot T_{\mathrm{SCR}} \cdot \dot{m}_{\mathrm{exh}}}{\rho \cdot \pi \cdot D_{\mathrm{SCR}}^2}, \tag{4}$$

where $R = 8.31\mathrm{J/mol}$ is the universal gas constant, T_{SCR} (K) is the temperature of the SCR, $\dot{m}_{\mathrm{exh}}$ (kg/s) is the mass flow of the gasses in the SCR, ρ ($\mathrm{kg/m^3}$) is the density of the gasses and D_{SCR} (m) is the diameter of the SCR. The parameters r_{a}, r_{d}, r_{std}, r_{fst}, r_{slw} are the reaction rates of the chemical species and are calculated with the following Arrhenius equations [4]

$$r_a = k_a \cdot e^{\frac{-E_{\mathrm{a}}}{R}\left(\frac{1}{T_{\mathrm{SCR}}} - \frac{1}{T_{\mathrm{ref}}}\right)} \cdot C_{\mathrm{NH_3}} \cdot (1 - \theta_{\mathrm{NH_3}}), \tag{5}$$

$$r_{\mathrm{d}} = k_{\mathrm{d}} \cdot e^{\frac{-E_{\mathrm{d}}}{R} \cdot (1 - \alpha \cdot \theta_{\mathrm{NH_3}})\left(\frac{1}{T_{\mathrm{SCR}}} - \frac{1}{T_{\mathrm{ref}}}\right)} \cdot \theta_{\mathrm{NH_3}}, \tag{6}$$

$$r_{\mathrm{std}} = k_{\mathrm{std}} \cdot e^{\frac{-E_{\mathrm{std}}}{R}\left(\frac{1}{T_{\mathrm{SCR}}} - \frac{1}{T_{\mathrm{ref}}}\right)} \cdot C_{\mathrm{NO}} \cdot \theta^*_{\mathrm{NH_3}} \cdot \left(1 - e^{\frac{-\theta_{\mathrm{NH_3}}}{\theta^*_{\mathrm{NH_3}}}}\right), \tag{7}$$

$$r_{\mathrm{fst}} = k_{\mathrm{fst}} \cdot e^{\frac{-E_{\mathrm{fst}}}{R}\left(\frac{1}{T_{\mathrm{SCR}}} - \frac{1}{T_{\mathrm{ref}}}\right)} \cdot C_{\mathrm{NO}} \cdot C_{\mathrm{NO_2}} \cdot \theta_{\mathrm{NH_3}}, \tag{8}$$

$$r_{\mathrm{slw}} = k_{\mathrm{slw}} \cdot e^{\frac{-E_{\mathrm{slw}}}{R}\left(\frac{1}{T_{\mathrm{SCR}}} - \frac{1}{T_{\mathrm{ref}}}\right)} \cdot C_{\mathrm{NO_2}} \cdot \theta_{\mathrm{NH_3}}, \tag{9}$$

where $\theta_{\mathrm{NH_3}}$ (%) is the NH_3 storage in the SCR; $\theta^*_{\mathrm{NH_3}}$ is a correction due to the NH_3 surface coverage ratio; T_{ref} (K) is the reference temperature of the SCR; E_{a}, E_{d}, E_{std}, E_{fst}, E_{slw} are activation energies for each reaction rate; and k_{a}, k_{d}, k_{std}, k_{fst}, k_{slw}, α are constants.

Finally, reaction rates are related by the following equation

$$\frac{\mathrm{d}\theta_{\mathrm{NH_3}}}{\mathrm{d}t} = r_{\mathrm{a}} - r_{\mathrm{d}} - r_{\mathrm{std}} - 2r_{\mathrm{fst}} - \frac{4}{3}r_{\mathrm{slw}} \tag{10}$$

The calibration of this model is conducted using a Particle Swarm Optimization (PSO) algorithm [5] where E_{a}, E_{d}, E_{std}, E_{fst}, E_{slw}, k_{a}, k_{d}, k_{std}, k_{fst}, k_{slw}, $\theta^*_{\mathrm{NH_3}}$, Ω and D_{SCR} are calibration parameters.

Due to the extreme complexity of the model, and the uncertainties associated with the experimental data, a deterministic calibration of the model is unfeasible. Therefore, this work proposes a statistical approach where the output of the model is a mean value with a Confidence Interval (CI), with the objective of capturing the maximum number of points of the experimental data.

2 Results and discussion

The statistical analysis conducted in this study relies on the outcomes derived from the PSO algorithm utilized for the model calibration. This algorithm stores the parameter sets employed for each model evaluation, along with their respective error. Subsequently, a database can be generated, showcasing the top-performing results sorted by error. These results serve as a representative sample of the parameter space, pinpointing the minimum in the error function. From

this database, mean values and confidence intervals are then computed.

The most relevant results obtained from the model consist of the NOx emissions generated by the SCR, presented as time series data. Figure 1 displays two sub-samples of experimental data alongside the model's output depicted as mean values and CI of 95%. Notably, the confidence bands encompass the majority of the experimental data, capturing approximately 90% of the data for these sub-samples.

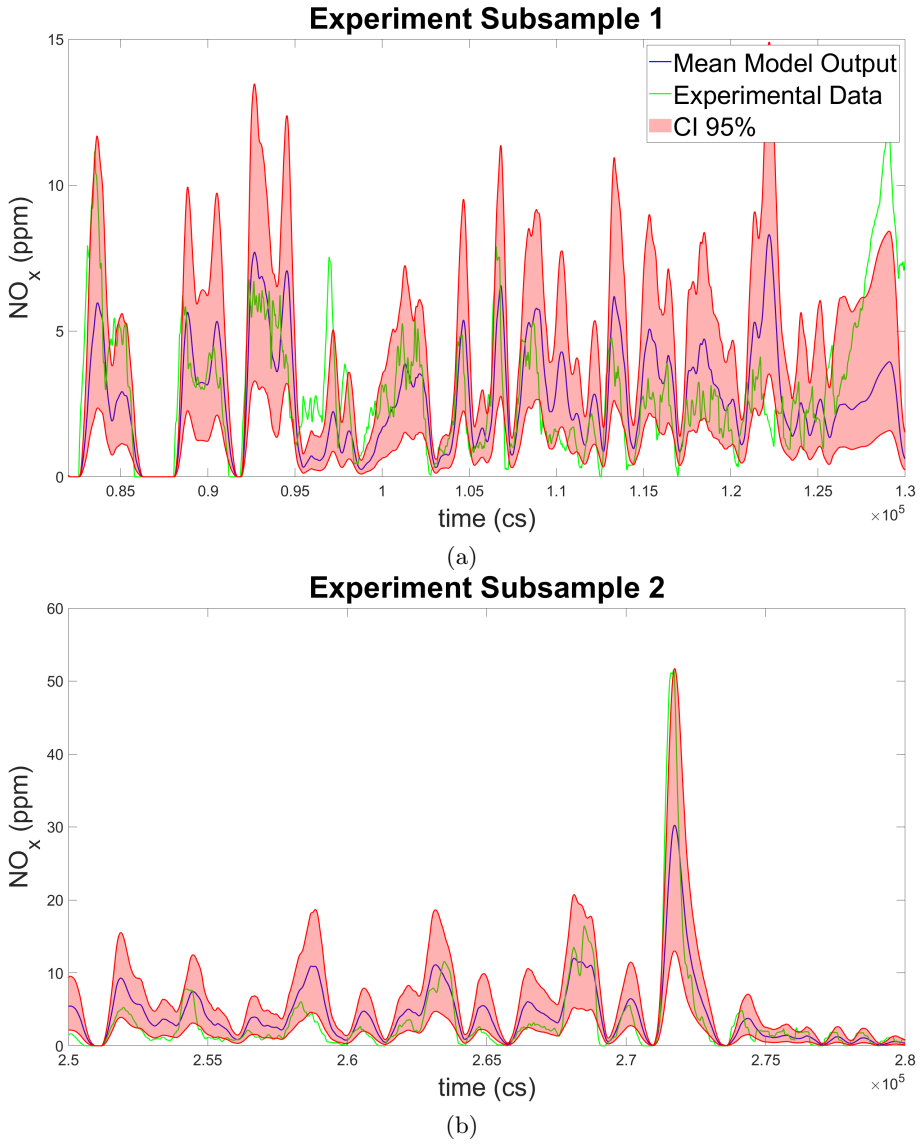

Figure 1: Statistical study of the Mean and the CI 95% of the model's output for the NO_x emissions time-series. The blue time-series represents the Mean of the model's output, the green time-series represents the experimental data and the red band represents the CI 95%.

3 Conclusions and Future work

The results of this study have achieved the objective of providing a response for the model outputs, in the form of mean and confidence interval, which encompass the majority of the points from the experimental data.

However, these results were attained by separately calibrating the multiple experiments that comprise the experimental dataset. Given the model's characteristics, it is preferable for the parameter set to remain consistent across all experiments. Consequently, this will be the focus of future work.

Acknowledgments

This work was supported by grant PDC2022-133527-100 financed by MCIN/AEI/10.13039501100011033 and the European Union Next Generation EU/PRTR.

References

[1] Willems F, Mentink P, Kupper F and Van den Eijnden E., Integrated emission management for cost optimal EGR-SCR balancing in diesels, IFAC Proceedings Volumes, Vol. 46 no 21, pp. 711–716, 2013.

[2] Upadhyay D. and Van Nieuwstadt M., Modeling of urea SCR catalyst with automotive applications, ASME 2002 International Mechanical Engineering Congress and Exposition.

[3] Mora Perez, J., Control-oriented modelling and diagnostics of diesel after-treatment catalysts, PhD UPV, 2018.

[4] Busca G, Lietti L, Ramis Go and Berti F., Chemical and mechanistic aspects of the selective catalytic reduction of NOx by ammonia over oxide catalysts: A review, Applied Catalysis B: Environmental, Vol. 18 no 1, pp. 1–36, 1998.

[5] Marini, Federico and Walczak, Beata, Particle swarm optimization (PSO). A tutorial, Chemometrics and Intelligent Laboratory Systems 149 2015.

Likelihood Measures for Classifying Frequency Response Functions from Posture Control Experiments

Vittorio Lippi[1,2⋆]

[1] Institut für Digitalisierung in der Medizin, University of Freiburg, Germany
[2] Neurozentrum der Uniklinik Freiburg, University of Freiburg, Germany

[1⋆]vittorio.lippi@uniklinik-freiburg.de

Abstract: The frequency response function (FRF) is an established way to describe the outcome of experiments in posture control literature. The FRF is an empirical transfer function between an input stimulus and the induced body segment sway profile, represented as a vector of complex values associated with a vector of frequencies. Having obtained an FRF from a trial with a subject, it can be useful to quantify the likelihood it belongs to a certain population, e.g., to diagnose a condition or to evaluate the human likeliness of a humanoid robot or a wearable device. In this work, a recently proposed method for FRF statistics based on confidence bands computed with Bootstrap will be summarized, and, on its basis, possible ways to quantify the likelihood of FRFs belonging to a given set will be proposed.

keywords: Frequency response function; Bootstrap; confidence bands.

MSC2020: 49-XX; 34-XX; 92-XX.

1 Introduction

The Frequency Response Function (FRF) is a common representation used in posture control experiments to describe the relationship between an input stimulus and the resulting body movement. The FRF is defined as an empirical transfer function. The FRF is a complex function of frequency, and its structure must be considered when performing statistical analysis to assess differences between groups of FRFs. An example of FRF is shown in Fig.1 with a brief explanation. For an extended description of FRFs in posture control that goes beyond the limits of this paper, see [7, 5]. The set used in the example is from [5]. Typically, statistics are performed by defining a scalar variable to be studied, such as the norm of the difference between FRFs, or by considering the components independently. However, this approach can introduce an arbitrary metric that may have little connection with the experiment. To properly consider the nature of the FRF, a method oriented to complex functions should be used. One method, based on random field theory[6], considers the two components (imaginary and real) as independent variables[3]. **The intuition** that an FRF, being a transfer function, can be transformed into a real-time domain signal without loss of information suggests an approach. On such real functions, the confidence bands can be defined using methods for continuous functions[1]. As the Fourier transform of a transfer function represents the impulsive response of a system, such function is referred to as *pseudo-impulse-response*, PIR. The method to use Bootstrap to define confidence bands on PIRs to perform statistics on FRFs is described in [4], and the code is available at [2]. The average PIR $\bar{x}(t) = 1/N \sum_N^{i=1} x_i(t)$ and the STD is $\hat{\sigma}_x(t) = \sqrt{(1/(N-1)) \sum_N^{i=1} |x_i(t) - \bar{x}(t)|^2}$. With these values, the prediction band

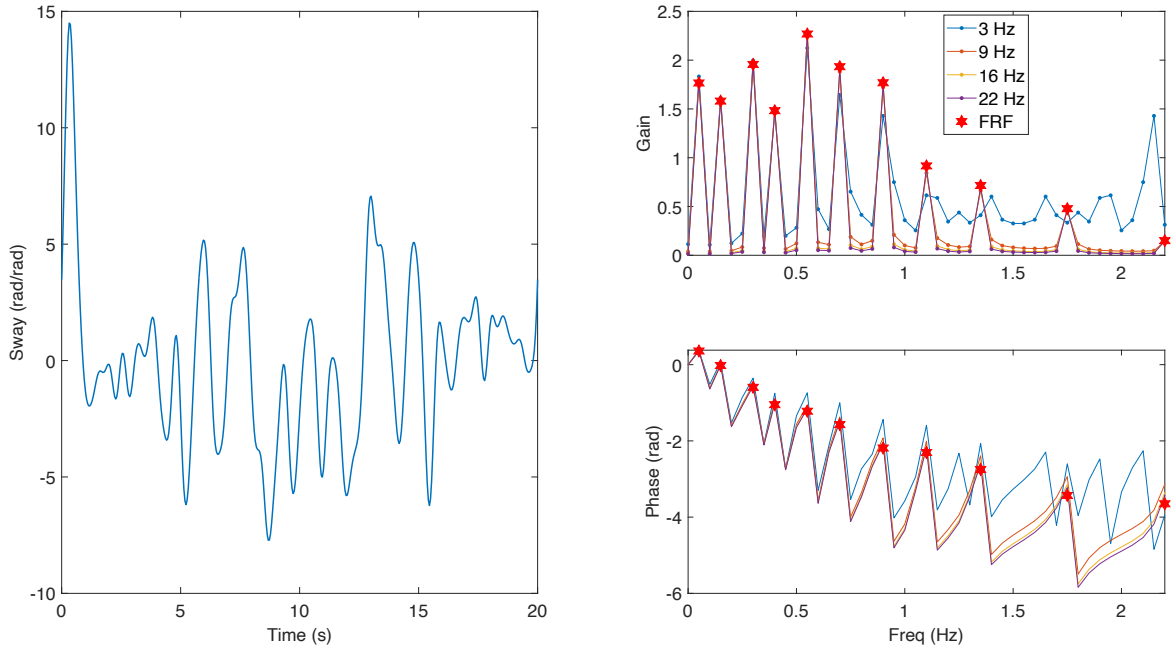

Figure 1: The PIR on the left, the FRF (red stars), and the DFT of the PIR (colored lines). The PIR is computed with eq. $x_i(t) = \sum_{k=1}^{M} \Re(H_{i,k}) \cos(2\pi\varphi_k t) + \Im(H_{i,k}) \sin(2\pi\varphi_k t)$. The peculiarity of the FRF as proposed in posture control analysis is that the frequencies $\varphi = [0.05,\ 0.15,\ 0.3,\ 0.4,\ 0.55,\ 0.7,\ 0.9,\ 1.1,\ 1.35,\ 1.75,\ 2.2]Hz$ are not equally spaced. The associated H is obtained as the average of the empirical transfer function over a range of frequencies. This was defined in for better plotting the signal[7]. Different sample times are tested to reconstruct the FRF through a DFT. The period of the PIR is defined as the inverse of the greatest common divisor of the frequencies in φ; the sample time used in the examples is set to ten times the highest frequency in φ, i.e., 22 Hz. Notice how the gain tends to converge to zero between the peaks.

can be defined for a new draw from the FRF distribution H_{n+1}, and hence for the respective PIR $x_{N+1}(t)$. With the desired confidence level $\alpha\%$, the constant C_p is defined to obtain the probability $P[\max_t |x_{N+1}(t) - \bar{x}(t)|/\hat{\sigma}_x(t) \leq C_p] = \alpha/100$ and the prediction band for a new FRF is $\bar{x}(t) \pm C_p \cdot \hat{\sigma}_x(t)$. This work proposes a further application of such bands to quantify the degree to which a sample FRF belongs to a distribution.

Can likeness be defined as likeliness? The need to classify FRFs in groups arises when the posturography is used to diagnose a condition or to assess the human likeness of a behavior produced by a robot humanoid or wearable as in [5]. A modified version of the function computing the prediction band from [4] can compute the minimal band, including a given sample. See fig. 2. This works by reversing the process used to compute the prediction band, i.e., finding the confidence α given the distance from the mean: the maximum distance between the test sample and the estimated mean in the histogram produced by the Bootstrap as shown in 2. Further measures can be defined as the empirical estimation of the probability density function (pdf) and cumulative density function (cdf). Here, they are defined on the distance $D = \int (x_i(t) - \hat{x}(t))^2 dt$, but the principle can be generalized. The cdf $F(x) = P[X \leq x]$is computed empirically with a bootstrap (a mean and a STD are provided for the estimate), the pdf is computed by approximating $f(x) = dF/dx \approx \Delta F(x)/(x_2 - x_1)$ where $\Delta F(x)$ is a fixed quantity (here $1/10$ of the number of samples N) and x_1 and x_2 are the values of x found in the vector ordered distances D produced by the Bootstrap moving back and forward of $N \cdot \Delta F(x)$ positions.

2 Results and Discussion and Conclusions

To show how the measures work, a sample has been removed from the set, and its minimum prediction band has been computed based on the rest of the samples, as shown in Fig. 2. The estimated probability

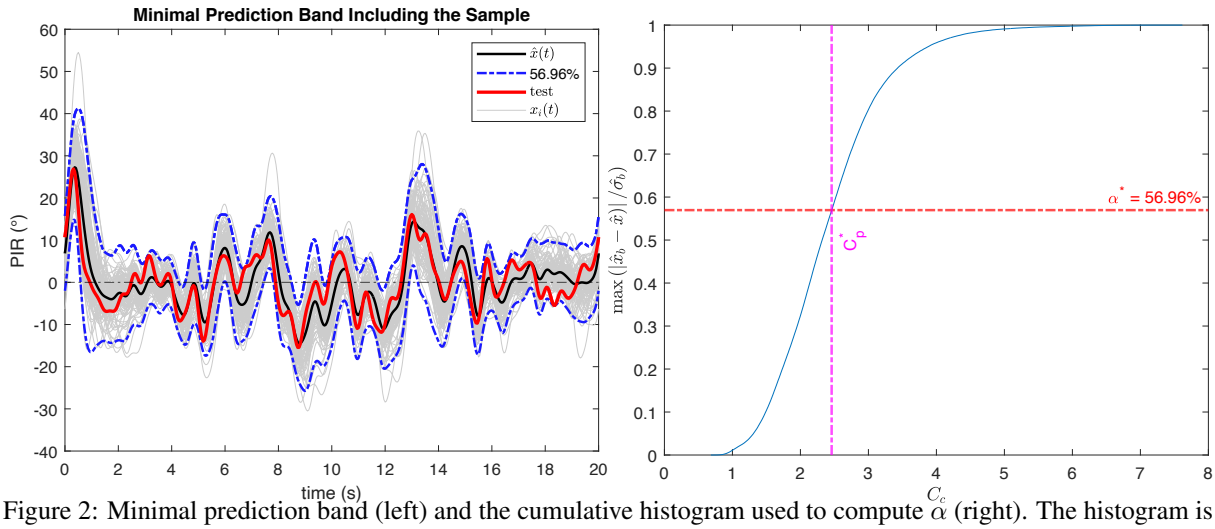

Figure 2: Minimal prediction band (left) and the cumulative histogram used to compute α (right). The histogram is produced by the Bootstrap approximating the probability as $\frac{1}{B}\sum_{b=1}^{B}\left[I\left(\max_t\left(\frac{|\hat{x}(t)-\hat{x}^b(t)|}{\hat{\sigma}_x^b(t)}\right)\right)\leq C_c\right]$. In this case, opposite to what is done in [4], the C_p is known (inferred using the tested sample), and the α is the quantity to be computed.

distribution features were: cdf ($F = 0.6075$, $\sigma_F = 0.0523$) and pdf ($f = 0.0042$, $\sigma_f = 0.0016$). Future work will consist of the application of these measures to quantify the difference between groups of patients (e.g., polyneuropathy) and a control group of healthy subjects and in humanoid robotics assessment to evaluate the human likeness of the produced motion pattern as an alternative to the pseudo-statistics based on the covariance matrix that was proposed in [5] with all the advantages discussed in the introduction. The computation of cdf and pdf can be used to evaluate the likelihood of the sample. Strictly speaking, they are based on an arbitrary scalar value (the integral of the distance). This may be useful as a further test to be performed on a sample after comparing it with a prediction band with a fixed α to have a continuous score beside the binary result of such a comparison with the band. Both measures can compare the output of different identified posture control models and decide the best one representing the sample population.

References

[1] M. W. Lenhoff, T. J. Santner, J. C. Otis, M. G. Peterson, B. J. Williams, and S. I. Backus. Bootstrap prediction and confidence bands: a superior statistical method for analysis of gait data. *Gait & Posture*, 9(1):10–17, 1999.

[2] V. Lippi. FRF statistics library. https://github.com/mcuf-idim/FRF-statistics.

[3] V. Lippi. Random Field Theory for Testing Differences Between Frequency Response Functions in Posturography. In *9th International Posture Symposium*, pages 130–134. Frontiers, 2023.

[4] V. Lippi. Bootstrap prediction and confidence bands for frequency response functions in posturography. forthcoming.

[5] V. Lippi, C. Maurer, and T. Mergner. Human-likeness indicator for robot posture control and balance. In *International Conference on Robotics, Computer Vision and Intelligent Systems*, pages 98–113. Springer, 2020.

[6] T. C. Pataky, M. A. Robinson, J. Vanrenterghem, R. Savage, K. T. Bates, and R. H. Crompton. Vector field statistics for objective center-of-pressure trajectory analysis during gait, with evidence of scalar sensitivity to small coordinate system rotations. *Gait & posture*, 40(1):255–258, 2014.

[7] R. Peterka. Sensorimotor integration in human postural control. *J. Neurophysiol.*, 88(3):1097–1118, 2002.

International Conference on Mathematical Analysis and Applications in Science and Engineering
ICMA^{2}SC'24
ISEP Porto-Portugal, June 20 - 22, 2024

Dynamics of the classical chemostat model with real random kinetics*

Javier López-de-la-Cruz

Departamento de Matemática Aplicada a las TIC
Escuela Técnica Superior de Ingenieros Informáticos
Campus de Montegancedo, Universidad Politécnica de Madrid
28660 Boadilla del Monte, Madrid, Spain

javier.lopez.delacruz@upm.es

Abstract: In this talk, the classical chemostat model with random kinetics will be derived, where the random terms will be bounded. The existence and uniqueness of non-negative global solution of the random systems will be proved, as well as the existence of deterministic compact absorbing and attracting sets. After that, the attracting sets will be studied in detail, which will allow us to provide conditions to ensure either the extinction or the persistence of the species, the most important goal in practice. In addition, several numerical simulations will be displayed to illustrate the theoretical results. Finally, we will compare our results with the ones obtained when using the standard Wiener process (the common way to model randomness in the literature), which is unbounded with probability one, to show the huge differences, particularly from the biological point of view.

keywords: chemostat model; real noise; Monod; Haldane.

MSC2020: 34A12; 34F05; 34D99.

1 Introduction

The chemostat is a laboratory device used for growing microorganisms in cultured environments. It has many applications in real life, for example, it can be used to study genetically altered organisms (see [13, 14]), models of mammalian large intestine (see [7, 8]), waste-water treatment processes (see [6, 11]) and models in ecology (see [10, 12]).

The classical chemostat device consists of three tanks, the *feed bottle*, the *culture vessel* and the *collection vessel*, which are interconnected by pumps. The substrate is stored in the feed bottle and pumped from there to the culture vessel, where it is consumed by the species. In order to keep the volume of the culture vessel constant, another flow is pumped from the culture vessel to the collection vessel. Then, the goal is to investigate the dynamics of the substrate and the species in the culture vessel.

*Symposium #9: Modeling with Differential and Difference Equations with Uncertainties

The mathematical model describing the evolution of the concentration of both the substrate and the species is given by the following differential system

$$\frac{ds}{dt} = D(s_{in} - s) - \mu(s)x, \tag{1}$$

$$\frac{dx}{dt} = -Dx + \mu(s)x, \tag{2}$$

where $s = s(t)$ and $x = x(t)$ denote the concentration of substrate and species, respectively, $s_{in} > 0$ describes the input concentration of substrate, $D > 0$ represents the dilution rate and $\mu = \mu(s)$ is a function describing how the species consume the substrate.

The most usual consumption function in the literature is knows as *Monod* and it is given by the following expression

$$\mu(s) = \frac{\mu_0 s}{a + s}, \tag{3}$$

where $\mu_0 > 0$ is the maximum specific growth rate of the microorganisms and $a > 0$ is the Monod constant.

Nevertheless, practitioners claim that some populations of species reduce the consumption of substrate if the substrate is at high concentration. In this case, it is necessary to consider an alternative consumption function, known as *Haldane*, which is given as follows

$$\mu(s) = \frac{\mu_0 s}{a + s + \dfrac{s^2}{k_i}},$$

where k_i is the inhibition constant and the rest of the parameters are defined as in (3).

The classical chemostat model (1)-(2) describes real devices in a good manner, in fact, it has been widely studied by researchers from many different areas, not only Mathematics, but also Biology, Ecology, Engineering..., specially when the consumption function is Monod (much less in the Haldane case), see [9] and references therein. Nevertheless, system (1)-(2) is deterministic and then it assumes strong restrictions, since real devices are subject to randomness.

For instance, the smooth consumption functions μ in (1)-(2) are typically derived as approximations of dotted lines from experimental data obtained in the laboratory, i.e., the value of $\mu(s)$ cannot be determined in real life for each value s in a deterministic way. As a consequence, we propose to consider random consumption functions in the classical chemostat model (1)-(2).

2 Random perturbations on the consumption function

Among the different ways to model random perturbations on the consumption function of the species in the classical chemostat model (1)-(2), our idea is to replace the maximum specific growth rate of the species μ_0 by $\mu_0 + \Phi(z^*(\theta_t\omega))$, where $\Phi(z^*(\theta_t\omega))$ denotes a bounded noise, motivated by the fact that real perturbations are usually random but bounded. This term concerning the bounded noise will be explained in detailed during the talk.

This way of modeling noise has proved to provide us a very powerful tool to model randomness in deterministic systems, not only in the case of the chemostat, but also in other models in

population dynamics (see [1]). On the one hand, this way of modeling random perturbations allows us to derive very realistic mathematical models that describe real phenomena in a very loyal way. On the other hand, the bounded noise allows us to provide conditions under which the consumer species persist, which is the most important goal in practice.

In this talk, firstly, the classical chemostat model with bounded random kinetics will be derived carefully. Then, the existence and uniqueness of non-negative global solution of the random systems will be proved, as well as the existence of deterministic compact absorbing and attracting sets. After that, the attracting sets will be studied in detail, which will allow us to provide conditions to ensure either the extinction or the persistence of the species, the most important goal in practice. In addition, we will prove that the absorbing and attracting sets are deterministic, i.e., do not depend on the realization of the noise, which is a very nice property. Moreover, several numerical simulations will be displayed to illustrate the theoretical results.

Finally, we will compare our results with the ones obtained when using the standard Wiener process (the common way to model randomness in the literature), which is unbounded with probability one, to show the huge differences, particularly from the biological point of view. In fact, even though the common mathematical study (using the theory of random dynamical systems and pullback convergence, see [4]) is totally accurate to handle the mathematical problem, several important drawbacks appear from the biological point of view when using the standard Wiener process. For instance, some state variables can take negative values, which is completely unrealistic in practice, and it is not possible to ensure the persistence of the species (see, for example, [2, 3]). This is an evidence of the importance of considering a bounded noise when modeling randomness in real systems.

The talk will be based on [5], which has been recently published.

References

[1] T. Caraballo, R. Colucci, J. López-de-la-Cruz, and A. Rapaport. A way to model stochastic perturbations in population dynamics models with bounded realizations. *Communications in Nonlinear Science and Numerical Simulation*, 77:239–257, oct 2019.

[2] T. Caraballo, M. J. Garrido-Atienza, and J. López-de-la-Cruz. *Some Aspects Concerning the Dynamics of Stochastic Chemostats*, volume 69, chapter 11, pages 227–246. Springer International Publishing, Cham, 2016.

[3] T. Caraballo, M. J. Garrido-Atienza, J. López-de-la-Cruz, and A. Rapaport. Modeling and analysis of random and stochastic input flows in the chemostat model. *Discrete & Continuous Dynamical Systems - Series B*, 24(8):3591–3614, 2018.

[4] T. Caraballo and X. Han. *Applied Nonautonomous and Random Dynamical Systems, Applied Dynamical Systems*. Springer International Publishing, 2016.

[5] T. Caraballo, J. López-de-la-Cruz, and V. Caraballo-Romero. Effects of real random perturbations on monod and haldane consumption functions in the chemostat model. *Mathematics and Computers in Simulation*, 218:482–497, 2024.

[6] G. D'Ans, P. Kokotovic, and D. Gottlieb. A nonlinear regulator problem for a model of biological waste treatment. *IEEE Transactions on Automatic Control*, 16(4):341–347, aug 1971.

[7] R. Freter. *Human Intestinal Microflora in Health and Disease*, chapter Mechanisms that control the microflora in the large intestine, pages 33–54. Academic Press, New York, 1983.

[8] R. Freter. An understanding of colonization of the large intestine requires mathematical analysis. *Microecology and Therapy*, 16:147–155, 1986.

[9] J. Harmand, C. Lobry, A. Rapaport, and T. Sari. *The Chemostat: Mathematical Theory of Micro-organisms Cultures*. Wiley, Chemical Engineering Series. John Wiley & Sons, Inc., Jun 2017.

[10] J. Kalff and R. Knoechel. Phytoplankton and their dynamics in oligotrophic and eutrophic lakes. *Annual Review of Ecology and Systematics*, 9(1):475–495, nov 1978.

[11] J. W. M. La Rivière. Microbial ecology of liquid waste treatment. In *Advances in Microbial Ecology*, volume 1, pages 215–259. Springer US, 1977.

[12] E. Rurangwa and M. C. J. Verdegem. Microorganisms in recirculating aquaculture systems and their management. *Reviews in Aquaculture*, 7(2):117–130, feb 2015.

[13] G. Stephanopoulos, R. Aris, and A.G. Fredrickson. A stochastic analysis of the growth of competing microbial populations in a continuous biochemical reactor. *Mathematical Biosciences*, 45(1-2):99–135, jul 1979.

[14] Frank Stewart and Bruce Levin. The population biology of bacterial plasmids: A priori conditions for the existence of conjugationally transmitted factors. *Genetics*, 87:209–228, 11 1977.

International Conference on Mathematical Analysis and Applications in Science and Engineering
ICMA^{2}SC'24
ISEP Porto-Portugal, June 20 - 22, 2024

A Magnus-based integrator for multidimensional parametric semi-linear stochastic oscillators

H. de la Cruz[1⋆] **R. D'Ambrosio**[2] **C. Scalone**[2]

[1] School of Applied Mathematics. FGV, Praia de Botafogo 190, Rio de Janeiro, Brazil
[2] Dipartimento di Ingegneria e Scienze dell'Informazione e Matematica, University of L'Aquila, Italy

[1⋆]hugo.delacruz@fgv.br

Abstract: We introduce a numerical method for solving second-order multidimensional stochastic differential equations of the form $\ddot{x} = A(t)x + f(t,x) + \Omega(t)\xi(t)$, describing a class of nonlinear oscillators with non-constant frequency, perturbed by white noise $\xi(t)$. The proposed scheme takes advantages of the Magnus approach to construct an stable integrator for this kind of stochastic oscillators. Its convergence properties are rigorously analyzed and selected numerical experiments on relevant stochastic oscillators in applications are carried out, confirming the effectiveness and the competitive behaviour of the proposed method, in comparison with standard integrators in the literature. This work extends recent results obtained by the authors in [1].

keywords: stochastic differential equations; stochastic oscillators; Magnus expansions, exponential integrators.

MSC2020: 65C30; 34F05; 60H35.

References

[1] R. D'Ambrosio, H. de la Cruz, C. Scalone, *A Magnus-based integrator for Brownian parametric semi-linear oscillators*, Applied Mathematics and Computation **472** (2024), 128610.

[2] H. de la Cruz, J. C. Jimenez, J. P. Zubelli, *Locally linearized methods for the simulation of stochastic oscillators driven by random forces*, BIT Numer. Math **57** (2017), 123–151.

[3] M. Gitterman, *The noisy oscillator, The first hundred years, from Einstein until now*. World Scientific (2005)

[4] A. Iserles, H.Z. Munthe-Kaas, S.P. NÃ¸rsett, A. Zanna, *Lie group methods*, Acta Numer. **9** (2005), 1–148.

International Conference on Mathematical Analysis and Applications in Science and Engineering
ICMA^{2}SC'24
ISEP Porto-Portugal, June 20 - 22, 2024

Probabilistic Analysis of Random Differential Equations with Nonlinearities via the Equivalent Linearization Technique

J.-C. Cortés[1] **E. López-Navarro**[1] **J.-V. Romero**[1] **M.-D. Roselló**[1]
J.F. Valencia Sullca[1⋆]

[1] Instituto Universitario de Matemática Multidisciplinar,
Universitat Politècnica de València, Camino de Vera s/n, Valencia/Spain

⋆joavasu2@teleco.upv.es

Abstract: The objective of this paper is to study the stochastic equivalent linearization method in order to obtain approximations of the main statistics of the steady-state solution of a class of nonlinear oscillators that depends on both the position and velocity, and driven by a stationary Gaussian stochastic process. Furthermore, we approximate the higher-order moments and the correlation function of the solution. Finally, we include a number of numerical experiments to illustrate the theoretical analysis, showing good results.
texto

keywords: Nonlinear oscillator; stationary Gaussian process; stochastic equivalent linearization

MSC2020: 49-XX; 34-XX; 92-XX.

1 Introduction

It is well known that vibratory systems have been widely studied and it is a topic of interest in several areas, such as Physics and Engineering [1]. In particular, nonlinear oscillators are described by nonlinear differential equations of the form

$$\ddot{X}(t) + 2\beta\dot{X}(t) + \epsilon g(X(t), \dot{X}(t)) + \omega_0^2 X(t) = Y(t), \quad t > 0, \tag{1}$$

where $X(t)$ denotes the position of the oscillatory system, $\beta > 0$ is the damping constant, $\omega_0 > 0$ is the undamped angular frequency, and ϵ is the perturbation that affects to the nonlinear term $g(X(t), \dot{X}(t))$. Finally, the term $Y(t)$ is an external source term acting upon the system usually called the input. This term characterizes the external vibrations of affecting the oscillator and often depends on factors that are not known in a deterministic form but stochastically. This motivates to treat $Y(t)$ as a stochastic process rather than a deterministic function.

To obtain reliable approximations of the Equation (1) with $Y(t)$ being a random function, the stochastic perturbation technique has been successfully applied in dealing with nonlinear oscillators subject to random vibrations [2]. Recently, in [3] has been proposed a family of nonlinear oscillators in the case that ϵ represents a small parameter and the nonlinear function is given by $g(t) = X^2(t)\dot{X}(t)$ (so depending on both the spatial position and the velocity), and whose forcing source is driven by a mean-square stationary zero-mean Gaussian process.

However, one of the main limitations of the stochastic perturbation technique is that it is restricted to problems with small nonlinearities ($|\epsilon| \ll 1$). To overcome this drawback, an effective method consists in constructing reliable approximations of Equation (1) in the case that the perturbation parameter (ϵ) is not necessary very small is the equivalent linearization technique [4].

This technique is based on the construction of an equivalent linear equation

$$\ddot{X}(t) + 2\beta_e \dot{X}(t) + \omega_e^2 X(t) = Y(t), \tag{2}$$

from the nonlinear differential equation

$$\ddot{X}(t) + f\left(X(t), \dot{X}(t)\right) = Y(t), \quad t > 0. \tag{3}$$

To this end, one minimizes the stochastic mean-square error defined by

$$\mathbb{E}\left\{(N(t))^2\right\} = \mathbb{E}\left\{\left[2\beta_e \dot{X}(t) + \omega_e^2 X - f\left(X(t), \dot{X}(t)\right)\right]^2\right\}, \tag{4}$$

where $\mathbb{E}\{\cdot\}$ denotes the expectation operator.

As previously indicated, in this contribution we consider model (1) with $g(t) = X^2(t)\dot{X}(t)$. Then, $f\left(X(t), \dot{X}(t)\right) = 2\beta\dot{X}(t) + \epsilon X^2(t)\dot{X}(t) + \omega_0^2 X(t)$. Then, it can be seen that in order for the error function be minimized, the parameters β_e and ω_e^2 must solve the following system of algebraic equations

$$\begin{aligned} 2(\beta_e - \beta)\,\mathbb{E}\left\{(\dot{X}(t))^2\right\} + \left(\omega_e^2 - \omega_0^2\right)\mathbb{E}\left\{X(t)\dot{X}(t)\right\} - \epsilon\mathbb{E}\left\{(X(t))^2(\dot{X}(t))^2\right\} = 0, \\ \left(\omega_e^2 - \omega_0^2\right)\mathbb{E}\left\{(X(t))^2\right\} + 2(\beta_e - \beta)\,\mathbb{E}\left\{X(t)\dot{X}(t)\right\} - \epsilon\mathbb{E}\left\{(X(t))^3\dot{X}(t)\right\} = 0. \end{aligned} \tag{5}$$

It can be seen that the stochastic process $X(t)$ is a mean-square differentiable stationary, zero-mean Gaussian process which is independent of $\dot{X}(t)$. Using these properties, one can obtain the following values of β_e and ω_e^2,

$$\begin{aligned} \beta_e &= \frac{2\beta + \epsilon E\left\{(X(t))^2\right\}}{2} = \frac{2\beta + \epsilon\sigma_X^2}{2}, \\ \omega_e^2 &= \omega_0^2, \end{aligned} \tag{6}$$

where it should be noticed that σ_X^2 does not depend on t since $X(t)$ is stationary.

The variance, σ_X^2, is obtained from the spectral density function, $S_{YY}(\omega)$, of $Y(t)$ and the frequency response, $y(i\omega)$, of the equivalent linear system given by Equation (2), [5]. Also, we can approximate $y(i\omega)$ by setting $\epsilon = 0$, in order to obtain $\beta_e = \beta$, $\omega_e = \omega_0$ and $\sigma_{X_0}^2$,

$$\begin{aligned} \sigma_X^2 &= \int_0^\infty S_{XX}(\omega)\mathrm{d}\omega = \int_0^\infty |y(i\omega)|^2 S_{YY}(\omega)\mathrm{d}\omega, \\ \sigma_{X_0}^2 &= \int_0^\infty |y_0(i\omega)|^2 S_{YY}(\omega)\mathrm{d}\omega = \int_0^\infty \frac{1}{\left(\omega_0^2 - \omega^2\right)^2 + 4\omega^2\beta^2} S_{YY}(\omega)\mathrm{d}\omega. \end{aligned} \tag{7}$$

The relation between the power spectral density of $Y(t)$ and the correlation function Γ_{YY} is given by

$$S_{YY}(\omega) = \frac{1}{\pi}\int_{-\infty}^\infty e^{-i\omega\tau}\Gamma_{YY}(\tau)\mathrm{d}\tau. \tag{8}$$

It can be proven that the solution of the linear Equation (2) is given by

$$X(t) = \int_0^\infty h(s)Y(t-s)\mathrm{d}s, \tag{9}$$

where

$$h(t) = \begin{cases} \left(\omega_e^2 - \beta_e^2\right)^{-\frac{1}{2}} e^{-\beta_e t} \sin\left[\left(\omega_e^2 - \beta_e^2\right)^{\frac{1}{2}} t\right], & \text{if } t > 0, \\ 0, & \text{if } t \leq 0, \end{cases} \tag{10}$$

is the impulse response function for the underdamped case, $\beta_e^2 < \omega_e^2$.

It can be proved that the statistical moments of odd order of the solution $X(t)$ are null

$$\mathbb{E}\left\{(X(t))^n\right\} = 0, \quad n = 1, 3, 5, \ldots \tag{11}$$

and the second-order moment for $X(t)$ is given by

$$\mathbb{E}\left\{X^2(t)\right\} = \int_0^\infty h(s) \int_0^\infty h(s_1)\Gamma_{YY}(s - s_1)\mathrm{d}s_1\mathrm{d}s. \tag{12}$$

As the first moment of $X(t)$ verifies $\mathbb{E}\left\{X(t)\right\} = 0$, then, the covariance and correlation functions of $X(t)$ coincide, namely, $\mathbb{C}\left\{X(t_1)X(t_2)\right\} = \Gamma_{XX}(\tau),\ \tau = |t_1 - t_2|$, where the correlation function of $X(t)$ is given by

$$\Gamma_{XX}(\tau) = \int_0^\infty h(s) \int_0^\infty h(s_1)\Gamma_{YY}(\tau - s_1 + s)\mathrm{d}s_1\mathrm{d}s. \tag{13}$$

2 Results and discussion

Let us consider as input excitation, $Y(t)$, the Gaussian white-noise process with zero-mean and correlation function $\Gamma_{YY}(\tau) = \pi S_0 \delta(\tau)$, where $\delta(\tau)$ is the Dirac delta function and $S_0 = \dfrac{1}{200\pi}$ is the noise power. Also, we have considered the following parameters $\beta = 0.05$ and $\omega_e^2 = \omega_0^2 = 1$, where $\sigma_{X_0}^2 = 0.025$. Then, the second-order moment is determined by

$$\mathbb{E}\left\{(X(t))^2\right\} = \frac{1}{40 + 10\epsilon}. \tag{14}$$

It can be proven the following approximation of the correlation function,

$$\Gamma_{XX}(\tau) = \begin{cases} f_1(\tau) & \text{if } \tau \geq 0, \\ f_2(\tau) & \text{if } \tau < 0, \end{cases} \tag{15}$$

$$f_1(\tau) = e^{\left(-\frac{1}{20} - \frac{\epsilon}{80}\right)\tau} \left[\frac{\cos\left(\sqrt{\frac{399}{400} - \frac{\epsilon}{800} - \frac{\epsilon^2}{6400}}\,\tau\right)}{40 + 10\epsilon} + \frac{\sin\left(\sqrt{\frac{399}{400} - \frac{\epsilon}{800} - \frac{\epsilon^2}{6400}}\,\tau\right)}{400\sqrt{\frac{399}{400} - \frac{\epsilon}{200} - \frac{\epsilon^2}{1600}}} \right], \tag{16}$$

$$f_2(\tau) = \frac{e^{\left(\frac{1}{20} + \frac{\epsilon}{80}\right)\tau}}{-255360 - 63520\epsilon + 120\epsilon^2 + 10\epsilon^3} \left[\left(-6384 + 8\epsilon + \epsilon^2\right) \cos\left(\sqrt{\frac{399}{400} - \frac{\epsilon}{800} - \frac{\epsilon^2}{6400}}\,\tau\right) + 40(4 + \epsilon)\sqrt{\frac{399}{100} - \frac{\epsilon}{200} - \frac{\epsilon^2}{1600}} \sin\left(\sqrt{\frac{399}{400} - \frac{\epsilon}{800} - \frac{\epsilon^2}{6400}}\,\tau\right) \right] \tag{17}$$

In Figure 1, it is shown the graphical representation of the correlation function, $\Gamma_{XX}(\tau)$, given in expression (15) for different values of ϵ.

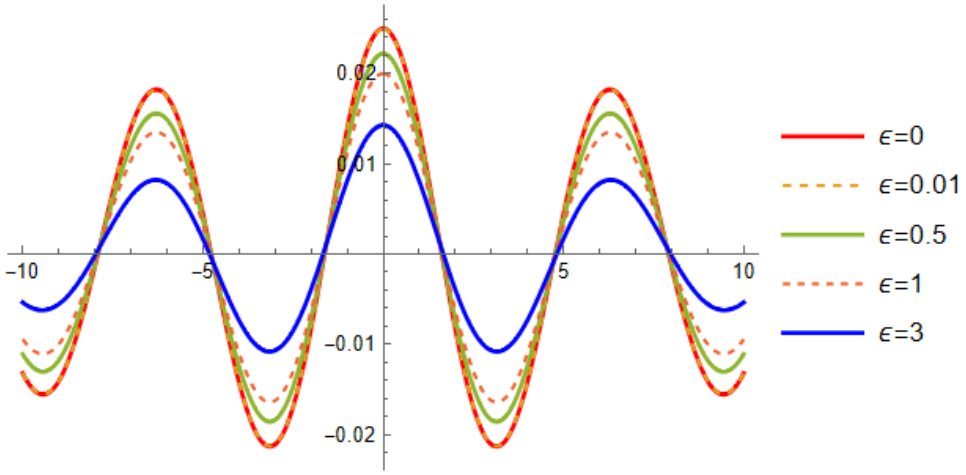

Figure 1: Correlation function $\Gamma_{XX}(\tau)$ of $X(t)$ for different values of ϵ.

3 Conclusions and future work

In this paper we have studied oscillators subject to perturbations on the nonlinear term that depends both upon the position and the velocity and driven by mean-square differentiable stationary zero-mean Gaussian processes. Additionally, we have obtained reliable approximations of the main statistics of the steady-state by means of the stochastic equivalent linearization technique. Finally, we have illustrated the case where the input excitation is a Gaussian white-noise stochastic process. In our future research, we plan to tackle this type of problems for other stochastic nonlinear oscillators.

Acknowledgments

This work has been supported by the grant PID2020-115270GB-I00 funded by MCIN/AEI/10.13039/501100011033.

References

[1] A. Yildirim, H. Askari, Z. Saadatnia, M. KalamiYazdi, and Y. Khan, Analysis of nonlinear oscillations of a punctual charge in the electric field of a charged ring via a Hamiltonian approach and the energy balance method. Computers & Mathematics with Applications, **62**(1) (2011), 486–490.

[2] S. H. Crandall, Perturbation techniques for random vibration of nonlinear systems. The Journal of the Acoustical Society of America, **35**(11) (1963), 1700-1705.

[3] J.-C. Cortés, E. López-Navarro, J.-V. Romero, and M.-D. Roselló, Approximating the density of random differential equations with weak nonlinearities via perturbation techniques. Mathematics, **9**(3) (2021), 204.

[4] T. K. Caughey, Equivalent linearization techniques. The Journal of the Acoustical Society of America, **35**(11) (1963), 1706–1711.

[5] T. T. Soong, Random differential equations in science and engineering (Book). New York, Academic Press, Inc. (Mathematics in Science and Engineering), **103** (1973).

The Linear Quadratic Optimal Control Problem for Stochastic Systems Controlled by Impulses

Vasile Drăgan [♭,♮], and Ioan-Lucian Popa[♢,†1]

(♭) Institute of Mathematics "Simion Stoilow" of the Romanian Academy,
P.O.Box 1-764, RO-014700, Bucharest, Romania
(♮) Academy of Romanian Scientists,
3 Ilfov, 050044, Bucharest, Romania
(♢) Department of Computing, Mathematics and Electronics, Faculty of Computing and Engineering,
"1 Decembrie 1918" University of Alba Iulia, Romania.
(†) Faculty of Mathematics and Computer Science, Transilvania University of Braşov,
Iuliu Maniu Street 50, 500091, Braşov, Romania.

1 Abstract

Consider the impulsive controlled linear stochastic system (ICLSS) described by:

$$dx(t) = A_0x(t)dt + A_1x(t)dw(t), \quad kh < t \leq (k+1)h \tag{1a}$$
$$x(kh^+) = \mathcal{A}_0x(kh) + \mathcal{B}_0u(k) + w_d(k)(\mathcal{A}_1x(kh) + \mathcal{B}_1u(k))$$
$$h > 0 \text{ is given }, \quad k \in \mathbb{Z}_+ = \{0, 1, \ldots\} \tag{1b}$$
$$x(0) = x_0 \tag{1c}$$

where $x(t) \in \mathbb{R}^n$ is the state vector of the system and $u(k) \in \mathbb{R}^m$ are the control parameters. In (1a) $\{w(t)\}_{t\geq 0}$ is an 1-dimensional standard Wiener process (or process of the Brownian motion) defined on a given probability space $(\Omega, \mathfrak{F}, \mathcal{P})$ and in (1b), $\{w_d(k)\}_{k\in\mathbb{Z}_+}$ is a sequence of independent random variables with zero mean and variance 1.

In (1) the controls $u(k)$ act at impulsive time instances $\tau_k = kh$, $k = 0, 1, \ldots$. That is why, this kind of system are called **impulsive controlled systems.**

$\mathcal{U}_{ad}(t_0, x_0)$ will be named the set of **admissible controls** associated to the initial pair (t_0, x_0).

To the pair formed by the ICLSS (1) and the set of admissible controls $\mathcal{U}_{ad}(t_0, x_0)$, we associate the quadratic functional:

$$J(t_0, \infty, x_0; \mathbf{u}) = \int_{t_0}^{\infty} \mathbb{E}[x_{\mathbf{u}}^\top(t)MX_{\mathbf{u}}(t)]dt \tag{2}$$
$$+ \sum_{k=\kappa(t_0)}^{\infty} \mathbb{E}[x_{\mathbf{u}}^\top(kh)M_dx_{\mathbf{u}}(kh) + 2x_{\mathbf{u}}^\top(kh)L_du(k) + u^\top(k)R_du(k)]$$

[1] lucian.popa@uab.ro

where $x_{\mathbf{u}}(\cdot) = x(\cdot; t_0, x_0, \mathbf{u})$.

We analyze the problem of the existence of the maximal solution and the stabilizing solution of a backward jump matrix linear differential equation.

Also, we shall provide conditions which guarantee that the optimal control problem under consideration is well posed and attainable. The main tool is a backward jump matrix matrix linear differential equation with the Riccati type jumping operator.

References

[1] B. Oksendal, Stochastic Differential Equations, Springer-Verlag Berlin Heidelberg, 2003

[2] A. Friedman, Stochastic Differential Equations and Applications, Volume 1, Academic Press, 1975.

[3] V. Drăgan, S. Aberkane, I.-L. Popa, T. Morozan, On the stability and mean square stabilization of a class of linear stochastic systems controlled by impulses, Ann. Acad. Rom. Sci. Ser. Math. Appl. 15 (2023) 45–72.

[4] V. Drăgan, T. Morozan, A.-M. Stoica, Mathematical Methods in Robust Control of Linear Stochastic Systems, Springer-Verlag New York, 2013.

[5] V. Drăgan, T. Morozan, A.-M. Stoica, Mathematical Methods in Robust Control of Discrete-Time Linear Stochastic Systems, Springer-Verlag New York, 2010. 10

International Conference on Mathematical Analysis and Applications in Science and Engineering
ICMA^{2}SC'24
ISEP Porto-Portugal, June 20 - 22, 2024

Maximum likelihood estimation of the Power Normal distribution parameters

Rui Gonçalves[1⋆]

[1] LIAAD INESC Tec, Faculdade de Engenharia, Universidade do Porto, Portugal.

[1⋆]rjasg@fe.up.pt

Abstract: The Power Normal (PN) distribution family was found by Goto et al. while investigating the original observations after applying the inverse Box-Cox transformation. This family includes the normal and log-normal distributions. In this paper we present an algorithm to calculate and refine the exact Maximum Likelihood Estimation (MLE) of the PN distribution parameters.

keywords: Power normal; Maximum likelihood; Box-Cox transformation

MSC2020: 46N30; 47N40.

1 Introduction

The Box-Cox (BC) transformation [6] of a positive random variable is defined by

$$Y = \begin{cases} \frac{X^\lambda - 1}{\lambda} & if \lambda \quad \neq 0 \\ \ln(X) & if \lambda \quad = 0, \end{cases}$$

where λ is the transformation parameter. Note that is required data is positive and this implies Y to be not lower than $-1/\lambda$. If the transformation is successful Y is normal or approximately normal. So, the question to be asked is, what is the probability distribution of the original variable (X)? The answer is the PN distribution first mentioned in [4] where the authors also give expressions for the moments in the form of power series. The PN probability density function (PDF) is given by,

$$f_X(x) = \frac{x^{\lambda-1}}{\sigma A(\lambda, \mu, \sigma)} \phi\left(\frac{x^{(\lambda)} - \mu}{\sigma}\right) \tag{1}$$

where $x > 0$ and $x^{(\lambda)} = \frac{x^\lambda - 1}{\lambda}$. We define $A(\lambda, \mu, \sigma)$ to be $\Phi(k)$, 1, $\Phi(k)$ if λ is > 0, $= 0$ and < 0, respectively. Note that Φ is the standard normal cumulative distribution function (CDF). The inverse BC transformation of a truncated normal variable Y for $\lambda \neq 0$ is $X = (\lambda Y + 1)^{\frac{1}{\lambda}}$. The PN distribution in the Box-Cox transformation context is also extensively studied in [7] where are calculated and presented expressions for the mean and variance. For practitioners carry out a data transformation it is required to estimate the parameters λ, μ and σ. In ordinary Box-Cox transformation, λ the Maximum Likelihood Estimation (MLE) assume $A(k) = 1$ implicitly

and the analysis was restricted to constancy of the error variance, near normality and the independence of the transformed observations. Although this could be enough to achieve near normality it is not appropriate if we aim to identify the particular PN on the original scale of the observations. In other words, to obtain consistent estimators of the parameters λ, μ and σ it is necessary to take $A(k)$ into account, [5].

2 Exact ML estimation of the parameters

If n observations $x_1, x_2, \cdots x_n$ have PN distribution with parameters λ, μ and σ then the log likelihood is given by,

$$\ln(L(x;\lambda,\mu,\sigma)) = -\frac{n}{2}\ln(2\pi) - \frac{n}{2}\ln(\sigma^2) - \frac{1}{2}\sum_{i=1}^{n}\left(\frac{x_i^{(\lambda)}-\mu}{\sigma}\right)^2 + (\lambda-1)\sum_{i=1}^{n}\ln(x_i) - n\ln(A(k)).$$

The procedure to estimate the parameters λ, μ and σ setting $A(k)=1$ by ordinary ML is referred to as the method M_1 proposed by [6], following [5]. For this approach the mu and σ^2 are the mean and variance of $X_i^{(\lambda)}$ $i = 1 \cdots n$. The second method which takes $A(k)$ in consideration we call the M_2 method. Remember that method M_2 assumes that the transformed data to be truncated normal distributed. For this method the estimators of μ and σ are consistent. In this work, for we will focus on the case $0 < \lambda < 1$ and in that case we may replace $A(k)$ by Φ (k). Differentiating the log-likelihood function with respect to each parameter we get the system:

$$\begin{cases} \frac{\partial \ln L}{\partial \lambda} &= \sum_{i=1}^{n}\ln(x_i) - n\frac{\phi(k)}{\Phi(k)}\left(-\frac{1}{\sigma\lambda^2}\right) - \frac{1}{\sigma^2}\sum_{i=1}^{n}\left(\frac{x_i^{\lambda}-1-\mu\lambda}{\sigma\lambda}\right)\left(\frac{\lambda x_i^{\lambda}\ln(x_i)-x_i^{\lambda}+1}{\sigma\lambda^2}\right) = 0 \\ \frac{\partial \ln L}{\partial \mu} &= -\sum_{i=1}^{n}\left(\frac{x_i-\mu}{\sigma}\right)\left(-\frac{1}{\sigma}\right) - n\frac{\phi(k)}{\Phi(k)}\frac{1}{\sigma} = 0 \\ \frac{\partial \ln L}{\partial \sigma} &= \sum_{i=1}^{n}\left(\frac{x_i-\mu}{\sigma}\right)\left(\frac{x_i-\mu}{\sigma^2}\right) - n\frac{\phi(k)}{\Phi(k)}\left(-\frac{k}{\sigma}\right) = 0 \end{cases}$$

Note that there is no closed form solution for the estimators since they are not independent from the parameters themselves. The system has to be solved numerically in a recurrent way, [5]. As usual in parameter estimation on Box-Cox transformation, for good results it is necessary to use a grid of initial values on the interval of possible values for the parameter. Note that for some initial values the Newton-Raphson (NR) method may converge to numbers distant from the natural candidates. For that reason the best estimate can only be obtained after processing the overall results. Let $\hat{\lambda}$, $\hat{\mu}$ and $\hat{\sigma}$ be the estimators of λ, μ and σ, respectively. The derivative of the log-likelihood function with respect to λ is given by:

$$\frac{\partial \ln L}{\partial \lambda} = \sum_{i=1}^{n}\ln(x_i) - \frac{n}{\Phi(k)}\frac{\partial \Phi(k)}{\partial \lambda} - \sum_{i=1}^{n} f(x_i)\frac{\partial f}{\partial \lambda}(x_i) \tag{2}$$

where $f(x_i) = \frac{x_i^{\lambda}}{\lambda\sigma} - k = \frac{x_i^{\lambda}-1-\mu\lambda}{\sigma\lambda}$. Then differentiating $\sum_{i=1}^{n} f(x_i)\frac{\partial f}{\partial \lambda}(x_i)$ we get

$$\sum_{i=1}^{n}\left[\left(\frac{\partial f}{\partial \lambda}\right)^2 + f(x_i)\frac{\partial^2 f}{\partial \lambda^2}\right]$$

where $\frac{\partial^2 f(x_i)}{\partial \lambda^2} = \frac{\lambda^2 x_i^{\lambda}(\ln^2(x_i) - 2x_i^{\lambda}\lambda\ln(x_i)) + 2\lambda x_i^{\lambda} - 2}{\sigma\lambda^3}$.
As for the first term of the derivative $\frac{\partial \ln L}{\partial \lambda}$ with respect to λ we should note that,

$$\frac{\partial \Phi(k)}{\partial \lambda} = \phi(k)\frac{\partial k}{\partial \lambda} = -\frac{\phi(k)}{\sigma\lambda^2} \tag{3}$$

Note that $\frac{\partial^2 \Phi(k)}{\partial \lambda^2} = -\frac{k - 2\lambda\sigma\phi(k)}{\lambda^4\sigma^2}$. After a few calculations we get the complete second derivative of the likelihood with respect to λ which is given by,

$$\frac{\partial^2 \ln L}{\partial \lambda^2} = -\sum_{i=1}^{n}\left\{\left(\frac{\partial f(x_i)}{\partial \lambda}\right)^2 + f(x_i)\frac{\partial^2 f(x_i)}{\partial \lambda^2}\right\} + \frac{n}{\Phi(k)}\left\{\frac{1}{\Phi(k)}\left(\frac{\partial \Phi(k)}{\partial \lambda}\right)^2 - \frac{\partial^2 \Phi(k)}{\partial \lambda^2}\right\} \tag{4}$$

The estimators $\hat{\mu}$ and $\hat{\sigma}$ are obtained from the (left) TN distribution (see [3]) which is the transformed scale. We have $\hat{\mu} = \bar{y} - \hat{\sigma}\frac{\phi(\hat{k})}{\Phi(\hat{k})}$ and $\hat{\sigma}^2 = \frac{s^2(y)}{1 - \hat{k}\frac{\phi(k)}{\Phi(\hat{k})} - \left(\frac{\phi(\hat{k})}{\Phi(\hat{k})}\right)}$ where y is the Box-Cox transformation of variable x.
The NR recurrence scheme is given by $\hat{\lambda}_{l+1} = \hat{\lambda}_l - \frac{\frac{\partial \ln L}{\partial \lambda}}{\frac{\partial^2 \ln L}{\partial \lambda}}\Big|\left(\lambda = \hat{\lambda}_l, \mu = \hat{\mu}_l, \sigma = \hat{\sigma}_l\right)$.
The algorithm to estimate the parameters is described below. As said earlier the estimation can only be effective using an adequate grid of values on the interval of possible values for λ. Each value of the considered partition is used as an initial value of the recurrence process. The used criterion to stop the recurrence scheme is the proximity between the consecutive estimates.

1 $a_0 = 0$ and $a_1 = 1$ and n, number of partition knots.

2 Set partition knots $[a_0, a_1]$, $A_i = A_1 + \frac{A_{m+1} - A_1}{m}$.

3 while $|(a0 - a1)| > 0.01$.

4 for $i = 1 : m - 1$ (for cycle for $m + 1$ knots).

5 while $\epsilon \geq 0.01$ (condition to stop recurrence process.)

6 Set $k(i) = \Phi^{-1}(A_i)$

7 Calculate $\phi(k)$, $\Phi(k)$, $f(x_i)$, $\left(\frac{\partial f}{\partial \lambda}\right)$, $\left(\frac{\partial f^2}{\partial \lambda^2}\right)$, $\left(\frac{\partial \Phi(k)}{\partial \lambda}\right)$, $\left(\frac{\partial^2 \Phi(k)}{\partial \lambda^2}\right)$.

8 Calculate $\hat{\mu}$ and $\hat{\sigma}$ (using given formulas).

9 Calculate $\hat{\lambda}_{l+1}$ and ϵ.

10 end while

11 Store $\hat{\lambda}$, $\hat{\mu}$, $\hat{\sigma}$ and corresponding likelihood (ml).

12 end for

13 Store best ml results for $\hat{\lambda}$, $\hat{\mu}$ and $\hat{\sigma}$. Let imle be the best.

14 $a_0 = A(imle - 1)$, $a_0 = A(imle + 1)$, calculate $|a_0 - a_1|$

15 end while

3 Conclusions and Future work

In a future work we will present a full simulation study to compare the two estimation methods.

References

[1] A. Atkinson, L. Pericchi and R. Smith, Grouped Likelihood for the Shifted Power Transformation, Journal of the Royal Statistic. Society, Series B., **39**,(1991), 473-482 .

[2] R. Gnanadesikan, *Fractional Integrals and Derivatives: Theory and Applications*, Wiley & Sons, 1977.

[3] D. Barr and T. Sherrill, Mean and Variance of Truncated Normal Distributions, The American Statistician, **53:4**, 357-361 (1999).

[4] M. Goto and T. Inoue, Some properties of power normal distribution, Journal of Biometrics, *1*, **1**, 28-54 (1980).

[5] M. Goto, T. Inoue and Y. Tsushihide, On estimation of parameters in power normal distribution, Bulletin of Informatics and Cybernetics, **21**, 41-53 (1984).

[6] G. E. Box and D. R. Cox, An analysis of transformations, Journal of the Royal Stat. Soc., Series B., (1964) **26**, 211-243.

[7] J. Freeman, R. Modarres, Inverse box-cox: The power-normal distribution, Statistics & Probability Letters, **1**, 764-772 (2006).

[8] R. Gonçalves, Inverse Box-Cox and the Power Normal distribution, *Innovation, Engineering and Entrepreneurship*,**505**(21), 805-810, (2019).

[9] R. Gonçalves, "The Power Normal distribution", Journal of Physics: Conference Series, *1334*, 012014, (2019).

[10] R. Gonçalves, "The Power Normal distribution", AIP Conference Proceeding, *2116*, 10009, (2019).

International Conference on Mathematical Analysis and Applications in Science and Engineering
ICMA^{2}SC'24
ISEP Porto-Portugal, June 20 - 22, 2024

Length-Biased-Weibull Probability Distribution, Characteristics and Application in Wind Energy

Brahim Taoussi[1⋆] **Sidi Mohammed Boudia**[2]

[1] National Higher School of Commerce, ESC, Algeria
[2] Centre de Developpement
des Energies Renouvelables, CDER, Algerie

[1⋆]b_taoussi@esc-alger.dz

Abstract: To effectively capture the stochastic nature of wind speed, which greatly impacts wind power generation, the Length-Biased-Weibull probability distribution is suggested. This study explores the viability of Length-Biased-Weibull as an alternative to the prevalent two-parameter Weibull model. Its appeal lies in its heavier right tail, which might suit the positively skewed nature of wind speed, and its ease transition from the conventional model. Wind speed data for three years were collected from a northern semi-arid and a southern saharn Algerian sites.Upon analysis, it became evident that the Length-Biased Weibull distribution outperformed other models based on RMSE, MAE and R^2.

keywords: Length-Biased-Weibull distribution; Parameter estimation methods; Wind power.

MSC2020: Challenges in Stochastic Modeling: Analysis, Numerical Simulation, and Applications

1 Introduction

Wind and solar PV energies contributed 12.1% to global electricity demand in 2022, showcasing its significance as a major renewable resource Renewables 2023 Report . Unlike other renewables, wind energy is non-dispatchable, which imposes challenges in energy grid management [1]. To attract investors, it is essential to provide precise feasibility studies. This involves a thorough assessment of the annual wind energy yield [2]. The stochastic nature of the wind turbine power output comes from its dependency on factors like geographic region, topography, and weather conditions such as wind speed, temperature, and direction [3]. Wind speed is the factor that affects the most the wind turbine power output as the wind power is proportional to the cube of wind speed, thus it is vital to describe the wind speed variations to optimize the design of wind turbines and effectively utilize the wind energy [4]. The average wind turbine power output $E[P_W]$ is given in Equation 1, where $P_W(x)$ is the wind turbine power output related to x and $f(x)$ is the probability density function (PDF) of x. Accurate estimation of $f(x)$ reduces uncertainty in predicting $E[P_W]$ [5].

$$E[P_W] = \int_0^\infty P_w(x) f_X(x) dx \tag{1}$$

The two-parameter Weibull (W2) is the most deployed PDF, following the recommendation of the International Electro-technical Commission [2]. However, W2 cannot fit all wind regimes. Thus, alternatives have been sought in the literature. This study investigates the capability of the Length-Biased-Weibull (WLB) in providing more precise modeling to the stochastic variability of wind velocity. Length-biased data occurs when every unit in the population does not have the same chance to be sampled [6]. Length-biased distribution is a particular case of the more general weighted distributions which were first introduced by Fisher (1934) then developed by Rao (1965) [7]. Length-biased PDFs have many applications in econometrics, survival analysis, renewal processes, biomedicine, and physics [7].

The reasons advocating the selection of WLB as an alternative to W2 are:

- It has a heavier right tail as indicated in Figure 1. This feature, in particular, might be useful in modeling the wind speed since it is heavily skewed to the right.
- Various studies suggested more sophisticated alternatives to the W2 that are either mixture distributions or unimodal PDFs with numerous parameters, thus complicating the estimation parameters process.
- Most wind power software packages like HOMER, WAsP, and WindSim predominantly rely on W2 for wind power statistics [8]. Consequently, the transition to WLB is facilitated as it represents a modification of W2.
- More importantly, the potential of WLB in enhancing wind speed modeling efficacy is unexplored, highlighting a promising investigation.

2 Materials and Methods

2.1 The Two-Parameter Weibull

Since the 1970s, the W2 distribution has been extensively utilized to model wind speed data due to its simplicity, requiring only two parameters α (scale) and β (shape), and its flexibility in mimicking various probability density functions (PDFs) such as exponential, Rayleigh, log-normal, and normal distributions [2, 9]. It is particularly suitable for describing occurrences of high wind speeds when $\beta < 3.6$, reflecting the positively skewed nature of wind speed phenomena [42]. The popularity of W2 arises from its efficacy in assessing wind potential at specific sites, with α indicating average wind speed and β characterizing the dispersion of wind speeds around the mean. A low β value suggests a higher percentage of low wind speeds [2, 4, 8, 9]. The probability density function (PDF), the cumulative distribution function (CDF), The r^{th} non-central moment , skewness, kurtosis are given in the following Equations [9].

$$X \sim W2\,(\alpha,\beta\,) \Leftrightarrow f_{W2}(x) = \frac{\beta}{\alpha^{\beta}} x^{\beta-1} e^{-(\frac{x}{\alpha})^{\beta}}; x \geq 0, \alpha, \beta > 0 \tag{2}$$

$$F_{W2}(x) = P\,[X \leq x] = 1 - e^{-(\frac{x}{\alpha})^{\beta}}; x \geq 0, \alpha, \beta > 0 \tag{3}$$

$$E\,(X^{r}) = \alpha^{r} \Gamma\left(1 + \frac{r}{\beta}\right) \tag{4}$$

$$\gamma_1 = \left[\Gamma\left(1+\frac{3}{\beta}\right) - 3\Gamma\left(1+\frac{2}{\beta}\right)\Gamma\left(1+\frac{1}{\beta}\right) + 2\left[\Gamma\left(1+\frac{1}{\beta}\right)\right]^3\right], \left[\Gamma\left(1+\frac{2}{\beta}\right) - \left[\Gamma\left(1+\frac{1}{\beta}\right)\right]^2\right]^{-3/2} \tag{5}$$

$$\gamma_2 = \left[\Gamma\left(1+\frac{4}{\beta}\right) - 4\Gamma\left(1+\frac{3}{\beta}\right)\Gamma\left(1+\frac{1}{\beta}\right) + 6\,\Gamma\left(1+\frac{2}{\beta}\right)\left[\Gamma\left(1+\frac{1}{\beta}\right)\right]^2 - 3\left[\Gamma\left(1+\frac{1}{\beta}\right)\right]^4\right]\left[\Gamma\left(1+\frac{2}{\beta}\right) - \left[\Gamma\left(1+\frac{1}{\beta}\right)\right]^2\right]^2 \tag{6}$$

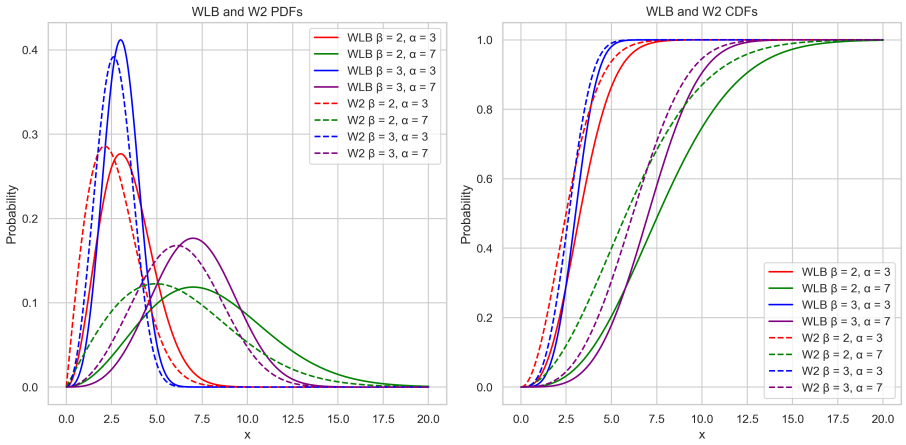

Figure 1: Length-Biased Weibull (WLB) and two-parameter Weibull (W2) distributions

2.2 The Length - Biased Weibull Distribution

Let X be a non negative random variable, X is said to have the Weibull length-biased distribution if its density function is given by [6, 7]

$$X \sim WLB\,(\alpha,\beta\,) \Leftrightarrow f_{WLB}(x) = \frac{\beta}{\alpha^{\beta+1}\,\Gamma(1+\frac{1}{\beta})} x^{\beta} e^{-(\frac{x}{\alpha})^{\beta}}; x \geq 0, \alpha\,, \beta > 0 \tag{7}$$

The relationship between WLB and W2 is expressed in Equation 8.

$$f_{WLB}(x) = \frac{x\, f_{W2}(x)}{\mathrm{E}[X]}; x \geq 0 \tag{8}$$

The CDF, the r^{th} non-central moment , skewness, and kurtosis are given in the following Equations, where $\gamma(.)$ is the lower gamma function [7].

$$F_{W2}(x) = \left[\Gamma(1+\frac{1}{\beta})\right]^{-1} \gamma\left(1+\frac{1}{\beta}, (\frac{x}{\alpha})^{\beta}\right); x \geq 0, \alpha\,, \beta > 0 \tag{9}$$

$$E\,(X^r) = \left[\Gamma(1+\frac{1}{\beta})\right]^{-1} \alpha^r \Gamma\left(1+\frac{r+1}{\beta}\right) \tag{10}$$

$$\gamma_1 = \left[\frac{\Gamma\left(1+\frac{4}{\beta}\right)}{\Gamma\left(1+\frac{1}{\beta}\right)} - \frac{3\Gamma\left(1+\frac{2}{\beta}\right)\Gamma\left(1+\frac{3}{\beta}\right)}{\left[\Gamma\left(1+\frac{1}{\beta}\right)\right]^2} + \frac{2\left[\Gamma\left(1+\frac{2}{\beta}\right)\right]^3}{\Gamma\left(1+\frac{1}{\beta}\right)}\right]\left[\frac{\Gamma\left(1+\frac{3}{\beta}\right)}{\Gamma\left(1+\frac{1}{\beta}\right)} - \left(\frac{\Gamma\left(1+\frac{2}{\beta}\right)}{\Gamma\left(1+\frac{1}{\beta}\right)}\right)^2\right]^{-3/2} \tag{11}$$

$$\gamma_2 = \left[\frac{\Gamma\left(1+\frac{5}{\beta}\right)}{\Gamma\left(1+\frac{1}{\beta}\right)} - \frac{4\Gamma\left(1+\frac{4}{\beta}\right)\Gamma\left(1+\frac{2}{\beta}\right)}{\left[\Gamma\left(1+\frac{1}{\beta}\right)\right]^2} + \frac{6\Gamma\left(1+\frac{3}{\beta}\right)\Gamma\left(1+\frac{2}{\beta}\right)^2}{\left[\Gamma\left(1+\frac{1}{\beta}\right)\right]^3} - \frac{\Gamma\left(1+\frac{2}{\beta}\right)^4}{\left[\Gamma\left(1+\frac{1}{\beta}\right)\right]^4}\right]\left[\frac{\Gamma\left(1+\frac{3}{\beta}\right)}{\Gamma\left(1+\frac{1}{\beta}\right)} - \left(\frac{\Gamma\left(1+\frac{2}{\beta}\right)}{\Gamma\left(1+\frac{1}{\beta}\right)}\right)^2\right]^{-2} \tag{12}$$

The coefficients of skewness and kurtosis are functions of the shape parameter β only. The Weibull distribution is symmetric for $\beta = 3.448$, positively skewed with a tail to the right for values $\beta < 3.448$ which might be interesting for wind power applications, and negatively skewed with a tail to the left for $\beta > 3.448$. The kurtosis is positive for values of the shape parameter that are $\beta \leq 2.164$ or $\beta > 5.455$ [7].

2.3 Parameter Estimation Methods

In this study, the maximum likelihood method (MLM), the method of moments, the method of linear moments (LMOM), the least square method (LSM), and the method of weighted least squares (WLSM) are deployed. MLM stands as a prominent and dependable point estimation technique widely employed in statistical inference. The estimates are obtained by maximizing the log-likelihood function's value. The MLM estimates for W2 and WLB are obtained through equations referenced as 13 and 14, respectively [9].

$$\arg\max_{(\alpha,\beta)}\left[n\ln\beta - n\ln\alpha + (\beta-1)\sum_{i=1}^{n}\ln x_i - \sum_{i=1}^{n}\left(\frac{x_i}{\alpha}\right)^{\beta}\right] \tag{13}$$

$$\arg\max_{(\alpha,\beta)}\left[n\ln\beta - n(\beta+1)\ln\alpha - n\ln\Gamma\left(1+\frac{1}{\beta}\right) + \beta\sum_{i=1}^{n}\ln(x_i) - \sum_{i=1}^{n}\ln\left(\frac{x_i}{\alpha}\right)\right] \tag{14}$$

In contrast to MLM, MOM estimates are derived by equating theoretical and empirical non-central moments. Although straightforward, computationally simple, and consistent, MOM estimates are deemed inefficient [9].

$$\begin{cases} \frac{\sum_{i=1}^{N} x_i}{n} = \alpha\Gamma\left(1+\frac{1}{\beta}\right) \\ \frac{\sum_{i=1}^{N} x_i^2}{n} = \alpha^2\Gamma\left(1+\frac{2}{\beta}\right) \end{cases} \tag{15}$$

$$\begin{cases} \frac{\sum_{i=1}^{N} x_i}{n} = \frac{\alpha\Gamma\left(1+\frac{2}{\beta}\right)}{\Gamma\left(1+\frac{1}{\beta}\right)} \\ \frac{\sum_{i=1}^{N} x_i^2}{n} = \frac{\alpha^2\Gamma\left(1+\frac{3}{\beta}\right)}{\Gamma\left(1+\frac{1}{\beta}\right)} \end{cases} \tag{16}$$

LSM serves as an alternative to MLM but exhibits lesser desirable characteristics. It involves minimizing the sum of squared deviations between the cumulative distribution function and the empirical cumulative distribution function [9]. WLSM, an extension of LSM, addresses challenges in regression analysis arising from violated assumptions of homoscedasticity and the presence of extreme outliers. By assigning lower weights to influential observations or outliers, WLSM mitigates their impact on parameter estimates [9].

$$\sum_{i=1}^{n}\left(F(x_i)-\hat{F}(x_i)\right)^2 \tag{17}$$

$$\sum_{i=1}^{n}\left(\frac{(n+1)^2(n+2)}{i(n-i+1)}\left(F(x_i)-\hat{F}(x_i)\right)^2\right) \tag{18}$$

3 Results and discussion

3.1 Data Description

In-Salah is a Saharan onshore location known as the windiest region in Algeria [10]. Hourly wind data sourced from the National Meteorological Office (ONM) were utilized, from the period January 2104 to December 2016, recorded at a height of 10 m AGL at In-Salah. Conversely, the Sidi-Bel-Abbas (SBA) site exhibits a semi-arid climate within Northern Algeria. SBA's data were obtained from NASA's MERRA2 dataset, covering hourly averages from January 2017 to December 2019. Table 1 presents the descriptive statistics of the utilized datasets. Notably, wind speeds at In-Salah exhibit higher velocity and greater variability compared to SBA, as evidenced by mean and standard deviation values. Both datasets demonstrate positive skewness (0.54 for In-Salah and 0.96 for SBA), yet the wind distribution at SBA displays a heavier-tailed right skew, as indicated by an excess kurtosis of 0.85.

Table 1: Descriptive Statistics for In-Salah and SBA Sites

Site	Mean	Median	Mode	Std	IQR	Min	Max	Skewness	Excess Kurtosis
In-Salah	6.97	6.7	5.1	2.8	3.7	0.1	21.6	0.54	-0.05
SBA	4.13	3.6	2.47	2.36	3.05	0.03	13.69	0.96	0.85

3.2 Data Analysis

Tables 2 and 3 present comprehensive metrics including shape and scale parameters, root mean square error (RMSE), mean absolute error (MAE), and coefficient of determination (R^2) criteria for assessing the goodness-of-fit of wind speed distributions at the In-Salah and SBA sites. At the In-Salah site (Table 2), a comparison between the WLB and W2 distributions reveals varying performance across different PEMs. For the WLB distribution, all PEMs, namely MLM, MOM, LSM, and WLSM demonstrate comparable goodness-of-fit, with R^2 values ranging from 0.9551 to 0.9615. Conversely, for the W2 distribution, MLM, MOM, and WLSM exhibit slightly lower R^2 values compared to the WLB distribution, suggesting a weaker fit. Notably, WLSM consistently yields the highest goodness-of-fit among the evaluated PEMs for both PDF types as indicated in Figure 2 (A). Similarly, at the SBA site, Table 3 and Figure 2 (B), a comparable trend is observed, although the differences between the performances of WLB and W2 distributions are more pronounced. Across various PEMs, the WLB distribution consistently demonstrates strong goodness-of-fit, with R^2 values ranging from 0.9868 to 0.9876. In contrast to In-Salah data, LSM emerged as the most effective estimation method form both WLB and W2 distribution according to RMSE and R^2. Having a high positive skewness and a large excess kurtosis may contributed to the evident disparity between WLB and W2, when analyzing the SBA data.

Table 2: Goodness-of-fit at In-Salah

	WLB					W2				
PEMs	**Shape**	**Scale**	**RMSE**	**MAE**	R^2	**Shape**	**Scale**	**RMSE**	**MAE**	R^2
MLM	2.1298	6.3232	0.0105	0.0068	0.9610	2.6614	7.8454	0.0123	0.0079	0.9467
MOM	2.1295	6.3217	0.0105	0.0068	0.9610	2.6768	7.8346	0.0122	0.0079	0.9477
LSM	2.0409	6.1812	0.0113	0.0074	0.9551	2.6063	7.7324	0.0125	0.0083	0.9451
WLSM	2.1370	6.3109	0.0105	0.0068	0.9615	2.7219	7.7799	0.0119	0.0078	0.9506

Table 3: Goodness-of-fit at SBA

	WLB					W2				
PEMs	**Shape**	**Scale**	**RMSE**	**MAE**	R^2	**Shape**	**Scale**	**RMSE**	**MAE**	R^2
MLM	1.3413	2.8718	0.0076	0.0049	0.9869	1.8450	4.6630	0.0121	0.0082	0.9671
MOM	1.3350	2.8600	0.0077	0.0049	0.9868	1.8160	4.6486	0.0122	0.0083	0.9663
LSM	1.3408	2.8463	0.0074	0.0051	0.9876	1.8745	4.5504	0.0109	0.0079	0.9734
WLSM	1.3443	2.8668	0.0075	0.0049	0.9873	1.8837	4.5975	0.0112	0.0079	0.9716

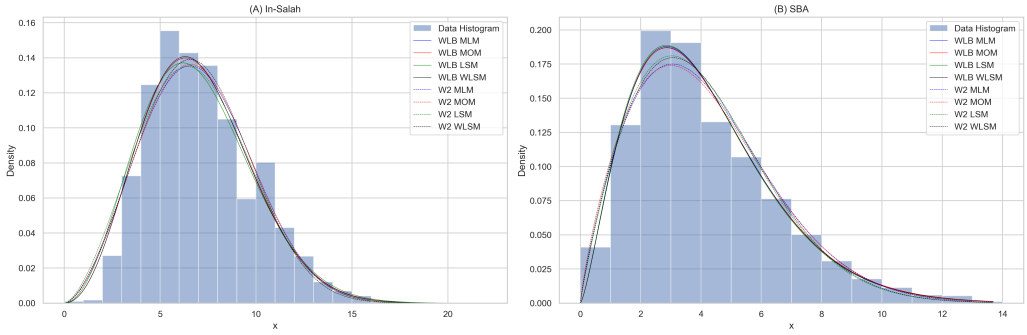

Figure 2: Wind speed at (A) In-Salah and (B) SBA superimposed with different models

4 Conclusion

Accurate modeling of wind speed variations is crucial for optimizing wind turbine design and energy utilization. While the W2 distribution is widely used, alternatives like WLB distribution offer potential improvements, especially in capturing the heavy right tail of wind speed distributions. The analysis based on wind speed data collected from two Algerian sites showed that WLB demonstrates strong performance particularly when equipped with WLSM and LSM methods.

References

[1] David Infield, Leon Freris, *Renewable energy in power systems*. John Wiley & Sons, 2020.

[2] Jung, Christopher, and Dirk Schindler. *Wind speed distribution selection-A review of recent development and progress*. Renewable and Sustainable Energy Reviews 114 (2019): 109290.

[3] Kim, Gyeongmin, and Jin Hur. *Probabilistic modeling of wind energy potential for power grid expansion planning*. Energy 230 (2021): 120831.

[4] Zhou, Junyi, et al. *Comprehensive evaluation of wind speed distribution models: A case study for North Dakota sites*. Energy Conversion and Management 51.7 (2010): 1449-1458.

[5] Jung, Christopher, and Dirk Schindler. *Global comparison of the goodness-of-fit of wind speed distributions*. Energy Conversion and Management 133 (2017): 216-234.

[6] Qin, Jing. Biased sampling, *over-identified parameter problems and beyond*. Vol. 5. Singapore: Springer, 2017.

[7] Shaban, S. A., and Naima Ahmed Boudrissa. *The weibull length biased distribution properties and estimation* InterStat 2 (2007): 1-26.

[8] Aries N, Boudia SM, Ounis H. *Deep assessment of wind speed distribution models: A case study of four sites in Algeria*. Energy Conversion and Management. 2018 Jan 1;155:78-90.

[9] Rinne H. *The Weibull distribution: a handbook*. Chapman and Hall/CRC; 2008 Nov 20.

[10] Boudia SM, Santos JA. *Assessment of large-scale wind resource features in Algeria.* Energy. 2019 Dec 15;189:116299.

International Conference on Mathematical Analysis and Applications in Science and Engineering ICMA²SC'24

ISEP **Porto-Portugal, June 20 - 22, 2024**

Statistical models, variational methods and engineering problems involved in the control of pharmaceutical pollutants

Irina Meghea

National University of Science and Technology POLITEHNICA Bucharest,
Faculty of Applied Sciences, Department of Mathematical Methods and Models
Romania

irina.meghea@upb.ro

Abstract: The existence of pharmaceutical pollutants (PhP) in water systems represents a significant worldwide problem. By searching innovative solutions for PhP removal from wastewater and drinkable waters, it was found that usual plants do not remove PhP. As a viable solution, the rehabilitation of the existing plants was proposed. A decision instrument, which provides a rigorous solution regarding the treatment efficiency is ANOVA factorial analysis with or without interaction. Two-factor, three-factor or multiple-factor factorial experiments can realize a more complex analysis of the possibilities to treat several PhP by different methods to choose the most appropriate way for their removal from wastewaters and drinkable waters. The increasing production and consumption of medicines multiply from one year to the next, and thus their increasing impact on the environment and people's health requires the intensification / continuation of research on this topic. The design of such an improved plant is presented with indications for technological objects including components, calculation details and examples, all these representing an important engineering solution to this capital problem. For the improvement of the existent plants, the introduction of corresponding membranes is proven by appropriate computations and all the necessary elements for such an action are described in accordance with specialty studies. The engineering solution is based on data collection, while the interpretation and organizing for appropriate statistical models are necessary for a deeper understanding of phenomena. Complex mathematical models can be formulated, and their solutions obtained via variational methods conduct, by usage of a proper numerical method, to the concrete solution. The aim of this work is to discuss different statistical models and variational methods which could be applied to draw solutions for real problems evolved during rehabilitation of TPs for pharmaceuticals removal.

keywords: modeling real phenomena; p-Laplacian; p-pseudo-Laplacian; treatment plant rehabilitation

MSC2020: 35A01; 35A15; 35J35; 35J40; 47J30.

1 Introduction

In the last years, the existence of pharmaceutical pollutants (PhP) in water systems represents a significant worldwide problem and they are considered an important class of emerging contaminants. Although the pharmaceutical wastes (due to their enormous amount) are toxic, non-biodegradable and bio-accumulative – like persistent organic pollutants, they are not nominated according to the Stockholm Convention [1]. Pharmaceutical residues were detected in surface and ground waters, wastewaters after processing, and more in drinkable waters. Traditional wastewaters treatment plants

(WTPs) are inadequate for the elimination of these contaminants. The negative effect caused by pharmaceutical contaminants on human health and terrestrial ecosystems is relatively recently established. The detection of these pollutants in aquatic systems implies significant financial efforts and highly qualified personnel.

By searching the innovative solutions for PhP removal from wastewater and drinkable waters, it was found that usual WTPs are not designed to remove PhP and the conventional plants with primary and secondary levels do not remove, generally, such pharmaceutical micropollutants. Treatment plants (TPs) which apply disinfection with residual free chlorine can eliminate only around 50% of them [1]. The advanced treatment techniques such as adsorption on activated carbon (AC), microfiltration (MF), ultrafiltration (UF), and advanced oxidation processes (AOPs) can remove efficiently these contaminants, while nanofiltration (NF) and reverse osmosis (RO) almost completely [1]. Among the technological operations of advanced treatment studied at level of laboratory, pilot, and, in cases of some operations, functional TP, the most attractive methods are adsorption on granulated AC, MF, UF, NF and RO. The first technique is considered as being more convenient since the investment costs are lower, needs smaller operating expenses (power, qualified personnel, reagents), there are no complicated problems to eliminate washing / cleaning of membranes which are sometimes more toxic than the substances dissolved in water and allow the reuse of exhausted adsorbent material [2]. TPs using membranes are appropriate for small population centers. Our attention was focused on two models of rehabilitated TP for surface and underground waters respectively [3] and for this reason, a mathematical model for passage of the PhP through the considered membranes is needed.

An important decision instrument, which provides a rigorous solution regarding the treatment efficiency is provided by ANOVA factorial analysis with or without interaction. Two-factor, three-factor or multiple-factor factorial experiments can realize a more complex analysis of the possibilities to treat several PhP by different methods to choose the most appropriate way for their removal from wastewaters and drinkable waters [2].

The rehabilitation of the existent TPs is a viable solution to clean the water also by removing this type of contaminants which cause hazardous effects on human health and on environment. In this paper, the design of such an improved plant [3] with indications for technological objects including components, calculation details and examples all these representing an important *engineering solution* to the above capital problem is completed by searching mathematical models for the passage of wastewater either through AC or a membrane.

To deepen the understanding of the phenomena involved in the considered when rehabilitating the existing plants, two problems will be formulated: flow through porous media, when we consider AC solution and membranes when AC, MF, UF, NF and RO are considered. Special conditions can be established for any concrete problem.

2 Results and discussion

In order to model the flow through AC, start with determination of porosity, compaction, compressibility of the considered porous medium, capillarity properties, i.e. saturation, wettability and, in the end, permeability. Starting from Darcy law, written for an incompressible or low-compressible fluid, obtain an equation with partial derivatives with p-Laplacian. The medium can be considered isotropic, the form of the set is cylindrical. A mathematical physics problem appears with boundary conditions given by the type of this cylinder. Since water can be well approximated as an incompressible fluid, a homogeneous p-Laplace equation for the pressure is obtained. Such a problem

can be solved either by considering a surjectivity method [4], or by obtaining a weak solution *via* an appropriate variational method [4] followed by corresponding numerical approach.

For the second case of the flow through a chosen membrane, a complete design solution with calculation examples is given in [3]. As an interesting mathematical model can be considered the vibration of the membrane, its displacement being an indicator of the membrane loading and hence the need to be changed. In [5], the problem of nonlinear elastic membrane with p-Laplacian and with p-pseudo-Laplacian is solved by using several results involving surjectivity and variational methods and they can be completed by appropriate numerical methods.

3 Conclusions and Future work

This work continues some studies of the author related to pharmaceutical pollutants from waste and drinkable waters. As a result of previous research, a viable solution for PhP removal it turned out to be the rehabilitation of the existent plants by adding the filtration through AC or membranes. Mathematical models for the flow through the porous medium – the cylinder with AC (for the pressure or the potential function) involving the p-Laplacian have been proposed. Also, for membrane usage, the mathematical physics problem for the displacement of the membrane with p-Laplacian of for p-pseudo-Laplacian could be of interest.

The two models can be visualized by applying Computational Fluid Dynamic (CFD) program. But the first future work is the detailed obtaining of the proposed models.

Acknowledgments

This work was supported by a grant from the National Program for Research of the National Association of Technical Universities – GNAC ARUT 2023, Grant no. 71/11.10.2023, MODEL FARMA.

References

[1] WHO. *Pharmaceuticals in Drinking Water*. WHO Library Cataloguing-in-Publication Data. ISBN: 978 924 150 2085, France, 2012.
[2] Irina Meghea, M. Lesnic, Ana-Maria Manea-Saghin, Innovative solutions for removal of pharmaceutical contaminants from water sources: statistical evaluation of method efficiency, Proceedings of International Structural Engineering and Construction, **11**(2) (2024), AAW-01.
[3] Irina Meghea, M. Lesnic, Ana-Maria Manea-Saghin, Design solutions for rehabilitation of a water treatment plant, Proceedings of International Structural Engineering and Construction, **11**(2) (2024), AAW-02.
[4] Irina Meghea, Solutions for Some Mathematical Physics Problems Issued from Modeling Real Phenomena: Part 1, Axioms, **12** (2023), 532.
[5] Irina Meghea, Solutions for Some Mathematical Physics Problems Issued from Modeling Real Phenomena: Part 2, Axioms, **12** (2023), 726.

International Conference on Mathematical Analysis and Applications in Science and Engineering
ICMA^{2}SC'24
ISEP Porto-Portugal, June 20 - 22, 2024

Optimal Control of a Class of Stochastic 3^{rd} Grade Fluids Equations

Raya Nouira[1⋆] **Fernanda Cipriano**[2]

[1] NOVA Math, NOVA School of Science and Technology, Portugal
[2] NOVA Math and Department of Mathematics, NOVA School of Science and Technology, Portugal

[1⋆]raya.nouira@gmail.com

Abstract: Partial differential equations with nonstandard growth and applications, Special Session #14.
In a bounded and simply connected domain $\mathcal{D} \subset \mathbb{R}^d$, $d = 2, 3$, with regular boundary $\partial\mathcal{D}$, we aim to control the dynamics of a class of stochastic incompressible third grade fluids. The control is introduced through a predictable stochastic force. The objective is to minimize a tracking-type cost functional, for which the velocity vector field is oriented towards a desired velocity profile, often referred to as the target. We recall the well-posedness results of the state equation, then prove some related stability results. Next, we study the well-posedness of the linearized state's solution and show that it coincides with the Gateaux derivative of the control-to-state mapping. Furthermore, we study existence and uniqueness results for the corresponding backward stochastic adjoint system and finally derive the duality relation and necessary optimality condition for the control problem.

keywords: Optimal control; Stochastic PDEs; Third grade fluids.

MSC2020: 76A05; 76D03; 60H15; 93D20; 76M35.

1 Introduction

Most real fluids are classified into two categories: Newtonian and non-Newtonian. Although many fluids exhibit a linear relationship between shear stress and shear rate, being classified as Newtonian fluids, an important class of natural fluids such as mud, quicksand, blood plasma and most fluids used in engineering and technology (e.g. nanofluids), food processing, the cosmetics industry, etc. do not possess such a linear relationship and belong to the class of non-Newtonian fluids.

Some of the relevant models describing non-Newtonian fluids are the second and third grade fluids equations. Throughout this work, we consider the latter.

Recall that stochastic incompressible third grade fluids equations for the random velocity vector field u, reads as follows

$$\begin{aligned} d(u - \alpha_1\Delta u) = (&-\nabla p + \mu\Delta u - u\cdot\nabla u + \alpha_1 \mathrm{div}(u\cdot\nabla A + (\nabla u)^T A + A(\nabla u)) \\ &+ \alpha_2 \mathrm{div}(A^2) + \beta \mathrm{div}(|A|^2 A) + \Phi\,)dt + \sigma(\cdot, u)d\mathcal{B}(\cdot), \end{aligned} \tag{1}$$

where p corresponds to the pressure, $\mu > 0$ denotes the viscosity of the fluid, α_1, α_2 are normal stress modulli, $\beta > 0$ is the specific material modulli and $A := A(u) = \nabla u + (\nabla u)^T$ represents the Rivlin-Ericksen kinematic tensor A_1. Moreover, Φ represents an external force and $\sigma(\cdot, u)d\mathcal{B}(\cdot)$ stands for the stochastic perturbation, also called the multiplicative Wiener noise. According to Fosdick-Rajagopal'80 and Dunn-Rajagopal'95, physical and thermodynamic considerations impose the following restrictions on the physical constants

$$\alpha_1 \geq 0, \quad |\alpha_1 + \alpha_2| \leq (24\mu\beta)^{\frac{1}{2}}.$$

Recently, the control problem for two-dimensional deterministic third grade fluids supplemented by Navier slip boundary conditions was addressed by Tahraoui and Cipriano'2023, [3]. Subsequently, in [4] the same authors studied the control problem for stochastic third grade fluids equations in $2d$ and $3d$, where the strong solution of the state equation exists only locally in time. In the above-mentioned works, the existence and uniqueness of an optimal control has been shown and necessary optimality conditions have been established.

2 Results and discussion

In a bounded and simply connected domain $\mathcal{D} \subset \mathbb{R}^d$, $d = 2, 3$, with regular boundary $\partial\mathcal{D}$, we aim to control the state dynamics of stochastic third grade fluids (1), for the particular case, $\alpha_1 = 0$, globally in time. The control is introduced through a predictable stochastic force, denotedΦ and the objective is to optimally minimize a tracking-type cost functional, for which the velocity vector field is oriented towards a desired velocity profile, often referred to as the target.

To achieve this, we follow two main steps:

Step 1. Show existence (and uniqueness) of an optimal controlΦ^* to the following control problem:

Let $\mathcal{U}_{ad}$ denote the set of admissible controls, which is a non-empty, bounded, closed and convex subset of $L^2(\Omega, L^2([0,T]; L^2(\mathcal{D})))$. Consider the cost functional $J : \mathcal{U}_{ad} \to \mathbb{R}$, given as

$$J(\Phi, U) = \frac{1}{2}\mathbb{E}\int_0^T \|U - u_d\|_2^2 dt + \frac{\Lambda}{2}\mathbb{E}\int_0^T \|\Phi\|_2^2 dt, \tag{2}$$

where$\Lambda > 0$ is given and $u_d \in L^2(0,T; L^2(\mathcal{D}))$ represents a desired target field. Thus, the control problem to be studied is given as follows

$$\min_{\Phi \in \mathcal{U}_{ad}} \{J(\Phi, U) : U \text{ is the solution to the state equation with the force} \Phi\},$$

more precisely,

$$\begin{cases} \text{Find} \Phi^* \in \mathcal{U}_{ad} \text{ such that} \\ J(\Phi^*, U^*) = \min_{\Phi \in \mathcal{U}_{ad}} J(\Phi, U). \end{cases}$$

Step 2. Derive the first order optimality condition by proving the following sub-steps

1. the linearised state equation admits a unique solution Z, with U replaced by U^* and the force Ψ replaced by$\Psi - \Phi^*$;
2. the stochastic backward adjoint equation admits a unique solution p^*, with U replaced by U^* and the force $\phi = U^* - u_d$;
3. the following duality property holds

$$\mathbb{E}\int_0^T (\Psi - \Phi^*, p^*)dt = \mathbb{E}\int_0^T (U^* - u_d, Z)dt, \qquad \forall \Psi \in \mathcal{U}_{ad}.$$

Finally, the necessary optimality condition holds, for any$\Psi \in \mathcal{U}_{ad}$

$$\mathbb{E}\int_0^T [\Lambda(\Phi^*, \Psi - \Phi^*) + (\Psi - \Phi^*, p^*)]dt \geq 0.$$

Acknowledgments

This work is funded by national funds through the FCT - Fundacao para a Ciencia e a Tecnologia, I.P., under the scope of the projects UIDB/00297/2020 (https://doi.org/10.54499/UIDB/00297/2020) and UIDP/00297/2020 (https://doi.org/10.54499/UIDP/00297/2020) (Center for Mathematics and Applications).

References

[1] R. Nouira, F. Cipriano, Y. Tahraoui, On the Existence and Long Time Behaviour of H^1-Weak Solutions for $2,3d$-Stochastic $3rd$-Grade Fluids Equations, arXiv preprint arXiv:2311.14596, 2023.

[2] Y. Tahraoui, F. Cipriano, Invariant Measures for a Class of Stochastic Third Grade Fluid Equations in $2D$ and $3D$ Bounded Domains, arXiv preprint arXiv:2401.04566, 2024.

[3] Y. Tahraoui, F. Cipriano., Optimal control of two dimensional third grade fluids. Journal of Mathematical Analysis and Applications, 523(2):127032, 2023.

[4] Y. Tahraoui, F. Cipriano, Optimal Control of Third Grade Fluids with Multiplicative Noise, arXiv preprint arXiv:2306.13231, 2023.

International Conference on Mathematical Analysis and Applications in Science and Engineering
ICMA^{2}SC'24
ISEP Porto-Portugal, June 20 - 22, 2024

Some Results for Equilibrium Problems

Lin, Yen-Cherng

Department of Applied Mathematics
College of Science, Tunghai University, Taichung, 407224, Taiwan

linyc2019@thu.edu.tw; linyc20171@gmail.com

Abstract: Our study addresses to delve into two different versions of equilibrium problems for set-valued mappings. What makes our approach distinctive is our ability to establish minimax theorems under non-continuous set-valued mappings as long as certain appropriate conditions are met. Furthermore, we explore the complexity of multilayer structures in this context.

keywords: Equilibrium problems; Minimax theorems.

MSC2020: 91B50; 49J35; 54C60.

1 Introduction

Recently, the existence of solutions for equilibrium problems have been discussed by many authors. For instance,[1] establishes new criteria for existence of solutions for equilibrium problems. [2] provides some sufficient and necessary conditions for existence of solutions for equilibrium problems. [3] studied the existence of projected solutions for generalized Nash equilibrium problems in Banach spaces settings. The existent solutions of equilibrium problems can be used to solve the price war in the business world [4], the Pareto-optimal solutions of a certain vector optimization problem [5], and so on. The concepts of weak and strong solutions for such problem are introduced by [13] as follows: let $\mathcal{X}, \mathcal{Y}, \mathcal{W}$ be three Hausdorff topological vector spaces, K a nonempty closed convex subset of $\mathcal{X}$, C a proper closed convex pointed solid cone in $\mathcal{W}$, given two set-valued mappings $F : \mathcal{Y} \times K \times K \rightrightarrows \mathcal{W}$ and $Q : K \rightrightarrows \mathcal{Y}$. A point $\bar{x} \in K$ is a *weak solution* of $(\mathrm{EP})_F$ if $F(\bar{s}, \bar{x}, y) \not\subset -intC$ for all $y \in K$ and for some $\bar{s} \in Q(\bar{x})$. A point $\bar{x} \in K$ is a *strong solution* of $(\mathrm{EP})_F$ if there is $\bar{s} \in Q(\bar{x})$ such that $F(\bar{s}, \bar{x}, y) \not\subset -intC$ for all $y \in K$. [13] also establishes both existences of weak and strong solutions of $(\mathrm{EP})_F$. We observed that there were many results concerned about the relation for these two kind solutions of $(\mathrm{EP})_F$ in [13]. In this paper, we further proposed two levels (EP) with a couple set-valued mappings, F and H, and realized how the weak solution of first level (EP) with respect to F, $(\mathrm{EP})_F$, determined the strong solution of second level (EP) with respect to H, $(\mathrm{EP})_H$. By employing some new techniques which are different from the ones that used in [12]-[13], we would like to investigate the dependent relationships between the both solutions for $(\mathrm{EP})_F$ and $(\mathrm{EP})_H$.

2 Scalar Minimax Theorems

We first present some fundamental concepts will be used in the sequel:

Let Q be a nonempty subset of $\mathcal{W}$. A point $q \in Q$ is called a *minimal point* of Q if $Q \cap (q - C) = \{q\}$; $MinQ$ means the set of all minimal points of Q; another analogous definitions for *maximal point, weakly minimal point, weakly maximal point* of Q can be found in [6, 7, 10]. We denote that, for a nonempty compact set Q, $MinQ \subset Min_wQ$ and $MaxQ \subset Max_wQ$. Both sets $MaxQ$ and $MinQ$ are nonempty, and both relations $Q \subset MinQ + C$ and $Q \subset MaxQ - C$ are valid. Furthermore, in $\mathbb{R}$, $MaxQ = Max_wQ = \max Q$, $MinQ = Min_wQ = \min Q$.

The following theorem will help us discuss the scalar hierarchical minimax results which play an important role to solve the set-equilibrium problem.

Theorem 1 *Let X be a nonempty compact (not necessary convex) subset of real Hausdorff topological vector spaces, Y be a nonempty (not necessary convex) subset of real Hausdorff topological vector spaces. Suppose that the set-valued mappings $F, S, T, G : X \times Y \rightrightarrows \mathbb{R}$ with nonempty compact values, $\max F(x,y), \max S(x,y), \max G(x,y)$ exist for all $(x,y) \in X \times Y$, and satisfy the following conditions:* (i) *the mapping $x \mapsto F(x,y)$ is lower semi-continuous on X for each $y \in Y$;* (ii) *the mapping $x \mapsto S(x,y)$ is above $\mathbb{R}_+$-convexlike[6] on X for each $y \in Y$, and the mapping $y \mapsto T(x,y)$ is below $\mathbb{R}_+$-concavelike[6] on Y for each $x \in X$; and* (iii) *for each $(x,y) \in X \times Y$, $\max F(x,y) \leq \max S(x,y)$, $T(x,y) \subset S(x,y) + \mathbb{R}_+$, and $G(x,y) \subset T(x,y) + \mathbb{R}_+$. Then, for each $t \in \mathbb{R}$, either there is $y_0 \in Y$ such that $\min G(x,y_0) \geq t$ for all $x \in X$ or there is $x_0 \in X$ such that $\max F(x_0,y) \leq t$ for all $y \in Y$.*

Theorem 2 *Under the framework of Theorem 1, in additional, Y is compact, the sets $\bigcup_{y\in Y} F(x,y)$ and $\bigcup_{x\in X} G(x,y)$ are compact for each $(x,y) \in X \times Y$, both mapping $y \mapsto G(x,y)$ is lower semi-continuous on Y for each $x \in X$. Then the relation (sH)*

$$\min \bigcup_{x\in X} \max \bigcup_{y\in Y} F(x,y) \leq \max \bigcup_{y\in Y} \min \bigcup_{x\in X} G(x,y)$$

holds.

Throughout this paper, unless stated otherwise, we assume that X, Y are two nonempty subsets of real Hausdorff topological vector spaces, respectively. Let $\mathcal{W}$ be a real Hausdorff topological vector space, C a proper closed convex pointed solid cone in $\mathcal{W}$. The Gerstewitz function ξ_{kv} with $k \in \text{int}C$ and $v \in \mathcal{W}$.

3 Hierarchical Minimax Theorems

As an appplication for scalar hierarchical minimax theorems, we first establish the following hierarchical minimax theorem:

Theorem 3 *Let X and Y be two compact (not necessarily convex) sets. Given the set-valued mappings $F, S, T, G : X \times Y \rightrightarrows \mathcal{W}$ with nonempty compact values, both sets $\cup_{y\in Y} F(x,y)$ and $\cup_{x\in X} G(x,y)$ are compact for each $(x,y) \in X \times Y$, and satisfy the following conditions:* (i) *$x \mapsto F(x,y)$ is lower semi-continuous on X for each $y \in Y$, $y \mapsto G(x,y)$ is lower semi-continuous on Y for each $x \in X$;* (ii) *$x \mapsto \xi_{kv} S(x,y)$ is above $\mathbb{R}_+$-convexlike for each $y \in Y$, $y \mapsto \xi_{kv} T(x,y)$ is below $\mathbb{R}_+$-concavelike for each $x \in X$;* (iii) *for each $(x,y) \in X \times Y$, we have*

$F(x,y) \subset S(x,y) - C$, $T(x,y) \subset S(x,y) + C$ *and* $G(x,y) \subset T(x,y) + C$*; and* (iv) *for each* $x \in X$, $\operatorname{Min} \bigcup_{x\in X} \operatorname{Max}_w \bigcup_{y\in Y} F(x,y) \subset \operatorname{Max}_w \bigcup_{y\in Y} F(x,y) - C$. *Then the relation*

$$\operatorname{Min} \bigcup_{x\in X} \operatorname{Max}_w \bigcup_{y\in Y} F(x,y) \subset \operatorname{Max} \bigcup_{y\in Y} \operatorname{Min}_w \bigcup_{x\in X} G(x,y) - C \qquad (I(F,G))$$

holds.

4 Hierarchical Equilibrium Problems

In this section, we will discuss how the weak solution of first level (EP) with respect to F, $(\mathrm{EP})_F$, determined the strong solution of second level (EP) with respect to G, $(\mathrm{EP})_G$. One of the existence results about the weak solution of first level $(\mathrm{EP})_F$, can be found in Theorem 15[12].

Theorem 4 *Let* K *be a nonempty compact convex subset of a Hausdorff topological vector space,* $Q : K \rightrightarrows \mathcal{Y}$ *have nonempty compact (not necessarily convex) values, and denote* $QK := \cup_{x\in K} Q(x)$. *The mappings* $F, S, T, H : QK \times K \times K \rightrightarrows \mathcal{W}$ *have nonempty compact values and satisfy the following conditions:* (i) $x \mapsto Q(x)$ *is upper semi-continuous on* K, $s \mapsto F(s,x,y)$ *is lower semi-continuous on* QK *for each* $(x,y) \in K \times K$, *and* $s \mapsto G(s,x,y)$ *is continuous on* QK *for each* $(x,y) \in K \times K$, $y \mapsto G(s,x,y)$ *is lower semi-continuous on* K *for each* $(s,x, \in QK \times K$*;* (ii) $y \mapsto \xi_{kv} T(s,x,y)$ *is below* $\mathbb{R}_+$*-concavelike on* K *for each* $(s,x) \in QK \times K$, $s \mapsto \xi_{kv} S(s,x,y)$ *is above* $\mathbb{R}_+$*-convexlike on* QK *for each* $(x,y) \in K \times K$*;* (iii) *for each* $(s,x,y) \in QK \times X \times Y$, *we have* $\max \xi_{kv} F(s,x,y) \leq \max \xi_{kv} S(x,y)$, $\xi_{kv} T(s,x,y) \subset \xi_{kv} S(s,x,y) + \mathbb{R}_+$, $\xi_{kv} G(s,x,y) \subset \xi_{kv} T(s,x,y) + \mathbb{R}_+$; *and* (iv) *for each* $(s,x) \in QK \times K$, *there is an* $w_{sx} \in K$ *such that* $\max \xi_{kv} H(s,x,w_{sx}) \leq \max \bigcup_{s\in TK} \min \bigcup_{y\in K} \xi_{kv} H(s,x,y)$. *Suppose that* $(EP)_F$ *has a weak solution, says* $\bar{x} \in K$ *and for some* $\bar{s} \in Q(\bar{x})$, $\cup_{y\in K} \xi_{kv} F(s,\bar{x},y)$ *and* $\cup_{s\in Q(\bar{x})} \xi_{kv} G(s,\bar{x},y)$ *are compact, then* $(EP)_H$ *has a strong solution.*

The following Theworewm is an existent result of strong solution for $(\mathrm{EP})_H$.

Theorem 5 *Let* K *be a nonempty compact convex subset of a Hausdorff topological vector space,* $Q : K \rightrightarrows \mathcal{Y}$ *have nonempty compact convex values, the mappings* $F, G, H : QK \times K \times K \rightrightarrows \mathcal{W}$ *have nonempty compact values and satisfy the following conditions:* (i) $x \mapsto Q(x)$ *is upper semi-continuous on* K, $y \mapsto F(s,x,y)$ *is lower semi-continuous on* K *for each* $(s,x) \in QK \times K$, $s \mapsto G(s,x,y)$ *and* $s \mapsto H(s,x,y)$ *are lower semi-continuous on* QK *for each* $(x,y) \in K \times K$, $s \mapsto F(s,x,y)$ *is upper semi-continuous on* QK *for each* $(x,y) \in K \times K$, *and* $y \mapsto H(s,x,y)$ *is continuous on* K *for each* $(s,y) \in QK \times K$*;* (ii) $s \mapsto \xi_{kv} F(s,x,y)$ *is above* $\mathbb{R}_+$*-concave on* QK *for each* $(x,y) \in K \times K$, $y \mapsto \xi_{kv} G(s,x,y)$ *is above* $\mathbb{R}_+$*-convex or above* $\mathbb{R}_+$*-quasi-convex on* K *for each* $(s,x) \in QK \times K$, $s \mapsto \xi_{kv} H(s,x,y)$ *is above* $\mathbb{R}_+$*-concave on* QK *for each* $(x,y) \in K \times K$*;* (iii) *for each* $(s,x,y) \in QK \times X \times Y$, *we have* $\operatorname{Max}_w F(s,x,y) \subset \operatorname{Max}_w G(s,x,y) - C$ *and* $\operatorname{Max}_w G(s,x,y) \subset \operatorname{Max}_w H(s,x,y) - C$*; and* (iv) *for each* $x \in K$ *and* $s \in Qx$, *there is an* $w_{sx} \in K$ *such that* $\max \xi_{kv} H(s,x,w_{sx}) \leq \max \bigcup_{s\in QK} \min \bigcup_{y\in K} \xi_{kv} H(s,x,y)$. *Suppose that* $(EP)_F$ *has a weak solution, says* $\bar{x} \in K$ *and for some* $\bar{s} \in Q(\bar{x})$, *then* $(EP)_H$ *has a strong solution.*

References

[1] M. Balaj, M. Castellani, M. Giuli, New criteria for existence of solutions for equilibrium problems, Computational Management Science **20** (2023).

[2] J. Cotrina, A. Svensson, The finite intersection property for equilibrium problems, Journal of Global Optimization **79** (2021), 941–957.

[3] O. Bueno, J. Cotrina, Existence of projected solutions for generalized Nash equilibrium problems, Journal of Optimization Theory and Applications, 191 (2021), 344–362.

[4] Y. Xie, Application of Nash equilibrium: taking the game between enterprises as an example, BCP Business & Management (2023), 915–918.

[5] Z. Feinstein, B. Rudloff, Characterizing and computing the set of Nash equilibria via vector optimization, Operations Research (2023), 1–15.

[6] Y.C. Lin, Q.H. Ansari and H.C. Lai, Minimax theorems for set-valued mappings under cone-convexities. Abstract and Applied Analysis (2012).

[7] S.J. Li, G.Y. Chen, K.L. Teo and X.Q. Yang, Generalized minimax inequalities for set-valued mappings, Journal of Mathematical Analysis and Applications **281** (2003), 707–723.

[8] C. Berge, *Topological Spaces*, Macmillan Co., New York (1963)

[9] J.P. Aubin, A. Cellina, *Differential inclusions*, Springer-Verlag, Berlin-Heidelberg-New York-Tokyo (1984)

[10] F. Ferro, Optimization and stability results through cone lower semi-continuity, Set-Valued Analysis **5** (1997), 365–375.

[11] C. Gerth, P. Weidner, Nonconvex separation theorems and some applications in vector optimization, Journal of Optimization Theory and Applications **67** (1990), 297–320.

[12] Y.C. Lin, C.T. Pang, The hierarchical minimax inequalities for set-valued mappings, Abstract and Applied Analysis (2014).

[13] Y.C. Lin, H.J. Chen, Solving the set equilibrium problems, Fixed Point Theory and Applications (2011).

[14] Y.C. Lin, The hierarchical minimax theorems, Taiwanese Journal of Mathematics **18** (2014), 451–462.

[15] Y.C. Lin, Minimax problems under hierarchical structures, Journal of Inequalities and Applications (2015).

[16] Y.C. Lin, P.J. Cheng, S.L. Lee, The convergent behavior for parametric generalized vector equilibrium problems, Journal of Mathematics (2012).

International Conference on Mathematical Analysis and Applications in Science and Engineering
ICMA^{2}SC'24
ISEP Porto-Portugal, June 20 - 22, 2024

Regularity of Solutions in L^2 Spaces for a Multidimensional Incompressible Flow under the $k-\varepsilon$ Turbulence Model

Jose Luis Diaz Palencia[1,2⋆]

[1] Department of Mathematics and its Education
Universidad a Distancia de Madrid, 28400 Madrid, Spain.
[2] Department of Information Technology, Escuela Politecnica Superior, Universidad San Pablo-CEU, CEU Universities, Campus Monteprincipe, Boadilla del Monte, Madrid 28668, Spain.

[1,2⋆]joseluis.diaz.p@udima.es or jose.diazpalencia@ceu.es

Abstract: Our study focuses on the Navier-Stokes equations in water flow. We incorporate the multidimensional Navier-Stokes equations and the $k-\varepsilon$ turbulence model. This work aims to establish the analysis of weak solutions for the velocity vector, turbulent kinetic energy, and dissipation rate $(\overline{\mathbf{u}}, k, \varepsilon)$ in a coupled system of nonlinear parabolic equations. Our model includes conditions for external forces and initial and boundary data within L^2 space in a finite domain Ω. The main result predicts the L^2 behaviour of solutions to the Navier-Stokes equations along with the $k-\varepsilon$ turbulence model.

keywords: Navier-Stokes Equations; Turbulence; Hydrodynamics; Regularity of Solutions.

MSC2020: 35A23; 76B03; 35A35.

1 Introduction

The Navier-Stokes equations are instrumental in understanding fluid behavior across various domains. In two dimensions, the regularity and uniqueness of solutions are relatively well-established. Thanks to the work of Ladyzhenskaya [1], it has been proven that solutions to the two-dimensional Navier-Stokes equations are regular and unique. In three dimensions (3D) the situation is challenging: Leray's work [2] introduced the existence of weak solutions for the 3D Navier-Stokes equations. In [3], Tao explores fluid motion under varying potentials. The Navier-Stokes equations in their most general 3D form for an incompressible fluid are given by: a) The continuity equation (Mass Conservation) $\nabla \cdot \mathbf{u} = 0$, where $\mathbf{u}$ is the velocity field. b) The Momentum Conservation $\rho\left(\frac{\partial \mathbf{u}}{\partial t} + \mathbf{u}\cdot\nabla\mathbf{u}\right) = -\nabla p + \mu\nabla^2\mathbf{u} + \mathbf{F}$, where ρ is the fluid density, p is the pressure, μ is the dynamic viscosity, and $\mathbf{F}$ represents external forces (like gravity). In what regards with the turbulence modeling, one common approach is to use Reynolds-Averaged Navier-Stokes (RANS) equations that can be expressed as: $\rho\left(\frac{\partial \overline{\mathbf{u}}}{\partial t} + \overline{\mathbf{u}}\cdot\nabla\overline{\mathbf{u}}\right) = -\nabla\overline{p} + \mu\nabla^2\overline{\mathbf{u}} + \mathbf{F} - \nabla\cdot\tau_{\mathrm{R}}$, where $\overline{\mathbf{u}}$ is the time-averaged velocity field, $\overline{p}$ is the time-averaged pressure, μ is the dynamic viscosity and τ_{R} is the Reynolds stress tensor that is given by: $\tau_{\mathrm{R}} = \rho\overline{\mathbf{u}'\mathbf{u}'}$, where $\mathbf{u}'$ represents the fluctuating component of the velocity field (i.e., $\mathbf{u} = \overline{\mathbf{u}} + \mathbf{u}'$). The challenge in RANS modeling is to accurately represent this Reynolds stress tensor. In our case,

we consider the Boussinesq hypothesis (refer to [4] for additional insights and Equation 22 in [5]), so that the tensor can be approximated as: $\tau_{\mathrm{R}} \approx -\rho\nu_t(\nabla\overline{\mathbf{u}} + (\nabla\overline{\mathbf{u}})^T) + \frac{2}{3}\rho k\mathbf{I}$, where ν_t is the eddy viscosity, k is the turbulent kinetic energy, and $\mathbf{I}$ is the identity matrix. Note that the first part involving the velocity gradients models the turbulent shear stresses while the term $\frac{2}{3}\rho k\mathbf{I}$ represents the isotropic part of the Reynolds stress tensor. The $\frac{2}{3}$ factor comes from the assumption of isotropic turbulence at the smallest scales, distributing the turbulent kinetic energy equally among the three directions. Hence, the RANS momentum equation with the Reynolds stress tensor becomes: $\rho\left(\frac{\partial\overline{\mathbf{u}}}{\partial t} + \overline{\mathbf{u}}\cdot\nabla\overline{\mathbf{u}}\right) = -\nabla\overline{p} + \nabla\cdot\left[(\mu+\rho\nu_t)(\nabla\overline{\mathbf{u}} + (\nabla\overline{\mathbf{u}})^T)\right] - \frac{2}{3}\rho k\nabla\cdot\mathbf{I} + \mathbf{F}$. To analyze the regularity of solutions, consider the coupled system of equations consisting of the RANS momentum equation along with the equations for k and ε in the turbulence model that are given as follows:

Momentum Equation:

$$\rho\left(\frac{\partial\overline{\mathbf{u}}}{\partial t} + \overline{\mathbf{u}}\cdot\nabla\overline{\mathbf{u}}\right) = -\nabla\overline{p} + \nabla\cdot\left[\left(\mu + \rho C_\mu\frac{k^2}{\varepsilon}\right)\left(\nabla\overline{\mathbf{u}} + (\nabla\overline{\mathbf{u}})^T\right)\right] - \frac{2}{3}\rho k\nabla\cdot\mathbf{I} + \mathbf{F}. \tag{1}$$

Turbulent Kinetic Energy Equation:

$$\frac{\partial k}{\partial t} + \overline{\mathbf{u}}\cdot\nabla k = \nabla\cdot\left[\left(\mu + \frac{C_\mu k^2}{\varepsilon\sigma_k}\right)\nabla k\right] + P_k(\overline{u}) - \varepsilon, \tag{2}$$

where P_k represents the production term of turbulent kinetic energy due to the mean velocity gradients in the fluid flow.

Dissipation Rate Equation:

$$\frac{\partial\varepsilon}{\partial t} + \overline{\mathbf{u}}\cdot\nabla\varepsilon = \nabla\cdot\left[\left(\mu + \frac{C_\mu k^2}{\varepsilon\sigma_\varepsilon}\right)\nabla\varepsilon\right] + C_{\varepsilon 1}\frac{\varepsilon}{k}P_k - C_{\varepsilon 2}\frac{\varepsilon^2}{k}. \tag{3}$$

We transform these equations into weak formulations. For a test function $\mathbf{v} \in \mathcal{V}$, where $\mathcal{V}$ is a suitable space of test functions (such as a Lebesgue space), the weak form is:

$$\begin{aligned}&\int_\Omega \rho\left(\frac{\partial\overline{\mathbf{u}}}{\partial t} + \overline{\mathbf{u}}\cdot\nabla\overline{\mathbf{u}}\right)\cdot\mathbf{v}\,d\Omega = \\ &\int_\Omega\left[-\overline{p}\nabla\cdot\mathbf{v} + \left(\mu + \rho C_\mu\frac{k^2}{\varepsilon}\right)(\nabla\overline{\mathbf{u}} + (\nabla\overline{\mathbf{u}})^T) : \nabla\mathbf{v} - \frac{2}{3}\rho k(\nabla\cdot\mathbf{I})\cdot\mathbf{v} + \mathbf{F}\cdot\mathbf{v}\right]d\Omega.\end{aligned} \tag{4}$$

For a scalar test function $\phi \in \mathcal{W}$, where $\mathcal{W}$ is an appropriate functional space:

$$\int_\Omega\left(\frac{\partial k}{\partial t} + \overline{\mathbf{u}}\cdot\nabla k\right)\phi\,d\Omega = \int_\Omega\left[-\left(\mu + \frac{C_\mu k^2}{\varepsilon\sigma_k}\right)\nabla k\cdot\nabla\phi + P_k\phi - \varepsilon\phi\right]d\Omega. \tag{5}$$

For a scalar test function $\psi \in \mathcal{W}$, the weak formulation of the dissipation rate equation is:

$$\int_\Omega\left(\frac{\partial\varepsilon}{\partial t} + \overline{\mathbf{u}}\cdot\nabla\varepsilon\right)\psi\,d\Omega = \int_\Omega\left[-\left(\mu + \frac{C_\mu k^2}{\varepsilon\sigma_\varepsilon}\right)\nabla\varepsilon\cdot\nabla\psi + C_{\varepsilon 1}\frac{\varepsilon}{k}P_k\psi - C_{\varepsilon 2}\frac{\varepsilon^2}{k}\psi\right]d\Omega. \tag{6}$$

The Neumann boundary condition is considered to reflect the posibility of non-slip at the borders because of turbulence: $\frac{\partial\overline{\mathbf{u}}}{\partial n} = \mathbf{g}_u \quad$ on $\partial\Omega$. Similarly: $\frac{\partial k}{\partial n} = g_k$, $\frac{\partial\varepsilon}{\partial n} = g_\varepsilon \quad$ on $\partial\Omega$, with g_u, g_k, $g_\varepsilon \in L^2(\Omega)$. We supplement the boundary condition with the initial data that will be further specified.

2 Results and discussion

Theorem 1: *Let $\Omega \subseteq \mathbb{R}^n$, with $n = 2, 3$, be a bounded domain with a sufficiently smooth boundary. Consider the RANS momentum equation* (1) *and the $k-\varepsilon$ model given in* (2) *and*

(3) *along with their weak formulations* (4), (5), *and* (6). *Suppose* $\mathbf{F} \in L^2(\Omega)$. *Assume initial conditions* $\overline{\mathbf{u}}_0 \in L^2(\Omega)$, $k_0 \in L^2(\Omega)$, *and* $\varepsilon_0 \in L^2(\Omega)$ *for the velocity, turbulent kinetic energy, and dissipation rate, respectively, and consider the Neumann boundary conditions. Then, there exist weak solutions* $(\overline{\mathbf{u}}, k, \varepsilon)$ *such that* $\overline{\mathbf{u}} \in L^2(\Omega)$, $k \in L^2(\Omega)$, *and* $\varepsilon \in L^2(\Omega)$.

The demonstration of the main lines in the theorem is presented herein, leaving an in depth proof to be discussed in more detail and extensive versions of this work. First, we construct a sequence $\{\overline{\mathbf{u}}_n, k_n, \varepsilon_n\}$ where each component of the sequence belongs to a finite-dimensional subspace of the L^2 space. Hence, consider a set of basis functions $\{\mathbf{v}_i\}$ for the velocity, $\{\phi_j\}$ for the turbulent kinetic energy, and $\{\psi_k\}$ for the dissipation rate. Each basis function belongs to the L^2 space. Then: $\overline{\mathbf{u}}_n = \sum_{i=1}^{n} a_i^n \mathbf{v}_i, \quad k_n = \sum_{j=1}^{n} b_j^n \phi_j, \quad \varepsilon_n = \sum_{k=1}^{n} c_k^n \psi_k$, where a_i^n, b_j^n, and c_k^n are coefficients to be determined. We shall now insert these approximations into the weak formulations (4), (5) and (6). For the system to be solvable, the residual of each equation (the difference between the left-hand side and right-hand side of the weak formulations) must be orthogonal to the space spanned by the basis functions. This leads to a system of algebraic equations generally expressed as $A(\mathbf{a}^n, \mathbf{b}^n, \mathbf{c}^n) = \mathbf{f}$, where A is a matrix representing the coefficients of the system, $(\mathbf{a}^n, \mathbf{b}^n, \mathbf{c}^n)$ is the vector of unknown coefficients, and $\mathbf{f}$ represents the forcing terms and initial conditions. We provide a qualitative discussion to ensure that solutions to the algebraic equation exist based on the Lax-Milgram theorem: It states that if $A : V \to V^*$ is a continuous, coercive (bounded below) linear operator from a Hilbert space V to its dual V^*, then for every $\mathbf{f} \in V^*$, there exists a unique $\mathbf{u} \in V$ such that $A(\mathbf{u}) = \mathbf{f}$. Hence, if we assume that the coefficients $\mathbf{a}^n, \mathbf{b}^n, \mathbf{c}^n$ belong to $L^2(\Omega)$ and that the operator A is continuous, we shall show that A is coercive, meaning there exists a constant $C > 0$ such that $\langle A(\mathbf{u}), \mathbf{u} \rangle \geq C\|\mathbf{u}\|^2, \quad \forall \mathbf{u} \in V$. Then, given the nature of the RANS equations, we consider the general bilinear form associated with A (refer to the convective derivative term on the left hand side in (4)): $\langle A(\mathbf{u}), \mathbf{v} \rangle = \int_\Omega a(\mathbf{x}, \mathbf{u}, \nabla \mathbf{u}) \cdot \mathbf{v} \, d\Omega$, where $a(\mathbf{x}, \mathbf{u}, \nabla \mathbf{u})$ represent the principal part of the differential operator, typically involving terms like $\nabla \mathbf{u}$. Poincare's inequality states that for functions in general spaces, there is a constant $C_P > 0$ such that $\|\mathbf{u}\|_{L^2(\Omega)} \leq C_P \|\nabla \mathbf{u}\|_{L^2(\Omega)}$. Now let us consider the energy functional $E(\mathbf{u})$ associated with the operator A: $E(\mathbf{u}) = \int_\Omega |\nabla \mathbf{u}|^2 \, d\Omega$. Using Poincare's inequality, we can establish a lower bound for $E(\mathbf{u})$: $E(\mathbf{u}) = \int_\Omega |\nabla \mathbf{u}|^2 \, d\Omega \geq \frac{1}{C_P^2} \|\mathbf{u}\|^2_{L^2(\Omega)}$. Given the above energy estimate, we can show the coercivity of A: $\langle A(\mathbf{u}), \mathbf{u} \rangle = \int_\Omega a(\mathbf{x}, \mathbf{u}, \nabla \mathbf{u}) \cdot \mathbf{u} \, d\Omega \geq \int_\Omega |\nabla \mathbf{u}|^2 \, d\Omega \geq \frac{1}{C_P^2} \|\mathbf{u}\|^2_{L^2(\Omega)}$. Certainly, we can apply the Lax-Milgram theorem, as stated previously, to conclude the existence and uniqueness of a solution to our system $A(\mathbf{u}) = \mathbf{f}$, at least in its linearized form. Now, we aim to show that the sequence of approximate solutions $\{\overline{\mathbf{u}}_n, k_n, \varepsilon_n\}$ converges in the respective L^2 spaces. This involves demonstrating the boundedness of the sequence and utilizing compactness arguments. The first step is to establish that the sequence of approximate solutions is bounded in the L^2 norm. Due to energy conservation or dissipation properties of the momentum equation, there exists a constant C_1 such that: $\|\overline{\mathbf{u}}_n\|_{L^2(\Omega)} \leq C_1$. Similarly, for the turbulent kinetic energy, we derive an estimate for k_n from the approximated kinetic energy equation, yielding a constant C_2 where $\|k_n\|_{L^2(\Omega)} \leq C_2$. Similarly for the dissipation rate $\|\varepsilon_n\|_{L^2(\Omega)} \leq C_3$. With the boundedness of the sequence preliminary established following our basic intuition about the dissipation mechanisms in a finite domain, we can apply compactness arguments to demonstrate convergence. Using the Rellich-Kondrachov compactness theorem, we can extract convergent subsequences from $\{\overline{\mathbf{u}}_n, k_n, \varepsilon_n\}$. Specifically, the boundedness in L^2 implies the existence of subsequences $\{\overline{\mathbf{u}}_{n_k}, k_{n_k}, \varepsilon_{n_k}\}$ that converge strongly in $L^2(\Omega)$. In addition, these subsequences converge strongly to some functions $\overline{\mathbf{u}}, k, \varepsilon$ in $L^2(\Omega)$, which are the limit points of the sequences, thereby proving the convergence of the sequence of approximate solutions in the respective L^2 spaces. We now need to show that these limit functions satisfy the weak formulations of the RANS equations and the $k - \varepsilon$ model. The key step is to pass to the limit in the weak formulations of the approximated equations. We select the main equation as (4) and provide the arguments for this case (similarly for (5) and (6) equations), hence and generally we have:

$\lim_{n\to\infty}\int_\Omega (\text{terms involving } \overline{\mathbf{u}}_n, k_n, \varepsilon_n)\, d\Omega = \int_\Omega (\text{corresponding terms involving } \overline{\mathbf{u}}, k, \varepsilon)\, d\Omega$. The n-th approximation is given by

$$\begin{aligned}&\int_\Omega \rho\left(\frac{\partial \overline{\mathbf{u}}_n}{\partial t} + \overline{\mathbf{u}}_n \cdot \nabla \overline{\mathbf{u}}_n\right)\cdot \mathbf{v}\, d\Omega = \\ &\int_\Omega \left[-\overline{p}_n \nabla\cdot\mathbf{v} + \left(\mu + \rho C_\mu \frac{k_n^2}{\varepsilon_n}\right)(\nabla\overline{\mathbf{u}}_n + (\nabla\overline{\mathbf{u}}_n)^T) : \nabla\mathbf{v} + \mathbf{F}\cdot\mathbf{v}\right] d\Omega.\end{aligned} \tag{7}$$

For linear terms, the convergence is straightforward due to the linearity of the integral and the strong convergence of the sequences in $L^2(\Omega)$. The convergence of nonlinear terms requires additional care. Hence, we focus on demonstrating the convergence of the most challenging nonlinear term, this is $\overline{\mathbf{u}}_n \cdot \nabla\overline{\mathbf{u}}_n$ in the weak formulation (a similar argument is applicable for the terms $\overline{\mathbf{u}}_n \cdot \nabla k_n$ and $\overline{\mathbf{u}}_n \cdot \nabla\varepsilon_n$ appearing in the weak formulations for each k_n and ε_n respectively). To introduce the analysis concerning this nonlinearity, we need a stronger form of convergence for $\overline{\mathbf{u}}_n$. This is where compactness arguments come in. We can assert the strong convergence of the nonlinear term by invoking the Rellich-Kondrachov theorem, so that we can extract a strongly convergent subsequence from $\overline{\mathbf{u}}_n$ and each term is bounded in L^2 as previously shown. As a consequence, we state that the nonlinear term converges in the sense that $\lim_{n\to\infty}\int_\Omega \overline{\mathbf{u}}_n \cdot \nabla\overline{\mathbf{u}}_n \cdot \mathbf{v}\, d\Omega = \int_\Omega \overline{\mathbf{u}}\cdot\nabla\overline{\mathbf{u}}\cdot\mathbf{v}\, d\Omega$. Similarly, $\overline{\mathbf{u}}_n \cdot \nabla k_n$ and $\overline{\mathbf{u}}_n \cdot \nabla\varepsilon_n$ in (5) and (6) respectively. After passing to the limit in each of the involved terms (linear and nonlinear), we conclude that there exist weak solutions $(\overline{\mathbf{u}}, k, \varepsilon)$ with finite norms in L^2 spaces for the model given in (4), (5) and (6).

3 Conclusions and Future work

We introduced Theorem 1, which established that the weak solutions $(\overline{\mathbf{u}}, k, \varepsilon)$ for the velocity, turbulent kinetic energy, and dissipation rate respectively in multidimensional Navier-Stokes equations with $k-\epsilon$ turbulence model belong to the $L^2(\Omega)$. This theorem provides a theoretical basis for understanding solution behavior in developing numerical models. As future works, we indicate the need for correlating our findings within applied scenarios under numerical simulations.

References

[1] Ladyzhenskaya, O. A., *The mathematical theory of viscous incompressible flow*. Gordon and Breach, 1963.

[2] Leray, J., Sur le mouvement d'un liquide visqueux emplissant l'espace, Acta Mathematica, (1934).

[3] Tao, T., On the universality of potential well dynamics, Dynam. Part. Differ. Eq., **14** (2017), 219-238.

[4] Schmitt, Francois G., About Boussinesq's turbulent viscosity hypothesis: historical remarks and a direct evaluation of its validity, Comptes Rendus Mecanique, **335**(9-10) (2007), 617-627, *doi:10.1016/j.crme.2007.08.004*.

[5] Rincon, M., Amarloo, A., Reclari, M., Yang, I.A., Abkar, M., Progressive augmentation of Reynolds stress tensor models for secondary flow prediction by computational fluid dynamics driven surrogate optimisation, Int J Heat Fluid Flow, **104** (2023).

International Conference on Mathematical Analysis and Applications in Science and Engineering
ICMA^{2}SC'24
ISEP Porto-Portugal, June 20 - 22, 2024

New approach to a Gartland-type mesh

G. Radojev[1⋆] **M. Brdar** [2] **Lj. Teofanov**[3]

[1] Faculty of Sciences, University of Novi Sad, Serbia
[2] Faculty of Technology, University of Novi Sad, Serbia
[3] Faculty of Technical Sciences, University of Novi Sad, Serbia

[1⋆]goran.radojev@dmi.uns.ac.rs

Abstract: The singular perturbation problem typically involves the boundary layers at the boundary of the domain and standard numerical methods applied to the uniform mesh - fail for these differential equations. The layer-adapted meshes were introduced to solve this issue. Gartland-type meshes (also known as Duran and Duran-Lombardi meshes) are one type of layer-adapted meshes, with some disadvantages that we resolved with our new approach. Theoretical and numerical results for different types of singular perturbation problems (ordinary as well as partial differential equations) will be presented.

keywords: singular perturbation, boundary layers, graded mesh, two parameters, layer-adapted mesh

MSC2020: 65N12, 65N30, 65N50

1 Introduction

The singular perturbation problems (SPP) are differential equations that depend on a small positive parameter ε and whose solutions (or their derivatives) approach a discontinuous limit as ε approaches zero. Such problems are said to be singularly perturbed, where we regard ε as a perturbation parameter, [8]. These problems typically involves the boundary layers at the boundary of the domain and standard numerical methods applied to the uniform mesh - fail for SPP. The layer-adapted meshes are introduced to solve this issue. Gartland-type meshes are one type of layer-adapted meshes. These type of meshes have some disadvantages that we want to resolve with new approach. We will construct the modifications of this type of layer-adapted meshes for the different 1D and 2D differential equations, with one and two perturbation parameters. The Gartland-type mesh [5] (also known as Duran mesh) that we will consider is introduced in [4]. The construction of these type of meshes is straightforward and depends only on mesh parameter $h \in (0, 1)$ given a priori. The error analysis of corresponding numerical methods is often much simpler than the one of widely used Shishkin and Bakhvalov-type meshes. However, a few disadvantages related to this type of meshes can be summarized as follows. First of all, for a fixed perturbation parameter(s), different meshes may have the same number of mesh points. For different values of the mesh parameter h, different meshes with the same number of the mesh points can be obtained. Second one, the mesh points are generated recursively so the last step size could be unacceptably smaller then the previous one. That may cause a problem in the error analysis, see [7]. Finally, for the multidimensional problems, the Gartland-type meshes usually do not have the same number of mesh points in each direction unlike the Shishkin and the Bakhvalov-type meshes.

2 Results and discussion

First modification that solved the mentioned issues of the Gartland-type mesh was defined in [7] for the following reaction-diffusion problem

$$\begin{aligned} -\varepsilon^2 \Delta u(x,y) + r(x,y)u(x,y) = f(x,y) \ \text{ in } \ \Omega = (0,1)\times(0,1), \\ u(x,y) = 0, \quad (x,y) \in \partial\Omega, \end{aligned} \tag{1}$$

where $\varepsilon \in (0,1]$, $\Delta = \partial^2/\partial x^2 + \partial^2/\partial y^2$ is the Laplace operator, $r, f \in C(\Omega)$ and $0 \le \beta < r$ on Ω with some positive constant β. The standard definition of Gartland-type mesh for 2D convection-diffusion problem can be found in [4]. This mesh can be easily adapted for reaction-diffusion problem (1). Let $\Delta_x : 0 = x_0 < x_1 < \ldots < x_{2M} = 1$, where

$$\begin{cases} x_0 = 0, & \\ x_i = ih\varepsilon, & \text{for } \ 1 \le i < \dfrac{1}{h} + 1, \\ x_i = x_{i-1} + hx_{i-1}, & \text{for } \ \dfrac{1}{h} + 1 \le i < M, \\ x_M = \dfrac{1}{2}, & \\ x_i = 1 - x_{2M-i}, & \text{for } \ M+1 \le i \le 2M, \end{cases} \tag{2}$$

and M is that uniquely defined integer with

$$x_{M-1} < \frac{1}{2} \quad \text{and} \quad x_{M-1} + hx_{M-1} \ge \frac{1}{2}.$$

Then $\Delta = \Delta_x \times \Delta_x$ is mesh that resolves boundary layers for the problem (1).
Instead of choosing h in (2), we first choose $N = 2M$ and then calculate h such that

$$\frac{1}{2} = x_{M-1} + hx_{M-1}.$$

The existence and uniqueness of h satisfying the last condition is proved.

Similarly, we can construct modification of this type mesh for 2D convection-diffusion problem

$$\begin{aligned} -\varepsilon\Delta u(x,y) - b(x,y)u_x(x,y) + c(x,y)u(x,y) &= f(x,y) \quad \text{in} \quad \Omega = (0,1)\times(0,1), \\ u(x,y) &= 0 \quad \text{on} \quad \partial\Omega, \end{aligned}$$

where $b \in W^{1,\infty}(\Omega)$, $c \in L^\infty(\Omega)$, $b, c \ge c_0 > 0$ on $\bar{\Omega}$. This problem has two different layers – an exponential layer at $x = 0$ and two parabolic layers at the characteristic boundaries $y = 0$ and $y = 1$. Accordingly, the mesh constructed in the described manner will have a different number of mesh points in the $x-$ and $y-$ direction [1]. So, in our modification, for a chosen N – two different parameters h_x and h_y are calculated so that the modified mesh has N mesh points in both directions:

$$\begin{cases} x_0 = 0, & \\ x_i = ih_x\varepsilon, & 1 \le i \le \lceil \frac{1}{h_x} \rceil =: K_x \\ x_{i+1} = x_i + h_x x_i, & K_x \le i \le N-2, \\ x_N = 1, & \end{cases} \tag{3}$$

and in y-direction by

$$\begin{cases} y_0 = 0, & \\ y_j = jh_y\sqrt{\varepsilon}, & 1 \le j \le \lceil \frac{1}{h_y} \rceil =: K_y \\ y_{j+1} = y_j + h_y y_j, & K_y \le j \le N/2 - 2, \\ y_{N/2} = 1/2, & \\ y_{N/2+j} = 1 - y_{N-j}, & j = 1, \ldots, N/2, \end{cases} \tag{4}$$

Also, we can construct modified Gartland-type mesh for the convection-diffusion-reaction problem (with two small parameters) [3] and for convection-diffusion problem with a large shift [2].

Finally, some theoretical and numerical results for our modified meshes will be presented on International Conference on Mathematical Analysis and Applications in Science and Engineering - ICMASC24.

3 Conclusions and Future work

New approach to Gartland-type meshe has several advantages over the usual approach: the obtained mesh is unique, it can be compared with other meshes (when the number of mesh points is fixed) and the recursive formula provides appropriate step size even in the last step. Finally, in a similar way, this approach for a Gartland-type can be applied to any other singular perturbation problem (as in the recent paper [6]).

Acknowledgments

The first and second authors gratefully acknowledge the financial support of the Ministry of Science, Technological Development and Innovation of the Republic of Serbia (Grants No. 451-03=66/2024-03/200134, 451-03=65/2024-03/200134 and No. 451-03-66/2024-03/200125, 451-03-65/2024-3/200125 respectively)..

References

[1] M. Brdar, G. Radojev, H. G. Roos, Lj. Teofanov, Superconvergence analysis of FEM and SDFEM on graded meshes for a problem with characteristic layers, Computers and Mathematics with Applications 93 (2021) 50-57.

[2] M. Brdar, S. Franz, H. G. Roos, A convection-diffusion problem with a large shift on Duran meshes, Calcolo, 61 (2024) https://doi.org/10.1007/s10092-023-00559-9, in the press.

[3] M. Brdar, H. Zarin, Lj. Teofanov, A singularly perturbed problem with two parameters in two dimensions on graded meshes, Computers and Mathematics with Applications, 72(10) (2016) 2582-2603.

[4] R. G. Durán, A. Lombardi, Finite Element Approximation of Convection Diffusion Problems using Graded Meshes, Applied Numerical Mathematics, 56 (2006) 1314-1325.

[5] E. C. Gartland, Graded-Mesh Difference Schemes for Singularly Perturbed Two-Point Boundary Value Problems, Mathematics of Computation, 51(184) (1988) 631-657.

[6] A. Kumar, S. Gowrisankar, Efficient numerical methods on modified graded mesh for singularly perturbed parabolic problem with time delay, Iranian Journal of Numerical Analysis and Optimization, 28 (2024) 77-106.

[7] G. Radojev, M. Brdar, A collocation method on a Gartland-type mesh for a singularly perturbed reaction-diffusion problem, Mathematical Communications, 24(1) (2019) 19-37.

[8] H.-G.Roos, M. Stynes, L. Tobiska.: Robust Numerical Methods for Singularly Perturbed Differential Equations, Springer Series in Computational Mathematics, vol. 24, 2nd edn. Springer, Berlin (2008)

NEW REFINEMENTS OF HERMITE-HADAMARD INEQUALITIES FOR LEFT AND RIGHT QUANTUM INTEGRALS

Sabah Iftikhar[1⋆] **Hüseyin Budak**[2]

[1] Xiamen University Malaysia
[2] Düzce University, Türkiye

[1⋆]sabah.iftikhar@xmu.edu.my, [2]hsyn.budak@gmail.com

Abstract: In this study, we first introduce two functions including quantum integrals. Then, we prove some properties of these mappings such as convexity and monotony. Moreover, by using the newly defined mappings, we prove some refinements of the left hand sides of Hermite-Hadamard inequality for left and right quantum integrals.

keywords: Convex functions; Hermite-Hadamard inequality; quantum integrals.

MSC2020: 26D10; 26D07; 26D15.

References

[1] N. Alp, M. Z. Sarikaya, M. Kunt and İ. İşcan, q-Hermite Hadamard inequalities and quantum estimates for midpoint type inequalities via convex and quasi-convex functions, J. King Saud Univ. Sci., **30** (2018), 193–203.

[2] S. Bermudo, P. Kórus and J. N. Valdés, On q-Hermite–Hadamard inequalities for general convex functions, Acta Math. Hung., **162**(2020), 364-374.

[3] H. Budak, Some trapezoid and midpoint type inequalities for newly defined quantum integrals, Proyecciones, **40** (2021), 199-215.

[4] V. Kac and P. Cheung, Quantum calculus, Springer (2001).

[5] M. A. Noor, K. I. Noor and M. U. Awan, Some quantum integral inequalities via preinvex functions, Appl. Math. Comput., **269** (2015), 242–251.

[6] W. Sudsutad, S. K. Ntouyas and J. Tariboon, Quantum integral inequalities for convex functions. *J. Math. Inequal.,* **9** (2015), 781–793.

[7] J. Tariboon and S. K. Ntouyas, Quantum integral inequalities on finite intervals, J. Inequal. Appl., 2014, 2014:121.

International Conference on Mathematical Analysis and Applications in Science and Engineering
ICMA^{2}SC'24
ISEP Porto-Portugal, June 20 - 22, 2024

Control of Multistability in a Parametrically Coupled Electromechanical Oscillator System

Godwin Sani[1⋆] **Zeric Tabekoueng Njitacke**[2] **Jan Awrejcewicz**[1]

[1] Department of Automation, Biomechanics and Mechatronics,
Lodz University of Technology, Stefanowskiego Str. 1/15, Lodz, 90-924, POLAND
[2] Department of Electrical and Electronic Engineering,
College of Technology (COT), University of Buea, PO Box 63, Buea, Cameroon

[1⋆]sanigodwin1@gmail.com

Abstract: The occurrence of coexisting attractors is one of the most interesting phenomena in dynamical systems. It appears in many applied nonlinear sciences and engineering where the final state of the system depends on the initial conditions. Multistability is undesirable in the design of devices with specific characteristics. On the other hand, it creates flexibility in the system with the appropriate control algorithm for switching between different desirable attractors. This work presents a sliding mode control for switching to any desired attractors in the pool of coexisting attractors. The designed controllers performed outstandingly on the tested system.

keywords: Parametric oscillator; Multistability; Control.

MSC2020: 49-XX; 34-XX; 92-XX.

1 Introduction

Multistability is the occurrence of coexisting attractors for a fixed set of parameters in dynamical systems under different initial conditions [1]. This phenomenon in nonlinear sciences allows a multi–mode operations of the same device for various applications. While it is undesirable in some appliances under strict specifications, it is useful in others for measurements or actuation. For this purpose, control algorithms are developed to influence the system's behavior. The conceptual model of the electromechanical system under consideration is presented in Fig. 1. It consists of the electrical subcircuit having the capacitor with the capacitance C, fully charged to the voltage V_c. The current i flowing through the nonlinear resistor R (with normalization resistance R_0), and the inductor (of inductance, L) energies the filament of mass m via the parametric coupling $M(t) = k_l + k_n\ cos(2\omega t)$. When the mass is displaced by q, the restoring force due to the stiffness of Duffing–type $k(q) = k_1 + k_2q^2$, and the viscous damper d, which forms the mechanical

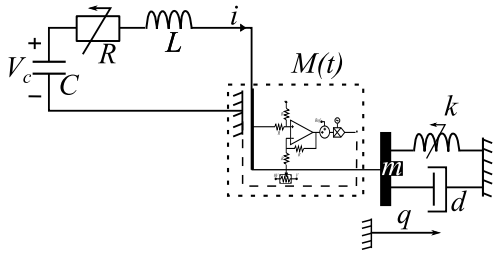

Figure 1: Electromechanical system model

substructure, causes the system to exchange energy via the parametric coupling. Given that the natural frequency Ω_e is anchored at $\frac{1}{\sqrt{LC}} = \sqrt{\frac{k_1}{m}}$, the non–dimensional governing equation has been established in [2] as

$$\begin{cases} \ddot{x} - \alpha\left(1 - x^2\right)\dot{x} + x - \lambda N_1(1 + \mu\ cos(2\Omega\tau))\,(y - x) = 0 \\ \ddot{y} + \beta\dot{y} + y + \gamma y^3 - \lambda\ (1 + \mu\ cos(2\Omega\tau))\,(x - y) \quad = 0 \end{cases} \tag{1}$$

where $\alpha = R_0 C\Omega_e$, $\beta = d\sqrt{\frac{1}{k_1 m}}$, $\gamma = \frac{k_2 y_{st}^2}{k_1}$, $\Omega = \frac{\omega}{\Omega_e}$, $\lambda = \frac{k_l}{k_1}$, $\mu = \frac{k_n}{k_l}$, and $N_1 = C \cdot k_1$. Initial investigation reveals that the system exhibits a multistability situation. We aim to design a sliding mode controller to move any of the attractors to the desired one by short entrainment. Let the sliding surface be $s = [s_1, s_2]^T = [\dot{\tilde{x}} + \kappa_1\tilde{x}, \dot{\tilde{y}} + \kappa_2\tilde{y}]^T$, where $\tilde{x} = x - x_d$ and $\tilde{y} = y - y_d$, and x_d, y_d are the desired trajectories. If the upper bounded disturbances d_1 and d_2 are introduced to cater for unmodeled dynamics, then the control law [3] can be defined as

$$\begin{cases} u_x = \ddot{x}_d - \kappa_1(\dot{x} - \dot{x}_d) - X - (\eta_1 + d_1)sign(s_1) \\ u_y = \ddot{y}_d - \kappa_2(\dot{y} - \dot{y}_d) - Y - (\eta_2 + d_2)sign(s_2), \end{cases} \tag{2}$$

where $\eta_1 > 0$, $\eta_2 > 0$, and X, Y are functions of the state variable respectively. If the Lyapunov function candidate is defined as $V(s, \tau) = \frac{1}{2}s^T s$, it can be proven that $\dot{V}(s, \tau) \leq -\eta_1|s_1| - \eta_2|s_2| \leq 0$. It implies that $\dot{V}(s, \tau) \to 0$ and the system converges to the desired attractor as $s \to 0$. The controller in (2) (first part) and the disturbance (i.e., $d_1 + u_x$) is added to the first part of system (1), and $d_2 + u_y$ is added to the second part of system (1) to achieve the control scheme.

2 Results and discussion

The numerical investigation of the system shows the six (6) coexisting attractors for the fixed parameter set: $\lambda = 0.48$, $N_1 = 0.98$, $\alpha = 0.8$, $\Omega = 2\pi/3$, $\beta = 0.5$, $\gamma = 0.3$, and $\mu = 0.816$ as presented in Fig. 2a under the initial conditions (a) [-0.4, 0, 0, 0], (b) [-0.4, 0, 5.8, 0], (c) [-1.72, 0, -2.61, 0], (d) [1.72, 0, 2.61, 0], (e) [7, 0, 7, 0], (f) [-7, 0, -7, 0]. The different initial

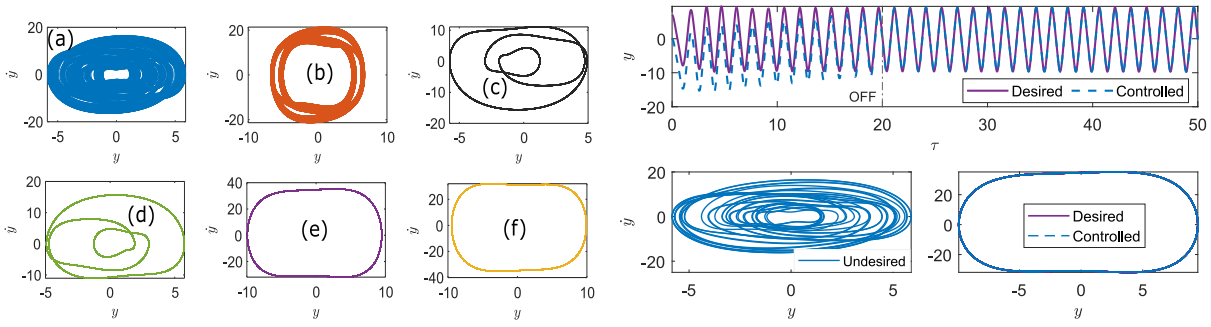

(a) Coexisting attractors (b) Attractor switching from (a) → (e).

Figure 2: The coexisting attractors (left), and controlled trajectories with phase portraits (right) under $\kappa_1 = 1.9$, $\kappa_2 = 1.9$, $\eta_1 = 0.7$, $\eta_2 = 0.6$

conditions lead to the different final states of the system in the form of attractors in Fig. 2a (a)–(f). When a desired attractor is selected by its initial condition, and the control scheme is applied to any undesired attractor (also selected by initial condition), the controlled state is entrained towards the trajectory of the desired state until the sliding surface approaches zero or a predefined threshold when the controlled trajectory enters the neighborhood of the desired attractor. Then, the controller is turned off as the controlled state is fully entrained to the

desired attractor. Figs. 2b–3b present the results of the controlled multistability phenomenon in the system. In Fig. 2b, with reference to Fig. 2a, attractor (e) is selected as the desired final state while (a) is undesirable. Then attractor (a) is controlled by entrainment towards (e), and the switching is complete at time $\tau = 20$, at which point the controller turns off. The parameters for the controller are listed in the figure caption, while $d_1 = d_2 = 0.001$ are fixed. Similarly, in Fig. 3a, attractor (a) is controlled to (f) as the desired final state. The controller

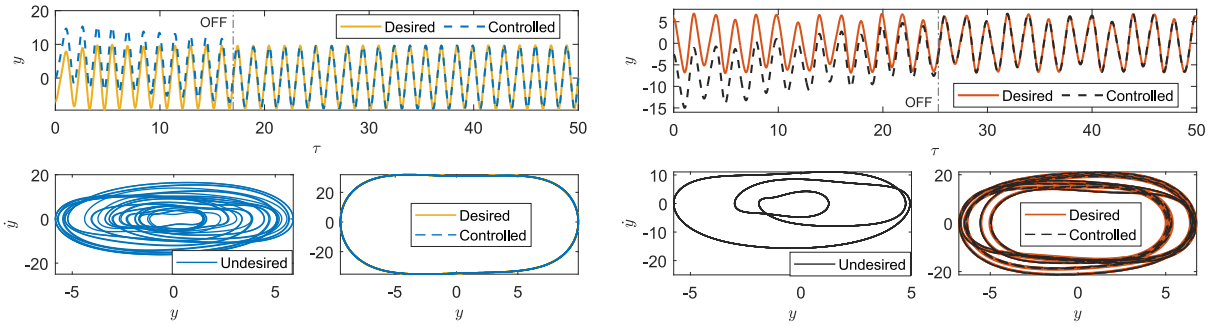

(a) Attractor switching from (a) → (f). $\kappa_1 = 1.9$, $\kappa_2 = 1.9$, $\eta_1 = 0.7$, $\eta_2 = 0.6$

(b) Attractor switching from (c) → (b). $\kappa_1 = 2$, $\kappa_2 = 2$, $\eta_1 = 0.1$, $\eta_2 = 0.6$

Figure 3: Controlled trajectories and phase portraits under two scenarios

turns off at $\tau = 17$. Finally, attractor (c) is entrained to (b) by the same controller, which turns off at $\tau = 25.3$ when the switching is complete.

3 Conclusions and Future work

The sliding mode control was designed and applied to the system to stabilize and entrain one attractor upon another. The short entrainment period is seen when the controlled attractor enters the neighborhood of the desired attractor, and the controller turns off. This method saves time and resources and enables attractor switching for various application scenarios. In the future, adaptation in the control law can be considered.

Acknowledgments

This work was completed while the first author, Godwin Sani, was a Doctoral Candidate in the Interdisciplinary Doctoral School, Lodz University of Technology, Poland, with support from the Polish National Science Centre, under the grant OPUS 18 No. 2019/35/B/ST8/00980

References

[1] Alexander N. Pisarchik, Ulrike Feudel Control of multistability, Physics Reports, **540** (4) (2014), 167–218.

[2] Godwin Sani, Jan Awrejcewicz, Zeric T. Njitacke, Modeling, analysis and control of parametrically coupled electromechanical oscillators, Mechanism and Machine Theory **191** (2024), 105514.

[3] Haji Hosseinloo, Ashkan, Jean-Jacques Slotine, Konstantin Turitsyn, Robust and adaptive control of coexisting attractors in nonlinear vibratory energy harvesters, Journal of Vibration and Control, **24** (12) (2018), 2532–2541.

International Conference on Mathematical Analysis and Applications in Science and Engineering
ICMA^{2}SC'24
ISEP Porto-Portugal, June 20 – 22, 2024

Zero-free regions of $\zeta^{(\alpha)}(s)$

Emanuel Guariglia

College of Science, Mathematics and Technology
Wenzhou-Kean University
88 Daxue Rd
325060 Wenzhou
China

School of Mathematical Sciences
Kean University
1000 Morris Avenue
07083 Union, NJ
USA

email: emanuel.guariglia@gmail.com

Abstract: This work concerns fractional calculus of the Riemann zeta function and its zero-free regions. The author already dealt with zero-free regions of the Lerch zeta functions. Here, we study with the case $\alpha > 3$ finding a corresponding zero-free region for $\zeta^{(\alpha)}(s)$. We also prove existence of a zero-free region in the left half-plane depending on α.

Keywords: Riemann zeta function, Grünwald-Letnikov fractional derivative, distribution of zeros, zero-free regions.

MSC2020: Primary 26A33, 11M06; Secondary 11M99, 11Y35.

References

[1] Belovas I. An inequality for the Riemann zeta function. Acta Math. Hungarica **170**(1), 367–378 (2023).

[2] Guariglia E. Riemann zeta fractional derivative – functional equation and link with primes. Adv. Difference Equ. **2019**(1), 261 (2019).

[3] Guariglia E. Fractional calculus of the Lerch zeta function – part II. Math. Methods Appl. Sci., Special Issue *Modelling, Analysis, and Applications* – ICMA2SC'2022, 1–15 (2024).

[4] Lee Y. Zeros of the derivatives of the Riemann zeta function on $\Re s < 1/2$. J. Number Theory **134**(1), 38–48 (2014).

[5] Li C, Dao X, Guo P. Fractional derivatives in complex planes. Nonlinear Anal. **71**(5-6), 1857–1869 (2009).

[6] Ortigueira MD, Trujillo JJ. Generalized Grünwald–Letnikov fractional derivative and its Laplace and Fourier transforms. J. Comput. Nonlinear Dyn. **6**(3), 034501 (2011).

[7] Spira R. An inequality for the Riemann zeta function. Duke Math. J. **32**(1), 247–250 (1965).

NEW INTEGRAL INEQUALITIES VIA HARDY-HILBERT AND MILNE INEQUALITIES

[1]**Mehmet Zeki Sarıkaya** [2⋆]**Mehmet Sabır Bingöl**

Düzce University, Türkiye

[1]sarikayamz@gmail.com, [2⋆]mehmetsabirbingol@gmail.com

Abstract: In this article, we aim to give some important new integral inequalities for the integrals of products of integrable non-negative functions with the help of Hardy-Hilbert inequalities and Milne Inequalities. Some applications are given for these inequalities.

keywords: Hardy-Hilbert's inequality; integral inequality; Milne's inequality.

MSC2020: 26D10; 26D07; 26D15.

References

[1] S. S. Dragomir, R. P. Agarwal and N. S. Barnett, Inequalities for beta and gamma functions via some classical and new integral inequalities, Journal of Inequalities and Applications, **5**(2) (2000), pp. 103– 165.

[2] S. S. Dragomir and and C.E.M. Pearce, *Selected Topics on Hermite–Hadamard Inequalities and Applications*, Internet Publication, http://rgmia.vu.edu.au,2000.

[3] M. Gurbuz and M. E. Özdemir, On some inequalities for product of different kinds of convex functions. Turkish Journal of Science, **5**(1)(2020), 23-27.

[4] G. Hardy, J.E. Littlewood and G. Polya, Inequalities, 2nd ed. Cambridge: Cambridge University Press; 1967.

[5] E.A. Milne, Note on Rosseland's integral for the stellar absorption, Mon. Not. R. Astron. Soc., **85**(9)(1925), 979–984.

[6] E. Set, ,M. E. Özdemir and S.Dragomir, On the Hermite-Hadamard inequality and other integral inequalities involving two functions, Journal of Inequalities and Applications, **2010**(2010), 1-9.

[7] B. G. Pachpatte, On some inequalities for convex functions. RGMIA Res. Rep. Coll, **6**(1)(2003), 1-9.

International Conference on Mathematical Analysis and Applications in Science and Engineering
ICMA^{2}SC'24
ISEP Porto-Portugal, June 20 - 22, 2024

Multifractals in Dynamical systems (On the Doubly non-monotonic perturbed map)

Ibrahim Alsendid

Mathematics Department, Faculty of Science, Sebha University, Sabha, Libya

Ibr.alsendid@sebhau.edu.ly

Submitted to the Special Session #12 (Dynamical Systems, Games and Applications).

Abstract: This paper considers the doubly non-monotonic perturbed map as a family of 2-dimensional piecewise linear area-preserving transformations on the 2-torus. Two parameters p and q take the transformation from a hyperbolic toral automorphism to the Cerbelli-Giona map which is a map known to exhibit multifractal properties. For certain parameter ranges, the map is ergodic, but the distribution of stable and unstable manifolds is far from uniform. We use the classical multifractal formalism to investigate the multifractal behavior of the map. The physical interpretations for the theoretical multifractal functions are shown by figuring out the numerical spectrum $f(\alpha)$ and computing the density (height of the $f(\alpha)$ curve), the dispersion (width of the $f(\alpha)$ curve), the clustering coefficient, and the skewed parameter. We also discuss the cancellation exponents for the map.

keywords: Multifractals; Dynamical systems; Mixing.

MSC2020: 49-XX; 34-XX; 92-XX.

1 Introduction

The dynamical system can be defined as a deterministic mathematical prescription for evolving the state of a system forward in time, either with continuous variable time or a discrete integer-valued variable time. Toral maps in dynamical systems are examples of a dynamical system in which time is a discrete variable. The dynamical systems can show an approach to mixing, and provide a minimal picture of mixing, some dynamical systems' maps are recognized as relevant (simple) models of the fluid mixing device. Hence, studying dynamical systems is an approach to understanding mixing. Multifractal behavior is important in practical settings to understand the performance of fluid mixing devices [1].
The study of multifractals has gained significant attention across various scientific disciplines such as image analysis, financial markets, biomedical signal analysis, climate science, and geographic information system, environmental monitoring, material science, and so on.
Examples in dynamical systems can be found in [2], while [3] explained the multifractal nature of turbulence and chaotic systems. The dynamical turbulence covered by [4], and chaotic systems discussed by [5]. Fractals and multifractal in fluid turbulence reviewed by [1]. Scaling and multifractal properties of mixing in chaotic flows provided by [6]. Persistent patterns and multifractality in fluid mixing are discussed in [7]. At its core, multifractal analysis delves into

the notion that different regions within a system can exhibit distinct scaling properties, challenging the traditional concept of uniform scaling. Unlike traditional fractals, which possess a single scaling exponent, multifractals capture the heterogeneity and self-similarity present in complex systems. This allows for a more nuanced understanding of the underlying dynamics, revealing hidden patterns and uncovering the intricate interplay between order and chaos. Multifractal analysis is a powerful mathematical tool used to study complex systems that exhibit self-similarity and scale invariance across multiple scales. It provides a quantitative framework for characterizing the heterogeneity and non-uniformity of various phenomena and exhibits a range of scaling behaviors across different scales [8].

The multifractality are addressed by several methods such as: the classical multifractal formalism, the multifractal detrended fluctuation analysis (MF-DFA), the wavelet transform modulus maxima (WTMM), and the multifractal detrending moving average (MFDMA). In [9] an efficient Python library are introduced (MFDFA library: from MFDFA import MFDFA; from MFDFA import fgn) for calculating the multifractal detrended fluctuation analysis (MFDFA). The MFDFA library in Python presented is a standalone package based integrally on Python's numpy. Available on `https://github.com/LRydin/MFDFA`.

The doubly non-monotonic perturbed map is a family of discrete-time dynamical systems from the 2-torus $T^2 = \mathbb{R}^2/\mathbb{Z}^2$ to itself, which includes maps in dynamical systems that are known for us such the Continuous Automorphism of the Toral map (CAT map) provided by Vladimir Arnold in [10], and the Cerbelli-Giona map (CG map) provided in [11] and deeply investigated by [12]. We studied these examples in order to replicate and extend Cerbelli & Giona's arguments for the perturbed CG map in [13] and investigate how uniformly distributed global stable and unstable manifolds can be.

In this research, the classical multifractal formalism is employed to investigate the multifractal behavior of the doubly non-monotonic perturbed map by taking a careful computational approach to show the results using Python data science. The ergodicity of the map will be investigated, which is the range of the parameters where the unstable and stable manifolds eventually cover the whole torus. Then, the distribution of the line-segments on the torus governed by the (forward/inverse) map will be tested. Then the following multifractal functions are computed: the fractal dimension D_0, the exponent α_0, the generalised fractal dimension D_q. Moreover, the q-representation (for which we display $f(q)$ versus D_q curves) will be illustrated. Furthermore, the monotonic function $\alpha(q)$ and the singularity multifractal spectrum $f(\alpha)$ for the map will also be provided. The advantage of multifractal techniques is that a $f(\alpha)$-spectrum integrates and quantifies spatial properties of a map in dynamical systems. Conceivably, multifractal parameters could be used to improve classifications of the structure of the map. Hence, an approximation to the shape and properties of a spectrum could be useful as physical interpretations. By representing the numerical spectrum $f(\alpha)$ we compute the density (height of the $f(\alpha)$ curve), the dispersion (width of the $f(\alpha)$ curve) $\Delta\alpha = \alpha_{\max} - \alpha_{\min}$, the clustering coefficient $\Delta f = f(\alpha_{\min}) - f(\alpha_{\max})$, and the skewed parameter $s = \frac{\alpha_{\max}-\alpha_0}{\alpha_0-\alpha_{\min}}$.

The cancellation exponent, as stated by [14], provides a quantitative characterization of the singularity inherent in the extreme tendency of the orientation of fast dynamo magnetic fields to oscillate rapidly in space. In this paper, we will also discuss the cancellation exponents for the doubly non-monotonic map.

2 Results

The results from this study suggest that the distribution of the line-segments of the manifold governed by the map affects the map's density, dispersion, and clustering.

3 Conclusions

In this research, the classical multifractal method is employed to set up a framework to study the multifractal behavior of discrete-time perturbed maps in dynamical systems, and Python data science is utilized to show our results.

Acknowledgments

I strongly admire and appreciate all the advice, time, help, and guidance from my Ph.D. supervisor Dr. Rob Sturman.

References

[1] Sreenivasan, KR. Fractals and multifractals in fluid turbulence. Annual review of fluid mechanics 23.1 (1991): 539-604.

[2] Halsey, Thomas C., et al. Fractal measures and their singularities: The characterization of strange sets. Physical review A 33.2 (1986): 1141.

[3] Benzi, Roberto, et al. On the multifractal nature of fully developed turbulence and chaotic systems. Journal of Physics A: Mathematical and General 17.18 (1984): 3521.

[4] McCauley, Joseph L. Introduction to multifractals in dynamical systems theory and fully developed fluid turbulence. Physics Reports 189.5 (1990): 225-266.

[5] McCauley, Joseph L. Multifractal description of the statistical equilibrium of chaotic dynamical systems. International Journal of Modern Physics B 3.06 (1989): 821-852.

[6] Muzzio, F. J., et al. Scaling and multifractal properties of mixing in chaotic flows. Physics of Fluids A: Fluid Dynamics 4.7 (1992): 1439-1456.

[7] Sundaram, Bala, Andrew C. Poje, and Arjendu K. Pattanayak. Persistent patterns and multifractality in fluid mixing. Physical Review E 79.6 (2009): 066202.

[8] Stanley, H. Eugene. Scaling, universality, and renormalization: Three pillars of modern critical phenomena. Reviews of modern physics 71.2 (1999): S358.

[9] Gorjao, L.R.; Hassan, G.; Kurths, J.; Witthaut, D. MFDFA: Efficient multifractal detrended fluctuation analysis in python. Computer Physics Communications 273 (2022): 108254.

[10] Arnold, Vladimir Igorevich and Avez, André, Ergodic problems of classical mechanics, 1968.

[11] Giona, Massimiliano, Stefano Cerbelli, and Alessandra Adrover. Invariant structures and multifractal measures in 2 d mixing systems. Fractals in Engineering: New Trends in Theory and Applications. London: Springer London, (2005): 141-155.

[12] MacKay, Robert S. Cerbelli and Giona's map is pseudo-Anosov and nine consequences. Journal of Nonlinear Science 16 (2006): 415-434.

[13] Alsendid, I.; Sturman, R. Multifractal properties of a family of non-monotonic toral mixing maps. SIAM Journal on Applied Dynamical Systems (2024): submitted 12 Feb 2024.

[14] Du, Y.; Ott, E. Physica D: Nonlinear Phenomena. Physics Letters A 67.4 (1993): 387-417.

International Conference on Mathematical Analysis and Applications in Science and Engineering
ICMA^{2}SC'24
ISEP Porto-Portugal, June 20 - 22, 2024

Theory of Hermite and Laguerre Bessel function from the umbral point of view

Umme Zainab

Department of Mathematics, National Institute of Technology, Kurukshetra,Haryana, India

umme.zainab15@gmail.com

Abstract: The theoretical underpinnings of hybrid families of special functions are examined through an umbral reformulation. Our discussion encompasses diverse families of Bessel-type functions and special polynomials, all situated within a unifying umbral-algebraic formalism. The method presented capitalizes on recent advancements in the formal treatment of higher transcendental functions, enabling novel and intriguing generalizations.

keywords: Hermite polynomials, Laguerre polynomials, Bessel functions, Tricomi functions, Operational rules, Definite integrals.

MSC2020: 33C10, 33C45, 33E20.

1 Introduction

This article explores various aspects of special functions, focusing on the category of hybrid special functions-analytic functions that are not expressed as series expansions of ordinary monomials but rather of special polynomials. Hermite Bessel functions (HBF) and Laguerre Bessel functions (LBF) serve as examples of such hybrid functions. Both HBF and LBF were introduced in reference [4], motivated initially by their incorporation into the theoretical foundations of the monomiality treatment of special functions (as discussed in ref. [4]). The study of these functions is further justified by their practical utility in applications, as elaborated upon later in this article. Many of the distinctive features of special functions cannot be adequately described through conventional approaches. Therefore, the significance of umbral techniques becomes apparent. These methodologies are extensively employed to elucidate myriad properties, including exponential and ordinary lacunary generating functions, umbral images, differential equations, among others, for both established and emerging special functions. Moreover, they are utilized to compute a variety of integrals that incorporate these functions. An outstanding application of umbral techniques lies in convolving two special functions, thereby introducing and exploring novel special functions, see for example [12, 13, 14, 15]. Therefore, this article present a new technique of umbral smbolic method to evaluate integrals hybrid special function.

Babusci *et al.* introduced certain concepts pertaining to umbral operators, including the establishment of a shift operator denoted as $\hat{c}$, acting on a vacuum function φ_0. It's worth noting that while this shift operator $\hat{c}$ can be defined on abstract grounds, Babusci and collaborators provided specific details and considerations regarding its implementation and properties.

The occurrence of shift operator $\hat{c}$ with vacuum φ_0 is given as [3]:

$$\hat{c}^{\mu}\varphi_0 = \frac{1}{\Gamma(1+\mu)}, \tag{1}$$

which satisfies the property

$$\hat{c}^{\mu}\hat{c}^{\nu} = \hat{c}^{\mu+\nu}, \tag{2}$$

consequently,

$$(\hat{c}^{\mu})^r = \hat{c}^{r\mu}. \tag{3}$$

The umbral image of Bessel function $J_n(x)$ is given by [2, 8]

$$J_n(x) = \left(\hat{c}\frac{x}{2}\right)^n e^{-\hat{c}\left(\frac{x}{2}\right)^2}\varphi_0. \tag{4}$$

The Hermite polynomials, classified among the orthogonal special polynomials, hold significant importance across various scientific domains. For instance, Hermite polynomials offer solutions to heat-type equations and are prevalent in applications related to quantum phase-space mechanics and optical beam transport problems, as discussed in [7]. The exponential expression of the generating functions of Hermite polynomials enhances their versatility, making them a potent tool for numerous applications. Recently, Hermite and Laguerre higher order polynomials have been studied in [5].

The 2-variable Hermite Kampé de Fériet polynomials (2VHKdFP) $H_n(x,y)$ defined by means of the following generating function [1]:

$$\sum_{n=0}^{\infty} H_n(x,y)\frac{t^n}{n!} = \exp(xt+yt^2), \tag{5}$$

$H_n(x,y)$ are solution of the heat equation too and can accordingly be defined through the operational rule

$$H_n(x,y) = e^{y\partial_x^2}x^n. \tag{6}$$

Dattoli *et al.* obtain the umbral image of $H_n(x,y)$ as:

$$H_n(x,y) = (x + \sqrt{y}\hat{h})^n\phi_0, \tag{7}$$

where ϕ_0 is known as polynomial vacuum and $\sqrt{y}\hat{h}$ is an umbra acting on the state ϕ_0 yields the 2VHP $H_n(x,y)$ given by

$$\sqrt{y}\hat{h}^{\,r}\phi_0 = \frac{y^{\frac{r}{2}}r!}{\Gamma(\frac{r}{2}+1)}\left|\cos r\frac{\pi}{2n}\right| \qquad (\phi_0 \neq 0). \tag{8}$$

In this article, we delve deeper into the investigation of hybrid functions and polynomials, employing a distinct variant of umbral theory developed over the last two decades, as summarized in [8, 2, 3, 10, 11]. This formulation, known as indicial umbral calculus, offers advantages such as simplifying the complexity of higher transcendental functions. According to this perspective, Bessel functions are treated akin to ordinary Gaussians or rational functions, while special polynomials are considered as Newton binomials [6].

2 Results and discussion

Theorem 1 The umbral images of Hermite-Bessel function ${}_HJ_n(x,y)$, Laguerre-Bessel function ${}_LJ_n(x,y)$, Hermite-Tricomi function ${}_HC_n(x,y)$ and Laguerre-Tricomi function ${}_LC_n(x,y)$ are given by

$$ {}_HJ_n(x,y) = \left(\hat{c}\frac{x+\sqrt{y}\hat{h}}{2}\right)^n e^{-\hat{c}\left(\frac{x+\sqrt{y}\hat{h}}{2}\right)^2}\varphi_0\phi_0 \tag{9}$$

$$ {}_LJ_n(x,y) = \left(\hat{c}\frac{y-x\hat{c}}{2}\right)^n e^{-\hat{c}\left(\frac{y-x\hat{c}}{2}\right)^2}\varphi_0. \tag{10}$$

$$ {}_HC_n(x,y) := C_n(x+\sqrt{y}\hat{h})\phi_0 = \hat{c}^n e^{-\hat{c}(x+\sqrt{y}\hat{h})}\varphi_0\phi_0 \tag{11}$$

and

$$ {}_LC_n(x,y) := C_n(y-\hat{c}_1 x)\varphi_{1,0} = \hat{c}_2^n e^{-\hat{c}_2(y-x\hat{c_1})}\varphi_{1,0}\varphi_{2,0}, \tag{12}$$

where $\hat{c}_1$ and $\hat{c}_2$ operate on vacuum $\varphi_{1,0}$ and $\varphi_{2,0}$, respectively.

Theorem 2 *The following integral identity for Hermite-Bessel functions ${}_HJ_n(x,y)$ holds true:*

$$ \int_{-\infty}^{\infty} {}_HJ_n(x,y)dx = \begin{cases} 0 & \text{if } n \text{ is odd,} \\ 2 & \text{if } n \text{ is even.} \end{cases} \tag{13}$$

Theorem 3 *The following integral identity for Laguerre-Bessel functions ${}_LJ_n(x,y)$ holds true:*

$$ I_n = \begin{cases} 0 & \text{if } n \text{ is odd,} \\ 2 & \text{if } n \text{ is even.} \end{cases} . \tag{14}$$

Theorem 4 The $0^{th}-$order Hermite-Bessel functions ${}_HJ_0(x,y)$ satisfies the following integral identity:

$$ \int_0^{\infty} {}_HJ_0(x,y)x\,dx = 2 - 2_{\sqrt{y}}\hat{h}\phi_0. \tag{15}$$

Theorem 5 The$0^{th}-$order TF $C_0(ux)$, $0^{th}-$order LTF ${}_LC_0(ux,uy)$ and $0^{th}-$order HTF ${}_HC_0(ux,u^2y)$ satisfy the following integral identities:

$$ \int_0^{\infty} C_0(ux)e^{-bu}dx = \frac{1}{b}e^{\frac{-x}{b}}, \tag{16}$$

$$ \int_0^{\infty} {}_LC_0(ux,uy)e^{-bu}\,du = \frac{1}{b}e^{\frac{-y}{b}}C_0\left(\frac{-x}{b}\right) \tag{17}$$

and

$$ \int_0^{\infty} {}_HC_0(ux,u^2y)e^{-bu}\,du = \frac{1}{b}e^{\frac{-x}{b}+\frac{y}{b^2}}. \tag{18}$$

3 Conclusions and Future work

The theory of Bessel and Tricomi functions constitutes a vast field of research with numerous applications. Many special functions are directly or indirectly connected to Bessel functions. Jekhowsky [9] explored multi-variable Bessel functions, which find applications in various branches of physics. The convolution of Bessel functions discussed in this paper has potential utility in solving existing and emerging problems in the realm of special functions and physics. This perspective provides a framework to explore new aspects and opens up analytical possibilities for further generalizations in the theory of special functions. Bessel functions and multi-variable Hermite and Laguerre polynomials have been shown to play a new and significant role within this framework. Their theories are explored in a simplified and unified manner using the umbral formalism, as discussed here.

References

[1] Appell, P.; Kampé de Fériet, J. *Fonctions Hypergéométriques et Hypersphériques: Polynômes d' Hermite. Gauthier-Villars, Paris,* 1926. https://doi.org/10.48550/arXiv.1103.3947

[2] Babusci, D.; Dattoli, G.; Górska, K.; Penson, K. A. The spherical Bessel and Struve functions and operational methods. *Appl. Math. Comput.* **238** (2014), 1-6.

[3] Babusci, D.; Dattoli, G.; Górska, K.; Penson, K. A. Lacunary generating functions for the Laguerre polynomials. *Sém. Lothar. Combin.* **76** (2017), Art. B76b, 19 pp.

[4] Dattoli, G. Hermite-Bessel and Laguerre-Bessel functions: a by-product of the monomiality principle. *Advanced special functions and applications (Melfi, 1999)*, 147-164, Proc. Melfi Sch. Adv. Top. Math. Phys., **1**, *Aracne, Rome*, 2000.

[5] Dattoli, G.; Garra, R. Licciardi S. Hermite, Higher order Hermite, Laguerre type polynomials and Burgers like equations. *Journal of Computational and Applied Mathematics,* **13** (2024) 115821.

[6] Dattoli, G.; Germano, B.; Martinelli, M. R.; Ricci, P. E. Lacunary Generating Functions of Hermite Polynomials and Symbolic Methods. *Ilirias Journal of Mathematics.* **4** (2015), 16-23.

[7] Dattoli, G.; Lorenzutta, S.; Maino, G.; Torre, A.; Cesarano, C. Generalized Hermite polynomials and super-Gaussian forms. *J. Math. Anal. Appl.* **203** (1996), no. 3, 597-609.

[8] Dattoli, G.; Licciardi, S. Operational, umbral methods, Borel transform and negative derivative operator techniques. *Integral Transforms Spec. Funct.* **31** (2020), no. 3, 192-220.

[9] Jekhowsky, B. Les fonctions de Bessel de plusieurs variables exprimées pour les fonctions de Bessel d'une variable, *CR Acad. Sci. Paris Sér. I Math.* **162** (1916), 38-319.

[10] Raza, N.; Zainab U.; Araci, S.; Esi, A. Identities involving 3-variable Hermite polynomials arising from umbral method. *Adv. in Differ. Equ.* **640** (2020), 1-16.

[11] Raza, N.; Zainab, U. The Mittag-Leffler-Legendre polynomials and their Lie-algebraic relations. *Rep. Math. Phys.* **89** (2022), no. 1, 97-129.

[12] Raza, N.; Zainab, U. Mittag-Leffler-Gould-Hopper polynomials: symbolic approach. *Rendiconti del Circolo Matematico di Palermo Series 2*, (2023) 1-28.

[13] Riyasat, M. A Riordan array approach to Apostol type-Sheffer sequences. *Filomat* **33** (2019), no. 18, 6025-6038.

[14] Riyasat, M. Densely generated 2D q-Appell polynomials of Bessel type and q-addition formulas, *Boletim da Sociedade Paranaense de Matemática*, **40** (2022) 1-9.

[15] Wani, S. A.; Riyasat, M. Integral transforms and extended Hermite-Apostol type Frobenius-Genocchi polynomials. *Kragujevac J. Math.* **48** (2024), no. 1, 41-53.

International Conference on Mathematical Analysis and Applications in Science and Engineering
ICMA^{2}SC'24
ISEP Porto-Portugal, June 20 - 22, 2024

BASIC PROBLEMS IN THE THEORY OF PSEUDO-DIFFERENTIAL EQUATIONS

Vladimir Vasilyev*

Belgorod State National Research University, Russia

*vbv57@inbox.ru

Abstract: A solvability problem for elliptic pseudo-differential equations in domains with a non-smooth boundary is studied. Digitization problem for these equations and certain problems related to a limit transform with a small parameter are considered also.

keywords: pseudo-differential equation; solvability; digitization; small parameter.

MSC2020: 35S05; 47G30; 65N15.

1 Introduction

The theory of pseudo-differential equations is based on a local principle, which asserts that for Fredholm property for a general equation one needs to describe of unique solvability for a special *model* equation in a certain *canonical* domain.

A model pseudo-differential operator has a symbol non-depending on a spatial variable, and canonical domain is a cone in Euclidean space $\mathbb{R}^m$. Equations in a whole space $\mathbb{R}^m$ and in a half-space $\mathbb{R}^m_+ = \{x \in \mathbb{R}^m : x = (x', x_m), x_m > 0\}$ were studied earlier in the starting part of the theory. Let us note, these cases present cones also. The work [3] has suggested an approach to studying solvability of model equations in conical domains, this idea is based on a special factorization of an elliptic symbol. General author's concept is presented in [4,5].

2 Results and discussion

1. Model equations. Model equation in a cone looks as follows

$$(Au)(x) = v(x), \quad x \in C, \quad x \in C, \tag{1}$$

where $A : H^s(C) \to H^{s-\alpha}(C)$ is a pseudo-differential operator with the symbol– $A(\xi)$ satisfying the condition

$$c_1(1 + |\xi|)^\alpha \le |A(\xi)| \le c_2(1 + |\xi|)^\alpha.$$

Under some additional assumptions with respect to the symbol $A(\xi)$ one can construct explicit solutions of the equation (1) for the cone C non-including a whole straight line [3].

2. Digitization. From computational point of view it is appropriately to consider the discrete analogue of the equation in a functional space with discrete variables, $u_d(\tilde{x}), \tilde{x} \in h\mathbb{Z}^m, h > 0$.

Let $C_d = h\mathbb{Z}^m \cap C$, be a discrete cone, $\hbar = h^{-1}, \mathbb{T} = [-\pi, \pi]$ and $A_d(\xi)$ be a measurable periodic function in $\mathbb{R}^m$ with basic cube of periods $\hbar\mathbb{T}^m$. A digital pseudo-differential operator A_d with the symbol $A_d(\xi)$ in the discrete cone C_d is defined by the formula

$$(A_d u_d)(\tilde{x}) = \sum_{\tilde{y} \in h\mathbf{Z}^m} h^m \int\limits_{\hbar\mathbf{T}^m} A_d(\xi) e^{i(\tilde{x}-\tilde{y})\cdot\xi} u_d(\tilde{y}) d\xi, \quad \tilde{x} \in C_d.$$

One can define discrete analogues of Sobolev–Slobodetskii functional spaces $H^s(C_d)$, and it is possible to describe solvability picture for discrete analogue of the equation (1) in discrete half-space, $C = \mathbb{R}^m_+$ [6,7]. It was established that discrete solution has good enough approximate properties for small h, and these discrete solutions can be treated as approximate solutions. Similar results were obtained in a discrete plane sector under some additional assumptions on the symbol. A comparison between discrete and continuous solutions is presented.

3. Small parameter. Each cone C has certain parameters as a rule, for example, $C^a_+ = \{x \in \mathbb{R}^2 : x = (x_1, x_2), x_2 > a|x_1|, a > 0\}$ has parameter a, the cone $C^{a,b}_+ = \{x \in \mathbb{R}^3 : x = (x_1, x_2, x_3), x_3 > a|x_1| + |x_2|, a, b > 0\}$ has two parameters a, b. It is natural question, what happens with solution of the equation (1) if some parameters tend to their endpoint values 0 and ∞. Some cases are considered in [8].

3 Conclusions and Future work

These studies continue in mentioned three directions. There are a lot of local situations, and we need to work for each situation separately. Of course, more difficulties are related to multi-dimensional situations.

References

[1] Mikhlin S.G., Prößdorf S. Singular Integral Operators. —Berlin, Akademie-Verlag, 1986.

[2] Eskin G. Boundary Value Problems for Elliptic Pseudodifferential Equations. AMS, Providence, RI, 1981.

[3] Vasil'ev, V.B. Wave Factorization of Elliptic Symbols: Theory and Applications. Kluwer Academic Publishers, Dordrecht–Boston–London,2000.

[4] Vasilyev V.B. Elliptic operators and their symbols. Demonstr. Math. **52** (2019) 361–369.

[5] Vasilyev V.B. Operator symbols and operator indices. Symmetry **12**:64 (2020) 1–12.

[6] Vasilyev V.B. Discreteness, periodicity, holomorhy, and factorization. In: C. Constanda et al. (eds.), Integral Methods in Science and Engineering, Volume 1, New York, Springer, 2017, pp. 315–324.

[7] Vasilyev A.V., Vasilyev V.B. Pseudo-differential operators and equations in a discrete half-space. Math. Model. Anal. **23**:3 (2018) 492–506.

[8] Vasilyev V.B. On certain 3-dimensional limit boundary value problems. Lobachevsmii J. Math. **41**:5 (2020) 917–925.

International Conference on Mathematical Analysis and Applications in Science and Engineering
ICMA^{2}SC'24
ISEP Porto-Portugal, June 20 - 22, 2024

STRONG CONVERGENCE OF INERTIAL SHRINKING PROJECTION METHOD FOR SPLIT BEST PROXIMITY POINT PROBLEM AND MIXED EQUILIBRIUM PROBLEM

Mohd Furkan[1⋆]

[1] University Polytechnic, Aligarh Muslim University, India

[1⋆]mohdfurkan786@gmail.com

Abstract: In this paper we introduce an inertial shrinking projection algorithm to approximate a solution of the best proximity point problem in such a way that the image of its solution under a bounded linear operator is the solution of the mixed equilibrium problem in the framework of real Hilbert spaces. Strong convergence theorem of the proposed algorithm has been established. We also derive some consequences from our main result. Further, we give a numerical experiment to determine the performance and superiority of the proposed algorithm. Finally, a comparison has also been carried out of our algorithm with an existing method.

keywords: mixed equilibrium problem; strong convergence; shrinking projection algorithm.

MSC2020: 49-29; 34-20; 92-25.

1 Introduction

Inspired and motivated by the work of Tiammee and Suantai [3], Husain et al. [1] and Suantai and Tiammee [2], our purpose in this paper is to introduce and analyze an inertial shrinking projection algorithm to find a solution of the split best proximity point problem and mixed equilibrium problem in the framework of real Hilbert spaces and we establish a strong convergence theorem. We also provide a numerical experiment to justify our method. Finally, a comparison has also been carried out of our algorithm with an existing method of Suantai and Tiammee [2].

2 Results and discussion

In this section, we prove strong convergence theorem based on the inertial shrinking projection algorithm for solving split best proximity point problem and mixed equilibrium problem.

Theorem 1. Let $\mathcal{M}_i \subset \Xi_1$ for i=1,2 and $\mathcal{N} \subset \Xi_2$ be nonempty, closed and convex subsets of Ξ_1 and Ξ_2, respectively. Let $\mathcal{B} : \mathcal{M}_1 \to \mathcal{M}_2$ be best proximally nonexpansive mapping such that $\mathcal{B}(\mathcal{K}_0) \subset \mathcal{D}_0$ with $\text{Best}_{\mathcal{M}_1}\mathcal{B} \neq \emptyset$. Let $\mathcal{A} : \Xi_1 \to \Xi_2$ be a bounded linear operator with adjoint operator $\mathcal{A}^*$. Let $g : \Xi_2 \to \Xi_2$ be a ξ-inverse strongly monotone mapping and let $\mathcal{Q}$: $\mathcal{N} \times \mathcal{N} \to \mathbb{R}$

be a bifunction satisfying $(\mathcal{C}_1)-(\mathcal{C}_4)$ with $\mathrm{MEP}(\mathcal{Q},g)\neq\emptyset$. Suppose that $\mathcal{B}$ satisfies the proximal property. Let $\{u_m\}$ be a sequence generated as follows:

$$\begin{cases} u_0, u_1 \in \mathcal{K}_0, \\ w_m = u_m + \delta_m(u_m - u_{m-1}), \\ y_m = (1-\xi_m)w_m + \xi_m P_{\mathcal{M}_1}\mathcal{B}w_m, \\ z_m = P_{\mathcal{M}_1}(y_m + \sigma\mathcal{A}^*(\mathcal{U}-\mathcal{I})\mathcal{A}y_m), \\ \mathcal{K}_{m+1} = \{u \in \mathcal{K}_m : \|z_m - u\| \leq \|y_m - u\| \leq \|w_m - u\|\}, \\ u_{m+1} = P_{\mathcal{K}_{m+1}}(u_0), \quad m = 1, 2, ..., \end{cases} \tag{1}$$

where $\mathcal{U} = \mathcal{F}^{\mathcal{Q}}_{\rho_m}(\mathcal{I} - \rho_m g)$, $\{\xi_m\} \subset (0,\, 1]$, $\{\rho_m\} \subset (0,\, \xi)$, $\xi > 0$, $\{\delta_m\} \subset [0, \delta]$, for some $\delta \in [0, 1)$ and $\sigma \in \left(0,\, \frac{1}{\|\mathcal{A}\|^2}\right)$. Suppose that $\mathcal{J} = \{\mathfrak{s}^* \in \mathrm{Best}_{\mathcal{M}_1}\mathcal{B} : \mathcal{A}\mathfrak{s}^* \in \mathrm{MEP}(\mathcal{Q}, g)\} \neq \emptyset$, Also, let the following conditions hold:

(i) $\limsup_{m\to\infty} \xi_m < 1$;

(ii) $\liminf_{m\to\infty} \rho_m > 0$.

Then the sequence $\{u_m\}$ converges strongly to a point $p^* \in \mathcal{J}$.

3 Conclusions and Future work

In this paper, we suggest and analyze an inertial shrinking projection algorithm for solving the split best proximity and mixed equilibrium problems. We approximate a solution of the best proximity problem in such a way that its image under a bounded linear operator is the solution of the mixed equilibrium problem under the setting of real Hilbert spaces. We construct an iterative algorithm for the proposed problem and prove a strong convergence theorem. Further, we deduce some special cases from our main convergence result. In addition, a numerical experiment has been presented to justify the convergence analysis of the proposed iterative algorithm. Finally, a comparison has also been carried out of our algorithm with an existing method and our algorithm (1) approached the stopping criteria faster than that of the sequence generated by the algorithm of Suantai and Tiammee [2].

Acknowledgments

Include acknowledgments, if any.

References

[1] S. Husain, F.A. Khan, M. Furkan, M.U. Khairoowala, N.H. Eljaneid, Inertial projection algorithm for solving split best proximity point and mixed equilibrium problems in Hilbert spaces, Axioms **11** (2022), 321.

[2] S. Suantai, J. Tiammee, The shrinking projection method for solving split best proximity point and equilibrium problems, Filomat, **35** (2021), 1133–1140.

[3] J. Tiammee, S. Suantai, On solving split best proximity point and equilibrium problems in Hilbert spaces, Carpathian Journal of Mathematics, **35** (2019), 385–392.

THERMAL NONEQILIBRIUM DOUBLE DIFFUSIVE CONVECTION IN A FLUID SATURATED ANISOTROPIC POROUS LAYER WITH SORET EFFECT

A.A. Altawallbeh1[1⋆] **Mohammed Z. Swalmeh2**[2] **Firas A. Alwawi3**[3]

[1] School of Basic and Marine Sciences, University of Jordan, 77110 Aqaba, Jordan
[2] Faculty of Arts and Sciences, Aqaba University of Technology, Aqaba, 77110, Jordan
[3] Prince Sattam Bin Abdulaziz University, Al-Kharj, 11942, Saudi Arabia

[1⋆] a.tawallbeh@ju.edu.jo

Abstract: Analytical study is investigated to report the Influence of Soret and anisotropy parameters on double-diffusive convection in a couple stress fluid-saturated anisotropic porous layer heated and salted from below. Fluid and solid phase are considered in local thermal nonequilibrium. A study based on Linear stability analysis has been conducted to study the effect of active parameters on the critical thermal Rayleigh number. The effect of anisotropy parameters, Soret parameter, and interphase heat transfer coefficient on the stationary convection are illustrated graphically. It was found that increasing the values of interphase heat transfer coefficient and negative values of Soret parameter stabilizes the system. On the other hand, increasing the values of mechanical anisotropy parameter and positive values of Soret parameter destabilize the system.

keywords: Thermal nonequilibrium; Anisotropic porous layer; Couple stress; Soret effect.

MSC2020: 49-XX; 34-XX; 92-XX.

1 Introduction

The problem of double-diffusive convection in porous media has received considerable attention, on account of its wide applications in natural systems and industries. When the heat transfer between the two phases (solid and liquid) is significant, then a local thermal non-equilibrium model (LTNM) must be considered. LTNM plays an important role in many applications such as drying, freezing of foods and other mundane materials and applications in everyday technology. Double diffusive convection in a porous layer saturated with viscoelastic fluid using thermal non-equilibrium model is investigated by [1]. Recently, [2] investigated the effect of thermal non-equilibrium and internal heat source on Brinkman-Benard convection.

Non-Newtonian fluids are more realistic for modeling some natural phenomena than Newtonian fluids. Double diffusive convection in a couple stress fluid saturated porous layer with internal heat source is studied by [3]. Recently, [4] investigated the influence of internal heat on double-diffusive convection in a couple stress fluid saturated anisotropic porous layer.

The gradients of temperature and concentration has a significant and cross influence on the flux of the other property. The influence of temperature gradient on the flow of pollutants is called the Soret effect. Different studies can be found in the literature concerning the Soret effects. see for example, [5], [6] and [7].

The aim of this work is to investigate the influence of Soret effect on local thermal non-equilibrium double diffusive convection in a couple stress fluid saturated isotropic porous layer.

2 Mathematical Model

The physical model under consideration, is an infinite horizontal anisotropic porous layer saturated with couple stress fluid confined between two parallel horizontal planes at $z = 0$ and $z = d$ with a distance d apart. Adverse temperature and concentration gradients are applied across the porous layer, and the lower and upper planes are kept at temperature $T0 + \Delta T$, concentration $S0 + \Delta S$, and $T0, S0$, respectively, where ΔT and ΔS are temperature difference and concentration difference between walls, respectively. A two-field model that represents the fluid and solid phases separately is employed for the energy equation. Soret effect is considered. Under these assumptions and after deriving the basic and perturbed states, the following non-dimensional governing equations are obtained:

$$\frac{1}{V}\frac{\partial}{\partial t}\nabla^2\psi + \left(\frac{\partial^2}{\partial x^2} + \frac{1}{\xi}\frac{\partial^2}{\partial z^2}\right)\left(1 - M\nabla^2\right)\psi + Ra_T\frac{\partial T_f}{\partial x} - Ra_s\frac{\partial S}{\partial x} = 0 \tag{1}$$

$$\frac{\partial T_f}{\partial t} - \left(\eta_f\frac{\partial^2}{\partial x^2} + \frac{\partial^2}{\partial z^2}T_f\right) - H(T_s - T_f) - \frac{\partial(\psi, T_f)}{\partial(x, z)} - \frac{\partial\psi}{\partial x}\frac{\mathrm{d}T_{fb}}{\mathrm{d}z} = 0 \tag{2}$$

$$\Gamma\frac{\partial T_s}{\partial t} - \left(\frac{\partial^2}{\partial x^2} + \frac{\partial^2}{\partial z^2}\right) + \gamma H(T_s - T_f) = 0 \tag{3}$$

$$\frac{\partial S}{\partial t} - \frac{1}{Le}\left(\frac{\partial^2}{\partial x^2} + \frac{\partial^2}{\partial z^2}\right)S - \frac{\partial(\psi, S)}{\partial(x, z)} + \frac{\partial\psi}{\partial x} - Sr\frac{Ra_T}{Ra_s}\nabla^2 T_f = 0 \tag{4}$$

Where $V = \frac{\epsilon P_r}{Da}$ Vadasz number, $Ra_T = \frac{\beta_T g\Delta T d K_z}{\nu\kappa_{f_z}}$ the thermal Rayleigh number , $Ra_s = \frac{\beta_s g K_z \Delta C d}{\nu\kappa_{f_z}}$ the concentration Rayleigh number, $M = \frac{\mu_c}{\mu d^2}$ couple stress parameter, $\nu = \mu/\rho_0$ the kinematic viscosity, $Le = \frac{\kappa_{f_z}}{D}$ the Lewis number, $H = \frac{hd^2}{\epsilon\kappa_{f_z}}$ the interphase heat transfer coefficient, $\gamma = \frac{\epsilon\kappa_{f_z}}{(1-\epsilon)\kappa_{s_z}}$ porosity modified conductivity ratio. $Sr = \frac{C_r\beta_s}{\kappa_f\beta_T}$ is the Soret parameter, $\xi = \frac{K_x}{K_z}$ mechanical anisotropy parameter, $\eta_f = \frac{\kappa_{f_x}}{\kappa_{f_z}}$ thermal anisotropy parameter for fluid phase, $P_r = \frac{\nu}{\kappa_f}$ Prandtil number and $Da = \frac{K_z}{d^2}$ Darcy number. Now, Eqs. (1)–(4) are solved with the boundary conditions $\psi = \frac{\partial^2\psi}{\partial\psi^2} = T_f = T_s = S = 0 \qquad at \quad z = 0 \quad and \quad z = 1.$

2.1 Linear stability theory

To make the linear stability study, we neglect the Jacobian in Eqs. (1)–(4), and assume the solutions to be periodic waves. For the nontrivial solution of the resulted system, the determinant of coefficient matrix must vanish.

For the existence of neutral stability and stationary convection the real and imaginary part of growth rate ω must be zero at marginal state. So, the stationary Rayleigh number is given by

$$Ra_T^{st} = -\frac{(Ma^4a_1^2 - Le\pi Ra_s\alpha^2 + a^2a_1^2)(Ha_2^2\gamma + a^2a_2^2 + Ha^2)}{\pi\alpha^2(LeSra^2 + a^2)(H\gamma + a^2)} \tag{5}$$

, where $a^2 = \pi^2(\alpha^2 + 1), a_1^2 = \pi^2(\alpha^2 + 1/\xi), a_2^2 = \pi^2(\alpha^2\eta_f + 1)$.

3 Results and discussion

The results given in Eq. (5) has been presented graphically. The neutral stability curves are drown, and the variation of the thermal Rayleigh number Ra_T for stationary convection with respect to wave number α is depicted. The results simulated for fix values of $Le = 1, Ra_s = 250, \gamma = 1, \eta_f = 0.5, \xi = 0.8, M = 0.5, H = 10, Sr = 0.01$, with variations of H, Sr and ξ in each case, as shown in the following figures. Influence of interphase heat transfer coefficient H on the stationary convection in terms of thermal Rayleigh number is presented in Fig. 1(a). It is noticed that an increment in parameter H increases the values of thermal Rayleigh number Ra_T, and thus stabilize the system.

Effect of mechanical anisotropy parameter ξ is depicted in Fig. 1(b). As shown from figure an increase in ξ decreases the stationary marginal curves and thus and Ra_T. So, the mechanical anisotropy parameter has a destabilizing effect. It can be noticed that both interphase heat transfer coefficient and mechanical anisotropy parameter exert a big and significant effects on the stationary convection.

Fig. 1(c) shows the effect of the Soret parameter (Sr) on the stationary mode, indicating that an increase in negative values of Sr increases the stationary marginal curves and Ra_T. On the other hand, an increment on positive values of Sr decreases marginal curves, as well as Ra_T, which means positive Sr has a stabilizing effect, while negative one has a destabilizing effect.

4 Conclusions

The influences of Soret and anisotropy parameters on the onset of LTNM double-diffusive convection in a couple stress fluid-saturated porous layer was studied analytically using linear stability analysis. It was found that increasing the values of interphase heat transfer coefficient H and negative values of Soret parameter Sr stabilizes the system. On the other hand, increasing the values of mechanical anisotropy parameter and positive values of Soret parameter destabilize the system.

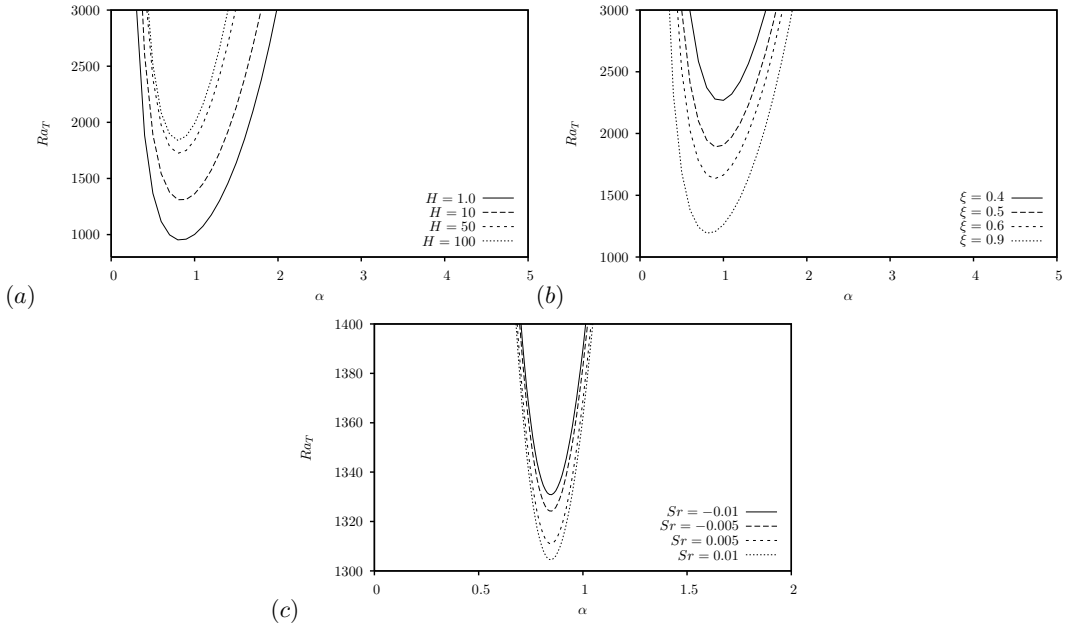

Figure 1: Effect of (a) H, (b) ξ, (c) Sr on the marginal stability curves for stationary convection, $Ra_s = 250, Le = 1, \eta_f = 0.5, \eta_s = 0.5, M = 0.5, \gamma = 1$

Acknowledgments

The authors gratefully acknowledge the Deanship of Scientific Research at the University of Jordan for their financial support.

References

[1] Anoj Kumar, B. S. Bhadauria, Double diffusive convection in a porous layer saturated with viscoelastic fluid using a thermal non-equilibrium model, Physics of Fluids, **23** (2011), 054101.

[2] C. Siddabasappa, T. Sakshath, Effect of thermal non-equilibrium and internal heat source on brinkman-benard convection, Phisica A, **566**(2021), 125617.

[3] S.N. Gaikwad, S. Kouser, Double diffusive convection in a couple stress fluid saturated porous layer with internal heat source, International Journal of Heat and Mass Transfer, **78**(2014), 1254–1264.

[4] A.A. Altawallbeh, S. Saraheen, A.A. Tawalbeh, Instability of a fluid saturated anisotropic porous layer using thermal nonequilibrium model, ASTFE Digital Library, **2023**, 1351–1359.

[5] A.A. Altawallbeh, B.S. Bhadauria, I. Hashim, Linear and nonlinear double diffusive convection in a in a saturated anisotropic porous layer with Soret effect and internal heat source, International Journal of Heat and Mass Transfer, **59** (2013), 103–111.

[6] A.A. Altawallbeh, B.S. Bhadauria, I. Hashim, Linear and nonlinear double-diffusive convection in a saturated porous layer with soret effect under local thermal non-equilibrium model, Journal of Porous Media, **21**(13) (2018), 1395–1413.

[7] A.A. Altawallbeh, Cross diffusion effect on linear and nonlinear double diffusive convection in a viscoelastic fluid saturated porous layer with internal heat sourcee, Fluids, **6** 182 (2021), 6050182.

International Conference on Mathematical Analysis and Applications in Science and Engineering
ICMA^{2}SC'24
ISEP Porto-Portugal, June 20 - 22, 2024

BASIC CONCEPTS ON ULAM STABILITY FOR BOUNDARY VALUE PROBLEMS FOR DIFFERENTIAL EQUATIONS

Snezhana Hristova[1⋆]

[1] Plovdiv University "P. Hilendarski", Bulgaria

[1⋆]snehri@gmail.com

Abstract: The main goal of this work is to emphasize on the application of Ulam type stability for boundary value problems for differential equations with various types of derivatives. We will give the basic concepts of the idea of Ulam type stability and we will discuss the main points in the application of Ulam type stability to boundary value problems. We will emphasize on some basic misunderstanding of this type of stability. We will give an idea how the common misunderstandings could be avoided in the study. The new ideas about the application of Ulam type stability will give a tool for further studies in this area.

keywords: Ulam stability; boundary value problems; differential equations; fractional derivatives.

MSC2020: 34D99; 34A08; 34B37.

1. Introduction

Ulam stability is an important type of stability studied and applied for different types of differential equations. This type of stability has applications in optimization, biology and economics etc. and it is a special type of data dependence of solutions. For boundary value conditions applied to differential equations there are some misunderstandings in the study of Ulam type stability and the main goal of this paper is to discuss this. First we provide several examples with simulations to illustrate the ideas involved and then we present one of the possible ways to connect both the solutions of the given problem and the solutions of the corresponding inequality. To be more precise we consider one type of nonlinear boundary condition to impulsive fractional differential equations with a general C

aputo fractional derivative and we define Ulam stability and we obtain sufficient conditions on a finite interval. As special cases several problems in the literature problems are considered and their Ulam stability is studied.

The main goal of this paper is to present the Ulam type stability for boundary value problems (BVP). We pointed out the basic misunderstangs in some published paper when this type of stability and give one of the possible ways to avoid these misunderstandings and to study Ulam type stability for boundary value problem in a similar way as in the case of initial value problems.

2. Results and discussion

Without loss of generality we assume the initial time point is 0.

The basic scheme of study of Ulam type stability could be described:

Step 1. Define the main problem of study which consists of two parts:

- the differential equation
$$D_t x(t) = F(t, x),\ t \in [0, b], \tag{1}$$
where $x : (0, b] \to \mathbb{R}^n$ is the unknown function D_t is an applied derivative. Note $b \leq \infty$, $n \geq 1$, the applied derivative could be an ordinary derivative or a fractional derivative and the function F could have more than two arguments (it could obtain any type of integral or derivative);
- the initial condition(IVP) or the boundary condition (BVP).

Step 2 Obtain equivalent integral presentation (integral equation) of the solution of the problem in Step 1.

Step 3 Define an operator based on the integral equation in Step 2 and prove the existence (and uniqueness) of its fixed point (or points), i.e. a solution of the problem defined in Step 1.

Step 4 Define Ulam type stability (US).

Step 5 Proof of US;

2.1. Some misunderstandings in study Ulam stability for boundary value problems

Consider the differential equation (1) with the boundary condition

$$G(x(0), x(b)) = 0. \tag{2}$$

Let $\varepsilon > 0$. Consider the differential inequality

$$||D_t y - F(t, y)|| \leq \epsilon,\ t \in [0, b]. \tag{3}$$

We will recall the definition for Ulam type stability based on the classical papers [1], [2], [3]:

Definition 1 *The BVP* (1), (2) *is Ulam-Hyers stable (UHS) if there exists a real number* $C_F > 0$ *such that for each* $\varepsilon > 0$ *and for each solution* $\nu \in C^1[0, b]$ *of the DI* (3) *there exists a solution* $x \in C^1[0, b]$ *of* (1), (2) *with* $|\nu(t) - x(t)| \leq C_F \varepsilon$ *for* $t \in [0, b]$.

Note that any solution of DI (3) does not satisfy the boundary condition (2) and the obtained in Step 2 integral presentation for the solution of the boundary value problem (BVP) (1),(2) could be not true for any solution of DI (3).

For example, let the derivative D_t in differential equation (1) be an ordinary derivative, $n = 1$, $b = 1$, $F(t, x) = 1.5x$, and $G(u, v) = u + e^{-1.5}v - 2$, i.e. consider the BVP

$$x'(t) = 1.5x(t),\ t \in (0, 1], \qquad x(0) + e^{-1.5}x(1) = 2. \tag{4}$$

The BVP (4) has a unique solution $x(t) = e^{1.5t},\ t \in (0, 1.$

Let $\varepsilon > 0$ be an arbitrary number. Choose an arbitrary solution of the DI

$$|\nu'(t) - 1.5\nu(t)| < \varepsilon,\ t \in [0,1]. \tag{5}$$

For example, let $\nu(t) = \varepsilon t^2,\ t \in [0,1]$. Then $\nu(t)$ does not satisfy the boundary condition $\nu(0) + e^{-1.5}\nu(1) = 2$. The difference $|\nu(t) - x(t)| = |\varepsilon t^2 - e^{1.5t}|$ depends significantly on ε and it is unbounded with respect to ε. There does not exist a constant $C > 0$ such that $|\nu(t) - x(t)| = |\varepsilon t^2 - e^{1.5t}| \leq C\varepsilon$ for any ε and $t \in [0,1]$, i.e. according to Definition 1 the BVP (4) is not Ulam-Hyers stable.

2.1.1. How to avoid the misunderstandings.

Note that in the above example there is not a connection between the unique solution of the given BVP (4) with the arbitrary solution of differential inequality (5). Note, there are several papers studying various types of BVP for different types of differential equations in which there is no connection between the solution $u(.)$ of the differential inequality of the type (3) and the solution $x(.)$ of the given BVP but incorrectly they apply the integral presentation for the solution $u(.)$ corresponding to the solution of the BVP for the differential equation (see, for example, [4], [5] ,[6]). In connection with this we will suggest one of the possible ways to avoid the above misunderstandings and to connect the solution of the given BVP and the arbitrary solution of the corresponding differential inequality ([7]).

In the general case change the boundary condition (2) to a boundary condition with a parameter

$$G(x(0), x(b)) = \mu, \tag{6}$$

where $\mu \in \mathbb{R}$ is a parameter. Then try to prove that the BVP (1),(2) has a solution for any parameter $\mu \in \mathbb{R}$. For an arbitrary $\varepsilon > 0$ choose an arbitrary solution $\nu(t)$ of the differential inequality (3) and let the parameter $\mu = G(\nu(0), \nu(b))$, i.e., consider the differential equation (1) with the boundary condition (6). Consider the solution $x(t),\ t \in [0,b]$ of BVP (1), (6) and study the difference between the solution $x(t)$ and the chosen solution $\nu(t)$ of the differential inequality (3).

For example, consider the particular case (4) and change the boundary condition $x(0)+e^{-1.5}x(1) = 2$ to a boundary condition with a parameter, i.e. consider the boundary condition $x(0) + e^{-1.5}x(1) = \mu$ and the new boundary value problem

$$x'(t) = 1.5x(t),\ t \in (0,1], \qquad x(0) + e^{-1.5}x(1) = \mu, \tag{7}$$

where $\mu \in \mathbb{R}$ is a parameter.

The BVP (7) has a unique solution $x(t) = 0.5\mu e^{1.5t},\ t \in [0,1]$ for any parameter $\mu \in \mathbb{R}$. Then for an arbitrary solution $\nu(t)$ of DI (5) we choose the parameter $\mu = \nu(0) + e^{-1.5}\nu(1)$. For example, if $\nu(t) = \varepsilon t^1$ then $\mu = e^{-1.5}\varepsilon$. Then the solution of BVP (7) is $x(t) = 0.5\varepsilon e^{1.5(t-1)},\ t \in [0,1]$ and $|\nu(t) - x(t)| = \varepsilon|t^2 - 0.5e^{1.5(t-1)}| \leq 0.5\varepsilon$ for any $\varepsilon > 0$ and $t \in [0,1]$. Therefore, according to Definition 1 the BVP (4) is Ulam-Hyers stable.

Acknowledgments

This work is partially supported by the Bulgarian National Science Fund under Project KP-06-PN62.

References

[1] I.A. Rus, Ulam stability of ordinary differential equations, *Studia Univ. "Babes-Bolyai", Mathematica*, **LIV**, 4, (2009), 125-133.

[2] S.M. Ulam, *A Collection of Mathematical Problems*. Interscience Tracts in Pure and Applied Mathematics, no. 8; Interscience Publishers: New York, NY, USA, 1960.

[3] D.H. Hyers, G. Isac, Th.M. Rassias, *Stability of Functional Equations in Several Variables*, Birkhauser, 1998.

[4] K. Shah, S. Tunc, Existence theory and stability analysis to a system of boundary value problem, *J. Taibah Uni. Sci.*, **11**, 6, 2017, 1330-1342.

[5] A. Zada, S. Ali, Y. Li, Ulam-type stability for a class of implicit fractional differential equations with non-instantaneous integral impulses and boundary condition. *Adv. Differ. Equ.*, **2017** , 317 (2017).

[6] M. Zamir, K. Shah, M. I. Chohan, Stability theory and existence of solution to a multi-point boundary value problem of fractional differential equations, *Math. Sci.* **13** (2019), 53-60.

[7] Agarwal, R.P.; Hristova, S. Ulam-Type Stability for a Boundary-Value Problem for Multi-Term Delay Fractional Differential Equations of Caputo Type. *Axioms* (2022), **11**, 742. https:// doi.org/10.3390/axioms11120742

International Conference on Mathematical Analysis and Applications in Science and Engineering
ICMA^{2}SC'24
ISEP Porto-Portugal, June 20 - 22, 2024

Regularity Results for Anisotropic PDEs

Eurica Henriques[1⋆]

[1] Center of Mathematics CMAT, University of Trás-os-Montes e Alto Douro, Portugal

[1⋆]eurica@utad.pt

Abstract: In this seminar we revisit several previous works concerning anisotropic differential equations (i.e. evolution equations in which the diffusion takes a different form within different space directions) whose prototypes are

$$u_t - \operatorname{div}\left(u^{\gamma(x,t)} Du\right) = 0 \ , \quad \gamma(x,t) > 0 \ ;$$

$$u_t - \sum_{i=1}^{N} \left(u^{m_i}\right)_{x_i x_i} = 0 \ , \quad m_i > 0 \ ;$$

$$u_t - \sum_{i=1}^{N} \left(|u_{x_i}|^{p_i - 2} u_{x_i}\right)_{x_i} = 0 \ , \quad p_i > 1 \ ,$$

written for nonnegative bounded functions u defined in $\Omega_T = \Omega \times (0, T]$, being Ω a bounded domain in $\mathbf{R}^N$ and $0 < T < \infty$. Recently, in a joint collaboration with S. Ciani and I. Skrypnik, we went back to these anisotropic PDEs, focusing on the singular ones, and started to work on some of their open problems. We'll briefly discuss this ongoing project pointing out some of the difficulties one needs to address and overcome.

keywords: Porous medium equation; Singular/Degenerate PDEs; Regularity theory; Intrinsic scaling; Anisotropic PDEs

MSC2020: 35B65; 35K55; 35K65; 35K55, 35K67; 35Q35; 35D30

International Conference on Mathematical Analysis and Applications in Science and Engineering
ICMA²SC'24
ISEP Porto-Portugal, June 20 - 22, 2024

Existence and global regularity properties for anisotropic parabolic equations with variable growth

Sergey Shmarev

University of Oviedo, Spain

shmarev@uniovi.es

Abstract: We consider the homogeneous Dirichlet problem for the anisotropic parabolic equation

$$u_t - \sum_{i=1}^{N} D_{x_i}\left(|D_{x_i}u|^{p_i(x,t)-2}D_{x_i}u\right) = f(x,t)$$

in the cylinder $\Omega\times(0,T)$, where $\Omega\subset\mathbb{R}^N$, $N\geq 2$, is a parallelepiped. The exponents of nonlinearity p_i are given Lipschitz-continuous functions. It is shown that if $p_i(x,t) > \frac{2N}{N+2}$,

$$\mu = \sup_{Q_T}\frac{\max_i p_i(x,t)}{\min_i p_i(x,t)} < 1+\frac{1}{N}, \quad |D_{x_i}u_0|^{\max\{p_i(\cdot,0),2\}}\in L^1(\Omega), \quad f\in L^2(0,T;W_0^{1,2}(\Omega)),$$

then the problem has a unique solution

$$u\in C([0,T];L^2(\Omega)) \text{ with } |D_{x_i}u|^{p_i}\in L^\infty(0,T;L^1(\Omega)),\ u_t\in L^2(Q_T).$$

Moreover,

$$|D_{x_i}u|^{p_i+r}\in L^1(Q_T) \quad \text{with some } r=r(\mu,N)>0, \qquad |D_{x_i}u|^{\frac{p_i-2}{2}}D_{x_i}u\in W^{1,2}(Q_T).$$

The assertions remain true for a smooth domain Ω if $p_i=2$ on the lateral boundary of Q_T. This is a joint work with Rakesh Arora, Indian Institute of Technology (BHU), Varanasi 221005, India.

keywords: anisotropic parabolic equations; global higher integrability; second-order regularity

MSC2020: 35K65; 35K67; 35B65; 35K55; 35K99

References

[1] Rakesh Arora, Sergey Shmarev Existence and global second-order regularity for anisotropic parabolic equations with variable growth, J. Differ. Equ. **349** (2023) 83-124

International Conference on Mathematical Analysis and Applications in Science and Engineering
ICMA^{2}SC'24
ISEP Porto-Portugal, June 20 - 22, 2024

INVERSE PROBLEM FOR THE PSEUDOPARABOLIC EQUATION WITH $p-$LAPLACIAN AND DAMPING TERM

Khompysh Khonatbek[1] **Aidos Shakir**[2⋆]

[1] Al-Farabi Kazakh National University, Kazakhstan

[1]konat_k@mail.ru, [2⋆]ajdossakir@gmail.com

1 Introduction

Let Ω be a bounded domain in $\mathbb{R}^d$ with smooth boundary $\partial\Omega$, and $Q_T = \{(x,t) : \ x \in \Omega,\ 0 < t \leq T\}$ is the cylinder with the lateral $\Gamma_T = \{(x,t) : \ x \in \partial\Omega,\ 0 \leq t \leq T\}$. In the present work, we study the following inverse problem of finding the function (solution) $u(x,t)$ and the unknown coefficient $f(t)$, which satisfy the pseudoparabolic equation with $p-$Laplacian diffusion and damping term

$$u_t - \Delta u_t - \operatorname{div}\left(|\nabla u|^{p-2}\nabla u\right) = \gamma\,|u|^{\sigma-2}\,u + f(t)\cdot g(x,t) \ \text{ in } \ Q_T, \tag{1}$$

the initial condition

$$u(x,0) = u_0(x) \text{ in } \Omega, \tag{2}$$

the Dirichlet boundary condition

$$u(x,t) = 0 \ \text{ on } \ \Gamma_T, \tag{3}$$

and the integral overdetermination condition

$$\int\limits_{\Omega} (u\cdot\omega + \nabla u\cdot\nabla\omega)\,dx = e(t), \ \ 0 \leq t \leq T. \tag{4}$$

Here, γ – the coefficient of the damping term might be positive $\gamma > 0$ either negative $\gamma < 0$. The functions $g(x,t),\ u_0(x),\ \omega(x)$ and $e(t)$ are given. The exponents p and σ are given positive numbers such that

$$1 < p,\ \sigma < \infty. \tag{5}$$

Acknowledgments

This research work has been funded by Grant number AP19676624 the Ministry of Science and Higher Education of the Republic of Kazakhstan.

International Conference on Mathematical Analysis and Applications in Science and Engineering
ICMA²SC'24
ISEP Porto-Portugal, June 20 - 22, 2024

New Asymmetry Measure of a Poincaré Plot for Heart Rate Assessment

Mijat Paunović[1*] Marko Ćosić[2] Nikola N. Radovanović[3] Nadica Miljković[1,4]

[1] University of Belgrade - School of Electrical Engineering, Belgrade, Serbia
[2] Laboratory of Physics, Vinča Institute of Nuclear Sciences - National Institute of the Republic of Serbia, University of Belgrade, Belgrade, Serbia
[3] Pacemaker Center, University Clinical Center of Serbia, Belgrade, Serbia
[4] Faculty of Electrical Engineering, University of Ljubljana, Ljubljana, Slovenia

Abstract: We propose a new Heart Rate Asymmetry (HRA) measure that quantifies the Poincaré plot asymmetry. Our approach represents Poincaré plots of the RR intervals corresponding to the elapsed time between two heart beats in the form of a square matrix that can be further used to quantify Asymmetry Magnitude Index (AMI). Data available from two open databases from two distinct groups of subjects (with normal sinus rhythm and congestive heart failure) are used to present the dynamics of the variations of AMI in comparison to the three HRA indices over different consecutive time intervals. The proposed analysis allows us to choose an appropriate signal duration that is short enough for convenience of recording electrocardiograms. Our results indicate that AMI exhibits relatively constant variations with the change of interval duration as opposed to the existing HRA indices which demonstrate a steady increase in variations as time interval shortens. This suggests that electrocardiograms as brief as 5 minutes can be used to calculate AMI, making it potentially suitable for standard clinical use as well as for application in wearable technology. Also, our results reveal that the largest difference in asymmetry between two groups of subjects is obtained with new AMI measure making it a promising tool for clinical application.

keywords: electrocardiogram; heart rate asymmetry; heart rate variability; matrix norm; Poincaré plot;

MSC2020: 49-XX; 34-XX; 92-XX.

1 Introduction

Heart Rate Variability (HRV) is a natural physiological phenomenon that describes temporal variations in subject's RR intervals that represent consecutive heart beats. The mechanisms that regulate Heart Rate (HR) are dynamic and complex. Thus, a common approach is to employ techniques that are used for the analysis of nonlinear dynamic systems [1]. For example, the Poincaré plot (PP), maps an RR interval series into a 2D phase space and can be used for HRV assessment [2]. PP in healthy subjects has shown to be asymmetric relative to a 45° angle line, known as the Line of Identity (LI) [2]. The position of a point, relative to the LI, indicates whether the current RR interval is longer (above the LI), shorter (below the LI), or equal (on the LI) to the previous RR interval. This phenomenon is known as Heart Rate Asymmetry (HRA) [2]. Efforts have been set in place to develop indices for HRA quantification [3]. The existing indices quantify HRA by: (1) separating the dataset based on the

position relative to the LI into two subsets, (2) calculating a proposed cumulative feature for each subset independently, and (3) comparing the two features to obtain their relative contributions [3]. Inspired by existing approaches, we quantify HRA by analyzing the asymmetry of 2D-histogram estimated distributions of points in a PP.

We aim to answer the following research questions: (1) could a new proposed Asymmetry Magnitude Index (AMI) be used for PP asymmetry assessment and how does it perform in comparison to other existing HRA indices, and (2) what is the appropriate interval duration that is both short enough for convenience of HR recording and long enough to be indicative of HRA as longer time intervals.

2 Methods and Materials

The experimental results are obtained using R peak annotations from PhysioNet open-access databases - the Normal Sinus Rhythm RR Interval Database (NSR) [5], [6] and Congestive Heart Failure RR Interval Database database (CHF) [5], [7]. Data of age-matched subjects with age between 29 and 43 years at the time of data collection are selected from these two databases to isolate possible comorbidities in elderly subjects [8]. Overall, five and six patients from the nsr2db and chf2db groups, respectively, met the inclusion criterion. Fig. 1 depicts the difference between the PPs of sample subjects from two different groups - NSR and CHF.

Processing steps are performed using Matlab ver. R2023b (The Mathworks, Natick, USA). Since heart rates lower than 30 bpm are uncommon in practice [9], RR intervals greater than 2000 ms are considered as non-physiological and we excluded them from further analysis.

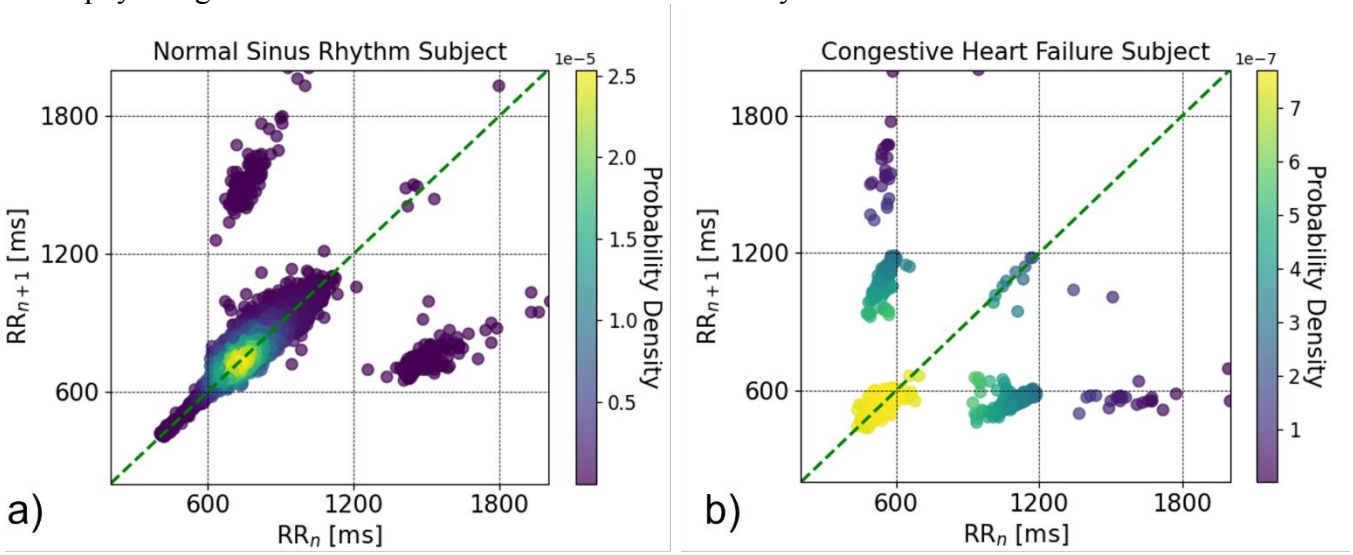

Figure 1 Poincaré plots (PPs) of sample subjects with a) normal sinus rhythm (NSR) and b) congestive heart failure (CHF)

Porta's index (PI) considers whether there are more points above or below the LI [10]. Guzik's index (GI) compares the cumulative squared distances between the points above and below the LI to the LI [2]. Asymmetric Spread Index (ASI) incorporates information on the position of a point along the LI, in addition to the distance. It merges this two information into a single feature, known as the arc length a_i. The a_i is calculated as a product of the distance of a point from the origin d_i, and the angle between the LI and the line connecting the point to the origin Θ_i. ASI compares the standard deviations of a_i of points above and below the LI [3].

We calculate the newly proposed AMI measure along with PI, GI, and ASI. AMI is calculated by the following steps: (1) Creating a 2D histogram of the points represented by a Poincaré plot. The result is the square matrix A, which represents an estimation of a 2D probability density function of the PP data; (2) Extracting the asymmetric component A_{asym} of the matrix A by taking the difference between matrix A and its reflection matrix over the main diagonal A^T; (3) Normalizing the A_{asym} matrix by its maximum value; and (4) Calculating the Frobenius norm (FN) of A_{asym} (Eq. 1).

$$||A_{asym}||_F = \sqrt{\sum_{i=1}^{m}\sum_{j=1}^{n}(A_{ij} - A_{ij}{}^T)^2} \quad (1)$$

The value of FN depends on the bin count, which reflects the duration of the original recording. Therefore, to obtain a duration-independent measure: (1) we define what we call "an ideal asymmetric component template", A_{IACT} as the matrix whose elements above and below the main diagonal are equal to +1 and -1, respectively, and (2) we define the normalization factor as the FN of the A_{IACT} as $||A_{IACT}||_F$. Finally, AMI is defined as the ratio between the $||A_{asym}||_F$ and the $||A_{IACT}||_F$. Matrices with greater symmetry are expected to yield AMI values closer to 0, while less symmetric ones should yield values closer to 1.

For each subject, we divide the R peak annotation data into *n* equal subsequent time intervals. The value of *n* varies from 3 to 300, corresponding to interval durations ranging approximately from 7 hours (for *n* = 3) to 4 minutes (for *n* = 300). For each set of *n* intervals, we proceed to calculate HRA indices for each interval. After obtaining HRA indices, we compute the standard deviation for each index at the given *n*, reflecting the variability of each HRA index across different interval durations within a 20-hour period. We report the median of Standard Deviation (SD) together with SD ranges across all subjects and all intervals for two distinct groups (NSR and CHF) and for all indices. This approach enables us to observe the fluctuation of each HRA index as the duration of the time intervals changes. Finally, we use relative ratios of median values to compare the performances of 20-hour AMI and the other existing HRA indices in differentiating between the NSR and CHF groups of subjects.

3 Results and Discussion

Median values and ranges for SDs of each index for two groups and across all intervals are presented in Table 1. AMI reveals the smallest median and maximal value of SD changes for all subjects and all intervals. ASI and PI have the lowest minimal SD values in NSR and CHF groups, respectively. However, the corresponding medians of ASI and PI are more than 16 and two times greater than the median of AMI. Such consistency across different time intervals may render AMI particularly suitable for standard clinical use and application in wearables where shorter time intervals are desirable.

Table 1. Median values and ranges for standard deviations normalized in range [0, 1] across all subjects and all intervals. Values are presented for proposed Asymmetry Magnitude Index (AMI), as well as for three indices found in literature: Porta Index (PI), Guzik Index (GI), and Asymmetric Spread Index(ASI). All indices are calculated separately for Normal Sinus Rhythm (NSR) and CHF (Congestive Heart Failure) groups of subjects.

	PI	**GI**	**ASI**	**AMI**
NSR	0.0186 [2.0810e-04 0.0720]	0.0337 [7.6850e-04 0.0974]	0.1091 [1.3962e-04 0.1687]	0.0068 [3.1641e-04 0.0193]
CHF	0.0159 [6.1679e-06 0.0357]	0.0128 [3.7238e-05 0.0623]	0.0648 [3.7685e-04 0.2184]	0.0068 [2.3306e-04 0.0220]

Median values for NSR group for PI, GI, ASI, and AMI are 0.4882, 0.5156, 0.5939, and 0.0389, respectively. Further, for CHF group, respective median values for HRA indices are 0.5019, 0.5000, 0.6678, and 0.0284. By their definition, PI, GI, and ASI yield values of 0.5 for symmetric PPs, while asymmetric plots have values closer to 0 or 1 depending on the feature contribution below or above the LI. For AMI, value of 0 indicates complete symmetry while 1 presents complete asymmetry. Therefore, medians of all indices suggest relatively high symmetries of PPs. It is expected that subjects with NSR experience more asymmetry than subjects with CHF [3]. The expectation is met for all indices except for ASI. Relative differences of medians for NSR and CHF groups in relation to the medians for NSR group are: 2.82% (PI), 3.03% (GI), 12.43% (ASI), and 27.16% (AMI). We can conclude that the largest

expected distinction between two groups of subjects is obtained by newly proposed AMI measure.

4 Conclusions and Future work

Our preliminary results on comparison of the proposed AMI measure with other existing asymmetry indices with the aim to present the analysis on small-time intervals (~5 min) and to differentiate between NSR and CHF subjects are promising. AMI shows the smallest dispersion for relatively short recordings, as well as the highest relative ratio when two groups of subjects are compared. Despite such encouraging results, a larger sample of diverse medical conditions is required to prove AMI usability and to apply appropriate tests for statistical significance.

Acknowledgments

NM is partly supported by the Ministry of Science, Technological Development and Innovation of the Republic of Serbia [Grant No. 451-03-65/2024-03/200103]. MĆ acknowledges the support from the Ministry of Science, Technological Development, and Innovation of the Republic of Serbia (grant No. 451-03-66/2024-03/ 200017).

Statement

Authors used GPT3.5 (ChatGPT) to improve readability. After the use of this tool, the first Author carefully reviewed the content of the paper.

References

[1] F. Shaffer and J. P. Ginsberg, "An Overview of Heart Rate Variability Metrics and Norms," *Front. Public Health*, vol. 5, p. 258, Sep. 2017, doi: 10.3389/fpubh.2017.00258.

[2] P. Guzik, J. Piskorski, T. Krauze, A. Wykretowicz, and H. Wysocki, "Heart rate asymmetry by Poincaré plots of RR intervals," *Biomed. Tech. Eng.*, vol. 51, no. 4, pp. 272–275, Oct. 2006, doi: 10.1515/BMT.2006.054.

[3] A. Rohila and A. Sharma, "Asymmetric spread of heart rate variability," *Biomed. Signal Process. Control*, vol. 60, p. 101985, Jul. 2020, doi: 10.1016/j.bspc.2020.101985.

[4] W. Ford, "Vector and Matrix Norms," in *Numerical Linear Algebra with Applications*, Elsevier, 2015, pp. 119–144. doi: 10.1016/B978-0-12-394435-1.00007-7.

[5] A. L. Goldberger *et al.*, "PhysioBank, PhysioToolkit, and PhysioNet: Components of a New Research Resource for Complex Physiologic Signals," *Circulation*, vol. 101, no. 23, Jun. 2000, doi: 10.1161/01.CIR.101.23.e215.

[6] P. Stein and R. Goldsmith, "Normal Sinus Rhythm RR Interval Database." physionet.org, 2003. doi: 10.13026/C2S881.

[7] R. Goldsmith, "Congestive Heart Failure RR Interval Database." physionet.org, 2003. doi: 10.13026/C2F598.

[8] M. J. Divo, C. H. Martinez, and D. M. Mannino, "Ageing and the epidemiology of multimorbidity," *Eur. Respir. J.*, vol. 44, no. 4, pp. 1055–1068, Oct. 2014, doi: 10.1183/09031936.00059814.

[9] P. Kligfield *et al.*, "Recommendations for the Standardization and Interpretation of the Electrocardiogram," *Circulation*, vol. 115, no. 10, pp. 1306–1324, Mar. 2007, doi: 10.1161/CIRCULATIONAHA.106.180200.

[10] A. Porta, S. Guzzetti, N. Montano, T. Gnecchi-Ruscone, R. Furlan, and A. Malliani, "Time Reversibility in Short-Term Heart Period Variability," 2006.

International Conference on Mathematical Analysis and Applications in Science and Engineering
ICMA^{2}SC'24
ISEP Porto-Portugal, June 20 - 22, 2024

Towards a nonlinear generalization of spectral decomposition

Jochen Merker[1⋆]

[1] HTWK Leipzig University of Applied Sciences, Germany

[1⋆]jochen.merker@htwk-leipzig.de

Abstract: We discuss a nonlinear generalization of the spectral theorem for selfadjoint linear operators by decomposing continuous absolutely homogeneous convex functionals with isolated minimum zero at the origin, i.e. powers of continuous norms. Our methods extend the case of one-homogeneous functional discussed in the paper "Nonlinear spectral decompositions by gradient flows of one-homogeneous functionals", Analysis & PDE, 2021, 14 (3), pp.823-860, by Leon Bungert, Martin Burger, Antonin Chambolle and Matteo Novaga, and allow various further generalizations.

keywords: nonlinear eigenvalue problems; nonlinear spectral decomposition; doubly nonlinear diffusion equations.

MSC2020: 35-P30; 47-J10.

1 Introduction

In this work, we discuss a nonlinear generalization of the spectral theorem for (possibly unbounded) self-adjoint linear operators A on a Hilbert space. This important theorem guarantees the existence of a Borel measure μ with values in the lattice of orthogonal projections, whose support is the spectrum $\sigma(A) \subset \mathbb{R}$ of the operator A and which allows decompositions

$$A = \int_{\sigma(A)} \lambda \, \mu(\mathrm{d}\lambda) \quad \text{and } \mathrm{Id} = \int_{\sigma(A)} \mu(\mathrm{d}\lambda)\,. \tag{1}$$

Since the 1970s, nonlinear spectral theory is concerned with the question how to define a spectrum for nonlinear operators, but this theory usually revolves around solvability of equations and not so much around existence of spectral decompositions. Particularly, given two (possibly nonlinear) operators $A : X \to X^*$, $B : Y \to Y^*$ on Banach spaces X, Y with a dense intersection, the problem to find those scalars λ and $u \in X \cap Y$ with $Bu \neq 0$ satisfying $Au = \lambda\, Bu$ is called a nonlinear eigenvalue problem, and if (λ, u) is a solution of this problem, then u is called a B-eigenvector of A to the B-eigenvalue λ. In the case that $B = \mathrm{Id}$ is the identification of a Hilbert space Y with its dual Y^* and $X \subset Y$ so that instead of the original $A : X \to X^*$ its strong realization $A_s : D(A) \subset X \subset Y \to Y^* \cong Y$ on $D(A) := \{u \in X \,|\, Au \in Y^* \subset X^*\}$ can be considered, those scalars λ, for which $\lambda\,\mathrm{Id} - A_s$ does not have a continuous inverse, define the so-called Rhodius spectrum [1] of A_s. Yet, this spectrum does not behave very well, therefore other notions of a nonlinear spectrum have been developed, for which we refer as basic reference to the monograph [2], or to the survey article [3].

Regarding a spectral decomposition of nonlinear operators, only very partial results seem to exist in literature. The case of Nemytskii operators is studied in [4], basis properties of eigenfunctions of the p-Laplacian are discussed in [5], and for basis properties of Fučík eigenfunctions see [6].

In this work, we consider subdifferentials $A = \partial\Phi_A$, $B = \partial\Phi_B$ of continuous absolutely homogeneous convex functionals $\Phi_A : X \to \mathbb{R}$, $\Phi_B : Y \to \mathbb{R}$ with isolated minimizer 0, i.e. monotone operators A, B having a power $\Phi_A(u) = \frac{1}{p}\|u\|_X^p$, $\Phi_B(u) = \frac{1}{q}\|u\|_Y^q$ of a continuous norm as potential, or equivalently duality mappings A, B on X, Y for powers $p, q > 1$. We follow the idea proposed by [7] for one-homogeneous functionals Φ_A, i.e. $p = 1$, and $B = \mathrm{Id}$ on a Hilbert space Y to obtain a nonlinear spectral decomposition via the (generalized nonlinear) gradient flow generated by the gradient system

$$\frac{dv}{dt} \in -Au\,, \quad v \in Bu \quad \text{for an initial value} \quad v(0) = v_0 \in Bu_0\,. \tag{2}$$

Such abstract doubly nonlinear diffusion equations have been studied e.g. in [8]. We show how to obtain from strong solutions of (2) a Borel measure μ_{v_0} on a measurable subset $\sigma_{v_0} \subset [0,\infty)$ satisfying

$$\Phi_A(u_0) = \int_{\sigma_{v_0}} \lambda\, \mu_{v_0}(\mathrm{d}\lambda) \quad \text{for } v_0 \in Bu_0 \quad \text{and} \quad \Phi_B^*(v_0) = \int_{\sigma_{v_0}} \mu_{v_0}(\mathrm{d}\lambda) \tag{3}$$

with the Fenchel conjugate Φ_B^* of Φ_B defined by $\Phi_B^*(v) := \sup_{u\in Y} (\langle v, u\rangle - \Phi_B(u))$. Further, $[0,\infty) \supset S \mapsto (v_0 \mapsto \mu_{v_0}(S))$ can be viewed as measure with values in the lattice of non-negative functionals on Y^*, and deserves to be named spectral measure due to the analogy of (3) and (1), where $q = 2$, $u_0 = v_0$ and $\mu_{v_0}(S) = \frac{1}{2}\langle \mu(S)u_0, u_0\rangle = \frac{1}{2}\|\mu(S)u_0\|^2$.

2 Nonlinear spectral decomposition via gradient flow

Theorem 1 *Assume that $\Phi_A : X \to \mathbb{R}$, $\Phi_B : Y \to \mathbb{R}$ are powers of continuous norms on reflexive Banach spaces X, Y with a dense and separable intersection such that $X \cap Y$ is separable and compactly embedded into Y, and that the subdifferential $B = \partial\Phi_B$ has a continuously differentiable inverse, then there exists a measure $[0,\infty) \supset S \mapsto (v_0 \mapsto \mu_{v_0}(S))$ with values in the lattice of non-negative functionals on Y^* such that* (3) *holds with the support σ_{v_0} of μ_{v_0}.*

Proof. Under the assumptions of the theorem, for an initial values $v_0 \in Y^*$ with $v_0 \in Bu_0$ for $u_0 \in Y$, the gradient system (2) admits a unique strong solution $v \in L^\infty(0,T;Y^*)$ with time derivative $\frac{\mathrm{d}v}{\mathrm{d}t} \in L^{p'}(0,T;X^*) \cap L^2(0,T;Y^*)$, $u \in L^p(0,T;X) \cap L^\infty(0,T;Y)$ with time derivative $\frac{\mathrm{d}u}{\mathrm{d}t} \in L^2(0,T;Y)$ for every $T < \infty$ (see [9, 11.2] for existence of weak solutions).

Particularly, (2) is valid as an equation in $L^{p'}(0,T;X^*) \cap L^2(0,T;Y^*)$, thus (2) can be tested by $u \in L^p(0,T;X)$ to obtain

$$\frac{\mathrm{d}}{\mathrm{d}t}\Phi_B^*(v(t)) = \langle \frac{\mathrm{d}}{\mathrm{d}t} v(t), B^{-1}v(t)\rangle = -\langle Au(t), u(t)\rangle \le 0 \tag{4}$$

due to $B^{-1}v(t) = u(t)$ and monotonicity of A with $A0 = 0$, and by $\frac{\mathrm{d}}{\mathrm{d}t}u(t) \in L^2(0,T;Y)$ to obtain

$$\frac{\mathrm{d}}{\mathrm{d}t}\Phi_A(u(t)) = \langle Au(t), \frac{\mathrm{d}}{\mathrm{d}t}u(t)\rangle = -\langle \frac{\mathrm{d}}{\mathrm{d}t}v(t), \frac{\mathrm{d}}{\mathrm{d}t}u(t)\rangle \le 0 \tag{5}$$

due to $\langle v(t+h) - v(t), u(t+h) - u(t)\rangle \ge 0$ for $v(t) \in Bu(t)$, $v(t+h) \in Bu(t+h)$ and every $h > 0$. i.e. monotonicity of B. Thus, $\Phi_A(u(t))$, $\Phi_B^*(v(t))$ are monotone decreasing w.r.t. time t and induce Lebesgue-Stieltjes measures $\mathrm{d}\Phi_A(u(t))$, $\mathrm{d}\Phi_B^*(v(t))$ on the time interval $[0,\infty)$.

Further, because $0 \in Au$ only if $u = 0$ and B^{-1} is continuous, we have $\lim_{t\to\infty} \Phi_A(u(t)) = 0$ and $\lim_{t\to\infty} \Phi_B^*(v(t)) = 0$, hence

$$\begin{aligned} \Phi_A(u_0) &= -\int_0^\infty \frac{\mathrm{d}\Phi_A(u(t))}{\mathrm{d}t}\,\mathrm{d}t = \int_0^\infty \mathrm{d}\Phi_A(u(t)) \quad \text{and} \\ \Phi_B^*(v_0) &= -\int_0^\infty \frac{\mathrm{d}\Phi_B^*(v(t))}{\mathrm{d}t}\,\mathrm{d}t = \int_0^\infty \mathrm{d}\Phi_B^*(v(t))\,. \end{aligned} \tag{6}$$

Now the Lebesgue-Stieltjes measure $\mathrm{d}\Phi_A(u(\cdot))$ on $[0,\infty)$ is absolutely continuous w.r.t. $\mathrm{d}\Phi_B^*(v(\cdot))$, because if $\Phi_B^*(v(\cdot)) = \text{const}$ on $T \subset [0,\infty)$, then $\langle Au(\cdot), u(\cdot)\rangle = 0$ on T so that T is a null set for $\mathrm{d}\Phi_A(u(t))$, too. Therefore, its Radon-Nikodym derivative $\lambda(t) := \frac{\mathrm{d}\Phi_A(u(t))}{\mathrm{d}\Phi_B^*(v(t))}$ mapping $[0,\infty)$ measurable onto a subset $\sigma_{v_0} \subset [0,\infty)$ can be used to obtain as image of $\mathrm{d}\Phi_B^*(v(t))$ under $\lambda(t)$ for each $v_0 \in Y^*$ a Borel measure μ_{v_0} on σ_{v_0}. This measure μ_{v_0} on σ_{v_0} is defined by $\mu_{v_0}(S) = \mathrm{d}\Phi_B^*(v(\cdot))(\lambda^{-1}(S))$ for measurable $S \subset [0,\infty)$ and satisfies by substitution rule

$$\begin{aligned} \Phi_A(u_0) &= \int_0^\infty \frac{\mathrm{d}\Phi_A(u(t))}{\mathrm{d}\Phi_B^*(v(t))}\,\mathrm{d}\Phi_B^*(v(t)) = \int_{\sigma_{v_0}} \lambda\,\mu_{v_0}(\mathrm{d}\lambda) \quad \text{for } v_0 \in Bu_0 \text{ and} \\ \Phi_B^*(v_0) &= \int_0^\infty \mathrm{d}\Phi_B^*(v(t)) = \int_{\sigma_{v_0}} \mu_{v_0}(\mathrm{d}\lambda)\,. \end{aligned} \tag{7}$$

Finally, for each measurable $S \subset [0,\infty)$ the functional $v_0 \mapsto \mu_{v_0}(S)$ is non-negative, because $\Phi_B^*(v) = \frac{1}{q'}\|v\|_{Y^*}^{q'}$ is non-negative and μ_{v_0} is just a reparametrization of the Lebesgue-Stieltjes measure $\mathrm{d}\Phi_B^*(v(\cdot))$ by $\lambda(t)$. Therefore, $[0,\infty) \supset S \mapsto (u_0 \mapsto \mu_{v_0}(S))$ can be viewed as measure on $0,\infty)$ with values in the lattice of non-negative functionals on Y^*. ■

3 Conclusions and Future work

The result presented in Section 2 can be extended into various directions:

If Φ_A is a power of a continuous seminorm (instead of a norm), then the limit $u_\infty := \lim_{t\to\infty} u(t)$ does not need to be zero, and instead $\Phi_A(u_0) - \Phi_A(u_\infty) = \int_{\sigma_{v_0}} \lambda\,\mu_{v_0}(\mathrm{d}\lambda)$ holds, where u_∞ is due to $Au_\infty = 0$ an eigenvector to the eigenvalue zero and $\Phi_A(u_\infty)$ is the part corresponding to this eigenvalue zero in the nonlinear spectral decomposition.

If Φ_A is just a general convex functional with minimum 0 at the isolated minimizer 0, then existence and uniqueness of solutions to (2) have to be carefully studied, but it seems so that the same result can be obtained. In this case the result can be further extended to differences of convex functionals (like selfadjoint operators are differences of positive self-adjoint operators).

If there is a positive cone Y_+^* on Y^*, then separately $\Phi_B(v_+)$ and $\Phi_B(v_-)$ could be decomposed leading to a decomposition w.r.t. Fučík spectrum. Yet, to rigorously obtain such results further research is needed.

References

[1] A. Rhodius, Der numerische Wertebereich und die Lösbarkeit linearer und nichtlinearer Operatorengleichungen, Math. Nachr. **79** (1977), 343–360.

[2] J. Appell, E. De Pascale, A. Vígnoli, *Nonlinear Spectral Theory.* Berlin, New York: De Gruyter, 2004.

[3] Alessandro Calamai, Massimo Furi, Alfonso Vígnoli, An Overview on Spectral Theory for nonlinear operators, Communications in Applied Analysis **13**(4) (2009), 509–534.

[4] Hermann Flaschka, A nonlinear spectral theorem for abstract Nemytskii operators, Indiana University Mathematics Journal **21**(3) (1971), 265–276.

[5] Paul Binding, Lyonell Boulton, Jan Čepička, Pavel Drábek, Petr Girg, Basis properties of eigenfunctions of the p-Laplacian, Proc. Amer. Math. Soc. **134** (2006), 3487–3494.

[6] Falko Baustian, Vladimir Bobkov, Basis Properties of Fučík Eigenfunctions, Anal Math **48** (2022), 619–648.

[7] Leon Bungert, Martin Burger, Antonin Chambolle, Matteo Novaga, Nonlinear spectral decompositions by gradient flows of one-homogeneous functionals, Analysis & PDE **14**(3) (2021), 823–860.

[8] Aleš Matas, Jochen Merker, Existence of weak solutions to doubly degenerate diffusion equations, Appl. Math. **57** (2012), 43–69.

[9] T. Roubíček, *Nonlinear partial differential equations with applications*. Basel: Birkhäuser, 2005.

International Conference on Mathematical Analysis and Applications in Science and Engineering
ICMA^{2}SC'24
ISEP Porto-Portugal, June 20 - 22, 2024

Approximation of fuzzy numbers and fuzzy-valued functions

M.I. Berenguer[1⋆] **D. Gámez**[1] **A.I. Garralda-Guillem**[1] **M. Ruiz Galán**[1]

[1] Departamento de Matemática Aplicada e Instituto de Matemáticas (IMAG), E.T.S. de Ingeniería de Edificación, Universidad de Granada

[1⋆]maribel@ugr.es

Abstract: In this talk, we present constructive methods for approximating fuzzy numbers and fuzzy-valued functions of a real variable. Our techniques are based on the use of appropriate Schauder bases in certain Banach spaces. We illustrate the approximations obtained in some particularly interesting cases by providing algorithms of great simplicity.

keywords: Fuzzy numbers; Schauder bases; approximation of functions.

MSC2020: 03E72; 46B15; 65D15.

1 Introduction

The difficulty involved in extending real models to models with uncertainty using arbitrary fuzzy numbers, as well as the difficulty of calculations with fuzzy numbers described by complex membership functions, has motivated the recent development of a large number of techniques that allow fuzzy numbers to be approximated by simpler ones. In the same way, the approximation of interval-valued functions and fuzzy-valued functions of a real variable has been approached over the years from various perspectives, on numerous occasions with the aim of being used in solving different types of equations in an environment with uncertainty. In the first part of this work we present a constructive method, that is based on the use of appropriate Schauder bases in certain Banach spaces, for the approximation of fuzzy numbers. We prove the convergence and study the properties of the approximation operator, such as its compatibility with arithmetic operations on fuzzy numbers and with some of its important characteristics. The second part is dedicated to presenting the results recently obtained to approximate continuous fuzzy-valued functions with particular attention to the case of interval-valued functions.

2 Approximation of fuzzy numbers

We refer the reader to [2] for the basic notation of interval and fuzzy calculus. The set of all compact (non empty) intervals of the real line is denoted by $\mathcal{K}_C$ and we denote the family of all fuzzy numbers as $\mathbb{F}$.

The relationship between fuzzy numbers and intervals allows us to give a representation of a fuzzy number u as a pair of functions $\underline{u}, \overline{u} : [0,1] \to \mathbb{R}$, defining the endpoints of the α-level sets of u.

Let $(X, \|\cdot\|)$ be a real Banach space of real-valued functions defined on $[0,1]$, and consider

$$\mathbb{F}_X := \{u \in \mathbb{F} : \ \underline{u}, \overline{u} \in X\}.$$

Suppose further that $\|\cdot\|^{(\cdot)}$ is a norm in $\mathbb{R}^2$ fulfilling the monotonicity condition

$$0 \leq x_1 \leq x_1', \ 0 \leq x_2 \leq x_2' \ \Rightarrow \ \|(x_1, x_2)\|^{(\cdot)} \leq \|(x_1', x_2')\|^{(\cdot)} \tag{1}$$

and that $\mathbb{F}_X$ is endowed with the distance $d_X^{(\cdot)}$ defined by

$$d_X^{(\cdot)}(u, v) := \| \left(\|\underline{u} - \underline{v}\|, \|\overline{u} - \overline{v}\|\right) \|^{(\cdot)}, \qquad (u, v \in \mathbb{F}_X). \tag{2}$$

The following result presents how to obtain an approximation of a fuzzy number $u \in \mathbb{F}_X$, which turns out to be compatible with the usual operations of fuzzy arithmetic.

Theorem 1 *(See [3]) Let $\{e_n\}_{n\geq 1}$ be a Schauder basis in a real Banach space $(X, \|\cdot\|)$ of real-valued functions defined on $[0,1]$, whose sequence of associated projections we denote by $\{P_n\}_{n\geq 1}$, and in a such a way that:*

i) *the functions e_n are bounded, left-continuous in $(0,1]$ and right-continuous at 0,*

ii) *if $g \in X$ is non-increasing and $g(1) \geq 0$, then $0 \leq \inf_{n\geq 1} P_n(g)(1)$,*

iii) *and when $g \in X$ is an non-decreasing function and $n \in \mathbb{N}$, $P_n(g)$ is also non-decreasing.*

Then:

a) *For each $u \in \mathbb{F}_X$ and $n \in \mathbb{N}$, $P_n(\underline{u})$ and $P_n(\overline{u})$ define the lower and upper branches of a fuzzy number $\mathbf{P_n}(u) \in \mathbb{F}_X$, that is, for any $\alpha \in [0,1]$,*

$$\underline{\mathbf{P_n}(u)}(\alpha) = P_n(\underline{u})(\alpha) \quad \text{and} \quad \overline{\mathbf{P_n}(u)}(\alpha) = P_n(\overline{u})(\alpha).$$

b) *If $u \in \mathbb{F}_X$, then the sequence $\{\mathbf{P_n}(u)\}_{n\geq 1}$ approximates u in the sense of the metric $d_X^{(\cdot)}$, i.e.,*

$$\lim_{n\to\infty} d_X^{(\cdot)}(u, \mathbf{P_n}(u)) = 0.$$

c) *For any $n \in \mathbb{N}$, the mapping $\boldsymbol{P_n} : \mathbb{F}_X \longrightarrow \mathbb{F}_X$ is a Lipschitz continuous projection and if $u, v \in \mathbb{F}_X$, then $d_X^{(\cdot)}(\mathbf{P_n}(u), \mathbf{P_n}(v)) \leq M d_X^{(\cdot)}(u, v)$, where M is the basic constant of the basis $\{e_n\}_{n\geq 1}$. In particular, if $\{e_n\}_{n\geq 1}$ is monotone, then $\mathbf{P_n}$ is non-expansive.*

3 Approximation of continuous interval-valued functions and fuzzy-number-valued functions

Given Ω a compact topological space, we will denote by $\mathcal{C}(\Omega)$ the Banach space of all continuous real valued functions defined on Ω with its usual max norm, $\|\cdot\|_\infty$, and by $\mathcal{C}(\Omega, \mathcal{K}_C)$ the set of all continuous functions from Ω into $\mathcal{K}_C$ endowed with the distance

$$H(f,h) := \sup_{\omega\in\Omega} \max\{|\underline{h}(\omega) - \underline{f}(\omega)|, |\overline{h}(\omega) - \overline{f}(\omega)|\}, \quad f = [\underline{f}, \overline{f})], \ h = [\underline{h}, \overline{h}].$$

In the following result we introduce an approximation of a continuous interval-valued function in the metric space $\mathcal{C}(\Omega, \mathcal{K}_C)$ in terms of a Schauder basis in the Banach space $\mathcal{C}(\Omega)$:

Theorem 2 *(See [1]) Let Ω be a topological compact space, $\{f_n\}_{n\geq 1}$ be a Schauder basis of $\mathcal{C}(\Omega)$ and let $\{\Pi_n\}_{n\geq 1}$ be the associated sequence of projections such that*

a) if $\omega \in \Omega$ and $n \geq 1$, then $f_n(\omega) \geq 0$, and

b) if $g \in \mathcal{C}(\Omega)$, $g \geq 0$, and $n \geq 1$, then $\Pi_n(g) \geq 0$.

Thus, given $f \in \mathcal{C}(\Omega, \mathcal{K}_C)$ and $\varepsilon > 0$ there exists $n \geq 1$ such that $H\left(f, P_n(f)\right) < \varepsilon$, where

$$P_n(f)(\omega) = \sum_{k=1}^{n} \alpha_k \phi_k(\omega) + \sum_{\substack{k=1 \\ \beta_k - \alpha_k \geq 0}}^{n} (\beta_k - \alpha_k)\psi_k(\omega) \ominus_{gH} \left(\sum_{\substack{k=1 \\ \beta_k - \alpha_k < 0}}^{n} |\beta_k - \alpha_k| \psi_k(\omega) \right)$$

with $\phi_k(\omega) = [f_k(\omega), f_k(\omega)]$, $\psi_k(\omega) = [0, f_k(\omega)]$ and certain real numbers $\alpha_1, \alpha_2, \ldots, \alpha_n$ and $\beta_1, \beta_2, \ldots, \beta_n$.

More general techniques allow us to obtain an analogous result for fuzzy-valued functions.

Acknowledgments

Research partially supported by Junta de Andalucia (Spain), Project FQM359 "Convex and Numerical Analysis".

References

[1] M. Arana-Jiménez, M.I. Berenguer, D. Gámez, A.I. Garralda-Guillem and M. Ruiz Galán (2020), *A perturbed collage theorem and its application to inverse interval integral problems*, Communications in Nonlinear Science and Numerical Simulation 90, 105365.

[2] B. Bede, *Mathematics of Fuzzy Sets and Fuzzy Logic*, Studies in Fuzziness and Soft Computing 295, Springer, 2013.

[3] M.I. Berenguer, D. Gámez, A.I. Garralda-Guillem and M. Ruiz Galán (2023), *A generalized and unified approach to the approximation of fuzzy numbers and its arithmetic and characteristics*, Fuzzy Sets and Systems, 473, 108727.

International Conference on Mathematical Analysis and Applications in Science and Engineering ICMA²SC'24

ISEP **Porto-Portugal, June 20 - 22, 2024**

Solving Abel type differential equations using multilayer perceptron

Tolga Recep Uçar[1] **Hasan Halit Tali**[2]

1. Yıldız Technical University, Turkey
2. Haliç University, Turkey

Abstract: We propose a machine learning-based algorithm as a new method for solving Abel type differential equations which is an important class of differential equations modeling magnetostatic problems and fluid dynamics. Our method does not rely on extensive formal numeric computing. It is a data-driven algorithm, hence a significant approach as data is more available each day. Our approximation function is a multilayer perceptron and we adjust parameters by backpropagation algorithm. We compare our results with some of the well-known methods' results.

keywords: Non-linear ordinary differential equations, Abel type equations, Neural networks, Multilayer perceptron, Backpropagation algorithm

MSC2020: 34A34; 65L05; 68T07

1. Introduction

Many nonlinear differential equations, especially those that arise in complex natural phenomena, have no analytical solution and thus various numerical methods are investigated to estimate the solutions to these equations. Accuracy of these methods as well as how effective their implementation is are important criteria. Here we focus on a fundamental class of differential equations called Abel type differential equations and the general form subject to our discussion is as follows:

$$\frac{dy}{dx} = p(x)y^3 + q(x)y^2 + r(x)y + s(x) \tag{1}$$

where $p(x) \neq 0$. With the substitution $y = \frac{1}{u}$ the equation (1) becomes the Abel equation of the second kind. It has many applications including electromagnetism and fluid dynamics [1,2]. Attempts on solving equations of this form include but are not limited to a recent work of Mak et al. [3] where a solution generating technique for Abel type equations is presented; another paper from Güler [4] proposing an algorithm based on Taylor matrix method; and Khuri [5] which introduces a Laplace decomposition algorithm and applies to a class of nonlinear differential equations.

Lately, many machine learning methods are being used to solve both ordinary and partial differential equations. Mathematical properties of neural networks are intensely investigated and it is a fundamental result that they have universal approximation capabilities (Pinkus [6]). The elegant implementation of the machine learning method is beneficial compared to the extensive formal numeric computing of other methods. Weinan E [7] reviews the relationship between machine learning and computational mathematics, proving a promising future for this class of numerical methods. Brunton et al. [8] reviews the advances in PDE research using machine learning.

Now we give some definitions and define our method.

1.1. Hypothesis Space. Consider the first-order initial value problem in the general form

$$G(x, y(x), y'(x)) = 0 \tag{2}$$

with $y(a) = A$ where $x \in \mathscr{D} = \{a, x_1, x_2, \ldots, x_{n-1}\}$, the discretized domain. Our aim is to approximate the solution $y(x)$.

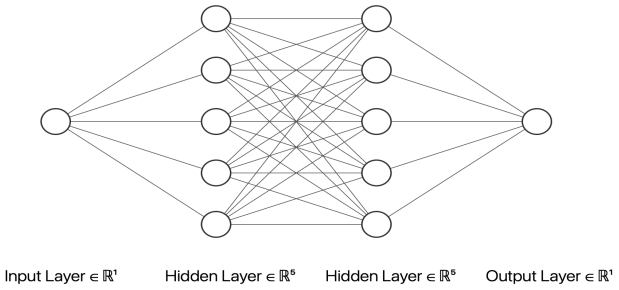

Fig. 1.1. Multilayer Perceptron (MLP) with scalar input, two hidden layers, and a scalar output [9].

We define a set of trial functions

$$H = \{y_t(x, \theta) = A + (x - a)f(x, \theta) \,|\, \theta \in \mathbb{R}\} \tag{3}$$

to optimize within and obtain the approximation from. For example, one could choose $f(\,.\,)$ to be a wavelet function or a polynomial, in order to approximate the unknown function. Our approach considers the ubiquitous multilayer perceptron with two hidden layers:

$$f(x, \theta) = w_2 \cdot h_1 + b_2 \tag{4}$$

where $h_1 = \sigma(w_1 \cdot h_0 + b_1)$ and $h_0 = \sigma(w_0 \cdot x + b_0)$. Here $\theta = \begin{bmatrix} w_0 \\ w_1 \\ w_2 \\ b_0 \\ b_1 \\ b_2 \end{bmatrix}$ $(w_j, b_j \in \mathbb{R})$ is the parameter vector to be optimized and $\sigma(z) = \dfrac{1}{1 + e^{-z}}$ is the sigmoid activation function that imposes nonlinearity to linearly transformed output.

1.2. Loss Function. Substituting the trial equation into the differential equation we get

$$G(x, y_t(x, \theta), y_t'(x, \theta)) \neq 0 \tag{5}$$

(assuming θ is not optimal). We transform the problem of making the left- and right-hand side of the above inequality approximately equal into the optimization problem

$$\min_{\theta} \sum_{x \in \mathscr{D}} \frac{1}{2} G(x, y_t(x, \theta), y_t'(x, \theta))^2 \tag{6}$$

and define the loss function

$$\mathscr{L}(x, \theta) = \sum_{x \in \mathscr{D}} \frac{1}{2} G(x, y_t(x, \theta), y_t'(x, \theta))^2. \tag{7}$$

1.3. Backpropagation. In order to minimize the loss function, we use the fundamental principle of gradient descent, that is, moving in the opposite way of the gradient of the loss function, which is the direction of the steepest descent. Gradient descent assumes the loss function $\mathscr{L}(\,.\,)$ to be differentiable in the parameter

domain. At each iteration we compute the loss for the whole discretized domain with the current parameters, and then compute the gradient with backpropagation. Each iteration ends with the update $\theta_{k+1} = \theta_k - \eta \nabla_\theta \mathscr{L}(x, \theta)$ where η is the learning rate adjusting the gain.

2. Results and Discussion

Now we consider some numerical examples to illustrate our method's performance. We define accuracy by the absolute error between the exact and approximate value $|y(x) - y_t(x, \theta)|$ for a given input x.

Example 1. We take the equation

$$y(x)y'(x) + xy(x) + y^2(x) + x^2y^3(x) = xe^{-x} + x^2e^{-3x} \tag{8}$$

with inital condition $y(0) = 1$ where $0 \leq x \leq 1$. The exact solution is $y = e^{-x}$ [8]. In Table 1 we compare the accuracy of our method with the Taylor matrix method and Padé approximation presented in [4]. Comparison with the exact solution is given in Figure 2.1(a).

Example 2. We also consider the equation

$$y'(x) = 4y(x) - y(x)^3 \tag{9}$$

with initial condition $y(0) = 0.5$. The exact solution is $\dfrac{2e^{4x}}{\sqrt{15 + e^{8x}}}$. In Table 2 we compare the accuracy of our method with the results of the Laplace transform algorithm presented in [5]. Comparison with the graph of the exact solution is given in Figure 2.1(b).

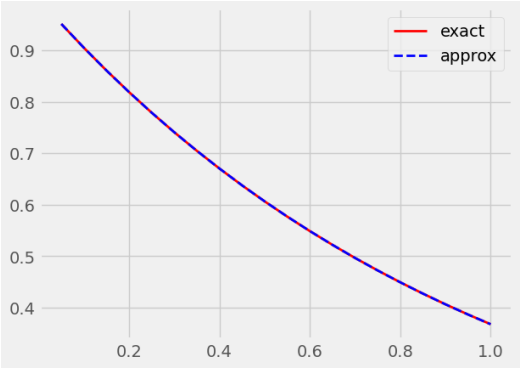

Fig. 2.1(a). Comparison between exact solution and MLP approximation (Example 1).

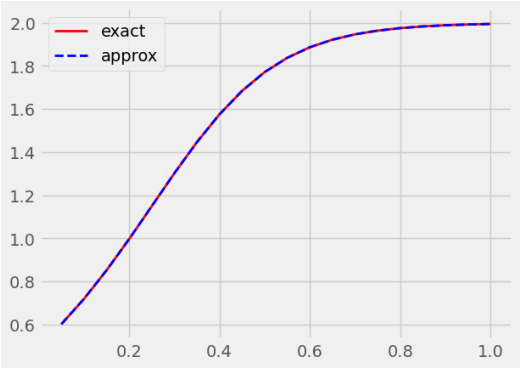

Fig. 2.1(b). Comparison between exact solution and MLP approximation (Example 2).

Table 1. Analytical and numerical outputs with absolute errors of the proposed method (Example 1).

Inputs	Exact solution	Taylor matrix method	Pade approximation	MLP	MLP Absolute error
0	1.0000000000	1.0000000000	1.0000000000	1.0000000000	0
0.1	0.9048374180	0.9048374167	0.9048374179	0.9049017	6.425381e-05
0.2	0.8187307531	0.8187306667	0.8187307455	0.8187502	1.943111e-05
0.3	0.7408182207	0.7408172500	0.7408181414	0.7408165	1.728535e-06
0.4	0.6703200460	0.6703146667	0.6703196347	0.67033315	1.311302e-05
0.5	0.6065306597	0.6065104167	0.6065292096	0.6065661	3.540516e-05
0.6	0.5488116361	0.5487520000	0.5488076312	0.54885244	4.082918e-05

Inputs	Exact solution	Taylor matrix method	Pade approximation	MLP	MLP Absolute error
0.7	0.4965853038	0.4964369167	0.4965759550	0.49661142	2.610683e-05
0.8	0.4493289641	0.4490026667	0.4493096647	0.44933373	4.768372e-06
0.9	0.4065696597	0.4059167500	0.4065333809	0.40656352	6.139278e-06
1.0	0.3678794412	0.3666666667	0.3678160920	0.36788034	8.940697e-07

Table 2. Analytical solution and absolute errors of numerical solutions (Example 2).

Inputs	Exact solution	Laplace decomposition absolute error	MLP	MLP Absolute error
0.05	0.6015262	2.5873e-07	0.6016848	1.586080e-04
0.10	0.71888816	1.5733e-05	0.7190194	1.312494e-04
0.15	0.85141754	1.6370e-04	0.85161024	1.927018e-04
0.20	0.9964629	7.9299e-04	0.99675953	2.966523e-04
0.25	1.1489644	2.3856e-03	1.1492543	2.899170e-04
0.30	1.301677	4.8087e-03	1.3018351	1.580715e-04
0.35	1.4463351	5.6245e-03	1.4463906	5.555153e-05
0.40	1.5755198	2.3004e-03	1.5756235	1.037121e-04

3. Conclusions and Future Work

We have introduced the machine learning approach to the effort of solving Abel type differential equations. Abel type equations have important physical applications. Previous methods include Taylor matrix based solutions and Laplace decomposition. From the results we conclude that the simple and low-cost multilayer perceptron with a very fundamental optimization approach achieves a significant accuracy and most importantly a well-balanced approximation.

The efficient convergence of the proposed approximation implies a bright future for machine learning in computational mathematics. The simplicity of the implementation enables the possibility of using it on many other differential equations. Future work may also include creative approaches to the choice of the hypothesis space. Finally, on the other hand, this direction of applied mathematics research can prove useful to the theory development of machine learning.

References

1. J.-P. M. Lebrun, "On two coupled Abel-type differential equations arising in a magnetostatic problem", Il Nuovo Cimento 103A(1990) 1369-1379.
2. S.Ş. Bayin, "Solutions of Einstein's field equations for static fluid spheres", Phys. Rev. D 18 (1978) 2745-2751.
3. M.K. Mak, "New method for generating general solution of Abel differential equation", Comput. Math. Appl. 43 (2002) 91–94.
4. C. Güler, "A new numerical algorithm for the Abel equation of the second kind", Int. J. Comput. Math 84 (2007) 109-119.
5. Suheil A. Khuri, "A Laplace decomposition algorithm applied to a class of nonlinear differential equations", Journal of Applied Mathematics 1:4 (2001) 141-155.
6. Allan Pinkus, "Approximation theory of the MLP model in neural networks", Acta Numerica 8 (1999) 143-195.
7. Weinan E, "Machine Learning and Computational Mathematics", arXiv:2009.14596 (2020)
8. Steven L. Brunton and J. Nathan Kutz, "Machine Learning and Partial Differential Equations", arXiv:2303.17078 (2023)
9. NN-SVG, Publication-ready NN-architecture schematics. http://alexlenail.me/NN-SVG/

International Conference on Mathematical Analysis and Applications in Science and Engineering ICMA²SC'24

ISEP **Porto-Portugal, June 20 - 22, 2024**

Fuzzy Big-M Method for Solving Fuzzy Linear Programming Problems using Horizontal Membership Function

Sukhpreet Kaur Sidhu[1*]

[1] Akal University, Talwandi Sabo, India

[*] sukhpreetkaursran@gmail.com

Abstract: In the real-life optimization problems, due to uncertainty and hesitancy, it might be challenging for the decision maker to identify the precise value of the parameters. To overcome this problem, fuzzy set theory came into existence. The fuzzy Big-M method is a mathematical technique used for solving fuzzy linear programming problem with inequality constraints. The concept of horizontal membership function was introduced by Piegat and Landowski in 2015. They define a fuzzy set not in the form of vertical membership function of type $\mu = f(x)$ but in the horizontal type $x = f(\mu)$. In this paper, an algorithm is proposed for fuzzy Big-M method using horizontal membership function. Numerical examples have been presented to illustrate the proposed algorithm.

Keywords: Fuzzy linear programming, Horizontal membership function, Fuzzy optimal solution, Horizontal fuzzy number, Big-M method

The smoothness of orbital measures on noncompact symmetric spaces

Sanjiv Kumar Gupta and Kathryn E. Hare

Abstract. Let G be a real, connected, noncompact, semisimple Lie group with finite center, and K a maximal compact subgroup of G. The quotient space, G/K, is a symmetric space of noncompact type, which we also assume to be irreducible. For $a \in G \diagdown N_G(K)$, we let ν_a denote the K-bi-invariant, orbital, singular measure supported on the compact double coset KaK in G. The smoothness properties of convolution products of these orbital measures has been of interest for many years and is related to questions about products of double cosets and spherical functions. Ragozin, in [**5**], proved that for $r \geq \dim G/K$, the convolution product measure, $\nu_{a_1} * \cdots * \nu_{a_r}$, is absolutely continuous with respect to any Haar measure on G, equivalently, its density function is a compactly supported function in $L^1(G)$. This was improved in a series of papers, culminating with [**2**] and [**4**], where r was reduced to either $rank G/K$ or $rank G/K + 1$ depending on the Lie type. See [**3**] for a good history of this problem.

For the special case of regular elements, a_j, it was shown in [**1**] that the density function of $\nu_{a_1} * \cdots * \nu_{a_r}$ belongs to the smaller space of compactly supported functions in $L^2(G)$ for $r \geq \dim G/K + 1$. The decay properties of spherical functions and the Plancherel theorem were used to prove this. In this paper, we develop a more refined analysis of the decay properties of spherical functions, using the classification of these symmetric spaces in terms of their restricted root systems, to significantly improve this result. This analysis allows us to both extend the L^2 result to convolutions of *all* orbital measures ν_a for $a \notin N_G(K)$, as well as to reduce the number of convolution products to approximately $rank G/K$; and obtain the precise values which depend only on the Lie and Cartan type of the symmetric space. In the special case of convolution products of orbital measures at regular elements, we prove that $r = 2$ suffices, except for one symmetric space (Cartan type AI of rank one) where $r = 3$ is both necessary and sufficient. This latter fact shows that, unlike the situation for the analogous problem in compact Lie groups and algebras, it is not true that ν_a^k belongs to L^2 if and only if ν_a^k is absolutely continuous (where the exponent means convolution powers). The decay properties are also applied to study the differentiability of orbital measures.

References

[1] B. Anchouche, *Regularity of the Radon-Nikodym derivative of a convolution of orbital measures on noncompact symmetric spaces,* preprint 2018.

[2] P. Graczyk and P. Sawyer, *Absolute continuity of convolutions of orbital measures on Riemannian symmetric spaces*, J. Func. Anal., **259**(2010), 1759-1770.

[3] P. Graczyk and P. Sawyer, *Convolution of orbital measures on symmetric spaces: a survey*, Contemporary Math **668**(2016), 81-110.
[4] S.K. Gupta and K.E. Hare, *The absolute continuity of convolutions of orbital measures in symmetric spaces*, J. Math. Anal. and Appl., **450**(2017), 81-111.
[5] D. Ragozin, *Zonal measure algebras on isotropy irreducible homogeneous spaces*, J. Func. Anal., **17**(1974), 355–376.

Dept. of Mathematics, Sultan Qaboos University, P.O.Box 36 Al Khodh 123, Sultanate of Oman
E-mail address: gupta@squ.edu.om

Dept. of Pure Mathematics, University of Waterloo, Waterloo, Ont., Canada, N2L 3G1

International Conference on Mathematical Analysis and Applications in Science and Engineering
ICMA^{2}SC'24
ISEP Porto-Portugal, June 20 - 22, 2024

A second kind formulation for algebraic contrained differential equations: The rare time when reckless differentiation makes things better

Vicente Gomez Herrera[1⋆] **David Stein**[2]

[1] Courant Institute, NYU, New York, NY 10012
[2] Center for Computational Biology, Flatiron Institute, New York, NY 10010, USA

[1⋆]vicente.g@nyu.edu

Abstract: Special Session 6 Computational Mathematics, Computational Statistics and Applications: A key characteristic of incompressible fluids is the disparity in the differential order of the equations. This discrepancy generates numerical difficulties that are often resolved by differentiating the applied force, adding boundary conditions, and/or using different discretization approaches for pressure and velocity. In this work, we introduce a new formulation for the periodic channel, presenting an unexpectedly simple yet effective solution to resolve the mismatch between pressure and velocity in incompressible fluids. By employing this seemingly unconventional approach, we craft a well-conditioned system that eliminates the traditional mismatch problem. Notably, this method's versatility extends beyond incompressible fluids and applies to various differential-algebraic equations, such as inelastic fibers and curl-free fluids.

keywords: Spectral Methods; Fluids

MSC2020:

1 Introduction

A common type of differential equation that appears in physical systems is partial differential equations with a differential algebraic constraint. The Stokes Equation (divergence-free vector field) and Semi-Elastic Inextensible Fibers (constant arc length) are two examples. Historically, three ways to solve these equations are (1) parametrizing the solution space [1, 2], (2) generating an auxiliary elliptic problem for the Lagrange multiplier (pressure or tension) [3, 4], and (3) generating a complete system where the primary variable and the Lagrange multiplier are solved at the same time [5]. Unfortunately, each of these has its drawbacks. Parametrizing the solution space can be complicated depending on the geometry and boundary conditions; generating the elliptic problem requires taking numerical derivatives of the external force in the system, and the linear system for all the variables generally has a condition number that grows as a function of the mesh size, leading to accumulation of errors or convergence issues in iterative methods.

To showcase our approach, in this work, we solve the Stokes Equation in the geometry $(-1, 1) \times \mathbb{S}_1$. After taking the Fourier Transform in the periodic dimension, the corresponding boundary value problem is

$$\begin{cases} -4\pi^2 n^2 \hat{\mathbf{u}}_n + \partial_x^2 \hat{\mathbf{u}}_n - \begin{pmatrix} \partial_x \\ 2\pi i n \end{pmatrix} \hat{p}_n = \hat{\mathbf{F}}_n, \quad x \in (-1,1) \\ \begin{pmatrix} \partial_x \\ 2\pi i n \end{pmatrix} \cdot \hat{\mathbf{u}}_n = 0, \quad x \in (-1,1) \\ \hat{\mathbf{u}}_n(-1) = \hat{\mathbf{g}}_n^{-1}, \\ \hat{\mathbf{u}}_n(1) = \hat{\mathbf{g}}_n^{1}. \end{cases} \tag{1}$$

This system will be a toy problem to showcase our method; however, our techniques can be extended to other semi-periodic geometries and other types of equations.

2 Results and discussion

Our idea is simple and direct: we take derivatives of the algebraic constraint until we match the number of derivatives in the main equation (for Stokes, this requires only one derivative). Information is lost when differentiating and must be recovered; a simple projection is sufficient here. In our toy model example, the resulting system looks like

$$\begin{cases} -4\pi^2 n^2 \hat{\mathbf{u}}_n + \partial_x^2 \hat{\mathbf{u}}_n - \begin{pmatrix} \partial_x \\ 2\pi i n \end{pmatrix} \hat{p}_n = \hat{\mathbf{F}}_n \\ \begin{pmatrix} \partial_x^2 \\ 2\pi i n \partial_x \end{pmatrix} \cdot \hat{\mathbf{u}}_n = 0 \\ \left\langle 1, \begin{pmatrix} 2\pi i n \\ \partial_x \end{pmatrix} \cdot \hat{\mathbf{u}}_n \right\rangle = 0 \\ \hat{\mathbf{u}}(-1) = \hat{\mathbf{g}}_n^{-1}, \\ \hat{\mathbf{u}}(1) = \hat{\mathbf{g}}_n^{1}. \end{cases} \tag{2}$$

This approach may seem counterintuitive since increasing the differential order of the system should only exacerbate the ill-conditioning. However, when the problem is appropriately reformulated (here using an integral formulation), something surprising happens. Define the variables

$$\hat{\mathbf{u}}_n = \mathbf{A}_n + \mathbf{B}_n x + \int \int \hat{\boldsymbol{\mu}}_n \tag{3}$$

$$\hat{p}_n = C_n + \int \hat{\rho}_n. \tag{4}$$

A direct integral reformulation for the densities (without differentiating the constraint equation) is given, in block form, by:

$$\left(\begin{pmatrix} \mathbb{I} & 0 & 0 \\ 0 & \mathbb{I} & \mathbb{I} \\ 0 & 0 & 0 \end{pmatrix} + \begin{pmatrix} -4\pi^2 n^2 \int\int & 0 & 2\pi i n \int \\ 0 & -4\pi^2 n^2 \int\int & 0 \\ 2\pi i n \int & \int & 0 \end{pmatrix} \right) \begin{pmatrix} \hat{\mu}_n^1 \\ \hat{\mu}_n^2 \\ \hat{\rho}_n \end{pmatrix} \tag{5}$$

For conciseness, boundary conditions have been omitted. Notably, the final block equation is not second-kind. An integral reformulation of our proposed method gives instead:

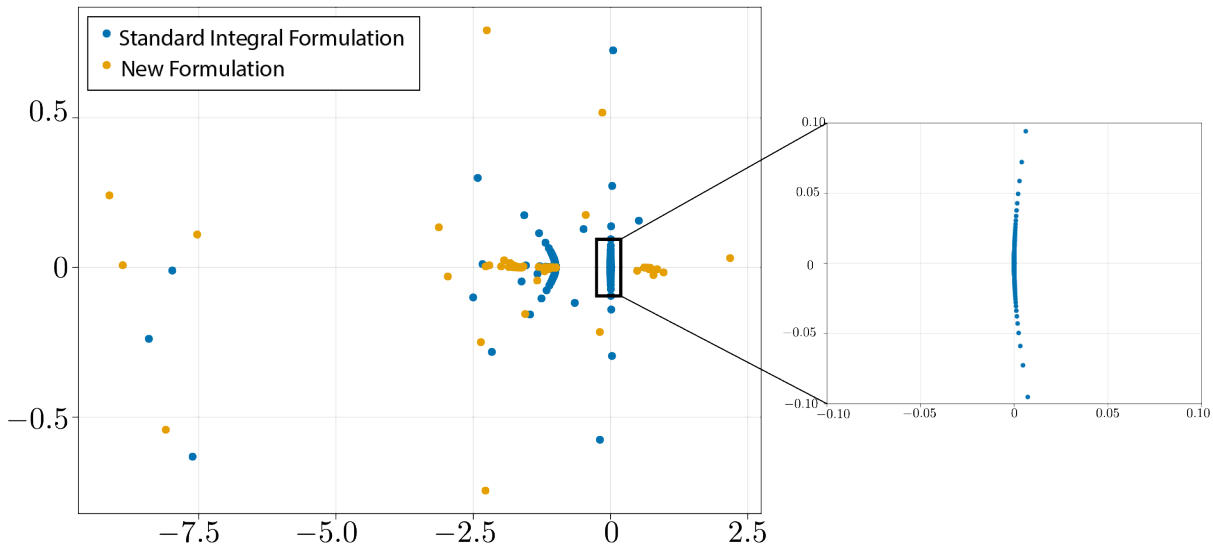

Figure 1: Comparison of the spectrum between a direct discretization using an integral method (blue dots) versus our new reformulation (yellow dots). A zoom-in around 0 is shown to show the accumulation of eigenvalues around 0 for the Standard integral formulation; note no eigenvalues from the New formulation appear in this zoom region.

$$\left(\begin{pmatrix}\mathbb{I} & 0 & 0\\ 0 & \mathbb{I} & \mathbb{I}\\ 0 & \mathbb{I} & 0\end{pmatrix}+\begin{pmatrix}-4\pi^2n^2\int\int & 0 & 2\pi in\int\\ 0 & -4\pi^2n^2\int\int & 0\\ 2\pi in\int & 0 & 0\end{pmatrix}\right)\begin{pmatrix}\hat{\mu}_n^1\\ \hat{\mu}_n^2\\ \hat{\rho}_n\end{pmatrix} \tag{6}$$

which is of the form of a compact operator plus an identity-like operator and is indeed second-kind. To show this technique's effectiveness, we compare the spectrum generated by the direct integral approach and our proposed meethod, shown in Fig. 1. We use 500 Chebyshev nodes and the integration rule following [6] to discretize the system. In the spectrum, we see an accumulation of eigenvalues towards 0 for a direct discretization, while in our new technique, the eigenvalues are bounded away from 0.

3 Conclusions and Future work

In this work, we have presented a new formulation of the Stokes Equation in Fourier space, which does not need to introduce numerical differentiation and generates a well-conditioned system. Even further, the technique is simple enough to be generalized to more complicated equations, like inelastic fibers, given by

$$\begin{cases}\mathbf{X}_t=(\mathbb{I}+\mathbf{X}_s\mathbf{X}_s)(-\mathbf{X}_{ssss}+(\mathbf{X}_sT)_s)\\ \mathbf{X}_s\cdot\mathbf{X}_s=1\\ \mathbf{X}_{ss}(0,L)=\mathbf{0}\\ \mathbf{X}_{sss}(0,L)=\mathbf{0}.\end{cases} \tag{7}$$

By the same principle, we take three derivatives of the constrain $\mathbf{X}_s\cdot\mathbf{X}_s=1$ until we get the same number of s derivative in $\mathbf{X}$.

Acknowledgments

The Flatiron Institute is a division of the Simons Foundation. We thank Michael Shelley, Leslie Greengard, and Daniel Fortunato for their insightful discussions.

References

[1] Maxian, O., Sprinkle, B., & Donev, A. (2023). Bending fluctuations in semiflexible, inextensible, slender filaments in Stokes flow: Toward a spectral discretization. The Journal of Chemical Physics, 158(15).

[2] Brubeck, P. D., & Trefethen, L. N. (2022). Lightning Stokes solver. SIAM Journal on Scientific Computing, 44(3), A1205-A1226.

[3] Tornberg, A. K., & Shelley, M. J. (2004). Simulating the dynamics and interactions of flexible fibers in Stokes flows. Journal of Computational Physics, 196(1), 8-40.

[4] Chorin, A. J. (1967). The numerical solution of the Navier-Stokes equations for an incompressible fluid. Bulletin of the American Mathematical Society, 73(6), 928-931.

[5] Burns, K. J., Vasil, G. M., Oishi, J. S., Lecoanet, D., & Brown, B. P. (2020). Dedalus: A flexible framework for numerical simulations with spectral methods. Physical Review Research, 2(2), 023068.

[6] Greengard, L., & Rokhlin, V. (1991). On the numerical solution of two-point boundary value problems. Communications on pure and applied mathematics, 44(4), 419-452.

International Conference on Mathematical Analysis and Applications in Science and Engineering
ICMA^{2}SC'24
ISEP Porto-Portugal, June 20 - 22, 2024

Choosing among different discrete approximations of a continuous random variable

Alessandro Barbiero[1⋆] **Asmerilda Hitaj**[2]

[1] Università degli Studi di Milano, Italy
[2] Università degli Studi dell'Insubria, Italy

[1⋆]alessandro.barbiero@unimi.it

Abstract: For many complex probabilistic problems involving continuous random variables, it is impossible to find a closed-form solution. Consequently, it is necessary to approximate a given continuous probability distribution with a discrete one. Several techniques are available for producing a discrete approximation to a continuous random variable, based on rather different criteria. In this work, we will examine and compare these main methods, by considering a well-known parametric distribution. Applications to real problems will finally be suggested.

keywords: discretization; moment-matching; quantization; representative points.

MSC2020: 62E15; 62E17.

1 Introduction

For many complex probabilistic problems involving continuous random variables, it is impossible to find a closed-form solution. Consequently, it is necessary to approximate a given continuous probability distribution with a discrete one. For a continuous random variable X with cumulative distribution function $F(x)$, one has to construct a discrete random variable $\tilde{X}$ defined on $\mathcal{S} = \{x_1, x_2, \ldots, x_k\}$, with probability mass function $P(\tilde{X} = x_i) = p_i$, $i = 1, \ldots, k$, ensuring that $\tilde{X}$ preserves the properties of X "as much as possible". Various discretization methods can be employed for determining the x_i and the p_i, relying on different criteria [1]. The most widely accepted criterion involves matching as many moments as possible of X. Alternatively, one can optimally select the values x_i in the sense of minimizing the expected mean squared error with X (optimal quantization). Another approach in based on minimizing the Cramér-von Mises distance between $F(x)$ and the step-wise cumulative distribution function of $\tilde{X}$. In this work, we will examine and compare these main methods and modifications thereof, by considering several well-known parametric distributions (normal, exponential, etc.). Possible applications to real problems will be finally hinted at.

2 Results and discussion

It is well-known that a k-point discrete random variable $\tilde{X}$, which is characterized by $2k$ values - the k support points $(x_1, x_2, \ldots, x_k)$ and the corresponding k probabilities $(p_1, p_2, \ldots, p_k)$ - can

preserve up to the first $2k-1$ moments of a continuous random variable X. The values of the x_i and p_i which lead to the exact matching of all the first $2k-1$ moments can be obtained by solving the corresponding non-linear system of $2k$ equations in the $2k$ unknowns:

$$\mathbb{E}(\tilde{X}) = \sum_{i=1}^{k} p_i \cdot x_i^r = m_r = \mathbb{E}(X^r), \quad r = 0, 1, \ldots, 2k-1, \tag{1}$$

where m_r is the r-th raw moment of the continuous random variable, and for $r = 0$ we have the trivial requirement that the p_i must sum up to 1. This can be done by resorting to the so-called Gaussian quadrature procedure and solving for the roots of an orthogonal polynomial [3] or computing the eigenvalues and first component of the orthonormalized eigenvectors of a symmetric tridiagonal matrix [4].

Alternatively, a k-point discrete approximation can be obtained by minimizing the following loss function, which is actually an expected mean squared distance:

$$\mathcal{L}_X(x_1, x_2, \ldots, x_k) = \int_{-\infty}^{\infty} \min_i (x - x_i)^2 f(x) \mathrm{d}x.$$

After defining a set of $k+1$ thresholds as $\delta_0 = -\infty$, $\delta_k = \infty$ and $\delta_i = (x_i + x_{i+1})/2$, $i = 1, \ldots, k-1$, the loss function above can be expressed in the form

$$\mathcal{L}_X(x_1, x_2, \ldots, x_k) = \sum_{i=1}^{k} \int_{\delta_{i-1}}^{\delta_i} (x - x_i)^2 f(x) \mathrm{d}x.$$

By minimizing $\mathcal{L}_X$ with respect to the x_i, one can obtain the optimal x_i, called the "principal points" [4], and the δ_i; the corresponding probabilities p_i are obtained as $p_i = \int_{\delta_{i-1}}^{\delta_i} f(x) \mathrm{d}x$. This approximation is also known as "optimal quantization" [5]. The resulting rv $\tilde{X}$ always preserves the first moment, but underestimates the variance of X.

[7] suggested a slight modification to "optimal quantization", in order to match the second moment of the continuous distribution (along with its expectation). The optimal k-point discrete approximation is derived as the solution to a nonlinear optimization problem and can be actually regarded as the discrete distribution which is the closest in mean-squared-error terms to the optimal quantizer, while preserving the first two moments. The probabilities are the same as for optimal quantization, whereas the modified support values are given by

$$x_i^* = \frac{\sigma_X}{\sigma_{\tilde{X}}} (x_i - \mathbb{E}(X)) + \mathbb{E}(X).$$

The three methods illustrated so far require the finiteness of (at least) the first two moments, a condition which is not satisfied by many heavy-tailed distributions used in quantitative finance, just think of stable distributions. In this case, one can perform discretization based on the minimization of some distance between the continuous cumulative distribution function of X, F, and the piece-wise constant cumulative distribution function of $\tilde{X}$, G, e.g,

$$d^2(F, G) = \int_{\mathbb{R}} [F(x) - G(x)]^2 w(x) \mathrm{d}x,$$

with $w(x)$ a (positive) weighting function. If $w(x) = F'(x)$ the function above reduces to Cramér-von Mises distance, and in this latter case, then the optimal discretization assigns constant weights $p_i = 1/k$ to the values $x_i = F^{-1}(u_i)$, with $u_i = (2i-1)/(2k)$ [7].

We now apply the four discretization methods discussed in this section to the exponential random distribution, which is characterized by the cumulative distribution function $F(x) = 1 - e^{-\lambda x}$ and

the probability density function $f(x) = \lambda e^{-\lambda x}$, $x > 0$, where $\lambda > 0$ is the rate parameter. The quantile function is $F^{-1}(u) = -\ln(1-u)/\lambda$, $0 < u < 1$. We recall that all the positive integer moments of the exponential distribution exist and are equal to $m_r = r!/\lambda^r$.

Table 1 displays the support values x_i and the corresponding probabilities p_i for a 7-point approximation of an exponential random variable with unit rate parameter. The last two rows reports the expectation and the variance of the approximating random variable.

Table 1: Approximation of an exponential rv with unit parameter through $k = 7$ points. Legend: MM=Moment Matching; OQ=Optimal Quantization; DZ=Drezner and Zerom (2016); minCvM=minimization of Cramér-von Mises distance.

MM		OQ		DZ		minCvM	
x_i	p_i	x_i	p_i	x_i	p_i	x_i	p_i
0.193	0.409	0.199	0.348	0.182	0.348	0.074	0.143
1.027	0.422	0.657	0.256	0.650	0.256	0.241	0.143
2.568	0.147	1.197	0.179	1.201	0.179	0.442	0.143
4.900	0.021	1.857	0.115	1.875	0.115	0.693	0.143
8.182	0.001	2.705	0.065	2.740	0.065	1.030	0.143
12.734	< 0.001	3.893	0.029	3.951	0.029	1.540	0.143
19.396	< 0.001	5.893	0.008	5.992	0.008	2.639	0.143
$\mathbb{E}(\tilde{X})$	1	$\mathbb{E}(\tilde{X})$	1	$\mathbb{E}(\tilde{X})$	1	$\mathbb{E}(\tilde{X})$	0.951
$\mathrm{Var}(\tilde{X})$	1	$\mathrm{Var}(\tilde{X})$	0.961	$\mathrm{Var}(\tilde{X})$	1	$\mathrm{Var}(\tilde{X})$	0.686

From Table 1, we can see that the different discretization techniques give rise to discrete random variables that can sensibly differ: one can note, in particular, that the range of the approximation induced by moment matching is quite larger than the others, and includes two points with a really small probability; to the contrary opposite, the discretization based on the minimization of the Cramér-von Mises distance leads to a distribution with the narrowest range and constant probabilities. Moreover, this latter approximation underestimates the first two moments, whereas the other three methods by construction preserve the first o the first two moments.

3 Conclusions and future work

A natural application of discrete approximation of a continuous random variable is scenario generation in stochastic programming. Here, the continuous stochastic quantity involved in the optimization problem is substituted by a random variable sitting on a finite number of points, the so-called "atoms" or "scenarios". Future work will consider some typical problems in stochastic programming, apply the different discretizations discussed in this work, and compare the resulting solutions.

Acknowledgments

The corresponding author acknowledges financial support from the Italian Ministry of University and Research through the PRIN2022 "The effects of climate change in the evaluation of financial instruments".

References

[1] R.K. Hammond, J.E. Bickel, Reexamining discrete approximations to continuous distributions, Decision Analysis, **10**(1) (2013), 6–25.

[2] G. H. Golub, J. H. Welsch, Calculation of Gauss quadrature rules, Mathematics of Computation, **23**(106) (1969), 221–230.

[3] C. F. Dunkl, Y. Xu, Orthogonal polynomials of several variables, Encyclopedia of Mathematics and its Applications, vol. 81, Cambridge University Press, Cambridge, UK (2001)

[4] B. A. Flury, Principal points, Biometrika, **77**(1) (1990), 33–41.

[5] S.P. Stuart Lloyd, Least squares quantization in PCM, IEEE Transations on Information Theory, **28**(2) (1982), 129–137.

[6] Z. Drezner, D. Zerom, A simple and effective discretization of a continuous random variable, Communications in Statistics - Simulation and Computation, **45**(10) (2016), 3798–3810.

[7] J. Kennan, A Note on Discrete Approximations of Continuous Distributions. Department of Economics, University of Wisconsin, 1180 Observatory Drive, Madison, WI, 2006.

International Conference on Mathematical Analysis and Applications in Science and Engineering
ICMA^{2}SC'24
ISEP Porto-Portugal, June 20 - 22, 2024

On the 4-D Nilpotent Feed-forward Network Dynamical Systems

Fahimeh Mokhtari[1⋆]

[1]Vrije Universiteit Amsterdam, Netherlands

[1⋆]f.mokhtari@vu.nl

Abstract: "In this paper, I investigate the normal form of a family of nilpotent feed-forward networks. This research is part of ongoing work on studying the normal form of networks with a feedforward architecture [2]. The system I am studying is described by the following equation:

$$\begin{bmatrix}\dot{x}_1\\ \dot{x}_2\\ \dot{x}_3\\ \dot{x}_4\end{bmatrix} = \begin{bmatrix}0 & 1 & \varepsilon p_1 & \varepsilon p_2\\ 0 & 0 & \varepsilon p_3 & \varepsilon p_4\\ 0 & 0 & 0 & 1\\ 0 & 0 & 0 & 0\end{bmatrix}\begin{bmatrix}x_1\\ x_2\\ x_3\\ x_4\end{bmatrix} + \begin{bmatrix}F_1(x_1,x_2,x_3,x_4)\\ F_2(x_1,x_2,x_3,x_4)\\ G_1(x_3,x_4)\\ G_2(x_3,x_4)\end{bmatrix}.$$

Here, F_1, F_2, G_1, G_2 are non-linear polynomial vector fields, and $\{p_i \mid i = 1..4\}$ represent parameters of order ϵ. The methodology employed in this study is based on $\mathfrak{sl}_2$-representation, transvectants, and generating functions [1].

keywords: Network dynamics; Normal form; Feed-forward.

MSC2020: 34C15; 37G05; 37G10.

References

[1] J. A. Sanders, F. Verhulst, and J. Murdock, *Averaging Methods in Nonlinear Dynamical Systems*, 2nd ed. New York: Springer, 2007.

[2] Fahimeh Mokhtari, *Nilpotent Feed-forward Network Dynamics*, Preprint, 2024.

International Conference on Mathematical Analysis and Applications in Science and Engineering
ICMA^{2}SC'24
ISEP Porto-Portugal, June 20 - 22, 2024

Continua of equilibrium states in ensembles with global coupling

Michael Zaks[1⋆]

[1] Humboldt University of Berlin, Berlin, Germany

[1⋆]zaks@physik.hu-berlin.de

Abstract: In the phase space of a generic dynamical system with continuous time, the equilibrium states are isolated; in presence of continuous symmetries such states can form continuous families. Here, a situation is presented in which dynamics of globally coupled one-dimensional units lacks symmetries, but high-dimensional continua of equilibrium states exist in the phase space nevertheless. Unlike equilibrium states in symmetry-related continua, here the eigenvalues of the corresponding Jacobian matrices are not shared by the whole family, but vary along the family. As a consequence, parts of the continua of steady states can be attracting whereas other parts can be repelling. This unusual situation is a consequence of the modeling assumption that the same global field(s) exert(s) the same action upon every element of the ensemble. If the overall number of elements in the ensemble exceeds the number of parameters in the description of the global field, the continua of steady states become generic. For several exemplary ensembles, we discuss geometry of the continua of steady states as well as their stability.

keywords: steady state; global coupling; continuum.

MSC2020: 34-C14; 34-D5; 37-C25.

Nonstandard Stummel Spaces and Applications

Alexandre Almeida

University of Aveiro, Portugal

jaralmeida@ua.pt

Abstract: In this talk, we present some function spaces involving special weights with nonstandard growth and discuss their conection with the study of PDE. Moreover, the role of uniform weighted norm inequalities will be emphasized in the study of mapping properties of classical operators in this setting.

keywords: Variable exponents; Stummel classes; Weights; Nonstandard growth.

MSC2020: 46E30, 42B35.

Acknowledgments

The research of A. Almeida was partially supported by the Portuguese Foundation for Science and Technology (FCT - Fundação para a Ciência e a Tecnologia), through CIDMA - Center for Research and Development in Mathematics and Applications, within project UIDB/04106/2020.

International Conference on Mathematical Analysis and Applications in Science and Engineering
ICMA^{2}SC'24

ISEP Porto-Portugal, June 20 - 22, 2024

REGULATORY NETWORKS WITH VARYING INTERACTIONS

Felix Sadyrbaev[1⋆] **Valentin Sengileyev**[2]

[1] Institute of Mathematics and Computer Science, University of Latvia, Latvia
[2] Daugavpils University, Latvia

[1⋆]felix@latnet.lv

Abstract: We consider the system of ordinary differential equations arising in the theory of gene regulatory networks, and more. The interaction between elements is described by the regulatory matrix W of dimension $n \times n$, where n is the number of elements in a network. Usually this matrix is supposed to be constant. We allow the entries of W be variable. The two dimensional case is considered.

keywords: network; ordinary differential equations; variable interactions.

MSC2020: 34C60, 34D45, 92B20

1 Introduction

Systems of the form

$$\begin{cases} x_1' = f(w_{11}x_1 + \ldots + w_{1n}x_n - \theta) - x_1, \\ x_2' = f(w_{21}x_1 + \ldots + w_{2n}x_n - \theta) - x_2, \\ \ldots \quad \ldots \quad \ldots, \\ x_n' = f(w_{n1}x_1 + \ldots + w_{nn}x_n - \theta) - x_n \end{cases} \tag{1}$$

arise in mathematical modeling of gene regulatory networks, telecommunication networks and neuronal networks ([1], [2], [3], [4]). The elements $x_i(t)$ are dependent on time, and their evolution over time is the main object of investigation. The functions $f_i(z)$ are supposed to be monotone, bounded and smooth. The sigmoidal functions satisfy these requirements. Most often the function $f(z) = \frac{1}{1+e^{-\mu z}}$ is used. The system (1) then takes the form

$$\begin{cases} x_1' = \dfrac{1}{1 + e^{-\mu_1 (w_{11}x_1 + w_{12}x_2 + \ldots + w_{1n}x_n - \theta_1)}} - \gamma_1 x_1, \\ x_2' = \dfrac{1}{1 + e^{-\mu_2 (w_{21}x_1 + w_{22}x_2 + \ldots + w_{2n}x_n - \theta_2)}} - \gamma_2 x_2, \\ \ldots \\ x_n' = \dfrac{1}{1 + e^{-\mu_n (w_{n1}x_1 + w_{n2}x_2 + \ldots + w_{nn}x_n - \theta_n)}} - \gamma_2 x_n \end{cases} \tag{2}$$

It contains multiple parameters. The values μ_i, θ_i and γ_i characterize the individual properties of elements. The coefficients w_{ij} describe relations between two elements x_i and x_j. Full information about interrelations between elements is collected in the matrix W, which in the theory of genetic networks is called regulatory matrix. In multiple studies of the properties of solutions of system

(1) or (2) the coefficients were constant. This makes systems autonomous and the analysis of solutions becomes easier. On the other hand, it is easy to imagine that the character of interrelations between elements of a network (in a model) may change in time. The activation may be varying. What happens with solutions, trajectories and future states of a network. We concern this problem for the two dimensional system of the form (2).

2 Results and discussion

So consider the system

$$\begin{cases} x_1' = \dfrac{1}{1+e^{-\mu_1\,(w_{11}x_1+w_{12}x_2-\theta_1)}} - \gamma_1 x_1, \\ x_2' = \dfrac{1}{1+e^{-\mu_2\,(w_{21}x_1+w_{22}x_2-\theta_2)}} - \gamma_2 x_2 \end{cases} \tag{3}$$

with the coefficient matrix

$$W = \begin{pmatrix} w_{11} & w_{12} \\ w_{21} & w_{22} \end{pmatrix}. \tag{4}$$

Our intent is to discuss first the activation case when all entries of W are positive constants. Then we allow the coefficients to be variable but positive. We will show that unexpected behavior of solutions can be observed.

2.1 Activation

Let the coefficient matrix

$$W = \begin{pmatrix} 1 & 1 \\ 1 & 1 \end{pmatrix}. \tag{5}$$

Other parameters are $\mu_1 = \mu_2 = 4$, $\theta_i = 0.5(w_{i1} + w_{i2})$, $i = 1, 2$; $\gamma_1 = \gamma_2 = 1$. The elements on the main diagonal of W say that both x_1 and x_2 are self-activating. The elements on the secondary diagonal of W say that x_2 activates x_1 and, in turn, x_1 activates x_2.

The two below pictures are for the system (3) with given values of parameters.

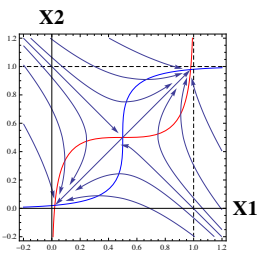

Figure 1: Vector field and nullclines.

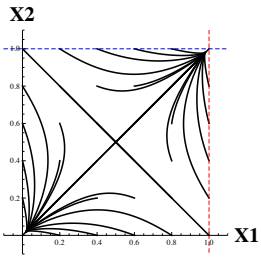

Figure 2: Some trajectories.

One can conclude that all trajectories tend to two attractors in the form of stable critical points located in the upper right and lower left corners of the unit square $0 < x_1 < 1$, $0 < x_2 < 1$. Generally similar structure of the phase plane is typical for the activation case. By activation case is meant system (3) with positive valued coefficients w_{ij} which are constant. Due to location of the nullclines (Figure 1) no whirling vector field is possible and no periodic or quasi-periodic trajectories can exist.

2.2 Variable coefficients

Consider system (3) with matrix (4) elements of which are variable and positive except finite number of points. Let the parameters μ, θ and γ be as above.

2.2.1 Matrix W_{ss}

Let

$$W = \begin{pmatrix} 0.5 + 0.5\sin t & 0.5 + 0.5\sin t \\ 0.5 + 0.5\sin t & 0.5 + 0.5\sin t \end{pmatrix}. \tag{6}$$

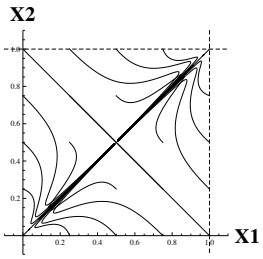

Figure 3: Trajectories for system (3) with (6).

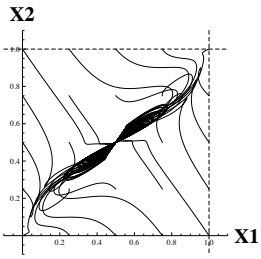

Figure 4: Trajectories for system (3) with (7).

2.2.2 Matrix W_{sc}

Let

$$W = \begin{pmatrix} 0.5 + 0.5\sin t & 0.5 + 0.5\sin t \\ 0.5 + 0.5\cos t & 0.5 + 0.5\sin t \end{pmatrix}. \tag{7}$$

Elements on the secondary diagonal oscillate now in opposite phase. The phase plane and trajectories are depicted in Figure 4. Evidently the vector field is rotating somewhere. A quasi-periodic solution is shown in Figure 5.

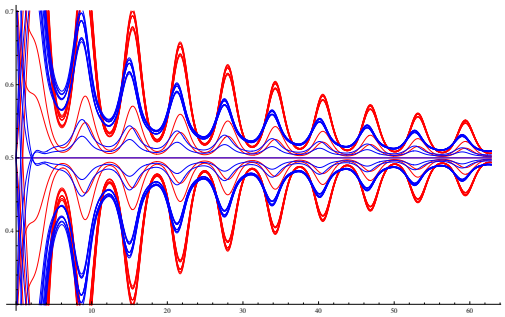

Figure 5: The solutions ($x_1$in red, x_2 in blue) of system (3) with matrix (7). The initial conditions are $x_1(0) = 0.25i$, $x_2(0) = 0.25j$, $i, j = 0, 1, 2, 3, 4$.

3 Conclusions and Future work

Activation systems of the form (3) with constant positive valued coefficients w_{ij} cannot have solutions of oscillatory type. This is possible however if the positive valued coefficients w_{ij} are t-dependent.

References

[1] C. Furusawa, K. Kaneko. A generic mechanism for adaptive growth rate regulation. PLoS Comput Biol, 4(2008), 1, e3, 0035–0042. https://doi.org/10.1371/journal.pcbi.0040003. [Google Scholar]

[2] Koizumi Y. et al. Adaptive Virtual Network Topology Control Based on Attractor Selection. Journal of Lightwave Technology. 2010; 28 (11): 1720-1731. DOI: 10.1109/JLT.2010.2048412

[3] J. Vohradský. Neural network model of gene expression. The FASEB Journal, Vol. 15, March 2001, 846–854.

[4] HR Wilson, JD Cowan. Excitatory and inhibitory interactions in localized populations of model neurons. Biophys J., vol 12 (1), 1972, pp. 1-24.

International Conference on Mathematical Analysis and Applications in Science and Engineering
ICMA^{2}SC'24
ISEP Porto-Portugal, June 20 - 22, 2024

Removable singularities of distributional solutions to the steady Navier-Stokes equations

Alfonsina Tartaglione[1⋆]

[1] Università degli Studi della Campania "Luigi Vanvitelli", Italy

⋆alfonsina.tartaglione@unicampania.it

Abstract: (Special Session #5 Difference & Differential Equations with Applications) Removable singularities for the steady Navier-Stokes equations in dimension $n \geq 3$ are considered. Starting from classical results by V.L. Shapiro [8] and Kim and Kozono [5] an improved condition on the velocity field u is presented in order to show that if u is a distributional solution in the punctured ball $\mathcal{B} \setminus \{o\}$ or in the punctured cone $\mathcal{K} \setminus \{o\}$, then u is a distributional solution in $\mathcal{B}$ or in $\mathcal{K}$.

keywords: Navier–Stokes equations; steady motions; removable singularities.

MSC2020: 35Q30; 35D30; 76D05.

1 Introduction

Let Ω be a bounded open connected set of $\mathbb{R}^n$ ($n \geq 3$) and consider the steady motions in Ω of a viscous incompressible fluid of Reynolds number λ. They are governed by the Navier–Stokes equations [4]

$$\begin{aligned} \Delta u - \lambda u \cdot \nabla u - \nabla p = 0, \\ \text{div } u = 0, \end{aligned} \tag{1}$$

where $u : \Omega \to \mathbb{R}^n$ and $p : \Omega \to \mathbb{R}$ represent the velocity and pressure fields, respectively.

We are interested in the analysis of possible isolated singularities for system (1) and particularly in the conditions assuring that they can be eventually removed. This problem continues to arouse interest since Landau [6] found a class of singular solutions of (1) for $n = 3$, which are regular everywhere except at a point (see also [11]).

The first result on removable isolated singularities for system (1) was obtained by Dyer and Edmunds [3]. They proved that if u is a smooth solution of (1) in the punctured unit ball $\mathcal{B} \setminus \{o\}$ and $u, p \in L^{n+\epsilon}(\mathcal{B})$, for some $\epsilon > 0$, than the singularity at o can be removed. Shapiro [8], [9] proved that the only condition on the velocity field is sufficient to remove the singularity. Kim and Kozono [5] improved Shapiro's result by showing that the singularity can be removed under the hyphotesis $u \in L^n(\mathcal{B})$.

As pointed out in [5], if we confine our attention to distributional solutions, by Shapiro's results [9] it follows that a condition assuring that if u is a distributional solution of (1) in $\mathcal{B} \setminus \{o\}$ it is also in $\mathcal{B}$ is that $u \in L^{2n/(n-1)}(\mathcal{B})$.

We aim to improve Shapiro's result by furnishing a weaker condition on the behaviour of u near o allowing to remove the singularity, also in the case of punctured cones.

Let $q \geq 2$. A weakly divergence free field $u \in L^q_\sigma(\Omega)$ (the subscript σ in the symbol denoting a function space stands for the free divergence condition) is a *distributional solution* to (1) in Ω if

$$\int_\Omega (u \cdot \Delta\phi + \lambda u \cdot \nabla\phi \cdot u) = 0, \quad \forall \phi \in C^\infty_{0,\sigma}(\Omega). \tag{2}$$

A distributional solution $u \in W^{1,q}(\Omega) \cap L^2(\Omega)$ is said *weak solution*.

We use the following notation: o is the origin of the reference frame, $\mathcal{B}_R = \{x \in \mathbb{R}^n : |x| = |x - o| < R\}$ is the ball of radius R centered at o, $\mathcal{B} = \mathcal{B}_1$, $\mathcal{T}_R = \mathcal{B}_{2R} \setminus \overline{\mathcal{B}_R}$, $\mathcal{K}_R = \{x \in \mathbb{R}^n : \lambda x \in \mathcal{K}_R,\ \forall \lambda < R\}$ is a cone with vertex o, $\mathcal{K} = \mathcal{K}_1$.

The following result holds true[1].

Theorem

(i) If $u \in L^{2q}_\sigma(\mathcal{B})$ $(q > 1)$ is a distributional solution to (1) in $\mathcal{B} \setminus \{o\}$ and

$$\|u\|^2_{L^{2q}(\mathcal{T}_R)} = o(R^{1-n/q'}), \tag{3}$$

then u is a distributional solution to (1) in $\mathcal{B}$.

(ii) If $u \in L^{2q}_\sigma(\mathcal{B})$ $(q > 1)$, $u - \kappa$ is a distributional solution to (1) in $\mathcal{B} \setminus \{o\}$ for every constant vector κ and

$$\|u\|^2_{L^{2q}(\mathcal{T}_R)} = o(R^{-n/q'}), \tag{4}$$

then u is a distributional solution to (1) in $\mathcal{B}$.

(iii) If $u \in L^{2q}_\sigma(\mathcal{K})$ $(q > 1)$ is a distributional solution to (1) in $\mathcal{K} \setminus \{o\}$, vanishing on $\partial\mathcal{K}$ and

$$\|u\|^2_{L^{2q}(\mathcal{K}_{2R} \setminus \mathcal{K}_R)} = o(R^{-n/q'}), \tag{5}$$

then u is a distributional solution to (1) in $\mathcal{K}$.

In the following section we give a proof sketch of the theorem.

2 Proof sketch

For simplicity we confine ourselves to the proof of (i).

Let $u \in L^{2q}_\sigma(\mathcal{B})$ $(q > 1)$ satisfy

$$\int_B (u \cdot \Delta\phi + \lambda u \cdot \nabla\phi \cdot u) = 0, \quad \forall \phi \in C^\infty_{0,\sigma}(\mathcal{B} \setminus \{o\}). \tag{6}$$

Consider a regular function w in $\mathbb{R}$, vanishing in $(-\infty, 0]$ and equal to 1 in $[1, +\infty)$ and the cut–off function

$$g(r) = w\left(\frac{r - R}{R}\right), \tag{7}$$

where $0 < R < 1/2$ and $r = |x| \equiv |x - o|$. Observe that $g = 0$ in $\mathcal{B}_R$ and $g = 1$ outside $\mathcal{B}_{2R}$. Moreover $\nabla g = w' R^{-1} e_r$, where $e_r = x/|x|$.

Let $\varphi \in C^\infty_{0,\sigma}(\mathcal{B})$ and consider the following auxiliary problem in divergence form

$$\begin{aligned} &\operatorname{div} h = -\operatorname{div}(g\varphi) \quad \text{in } \mathcal{T}_R \\ &\|\nabla_k h\|_{L^q(\mathcal{T}_R)} \leq c(q) \|\nabla_{k-1}(\varphi \cdot \nabla g)\|_{L^q(\mathcal{T}_R)} \end{aligned} \tag{8}$$

[1]The complete proof is contained in [13]

with $k = 1, 2$. Problem (8) admits a (not unique) solution $h \in W^{2,q}(\mathcal{T}_R)$ [4].

Let consider the function $\phi = g\varphi + h$. Observe that ϕ can be used as a test function in (6). So we have

$$\begin{aligned} \int\limits_{\mathcal{B}\setminus\mathcal{B}_R} gu \cdot \Delta\varphi + \lambda \int\limits_{\mathcal{B}\setminus\mathcal{B}_R} gu \cdot \nabla\varphi \cdot u = &- \int\limits_{\mathcal{T}_R} \big(u \cdot \varphi\Delta g + 2\nabla g \cdot \nabla\varphi \cdot u + u \cdot \Delta h\big) \\ &- \lambda \int\limits_{\mathcal{T}_R} \big[(u \cdot \varphi)u \cdot \nabla g + u \cdot \nabla h \cdot u\big]. \end{aligned} \tag{9}$$

A combination of classical inequalities, $(8)_2$ and (3), letting $R \to 0$ in (9) implies that u is a distributional solution to (1) in $\mathcal{B}$.

3 Conclusions and future work

A sufficient condition to remove an isolated singularity for distributional solutions to the steady Navier–Stokes equations in the punctured ball or cone has been presented for dimension $n \geq 3$. On the basis of this result the aim of a future work is the analysis of the problem of existence of singular solutions (different from Landau solutions for $n = 3$). This is an open problem as pointed out in [11]. Also, following [1], we aim to investigate the problem of isolated singularities by means of potential methods (see, [10], [12] where the elastic layer potentials have been considered). We are also interested in the non–homogeneous case $\lambda = \lambda(x)$ (see, *e.g.*, [7], [14] and [2]).

References

[1] H.J. Choe and H. Kim: Isolated singularity for the stationary Navier–Stokes system, *J. Math. Fluid Mech.* **2** (2000), 151–184.

[2] A. Ferone, R. Russo and A. Tartaglione: The Stokes Paradox in Inhomogeneous Elastostatics, *Journal of Elasticity* **142** (2020), 35–52.

[3] R. H. Dyer and D. E. Edmunds: Removable singularities of solutions of the Navier-Stokes equations, *J. London Math. Soc.* **2** (2) (1970), 535–538.

[4] G.P. Galdi: *An Introduction to the Mathematical Theory of the Navier–Stokes Equations. Steady–state problems*, Springer (2011).

[5] H. Kim and H. Kozono: A removable isolated singularity theorem for the stationary Navier–Stokes equations, *J. Differential Equations* **220** (2006), 68–84.

[6] L.D. Landau: A new exact solution of the Navier-Stokes equations, *Dokl. Akad. Nauk SSSR* **43** (1944), 286–288.

[7] R. Russo and A. Tartaglione The Plane Exterior Boundary-Value Problem for Non-homogeneous Fluids, *Journal of Mathematical Fluid Mechanics* **22** (2020), 14.

[8] V.L. Shapiro: Isolated singularities of solutions of the nonlinear stationary Navier–Stokes equations, *Trans. Amer. Math. Soc.* **187** (1974), 335–363.

[9] V.L. Shapiro: Isolated singularities in steady state fluid flow, *SIAM J. Math. Anal.* **7** (1976), 577–601.

[10] G. Starita and A. Tartaglione: On the Fredholm Property of the Trace Operators Associated with the Elastic Layer Potentials, *Mathematics* **7** (2019), 134.

[11] V. Šveràk: On Landau's solutions of the Navier–Stokes equations, *J. Math. Sci. (N.Y.)* **179** (2011), 208–228.

[12] A. Tartaglione: A Note on the Displacement Problem of Elastostatics with Singular Boundary Values, *Axioms* **8** (2019), 46.

[13] A. Tartaglione: On isolated singularities for the stationary Navier–Stokes system, *submitted*.

[14] A. Tartaglione: Regularity of weak solutions to the inhomogeneous stationary Navier–Stokes equations, *Symmetry* **13** (2021) 1336.

International Conference on Mathematical Analysis and Applications in Science and Engineering
ICMA^{2}SC'24

ISEP Porto-Portugal, June 20 - 22, 2024

Development and Validation of Large Eddy Simulation with Correction - a novel class of turbulence models

Alexander Labovsky[1⋆]

[1] Michigan Technological University, USA

[1⋆]aelabovs@mtu.edu

Abstract: We introduce and discuss the newly proposed class of turbulence models, Large Eddy Simulation with Correction (LES-C). These models improve the efficiency of existing LES models by reducing the modeling error, as well as the temporal discretization error. The improved accuracy is achieved by the defect correction procedure, where the original LES turbulence model is viewed as a "defect" approximation of the quantities of interest, and the whole model is then "corrected" via an algorithm proposed by the author. The problem is solved twice, on the same spacial mesh, using several cores for an effective parallelized implementation. We will present some of the recent results in validation and development of the LES-C models, including the fluid-fluid interaction problem with nonlinear coupling, aiming at the atmosphere-ocean applications. We will also discuss some new findings, that have not been published yet: a three-step LES-C model, where the second correction step is introduced to further improve the solution quality.

keywords: turbulence modeling; large eddy simulation with correction; fluid-fluid interaction.

MSC2020: 76D05; 76M10; 86A05.

1 Introduction

Turbulent fluid flows are ubiquitous in nature, including atmospheric and ocean currents, flows through turbines and pipes, air flows past a moving car or plane, blood flow in arteries, etc. Accurate prediction of turbulent flows is important and sometimes crucial for human life; yet, the complexity of these flows makes the direct numerical simulation prohibitively expensive (now and in the foreseeable future). Thus, the only viable approach to studying turbulence flows is through modeling. There exist so many turbulence models that, clearly, no one model/approach can be viewed as the ultimate success. Herein, we propose to further improve, validate and better understand the strengths and weaknesses of the method, proposed by the PI in 2020, [1]; the method improves the efficiency of the existing popular turbulence models, by reducing the modeling errors and the time discretization errors.

The k-step ($k \geq 2$) defect correction method, applied to turbulence modeling, seeks k consecutive approximation pairs (w_i, q_i), $i = 1, ..., k$ of the Quantity of Interest (QoI). The QoI could be the velocity-pressure pair (u, p), the pair of spatially filtered velocity $\bar{u}$ and pressure p, or any other pair of functions $(h(u), g(p))$. If a turbulence model (TM) is chosen from the Large Eddy Simulation (LES) family of models, then a LES-C (Large Eddy Simulation with Correction, "Lessi") model is obtained via the following procedure.

Algorithm 1 *Turbulence Modeling with Correction.*

1. If needed, rewrite the NSE system so that the velocity-pressure pair (u, p) is transformed into the QoI pair $(h(u), g(p))$:

$$\widetilde{NSE}(QoI) = 0.$$

2. Using the turbulence model (TM), find the defect step approximation of the QoI:

$$TM(w_1, q_1) = 0.$$

3. The correction steps provide a more accurate approximation of the QoI, via

$$TM(w_i, q_i) = TM(w_{i-1}, q_{i-1}) - \widetilde{NSE}(w_{i-1}, q_{i-1}), \qquad i = 2, ..., k.$$

2 Results and discussion

The author, along with his current and former PhD students, are in the process of testing a three-step LES-C procedure (with two correction steps) in various settings, including the fluid-fluid interactions and MHD. Below is the test of Flow Past a Step - a well-known benchmark problem, where eddies form behind a step, then shed and travel to the right. The known LES model Leray-α, is followed by the two corresponding correction steps of Algorithm 1 to form Leray-α-C1 and Leray-α-C2. These three solutions of the Leray-α-C turbulence model are plotted in Figures 2 - 4. These should be compared to the true solution in Figure 1, computed via direct numerical simulation at a finer mesh, with smaller time step. The second correction in the three-step LES-C model gives a better prediction of the position of the traveling vortex, further improving the result of the two-step LES-C.

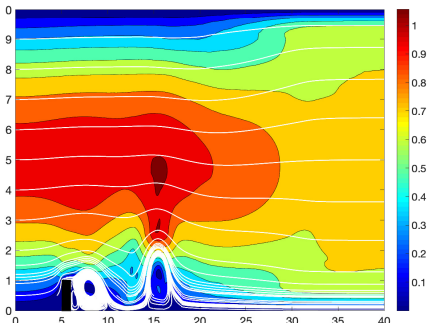

Figure 1: Filtered True Velocity, $Ndofs = 33,820$

Fluid-Fluid Interaction. Next, consider the two-dimensional spatial domain Ω, comprised of two subdomains Ω_1 and Ω_2, coupled across an interface I.

The fluid-fluid interaction problem, introduced below, could be viewed as the important first step in studying turbulent atmosphere-ocean problems. The nonlinear coupling equation, known as the rigid lid condition, allows for the exchange of energies between the subdomains, while having the global energy of the system conserved. This extra nonlinearity poses substantial difficulties in both the numerical analysis of the problem, and in formulating the turbulence models.

The problem for the velocity-pressure pair (u, p) reads: *given* $\nu_i > 0$, $f_i : [0, T] \to H^1(\Omega_i)^d, u_i(0) \in H^1(\Omega_i)^d$ *and* $\kappa \in \mathbb{R}$, *find (for* $i = 1, 2$*)* $u_i : \Omega_i \times [0, T] \to \mathbb{R}^d$ *and* $p_i : \Omega_i \times [0, T] \to \mathbb{R}$ *satisfying*

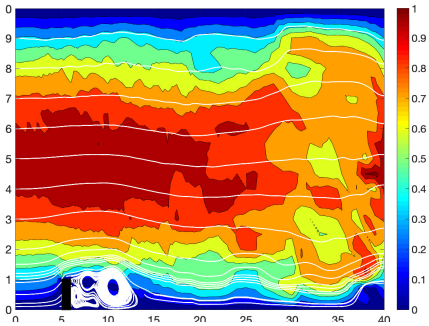

Figure 2: Leray-α model (Defect Step), $Ndofs = 8,897$

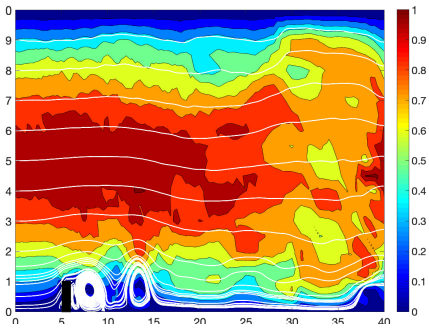

Figure 3: Leray-α-C model, First Correction Step, $Ndofs = 8,897$

(for $0 < t \leq T$*)*

$$
\begin{aligned}
u_{i,t} &= \nu_i \Delta u_i - u_i \cdot \nabla u_i - \nabla p_i + f_i, \quad \text{in } \Omega_i, && (1)\\
-\nu_i \hat{n}_i \cdot \nabla u_i \cdot \tau &= \kappa |u_i - u_j|(u_i - u_j) \cdot \tau, \quad \text{on } I,\ i,j = 1,2\,,\ i \neq j\,, && (2)\\
u_i \cdot \hat{n}_i &= 0 \quad \text{on } I, i = 1,2 && (3)\\
\nabla \cdot u_i &= 0, \quad \text{in } \Omega_i && (4)\\
u_i(x,0) &= u_i^0(x), \quad \text{in } \Omega_i, && (5)\\
u_i &= 0, \quad \text{on } \Gamma_i = \partial\Omega_i \setminus I. && (6)
\end{aligned}
$$

The vectors $\hat{n}_i$ are the unit normals on $\partial\Omega_i$, and τ is any vector such that $\tau \cdot \hat{n}_i = 0$. The parameters ν_i represent kinematic viscosities. We include generic body forces f_i, for generality.

The models NS-ω and NS-ω-C were first compared in a setting, where a circular object was flying at high speed in the air, very close to the still water surface. The energy exchange between the domains can affect the formation of the vortex street; also, the energy of the air flow creates coherent structures in the ocean domain. Figure 5 shows that the NS-ω-C correctly depicts the motion in both domains, while the NS-ω solution fails to capture any of the structures in the water.

References

[1] A. Labovsky, *Approximate Deconvolution with Correction - a member of a new class of models for high Reynolds number flows*, SIAM Journal on Numerical Analysis, vol. 58 (5), 2020, pp. 3068 – 3090.

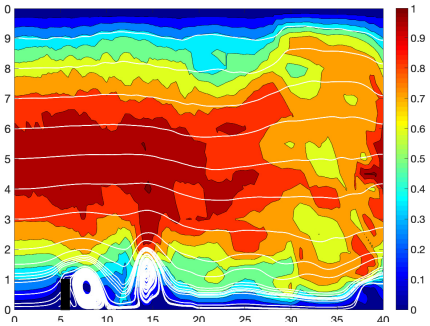

Figure 4: Leray-α-C model, Second Correction Step, $Ndofs = 8,897$

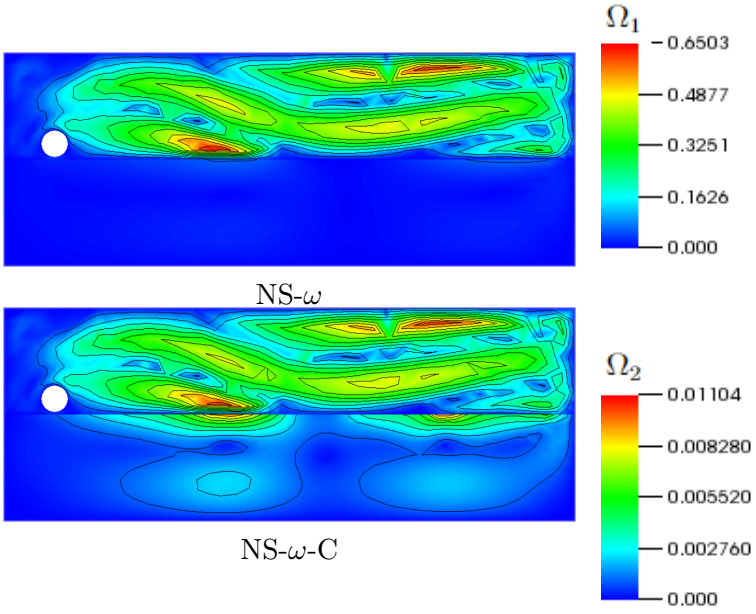

Figure 5: Velocity magnitudes for NS-ω and NS-ω-C for $Re = 1,000$.

[2] M. Aggul, A. Labovsky, E. Onal, K. Schwiebert, *Fluid-Fluid Interaction Problems at High Reynolds Numbers: Reducing the Modeling Error with LES-C*, SIAM Journal on Numerical Analysis, 61(2), 2023, pp. 707–732.

[3] M. Aggul, J. Connors, D. Erkmen, A. Labovsky, *A Defect-Deferred Correction Method for Fluid-Fluid Interaction*, SIAM J. Numer. Anal., 56(4), pp. 2484 - 2512, 2018.

[4] Y. Batugedara, A. Labovsky, K. Schwiebert, *Validation of LES-C turbulence models*, Computer Methods in Applied Mechanics and Engineering, vol. 478(A), 2024, 116458.

[5] Y. Batugedara, A. Labovsky, K. Schwiebert, *Higher Temporal Accuracy for LES-C Turbulence Models*, Computer Methods in Applied Mechanics and Engineering, vol. 377, 2021, 113696.

[6] Y. Batugedara, A. Labovsky, *Approximate Deconvolution with Correction - a high fidelity model for Magnetohydrodynamic flows at high Reynolds and magnetic Reynolds numbers*, Computational Methods in Applied Mathematics, 2023, https://doi.org/10.1515/cmam-2022-0254

International Conference on Mathematical Analysis and Applications in Science and Engineering
ICMA^{2}SC'24
ISEP Porto-Portugal, June 20 - 22, 2024

From Einstein on the Beach to Collatz on the Web

Miguel CASQUILHO[1⋆] **Rui GALHANO**[2] **Jorge BUESCU**[3]

[1]IST (*Instituto Superior Técnico*), University of Lisbon, and CERENA,
Ave. Rovisco Pais, IST, 1049-001 Lisboa, Portugal
[2]IST, University of Lisbon, and CERENA,
Ave. Rovisco Pais, IST, 1049-001 Lisboa, Portugal
[3]FCUL (*Faculdade de Ciências*), University of Lisbon, and CMAFCIO,
Campo Grande, 1749-016 Lisboa, Portugal

[1⋆]mcasquilho@tecnico.ulisboa.pt [2]rui.galhano@tecnico.ulisboa.pt [3]jsbuescu@fc.ul.pt

Abstract: In this study, we address the famous Collatz conjecture, which reminded us of Philip Glass's musical style. After a brief review of the mechanism of calculating the sequence in the conjecture, we directly focus on two objectives: offering the practical numerical operation of the conjecture on a public web page of ours; and, in another web page, seeking a relation of the number of steps in the sequence as a function of the initial values, n, of the sequence, in a long range of values of n. Moreover, we make it possible to use other conjecture parameters, instead of the classical "3, 1, 2". Other web pages to run the Collatz conjecture seemed unclear or unfriendly, motivating our study. The relation mentioned was accomplished, to good agreement, by a Gamma probability density function. Web-based computing is a way both to make computation accessible and usable, and to promote the desirable academia-industry interchange.

keywords: Collatz conjecture; computing; web-based; Philip Glass.

MSC2020: 11-04; 68-04; 68R-99; 97N-80.

1 Introduction

In 1937, the German mathematician Lothar Collatz (1910–1990) revealed his subsequently famous conjecture, described simply in Eq. (1): with n an arbitrary positive integer, repeat

$$\begin{cases} n := 3n+1 & \text{if } n \text{ is odd} \\ n := \dfrac{n}{2} & \text{if } n \text{ is even} \end{cases} \tag{1}$$

(with attributive ':='). This repetitive, "obstinate" structure or algorithm leads always —as far as is known— to a single final result: $n = 1$. Once, Paul Erdős gravely said ([1]) on the conjecture (verified numerically till $\sim 10^{18}$) that Mathematics is not ready to confirm it.

Two decades after the advent of the conjecture, in 1975, the American composer and pianist Philip Glass finished an opera entitled "Einstein on the Beach". We find relationships between both authors, besides the fact that the musician was born in 1937, the same year the mathematician presented his conjecture: more important is Glass's obstinate style, leading to his

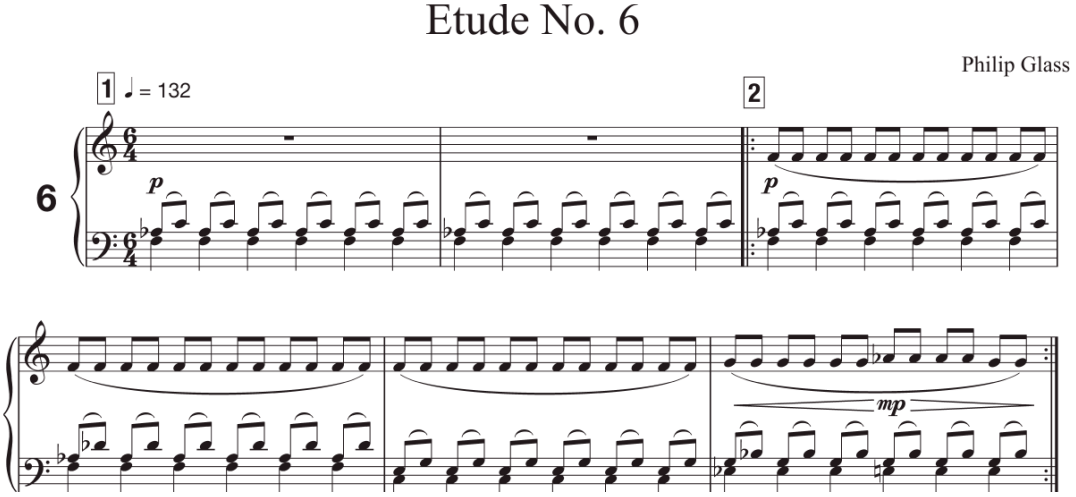

Figure 1: First two staves of Glass's Étude No. 6.

characteristic musical effects. The minimalist, *"ostinato"*[1] structure in his style is well represented, e.g., in his Étude No. 6, for piano, of which the two initial staves are shown in Fig. 1. Remark, even in this short excerpt, a segment itself to be repeated (meaning of the starting and ending ":") from the "2" (in a square) till the end.

For the numerical mechanism of the conjecture, some examples (skipping the first, trivial $n = 1, 2$) can be the following (where $\mathbf{10} = 3 \times \mathbf{3} + 1$), with more striking sequences in Section 2.

$$n = 3\text{: } 10\ 5\ 16\ 8\ 4\ 2\ 1; \qquad n = 5\text{: } 16\ 8\ 4\ 2\ 1$$

Our two objectives in this study are made operational for free use as per these reference links:

Ref.s: [4], [5].

The 1.st permits to run the conjecture to generate the sequence from n, allowing even to change the *multiplier*, *addend*, and *divisor* (respectively, 'Mult', 'Add', 'Div' in the plots), from 3, 1, 2. The 2.nd adjusts a function to estimate the number of steps in the sequence as a function of n in a long range of n's. The web pages reside at the University computing Centre (CIIST, [8]).

It would be implausible to miss texts and web pages on the "Collatz conjecture", for which Google gives 500 000 results. We just mention a few references, since either they did contain no computing or it was not visible (best first): [10], [2], [3], [12], [11], [9]. Many web pages explain the theme, e.g., in universities, but the said scarcity led us to build our own, hopefully more practical. Our use of the Internet as a computing medium has been consistent (e.g., [6], [7]), whereas the general technical articles have circumvented this means to let us verify and use their results and methods.

In the following: Section 2 shows the use of the conjecture, and a further characterization for a range of initial values; and Section 3 synthesizes some of the acquirements and recommendations.

2 Results and discussion

Several Collatz sequences are now shown through the use of the constructed web page [4], and, in the end, through [5], to obtain a relation of the number of steps, S, as a function of n.

For $n = 7$, 16 steps are necessary, as in Fig. 2 (left), a relatively long sequence for a small n, and (right) for $n = 15$, with 17 steps. For $n = 2024$, Fig. 3 shows 112 steps, (left) original, and (right) "reduced", with the y-axis limited to 2000 for better visibility of the final points.

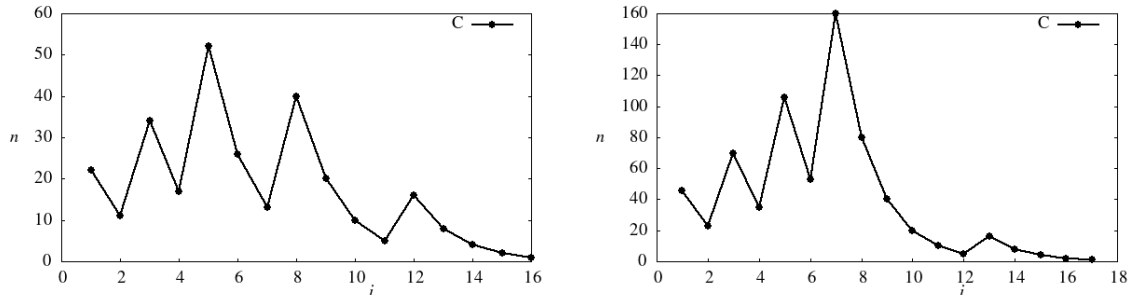

Figure 2: Collatz sequences for (left) $n = 7$, with 16 steps, and (right) $n = 15$, with 17 steps.

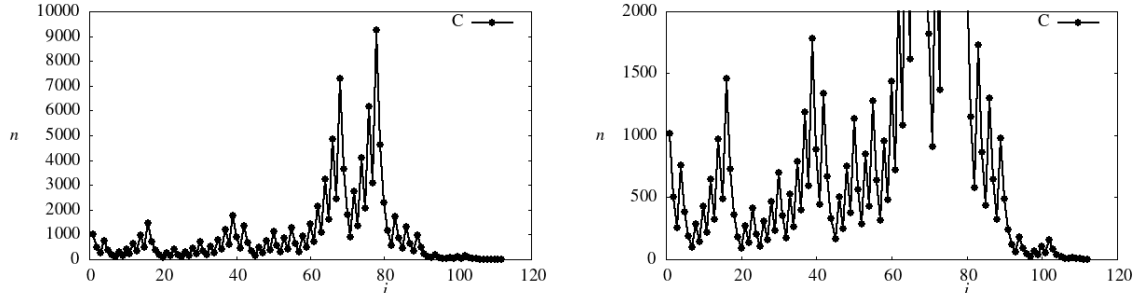

Figure 3: Collatz sequence for $n = 2024$, with 112 steps, (left) original, and (right) "reduced".

A function to relate the initial n for the conjecture with the number of steps till the end, S, was sought. A good agreement (after abandoning an inadequate fit with a Poisson distribution) was obtained with a Gamma density with $\alpha = 5.57$ and $\beta = 23.5$ (approx.) or $\mu = 131$ and $\sigma = 3087$, visible in Fig. 4. The programming was in Python, and, for the adjustment through simple least-squares, a segment in Fortran was used for speed.

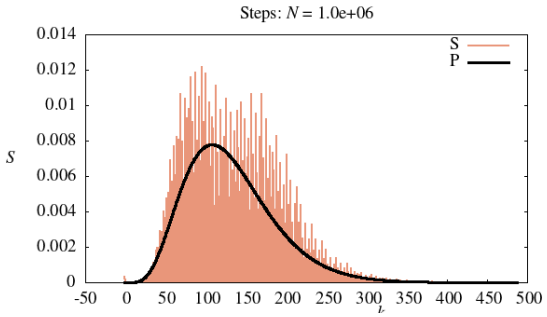

Figure 4: Collatz sequence "sweep" for $2 \leq n \leq 10^6$, with adjusted Gamma 'pdf'.

3 Conclusions and Future work

We briefly reviewed the famous Collatz conjecture (suggestive of Glass's music style) and, more importantly, present its computation on a dedicated web page of ours. There, maintaining the conjecture's structure, the user can also try other values of the multiplicand, addend and divisor, which are, respectively, 3, 1, and 2 in the original setting. We sought websites for these matters, but found none remarkable, among numerous explanatory web pages. We also constructed a relation between the starting n and the number of steps till end, S, in a long range of consecutive values of n, finding a satisfactory function, a Gamma probability density. We recommend the

[1] "Ostinato", Italian musical term for "obstinate" play, indicates a persistent repetition of a phrase, with little or no alterations.

Internet as a computing medium, for this and many other scientific problems, a medium that we will keep using, and is still scarcely active in the scientific literature.

Acknowledgments

The author MC does research at the Department of Chemical Engineering, IST (Instituto Superior Técnico), University of Lisbon, Lisbon, Portugal, and CERENA, "Centro de Recursos Naturais e Ambiente" (*Centre for Natural Resources and the Environment*), under Project UID/04028/2020, funded by FCT, "Fundação para a Ciência e a Tecnologia" (Portuguese *National Science Foundation*); RG teaches and does research at the Dept. of Chemical Eng.[ing], IST, University of Lisbon, and CERENA (Project above); and JB teaches and does research at Dept. of Mathematics, FC (Faculty of Sciences), University of Lisbon, Project UIDB/04561/2020, doi: https://doi.org/10.54499/UIDB/04561/2020. CIIST, "Centro de Informática do IST" (Informatics Centre of IST) supplies the computing system.

References

[1] AMS Blogs (American Mathematical Society), "The Collatz Conjecture", https://blogs.ams.org/mathgradblog/2013/08/01/collatz-conjecture/, accessed 15-Jan-2024.

[2] Barina, D. (2020), "Convergence verification of the Collatz problem", J. Supercomputing.

[3] Carletti, T., D. Fanelli (2018), "Quantifying the degree of average contraction of Collatz orbits", Boll. Unione Mat. Ital., 11:445–468.

[4] Casquilho, Miguel, "Collatz conjecture on the Web", http://web.tecnico.ulisboa.pt/~mcasquilho/compute/ICMASC_24/Collatz/P-Collatz.php.

[5] Casquilho, Miguel, "Collatz conjecture, Web sweeping", http://web.tecnico.ulisboa.pt/~mcasquilho/compute/ICMASC_24/sweep/P-sweep.php.

[6] Casquilho, Miguel, Jorge Buescu (2022), "Standard deviation estimation from sums of unequal size samples", Monte Carlo Methods and Applications, August, doi: https://doi.org/10.1515/mcma-2022-2118.

[7] Casquilho, Miguel, Pedro Pacheco (2023), "Three languages simulate polygons and perform on the Web", icSoftComp2023, CHARUSAT, Changa, India.

[8] CIIST, "Centro de Informática do IST" (Informatics Centre of IST), https://si.tecnico.ulisboa.pt/en/, accessed 15-Jan-2024.

[9] Gründsatzlich Informatie Technologie, "Collatz Calculator", https://www.grundsatzlich-it.nl/collatz.html, accessed 15-Jan-2024.

[10] Lagarias, J. C. (2011), "The Ultimate Challenge: the 3x+1 Problem", AMS, RI (USA).

[11] Notre Dame University, "Challenge 05: Collatz Conjecture", https://www3.nd.edu/~pbui/teaching/cse.30872.fa22/challenge05.html, accessed 15-Jan-2024.

[12] Wolfram Alpha, "collatz conjecture", https://www.wolframalpha.com/input/?i=collatz+conjecture, accessed 15-Jan-2024.

International Conference on Mathematical Analysis and Applications in Science and Engineering
ICMA^{2}SC'24
ISEP Porto-Portugal, June 20 - 22, 2024

Discrete-Time Octonion Orbital Dynamics in a Recurrent Frenet Frame with Symmetries

Bernd Binder[1⋆]

[1] Quanics, 89182 Bernstadt, Germany

[1⋆]bernd@binders.de

Abstract: Following a minimalist approach to establish a discrete-time co-moving Frenet frame, we propose an autonomous difference equation system given by $X_i = X_{i-2} + X_{i-1} \times f_i\left(X_{i-1}, X_{i-2}, X_{i-3}\right) \in \mathbb{R}^3$ or $\in \mathbb{R}^7$ based on three former position vectors $X_{i-1}, X_{i-2}, X_{i-3}$, with $X_{i-1} - X_{i-3}$ orthogonal to X_{i-2}. We recurrently determine both, the orthogonal co-moving components (normal, tangential, binormal) and dynamics of a discrete Frenet frame with non-zero torsion and curvature parameter. Symmetries are given by the invariant $X_i \cdot X_{i-1}$ and reflection sign flip operations at every memorizing step. The necessary cross and dot vector product (split-)algebra is encoded in variable multiplication tables in $3d$ (quaternion) and $7d$ (octonion). We discuss solutions showing orbital waves with spin and characteristic non-linear modal transitions.

keywords: Frenet; Octonion; Quaternion.

MSC2020: 60-J74; 57-R25; 35-A04.

1 Introduction

Recently we pointed to symmetries in a discrete-time delay autonomous difference equation system using a normed cross product algebra. By reflection we could generated two opposite "charged" mirror density pairs showing interaction and non-linear but stable spin dynamics on curved surfaces [1, 2, 3]. Initially, we started with computer experiments in two dimensions or on spherical surfaces [1] producing some chaotic and regular pattern by discrete-time Rotation-Translation-Reflection chaotic algorithms inspired by [4]. It became clear, how symmetry and regular non-linear flow-type structures can arise out of a time-discrete chaotic dynamics. As the central concept of this work, the change of the actual position will be given by the three position memory terms $X_{i-1}, X_{i-2}, X_{i-3}$ recurrently. These three points will also be used to define the normal, tangential, and binormal components of the co-moving Frenet frame. So both, the orthogonal frame and the change of the frame are represented by the three former position vectors. The simulation software part of the presentation shows the fading vector "jump" density in real-time, where the curvature and torsion parameters and initial conditions can be changed, saved, and recovered.

2 Results and discussion

The following multidimensional, recurrent, autonomous, and discrete-time delay difference equation including reflection was initially presented in [3]

$$X_i = X_{i-2} - X_{i-1} \times f_i \left(X_{i-1}, X_{i-2}, X_{i-3} \right) \in \mathbb{R}^3 \text{ or } \in \mathbb{R}^7, \tag{1}$$

where the reflection sign flip operations at every step are given by

$$X_{i-3} = -X_{i-2}, \;\; X_{i-2} = -X_{i-1}, \;\; X_{i-1} = -X_i. \tag{2}$$

The resulting density pattern show a lot of orbital spin and wave dynamics with symmetries. According to Noethers Theorem, symmetry exhibits an observable quantity that is conserved. Reflection in Eq.(2) as a permanent sign-flip shows long range jumps between spatial separated co-orbiting mirror-image density pattern. It provides for a kind of pattern-antipattern symmetry, see Fig.1 and 2, which are two spatially separated counter sets appearing as even/odd tuples (even/odd index i) [1] defining opposite "charge" sets based on the alternating "jumps". Since the cross product $X_{i-1} \times f_i$ equal to the tangential difference $X_i - X_{i-2}$ in Eq.(1) is orthogonal to the intermediate point X_{i-1} located on the other side of the center, we have the invariant C

$$(X_{i-2} - X_i) \cdot X_{i-1} = 0, \quad C = X_i \cdot X_{i-1} = X_{i-1} \cdot X_{i-2} = ..., \tag{3}$$

where $C = -\left|X_i\right| \left|X_{i-1}\right| \cos\left(s_i - s_{i-1}\right)$ and $s_i - s_{i-1}$ is the rotation angle. This way we already found very interesting conditions showing orbital wave function mirror pairs with eigenstates, where we could stimulate spin-transitions and a lot of non-linear dynamics like decays or spontaneous phase changes showing hysteresis and pairing effects.

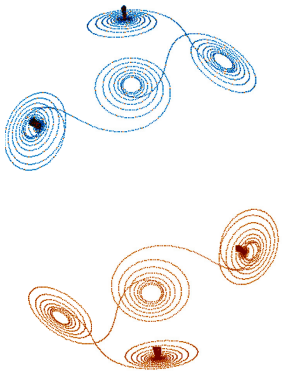

Figure 1: Type 2 octonion connected pair group, acting in $7d$ with more than 3 modes excited (orbital modes and some radial "nipples"). The orbital modes are point symmetric, the nipples not, constant $C = 1$.

A co-moving frame can provide for kinematic properties like local orientation, velocity, acceleration, curvature, and torsion along the arc. Regarding the discrete change of the frame, in a limit cycle which is closed after m steps, the angular change or arc length difference after one loop is infinitesimally small with arbitrary slow rotation $s_{i-m} - s_i$ and can go to zero $\varepsilon = |X_i - X_{i\pm m}| \to 0$. In this case the fixed point drift is arbitrary smooth and can be a differential $\Delta s_{i,m} = s_{i-m} - s_i \to ds_{i,m}$. To get the geometric properties of the curves itself, the discrete Frenet-Serret formulas Hu[5], Konno[6] provide for an standard model of orthogonal frame vectors given by the so-called tangent T_i, normal N_i, and binormal B_i unit vectors in terms of each other.

First we note, that in osculating symmetry the normal vector N_i points to the center of motion $N_i = -X_i/|X_i|$, which means that the coordinate center is equal to the reflection center and

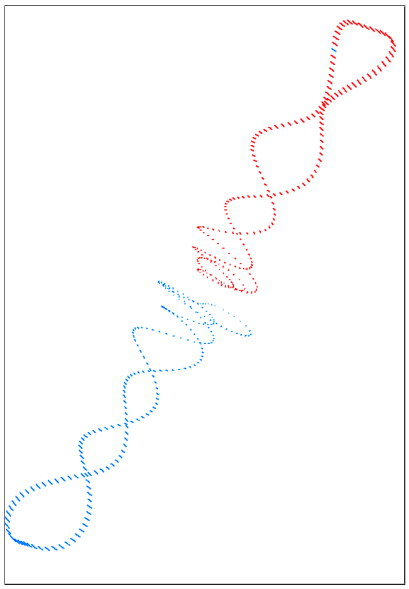

Figure 2: A type 1 quaternion limit cycle "hosted" in an octonian. The cycle has $m = 470$ points, $\tau \approx 0.01264$, $\kappa \approx 0.09656$, $C = \alpha = 1$.

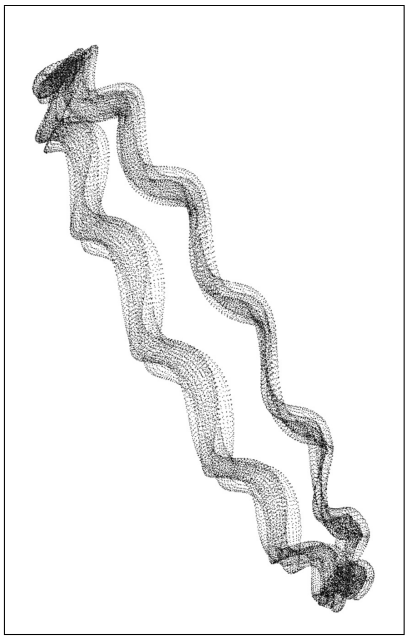

Figure 3: A type 2 split-octonion orbital wave. 3 out of 7 dimension are projected into $2d$.

the normal vector is anti-parallel to the position vector. The change in the normal component after a closed loop with m steps and infinitesimal position change can be directly related to the continuous Frenet-Serret formula

$$\frac{N_{i-m} - N_i}{s_{i-m} - s_i} = \frac{\Delta N_{i,m}}{\Delta s_{i,m}} \rightarrow \frac{dN_{i,m}}{ds_{i,m}} = \tau_{i,m}\ B_{i,m} - \kappa_{i,m}\ T_{i,m}\ , \tag{4}$$

where $\kappa_{i,m}$ is the curvature and $\tau_{i,m}$ the torsion parameter in discrete time on a closed loop. Since $B_{i,m}$ and $T_{i,m}$ must be both orthogonal to $N_{i,m}$, the central requirement of orthogonal change in the Frenet continuous case can be written as

$$\frac{dN_{i,m}}{ds_{i,m}} \cdot N_{i,m} = 0. \tag{5}$$

In our approach this orthogonal change can be represented by the three actual vectors, where we have in circular osculating symmetry on both sides (even/odd index) $|X_i| = |X_{i-2}|$. This means, after two steps $m = 2$ the orthogonal reflection change is with Eq.(3) given by

$$\frac{\Delta N_{i,2}}{\Delta s_{i,2}} \cdot N_{i-1} = 0. \tag{6}$$

With this orthogonal frame and orthogonal evolution set we found two Frenet types of vector functions f_i showing some interesting dynamics in $3d$ and $7d$.

2.1 Type 1 recurrent Frenet unit frame function

Our f_i type 1 is based on the standard discrete Frenet frame apparatus and the three basic orthogonal terms. Similar to the standard Frenet frame, the binormal and tangential unit frame vectors for the first type 1 are given by

$$B_i = c_B^{-1} X_{i-1} \times X_{i-2},\ T_i = c_T^{-1} X_{i-1} \times X_{i-3}, \tag{7}$$

which are normalized by c_B and c_T

$$c_B = |X_{i-1} \times X_{i-2}|\,,\ c_T = |X_{i-1} \times X_{i-3}|\,. \tag{8}$$

With these orthogonal memory terms we have the type 1 function with the Frenet type curvature and torsion parameter

$$f_i\left(X_{i-1}, X_{i-2}, X_{i-3}\right) = \alpha_i \left[X_{i-2} c_B^{-1} \tau_{i-1} - X_{i-3} c_T^{-1} \kappa_{i-1}\right]. \tag{9}$$

2.2 Type 2 recurrent Frenet power-law frame vector function

In our computer experiments we have been looking for variants of f_i in the three-memory term Frenet concept and found the f_i type 2 as a modification containing no unit vector normalization terms, but power-law distance dependent terms

$$f_i\left(X_{i-1}, X_{i-2}, X_{i-3}\right) = \alpha_i \left[c_1 \frac{X_{i-2}}{|X_{i-2} - X_{i-1}|^{p_1}} + c_2 \frac{X_{i-3}}{|X_{i-3} - X_{i-1}|^{p_2}}\right]. \tag{10}$$

Note, that a power-law distance dependence was also part of [4]. Now we have two power-law dependent torsion and curvature terms part of f_i type 2

$$\tau_{i-1} = \frac{c_1 c_B}{|X_{i-2} - X_{i-1}|^{p_1}}\ , \kappa_{i-1} = \frac{c_2 c_T}{|X_{i-3} - X_{i-1}|^{p_2}}\ . \tag{11}$$

Default values for the exponents are $p_1 = p_2 = 1$, where we have a scale-invariant vector function.

2.3 Quarternion and (split-)Octonion algebra

The cross operations are important for generating the tangential, normal, and binormal parts of a co-moving Frenet frame. The cross product is usually defined by the algebra of pure imaginary (split-)quaternions in $3d$ part of (split-)octonions in $7d$, where the algebra is encoded in matrix multiplication tables. The standard cross products of normed division and split-algebras can exist in $\mathbb{R}^n$ if and only if $n = 0$, 1, 3 or 7, see [7]. This means we will operate our discrete space vector $X_i \in \mathbb{R}^3$ or $\in \mathbb{R}^7$ and apply in both algebras the cross product leading to orthogonal vectors. The $7d$ cross product has the same relationship to the $8d$ (split-)octonions $\mathbb{O}$ as the $3d$ cross product does to the $4d$ (split-)quaternions $\mathbb{H}$. The (split-)octonions correspond to the largest of the four normed algebras and are like the (split-)quarternions a division algebra over the real numbers, a kind of hypercomplex number system. As usual, the cross operations in $7d$ will be carried out by variable multiplication tables that can be choosen by the simulation software.

3 Conclusions and Future work

The two step change from X_{i-2} to X_i orthogonal to last value X_{i-1} in Eq.(1) provides for a symmetry invariant and suggests according to Eq.(3) - Eq.(6) to change the frame recurrently by the curvature and torsion parts in the sense of Frenet-Serret.

Bringing the quaternion and (split-)octonion system to life by algebras supporting vector dot and cross products delivering orthogonal vector shifts in a time-discrete co-moving recurrent frame, we have found two related vector Frenet-Serret type functions driving the frame path recurrently. These two functions take as an input the three last vectors from the past not located on one straight line to establish the three orthogonal frame vectors of normal, tangential, and binormal components with a normed algebra. Computer simulations confirm that we can extend

the basic recurrent nonlinear algebraic system from $\mathbb{R}^3$ to $\mathbb{R}^7$. The two main symmetries are given by the reflection mirror symmetry, see Fig.1 and 2, and the invariant C. Split-octonions often show a very rich dynamics with a lot of torsion, see Fig.3, where different frequencies can be observed, like a slow wave or orbit in some dimensions superimposed by a fast vibration or orbit in other dimension pairs. In this context it should be noted, that we can also use a $3d$ quaternion sub-algebra of the $7d$ algebra for quaternion frames, where the other 4 dimensions are zero. Geometric shifts induced by parallel transport can be related to the surface curvature and torsion, where extra angles or angular shifts are responsible for pattern generation. Building this way complex structures, modular arithmetic gives the extra angles and geometric shifts on closed, discrete, and curved paths. This relation is still open.

The recurrent operations approach could be interesting in all fields the algebras already have been applied, which are Clifford algebras and spinors, projective geometry with Hopf fibrations and Lorentzian geometry, Jordan algebras, and the exceptional Lie groups - and there are many applications in quantum physics, relativity, and supersymmetry. Since relativistic quantum physics (Dirac) can be formulated by this algebra [8, 9], and the Frenet frame approach directly shows the geometric role of torsion and curvature in the context of electromagnetism, we could try to link to quantum and relativistic physics and eventually identify some interesting real existing orbital wave solutions that could be relevant in this context. The concept of long-range reflection jumps introduces a kind of non-locality, which is important in the context of quantum physics. Curvature and torsion properties have already be related to electromagnetic fields.

We also see atomic-types eigenstates with a core, instability, hysteresis, and transition to chaos. Very interesting in this context are the stimulations, transitions, and relations between different modes, like orbital and radial modes. The spin anomaly found in the context of a radial mode excitation threshold with hysteresis could be a good starting point (to be published).

In future works we will consider not only one isolated system with one algebra, we will apply different algebras parallel, where we can modify, couple or split algebras in variable multiplication tables. But this approach requires more understanding and improvement of the simulation methods. There are still a lot of interesting open points, some of which will be clarified sooner or later. Videos from simulations can be found on the internet with the tag #DACOP.

References

[1] B. Binder, *"Dynamic Localized Autonomous Chaotic Orbital Patterns from Rotation-Translation Sequences"*, Springer Proceedings in Complexity, 14th Chaotic Modeling and Simulation International Conference, Y. Dimotikalis and C. Skiadas, (Eds), Springer Nature, 45-54, (2022).

[2] B. Binder, *"Orbital Waves and Quantum Densities from Time-Discrete Chaotic Sequences"*, Springer Proceedings in Complexity, 15th Chaotic Modeling and Simulation International Conference, Y. Dimotikalis and C. Skiadas, (Eds), Springer Nature, 29-40, (2023).

[3] B. Binder, *"Time-Discrete SO(3) Jump Sequences Showing a Quantum Type Orbital Wave Dynamics"*, presentation in: Days Of Applied Nonlinearity and Complexity (DANOC), Book of Abstracts, January 12-14, (2024).

[4] C. H. Skiadas, *"Von Karman Streets Chaotic Simulation, Topics on Chaotic Systems"*, C.H. Skiadas, Y. Dimotikalis and C. Skiadas, (Eds), World Scientific, 309-313, (2009).

[5] S. Hu, M. Lundgren and A. J. Niemi, *"Discrete Frenet frame, inflection point solitons, and curve visualization with applications to folded proteins"*, Phys. Rev. E 83, 061908,(2011).

[6] D. E. Blair and T. Konno, *"Discrete torsion and its application for a generalized van der Waerden's theorem"*, Proc. Japan Acad., 87, Ser. A, No.10, 209-214, (2011).

[7] A. Hurwitz, *"Ueber die Composition der quadratischen Formen von beliebig vielen Variabeln (On the composition of quadratic forms of arbitrary many variables)" (in German)*. Nachr. Ges. Wiss. Goettingen: 309-316, (1898).

[8] D. B. Shapiro, *"Compositions of Quadratic Forms"*, W. de Gruyter Verlag, (2000).

[9] John, Baez, *"The Octonions"*, Bull. Amer. Math. Soc. 39 (02): 145-205. Electronic copy found at: http://www.ams.org/journals/bull/2002-39-02/S0273-0979-01-00934-X/S0273-0979-01-00934-X.pdf

International Conference on Mathematical Analysis and Applications in Science and Engineering ICMA²SC'24

ISEP **Porto-Portugal, June 20 - 22, 2024**

ESSENTIAL SPECTRA OF WEIGHTED ENDOMORPISMS OF UNIFORM ALGEBRAS

Arkady Kitover[1*] **Mehmet Orhon**[2]

[1] Community College of Philadelphia, USA
[2] University of New Hampshire, USA

[1*] akitover@ccp.edu

[2*] mo@unh.edu

Abstract: We obtain some results about the spectrum and the semi-Fredholm spectra of weighted isometrical endomorphisms of uniform algebras. In particular, we show that in the case of analytic uniform algebras the spectrum is a connected rotation invariant subset of the complex plane and that the semi-Fredholm spectra are rotation invariant.

keywords: weighted composition operators; spectrum; essential spectra

MSC2020: 47B33; 47B48; 46B60.

1 Introduction

The goal of this paper is to present some results about the spectra of weighted isometrical endomorphisms of uniform algebras. These results extend and complement the previous results of the authors in [1] and [2].

The first of our main results, Theorem 1, states that the upper semi-Fredholm spectrum of an isometrical weighted automorphism coincides with its approximate spectrum.

Theorem 2 states that the spectrum of a weighted isometrical isomorphism of an analytic

(see Definition 1) unital uniform algebra is a rotation invariant connected subset of the complex plane.

We conclude the paper with the partial description of essential spectra of weighted automorphisms of the disc-algebra, thus complementing the results of H. Kamowitz, who described the spectrum of these operators in [3].

Throughout the paper we use the following notations.

A is a unital uniform algebra.

∂A is the Shilov boundary of A.

$C(K)$ is the space of all complex-valued continuous functions on a Hausdorff compact space K.

$\mathbf{N}$ is the set of all positive integers.

$\mathbf{C}$ is the field of all complex numbers. All linear spaces are considered over the field $\mathbf{C}$.

$\mathbf{T}$ is the unit circle, $\mathbf{U}$ is the open unit disc, $\mathbf{D}$ is the closed unit disc.

Let $T: X \to X$ be a bounded linear operator on a Banach space X.

$\sigma(T)$ is the spectrum of T.

$\sigma_{a.p.}(T)$ is the approximate point spectrum of T, i.e.

$\sigma_{a.p.}(T) = \{\lambda \in \mathbf{C}: \quad \exists x_n \in X, \| x_n \| = 1, Tx_n - \lambda x_n \to 0\}$.

Recall that a continuous linear operator on a Banach space X is called upper semi-Fredholm (respectively, lower semi-Fredholm) if its image $R(T)$ is closed in X and $\dim \ker T < \infty$ (respectively, $\operatorname{codim} R(T) < \infty$).

$\sigma_{usf}(T)$ is the upper semi-Fredholm spectrum of T, i.e.

$\sigma_{usf}(T) = \{\lambda \in \mathbf{C}: \lambda I - T$ is not upper semi-Fredholm$\}$.

$\sigma_{lsf}(T)$ is the lower semi-Fredholm spectrum of T, i.e.

$\sigma_{lsf}(T) = \{\lambda \in \mathbf{C}: \lambda I - T$ is not lower semi-Fredholm$\}$.

$\sigma_{sf}(T) = \sigma_{usf}(T) \cap \sigma_{lsf}(T)$ is the semi-Fredholm spectrum of T.

$\sigma_{f}(T) = \sigma_{usf}(T) \cup \sigma_{lsf}(T)$ is the Fredholm spectrum of T.

Let A be a unital uniform algebra and U be an isometric isomorphism of A. Let φ be the corresponding map of the space of maximal ideals of A into itself. Then, $\varphi(\partial A) = \partial A$. We will denote the endomorphism U as T_φ.

2 Results and discussion

Theorem 1. Let A be a unital uniform algebra, T_φ be an isometric endomorphism of A and let $w \in A$. Assume that ∂A has no isolated points and that φ is an open map of ∂A onto itself. Then,

$$\sigma_{usf}(T) = \sigma_{a.p.}(T) = \sigma_{a.p.}(T, C(\partial A)).$$

Definition1. A unital uniform algebra A is called *analytic* if for any nonempty subset U of ∂A and any $a \in A$ we have $a|U \equiv 0 \Rightarrow a = 0$.

Theorem 2. Let A be a unital analytic uniform algebra, T_φ be an isometric endomorphism of A and let $w \in A$. Assume that φ is an open map of ∂A onto itself and that $T_\varphi^n \neq I, n \in \mathbf{N}$. Then, $\sigma(T)$ and $\sigma_{usf}(T)$ are rotation invariant subsets of $\mathbf{C}$.

Moreover, the set $\sigma(T)$ is connected.

The next three propositions provide information about the essential spectra of weighted automorphisms of the disc algebra $\mathbf{A}$: the algebra of all functions analytic in $\mathbf{U}$ and continuous in $\mathbf{D}$. For the sake of brevity, we will consider below only the case when the weight w is invertible in $\mathbf{A}$. Thus, we assume that $T = wT_\varphi$ is an invertible weighted automorphism of $\mathbf{A}$.

Proposition 1. If φ is an elliptic (nonperiodic) Möbius transformation, ω is the fixed point of φ in $\mathbf{U}$, and $w(z) = (z-\omega)^n w_1(z)$, where $n \geq 0$ and $w_1(\omega) \neq 0$. Then,

$$\sigma_{sf}(T) = \sigma(T) = w_1(\omega)\mathbf{T}.$$

Proposition 2. If φ is a parabolic Möbius transformation and ω is the fixed point of φ in $\mathbf{T}$. Then,

$$\sigma_{sf}(T) = \sigma(T) = w(\omega)\mathbf{T}$$

Proposition 3. Let φ be a hyperbolic Möbius transformation and ω_1, ω_2 be the fixed points of φ in $\mathbf{T}$. Assume that ω_1 is the attracting point of φ.

1. If $|w(\omega_1)| \leq |w(\omega_2)|$, then
$$\sigma(T) = \sigma_{lsf}(T) = \{\lambda \in \mathbf{C}: \ |w(\omega_1)| \leq |\lambda| \leq |w(\omega_2)|\},$$
$$\sigma_{usf}(T) = w(\omega_1)\mathbf{T} \cup w(\omega_2)\mathbf{T}.$$
2. If $|w(\omega_1)| \geq |w(\omega_2)|$, then
$$\sigma(T) = \sigma_{usf}(T) = \{\lambda \in \mathbf{C}: \ |w(\omega_2)| \leq |\lambda| \leq |w(\omega_1)|\},$$
$$\sigma_{lsf}(T) \supseteq w(\omega_1)\mathbf{T} \cup w(\omega_2)\mathbf{T}.$$

Remark. The authors will provide the proofs of the results stated above and considerably more details about the spectra of weighted automorphisms of the disc algebra and the polydisc algebras (including the case of a noninvertible weight w) in future publications.

3 Conclusions and Future work

To illustrate on the one hand the usefulness and on the other hand the shortcomings of the results stated in the current paper we invite the reader to look together with us at the following example.

Let $Tf(z) = w(z)f(B(z)), z \in \mathbf{D}, f \in \mathbf{A}$, where $\mathbf{A}$ is the disc algebra and B is a finite Blaschke product containing at least two Möbius factors.

The theorems 1 and 2 guarantee that $\sigma(T)$ is connected and rotation invariant and that $\sigma_{usf}(T)$ is also rotation invariant. But, with the exception of some special examples, we cannot provide any effective way to compute the spectral radius of T, even less, to provide an exact description of the sets $\sigma_{usf}(T)$ and $\sigma_{lsf}(T)$.

We hope that either our future work will provide some progress, or that the problems outline here will attract the attention of other researchers.

References

[1] Kitover A.K., Spectrum of weighted composition operators: part 1. Weighted composition operators on $C(K)$ and uniform algebras. Positivity, **15** (2011), 639 - 659.

[2] Kitover A.K., Orhon M., Spectrum of weighted composition operators, part V, spectrum and essential spectra of weighted rotation-like operators. Positivity, **24** (2020), 973 – 1015.

[3] Kamowitz H., The spectra of a class of operators on the disc algebra, Indiana University Mathematics Journal, **27** No 4, (1978), 581 – 610.

International Conference on Mathematical Analysis and Applications in Science and Engineering
ICMA^{2}SC'24
ISEP Porto-Portugal, June 20 - 22, 2024

WEIGHTED NEWTON-TYPE INEQUALITIES VIA RIEMANN-LIOUVILLE FRACTIONAL INTEGRALS

Hüseyin Budak

Düzce University, Türkiye

hsyn.budak@gmail.com

Abstract: In this study, we present weighted Newton-type inequalities for different classes of functions using Riemann-Liouville fractional integrals. We start by using a positive weighted function to show an essential integral equality needed to establish the main results. By utilizing this equality and Riemann-Liouville fractional integrals, we prove several weighted Newton-type inequalities for different function classes, including differentiable convex functions, bounded functions, Lipschitzian functions, and functions of bounded variation. The results provide insights into the implications of Newton-type inequalities and suggest potential avenues for future research.

keywords: Riemann-Liouville fractional integrals; Newton-type inequalities; weighted integral inequalities.

MSC2020: 26D10; 26D07; 26D15.

References

[1] M. R. Delavar, A. Kashuri, and M. De La Sen, On weighted Simpson's $\frac{3}{8}$ rule, Symmetry, **13**(10) (2021), 1933.

[2] F. Hezenci, H. Budak, and P. Kösem, A new version of Newton's inequalities for Riemann-Liouville fractional integrals, Rocky Mountain Journal of Mathematics, **52**(6) (2022), 49–64.

[3] S. Erden, S. Iftikhar, P. Kumam, and M. U. Awan, Some Newton's like inequalities with applications, Revista de la Real Academia de Ciencias Exactas, Fisicas y Naturales. Serie A. Matematicas, **114**(4) (2020), 1–13.

[4] S. Gao and W. Shi, On new inequalities of Newton's type for functions whose second derivatives absolute values are convex, International Journal of Pure and Applied Mathematics, 74(1) (2012), 33–41.

[5] M. A. Noor, K. I. Noor, S. Iftikhar, Some Newton's type inequalities for harmonic convex functions, Journal of Advanced Mathematical Studies, **9**(1) (2016), 7–16.

[6] T. Sitthiwirattham, K. Nonlaopon, M. A. Ali, and H. Budak, Riemann-Liouville fractional Newton's type inequalities for differentiable convex functions, Fractal and Fractional, 6(3) (2022), 175.

[7] A.A. Kilbas A.A.; Srivastava H.M.; and Trujillo J.J. *Theory and applications of fractional differential equations*, Elsevier, Amsterdam, 2006.

International Conference on Mathematical Analysis and Applications in Science and Engineering
ICMA^{2}SC'24
ISEP Porto-Portugal, June 20 - 22, 2024

Linear Statistical Inverse Problems for Hilbert Space Processes in Hilbert Scales

Mihaela Pricop-Jeckstadt[1⋆]

[1] University POLITEHNICA of Bucharest, Romania

[1⋆]Mihaela.Pricop@upb.ro

Abstract: In this talk, we introduce and characterize Hilbert space processes in Hilbert scales (s-HSP) and we study linear statistical inverse problems between s-HSPs. The smoothness of the exact solution and of the noise as well as the ill posedness of the linear operator are expressed with the help of indeces of Hilbert spaces in Hilbert scales. Finally, conditions for the well-posedness of the inverse problem are presented

keywords: statistical inverse problems; Hilbert scales; lHilbert space process.

MSC2020: 49-XX; 34-XX; 92-XX.

1 Introduction

In this paper, we study the problem of reconstructing the linear, continuous stochastic process $X : H \to \mathbf{L}^2(\Omega, \mathbf{A}, \mathbf{P})$ with covariance operator R_X from (noisy) values of

$$Y^\sigma = F(X) + \sigma W$$

$F(X) : H \to \mathbf{L}^2(\Omega, \mathbf{A}, \mathbf{P})$, $F(X)(\varphi) = X(F^*(\varphi)), \forall \varphi \in H$
where $W : H \to \mathbf{L}^2(\Omega, \mathbf{A}, \mathbf{P})$ is white noise independent from X. The best linear estimate of X is a well-posed problem in this setting ([1, 2]).
We introduce and characterize the Hilbert space processes in Hilbert scales (s-HSP) in the following and we study linear statistical inverse problems for s-HSP on Hilbert scales for a linear, bounded, compact operator $F : H \to H$ and a separable Hilbert space H.

2 Results and discussion

We recall first the definition of Hilbert scales.

Definition 2.1 *Consider an operator $L : D(L) \to H$ unbounded, selfadjoint, strictly positive, $D(L) \subset H$ dense over the separable Hilbert space H. Then, we define the Hilbert space $\mathcal{H}_s := D(L^s)$, $s \geq 0$, $H_0 = H$ with the norm*

$$\langle x, y \rangle_s := \langle L^s x, L^s y \rangle_H, \qquad x, y \in \mathcal{H}_s$$

For $s < 0$ we define $\mathcal{H}_s$ as completion of H under the norm $\|x\|_s :=< x, x >_s^{1/2}$. $(\mathcal{H}_s)_{s \in \mathbf{R}}$ is the Hilbert scale induced by L.

A new class of smo0thness for generalized stochastic processes is introduced in the next definition starting from [3].

Definition 2.2 *Let $(\mathcal{H}_s)_{s\in\mathbf{R}}$ be a Hilbert scale defined as before and $\mathbf{L}^2(\Omega,\mathbf{A},\mathbf{P})$ be the Hilbert space of mean-square integrable random variables on the probability space $(\Omega,\mathbf{A},\mathbf{P})$.*
A random element $\mathcal{X}_s:\mathcal{H}_s\to\mathbf{L}^2(\Omega,\mathbf{A},\mathbf{P})$ is a s-Hilbert space process (s-HSP) if it is linear and continuous in the mean square sense with respect to the $\mathcal{H}_s-$topology for any $s\in\mathbf{R}$.

Definition 2.3 *The minimum Hilbert scale singularity order u (or the maximum Hilbert scale regularity order $-u$) is the minimum Hilbert scale order s for which a Hilbert space process is a s-HSP.*

The existence of an extension of a stochstic process to a $u-HSP$ can be proved.

Lemma 1 *For any $X:\mathbf{M}\to\mathbf{L}^2(\Omega,\mathbf{A},\mathbf{P})$ linear and continuous where $\mathbf{M}=\cap_{k\geq 0}H_k$ dense in H_0 there exists $X_u:H_u\to\mathbf{L}^2(\Omega,\mathbf{A},\mathbf{P})$ a $u-HSP$ version of X.*

We assume that our process has a continuous, linear covariance operator defined implicitely as beneath.

Definition 2.4 *The covariance operator $R_s:\mathcal{H}_s\to\mathcal{H}_{-s}$ of the s-HSP $\mathcal{X}_s$ is defined as $<(R_s\varphi)^*,\Phi>_{\mathcal{X}_s}=\mathbf{E}(\mathcal{X}_s(\varphi)\mathcal{X}_s(\Phi)),\forall\varphi,\Phi\in\mathcal{H}_s$,*

The theoretical results are based on the following spaces of random variables.

Definition 2.5 *The Hilbert space of random variables associated with $\mathcal{X}_s$, $K(\mathcal{X}_s)$ is the closed span with respect to the mean-square norm of the subspace $\{\mathcal{X}_s(\varphi):\varphi\in\mathcal{H}_s\}$ in $\mathbf{L}^2(\Omega,\mathbf{A},\mathbf{P})$.*

Definition 2.6 *The reproducing kernel Hilbert space (RKHS) $\mathcal{K}(\mathcal{X}_s)$ of $\mathcal{X}_s$ is the space of functions $u\in\mathcal{H}_{-s}$ such that for a certain $Y\in K(\mathcal{X}_s)$, $u(\varphi)=\mathbf{E}(Y\mathcal{X}_s(\varphi))\forall\varphi\in\mathcal{H}_s$.*
The inner product is defined as $<u,v>_{\mathcal{K}(\mathcal{X}_s)}=\mathbf{E}YZ$ with Y,Z are the random variables from the definition of $\mathcal{K}(\mathcal{X}_s)$.

Moreover, the existence of an $s-dual$ stochastic process proves to be crucial.

Definition 2.7 *The s-HSP $\mathcal{X}'_s:\mathcal{H}_{-s}\to\mathbf{L}^2(\Omega,\mathbf{A},\mathbf{P})$ is the s-dual of $\mathcal{X}_s$ if*

$$K(\mathcal{X}_s)=K(\mathcal{X}'_s)$$
$$<\mathcal{X}_s(\varphi),\mathcal{X}'_s(\Phi)>_{K(\mathcal{X}_s)}=<\varphi,\Phi'>_{\mathcal{H}_s}$$

$\forall\varphi\in\mathcal{H}_s,\Phi\in\mathcal{H}_{-s}$, Φ' is the dual of Φ in the $\mathcal{H}_s$ topology.
$K(\mathcal{X}'_s)$ is the Hilbert space of associated random variables with $\mathcal{X}'_s$ and $\mathcal{K}(\mathcal{X}'_s)$ is the RKHS of the s-HSP $\mathcal{X}'_s$.

The first theoretical result regarding the characterization of the existence of the an $s-$dual process is based on the Assumption 1: There are $c,C>0$ such that $\forall\varphi\in H$

$$c\|\varphi\|_{-2s}\leq\|R_X\varphi\|_H\leq C\|\varphi\|_{-2s}.$$

Theorem 2.1 *$\mathcal{X}_s$ and $\mathcal{X}'_s$ are s-dual (relative to $\mathcal{H}_s$) and have minimum singularity s iff Assumption 1 holds.*

Our inverse problem in this setting becomes to reconstruct the s-HSP $\mathcal{X}_s : \mathcal{H}_s \to \mathbf{L}^2(\Omega, \mathbf{A}, \mathbf{P})$ from (noisy) values of

$$Y_q^\sigma = F(\mathcal{X}_s) + \sigma W_q$$

$F(\mathcal{X}_s) : \mathcal{H}_q \to \mathbf{L}^2(\Omega, \mathbf{A}, \mathbf{P})$ q-HSP, $F(\mathcal{X}_s)(\varphi) = \mathcal{X}_s(F^*(\varphi)), \forall \varphi \in \mathcal{H}_{-q}$
where $W_q : \mathcal{H}_q \to \mathbf{L}^2(\Omega, \mathbf{A}, \mathbf{P})$ is white noise on $\mathcal{H}_q$ i.e. $R_{W_q} = I_{\mathcal{H}_q}$.
The best linear estimate of $\mathcal{X}_s$ is now given with the help of the linear, continuous operator $S : \mathcal{H}_q \to \mathcal{H}_s$ such that $\hat{\mathcal{X}}_s = SY_q^\sigma$ minimizes the mean square error $E(\varphi; S, \sigma) = \mathbf{E}(| < \mathcal{X}_s - SY_q^\sigma, \varphi >_q |^2) \forall \varphi \in \mathcal{H}_{-q}$
Finally, it holds that

Theorem 2.2 *i)If $\mathcal{X}_s$ and $F(\mathcal{X}_s)$ have order of duality s respectively $q > s$ then there exists a unique solution for the linear statistical inverse problem for s-HSP with exact data $F(\mathcal{X}_s)$ given by $S^*(\Phi) = R_{F(\mathcal{X}_s)} R^*_{\mathcal{X}_s F(\mathcal{X}_s)}(\Phi), \forall \Phi \in \mathcal{H}_{-q}$.*
ii) If $\mathcal{X}_s$ and and the noisy data Y_q^σ have order of duality s respectively $q > s$ then there exists a unique solution for the linear statistical inverse problem for s-HSP with noisy data $S^*(\Phi) = R_{Y_q^\sigma} R^*_{\mathcal{X}_s Y_q^\sigma}(\Phi), \forall \Phi \in \mathcal{H}_{-q}$.
In these cases, the solution is stable w.r.t. the considered Hilbert scales topologies.

3 Conclusions and Future work

We defined and characterized new classes of generalized stochastic processes and characterized the solution of a statistical inverse problem in this framework. The knowledge of the covariance operator is required and it would be a great improvement to overcome this assumption in the future.

Acknowledgments

This work was supported by the M-ERA Net Project SMILE, grant number 315/2022.

References

[1] Franklin J.N., Well-posed stochastic extensions of ill-posed linear problems, Journal of Mathematical Analysis and Applications, **31**(3) (1970), 682–716.

[2] Stuart AM., Inverse problems: A Bayesian perspective, Acta Numerica, **19** (2010), 451–559.

[3] Angulo J. , Ruiz-Medina MarÃa, Estimation and filtering of fractional generalised random fields, Journal of the Australian Mathematical Society, **69** (12) (2000), 336 – 361.

International Conference on Mathematical Analysis and Applications in Science and Engineering ICMA²SC'24

ISEP **Porto-Portugal, June 20 - 22, 2024**

ESSENTIAL SPECTRA OF WEIGHTED AUTOMORPISMS OF THE POLYDISC ALGEBRA

Arkady Kitover[1*] **Mehmet Orhon**[2]

[1] Community College of Philadelphia, USA
[2] University of New Hampshire, USA

[1*] akitover@ccp.edu

[2*] mo@unh.edu

Abstract: We investigate the spectrum and the essential spectra of the weighted automorphisms of the polydisc algebra $\mathbf{A}^n$. In the case $n = 2$ we provide a detailed and, in most cases, complete description of these spectra.

keywords: spectrum, essential spectra, weighted composition operators, polydisc algebra.

MSC2020: 47B33; 47B48; 46B60.

.

1 Introduction

The spectrum of weighted automorphisms of the disc algebra was described by Kamowitz in [1]. In [2] the first named author obtained a full description of the spectrum of weighted automorphisms of unital uniform algebras. The paper [3] contains a description of essential

spectra of weighted automorphisms of $C(K)$. In [4] the authors obtained some general results about the spectrum and essential spectra of weighted isometrical endomorphisms of uniform algebras. The goal of the current paper is to apply the results obtained in [2 - 4] to the problem of describing essential spectra of weighted automorphisms of the polydisc algebra $\mathbf{A}^n$.
While our methods can be applied in the case of any $n \in \mathbf{N}$, we decided to provide as many details as possible in the case $n = 2$. As the reader will see, even in this case the multitude of distinct possibilities is quite large.

The following notations are used throughout the paper.
$\mathbf{N}$ and $\mathbf{Z}$ are the sets of all positive integers and of all integers, respectively.
We denote by $\mathbf{T}, \mathbf{U}$ and $\mathbf{D}$ the unit circle, the open unit disc, and the closed unit disc, respectively.
$\mathbf{A}^n, n \geq 2$, is the polydisc algebra: the algebra of all functions analytic in $\mathbf{U}^n$ and continuous in $\mathbf{D}^n$.
Let $T : X \to X$ be a bounded linear operator on a Banach space X.
$\sigma(T)$ is the spectrum of T.
$\sigma_{a.p.}(T)$ is the approximate point spectrum of T, i.e.
$\sigma_{a.p.}(T) = \{\lambda \in \mathbf{C} : \ \exists x_n \in X, \| x_n \| = 1, Tx_n - \lambda x_n \to 0\}$.
Recall that a continuous linear operator on a Banach space X is called upper semi-Fredholm (respectively, lower semi-Fredholm) if its image $R(T)$ is closed in X and $\dim \ker T < \infty$ (respectively, $\operatorname{codim} R(T) < \infty$).
$\sigma_{usf}(T)$ is the upper semi-Fredholm spectrum of T, i.e.
$\sigma_{usf}(T) = \{\lambda \in \mathbf{C} : \lambda I - T$ is not upper semi-Fredholm$\}$.
$\sigma_{lsf}(T)$ is the lower semi-Fredholm spectrum of T, i.e.
$\sigma_{lsf}(T) = \{\lambda \in \mathbf{C} : \lambda I - T$ is not lower semi-Fredholm$\}$.
$\sigma_{sf}(T) = \sigma_{usf}(T) \cap \sigma_{lsf}(T)$ is the semi-Fredholm spectrum of T.
$\sigma_{f}(T) = \sigma_{usf}(T) \cup \sigma_{lsf}(T)$ is the Fredholm spectrum of T.
$\rho(T)$ is the spectral radius of T.

2 Results and discussion

It is well known (see [5]) that if U is an automorphism of the algebra $\mathbf{A}^2$, then $U = T_\Phi$, where either $\Phi(z_1, z_2) = (\varphi(z_1), \psi(z_2))$, or $\Phi(z_1, z_2) = (\psi(z_2), \varphi(z_1))$, where φ and ψ are Möbius transformations of $\mathbf{U}$. The second case can be reduced to the first one via the spectral mapping theorem for essential spectra (see [6, Corollary 3.61] and therefore we will consider only automorphisms of the first form. Moreover, we will assume without loss of generality that an elliptic Möbius transformation of $\mathbf{U}$ is of the form $\varphi(z) = \alpha z$, where α is not a root of unity.

In the following propositions we will assume for brevity that the weight w is an invertible element of the algebra $\mathbf{A}^2$.

Proposition 1. Let $T = wT_\Phi$, where $\Phi(z_1, z_2) = (\alpha_1 z_1, \alpha_2 z_2)$ and $w \in (\mathbf{A}^2)^{-1}$. Then,
(1) $\sigma_{sf}(T) = \sigma(T) = \{\lambda \in \mathbf{C} : 1/\rho(T^{-1}) \leq |\lambda| \leq \rho(T)\}$.

(2) If we assume that either $\alpha_1^p \alpha_2^q \neq 1, p, q \in \mathbf{Z}$, or $\alpha_1^p = \alpha_2^q$ for some $p, q \in \mathbf{N}$, then

$$\sigma_{sf}(T) = \sigma(T) = w(0,0)\mathbf{T}.$$

Example 1. Let $\alpha \in \mathbf{T}$ be not a root of unity. Let $Tf(z_1, z_2) = (2 + z_1 z_2) f(\alpha z_1, \overline{\alpha} z_2)$, $f \in \mathbf{A}^2$. Then,

$$\sigma_{sf}(T) = \sigma(T) = \{\lambda \in \mathbf{C} : 1 \leq |\lambda| \leq 3\}.$$

Proposition 2. Let $\Phi(z_1, z_2) = (\alpha z_1, \psi(z_2))$, where $\alpha \in \mathbf{T}$ is not a root of unity and ψ is a parabolic Möbius transformation. Let $\zeta \in \mathbf{T}$ be the fixed point of ψ. Let $w \in (\mathbf{A}^2)^{-1}$ and $T = wT_\Phi$. Then,

$$\sigma(T) = \sigma_{sf}(T) = w(0, \zeta)\mathbf{T}.$$

Proposition 3. Let $\Phi(z_1, z_2) = (\varphi(z_1), \psi(z_2))$, where φ and ψ are parabolic Möbius transformations. Let $\xi, \zeta \in \mathbf{T}$ be the fixed points of φ and ψ, respectively. Let $w \in (\mathbf{A}^2)^{-1}$ and $T = wT_\Phi$. Then,

$$\sigma(T) = \sigma_{sf}(T) = w(\xi, \zeta)\mathbf{T}.$$

Proposition 4. Let $\Phi(z_1, z_2) = (\alpha z_1, \psi(z_2))$, where $\alpha \in \mathbf{T}$ is not a root of unity and ψ is a hyperbolic Möbius transformation. Let $\zeta_1, \zeta_2 \in \mathbf{T}$ be the fixed points of ψ. We assume that ζ_1 is the attracting point of ψ. Let $w \in (\mathbf{A}^2)^{-1}$ and $T = wT_\Phi$.

(1) If $|w(0,\zeta_1)| \leq |w(0,\zeta_2)|$, then $\sigma(T) = \sigma_{lsf}(T) = \{\lambda \in \mathbf{C} : |w(0,\zeta_1)| \leq |\lambda| \leq |w(0,\zeta_2)|\}$ and $\sigma_{usf}(T) = w(0,\zeta_1)\mathbf{T} \cup w(0,\zeta_2)\mathbf{T}$.

(2) If $|w(0,\zeta_2)| \leq |w(0,\zeta_1)|$, then $\sigma(T) = \sigma_{usf}(T) = \{\lambda \in \mathbf{C} : |w(0,\zeta_2)| \leq |\lambda| \leq |w(0,\zeta_1)|\}$ and $\sigma_{usf}(T) \supseteq w(0,\zeta_1)\mathbf{T} \cup w(0,\zeta_2)\mathbf{T}$.

Proposition 5. Let $\Phi(z_1, z_2) = (\varphi(z_1), \psi(z_2))$, where φ and ψ are a parabolic and a hyperbolic Möbius transformations, respectively. Let $\xi \in \mathbf{T}$ be the fixed point of φ and let $\zeta_1, \zeta_2 \in \mathbf{T}$ be the fixed points of ψ. We assume that ζ_1 is the attracting point of ψ. Let $w \in (\mathbf{A}^2)^{-1}$ and $T = wT_\Phi$.

(1) If $|w(\xi,\zeta_1)| \leq |w(\xi,\zeta_2)|$, then $\sigma(T) = \sigma_{lsf}(T) = \{\lambda \in \mathbf{C} : |w(\xi,\zeta_1)| \leq |\lambda| \leq |w(\xi,\zeta_2)|\}$ and $\sigma_{usf}(T) = w(\xi,\zeta_1)\mathbf{T} \cup w(\xi,\zeta_2)\mathbf{T}$.

(2) If $|w(\xi,\zeta_2)| \leq |w(\xi,\zeta_1)|$, then $\sigma(T) = \sigma_{usf}(T) = \{\lambda \in \mathbf{C} : |w(\xi,\zeta_2)| \leq |\lambda| \leq |w(\xi,\zeta_1)|\}$ and $\sigma_{usf}(T) \supseteq w(\xi,\zeta_1)\mathbf{T} \cup w(\xi,\zeta_2)\mathbf{T}$.

It remains to look at the case when $\Phi(z_1, z_2) = (\varphi(z_1), \psi(z_2))$ where φ and ψ are hyperbolic Möbius transformations. Let ξ_1, ξ_2 and ζ_1, ζ_2 be the fixed points of φ and ψ, respectively. We assume that ξ_1 and ξ_2 are the attracting points of φ and ψ, respectively. Assume that $w \in (\mathbf{A}^2)^{-1}$. The description of essential spectra of $T = wT_\Phi$ in this case depends on the order of the numbers $|w(\xi_1,\zeta_1)|, |w(\xi_1,\zeta_2)|, |w(\xi_2,\zeta_1)|$ and $|w(\xi_2,\zeta_2)|$ on the real line and therefore there are 24 distinct cases. One of them is considered in our last proposition.

Proposition 6. Let $|w(\xi_1,\zeta_1)| \leq |w(\xi_1,\zeta_2)| \leq |w(\xi_2,\zeta_1)| \leq |w(\xi_2,\zeta_2)|$. Then

$\sigma_{lsf}(T) = \sigma(T) = \{\lambda \in \mathbf{C} : |\, w(\xi_1, \zeta_1)\,| \le |\, \lambda\,| \le |\, w(\xi_2, \zeta_2)\,|\}$ and

$\sigma_{usf}(T) = w(\xi_1, \zeta_1)\mathbf{T} \cup w(\xi_1, \zeta_2)\mathbf{T} \cup w(\xi_2, \zeta_1)\mathbf{T} \cup w(\xi_2, \zeta_2)\mathbf{T}$.

We intend to provide the proofs of the propositions 1 -6 as well as the discussion of the case when the weight w is not invertible in a different publication.

3 Conclusions and Future work

The exact description of the lower semi-Fredholm spectrum of the operators considered in this paper remains elusive. Another, in our opinion, interesting open question is to find an effective formula for the spectral radius of T if the conditions (2) of Proposition 1 are not satisfied.

References

[1] Kamowitz H., The spectra of a class of operators on the disc algebra, Indiana University Mathematics Journal, **27** No 4, (1978), 581 – 610.

[2] Kitover A.K., Spectrum of weighted composition operators: part 1. Weighted composition operators on $C(K)$ and uniform algebras. Positivity, **15** (2011), 639 - 659.

[3] Kitover A.K., Spectrum of Weighted Composition Operators. Part III: Essential Spectra of Some Disjointness Preserving Operators on Banach Lattices. Ordered Structures and Applications: Positivity VII Trends in Mathematics, Springer International Publishing (2016), 233–261.

[4] Kitover A.K., Orhon M., Essential spectra of weighted automorphism of uniform algebras. Submitted to the proceedings of the conference ICMASC'2024, Porto, Portugal, 2024.

[5] Rudin W. Function theory in polydiscs, W. A. BENJAMIN, INC. (1969).

[6] Aiena P., Fredholm and local spectral theory with applications to multipliers, Kluwer Academic Publishers (2004).

International Conference on Mathematical Analysis and Applications in Science and Engineering
ICMA^{2}SC'24
ISEP Porto-Portugal, June 20 - 22, 2024

Scoring system for predicting student failure in maths courses

Ivan Dražić[1⋆] **Vanja Čotić Poturić**[1,2] **Sanja Čandrilić**[2]
Maja Gligora Marković[3]

[1] University of Rijeka, Faculty of Engineering, Croatia
[2] University of Rijeka, Faculty of Informatics and Digital Technologies, Croatia
[3] University of Rijeka, Faculty of Medicine, Croatia

[1⋆]ivan.drazic@uniri.hr

Abstract: Understanding and addressing the factors that contribute to student failure is critical to success and retention in mathematics education. In this study, multiple data sources are examined in depth, including engagement metrics, assessment performance, and demographic variables to identify key indicators of academic difficulty. Using data from the e-learning platform for maths courses at the Faculty of Engineering, University of Rijeka, various correlation methods are employed, with a focus on the use of Cramer's V-measure. This measure forms the basis for the development of a scoring system for predicting student failure. The scoring system is refined weekly, with the threshold for each week determined by retrospective analysis and the predictive quality of failure assessed. Furthermore, the practical implications of these findings for educators are explained and strategies for tailored interventions and personalised support mechanisms are presented. By equipping educators with proactive insights, we aim to enable the early identification and support of at-risk students, fostering a more inclusive and supportive environment for maths learning.

keywords: mathematics education; at-risk students; scoring system.

MSC2020: 97-02; 97-11.

1 Introduction

Mathematics education is a cornerstone of academic development, playing a critical role in various fields ranging from engineering and technology to economics and social sciences. However, a significant number of students struggle with mathematics, leading to high failure rates and subsequent academic challenges. This issue not only affects individual student outcomes but also has broader implications for educational institutions and society at large. To address this pervasive problem, it is crucial to identify students who are at risk of failing math courses early in their academic journey.

The objective of this work is to present a comprehensive scoring system specifically designed to predict student failure in mathematics courses. Our approach is grounded in the analysis of diverse data points encompassing academic performance, behavioral indicators, and demographic information. By leveraging these multifaceted factors, our scoring system aims to provide a nuanced and accurate prediction model.

Academic performance metrics, such as previous grades and test scores, offer insights into a student's historical aptitude and consistency in mathematics. Behavioral indicators, including attendance records and participation in class activities, reveal patterns that may signify a student's engagement and commitment to the subject. Moreover, additional factors such as motivation are considered to understand the broader context influencing a student's learning experience.

The development of this scoring system involved a rigorous process of data collection, statistical analysis, and model validation. The foundation of our scoring system is based on the statistical measure Cramer's V, which quantifies the strength of association between categorical variables. We collected data on academic performance, behavioral indicators, and demographic factors from various educational records. Using Cramer's V, we identified key variables that significantly impact math course success. High Cramer's V values highlighted strong associations, such as between attendance and test scores. These variables were then weighted accordingly in our predictive model. The scoring system was developed through normalization and weighting of these factors, followed by rigorous validation to ensure accuracy and reliability in predicting student failure. The data utilized in this study were extracted from the dedicated e-learning platform tailored for mathematics courses at the Faculty of Engineering, University of Rijeka.

Moreover, we discuss the practical applications of this predictive tool in educational settings. By identifying at-risk students early, educators can implement targeted interventions, such as tutoring, mentoring, and tailored instructional strategies, to mitigate the risk of failure. This proactive approach not only improves individual student outcomes but also enhances overall academic performance and retention rates within institutions.

2 Results and discussion

Based on the analysis using Cramer's V measure, several significant predictors were identified. These include the average math grade from high school, the percentage achieved on the national math exam, and extrinsic motivation - both imposed and externally regulated. Other important predictors are the maximum percentage achieved by the student on tasks identical to those in tutorial exercises, the number of attempts at solving similar tasks, and the maximum percentage achieved on similar tasks in all previous weeks. Additionally, the number of times video lectures were viewed, whether the necessary teaching materials were downloaded for the week, and the percentage of points scored on the first bonus test in the fourth week, the first midterm in the fifth week, the second bonus test in the seventh week, the second midterm in the eleventh week, and the fourth bonus test in the thirteenth week were all significant factors.

For each teaching week, a different scoring system was developed. For example, the system for the 4th week is as follows. If a student had an average high school math grade greater than 3.59, the score for that variable is 11. If the student achieved a percentage greater than 66.34 on the national exam, the score is 10. If the student scored higher than 6.13 on the Academic Motivation Scale survey for the type extrinsic motivation (imposed), the score is 10. For a score higher than 5.63 on the same scale for extrinsic motivation (externally regulated), the score is 12. If the student achieved a maximum percentage greater than 0.61 on tasks identical to those in the exercises, the score is 13. If the number of attempts at solving tasks similar to those in the exercises is greater than 1.5, the score is 10. If the student achieved a maximum percentage greater than 0.67 on tasks similar to those in the exercises, the score is 11. If the number of video lectures viewed is greater than 15.5, the score is 11. If the percentage of points scored on the first test is greater than 0.25, the score is 12. In that week, the threshold score that placed a student at risk of failing the course was 39.

The retrospective analysis of the prediction quality based on this score is given in the following table.

Accuracy	Precision	Sensitivity	PPV	NPV	AUC_ROC	F1 Score
0.88	0.88	0.97	0.88	0.90	0.89	0.92

Table 1: Retrospective Analysis of Prediction Quality Based on the Score

These results indicate a high level of prediction quality based on the scoring system. Metrics suggest that the scoring system effectively identifies students at risk of failure, demonstrating its potential to support early intervention strategies and improve overall academic outcomes.

3 Conclusions and Future work

In conclusion, our scoring system represents a significant advancement in educational predictive analytics, offering a valuable resource for educators aiming to support students in their mathematical pursuits. By providing a reliable mechanism for early identification of students at risk of failing, this tool has the potential to transform educational practices and foster a more supportive learning environment.

In the continuation of the research, a prospective analysis of the score quality will be conducted, and it will be attempted to apply it to various subjects within STEM. Additionally, the e-learning system will be enhanced to extract additional parameters that could serve as quality predictors, and based on these results, the existing score will be improved.

Acknowledgments

All authors of this work are supported by the University of Rijeka, Croatia under the project Development of an information system for early detection of failure among students at STEM subjects (uniri-iskusni-drustv-23-236).

References

[1] Alan Agresti, Categorical Data Analysis, John Wiley & Sons, 2013

[2] Kurt VanLehn, The Relative Effectiveness of Human Tutoring, Intelligent Tutoring Systems, and Other Tutoring Systems. Educational Psychologist, 46(4) (2011), 197-221

[3] Vanja Čotić Poturić, Angela Bašić-Šiško, I. Dražić, Motivation as a Predictor of Student Success in University Maths Courses, INTED2024 Proceedings, (2024), 3844-3850.

International Conference on Mathematical Analysis and Applications in Science and Engineering ICMA²SC'24

ISEP **Porto-Portugal, June 20 - 22, 2024**

Computer Algebra System integrated in Computer-Assisted Assessment with Stack in Fourier Series experience

António Sousa[1] [0000-0003-2015-7980], Luís Afonso[2] [0000-0003-4032-7019], Jorge Mendonça[3] [0000-0002-8359-139X]

[1]*LEMA, ISEP, Polytechnic of Porto, Portugal, ats@isep.ipp.pt*

[2]*ISRC, ISEP, Polytechnic of Porto, Portugal, lma@isep.ipp.pt*

[3]*SIIS, ISEP, Polytechnic of Porto, Portugal, jpm@isep.ipp.pt*

Abstract

Computer-assisted assessment (CAA) tools, such as the Moodle plugin STACK, based on the Maxima Computer Algebra System (CAS), offer the ability to create questions with varying levels of complexity and provide students with immediate feedback. This approach addresses the persistent challenge of complex topics in higher education courses by integrating CAS into CAA, enabling the provision of necessary tools to students in alignment with the curricular unit's syllabus.

STACK facilitates the creation of complex question parametrized models and their subdivision into simpler sub-problems, which are then dynamically evaluated using decision trees. However, the process of designing and developing these question models demands technical skills from instructors. CAS can assist students in solving complex problems more efficiently, while also enabling teachers quickly assess student resolutions.

By automating and uniformizing the grading process, STACK can significantly reduce instructor's workload, allowing them to focus more on teaching and student interaction, thereby enhancing assessment objectivity. This is particularly beneficial in large classes where manual grading would be impractical and time-consuming. The initial application of this procedure was in the context of the mathematical topic of Fourier series, conducted in a laboratory environment using Python for individual and group problem-solving.

The integration of CAS into STACK based CAA enables the elaboration of complex questions by connecting multiple topics within a theme. This allows students to submit answers obtained from various symbolic calculation platforms without increasing the difficulty of obtaining the answer, thereby optimizing the evaluation process. By leveraging the capabilities of CAS and CAA, instructors can create engaging and challenging assessments that provide students with immediate feedback and support their learning process.

keywords: STACK; Computer Algebra System; Computer-Assisted Assessment; Fourier Series; Feedback

MSC2020: 42A16 ; 49-XX; 34-XX; 92-XX.

1 Introduction

The integration of Computer Algebra Systems (CAS) and Computer-Assisted Assessment (CAA) has increasingly influenced educational approaches to mathematical problem-solving and assessment [1]. CAS, such as Mathematica, Maple, MATLAB, and Python's SymPy, are powerful tools capable of symbolic computation, including the manipulation of mathematical expressions, solving equations, and performing algebraic operations. These capabilities make CAS useful in both educational and research settings by enabling the visualization of mathematical concepts and the automation of high-level calculations.

CAA systems make use of computer technology to design, deliver, and evaluate assessments. They can automatically grade objective questions and provide instant feedback. Advanced features of CAA include adaptive testing, where question difficulty adjusts based on the student's performance, and the ability to randomize question order to maintain assessment integrity. Automated grading saves educators time, while instant feedback and performance analytics help tailor educational experiences to individual needs.

The STACK stands for System for Teaching and Assessment using a Computer algebra Kernel) is a popular tool integrating CAS and CAA working under Moodle platform [2]. STACK leverages CAS to provide dynamic and individualized assessment of students' mathematical understanding. It enables detailed and controlled feedback through a process where student responses are evaluated by comparison with expected answers using the Maxima CAS tool. This system supports both formative and summative assessments and offers feedback based on Potential Response Trees (PRTs), which can consider answers to previous questions for a more precise evaluation [3]. The use of STACK has the potential to enhance the learning process by providing immediate, specific feedback, and facilitating complex problem-solving. However, integrating CAS and CAA also presents difficulties requiring specialized training for instructors in design and development (Coding) of STACK models to explore STACK potential [4]. Students also need training to input computational formulations equivalent to traditional mathematical expressions of intended answers (Figure 1).

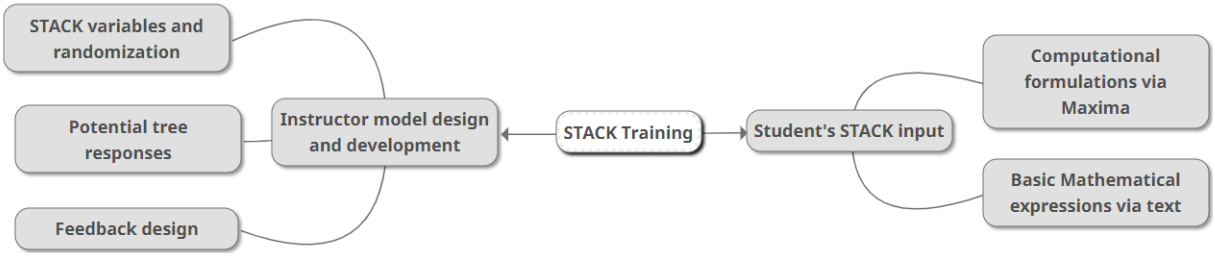

Fig 1. STACK training requirements.

In this work, we present the outline of a STACK experience concerning Fourier Series conducted in the "Mathematical Laboratories" course during the second semester of the first year of the Electrical Engineering degree in the academic year 2024.

2 Results and discussion

Students studied the Fourier Series using the SymPy CAS Python library. The instruction process and assessment model are shown in Figure 2. Two formative sessions covered Python and SymPy basics, followed by SymPy Python notebook-based lectures on Fourier Series concepts. A demonstration of STACK was sufficient because Maxima CAS input is similar to SymPy's.

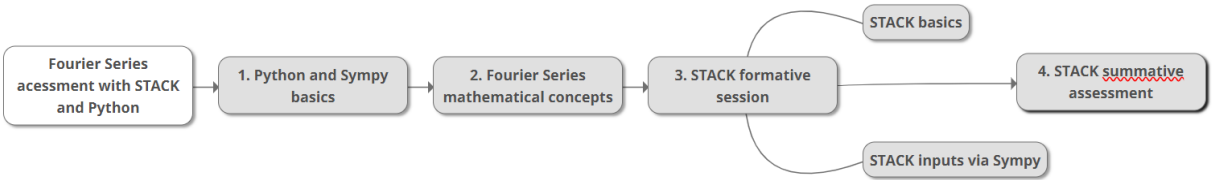

Fig 2. Fourier Series instruction and assessment process.

Students entered their solutions into the STACK system using Python expressions. The STACK formative sessions lasted two weeks, with additional offline sessions via Moodle. Finally, a summative assessment using CAA tools was conducted. Two STACK PRT codes are presented in Figure 3. Figure 3a shows a PRT used for controlled feedback and grading of two dependent questions. Figure 3b depicts an example of a PRT grading and feedback for an independent question. The PRT allows the customization of the feedback at each step. The corresponding STACK test fragment is depicted in Figure 4.

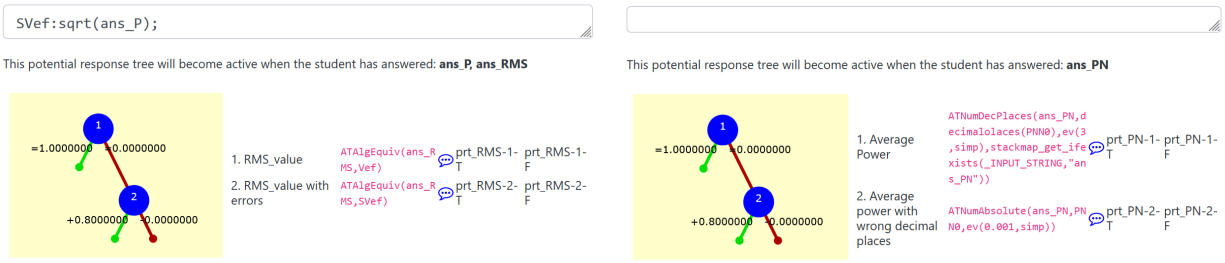

Fig 3. PRT Feedback and grading design: (a) two dependent questions; (b) one independent question.

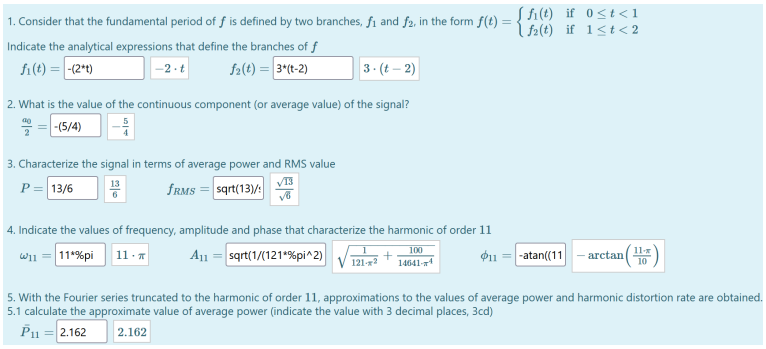

Fig 4. STACK test fragment with teacher answers (TA).

The results using STACK were consistent with previous course editions that used traditional assessment methods. While the workload for instructors increased in developing STACK models, this was offset by a significant decrease in evaluation work.

3 Conclusions and Future work

The assessment results of the course using STACK were promising, significantly reducing instructors' workload without compromising grading precision. However, developing model problems with strong discriminatory power and providing constructive feedback remains challenging. STACK developers would greatly benefit from systematizing the construction of model problems, which warrants further research.

References

[1] Engelbrecht, J., & Borba, M. C. (2023). Recent developments in using digital technology in mathematics education. *ZDM–Mathematics Education*, 1-12.

[2] Sangwin, C. (2013). *Computer aided assessment of mathematics*. OUP Oxford.

[3] Sangwin, C. (2015, July). Computer aided assessment of mathematics using STACK. In *Selected regular lectures from the 12th international congress on mathematical education* (pp. 695-713). Cham: Springer International Publishing.

[4] Exercises Using JSXGraph for Online Course: Exploring Strategies for Supporting Students with Mathematical Challenges. In *Proceedings of the 16th International Conference on Computer Supported Education-Volume 2: CSEDU*. SCITEPRESS Science And Technology Publications.

International Conference on Mathematical Analysis and Applications in Science and Engineering
ICMA^{2}SC'24
ISEP Porto-Portugal, June 20 - 22, 2024

Implementation of Moodle Stack Questions on Numerical Methods Course in an Engineering Degree

António Sousa[1⋆] **Ana Júlia Viamonte**[1]

[1] LEMA, ISEP, Polythecnic of Porto, Porto, Portugal

[1⋆]ats@isep.ipp.pt

Abstract: The integration of Stack questions in Moodle offers an innovative approach for higher education assessment. It effectively tests students' knowledge, promoting critical thinking, problem-solving, and the practical application of learned concepts. The strong characteristics of Stack questions are their ability to generate a wide variety of questions based on a set of parameters defined by the teacher, and their capability to handle different answer types. Stack questions have the ability to integrate with Computer Algebra Systems (CAS), such as Maxima. This integration enables them to process complex mathematical expressions and provide detailed step-by-step solutions. Another important benefit is that when students answer questions, the system can provide feedback, pointing whether the answer is correct or incorrect, and in some cases, offer detailed explanations to help them understand where they went wrong. Furthermore, Stack questions in Moodle provide the opportunity to assess skills beyond simple mathematical calculations. For example, students can be evaluated based on whether they present the exact result, the result with the correct number of decimal places, or the result with the correct number of significant figures. In this study, we share an experience from a numerical methods course in an engineering degree program. The assessment included two tests, each with two parts: one with closed-response questions, and another with open-response questions, including two Stack questions and one closed-ended question. Upon completion, students were surveyed to gauge their perceptions of Stack questions compared to other question types. This paper detail the experience and the results obtained.

keywords: STACK; CAA; Maxima.

MSC2020: 49-XX; 34-XX; 92-XX.

1 Introduction

Computer-assisted assessment (CAA), like Moodle, offers several advantages that teachers can use to streamline the assessment process for their students, both during formative and summative evaluation phases. The question types provided by these tools cover a wide range of options and allow for varying levels of assessment depth [1]. Teachers can choose between closed or open questions, although the latter are often avoided by teachers due to the need for careful question design to enable automatic grading. Two special question types within this context are Cloze and STACK questions [2], which enable more sophisticated student assessment. While Cloze questions rely on predetermined answers for automatic grading, STACK questions can pre-process student responses and compare them to the expected Teacher Answer (TA) at different levels of correctness, allowing for more nuanced scoring, particularly in mathmatics where answers can

take multiple correct forms. An additional benefit of this system is its capability to re-evaluate subsequent questions that are contingent on the response to a preceding question. Consequently, in case a student submits an incorrect answer, their dependent responses can be reviewed.

Potential Response Tree (PRT) is a STACK tool enabling detailed marking of Student Answers (SA). PRTs are decision trees representing possible response paths, allowing granular SA analysis. They enable the assignment of partial credit based on correct intermediate steps and the re-evaluation of subsequent questions that depend on the response to a previous question. In this way, PRTs are essential for leveraging STACK's advanced assessment features, especially in areas like Numerical Analysis, which permit diverse correct answer formats.

In this work, we will explore some aspects of STACK questions related to partial question correction and the re-evaluation of responses to dependent questions. Specifically, we will delve into the implementation of the PRT to achieve a fine-grained assessment of answers in the field of Numerical Analysis.

2 Results and discussion

The process of assessment began with the creation of a test consisting of two parts: the *first part* included open-ended answers, while the *second part* contained closed-ended answers. In the *first part*, there were two STACK-type questions: one related to general error handling in numerical calculations with error-affected data, and the other related to root finding in non-linear equations, using the bisection method and Newton's method. This parte of asseessment concluded with a Cloze question focusing on solving systems of linear equations. The *second part* with multiple-choice questions focused on more theoretical aspects.

When developing the STACK questions, care was taken to solve fully parameterized model problems using the Python library Sympy, as it is the adopted CAS in the course. The results were compared with an alternative solution provided by the CAS Maxima. This step was necessary since Maxima is the tool implemented in STACK, ensuring consistency in the outcomes. In Listing 1, we present a sketch with the main steps of the implementation for one of these questions, along with comments that guided its development in both Python and Maxima.

Listing 1: Steps of implementation coded in STACK Question variables field.

```
% 1. Select an instance of random parameters a, b, c, n
[...]
% 2. Equation and auxiliary function, f(x)=(x - a) - exp(-b*(x-a)
[...]
% 3. RESOLUTION
%  a) Graphical location of the root near to a: I=[a-2c, a+3c]
%      Find limits of I, amplitude and perform Bolzano test,...
[...]
%      TA_a: [Il,Ir,ampl,test,...];
%  b) Bisection method based on a suggested initial interval, I
%      Find minimum number of iterations, final I, rounded solution,...
[...]
%      TA_b: [nmi,Ikl,Ikr,xkb,...];
%  c) Newton method
%      Initial parameters and perform k iterations of Newton method
%      Calculation of nsf, ndp, rounded solution,...
[...]
%      TA_c: [k,nsf,ndp,kxn,...];
```

In Figure 1, the corresponding question text of an instance is shown. This question includes various sub-questions, allowing for a more detailed assessment of the topics. The TA of these sub-questions were partially calculated by Maxima during the generation of this instance.

In Figure 2, the PRT for Question 1 of Figure 1 is presented. It includes the necessary Maxima code for evaluating the SA. Reevaluation takes place when the student's response differs from the TA at node 1 or when different scoring levels are assigned (nodes 2 and 3), based on the quality of the SA. Furthermore, the PRT provides comments for each evaluation node and offers appropriate feedback to the student.

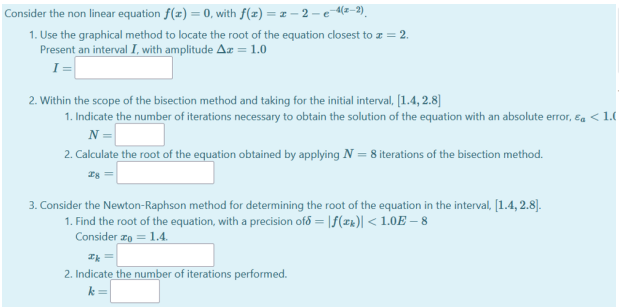

Figure 1: A instance of Question text

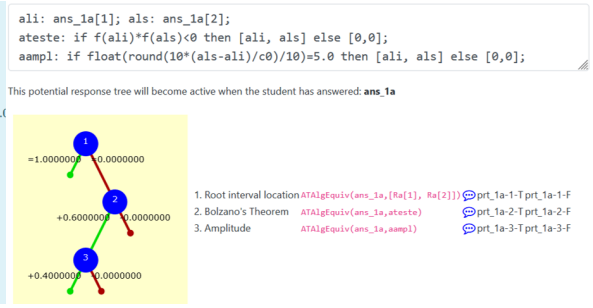

Figure 2: Feedback based on PRT.

A survey was made available to students on Moodle and was anonymous. Forty percent of the students responded to the survey, of which the majority, 90%, were taking the course for the first time, and the remainder had enrolled three or more times. Among those who completed the survey, a preference emerged for including both types of questions in assessments. However, closed-ended questions were favored over open-ended ones. They did not notice a difference between Cloze and STACK questions and within the closed-ended questions, they preferred multiple-choice questions over fill-in-the-blank questions.

3 Conclusions and Future work

This study explores the application of Moodle STACK tool in evaluating the students of a Numerical Methods course within an engineering degree at ISEP. The experience illustrate the feasibility of automating the grading process for typical summative assessment questions, utilizing the automatic assessment tool, STACK, to facilitate open-ended inquiries. The survey results suggest that when an appropriate formalism is adopted for STACK type questions, they do not significantly differ from other open-ended question types in Moodle, such as Cloze questions. An additional insight from the survey reveals a student preference for closed-ended questions over open-ended ones. The authors advocate for a balanced use of closed and open-ended questions in summative assessments to ensure a more holistic assessment of the knowledge that students have acquired.

References

[1] Sangwin, C. *Computer Aided Assessment of Mathematics Using STACK*. In: Cho, S. (eds) Selected Regular Lectures from the 12th International Congress on Mathematical Education. Springer, Cham. (2015) https://doi.org/10.1007/978-3-319-17187-6_39

[2] Moodle Docs. *Question types*. Available: https://docs.moodle.org/400/en/Question_types. Accessed on May 8, 2024

International Conference on Mathematical Analysis and Applications in Science and Engineering ICMA²SC'24

ISEP **Porto-Portugal, June 20 - 22, 2024**

Fractional Operators, Topos and Grothendieck Schemes: Outline about a Sheaf Approach of the "Arrow of Time".

Alain Le Méhauté[1], Alina Gavrilut[2] et Dmitrii Tayurskii[3]

(1) Materials Design SARL and Inc, 42 Avenue Verdier, 92120 Montrouge France
(2) Mathematical Department, IASI Cusa University, Carol avenue 18, 700506 Iasi, Romania
(3) Kazan Federal University, Kremlevskaia avenue 18, 420008 Kazan Tatarstan.

[1*]alm@materialsdesign.com

Abstract: The purpose of this note is to show why and how the fractional operators required for formalizing dynamic issues in complex environment, mobilize among the most advanced mathematical concepts : topos, site, spectrum, sheaf, ringed spaces, p-adic numbers, etc. In the context of physical exchanges in spaces crumpled by long range interaction (hyperbolic geometries), geodesics no longer respond to Noether invariance principles but to memory effects and to the categorical limits imposed by some requirements for completion. This completion is in fine based upon algebra-topology coupling. This coupling may be expressed through the zeta function which, as a bridge, ensures the formal closure of the representation and implicitly the space-time relationship. The analysis points out the existence of a particular case corresponding to the Riemann hypothesis (Martin's axiom). Above approach involves a new viewpoint upon quantum mechanics. In all other cases, time is discretized and an arrow of time naturally emerges from the analysis. The note relates this arrow to anti entropic properties of dissipative complex systems.

.

keywords: a-Operators; Topos, Time;

1 Introduction

There is an irreducible link between the zeta function, fractional operators, fractal geometries (1) and beyond that the classifying Grothendieck topos (2). To show this, the approach supports the construction of ring sheaves (3) associated with transfer functions Z_α of the Cole and Cole type (4) process associated with α-non-integer differential equations. We know that such functions are constrained by a constant phase angle $\varphi(\alpha)$ and that, except in special cases (α=1/2 Riemann hypothesis) inverse Fourier transformation does not exist. Therefore, dynamics cannot use the standard time variable. We called α-exponential such a site of analysis because its representation is an arc of a circle shored up by a 1/2 arc of a circle which represents the standard transfer function of an exponential law in the complex plane $\mathbb{C}$. It trivially results from this representation the existence of a geometric completion arc denoted $Z_{1-\alpha}$.

2 Results and discussion

The particular status of such arcs in $\mathbb{C}$ as parameterized via an inversion of a straight line and here featured by gaps at the origins, makes it possible to associate Z_α with the ring $\mathbb{Z}$ and a stratified structure ${}^nZ_{1-\alpha}$ based on the spectrum of $\mathbb{Z}$ (3). This spectrum makes it possible to identify the existence of local rings built on overlaps of topological opens responding to an order of inclusion (5) and ultimately leading to the parameterization of $Z_{1-\alpha}$ not in $\mathbb{R}$ as the inverse Fourier transformation would suppose, but in the field of p-adic numbers $\mathbb{Q}_p$ (6) The notion of time then splits into a set of distinct time constants. The foliation attached to ${}^nZ_{1-\alpha}$ responds to Algebra Z_α/Topology(${}^nZ_{1-\alpha}$) duality (5) formally explained in the arithmetic coupling between Z_a and ${}^nZ_{1-a}$. We are thus led to the design of a topos $Z_\alpha \oplus Z_{1-\alpha}$, which, among other conceivable topos, conceals nevertheless two classes of dynamic distinct morphisms whose coupling is based for both on the algebraic relation related to scales: $\eta.(in)^\alpha = 1^\alpha$ (4) with scale η (space of quantity) and n (quantity of space) (7) equation leading two dynamical renormalizations. This generic bi category opens the way to the role of the zeta function (8) because ${}^nZ_{1-\alpha}$, is not only a ringed vector space but a Grothendieck scheme featured by points almost certainly open at boundary (5).

Parameterized using prime numbers, the highly entangled geometry associated to the topos questions the physicist who does not , a priori, imagines any empiricism in the status of ${}^nZ_{1-\alpha}$. Indeed the entropy of the process associated with the transfer function seems entirely concentrated in the "concrete" part of the process. However, this is an illusion because this a priori only objective part, depends on the mode of representation. When referred to the toposic overall exponential, the representation makes it possible to separate the correlations due (i) to the irreversible nature of the physical process from those (ii) due to the here self-similar geometry associated with the renormalization constraints and with the p-adic structures of the dynamic correlations, therefore of an entropic component of geometric origin (9). In this particular dynamic context, it is important to distinguish the renormalization of scales and the renormalization of spectral energy (7). The zeta function $\zeta_\alpha(s)$ appears to be the most natural fiber functor capable of guaranteeing the classifying character of the topos, in particular through the functional relationship which leads it. The parameter "$i\theta$" formalizes a canonical fibration "f_θ" which, through the parameter $s=\alpha \pm i\theta$, gives rise to $\zeta_\alpha(s)$ foliated ring structure pinning "η" over Z_α in a manner distinct or not from what the set derivation ∂_n can do from the fundamental law of arithmetic, to obtain the foliation of ${}^nZ_{1-\alpha}$, (1). In the categorical framework both stratified structures can be compared using the Kan extension functor, namely via the commutativity of the respective fibrations process $[f_\theta \circ \partial_n - \partial_n \circ f_\theta]$. This mathematical commutator is only zero if $\alpha = 1/2$. This conclusion leads two classes of consequences (3) :

1. Noether's principles and the resulting mechanical invariants are only valid in the hypothesis which reduces the self-similarity conditions to the arithmetic constraints given by $\mathbb{N} = \mathbb{N} \times \mathbb{N}$, i.e. $\alpha = 1/2$. The compact diffusion processes, therefore the Schrodinger equations, are the only discretized, closed processes in $\mathbb{C}$ matching the fundamental law of algebra in space-time and scale-frequency jointly (8). The underlying 2D fractal geometry is a pure Peano space ($d = 1/\alpha = 2$) . The archetypal example of this type of Euclidean topos is given by the space of Quantum Mechanical States (no tensor coupling between states). The phase angle is an integer divisor of the module. The transfer function has an inverse Fourier transformation. This conclusion is easily expressed by means of the functional relation relating to the zeta function $\zeta_\alpha(s)) = F[\zeta_{1-\alpha}(1-s)]$ which here ensures the interoperability (2). of $Z_{1/2}$ and ${}^nZ_{1/2}$
2. In the hypothesis where the Kan commutator is not zero $\alpha \neq (1 - \alpha)$ then $\pm \theta_\alpha \neq \mp \theta_{1-\alpha}$ The function F which implicitly assumes that the commutator is zero, must be revisited in the frame of categorical approach. The re-examination can be carried out by changing the physical and geometric reference background, by writing $+\beta = \alpha - 1/2$, therefore $-\beta = 1/2 - \alpha$. β is obviously zero for $\alpha = 1/2$ but it is not in the general case. White noise and chance become the standard.

Therefore, if we assume that "θ" is the variable associated with a "universal" clock time in our issue, we demonstrate that the existence of $\beta \neq 0$ entering dynamic categories associated with multi-scale constraints leads Z_α and ${}^{\theta}Z_{1-\alpha}$, obtained via $\zeta_{1-\alpha}(1\text{-}s)$ to be non-adjunct categories justifying the role of the topos as a dissymmetrical bridge (2) herein giving birth to the existence of an arrow of time (11). The role of the classifying topos becomes fundamental (2) and the classification then involves a clear distinction between both complementary zeta functions $\zeta_\alpha(s)$ and $\zeta_{1-\alpha}(s)$. Geometry loses its atomicity (10) but keep fractality by introducing in particular a thickening of the present certainly oriented towards the anterior but also towards the future through the open at the edge of the Grothendieck scheme. We demonstrate that the two classes of renormalization relating to the external clock (quantity of space n) and internal clock (space of quantity η) (7) then not fully interoperable due to the phase angle $\varphi(\alpha)$, formalizes this thickness, by bringing out a valid monadic distinction especially at categorical limits. Analytical approach (concrete entropic process) and the synthetic approach (anti-entropic completion functor) must be distinguished. Duality leads to a flat functor according to a creative rationality based over an intuitionist logic (8).

3 Conclusions and Future work

It is known that non-integer integro-differentiation operators naturally lead to a thickening of local properties. The categorical approach proposed by the authors leads to understand the monadic aspect of this width and the importance of the distinction that must be made between the notions of co-limit (analytical approach) and limit (projective approach) associated with k-algebras in any space characterized by scaling properties led by "k". Certainly, in the simplest cases of arithmetic self-similarity the two notions are in simple interoperative duality ($\alpha=1/2 \sim \mathbb{N} = \mathbb{N} \times \mathbb{N}$) and the final object and also an initial object (Euclidean Topos. Standard cohomology (12) Quantum Mechanics Riemann Hypothesis, probability normalization). However, in the cases of dual self-similarities, α and $\alpha_{ref} = 1/2$, with $\alpha \neq 1/2$, the dualities concerned require the use of a non-commutative square scheme of which the direct and inverse zeta functions leave open sets at (coupled punctuated two holes torus) whose role is fundamental for the overall coherence of issue. It is these open sets that give birth to the arrow of time. The dynamical topos then in fine physically relevant, namely $\zeta_\alpha(s) \oplus {}^{-\theta}Z_{1-\alpha}$ builds a bridge between the two non-interoperable categories which are ${}^{n}Z_{1-\alpha}$ on the one hand and ${}^{-\theta}Z_{1-\alpha}$ fibered by a negative standard time that is to say, between a dissipative dynamic and the stratified anti-entropic component of geometric completion. The square scheme allows us to find a logic which, even intuitively, allows us to access rationality despite the complexity and of entanglement of multi-causal fibers. We assume that any creative process relies explicitly or implicitly on this toposic approach. Although this is only a first sketch (3) requiring further work developed by mathematicians (13), we can observe here how a practical problem (4) was able to give birth to a heuristic raised from engineering questions (control of chaos in automatic, optimization of batteries in electrochemistry, damping or reconstruction of waves in heterogeneous wires or environments, etc.).

In memoriam

This work is dedicated to the memory of my friends, ***Michel Mendes France*** who carries so gripping works on iteratives systems and primes numbers and ***Jose Tenreiro Machado***, who was one of the active promoters of the school of fractional operators for engineering. Among the first, he understood the irreducible link that exists between this class of operators and the notion of entropy. For all this our community owes him a lot of gratitude.

References

(1) P. Riot,, A. Le Méhauté, D. Tayurskii, *Fractional Dynamics, Riemann Zeta Function and Self Similarity through Category Theory*, in Advances in "Special Functions and Analysis of Differential Equations" (Chapter 14) Agarwal Praveen, Agarwal Ravi P., Ruzhansky M. Editors. CRC Press Deleware, 2019

(2) Caramelo Olivia : *Theories, Sites, Toposes : Relating and Studying Mathematical Theories Through Topos-Theoretic* bridges, Oxford University Press Oxford ,2017. (see for instance www.bing.com/videos/riverview/relatedvideo?&q=olivia+caramelo+&&mid=713FD860D4ECE6D264F4713FD860D4ECE6D264F4&&FORM=VRDGAR)

(3) Le Méhauté Alain, Gavrilut Alina and Taryurskii Dmitrii, *Fractional Operator Topos and Grothendieck schemes for creativity management*. Bucarest Roumania Hyperion International journal of Econophysics and modern economy (2023) to be published

(4) Le Méhauté Alain *Transfer process in fractal*, J. Stat. Phys. 36 (1984) 665-670

(5) Valence Arnaud, *Montrer et démontrer : la dualité d' Isbell ou les voies à doubles sens des raisonnements scientifiques*, Paris, Edition de la Sorbonne, 2019.

(6) Colmez Pierre, *Représentations de $GL_2(Q_p)$ et (j, G)-modules*, 216 pages, To be published in Astérisque, http ://people.math.jussieu.fr/ colmez/publications.html.

(7) Lawvere William, *Categories of space and quantity , the space of mathematics,* Eds Javier Echeveria, Andoni Ibassa, Thomas Marmam, "The space of mathematics" de Gruyter (2012) 14-35

(8) Berry Michael and Keating Jonathan, *The Riemann Zeros and Eigenvalue Asymptotics* , SIAM Review, 1999 (41), 236-266.

(9) Baudot P and Bennequin D, *The homological nature of entropy*, 17 (2015) 3253-3318

(10) Gavrilut, Alina. Merches, Ioan. And Agop, M. : *Atomicity through fractal measure theory*, Zurich, Springer, 2019

(11) Coveney Peter and Highfield Roger, *The arrow of time* (Introduced by I. Prigogine) New York, Fawcett Colombine ,1992.

(12) Baudot P and Bennequin D, *The homological nature of entropy*, 17 (2015) 3253-3318

(13) Leinster Thom, arXiv:2012.02113V3[q-bioPE]22 oct 2022.

[

International Conference on Mathematical Analysis and Applications in Science and Engineering
ICMA^{2}SC'24
ISEP Porto-Portugal, June 20 - 22, 2024

Study of non-smooth solutions for fourth order multi-term fractional reaction-diffusion equation

Reetika Chawla[1⋆] **Devendra Kumar**[1]

[1] Department of Mathematics, Birla Institute of Technology and Science, Pilani, Rajasthan, India

[1⋆] reetika.chawla285@gmail.com

Abstract: This work presents the numerical analysis of non-smooth solutions for the multi-term time-fractional fourth-order reaction-diffusion equation using the Caputo derivative. The non-smooth solutions have a weak singularity near $t = 0$ that can be effectively handled by non-uniform mesh. Therefore, the graded mesh with optimal grading parameters is used to evaluate the numerical solution to regain accuracy. Moreover, the trigonometric quintic B-spline approach is used to solve this problem. Through rigorous analysis, we proved the unconditional stability and convergence of the numerical scheme. Numerical experiments are broadly discussed through tabulated results and plots that manifest the uniform and non-uniform mesh comparison and validate our theoretical findings. Moreover, we observed that the results obtained by utilizing non-uniform mesh for solving the problem with non-smooth solutions are more efficient and accurate than those obtained through uniform mesh.

keywords: Caputo derivative; Multi-term time-fractional; fourth order reaction diffusion equation; Trigonometric quintic B-spline; Stability and convergence; Graded mesh

MSC2020: 35R11, 65D07, 35B65, 35G10, 65M12.

International Conference on Mathematical Analysis and Applications in Science and Engineering
ICMA^{2}SC'24
ISEP Porto-Portugal, June 20 - 22, 2024

What is a fractional derivative? – a constructive approach

Manuel D. Ortigueira*

NOVA School of Science and Technology, UNINOVA-CTS and LASI,
NOVA University of Lisbon, Portugal

*mdo@fct.unl.pt

Abstract: The construction of fractional derivatives from order one versions is described. This is done in a few steps, the more important being the eigendecomposition of the derivative.

keywords: Fractional derivative; Generalized Laplace transform; Transfer function.

MSC2020: 26A33; 93C55.

1 Introduction

The first formal introduction of the concept of fractional derivative (FD) by Liouville (1832) gave rise to the main definitions we find today, mainly the Riemann–Liouville [9], (Dzherbashian)-Caputo [2], and Grünwald-Letnikov [9] definitions. However, and based on these derivatives, new ones have been proposed alongside these, such as Hadamard's [2] or Marchaud's [9]. The success of the "fractional derivative" designation motivated and originated proposals of "new fractional derivatives". In the last 20 years, many modifications or combinations of the above derivatives have been introduced, along with other operators claiming to be "fractional derivatives". Some are mere linear systems and others are disguised order 1 derivatives. If we also consider the pseudo-derivatives, we conclude that the situation is really confused and confusing as shown by Teodoro et al., [11], that listed such operators and introduced a classification according to some specified criteria. Since 2015, a great discussion took place in forums, conferences and articles, where we verify that most people is unaware of the distinction between the concepts of system and derivative. This situation was the main reason for the attempt, described in [6], to give a methodology for testing whether a given operator is suitable to be a fractional derivative. Such a goal was continued with the formalizations introduced in [7, 12]. However, new generalized attempts appeared recently having as base the Abel's algorithm for the tautochrone problem. This was done first by Kochubei [3], and after, by Luchko [4], and Tarasov [10]. Hanyga [1] used Abel's approach in the discussion of the concept of fractional derivative. However, it is important to note that these developments only deal with shift-invariant operators in continuous-time, without considering scale-invariant and discrete-time operators.
Here, we consider a very general approach valid for functions defined on any time scale: continuous, discrete, mixed, fractal, and son on.

2 Framework for fractionalizing derivatives

We are going to present the steps required to define fractional derivatives. In particular, we will compute their transfer function and, from it, the impulse response, $g(t)$. Let $\mathbb{T}$ denote any non-empty closed subset of $\mathbb{R}$ that is called time scale or time sequence. The steps are:

1. In $\mathbb{T}$, we define an operator $\mathcal{D}_f$ which we will generically call *derivative* and which is basically an incremental ratio. We can consider three types: nabla (causal), delta (anti-causal) and theta (bilateral). We will described the nabla case.

2. Define the impulse distribution by

$$\delta_f(t) = D_f u(t). \tag{1}$$

   In the usual domain ($\mathbb{R}$) with the classic derivative, $\delta_f(t)$ coincides with the Dirac impulse.

3. For such a derivative, compute the pair eigenfunction/eigenvalue from

$$\mathcal{D}_f e_f(t,s) = s\ e_f(t,s), \tag{2}$$

   where $t \in \mathbb{T}$ and $s \in \mathbb{C}$. The eigenfunction $e_f(t,s)$ will be called *generalized exponential*.

4. Define the corresponding fractional derivative, $\mathcal{D}_f^\alpha$, through

$$\mathcal{D}_f^\alpha e_f(t,s) = s^\alpha\ e_f(t,s), \tag{3}$$

   where $\alpha \in \mathbb{R}$ is the derivative order. The elemental system characterized by $H(s) = s^\alpha$ with a suitable region of convergence is called *differintegrator*.

5. With the generalized exponential, above introduced, define a (generalized Laplace) transform,

$$X(s) = \mathcal{L}_f\left[x(t)\right],$$

   so that

   - Any function, $x(t)$, can be expressed in terms of the eigenfunction (synthesis equation) by

$$x(t) = \mathcal{L}_f^{-1} X(s) = \frac{1}{2\pi j}\int_\gamma X(s) e_f(t,s)\mathrm{d}s, \tag{4}$$

     where γ is in general a closed simple integration path in a region of the complex plane where $X(s)$ is analytic. It may happen we have to make an adjustment in (4) so that

$$\mathcal{L}_f\left[\delta_f(t)\right] = 1,$$

     in the whole complex plane.
   - From (4) and using (3), the classic relation

$$\mathcal{L}_D\left[\mathcal{D}^\alpha x(t)\right] = s^\alpha X_D(s) \tag{5}$$

     emerges and is valid in a suitable ROC.
   - From (5), we conclude that the fractional derivative is defined by

$$D_f^\alpha\left[g(t) * x(t)\right] = D_f^\alpha g(t) * x(t) = g(t) * D_f^\alpha x(t). \tag{6}$$

   - The analysis equation (direct transform) is defined, for each case, in agreement with the properties of the eigenfunction.

The above definition of fractional derivative, *an elemental system having TF equal to* $H(s) = s^\alpha$, brings some properties that are fundamental in applications and are easily deduced from (4):

1. Associativity of the orders
$$\mathcal{D}_f^\alpha \mathcal{D}_f^\beta x(t) = \mathcal{D}_f^{\alpha+\beta} x(t); \tag{7}$$
This relationship ensures that a given system can be implemented using different structures.

2. Identity
$$\mathcal{D}_f^0 x(t) = x(t); \tag{8}$$

3. Inverse (anti-derivative)
$$\mathcal{D}_f^\alpha \mathcal{D}_f^{-\alpha} x(t) = \mathcal{D}_f^{-\alpha} \mathcal{D}_f^\alpha x(t) = x(t). \tag{9}$$
This result establishes a fundamental difference between anti-derivative and primitive.

These properties, together with the generalized Leibniz rule, constitute a criterion for deciding if a given elemental system can be considered as a fractional derivative [6]. However, in most applications, such a relation does not have any special role..

Example 1 *We will study the discrete-time Euler fractional causal derivative. We will assume that our domain is the discrete-time (DT) sequence* $\mathbb{T} = h\mathbb{Z}$. *The positive real parameter,* h, *is the graininess or sampling interval of the time sequence.*
Set $t = nh$. *We define the nabla derivative by:*
$$D_\nabla f(t) = \frac{f(t) - f(t-h)}{h} \tag{10}$$
Therefore, taking this derivative we deduce immediately:

1. *The nabla exponential is sgiven by*
$$e_\nabla(nh, s) = (1 - sh)^{-n}, \quad n \in \mathbb{Z}, s \in \mathbb{C}, \tag{11}$$

2. *We define the nabla fractional derivative through*
$$D_\nabla^\alpha e_\nabla(nh, s) = s^\alpha e_\nabla(nh, s) \tag{12}$$
For non integer orders we have to consider a branchcut line starting at $s = 0$ *and lying in the left complex half-plane.*

3. *The transform implied by (11) is called nabla Laplace transform (NLT) . The analysis equation for the NLT is given by*
$$\mathcal{N}\left[f(nh)\right] = F_\nabla(s) = h \sum_{n=-\infty}^{+\infty} f(nh) e_\nabla\left(-nh, s\right). \tag{13}$$
Its inverse transform (synthesis equation) is given by
$$f(nh) = -\frac{1}{2\pi i} \oint_\gamma F_\nabla(s) e_\nabla\left((n+1)h, s\right) ds, \tag{14}$$
where the integration path, γ, *is any simple closed contour in a region of analyticity of the integrand that includes the point* $s = \frac{1}{h}$. *The simplest path is a circle with centre at* $s = \frac{1}{h}$.

4. *Fractional derivative*
$$D_\nabla^\alpha x(nh) = h^{-\alpha} \sum_{k=0} \frac{(-\alpha)_k}{k!} x(nh - kh), \tag{15}$$

to see more rich behaviors unveiled with the effect of drift in complex system in the fields of hydrology, finance and turbulence.

From the theoretical perspective, the time and Hurst index dependent scale boundary of the crossover is very essential to distinguish the central parts with Gaussian and the tail parts with non-Gaussian behaviors. It is known that all Laplace processes reduce to their Gaussian for sufficiently large lags [2], which may explain the apparent contradiction between large-scale models based on fractional Brownian motion and non-Gaussian behavior on smaller scales. In future developments of the FLM-type dynamics to provide mechanics tools for anomalous diffusion data, the nonlinear forces on the diffusion particles can be considered, also including the confined and reset scenarios.

Acknowledgments

Y.L. acknowledges financial support from the Alexander von Humboldt Foundation (Grant No. 1217531) and the National Natural Science Foundation of China (Grant No. 12372382). R.M. acknowledges financial support from the German Science Foundation (DFG, Grant No. ME 1535/12-1).

References

[1] T. J. Kozubowski, M. M. Meerschaert, and K. Podgorski, Fractional Laplace motion. Adv. Appl. Probab. **38**, 451 (2006).

[2] M. M. Meerschaert, T. J. Kozubowski, F. J. Molz, and S. Lu, Fractional Laplace model for hydraulic conductivity, Geophys. Res. Lett. **31**, L08501 (2004).

[3] V. Ganti, A. Singh, P. Passalacqua, E. Foufoula-Georgiou, Subordinated Brownian motion model for sediment transport, Phys. Rev. E **80**, 011111 (2009).

[4] J. Gajda, A. Wylomanska, and A. Kumar, Generalized fractional Laplace motion, Stat. Probabil. Lett. **124**, 101 (2017).

International Conference on Mathematical Analysis and Applications in Science and Engineering
ICMA^{2}SC'24
ISEP Porto-Portugal, June 20 - 22, 2024

Paradoxical non-Gaussian behavior in fractional Laplace motion with drift

Yingjie Liang[1⋆] **Wei Wang**[2] **Ralf Metzler**[3]

[1] Hohai University, China
[2] University of Potsdam, Germany
[3] University of Potsdam, Germany

[1⋆]liangyj@hhu.edu.cn

Abstract: Special Session 7-Fractional Modelling and Artificial Intelligence in biomedical/diseases. In general, the kurtosis approaches 3, implying the probability density function (PDF) of a stochastic process becomes Gaussian. Recently, a new process, named Fractional Laplace motion (FLM) was demonstrated to have PDF with non-Gaussian tail even through the kurtosis approaches 3. In the current study we develop and analyze the statistics of FLM with drift in the two different mechanisms: the drift may keep acting on the system all the time or the drift only acts at the moments of jump. The non-Gaussianity of particle displacements, mean squared displacement and kurtosis are quantified. We thoroughly determine the crossover from non-Gaussian to Gaussian behaviors in the PDF and show that in the present and absent of drift, as time progresses an inner core region reaches the Gaussianity, while the region outside the core is non-Gaussian, with the boundaries of the core region growing with time as power laws. The results of our computer simulations are fully consistent with the analytical predictions. Our model is applicable on external forces superimposed onto the FLM-type dynamics.

keywords: Fractional Laplace motion; non-Gaussian; drift.

MSC2020: 37A60; 60G22; 982C03.

1 Introduction

Anomalous diffusion is well described by different generalized stochastic models depending on the system. The continuous time random walk (CTRW) model and fractional Brownian motion (FBM) are two such processes suited to describe anomalous diffusion in a wide range of systems. FBM is a Gaussian process with stationary increments which are persistent and anti-persistent for the anomalous Hurst exponent H in the range $2H > 1$ and $0 < 2H < 1$, respectively. FBM with $2H = 1$ reduces to BM. It is widely used to describe subdiffusion in cellular cytoplasm and complex liquids, and superdiffusion in amoeboid cells, and for densities of persistently growing brain fibers.

Here we address a compound process, i.e., fractional Laplace motion (FLM) [1, 2, 3, 4], to describe the system with anomalous diffusion and non-Gaussian behaviors. FLM introduced by Meerschaert and Kozubowsk [2], is obtained by subordinating fractional Brownian motion to a gamma process. The parent process is FBM and the gamma process is a strictly increasing

and pure jump Levy process. Increments in the gamma process has a gamma distribution. The gamma process was first applied by Moran to model water flow into a dam, and is widely used in different fields, such as maintenance, finance and degradation. In the context of subordinator, it represents the trading time or volume in financial application and the number of depositional features encountered over a distance in hydrology. FLM has been applied in hydraulic conductivity, subsurface hydrology and sediment transport. Interestingly, the probability density function (PDF) of FLM has a heavy tail with stretched Gaussian at small scales, but approaches Gaussian with increasing measurement time. Its increments called fractional Laplace noise is a stationary process. The increments in FLM is Laplace PDF at small scales in the uncorrelated case and approaches Gaussian PDF with increasing scales. The Laplace PDF merges from the geometric central limit theorem, which states that the sum of a random number of independent identically distributed with finite variance is asymptotically Laplace if the random count is geometrically distributed. Specifically, FLM has stochastic self-similarity.

We here go one step beyond and study FLM in the presence of a constant external force, and to determine the boundaries to separate the Gaussian and non-Gaussian parts in the PDFs both in the cases with and without drift. It is acknowledged that drift is action of the deterministic force on particle and accelerates its movement to the ballistic motion in an empty space. The effect of drift is found in the transient current in an amorphous material with an electric field, drying of porous media with temperature and pressure gradients, fluctuating interactions in gel electrophoresis and hydrodynamic dispersion in a flow field. In this study, we will consider two different mechanisms of drift, one is the drift may keep acting on the system all the time, even when the particle is trapped and the other is the drift only acts at the moments of jump and does not affect the particle during trapping events.

2 Results and discussion

In Fig. 1 we show the results of our analytical calculations and stochastic simulations of the PDF for FLM with drift $v = 1$ acting on the subordinated process $x(t)$ at three different times for the Hurst exponents $H = 0.5$, $H = 0.8$ and $H = 0.2$. The analytical results agree well with the simulations for all cases. The PDFs are also symmetric and they have a central Gaussian with stretched exponential tails, which can be accurately distinguished the Gaussian central part and non-Gaussian tail part by using the left boundary $vt - t^{H+1/2}$ and the right boundary $vt + t^{H+1/2}$. Interestingly, the left and right boundaries are centered exactly on vt.

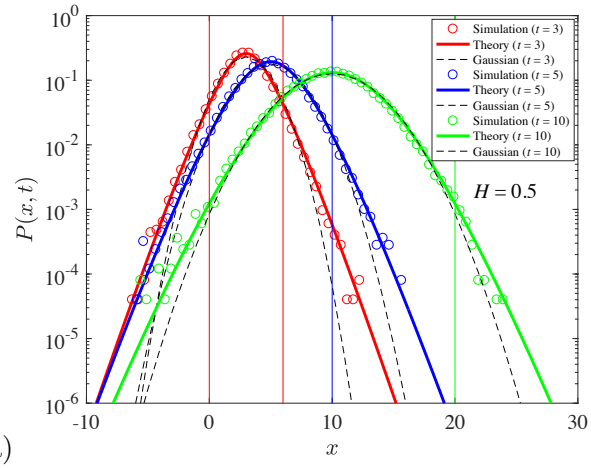

(a)

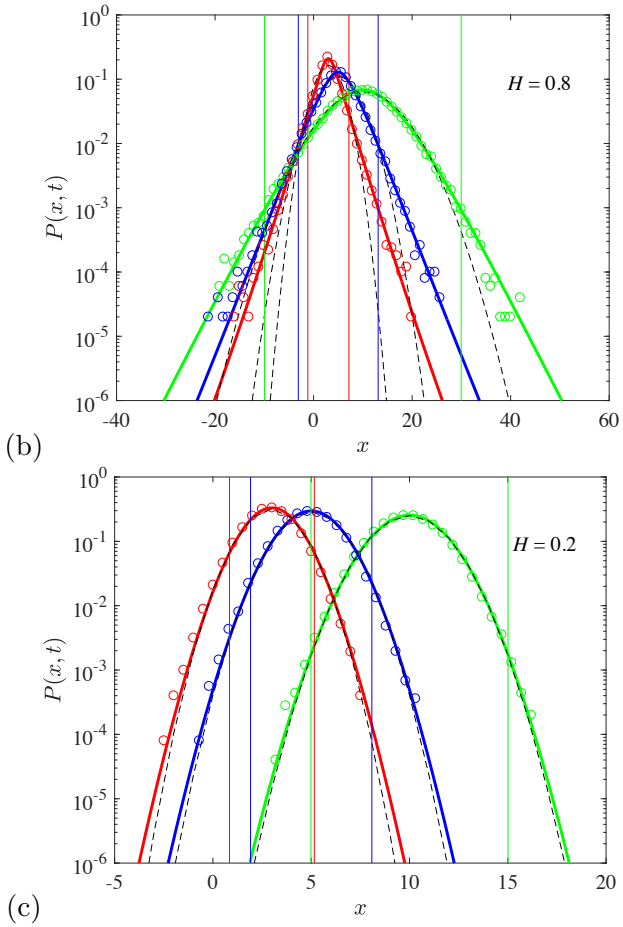

Fig. 1. Simulations (circles) and analytical results (colored solid curves) for the PDF of FLM with drift $v = 1$ acting on the subordinated process $x(t)$ at times $t = 3$, $t = 5$, and $t = 10$ with (a) $H = 0.5$, (b) $H = 0.8$ and (c) $H = 0.2$. The same colored vertical solid lines are the left boundary $vt - t^{H+1/2}$ and the right boundary $vt + t^{H+1/2}$ used to separate the Gaussian and non-Gaussian domains. For $H = 0.5$, the left boundary is 0 for the three different cases.

3 Conclusions and Future work

In this paper, we examined the diffusion process subordinating fractional Brownian motion to a gamma process in the presence of drift with two different mechanisms, both analytically and via stochastic computer simulations. As expected, the drift term dominates the diffusion behavior at long times in both moments and PDF. The PDF is non-Gaussian at short times, and approaches Gaussian at long times, which is asymptotically identical to the dynamics of free FBM with drift. The PDF has a stretched exponential tail. In the intermediate time, we find a relaxation region of the PDF, whose right and left frontiers grow with time and also depend on the Hurst exponent. Inside the region, the PDF is Gaussian and outside the region, the PDF has stretched exponential tail. At long times the tail become so suppressed by the central Gaussian parts that they do not significantly contribute.

From the experimental perspective, the time scale dependent non-Gaussian behavior plays a key role in the FLM-type dynamics. FLM in the absence of drift was proposed to examine the increments of the hydraulic conductivity data. The FLM was extended to accurately capture the sampling time scales dependent PDF of bed elevation and sediment transport rates, in which the operational time was reasoned on the basis that the stochastic nature of turbulent velocity fluctuations near the bed induces randomness in particle entrainment. It should be expected

3 Conclusions and Future work

The fundamental idea here described was to formalize a general framework that supports the development of fractional derivatives, while maintaining complete coherence with classical definitions, in order to create a structure for modelling many fractional systems we find in practice. It can be shown that the proposed scheme allows us to obtain different structures for dealing with continuous/discrete shift-invariant or scale-invariant systems. This opens many doors for applications.

Acknowledgments

This work was partially funded by National Funds through the Foundation for Science and Technology of Portugal, under the projects UIDB/00066/2020.

References

[1] Hanyga, A.: A comment on a controversial issue: A generalized fractional derivative cannot have a regular kernel. Fractional Calculus and Applied Analysis **23**(1), 211–223 (2020)

[2] A. A. Kilbas, H. M. Srivastava, and J. J. Trujillo, *Theory and Applications of Fractional Differential Equations*. Amsterdam: Elsevier, 2006.

[3] Kochubei, A.N.: General fractional calculus, evolution equations, and renewal processes. Integral Equations and Operator Theory **71**(4), 583–600 (2011).

[4] Luchko, Y., Yamamoto, M.: The general fractional derivative and related fractional differential equations. Mathematics **8**(12), 2115 (2020)

[5] M. D. Ortigueira and F. J. V. Coito, "System initial conditions vs derivative initial conditions," *Computers & Mathematics with Applications*, vol. 59, no. 5, pp. 1782–1789, 2010.

[6] M. D. Ortigueira and J. T. Machado, "What is a fractional derivative?" *Journal of Computational Physics*, vol. 293, no. 15, pp. 4–13, 2015.

[7] M. D. Ortigueira and J. A. T. Machado, "Fractional derivatives: The perspective of system theory," *Mathematics*, vol. 7, no. 2, 2019.

[8] Ortigueira, M.D.; Valério, D. *Fractional Signals and Systems*; De Gruyter: Berlin, Boston, 2020.

[9] S. G. Samko, A. A. Kilbas, and O. I. Marichev, *Fractional integrals and derivatives*. Yverdon: Gordon and Breach, 1993.

[10] Tarasov, V.E.: Multi-kernel general fractional calculus of arbitrary order. Mathematics **11**(7), 1726 (2023)

[11] G. S. Teodoro, J. T. Machado, and E. C. De Oliveira, "A review of definitions of fractional derivatives and other operators," *Journal of Computational Physics*, vol. 388, pp. 195–208, 2019.

[12] Valério, D.; Ortigueira, M.D.; Lopes, A.M. How Many Fractional Derivatives Are There? *Mathematics* **2022**, *10*.

International Conference on Mathematical Analysis and Applications in Science and Engineering
ICMA^{2}SC'24
ISEP Porto-Portugal, June 20 - 22, 2024

Generalized differentiation meets generalized probabilities

Igor Podlubny

Technical University of Kosice, Slovakia

igor.podlubny@ituke.sk

Abstract: The talk is based on the joint results with N. Leonenko (Cardiff University). The Monte Carlo method for fractional differentiation will be presented. Extending this method for fractional-order derivatives of order higher than one leads to using signed probability distributions (with positive and negative probabilities). Several methods for simulation of signed probability distributions will be presented and applied for numerical fractional-order differentiation by the Monte Carlo method.

keywords: fractional differentiation; signed probabilities; Monte Carlo method

MSC2020: 26A33, 65C05, 65D25

1 Introduction

In this work two seemingly unrelated fields of mathematics are presented and linked together. The first field is the so-called fractional calculus, which is the theory of differentiation and integration of arbitrary real order (integer and non-integer). The second field is the probability theory with signed probabilities – that is, with positive and negative probabilities.

While the fractional calculus has the history more that three centuries long, the idea of working with negative probabilities has less than one third of that. No surprise that that were open-minded physicists working in quantum mechanics who first came to using negative probabilities in there work. The first known remark was made by E. Wigner in 1932 [1], followed by P. Dirac in his 1940 lecture (published in 1942 [2]), and then by R. Feynman in 1987 [3]. It is remarkable that all three were the laureates of the Nobel Prize.

And exactly like P. Dirac's invention of his delta function $\delta(t)$, inspired Laurent Schwarz to develop the theory of distributions, or generalized functions, for which Schwarz was awarded the Fields Medal, Dirac's lecture [2] inspired M. Bartlett to elaborate the mathematical notion of negative probability [4].

Late professor Jose A. Tenreiro Machado, to whose memory this conference is dedicated, was also a man of remarkable creativity and open-mindedness. He was the first, who noticed the possible link between the fractional-order differentiation and probability distributions [5]. Namely, he noticed that the coefficients in the Grünwald–Letnikov definition of fractional differentiation for orders between zero and one can be considered as probabilities, and tried to develop a probabilistic interpretation of fractional derivatives.

Recently, we succeeded in taking Machado's observation to more advanced level, and developed the Monte Carlo methods for numerical fractional-order differentiation, initially for the case of orders between zero and one [6] .

However, consideration of orders higher than one took us to the necessity of working with signed probabilities [7], and we demonstrated how the negative probabilities can be handled in the framework of the Monte Carlo method.

2 The basic outline of the Monte Carlo method for fractional-order differentiation

Let us recall that the Grünwald–Letnikov fractional derivative [8]

$$D^{\alpha} f(t) = \lim_{h \to 0} A_h^{\alpha} f(t), \quad \alpha > 0, \quad h > 0, \tag{1}$$

where

$$A_h^{\alpha} f(t) = \frac{1}{h^{\alpha}} \sum_{k=0}^{\infty} \gamma(\alpha, k) f(t - kh), \tag{2}$$

$$\gamma(\alpha, k) = (-1)^k \frac{\Gamma(\alpha + 1)}{k! \, \Gamma(\alpha - k + 1)}.$$

For $f(t) = 0$ for $t < 0$, the fractional-order difference (2) can be used for numerical evaluation of the Grünwald–Letnikov fractional order derivative, the Riemann–Liouville fractional derivative, and the Caputo fractional derivative when it is equivalent to the Riemann–Liouville one [8].

The outline of the Monte Carlo method for the case of orders of differentiation between zero and one, following our paper [6], is the following.

Let Y be a discrete random variable such that

$$\mathbb{P}\{Y = k\} = p_k = p_k(\alpha) = -\gamma(\alpha, k), \quad k = 1, 2, \ldots \tag{3}$$

and let Y_1, Y_2,..., Y_n, ..., are independent copies of the random variable Y.

For the simulation of the random variable Y with distribution (3), we introduce the cumulative distribution function

$$F_j = \sum_{i=1}^{j} p_i,$$

where $p_k = p_k(\alpha)$ are defined in (3).

If U is a random variable uniformly distributed on $[0, 1]$, then

$$\mathbb{P}(F_{j-1} < U < F_j) = p_j,$$

and hence, to generate $Y \in \{1, 2, \ldots\}$, we set

$$Y = k, \text{ if } F_{k-1} \le U < F_k. \tag{4}$$

Each trial (draw) of the developed Monte Carlo method includes the following steps.

1. Compute $p_i = p_i(\alpha)$ defined in (3), and $F_j = \sum_{i=1}^{j} p_i$.

2. Generate N uniformly distributed random points, and compute the values Y_i using (4).

3. Evaluate the expression

$$A^{\alpha}_{N,h} f(t) = \frac{1}{h^{\alpha}} \left[f(t) - \frac{1}{N} \sum_{k=1}^{N} f(t - Y_k h) \right] . \tag{5}$$

Repeat steps 1–3 K times (trials). The mean of the obtained K values of $A^{\alpha}_{N,h} f(t)$, obtained in step 3, gives an approximation of the value of the fractional derivative of order α, $0 < \alpha \leq 1$, at the point t.

The case of derivatives of orders higher than one, as well the necessary methods for numerical simulation of related signed probability distributions, will be presented at the conference. Detailed explanations, references, and further algorithms can be found in [6] and [7].

3 Conclusions and Future work

The Monte Carlo method for numerical evaluation of integrals has become a standard topic in textbooks even for undergraduate students. It was surprising that there was not the Monte Carlo method for numerical differentiation. That was done for the first time in the works [6] and [7], and these works also provided the understanding that for developing the Monte Carlo method for numerical differentiation it was necessary to consider the case of arbitrary orders, in which the case of integer orders of differentiation is included.

The Monte Carlo method, developed in [6] and [7], provided also a certain understanding of how the non-equidistant grids for numerical fractional-order differentiation work. Even more, it became clear that the optimal locations of the nodes of a non-equidistant grid should be based on the order of differentiation.

It should be mentioned that the Monte Carlo method finally allows development of parallel algorithms for numerical fractional-order differentiation, and potentially for solution of ordinary fractional-order differential equations and their systems.

Our current work is focused on studying and exploring the properties of signed probability distributions and their applications.

Acknowledgments

The author would like to thank the Isaac Newton Institute for Mathematical Sciences, Cambridge, for support and hospitality during the programme Uncertainty quantification and stochastic modelling of materials, which was supported by EPSRC grant EP/R014604/1. The work of Igor Podlubny is also partially supported by grants APVV-22-0508, ARO W911NF-22-1-0264, and VEGA 1/0674/23.

References

[1] Wigner, E. On the quantum correction for thermodynamic equilibrium. *Physical Review*, **40** (1932) 749–759.

[2] Dirac, P. The physical interpretation of quantum mechanics. *Proceedings of the Royal Society A*, **180** (1942) 1–40.

[3] Feynman, R.: Negative probability. In: Hiley, B. J., and Peat, F. D. (Eds.) *Quantum Implications. Essays in Honour of David Bohm.* Routledge, London and New York, Chapter 13 (1987) 235–248.

[4] Bartlett, M. Negative probability. *Mathematical Proceedings of the Cambridge Philosophical Society*, **41**(1) (1945) 71–73.

[5] Machado, J.A.T. A probabilistic interpretation of the fractional-order differentiation. *Fractional Calculus and Applied Analysis*, **6**(1) (2003) 73–80.

[6] Leonenko, N., Podlubny, I. Monte Carlo method for fractional-order differentiation. *Fractional Calculus and Applied Analysis*, **25**(2) (2022) 346–361.

[7] Leonenko, N., Podlubny, I. Monte Carlo method for fractional-order differentiation extended to higher orders. *Fractional Calculus and Applied Analysis*, **25**(3) (2022) 841–857.

[8] Podlubny, I. *Fractional Differential Equations.* Academic Press, San Diego (1999).

New Perspectives on Integral Inequalities by Means of Generalized Fractional Integrals

Hasan Kara[1,⋆], **Hüseyin Budak**[2], **Fatih Hezenci**[3]

Düzce University, Türkiye

[1,⋆]hasan64karagmail.com, [2]hsyn.budak@gmail.com, [3]fatihezenci@gmail.com

Abstract: This research establishes an identity for differentiable convex functions with generalized fractional integrals. We utilize this identity to demonstrate novel parameterized inequalities through generalized fractional integrals. Using special choices of the parameter, we obtain both previously obtained and novel results. The outcomes are also demonstrated using an example. Moreover, graphics support the correctness of the example.

keywords: Convex functions; integral inequalities; fractional integrals

MSC2020: 26D10; 26D07; 26D15.

References

[1] H. R. Hwang, K. L. Tseng, and K. C. Hsu, New inequalities for fractional integrals and their applications, Turkish Journal of Mathematics, **40** 3, (2016), 471–486, .

[2] S. Hwang and K. Tseng, New Hermite–Hadamard-type inequalities for fractional integrals and their applications, Revista de la Real Academia de Ciencias Exactas, Físicas y Naturales. Serie A. Matemáticas, **112** (2018), 1211–1223, .

[3] A. Hyder, A.H. Soliman, A new generalized θ-conformable calculus and its applications in mathematical physics, Physica Scripta, **96** (2020), 015208.

[4] M. Iqbal, B. M. Iqbal, and K. Nazeer, Generalization of Inequalities Analogous to Hermite-Hadamard Inequality via Fractional Integrals, Bulletin of the Korean Mathematical Society, **52**(3) (2015), 707–716.

[5] F. Jarad, T. Abdeljawad, D. Baleanu, On the generalized fractional derivatives and their Caputo modification, J. Nonlinear Sci. Appl., **10** (5) (2017), 2607–2619.

[6] R. Khalil, M. Al Horani, A. Yousef, and M. Sababheh, A new definition of fractional derivative, Journal of Computational and Applied Mathematics, **264** 2014, 65–70.

[7] E. Set, J. Choi, and A. Gozpinar, Hermite-Hadamard type inequalities involving nonlocal conformable fractional integrals. Malaysian Journal of Mathematical Sciences, **15** (2021), 33–43.

International Conference on Mathematical Analysis and Applications in Science and Engineering
ICMA^{2}SC'24
ISEP **Porto-Portugal, June 20 - 22, 2024**

Special Session #1 – Impact of fractional calculus in modelling and control applications

Controllability of fractional dynamical systems with (k, ψ)-Hilfer fractional derivative

Javid Ali

Department of Mathematics, Aligarh Muslim University, Aligarh 202002, India

javid.mm@amu.ac.in

Abstract: In this paper, we study the controllability of dynamical systems with (k, ψ)-Hilfer fractional derivative. The Gramian matrix is used to get at necessary and sufficient controllability requirements for linear systems, which are characterized by the Mittag-Leffler (M-L) functions, while the fixed point approach is used to arrive at adequate controllability criteria for nonlinear systems. The novel feature of this study is to inquire into the controllability notion by using (k, ψ)-Hilfer fractional derivative, the most generalized variant of the Hilfer derivative. The advantage of this type of fractional derivative is that it recovers the majority of earlier studies on fractional differential equations (FDEs). Finally, we provide numerical examples to illustrate our main results.

Keywords: fractional dynamical systems; ψ-Hilfer FDEs; M-L functions; controllability Gramian; fixed point theorem.

MSC2020: 47H10, 34A08, 26A33, 34K37, 93B05, 93C10.

References

[1] D. Baleanu, J.A.T. Machado, A.C.J. Luo, *Fractional Dynamics and Control*, Springer, Berlin, 2012.

[2] J. Sausa, E. De Oliveira, On the ψ-Hilfer fractional derivative, Commun. Nonlinear Sci. Numer. Simul., 60 (2018), 72-91.

[3] S. Samko, A. Kilbas, O. Marichev, *Fractional Integrals and Derivatives: Theory and Applications*. London: Gordon and Breach Science Publishers, 1993.

International Conference on Mathematical Analysis and Applications in Science and Engineering
ICMA^{2}SC'24
ISEP Porto-Portugal, June 20 - 22, 2024

On a Certain Singular Caputo-Fractional Problem With Two Boundary Intgral Conditions

Aboubaker El-Saddik Bouziane[1⋆] **Berrabah Bendoukha**[1]

[1] Abdelhamid Ibn Badis University, Algeria

[1⋆]aboubaker27@gmail.com

Abstract: This paper presents some uniqueness and existence results for a certain singular Caputo-fractional differential equation with two integral boundary conditions. The problem is firstly converted to an equivalent fractional integral equation and well known fixed point theorems are then used.

keywords: Banach fixed point; Completely continuous operator; Fractional differential equations.

MSC2020: 49-XX; 34-XX; 92-XX.

1 Introduction

Fractional differential equations have been of great interest recently. It is caused both by the intensive developpement of the theory of fractional calculus itself and its applications in various sciences such as physics, mechanics, chemistry, engineering,...(see [1, 3, 9]). The existence and uniqueness of solutions for Caputo fractional equation ([2]) still attract interest of authors. Futheremore, many results of fractional differential problems with boundary conditions have been studied and surveyed using differents functional analysis creteria (Banach, Schauder fixed point...([7])). For more information, the reader is invited to see ([4, 6, 8, 10]). In 2015, Rezapour et al. ([5]), considered the following problem:

$$\begin{cases} {}^cD^{\alpha}x(t) + f(t, x(t)) = 0, & t \in [0,1]\,,\ n = [\alpha] + 1 \\ x(0) = x'(0) = x^{(3)}(0) = ... = x^{(n-1)}(0) = 0 & \\ ax(1) = I^p x(1), & a \geqslant 1,\ \alpha \geqslant 3,\ p \geqslant 1. \end{cases},$$

with $f :]0,\ 1] \times \mathbb{R} \longrightarrow [0,\ +\infty[$ continuously defined from $]0,\ 1] \times \mathbb{R}$ into $\mathbb{R}^+$ with a certain singularity at the point 0. For this problem, they gave in particular a sufficient uniqueness condition by mean of Banach contraction principle and a sufficient positive existence condition by using the compressive Krasnosel'skii cone fixed point theorem. All investigations have been done under the condition $2\Gamma(p) \geqslant \Gamma(\alpha)$. In the present work, we consider the Caputo-fractional problem with two integral boundary conditions

$$\begin{cases} {}^cD^{\alpha}_{0^+}x(t) + f(t, x(t)) = 0, \quad (t \in [0,1]\,,\ n-1 < \alpha < n, \quad n = [\alpha] + 1) \\ x^{(j)}(0) = 0, \quad (j \in \{0, 1, \cdots, n-1\} \setminus \{j_1, j_2\}) \\ a_k x^{(q_k)}(1) = I^{p_k}x(1), \quad (1 \leqslant a_k,\ 1 \leqslant p_k,\ k = \overline{1,2}) \end{cases} \tag{1}$$

where, $j_1,\ j_2,\ q_1,\ q_2,\ p_1,\ p_2$ are positive integers such that

$$0 \leqslant q_1 \leqslant j_1 < q_2 \leqslant j_2 \leqslant \alpha - 1. \tag{2}$$

f has the singularity

$$\lim_{t \longrightarrow 0^+} |f(t,s)| = +\infty, \quad \forall\ s \in \mathbb{R}, \tag{3}$$

and satisfies the conditions (4), (5). Setting $j_1 = j_2 = 2,\ q_1 = q_2 = 0$, one retrieves problem investigated in [5] without the condition $2\Gamma(p) \geqslant \Gamma(\alpha)$. We will also suppose that there exist three real constants $k > 0,\ m > 0,\ 0 < \sigma < 1$ such that:

$$|t^\sigma f(t,0)| \leqslant m, \quad \forall\ t \in [0,\ 1]\,, \tag{4}$$

$$|t^\sigma (f(t,x(t)) - f(t,y(t)))| \leqslant k\|x-y\|, \quad \forall\ (x,y) \in \mathcal{E}^2, \quad \forall\ t \in [0,\ 1]\,, \tag{5}$$

$\mathcal{E}$ is the Banach space $C_{\mathbb{R}}[0,\ 1]$ of continuous functions in $[0,\ 1]$ equipped with the norm:

$$\|x\|_{\mathcal{E}} := \|x\| = \max_{0 \leqslant t \leqslant 1} |x(t)|, \quad x \in \mathcal{E}.$$

2 Main results

Lemma 1 *A function $x \in \mathcal{E}$ is a solution of problem (1)-(2), if and only if it satisfies the integral equation*

$$x(t) = \int_0^1 G(t,s) f(s,x(s)) ds, \quad (t \in [0,1])$$

where,

$$G(t,s) = \begin{cases} \frac{-(t-s)^{\alpha-1}}{\Gamma(\alpha)} + t^{j_1} g_1(s) + t^{j_2} g_2(s) & ,\ (s \leqslant t) \\ \\ t^{j_1} g_1(s) + t^{j_2} g_2(s) & ,\ (t \leqslant s) \end{cases}$$

and

$$g_1(s) = \frac{\Gamma(j_2+1)}{detS} \begin{pmatrix} \frac{a_2\Gamma(p_2+j_2+1)-\Gamma(j_2-q_2+1)}{\Gamma(j_2-q_2+1)\Gamma(p_2+j_2+1)} \frac{a_1\Gamma(\alpha+p_1)(1-s)^{\alpha-q_1-1}-\Gamma(\alpha-q_1)(1-s)^{\alpha+p_1-1}}{\Gamma(\alpha-q_1)\Gamma(\alpha+p_1)} \\ \\ -\frac{a_1\Gamma(p_1+j_2+1)-\Gamma(j_2-q_1+1)}{\Gamma(j_2-q_1+1)\Gamma(p_1+j_2+1)} \frac{a_2\Gamma(\alpha+p_2)(1-s)^{\alpha-q_2-1}-\Gamma(\alpha-q_2)(1-s)^{\alpha+p_2-1}}{\Gamma(\alpha-q_2)\Gamma(\alpha+p_2)} \end{pmatrix},$$

$$g_2(s) = \frac{\Gamma(j_1+1)}{detS} \begin{pmatrix} \frac{1}{\Gamma(p_2+j_1+1)} \frac{a_1\Gamma(\alpha+p_1)(1-s)^{\alpha-q_1-1}-\Gamma(\alpha-q_1)(1-s)^{\alpha+p_1-1}}{\Gamma(\alpha-q_1)\Gamma(\alpha+p_1)} \\ \\ +\frac{a_1\Gamma(p_1+j_1+1)-\Gamma(j_1-q_1+1)}{\Gamma(j_1-q_1+1)\Gamma(p_1+j_1+1)} \frac{a_2\Gamma(\alpha+p_2)(1-s)^{\alpha-q_2-1}-\Gamma(\alpha-q_2)(1-s)^{\alpha+p_2-1}}{\Gamma(\alpha-q_2)\Gamma(\alpha+p_2)} \end{pmatrix}$$

with

$$\begin{aligned} detS &= \Gamma(j_1+1)\Gamma(j_2+1) \\ &\times \left(\frac{a_1\Gamma(p_1+j_2+1)-\Gamma(j_2-q_1+1}{\Gamma(p_2+j_1+1)\Gamma(p_1+j_2+1)\Gamma(j_2-q_1+1)} + \prod_{k=1}^{2} \frac{a_k\Gamma(p_k+j_k+1)-\Gamma(j_k-q_k+1)}{\Gamma(p_k+j_k+1)\Gamma(j_kq_k+1)} \right). \end{aligned}$$

Setting

$$\begin{aligned}\Delta &= \frac{1}{\Gamma(\alpha)}+\frac{\Gamma(p_2+j_1+1)}{\Gamma(j_1+1)}\frac{a_2}{\Gamma(\alpha-q_2)}\\ &+\frac{\Gamma(p_1+j_2+1)}{\Gamma(j_2+1)}\frac{a_1\Gamma(j_2-q_1+1)}{\Gamma(\alpha-q_1)\left[a_1\Gamma(p_1+j_2+1)-\Gamma(j_2-q_1+1)\right]}\\ &+\sum_{i=1}^{2}\frac{\Gamma(p_i+j_i+1)}{\Gamma(j_i+1)\Gamma(\alpha-q_i)}\frac{a_i\Gamma(j_i-q_i+1)}{a_i\Gamma(p_i+j_i+1)-\Gamma(j_i-q_i+1)},\end{aligned} \tag{6}$$

and remarking that

$$\max\left\{|g_1(s)|,|g_2(s)|,|G(t,s)|\right\}\leqslant\Delta\ ,\quad 0\leqslant s,t\leqslant 1.$$

One can prove the following useful result.

Proposition 2 *For each $x\in\mathcal{E}$, operator F given by formula*

$$x\longmapsto F_x:=F(x)=\int_0^1 G(.,s)f(s,x(s))ds, \tag{7}$$

is well defined from $\mathcal{E}$ into $\mathcal{E}$. Moreover, it is completely continuous mapping and for all $x\in\mathcal{E}$,

$$\|F_x\|=\max_{0\leqslant t\leqslant 1}|F_x(t)|\leqslant\frac{k\|x\|+m}{1-\sigma}\Delta.$$

Theorem 3 *If constants σ and k in formulas (4), (5) satisfy inequality $0<k<\frac{1-\sigma}{2\Delta}$. Then, Problem (1)-(2) has a unique solution. Moreover, the norm of this solution does not exceed $\frac{2m\Delta}{1-\sigma}$.*

Indeed, under assumptions of the theorem, mapping F has a unique fixed point x_0 which is the unique solution in $\mathcal{E}$ of our initial problem. The majoration

$$\|x_0\|_{\mathcal{E}}\leqslant\frac{2m\Delta}{1-\sigma}$$

follows from the invariance with respect to F of the closed subset

$$B_r=\left\{x\in\mathcal{E}:\|x\|\leqslant r,\quad r=\frac{2m\Delta}{1-\sigma}\right\}$$

since this invariance implies that x_0 is necessarly in B_r.
We obtain the following existence result:

Theorem 4 *Assume that constants σ and k in formulas (4), (5) satisfy inequality $0<k<\frac{1-\sigma}{\Delta}$. Then, Problem (1)-(2) has at least one solution.*

Indeed, for $r\geqslant\frac{m\Delta}{1-\sigma-k\Delta}$, Ω be the closed ball, centered at the origin with radius r. This is clearly a convex and closed subset of $\mathcal{E}$. It follows from proposition 2 that

$$x\in\Omega\Longrightarrow\|F_x\|\ =\ \sup_{0\leqslant t\leqslant 1}\left|\int_0^1 G(t,s)f(s,x(s))ds\right|\leqslant\frac{kr+m}{1-\sigma}\Delta\leqslant r.$$

Hence, the completely continuous operator F applies Ω on Ω. To conclude, it siffices to use the following Schauder fixed point.

Theorem 5 *[7] If Ω is a closed ball, bounded and convex in a Banach space $\mathcal{E}$ and $F:\Omega\longrightarrow\Omega$ is completely continuous operator, So F has a fixed point in Ω.*

3 Conclusion and Future work

In this paper, we analyzed a class of singular fractional boundary value problem using Caputo fractional derivative applying several functional analysis criteria (the banach, Schauder fixed point theorem). We have proved conditions to garantee the existence and uniqueness of the solution. Next future studies will be grounded to research the existence and uniqueness conditions for complicated fractional differential problems and using an others kinds of fixed point principles.

Acknowledgments

This study is a colaborate work between the professor Bendoukha Berrabh and the PHD student Bouziane Aboubaker El Saddik. It is supported by the Laboratory of pure and applied Mathematics, Abdelhamid Ibn Badis University, Mostaganem, Algeria.

References

[1] D. Baleanu, *Fractional variational principles in action*, Physica scripta, **2009** (T136) (2009).

[2] M. Caputo, F. Mainardi, *Linear models of dissipation in anelastic solids*, La Rivista del Nuovo Cimento, **1** (2) (1971), 161–198.

[3] R. Hilfer, *Applications of fractional calculus in physics*, Singapore: World Scientific Publ. Co, 2000.

[4] S. Kumar, R. K. Vats, H. K. Nashine, *Existence and uniqueness results for three-point nonlinear fractional (arbitrary order) boundary value problem*, Matematicki Vesnik, **70** (4) (2018), 314–325.

[5] Sh. Rezapour, M. Shabibi, *A singular fractional differential equation with Reimann-Liouville integral boundary condition*, Journal of Advanced Mathematical Studies, **8** (4) (2015), 80–88.

[6] S. G. Samko, A. A. Kilbas, O. I. Marichev, *Fractional integrals and derivatives, Theory and applications*, Gordon and Breach Science Publishers, Amsterdam, 1993. *Engl. transl. from Russian, Integrals and derivatives of fractional order and some of their applications*, Nauka i Tekhnika, Minsk, 1987.

[7] J. Schauder, *Der fixpunktsatz in funktionalraumen*, Studia Math, **2** (1) (1930), 171–180.

[8] M. Shabibi, Sh. Rezapour, S. M. Vaezpour, *A singular fractional integro- differential equation*, UPB Scientific Bulletin; Series A: Applied Mathematics and Physics, **79** (1) (2017), 109–118.

[9] H. Sun, Y. Zhang, D. Baleanu, W. Chen, Y. Chen, *A new collection of real world applications of fractional calculus in science and ingineering*, Communications in Nonlinear Science and Numerical Simulation, **64** (2018), 213–231.

[10] S. K. Verma, K. R. Vats, K. A. Nain, *Existence and uniqueness results for a fractional differential equations with nonlocal boundary conditions*, Boletim da Sociedade Paranaense de Matematica, **40** (3) (2022) 1–7.

International Conference on Mathematical Analysis and Applications in Science and Engineering ICMA²SC'24

ISEP **Porto-Portugal, June 20 - 22, 2024**

Dissecting fractional order calcium dynamics with Amyloid beta and Orai channel

Vora Hardagna Vatsal[1] **Brajesh Kumar Jha**[2*] **Tajinder Pal Singh**[3]

1Department of Mathematics, Pandit Deendayal Energy University, Gandhinagar, 382426, Gujarat, India

[2*]brajeshjha2881@gmail.com

Abstract: Calcium is a ubiquitous signaling component of neuronal functions. Calcium regulation is a complex phenomenon that is controlled by cellular organelles. Abnormality created by amyloid plaques is a crucial phenomenon in which the [Ca2+] flux enters through the plasma membrane. Entry of such flux is managed by intracellular homeostasis. In the neuronal calcium homeostasis, any alteration could lead to neurodegeneration. In this paper, the effect of various parameters like SERCA, IPR, Leak, VGCC, etc. has been investigated. A mathematical model has been developed by considering a time-fractional differential approach to investigate the non-local impact on cytosolic [Ca2+]. An analytic solution was obtained by applying the Laplace transform, Fourier cosine transform, and Green's function. The significant implication of amyloid beta, endoplasmic reticulum flux, and plasma membrane flux on calcium signaling was observed. It is also observed that Amyloid beta created pores are toxic to the neuron. The effect of S100B, EGTA, and BAPTA with different diffusion coefficients could show neuroprotective properties for calcium signaling. From all this simulation, therapeutic insight from different buffers, differential order, and amyloid plaques can be observed, which is a better fit as per realistic physiology.

keywords: Calcium distribution, ER fluxes, Buffer, Neuron, Laplace transforms, Fractional derivative

1 Introduction

The central nervous system has signal processing activity with neurons, a basic processing cell. Neuron is also known as a basic building block of the nervous system. Several elevations and depletions of ion concentration occur repetitively to play their role in neuronal networks. The biochemical process in neuron cells can be understood by using mathematical modeling and simulation. Modeling can be done for the homeostasis of different ions proteins and different molecules. Among them, calcium mediates in many neuronal features[1].

Mimicking the calcium oscillations for neuron cell modeling is the theoretical backbone. This analysis develops an understanding of the background parameter mechanism like buffer, diffusion coefficient, different calcium channels, etc. These parameters are located on different regions of neurons like organelle membrane, and plasma membrane, which have a different role in neuronal functions. Some proteins are also associated to play a key role in the cellular homeostasis [2]. Amyloid beta is a major protein that associates with cellular functions like neurite outgrowth, and calcium homeostasis. Amyloid precursor protein (APP) has several physiological properties to perform in neurons. Amyloid beta(Aβ) is created by the deformation of APP. Neuroprotective

property flips while this breakdown and it becomes toxic for neurons. This amyloid beta abnormal plaques form within the cytosol and extracellular fluids. Which increases the calcium flux entry to the neurons. This mechanism in addition to the calcium channel or pore leads to increased calcium concentration. It could be possible to absorb this calcium but after some extent, it will overload for endoplasmic reticulum and mitochondria. This situation triggers neuronal dysregulation.

S. Tiwari et al. have studied the cardiac mitochondrial calcium pathway [3]. N. Wei and A. Layton examined a quantitative analysis of the smooth muscle cell for calcium homeostasis [4]. Y Jagtap and N. Adlakha have studied the calcium and IPR dynamics by using the finite volume method [5]. A. Kothiya and N. Adlakha has studied the calcium dynamics with nitric oxide by using the finite element method [6]. H Joshi and Jha have explored fractional diffusion through the analytical and numerical solution for neurons incorporated with Parkinson's disease [7]. Other researchers have also modeled the calcium diffusion using different approaches to understand the biophysical nature of the calcium in different cells.

From this literature exploration, it is observed that the Amyloid beta calcium flux, which is taken at the boundary membrane flux with different channels, is not taken into consideration to examine the neuronal calcium flux for nonlocal behavior and with endoplasmic reticulum flux. Also new buffer S100B impact is considered in the paper.

we obtain the proposed model,

$$\frac{\partial^u [Ca^{+2}]}{\partial t^\alpha} = D_{Ca}\nabla^2[Ca^{+2}] - k^+[B][Ca^{+2}] + k^-[CaB] + J_{IPR} - J_{SERCA} + J_{leak} + J_{channel}$$

Taking the physiological condition of calcium flux on the plasma membrane in neuron, the boundary condition with flux is considered as,

$$\left.\frac{\partial [Ca^{+2}]}{\partial x}\right|_{x=0} = J_{Ab} + J_{\text{Orai}} - J_{PMCA} + J_{VGCC}$$

2 Results and discussion

This model is developed to simulate the neuronal calcium distribution and study the effect of various parameters on cytosolic calcium concentration distribution in neuron cells. This study helps to understand calcium homeostasis and intracellular calcium signaling for the neuron cell. Calcium stream can be visualized for amyloid beta pores and other channels. This visualization can lead to estimation better with Caputo fractional derivative order Neuronal cytosolic calcium ions are a decisive component of cellular functions. Its concentration is the decisive factor for neurotransmitter release. To mimic neuronal degeneration for conditions like real physiology, appropriate data is used. Literature suggests that the hippocampal and entorhinal cortex are primarily damaged areas in Alzheimer's disease. For neuronal geometry, several researchers applied the finite element approach successfully.

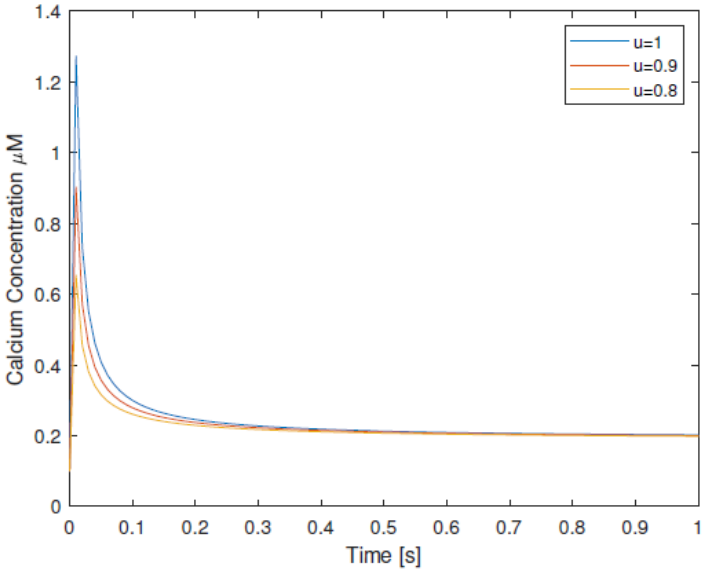

In above, the temporal calcium distribution is shown for different values of fractional order u. This calcium flux diffuses throughout the plasma membrane via different parts of the cell. For lower values of fractional order, it is observed that calcium sequestered rapidly with buffer and ER while entering into the neuron. In a fraction of time, it attains background calcium concentration. Different graphs of non-local lines converge with the same nature of the curve.

Quark, blip, and wave are the result of the calcium's incoming flux, which is determined by the quantity of calcium in the ER sensor STIM. If the calcium level is less than 250 micromolar it binds to Orai. Associated clusters with the STIM Orai channel create the calcium stream. The second calcium wave starts with a previous stage basal calcium concentration.

Different buffer concentration, various protein bound impact, different diffusion coefficient is shown graphically to evaluate the neuronal calcium in the paper. The graphical presentation shows the various behaviour of the calcium concentration for various parameter and memory impact on neuronal cell.

3 Conclusions and Future work

In this paper, we have studied the effect of various parameters like neuronal cell plaques formed by amyloid beta on cytosolic calcium ions concentration and incorporated with Orai channel. These two parameters are not explored but they have potential pathways for neurodegeneration. Also, S100B buffer is considered to check the impact on calcium-free ions concentration. Mechanism of amyloid beta, IPR, SERCA, PMCA, VGCC, leak modeled with time fractional partial differential equation. To solve this reaction-diffusion equation of calcium distribution we have used the singular kernel-based Caputo fractional differential definition. This approach is handled with Laplace and Fourier cosine transform to get an analytical solution of the model and using Green's function. The fractional differential equation approach simulates the result to incorporate the anomalous diffusion problem. This gives better insight into neuronal calcium signaling with memory effect. Physiological parameters of the plasma membrane are considered with boundary flux which increases the calcium signaling complexity. The obtained results for local and non-local impact on space and time are found significant. Graphical representation of spatiotemporal calcium shows the significant consequences of Orai and amyloid-created pores. Different fractional order gives insight into the previous stage's effect on the upcoming state of calcium ions. Using the different buffer species and concentrations the results were obtained to see the different impacts of Alzhemeric affected neuronal physiology and normal neuron calcium signaling. The effect of the diffusion coefficient is found significant. Therefore, this fractional nonlocal approach gives a memory effect to the calcium signaling phenomena and fits more accurately

than the classical approach. This work can be extended by a non-singular kernel and using other parameters.

Acknowledgment

The authors are highly thankful to the SHODH scheme, the education department, Government of Gujarat, India for financial support for carrying out this research work.

References

[1] F.M. LaFerla, Calcium dyshomeostasis and intracellular signaling in Alzheimer's disease, Nat Rev Neurosci. 3 (2002). https://doi.org/10.1038/nrn960.

[2] I. Bezprozvanny, Calcium signaling, and neurodegenerative diseases, Trends Mol Med. 15 (2009). https://doi.org/10.1016/j.molmed.2009.01.001.

[3] S.G. Tewari, A.K.S. Camara, D.F. Stowe, R.K. Dash, Computational analysis of Ca2+ dynamics in isolated cardiac mitochondria predicts two distinct modes of Ca2+ uptake, Journal of Physiology 592 (2014). https://doi.org/10.1113/jphysiol.2013.268847.

[4] N. Wei, A.T. Layton, Theoretical assessment of the Ca 2 + oscillations in the afferent arteriole smooth muscle cell of the rat kidney, International Journal of Biomathematics 11 (2018). https://doi.org/10.1142/S1793524518500432.

[5] Y. Jagtap, N. Adlakha, Numerical model of hepatic glycogen phosphorylase regulation by nonlinear interdependent dynamics of calcium and $$IP_{3}$$, The European Physical Journal Plus 138 (2023) 399. https://doi.org/10.1140/epjp/s13360-023-03961-y.

[6] A. Kothiya, N. Adlakha, Model of Calcium Dynamics Regulating IP3 and AT P Production in a Fibroblast Cell, Adv Syst Sci Appl 22 (2022). https://doi.org/10.25728/assa.2022.22.3.1219.

[7] H. Joshi, B.K. Jha, On a reaction–diffusion model for calcium dynamics in neurons with Mittag–Leffler memory, Eur Phys J Plus 136 (2021). https://doi.org/10.1140/epjp/s13360-021-01610-w

[8] D.D. Dave, B.K. Jha, 2D finite element estimation of calcium diffusion in Alzheimer's affected neuron, Network Modeling Analysis in Health Informatics and Bioinformatics 10 (2021). https://doi.org/10.1007/s13721-021-00322-6.

[9] P.A. Naik, K.R. Pardasani, Three-Dimensional Finite Element Model to Study Effect of RyR Calcium Channel, ER Leak and SERCA Pump on Calcium Distribution in Oocyte Cell, Int J Comput Methods 16 (2019). https://doi.org/10.1142/S0219876218500913.

[10] H. Joshi, M. Yavuz, I. Stamova, Analysis of the disturbance effect in intracellular calcium dynamic on fibroblast cells with an exponential kernel law, Bulletin of Biomathematics (2023). https://doi.org/10.59292/bulletinbiomath.2023002.

International Conference on Mathematical Analysis and Applications in Science and Engineering
ICMA^{2}SC'24
ISEP Porto-Portugal, June 20 - 22, 2024

Qualitative analysis of a fractional-order for a within-host infection dynamics with adaptive immunity using Caputo derivative

Marya Sadki[1⋆]

[1] Laboratory of Mathematics, Computer Science and Applications, Faculty of Sciences and Technologies, University of Hassan II of Casablanca, Mohammedia, Morocco

[1⋆]maryasadki@gmail.com

Abstract: The objective of this paper is to introduce and study a within-host viral infection model via both modes of viral transmission mechanism; virus-to-cell and cell-to-cell. The proposed model incorporates the role of adaptive immunity in limiting viral pathogen spread, including humoral and cellular immune responses. This paper focuses on describing the long memory effect using the Caputo derivative. This work begins with the investigation of the well-posedness of our mathematical model concerning demonstrating the existence, positivity and boundedness of solutions. The paper moves to introduce all the problem's steady states, which are determined by specific reproduction numbers. Subsequently, the paper proceeds to demonstrate the global stability of the five equilibria points. To evaluate the theoretical findings of global stability, we employ a numerical technique based on the fundamental theorem of fractional calculus, in addition to utilizing a three-step Lagrange polynomial interpolation method.

keywords: Global stability; Fractional-order model; Numerical simulation.

MSC2020: 34A08; 34K37; 26A33.

1 Introduction

Despite significant advancements in medical treatment and prevention, numerous infectious diseases continue to affect large populations, causing high morbidity and mortality rates. Hence, scientists are consistently motivated to understand and study how viral foreign bodies impact the health of cells within the body, while also seeking to understand the immune system's response to these transformative changes. Mathematical modeling is vital in minimizing the costly public health effects and loss of lives. It provides insights into the viral dynamics of infections in the human body [1], predicting their progression and future growth patterns. This knowledge empowers public health authorities to take informed measures and diminish the impact of diseases effectively.

Many researchers have formulated and studied mathematical biological models for describing and studying the viral infection dynamics (see for example [2, 3, 4, 5, 6]). Based and motivated

by this works and other works which are not yet mentioned, we formulate the fractional-order mathematical model:

$$\begin{cases} D^{\alpha}T = \lambda - \beta_1 TV - \beta_2 TI - d_1 T, \\ D^{\alpha}I = \beta_1 TV + \beta_2 TI - qIZ - d_2 I, \\ D^{\alpha}V = kI - pVW - d_3 V, \\ D^{\alpha}W = cVW - d_4 W, \\ D^{\alpha}Z = gIZ - d_5 Z. \end{cases} \tag{1}$$

Here D^{α} stands for the Caputo fractional derivative of order α, and $(T(0), I(0), V(0), W(0), Z(0)) \in \mathbb{R}^5_+$.

We mentioned that the functions T and I designate the density of the uninfected and infected cells, respectively. V signifies the viral load, while W stands for the humoral immune response and Z represents the cellular immune response. From the liver, susceptible cells are created at a rate λ; the extinction of each uninfected cell is natural at a rate d_1 and its infection is at a rate β_1 and β_2 by free virions and infected cells, respectively. For each infected cell dies at a rate d_2, and gets eliminated by the B cells at a rate q. Also, each free virion which is born by infected cells at rate k, dies naturally at a rate d_3, is decay antibodies at a rate p. Because of the presence of the virions and the infected cells, the humoral immune response and the cellular immune response are activated, by the production of B cells and T cells with a rate c and g, respectively. Furthermore, both B cell and T cells is cleaned naturally with a rate d_4 and d_5, respectively. We suppose that all these parameters noted below are positive.

2 Results and discussion

After formulating a fractional-order for a within-host infection dynamics with adaptive immunity using Caputo derivative operator, some basic results are given in terms of the existence, uniqueness, positivity of solutions. Then, we find five steady states of the fractional-order viral model. Moreover, the formula of the basic reproduction number is achieved. We noticed that the basic reproduction number is written in terms of β_1 and β_2, which are the infection rate via the transmission mode virus-to-cell and cell-to-cell, respectively. The theoretical findings regarding the global stability of the steady states demonstrates that the free-endemic equilibrium is stable when the basic reproduction number is below than one. Additionally, the other endemic steady states are globally asymptotically stable under some specific optimal conditions. Numerical results are obtained via employing a numerical method derived in the fundamental theorem of fractional calculus and a three-step Lagrange polynomial interpolation technique. The numerical findings have two objectives; which are, firstly to validate the theoretical investigation regarding the global stability of the steady states and secondly to demonstrate the impact of the fractional order on the dynamical behavior of the infection. The numerical results show a strong agreement between the theoretical and numerical findings, indicating that variations in the value of α do not influence the stability of any equilibrium points. Based on the numerical findings, our observations reveal that the value of the fractional order derivative influence the speed of convergence towards the respective equilibrium. More specifically, when the value of α is small, the convergence of the problem's solution towards the equilibrium points is faster.

3 Conclusions and Future work

The current paper formulated and studied a fractional-order viral model using the Caputo fractional derivative operator. The model includes five fractional derivatives equations describing

and exploring the interaction between healthy cells, unhealthy ones, the viral load, and the adaptive immunity. Moreover, the fractional-order model investigates how viral infection disseminates in the human body through the two crucial modes of infection transmission; virus-to-cell and cell-to-cell and how adaptive immunity fight against the spread of infection. We established some important results, which are, the existence, positivity and boundedness of the problem's solutions, along with determining the basic reproduction number. The proof of global stability for the equilibria is achieved through the utilization of the Lyapunov approach and La-Salle's fractional invariance principle. In order to apply numerical simulations, a numerical method is developed based on a three-step Lagrange polynomial interpolation technique and arising from fundamental theorem of fractional calculus. As future perspective, we aim to make a comparison between our theoretical findings and the clinical data for some viruses such as COVID-19, hepatitis B virus or hepatitis C virus. As a second purpose, we are interested by applying and suggesting a new numerical method this time with four-step Lagrange polynomial interpolation technique and built via fundamental theorem of fractional calculus.

References

[1] Martin A. Nowak, Charles R.M. Bangham, Population dynamics of immune responses to persistent viruses, Science, **272**(5258) (1996), 74–79.

[2] Marya Sadki, Sanaa Harroudi, Karam Allali, Local and global stability of an HCV viral dynamics model with two routes of infection and adaptive immunity, Computer Methods in Biomechanics and Biomedical Engineering, (2023), 1–28.

[3] Marya Sadki, Sanaa Harroudi, Karam Allali, Dynamical analysis of an HCV model with cell-to-cell transmission and cure rate in the presence of adaptive immunity, Mathematical modeling and computing, **9**(3) (2022), 579–593.

[4] Marya Sadki, Jaouad Danane, Karam Allali, Hepatitis C virus fractional-order model: mathematical analysis, Modeling Earth Systems and Environment, **9**(2) (2023), 1695–1707.

[5] Mouhcine Naim, Zakaria Yaagoub, Anwar Zeb, Marya Sadki, Karam Allali, Global analysis of a fractional-order viral model with lytic and non-lytic adaptive immunity, Modeling Earth Systems and Environment, (2023), 1–21.

[6] Marya Sadki, Sanaa Harroudi, Karam Allali, Fractional-order SIR epidemic model with treatment cure rate, Partial Differential Equations in Applied Mathematics, **8** (2023), 100593.

International Conference on Mathematical Analysis and Applications in Science and Engineering
ICMA^{2}SC'24
ISEP Porto-Portugal, June 20 - 22, 2024

Exact solution of fractional order Chagas virus model

S. Gimnitz Simon[1] **B. Bira**[1] **Dia Zeidan**[2⋆]

[1] Department of Mathematics, SRM Institute of Science and Technology, Kattankulathur, Chennai - 603203, Tamilnadu, India
[2] School of Basic Sciences and Humanities, German Jordanian University, Amman, Jordan

[2⋆]dia.zeidan@gju.edu.jo

Abstract: In this article, we investigate the system of fractional order Chagas vector spreading model caused by the parasite Trypanosoma cruzi under symmetry analysis. First, we derive the infinetisimal transformations under which the governing model remain invariant . Then, we construct the exact group invariant solution.

keywords: symmetry reduction; first order fractional ODE ; chagas vectors.

MSC2020: 34C14; 34A08; 34B08.

1 Introduction

Chagas disease, also called American trypanosomiasis, is primarily found in rural South and Central America. This life-threatening disease is mostly transmitted to humans via the bite of hematophagous insects from the Triatomine subfamily, popularly known as "kissing bugs". They usually live in the wall or roof cracks of poorly built homes in rural or suburban areas, becoming active at night, biting exposed skin, and defecating near the bite. Chagas disease can also be spread through blood or blood product transfusions from infected donors, congenital etc. *Deltamethrin* is the widely used insecticide for to control the spread of vectors. It is also be observed that, after the strength of insecticide vanishes, the spread may reoccur. Therefore, instead of going in trial and error methods, it is essential to frame a mathematical model to study this phenomena effectively.

Many researchers have formulated mathematical models considering different factors affecting the spread of Chagas and its control. For example, the authors in [1], have studied about Chagas spread by tourists and migrants in European countries. In [2], the authors have studied about the challenges in treating the disease. The optimised cost effective preventive measure of Chagas is studied in [3]. For the Chagas re-infestation model and analysis of distinct insecticide spraying and its effects on the spread of Chagas, we refer[4, 5].

Lie symmetry analysis is one of the powerful and systematic tool to compute exact solutions for a given nonlinear system of FODEs. Although, the application of symmetry analysis to PDEs[6, 7] and FPDEs[8, 9] are prevalent, but rarely it is applied to study system of FODEs. The authors in [10], considered a FODE and derived the point symmetries. For the exact solution of certain FODEs, we refer [11] whereas, for the exact solution of coupled FODEs, we refer [12]. However, the system of FODEs with first order[13, 14, 15] is yet to be explored under symmetry analysis. Hence, this motivates us to carry on the present study.

2 Basic model and Lie symmetry

In the year 2021 Iyiola et.al [4], derived the model:

$$\begin{aligned} \frac{d^{\rho}S}{dt^{\rho}} &= -bIS - r_0S - cS + w(N - S - I), \\ \frac{d^{\rho}I}{dt^{\rho}} &= bIS + cS - (r + r_0)I, \\ S(0) &= S_0; \quad I(0) = I_0, \end{aligned} \tag{1}$$

with $(0 < \rho < 1)$, the parameters b is unit to unit infestation, c is the rate of triatomine migration from sylvatic areas, w is the decay in insecticide strength, r_0 is the spraying rate of general insecticide and r is the spraying of deltamethrin insecticide (specific for triatomine) after detecting triatomine also N is the number of homes present, S is the susceptible homes present and I is the infested homes, with the initial susceptible homes $S(0) = S_0$, initial infested homes $I(0) = I_0$. In our present study, we consider the model (1) and construct the exact solution using Lie symmetry. Applying prolongation on (1), we obtain:

$$\begin{aligned} \phi_t^{(\rho,t)} &= -b\phi I - b\psi S - r_0\phi - c\phi - w\phi - w\psi, \\ \psi_t^{(\rho,t)} &= b\phi I + b\psi S + c\phi - (r + r_0)\psi. \end{aligned} \tag{2}$$

We get the infinitesimal transformations as:

$$\begin{aligned} \tau &= c_1 t, \\ \phi &= -\frac{1}{2}\rho c_1 \frac{(2c^2 + cr_0 + r_0w + 3c + w)}{cb} S - c_2 \frac{(2c + r_0 + 1)}{2c}, \\ \psi &= c_1 \frac{1}{2}\rho \frac{b}{(r_0 + 1)} I - c_2, \end{aligned} \tag{3}$$

and the corresponding symmetry generators:

$$\begin{aligned} X_1 &= t\frac{\partial}{\partial t} - \frac{1}{2}\rho \frac{(2c^2 + cr_0 + r_0w + 3c + w)}{cb} S\frac{\partial}{\partial S} + \frac{1}{2}\rho \frac{b}{(r_0 + 1)} I\frac{\partial}{\partial I}, \\ X_2 &= -\frac{(2c + r_0 + 1)}{2c}\frac{\partial}{\partial S} - \frac{\partial}{\partial I}. \end{aligned}$$

3 Exact solution

To construct exact solution, we consider the more general symmetry generator X_1 and its associated characteristic equation is written as:

$$\frac{dt}{t} = \frac{dS}{-\frac{1}{2}\rho c_1\Big(\frac{2c^2 + cr_0 + r_0w + 3c + w}{cb}\Big)S} = \frac{dI}{\frac{1}{2}\rho\Big(\frac{b}{r_0 + 1}\Big)I}. \tag{4}$$

Solving the characteristic equation (4), one can obtain the solution of (1) as:

$$S = \frac{1}{t^{\frac{\rho}{2}\Big(\frac{2c^2 + cr_0 + rw + 3c + w}{cb}\Big)} + k_1}, \qquad I = t^{\frac{\rho}{2}\Big(\frac{b}{r_0 + 1}\Big)} + k_2, \tag{5}$$

where k_1 and k_2 are two integration constants. Since, the considered model represents the spread of Chagas virus, hence we choose $I(0) > 0$. For our computational work in this paper, we choose $S(0) = 80,\ I(0) = 20$ and $N = 100$. Consequently, the exact solution of (1) can be rewritten as:

$$S = \frac{1}{\frac{\rho}{t}\frac{2}{2}\left(\frac{2c^2 + cr_0 + rw + 3c + w}{cb}\right) + 0.0125}, \qquad I = t^{\frac{\rho}{2}\left(\frac{b}{r_0 + 1}\right)} + 20. \tag{6}$$

4 Conclusions and Future work

The fractional order reinfestation model of Chagas virus is studied under symmetry analysis. We derive the symmetry generators and with the help of method of characteristics, we construct the exact group invariant solution for the given model. Further, this work can be extended to discuss the spread of Chagas virus and reinfestation under various physical parameters such as unit to unit infestation rate b, bug migration from sylvatic areas c, spraying of general r_0 and specific r insecticides and its decay w. Furthermore, we are planning to investigate the behaviour of the solution under the influence of the fractional derivative ρ.

References

[1] Basile, Luca and Jansà, Josep Maria and Carlier, Yves and Salamanca, Dominique Dejour and Angheben, Andrea and Bartoloni, Alessandro and Seixas, J and Van Gool, Tom and Cañavate, Carmen and Flores-Chávez, María and others, Chagas disease in European countries: the challenge of a surveillance system, Eurosurveillance, **16**(37) (2011).

[2] Mills, Roger M, Chagas disease: epidemiology and barriers to treatment, The American journal of medicine, **133**(11) (2020), 1262–1265.

[3] Oduro, Bismark and Grijalva, Mario J and Just, Winfried, Models of disease vector control: When can aggressive initial intervention lower long-term cost?, Bulletin of Mathematical Biology, **80** (2018), 788–824.

[4] Iyiola, Olaniyi and Oduro, Bismark and Akinyemi, Lanre, Analysis and solutions of generalized Chagas vectors re-infestation model of fractional order type, Chaos, Solitons & Fractals, **145** (2021), 110797.

[5] Oduro, Bismark and Grijalva, Mario J and Just, Winfried, A model of insect control with imperfect treatment, Journal of Biological Dynamics, **13**(1) (2019), 518–537.

[6] Satapathy, Purnima and Raja Sekhar, T, Analytic solutions for (2+ 1)-dimensional shallow water equations with flat bottom through Lie symmetry approach, The European Physical Journal Plus, **137**(10) (2022), 1183.

[7] Shagolshem, Sumanta and Bira, B and Sil, S, Application of symmetry analysis to viscoelastic fluid model, Communications in Nonlinear Science and Numerical Simulation, **125** (2023), 107417.

[8] Cheng, Xiaoyu and Hou, Jie and Wang, Lizhen, Lie symmetry analysis, invariant subspace method and q-homotopy analysis method for solving fractional system of single-walled carbon nanotube, Computational and Applied Mathematics, **40** (2021), 1–17.

[9] Chatibi, Youness and El Kinani, El Hassan and Ouhadan, Abdelaziz, On the discrete symmetry analysis of some classical and fractional differential equations, Mathematical Methods in the Applied Sciences, **44**(4) (2021), 2868–2878.

[10] Bakkyaraj, T and Sahadevan, R, Invariant analysis of nonlinear fractional ordinary differential equations with Riemann–Liouville fractional derivative, Nonlinear Dynamics, **80** (2015), 447–455.

[11] Prakash, P and Sahadevan, R, Lie symmetry analysis and exact solution of certain fractional ordinary differential equations, Nonlinear Dynamics, **89** (2017), 305–319.

[12] Sethukumarasamy, K and Vijayaraju, P and Prakash, P, On Lie symmetry analysis of certain coupled fractional ordinary differential equations, Journal of Nonlinear Mathematical Physics, **28**(2) (2021), 219–241.

[13] Sujitha, S and Jayakumar, T and Maheskumar, D, Fractional model of brain tumor with chemo-radiotherapy treatment, Journal of Applied Mathematics and Computing, **69**(5) (2023), 3793–3818.

[14] Li, Yong-Min and Ullah, Saif and Khan, Muhammad Altaf and Alshahrani, Mohammad Y and Muhammad, Taseer, Modeling and analysis of the dynamics of HIV/AIDS with non-singular fractional and fractal-fractional operators, Physica Scripta, **96**(11) (2021), 114008.

[15] Ali, Zeeshan and Rabiei, Faranak and Shah, Kamal and Khodadadi, Touraj, Fractal-fractional order dynamical behavior of an HIV/AIDS epidemic mathematical model, The European Physical Journal Plus, **136**(1) (2021), 36.

International Conference on Mathematical Analysis and Applications in Science and Engineering
ICMA^{2}SC'24
ISEP Porto-Portugal, June 20 - 22, 2024

Exact solutions of time-fractional (2+1) Chemotaxis model using Lie symmetry

S. Gimnitz Simon[1] **B. Bira**[1⋆] **Dia Zeidan**[2]

[1] Department of Mathematics, SRM Institute of Science and Technology, Kattankulathur, Chennai - 603203, Tamilnadu, India
[2] School of Basic Sciences and Humanities, German Jordanian University, Amman, Jordan

[1⋆]bibekanb@srmist.edu.in

Abstract: In this paper, we consider the time-fractional (2+1)-dimensional Patlak-Keller-Segal system describing chemotaxis process. We construct infinetisimal transformations of the given model under Lie symmetry analysis. Further, the given system of time-fractional partial differential equations (PDEs) is reduced to ordinary differential equations (ODEs) with integer order. Finally, we derive the exact group invariant solution for the given model.

keywords: Patlak-Keller-Segal; exact solution; non-classical symmetry.

MSC2020: 76M60; 35R11 ; 35B30.

1 Introduction

A human being falls sick if the fundamental composition of the human body (cells) becomes disordered. Over time, medical practitioners started to analyse, simulate and study about the disease and its remedy. The essential factor involving cure is that how the chemical component present in medicine is going to react with infected cell or tumor. The process of cells reacting to the chemical stimuli in medicine is called Chemotaxis.

Evelyn F Keller and Lee A Segal have formulated a mathematical model for chemotaxis which was named after them as Keller-Segal model opened new doors for the theoretical study. Later, the work of Clifford S Patlak has been incorporated and we obtained Patlak-Keller-Segal model which also considers the direction of chemical and cell movement. Parameters affecting chemotaxis include the sensitivity of cells to chemical compounds and reaction nature of both cells and chemical. In our present work, we consider the Patlak-Keller-Segal model with time-fractional derivative in the sense of Riemann-Liouville.As differential equations (DEs) with fractional order are very much useful to model the system with memory and hereditary. Recently, many models have been framed in fractional order to represent different non-linear phenomena more accurately[1, 2, 3].

To analyse the given FPDEs, several researchers have developed many effective techniques such as ARA power series method[4], soliton solutions[5], numerical approximation using Fibonacci wavelets operational matrix approach[6], natural transform decomposition method[7] and integrated Bernoulli polynomials combined with iteration methods[8].

On the other hand, Lie's symmetry analysis is one of the systematic and distinguished method to construct group invariant exact solution for a given FPDEs[9, 10]. Hence, in our study we apply Lie symmetry analysis to solve the given model.

1.1 Preliminary

Riemann-Liouville (RL) fractional derivative: For $0 < m-1 < \beta < m$, the Riemann-Liouville (RL) fractional derivative with order β is given as:

$$\partial_t^\beta f = \begin{cases} \frac{1}{\Gamma(m-\beta)} \frac{\partial^m}{\partial t^m} \int_0^t \frac{f(s)}{(t-s)^{\beta+1-m}} ds, & 0 < m-1 < \beta < m, \\ \frac{d^m f}{dt^m}, & \beta = m. \end{cases} \tag{1}$$

Erdelyi-Kober integral operator: Let $U(\theta)$ be a smooth function with similarity variable θ, then the Erdelyi-Kober fractional integral operator is defined as:

$$J_\xi^{\tau,\beta} U(\theta) = \frac{1}{\Gamma(\beta)} \int_1^\infty \frac{z^{-(\tau+\beta)}}{(z-1)^{1-\beta}} U(\theta z^{\frac{1}{\xi}}) dz. \tag{2}$$

The Erdelyi-Kober fractional integral operator can be approximated as [11]:

$$J_\xi^{(\tau,\beta)} U(\theta) = \sum_{s=0}^{\infty} \lambda_s U^{(s)}(\theta) \frac{\theta^s}{s!}, \quad \text{where} \quad \lambda_s = \sum_{j=0}^{s} s C_j (-1)^{s-j} \frac{\Gamma(\tau + \frac{j}{\xi} + 1)}{\Gamma(\tau + \beta + \frac{j}{\xi} + 1)}. \tag{3}$$

2 Symmetry reduction

The (2+1) Keller-Segal fractional model is considered as[12]:

$$\frac{\partial^\beta u}{\partial t^\beta} + a(u_x v_x + u v_{xx} + u_x v_y + u v_{xy} + u_y v_x + u v_{yx} + u_y v_y + u v_{yy}) = 0, \tag{4}$$

$$\frac{\partial^\beta v}{\partial t^\beta} + \Delta v + b_v v - b_u u = 0, \tag{5}$$

where $u(x, y, t)$ denotes the cell density, $v(x, y, t)$ denotes the chemoattractant concentration, a is chemotactic sensitivity constant and b_u, b_v are reaction coeffecients of u, v respectively.
From the application of symmetry analysis, one can get the infinitesimal transformations as:

$$\gamma = \frac{\gamma}{2} c_1 + c_2, \quad \xi = 2c_1 t, \quad \eta = \frac{\gamma}{2} c_1 - c_2, \quad \nu = \beta u c_1, \quad \phi = \beta v c_1,$$

and the corresponding generators are:

$$X_1 = \frac{\beta}{2} \frac{\partial}{\partial x} + \frac{\beta}{2} \frac{\partial}{\partial y} + 2t \frac{\partial}{\partial t} + \beta u \frac{\partial}{\partial u} + \beta v \frac{\partial}{\partial y}, \qquad X_2 = \frac{\partial}{\partial x} - \frac{\partial}{\partial y}. \tag{6}$$

2.1 Symmetry reduction

To construct the exact solution of the given model, we consider the two-dimensional optimal algebra $< X_1, X_2 >$. First, we consider characteristic equation of X_2 as:

$$\frac{dx}{1} = \frac{dy}{-1}.$$

and obtained,

$$x + y = k_1. \tag{7}$$

Using (7) in X_1 gives: $X_{11} = \frac{\beta}{2}\frac{\partial}{\partial k_1} + 2t\frac{\partial}{\partial t} + \beta u\frac{\partial}{\partial u} + \beta v\frac{\partial}{\partial y}$ whose characteristic equation is given as:

$$\frac{dk_1}{\frac{\beta}{2}} = \frac{du}{\beta u} = \frac{dv}{\beta v} = \frac{dt}{2t}.$$

Solving the above equation yields the similarity variables:

$$\tau = t^{-\frac{\beta}{4}}k_1, \quad u = t^{\frac{\beta}{2}}U(\tau), \quad v = t^{\frac{\beta}{2}}V(\tau), \tag{8}$$

Using (8) through (1) and (2) in (4) we obtain the following reduced FODEs:

$$\begin{aligned}(1 - \frac{3\beta}{2} - \frac{\beta}{2}\xi\frac{d}{d\xi})K^{1-\frac{\beta}{2},1-\beta}_{\frac{4}{\beta}}U + a(4U'V' + 4UV'') &= 0,\\ (1 - \frac{\beta}{2} - \frac{\beta}{2}\xi\frac{d}{d\xi})K^{1-\frac{3\beta}{2},1-\beta}_{\frac{4}{3\beta}}V + b_vV - b_uU &= 0.\end{aligned} \tag{9}$$

3 Exact solutions

To derive the exact solution, the system of FODEs in (9) is converted to system of ODEs with integer order through (3) as:

$$\begin{aligned}\left(1 - \frac{3\beta}{2}\right)\frac{\Gamma(2-\frac{\beta}{2})}{\Gamma(3-\frac{3\beta}{2})}U - \frac{\beta}{2}\tau\frac{\Gamma(2-\frac{\beta}{2})}{\Gamma(3-\frac{3\beta}{2})}U' + 4a(U'V' + UV'') = 0,\\ \left(1 - \frac{\beta}{2}\right)\frac{\Gamma(2-\frac{3\beta}{2})}{\Gamma(3-\frac{5\beta}{2})}V - \frac{\beta}{2}\tau\frac{\Gamma(2-\frac{3\beta}{2})}{\Gamma(3-\frac{5\beta}{2})}V' - b_vV + b_uU = 0.\end{aligned} \tag{10}$$

Further, (10) can be rewritten as:

$$\begin{aligned}K_1U - K_2\tau U' + 4a(U'V' + UV'') &= 0,\\ K_3V - K_4\tau V' - b_vV + b_uU &= 0,\end{aligned} \tag{11}$$

with $K_1 = (1 - \frac{3\beta}{2})\frac{\Gamma(2-\frac{\beta}{2})}{\Gamma(3-\frac{3\beta}{2})}$, $K_2 = \frac{\beta}{2}\frac{\Gamma(2-\frac{\beta}{2})}{\Gamma(3-\frac{3\beta}{2})}$, $K_3 = (1 - \frac{\beta}{2})\frac{\Gamma(2-\frac{3\beta}{2})}{\Gamma(3-\frac{5\beta}{2})}$, $K_4 = \frac{\beta}{2}\frac{\Gamma(2-\frac{3\beta}{2})}{\Gamma(3-\frac{5\beta}{2})}$.
In order to find the group invariant exact solutions, we consider $U = C\tau^{\theta_1}$, $V = D\tau^{\theta_2}$. Substituting it in (11), we get:

$$\begin{aligned}K_1C\tau^{\theta_1} - K_2C\theta_1\tau^{\theta_1} + 4a(\theta_1\cdot\theta_2\cdot C\cdot D\tau^{\theta_1+\theta_2-2} + C\cdot D\theta_2(\theta_2-1)\tau^{2\theta_2-2}) = 0,\\ K_3D\tau^{\theta_2} - \theta_2K_4D\tau^{\theta_2} - b_vD\tau^{\theta_2} + b_uC\tau^{\theta_1} = 0.\end{aligned} \tag{12}$$

Under the invariant condition $\theta_1 = \theta_2 = 2$, the system (12) gives:

$$C = \frac{2K_2 - K_1}{24ab_u}\cdot(2K_4 + b_v - K_3), \quad D = \frac{2K_2 - K_1}{24a}. \tag{13}$$

Further, giving rise the exact solution of (4) as:

$$u = \frac{(2K_2 - K_1)}{24ab_u}\cdot(2K_4 + b_v - K_3)\cdot(x+y)^2\cdot t^{-\frac{\beta}{2}}, \tag{14}$$

$$v = \frac{2K_2 - K_1}{24a}\cdot(x+y)^2\cdot t^{-\frac{\beta}{2}}. \tag{15}$$

References

[1] Ahmad, Imtiaz, Ibrahim Mekawy, Muhammad Nawaz Khan, Rashid Jan, Salah Boulaaras, Modeling anomalous transport in fractal porous media: A study of fractional diffusion PDEs using numerical method, Nonlinear Engineering, **13** 1 (2024), 20220366.

[2] Bandekar, Shraddha Ramdas, Mini Ghosh, C. Rajivganthi, Impact of vaccination on the dynamics of COVID-19: A mathematical study using fractional derivatives, International Journal of Biomathematics, **17.02** (2024), 2350018.

[3] Sofia, I. R., Shraddha Ramdas Bandekar, Mini Ghosh, Mathematical modeling of smoking dynamics in society with impact of media information and awareness, Results in Control and Optimization, **11** (2023), 100233.

[4] Burqan, Aliaa, Rania Saadeh, Ahmad Qazza, Shaher Momani, ARA-residual power series method for solving partial fractional differential equations, Alexandria Engineering Journal, **62** (2023), 47-62.

[5] Pavani, K., K. Raghavendar, K. Aruna, Soliton solutions of the time-fractional Sharma-Tasso-Olver equations arise in nonlinear optics, Optical and Quantum Electronics, **56.5** (2024), 748.

[6] Manohara, G., S. Kumbinarasaiah, Numerical approximation of fractional SEIR epidemic model of measles and smoking model by using Fibonacci wavelets operational matrix approach, Mathematics and Computers in Simulation (2024).

[7] Bushnaq, Samia, Amjad Ali, Numerical investigation of fractional Fisher partial differential equation via natural transform decomposition method, Partial Differential Equations in Applied Mathematics, **9** (2024), 100642.

[8] Azarnavid, Babak, Mahdi Emamjomeh, Mohammad Nabati, Abdollah Dinmohammadi, An efficient iterative method for multi-order nonlinear fractional differential equations based on the integrated Bernoulli polynomials, Computational and Applied Mathematics, **43** 1 (2024), 68.

[9] Hashemi, Mir Sajjad, A. Haji-Badali, F. Alizadeh, Mustafa Inc, Classical and non-classical Lie symmetry analysis, conservation laws and exact solutions of the time-fractional Chen-Lee-Liu equation, Computational and Applied Mathematics, **42** 2 (2023), 73.

[10] Zhu, Hui-Min, Jia Zheng, Zhi-Yong Zhang, Approximate symmetry of time-fractional partial differential equations with a small parameter, Communications in Nonlinear Science and Numerical Simulation, **125** (2023), 107404.

[11] Plociniczak, Lukasz, Approximation of the Erdelyi-Kober operator with application to the time-fractional Porous medium equation, SIAM journal on applied mathematics, **74.4** (2014), 1219-1237.

[12] Chertock, Alina, Yekaterina Epshteyn, Hengrui Hu, Alexander Kurganov, High-order positivity-preserving hybrid finite-volume-finite-difference methods for chemotaxis systems, Advances in Computational Mathematics, **44** (2018), 327-350.

International Conference on Mathematical Analysis and Applications in Science and Engineering
ICMA^{2}SC'24
ISEP Porto-Portugal, June 20 - 22, 2024

A New Class of Fractional Problems of the Calculus of Variations

Om Kalthoum Wanassi[1,2] **Delfim F. M. Torres**[1]

[1]Center for Research and Development in Mathematics and Applications (CIDMA), Department of Mathematics, University of Aveiro, 3810-193 Aveiro, Portugal
[2]LR18ES17, Faculty of Sciences of Monastir, University of Monastir, Tunisia

{om.wanassi, delfim}@ua.pt

Abstract: The Fractional Calculus of Variations was introduced in 1996/1997 by Riewe in the context of classical mechanics. Since then, the theory of fractional calculus of variations and fractional optimal control has been greatly developed: see [1] and references therein. In this work we introduce a new fractional problem of the calculus of variations with nonstandard boundary conditions. We prove new necessary optimality conditions of Euler–Lagrange type, providing an illustrative example. Moreover, we develop a power-series method to approximate the solution of the new class of fractional variational problems. An illustrative example shows the fast convergence of the proposed method to the solution.

keywords: optimization; calculus of variations; fractional calculus; power series method.

MSC2020: 26A33; 49K05; 49M99.

Acknowledgments

This work was supported by The Portuguese Foundation for Science and Technology (FCT) under Grants UIDB/04106/2020 and UIDP/04106/2020.

References

[1] R. Almeida, D. F. M. Torres, A survey on fractional variational calculus, Handbook of fractional calculus with applications, Vol. 1, 347–360, De Gruyter, Berlin, 2019.

International Conference on Mathematical Analysis and Applications in Science and Engineering
ICMA^{2}SC'24
ISEP Porto-Portugal, June 20 - 22, 2024

On a class of p-Kirchhoff equations with nonlocal logarithmic nonlinearity

Uğur Sert

Hacettepe University, Turkey

usert8483@gmail.com

Abstract: (*Special Session 14*: *Partial differential equations with nonstandard growth and applications*)
In this talk, we present the Dirichlet problem for a class of Kirchhoff-type degenerate evolution equations involving the p-Laplace operator

$$u_t - a\left(\|\nabla u\|^p_{L^p(\Omega)}\right)\Delta_p u = \ln\left(\|u\|^2_{L^2(\Omega)}\right)|u|^{q(x,t)-2}u, \quad (x,t)\in\Omega\times(0,T)$$

where the coefficient of diffusion and the source term nonlocally depend on the sought solution. In particular, we investigate the effects of the presence of nonlocal logarithmic nonlinearity to the problem. We establish sufficient conditions for local and global in time solvability of the problem. Sufficient conditions for the blow-up or vanishing of solutions in a finite time are derived. In addition, the upper bound for the blow-up moment is found.

This talk is based on joint work with Sergey Shmarev.

keywords: p-Kirchhoff; variable exponent; blow-up; logarithmic nonlinearity; non-local; asymptotic behaviour.

MSC2020: 35A01; 35B44; 35K65; 35K55; 35K92; 35K99.

References

[1] U. Sert, S. Shmarev, *On a class of nonlocal parabolic equations of kirchhoff type: Nonexistence of global solutions and blow-up*, Math. Methods Appl. Sci. **45**(14) (2022), 8674–8700

[2] U. Sert, S. Shmarev, *On a degenerate nonlocal parabolic equation with variable source*, J. Math. Anal. Appl. **484** (2020), no. 1, 123695.

International Conference on Mathematical Analysis and Applications in Science and Engineering
ICMA^{2}SC'24
ISEP Porto-Portugal, June 20 - 22, 2024

Gradient Controllability of Time-Fractional Systems involving Psi-Caputo Fractional Derivative

Asmae Tajani [1⋆] **Delfim F. M. Torres**[1]

[1] Center for Research CIDMA, Department of Mathematics,
University of Aveiro, 3810-193 Aveiro, Portugal

[1⋆]tajaniasmae@ua.pt

Abstract: The main goal of this work is to investigate the gradient controllability of fractional sub-diffusion equations involving $\psi-$Caputo derivative of order $\alpha \in (0,1)$. We first introduce a new definition of gradient controllability for the fractional systems, which recovers the usual definition of gradient controllability as $\alpha \to 1$. An approach to guarantee the gradient controllability of the problem studied using a generalization of HUM Approach is presented. several examples are presented in the end to illustrate the effectiveness of our results, where zone actuators and pointwize actuators are respectively considered.

keywords: Gradient controllability; Fractional calculus; Operator theory.

MSC2020: 93B05; 26A33; 47A13.

References

[1] Sonuc Zorlu and Adham Gudaimat, Approximate Controllability of Fractional Evolution Equations with ψ-Caputo Derivative, Symmetry 2023, 15, 1050. https://doi.org/10.3390/sym15051050.

[2] Ruiyang Cai, Fudong Ge, YangQuan Chen, Chunhai Kou, Regional gradient controllability of ultra-slow diffusions involving the Hadamard-Caputo time fractional derivative, Mathematical Control and Related Fields , **10** (2020), 141–156. Doi: 10.3934/mcrf.2019033

[3] S. Samko, A. Kilbas, O. Marichev, *Fractional Integrals and Derivatives: Theory and Applications*. London: Gordon and Breach Science Publishers, 1993.

International Conference on Mathematical Analysis and Applications in Science and Engineering ICMA²SC'24

ISEP **Porto-Portugal, June 20 - 22, 2024**

Fractional Transformations of Distributions with Applications

Ahmed I. Zayed

Department of Mathematical Sciences

DePaul University

Chicago, IL 60614, USA

azayed@depaul.edu

The subject of fractional integral transforms started in the early 1980's with the publication of Namias's paper on the fractional Fourier transform [1]. The fractional Fourier transform, which is a generalization of the Fourier transform, did not receive much attention until the 1990's when many engineers and physicists realized a number of applications of the transform in optics and signal processing [2].

More recently, several other fractional integral transformations, such as fractional Hankel, fractional Radon, and fractional wavelet transforms were introduced in the literature, see [3]. The domains of these fractional transformations have been extended to larger function spaces, including generalized functions and Schwartz distributions and taking values in quaternion and Clifford algebras.

In this talk we will give a brief introduction to the subject of fractional transformations and their extensions and then discuss some recent developments on the extensions of the two-dimensional coupled fractional Fourier transform and pseudo-differential operators.

Unlike the standard two-dimensional fractional Fourier transform which is a tensor product of two one-dimensional transforms, one with parameter α and one with parameter β, the coupled fractional Fourier transform is an authentic two-dimensional transform in which the two parameters are $(\alpha + \beta)/2$ and $(\alpha - \beta)/2$.

Keywords: Fractional transformations, distributions, generalized functions.
MSC: **2020:** 44A15; 46F12.

References:

1) V. Namias, The fractional order Fourier transform and its application to quantum mechanics. IMA J. Appl. Math. Vol. 25 (1980).
2) H. M. Ozaktas, Z. Zalevsky, M. Kutay, The fractional Fourier transform with applications in optics and signal processing, John Wiley, New, York (2001).
1) A. I. Zayed, Fractional Integral Transforms: Theory and Applications, CRC Press (2024).

International Conference on Mathematical Analysis and Applications in Science and Engineering
ICMA^{2}SC'24
ISEP Porto-Portugal, June 20 - 22, 2024

On the construction of fractional operators with normalization

Marc Jornet[1⋆]

[1] Departament de Matemàtiques, Universitat de València, Burjassot, Spain

[1⋆]marc.jornet@uv.es

Abstract: I present some results from arXiv:2403.06198. We show how a rescaling of fractional operators may improve their properties and their applicability in differintegral models. In the Caputo case, the normalization gives rise to the L-fractional operator, which entails units time^{-1}, differential form, and finite ordinary derivative at the initial condition. For non-singular kernels, some of their deficiencies may be overcome with normalization, because the fundamental theorem of calculus holds and there is no inconsistency at the origin. By generalizing the L-fractional modification, a new probabilistic derivative can be defined, that is of application in differintegral equations.

keywords: fractional calculus; rescaled operator; probabilistic derivative

MSC2020: 34A08; 60E05

1 Introduction

In [1], we consider and modify fractional operators proposed in the literature. We use the generic notation $Dx(t)$ here, for the operator D and its evaluation at functions x, where t is the independent variable (the time). We investigate whether dividing by Dt improves the properties of the operator:

$$\tilde{D}x(t) := \frac{Dx(t)}{Dt}. \tag{1}$$

We also address the associated fractional differential equation,

$$\tilde{D}x(t) = f(t, x(t)). \tag{2}$$

In general, with (1) and (2), we will see that the values of $x'(0)$ and $\tilde{D}x(0)$ are more consistent, and that the vector field f has units time^{-1}. Even though the normalization with Dt may seem simple, it requires the building of a new theory on fractional calculus, especially with regard to the search of explicit and closed-form solutions. In addition, it provides insight on how to design a general definition of operator with memory that extends the ordinary derivative.

2 L-fractional operator (normalization of Caputo)

The L-fractional derivative [2, 3] is defined as the normalization of the Caputo operator,

$$ {}^{L}D^{\alpha}x(t) = \frac{{}^{C}D^{\alpha}x(t)}{{}^{C}D^{\alpha}t} = \frac{\Gamma(2-\alpha)}{t^{1-\alpha}}\,{}^{C}D^{\alpha}x(t), \tag{3} $$

from $\mathrm{AC}[0,T]$ into $\mathrm{L}^1[0,T]$. When $x \in \mathcal{C}^2[0,T]$,

$$ {}^{L}D^{\alpha}x(t) = x'(0) + \frac{1}{t^{1-\alpha}}\int_0^t (t-\tau)^{1-\alpha}x''(\tau)\mathrm{d}\tau, \tag{4} $$

pointwise on $(0,T]$. The kernel $(t-\tau)^{1-\alpha}$ is non-singular, although the denominator $t^{1-\alpha}$ controls the value of ${}^{L}D^{\alpha}x(0+)$ to avoid inconsistencies. It holds $x'(0) = {}^{L}D^{\alpha}x(0) \in (-\infty,\infty)$. Considering (3), an L-fractional differential equation is

$$ {}^{L}D^{\alpha}x(t) = f(t,x(t)), $$

for $t \in (0,T]$, with an initial condition or state $x(0) = x_0$. The integral operator is

$$ {}^{L}J^{\alpha}x(t) = \frac{1}{\Gamma(\alpha)\Gamma(2-\alpha)}\int_0^t (t-s)^{\alpha-1}s^{1-\alpha}x(s)\mathrm{d}s. $$

The link of L-fractional calculus with probability theory is

$$ {}^{L}J^{\alpha}y(t) = t\mathbb{E}[y(tV)], \quad {}^{L}D^{\alpha}y(t) = \mathbb{E}[y'(tW)], \tag{5} $$

where $V \sim \mathrm{Beta}(2-\alpha,\alpha)$ and $W \sim \mathrm{Beta}(1,1-\alpha)$.

3 A new probabilistic derivative

Based on (5), we define the new linear operator

$$ \mathcal{D}x(t) = \mathbb{E}[x'(tW)], \tag{6} $$

where $t \in [0,T]$, $x : [0,T] \to \mathbb{C}$ is (at least) an absolutely continuous function, and W is a random variable with the requirements:

$$ \mathrm{support}(W) \subseteq [0,1], \quad \|W\|_\infty = 1, \quad \lim_{n\to\infty} n\mathbb{E}[W^n] = \infty. \tag{7} $$

Let W be a fixed random variable satisfying (7). Suppose that there exists another random variable V, independent of W and with support in $[0,1]$, such that

$$ WV = U \sim \mathrm{Uniform}(0,1). $$

The associated integral operator to (6) is

$$ \mathcal{J}x(t) = t\mathbb{E}[x(tV)]. $$

We define the new Mittag-Leffler-type function

$$ \mathcal{E}(s) = \sum_{n=0}^{\infty} \frac{s^n}{n!\prod_{j=1}^{n-1}\mathbb{E}[W^j]}. $$

Some examples of results:

Theorem 1 *If $x : [0,T] \to \mathbb{C}$ is a continuously differentiable function, then*

$$\mathcal{J} \circ \mathcal{D}x(t) = x(t) - x(0), \quad \mathcal{D} \circ \mathcal{J}x(t) = x(t)$$

for every $t \in [0,T]$. If x is given by an ordinary power series, then

$$\mathcal{J}x(t) = \sum_{n=0}^{\infty} x_n \mathcal{J}t^n = \sum_{n=0}^{\infty} x_n \frac{t^{n+1}}{(n+1)\mathbb{E}[W^n]}.$$

Theorem 2 *If $A \in \mathbb{C}^{d\times d}$ and $x_0 \in \mathbb{C}^d$, then*

$$x(t) = \mathcal{E}(tA)x_0$$

solves

$$\mathcal{D}x(t) = Ax(t)$$

with $x(0) = x_0$, pointwise on $[0,\infty)$.

4 Modification of operators with non-singular kernel

We consider operators of exponential kernel (Caputo-Fabrizio). Analogous results hold for those with Mittag-Leffler kernel. Since

$${}^{CF}D^{\alpha}t = \frac{1}{\alpha}\left(1 - \mathrm{e}^{-\frac{\alpha}{1-\alpha}t}\right) = c_{\alpha}(t) \sim \frac{1}{1-\alpha}t,$$

we define

$${}^{NCF}D^{\alpha}x(t) = \frac{1}{(1-\alpha)c_{\alpha}(t)} \int_0^t \mathrm{e}^{-\frac{\alpha}{1-\alpha}(t-s)} x'(s)\mathrm{d}s. \tag{8}$$

It is clear that the units of (8) are time^{-1}, by the division by $c_{\alpha}(t)$. Therefore, the new operator represents some sort of rate of change, in contrast to the standard one. Definition (8) is well posed for $t = 0$:

$${}^{NCF}D^{\alpha}x(0) = \lim_{t\to 0^+} \mathrm{e}^{-\frac{\alpha}{1-\alpha}t} \cdot \frac{1}{t} \int_0^t \mathrm{e}^{\frac{\alpha}{1-\alpha}s} x'(s)\mathrm{d}s = x'(0).$$

One can thus work with differential equations of the form

$${}^{NCF}D^{\alpha}x(t) = f(t, x(t)),$$

avoiding inconsistencies at $t = 0$. The associated integral operator,

$${}^{NCF}J^{\alpha}x(t) = (1-\alpha)c_{\alpha}(t)x(t) + \alpha \int_0^t c_{\alpha}(s)x(s)\mathrm{d}s,$$

does satisfy the fundamental theorem of calculus: for a continuously differentiable function x,

$${}^{NCF}J^{\alpha} \circ {}^{NCF}D^{\alpha}x(t) = x(t) - x(0), \quad {}^{NCF}D^{\alpha} \circ {}^{NCF}J^{\alpha}x(t) = x(t).$$

References

[1] M. Jornet, Theory on new fractional operators using normalization and probability tools, ArXiv preprint, arXiv:2403.06198 (2024).

[2] M. Jornet, J.J. Nieto, Power-series solution of the L-fractional logistic equation, Applied Mathematics Letters, **154** (2024), 109085.

[3] M. Jornet, Theory on linear L-fractional differential equations and a new Mittag-Leffler-type function, ArXiv preprint, arXiv:2403.00341 (2024).

International Conference on Mathematical Analysis and Applications in Science and Engineering
ICMA^{2}SC'24
ISEP Porto-Portugal, June 20 - 22, 2024

Modelling optimal control of the piecewise-fractional Ebola model

Silvério Rosa[1⋆⋆] **Faïçal Ndaïrou**[2]

[1] Instituto de Telecomunicações (IT) and Department of Mathematics, University of Beira Interior, Covilhã, Portugal
[2] Center for Research and Development in Mathematics and Applications (CIDMA), University of Aveiro, Portugal

[1⋆]rosa@ubi.pt

Abstract: A recently proposed fractional-order mathematical model of the Caputo type was developed for Ebola [1]. We improve and generalise that model, beginning with its correction. We then formulate and numerically solve a fractional optimal control (FOC) problem using the rate of vaccination as the control variable. This work presents research on fitting real data from Guinea, Liberia, and Sierra Leone, which is available at the World Health Organisation (WHO). We perform a cost-effectiveness analysis to evaluate the cost and effectiveness of the control measure during the intervention. We conclude that the fractional control is only more efficient than classical control for a portion of the time interval. Hence, we suggest a system where the derivative order changes over time, becoming fractional or classical when it makes sense. This type of variable-order fractional model, known as piecewise derivative with fractional Caputo derivatives, is the most successful in managing the illness.

keywords: Ebola; compartmental mathematical models; fractional-order optimal control; piecewise derivative.

MSC2020: 34A08; 49M05; 92C60.

References

[1] Faïçal Ndaïrou, Moein Khalighi, and Leo Lahti. Ebola epidemic model with dynamic population and memory. *Chaos Solitons Fractals*, 170:Paper No. 113361, 7, 2023.

⋆Supported by The Portuguese Foundation for Science and Technology (FCT-Fundação para a Ciência e a Tecnologia), grants number UIDB/50008/2020 (S.R.)

International Conference on Mathematical Analysis and Applications in Science and Engineering
ICMA^{2}SC'24
ISEP Porto-Portugal, June 20 - 22, 2024

Extension of a fractional model identification method for fractional dual-pole plus dead-time models

Juan J. Gude[1⋆] **Gaizka Heppe**[1] **Pablo García Bringas**[1]

[1] University of Deusto, Spain

[1⋆]jgude@deusto.es

Abstract: This paper proposes the extension of a recently proposed analytical identification method of fractional-order models based on the process reaction curve for the fractional double-pole plus dead-time model. This procedure is based on three arbitrary points of the process reaction curve, which is obtained by an open-loop step-test experiment.

keywords: fractional dual-pole plus dead-time model; fractional first-order plus dead-time model; fractional-order systems; process identification.

MSC2020: 26A33; 23A08; 93-10.

1 Introduction

Recently, different analytical procedures have been presented for identifying fractional first-order plus dead-time (FFOPDT) models for processes with overdamped step response [1]. These procedures are characterized by being based on fitting three points on the process reaction curve and by their simplicity of implementation.

In this work, a fractional dual-pole plus dead-time (FDPPDT) model identification procedure is proposed based on three arbitrary points on the process reaction curve, which is obtained by an open-loop step-test experiment.

2 Results and discussion

The processes considered in this work are characterized by having an S-shaped step response and can be represented by an FDPPDT model, which transfer function can be expressed as:

$$P(s) = \frac{Y_\alpha(s)}{U(s)} = \frac{Ke^{-Ls}}{(1+Ts^\alpha)^2}, \tag{1}$$

where $y_\alpha(t)$ is the process output, $u(t)$ is the input signal, K is the process gain, $T > 0$ its dual-pole time constant, $L \geq 0$ its apparent dead time, and α the fractional order of the model.

The time-domain expression for the FDPPDT model (1) response to a step-input signal with amplitude Δu is:

$$y_\alpha(t) = \begin{cases} 0, & 0 \leq t < L \\ K\Delta u \left\{ 1 - \left(1 + \frac{(t-L)^\alpha}{T} \right) E_\alpha \left[-\frac{1}{T}(t-L)^\alpha \right] \right\}, & t \geq L \end{cases} \tag{2}$$

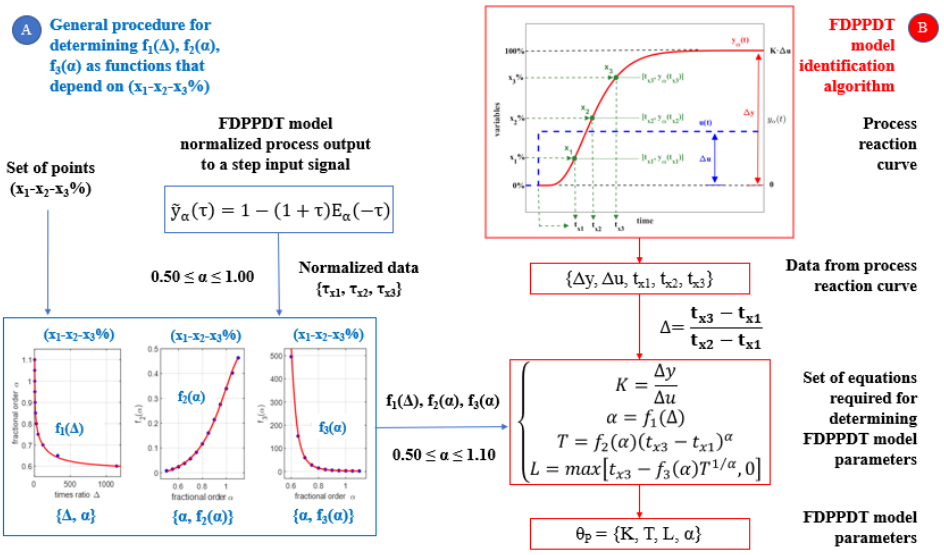

Figure 1: Complete diagram of the procedure to identify the parameters of the fractional-order model considering three arbitrary points on the process reaction curve.

where the output signal change is $\Delta y = K \cdot \Delta u$ and E_α is the one-parameter Mittag-Leffler function.

General equations:

The following set of equations includes the general expressions that have been derived for determining the parameters of the FDPPDT model, $\theta_P = \{K, T, L, \alpha\}$, using the times required for the response to reach any three points on the reaction curve, $\{\Delta y, \Delta u, t_{x1}, t_{x2}, t_{x3}\}$:

$$\begin{cases} K = \dfrac{\Delta y}{\Delta u} \\ \alpha = f_1(\Delta) \\ T = f_2(\alpha)\left(t_{x3} - t_{x1}\right)^{\alpha} \\ L = max\left[t_{x3} - f_3(\alpha)T^{1/\alpha}, 0\right] \end{cases} \tag{3}$$

Figure 1 shows schematically the procedure to obtain the functions $f_1(\Delta)$, $f_2(\alpha)$ and $f_3(\alpha)$ from experimental data. It also shows the procedure to estimate the parameters of the FDPPDT model from three arbitrary points (x_1-x_2-x_3%) on the process reaction curve.

Experimental results:

For illustrative purposes, the following higher-order lag-dominated fractional-order process model, suggested in [4], is used:

$$P_1(s) = \frac{K_1}{(1 + T_1 s^{\lambda_1})^n}, \tag{4}$$

where $K_1 = 2$, $T_1 = 1$ s, $n = 5$, and $\lambda_1 = 0.85$.

The parameters of the FDPPDT model have been determined using the proposed method. In addition, several FFOPDT models for the process P_1 have also been obtained using various fractional identification methods. More specifically, FFOPDT models have been obtained using the methods based on the reaction curve of the process proposed by Gude et al. in [2], in [3] for the symmetrical set of points (5-50-95%) and (10-50-90%), and following the three strategies proposed by Tavakoli-Kakhki in [4].

Table 1 shows the accuracy of each of the identified models in terms of the mean squared error (S) between the step response of the identified model and the reaction curve of process P_1.

Table 1: Time-domain performance index values $S(\theta_{1,j})$ determined using the models estimated using different identification procedures for the process P_1.

j	**Technique**	**Model**	**Set of points**	$S(\theta_{1,j})$
1	Proposed	FDPPDT	(10-50-90%)	$6.25 \cdot 10^{-5}$
2	Gude Mittag-Leffler [2]	FFOPDT	(10-90%)	$2.56 \cdot 10^{-4}$
3	Gude Symmetrical [3]	FFOPDT	(5-50-95%)	$6.29 \cdot 10^{-4}$
4	Gude Symmetrical [3]	FFOPDT	(10-50-90%)	$9.19 \cdot 10^{-4}$
5	Tavakoli-Kakhki 1 [4]	FFOPDT	–	$1.10 \cdot 10^{-3}$
6	Tavakoli-Kakhki 2 [4]	FFOPDT	–	$1.80 \cdot 10^{-3}$
7	Tavakoli-Kakhki 3 [4]	FFOPDT	–	$5.58 \cdot 10^{-4}$
		$N_S = 2,501$		

This table illustrates that the proposed method reduces the value of S by 74%, 90%, 93%, 94%, 96%, and 87% compared to the procedures proposed by Gude with the Mittag-Leffler based method, for the symmetrical method with (5-50-95%) and (10-50-90%), and for the three strategies proposed by Tavakoli-Kakhki, respectively.

3 Conclusions and Future work

This paper presents a new method to identify FDPPDT models applied to describe the dynamic behavior of processes with overdamped step response. The proposed approach uses information collected from the process reaction curve obtained by applying an open-loop step test experiment.

The authors believe that this approach that finds an appropriate balance between simplicity of the procedure and accuracy of the identified model will promote the adoption of this type of reduced-order fractional models at the industrial level.

Acknowledgments

Juan J. Gude and Pablo García Bringas thank the Basque Government for its funding support through the BEREZ-IA Elkartek project (ref. KK-2023/00012).

References

[1] Juan J. Gude, Contributions to fractional-order modelling and control of dynamic systems: A theoretical and practical approach, University of Deusto, (2023).

[2] Juan J. Gude, A. Di Teodoro, O. Camacho, P. García Bringas, A new fractional reduced-order model-inspired system identification method for dynamical systems, IEEE Access, **11**, (2023), 103214–103231.

[3] Juan J. Gude, P. García Bringas, Proposal of a general identification method for fractional-order processes based on the process reaction curve, Fractal and Fractional, **6**(9), (2022), 526.

[4] M. Tavakoli-Kakhki, M. Haeri, M.S. Tavazoei, Simple fractional order model structures and their applications in control system design, European Journal of Control, **16**(6), (2010), 680–694.

International Conference on Mathematical Analysis and Applications in Science and Engineering ICMA²SC'24

ISEP **Porto-Portugal, June 20 - 22, 2024**

TWO NEW RHEOLOGICAL MODELS AND TWO RHEOLOGICAL DYNAMICAL SYSTEMS FRACTIONAL TYPE

(In Honor of Prof Tenreiro Machado, Scientist and our Scientific Friend)

Katica R. (Stevanović) Hedrich[1*,2,3]

[1] Mathematical Institute of Serbian Academy of Science and Arts, Serbia
[2] University of Niš,Faculty of Mechanical Engineering, Serbia
[3] Serbian Scientific Society, Serbia

1*katicah@mi.sanu.ac.rs,katicahedrih@gmail.com

Abstract: Two new basic complex rheological models of ideal materials, fractional type are defined by structural formulas and constitutive relations. A new model the fluid - Newron's ideally viscous fluid flow, fractional type, was introduced. A new modified Kelvin-Voigt's model, fractional type, was defined in parallel coupling of Newron's ideally viscous fluid flow, fractional type with Hooke's ideally elastic material model. By series linking the new model the fluid - Newron's ideally viscous fluid flow, fractional type with the model Hooke's ideally elastic material, a new modified model Maxwell's model of fractional type is defined, which is one of the two basic complex models of ideal materials. Two new rheological dynamic systems of the fractional type, oscillator or crawler type were formed as dynamic systems, which in their structure contain, as a link, standard light models of the fractional type, defined as complex rheological models of materials. Their dynamics are described by differential equations of fractional order and the dualities of their dynamics are shown. The emergence of internal degrees of freedom of movement was indicated.

keywords: rheological models of ideal materials of the fractional type, Newron's ideally viscous fluid flow of the fractional type, new rheological dynamic systems of the fractional type, internal degrees of freedom of movement

MSC2020: 34A08; 74B05; 74A20;74-xx; 74hXX.

1 Introduction

The author, together with his colleagues, previously researched the dynamics of oscillating discrete systems with one and more degrees of freedom of oscillation, of the fractional type, applying the mathematical description with differential equations of the fractional order. For details, see References [1, 2]. Reference [3] shows the results of research on the topic Elements of mathematical phenomenology and analogies of electrical and mechanical oscillators of the fractional type with finite number of degrees

of freedom of oscillations: linear and nonlinear modes.
In this paper, only a small part of the author's new, not jet published, scientific results, which she obtained in a more complex research on rheological models [4] of ideal materials and the dynamics of rheological dynamic systems, fractional type, is obtained. The author, in a more complex investigation, obtained a large number of results about numerous new rheological models, of fractional type, with appropriate structural, formulas and constitutive relations, which contain differential operators of fractional order. Graphs of the structures of the basic complex rheological models of ideal materials, of the fractional type, with the accompanying differential connections of normal stresses and axial dilations, of the fractional order, are obtained. The compensation elasticity surface, as well as the stress relaxation property, are obtained as a function of time and the exponent of the order of fractional differentiation. An overview of a series of complex rheological models, fraction type with accompanying constitutive relations, fractional order and corresponding Laplace transformations of the solution, which describe the properties of normal stress or axial dilatation of the material model is also new research results. Some models describe the properties of ideal materials, which can be elasto-viscous solids, or visco-elastic fluids.
Using the newly introduced basic complex, as well as hybrid complex rheological models, of the fractional type, the dynamics of a series of mechanical rheological systems of oscillators or pulsators, of the fractional type, with corresponding independent generalized coordinates, external and internal degrees of freedom of movement were studied. Laplace transformations of solutions for independent generalized coordinates, external and internal degrees of freedom of system dynamics were determined. On those specimens, it was shown that complex rheological models, of the fractional type, introduce internal degrees of freedom into the dynamics of the rheological dynamical system. New tasks appear, as challenges for mathematicians, translating Laplace transformations of solutions by coordinates, by mechanical normal stress or axial dilations into the time domain. A number of those translations of Laplace transformations of solutions into the time domain were done by the author.

2 Two models of basic complex ideal materials fractional type

The basic material models are [4]:
* Hooke's ideally elastic material – a solid body with the property of ideal elasticity
* Newron's ideal viscous material - viscous fluid with the property of viscous fluid flow
* Saint Venant's ideal plastic material - a rigid body with the property of plastic yielding when the load exceeds the yield point
In this paper, we intend to introduce one more ideal models based on their characteristics. The first new model is a generalization of the model of Newron's ideally viscous material based on the constitutive relationship between the normal stress and the rate of axial dilatation by derivation of non-integer order, by introducing a differential operator of non-integer, fractional order [3],

$$\mathfrak{D}_t^{\alpha}\left[x(t)\right]=\frac{d^{\alpha}x(t)}{dt^{\alpha}}=x^{(\alpha)}(t)=\frac{1}{\Gamma(1-\alpha)}\frac{d}{dt}\int_0^t\frac{x(\tau)}{(t-\tau)^{\alpha}}d\tau,\quad for\quad 0<\alpha\le 1 \tag{1}$$

(for example, $\sigma_{z,\alpha}=\mathbf{E}_{\alpha}\mathfrak{D}_t^{\alpha}\left[\varepsilon_z\right]$), in which is determined by an exponent $0<\alpha<1$ between zero and one. It is a generalization of the viscous dissipative element and includes it.
Such models of basic ideal materials with pure ideal properties, can be combined into hybrid complex models, where by one pair of models of basic materials can be connected in two ways:
a*serial – in a series, which is indicated by a horizontal line "-" between the elements;
and b* parallel, which is indicated by a vertical line "/" between the elements.
The picture shows the models of basic complex materials from two basic models of ideal materials,

fractional type. Modified Kelvin's or Voigt's model of the fractional type, denoted by and it is one of the two basic complex models of ideal materials, created from two basic models of ideal materials connected in parallel, Hooke's ideally elastic and modified Newton's fractional fluid type and has structural formula $\mathbf{K}_\alpha = (\mathbf{H}/\mathbf{N}_\alpha)$, see model presented at right part in Figure 1. Modified Maxwell's model of fractional type, is one of the two basic complex models of materials, $\mathbf{M}_\alpha$, ordinarily (serially) connected basic models of ideal materials Hooke's $\mathbf{H}$ ideally elastic and modified and Newton's ideal fluid $\mathbf{N}_\alpha$ fractional type has the structural formula $\mathbf{M}_\alpha = (\mathbf{H} - \mathbf{N}_\alpha)$, see model presented at left part in Figure 2.

3 Two rheological dynamical systems fractional type

3.1. The rheological dynamical oscillator fractional type

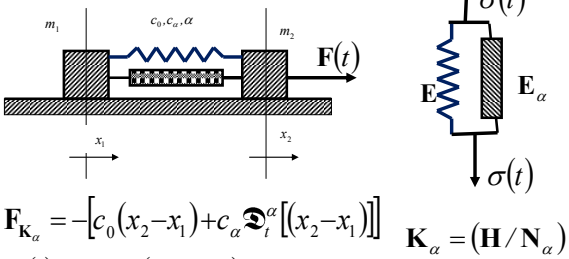

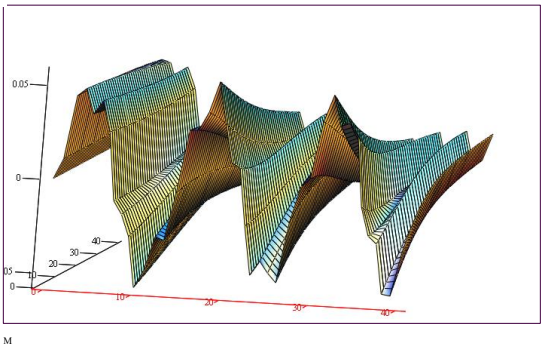

Figure 1. a)System of two material points, mass m_1 and m_2 bound by an easy modified Kelvin-Voigt model, fractional type, stiffness c_0 and c_α, , as a system with two degrees of freedom of movement, and one degree of freedom of oscillation, of one material point in relation to the second, whose positions are determined by coordinates x_1 and x_2; b) Graphic representation of the space surface of a particular solution of an ordinary inhomogeneous differential equation, fractional order, which describes the elongation $x_{prtt}(t)$ of the forced mode, fractional type, for an oscillator with one degree of freedom of forced oscillations, fractional type, in the coordinate system: $x_{prtt}(t)$ elongation of the forced mode, time and exponent α of the fractional order of differentiation in the interval, $0 < \alpha < 1$, and for the circular frequency . $\Omega_0 = 10$

We introduce the symbols $\tilde{\omega}_0^2 = \frac{c(m_1 + m_2)}{m_1 m_2}$, $\tilde{\omega}_\alpha^2 = \frac{c(m_1 + m_2)}{m_1 m_2}$ and $\tilde{h} = \frac{m_1 F_0 sin(\Omega t + \varphi_0)}{m_1 m_2}$,we introduce a new independent generalized coordinate $x(t) = [x_2(t) - x_1(t)]$, which represents the relative displacement of one material point in relation to another. Now, we write the ordinary inhomogeneous differential equation, of fractional order, of the oscillation of one material point with respect to another, in the form:

$$\ddot{x}(t) + \tilde{\omega}_0^2 x(t) + \tilde{\omega}_\alpha^2 \mathfrak{D}_t^\alpha [x(t)] = \tilde{h}\, sin(\Omega t + \varphi_0)$$

Then the analytical approximate solution of the previous non-homogeneous ordinary differential equation, of fractional order, from the interval is of the form:

$$x(t) = \sum_{k=0}^{\infty} (-1)^k \omega_\alpha^{2k} t^{2k} \sum_{j=0}^{k} \binom{k}{j} \frac{\omega_\alpha^{2j} t^{-\alpha j}}{\omega_o^{2j}} \left[\frac{x_0}{\Gamma(2k + 1 - \alpha j)} + \frac{\dot{x}_0 t}{\Gamma(2k + 2 - \alpha j)} \right] + \\ + \int_0^t \left\langle h\, sin(\Omega(t - \tau)) + \varphi_0 \right\rangle \left\langle \sum_{k=0}^{\infty} (-1)^k \omega_\alpha^{2k} \tau^{2k+1} \sum_{m=0}^{k} \binom{k}{m} \frac{\omega_\alpha^{-2m} \tau^{-\alpha m}}{\omega_0^{2m} \Gamma(2k + 2 - \alpha m)} \right\rangle d\tau \qquad , \alpha \in (0.1) \qquad (2)$$

3.2. The rheological dynamical crawler, fractional type

Let's introduce the following notations: $\omega_0^2 = \frac{c_0}{m}$ $\omega_\alpha^2 = \frac{c_\alpha}{m}$ $h_0 = \frac{F_0}{m}$, and cores-ponding systems of inhomogeneous differential equations of fractional order, dynamics of rheological

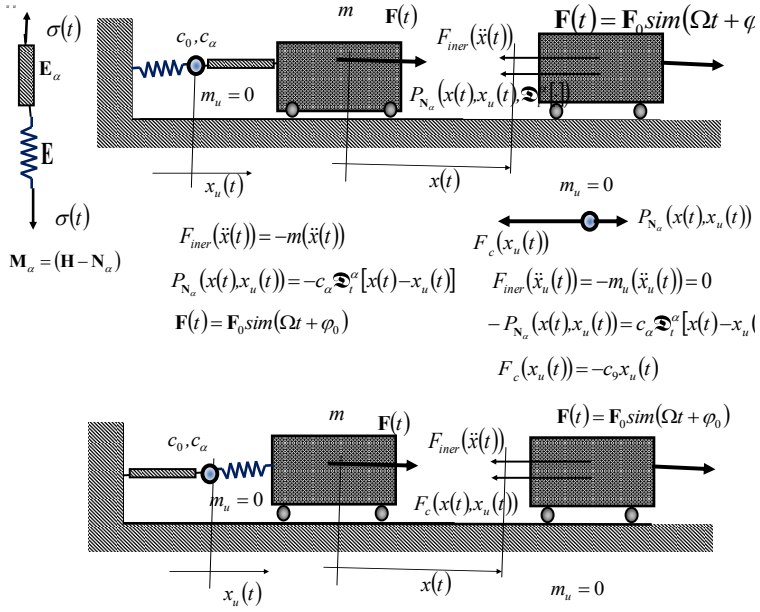

Figure 2. Rheological dynamic system (shown in up part of the figure) of one material point, mass m bound by a basic complex Maxwell model of ideal, fractional type of material, with the property of stress relaxation, stiffness c and c_α, as a system with one external and one internal degree of freedom of movement, whose positions are determined by independent generalized coordinates x and $x_{u,1}$; On the lower part of the scaffold, reverse the order of tying the structure of the light basic complex Maxwell model of the ideal, fractional type, material;

dynamic systems of fractional order from Figure 2, are in the form:

$$\ddot{x}+\omega_\alpha^2 \mathfrak{D}_t^\alpha\left[x(t)-x_{u,1}(t)\right]=h_0 sin(\Omega t+\varphi_0) \qquad \ddot{x}+\omega_0^2\left(x(t)-x_{u,1}(t)\right)==h_0 sin(\Omega t+\varphi_0)$$

$$-\omega_\alpha^2 \mathfrak{D}_t^\alpha\left[x(t)-x_{u,1}(t)\right]+\omega_0^2 x_{u,1}(t)=0 \qquad -\omega_0^2\left(x(t)-x_{u,1}(t)\right)+\omega_\alpha^2 \mathfrak{D}_t^\alpha\left[x_{u,1}(t)\right]=0 \quad (3)$$

Laolace's transformation $\mathfrak{L}\{x(t)\}$ of the external independent generalized coordinate $\{x(t)\}$ and Laolace's transform $\mathfrak{L}\{x_{u,1}(t)\}$ of the internal independent generalized coordinate $x_{u,1}(t)$ in the form:

$$\mathfrak{L}\{x(t)\}=\frac{(px_0+\dot{x}_0)}{\left\langle p^2+\omega_\alpha^2 p^\alpha-\frac{\omega_\alpha^4 p^{2\alpha}}{\left\langle \omega_0^2+\omega_\alpha^2 p^\alpha\right\rangle}\right\rangle}+\frac{1}{\left\langle p^2+\omega_\alpha^2 p^\alpha-\frac{\omega_\alpha^4 p^{2\alpha}}{\left\langle \omega_0^2+\omega_\alpha^2 p^\alpha\right\rangle}\right\rangle}\cdot\frac{h_0\Omega}{p^2+\Omega^2},\ \mathfrak{L}\{x_{u,1}(t)\}=\frac{\omega_\alpha^2 p^\alpha}{\left\langle \omega_0^2+\omega_\alpha^2 p^\alpha\right\rangle}\mathfrak{L}\{x(t)\} \quad (4)$$

4 Conclusions and Future work

By comparing the obtained expressions for both natural and forced movements of the material point, we see that the way of predicting this structure of the modified rheological Maxwell model of the ideal, fractional type, has a greater influence on the resulting movement-creep of the system elements.

Acknowledgments. The Author presented some ideas and results, which is in the field of application to biomaterials. Dr. Andjelka Hedrich, was the inspiration for the basic ideas of this research rheological models in biomaterials.

References

[1] Hedrih (Stevanović), K. R, Machado, J. T. (2015), Discrete fractional order system vibrations, International Journal Non-Linear Mechanics, 73, 2–11

[2] Hedrih (Stevanović), K. R, Hedrih, A. N. (2023), "The Kelvin–Voigt visco-elastic model involving a fractional-order time derivative for modelling torsional oscillations of a complex discrete biodynamical system," Acta Mechanica, 234, pp. 1923–1942.

[3] Hedrih (Stevanović), R. K, Milovanović, V. G. Elements of mathematical phenomenology and analogies of electrical and mechanical oscillators of the fractional type with finite number of degrees of freedom of oscillations: linear and nonlinear modes (under review).

[4] Hedrih (Stevanović), R. K, Izabrana poglavlja Teorije elastičnosti (Selected chapters of Theory of Elasticity), Izdanje - prošireno i dopunjeno, Mašinski fakultet u Nišu, 1988, p. 425. http://elibrary.matf.bg.ac.rs/handle/123456789/3766

International Conference on Mathematical Analysis and Applications in Science and Engineering
ICMA^{2}SC'24
ISEP Porto-Portugal, June 20 - 22, 2024

A Novel Crossover Dynamics of Monkeypox Disease Mathematical Model Using Fractional Differential Equations Based on the Ψ-Caputo Derivative: Numerical Treatments

N. H. Sweilam[1,*], S. M. AL-Mekhlafi[2]

[1,*] Mathematics Department, Faculty of Science, Cairo University, Giza, Egypt
[2]Department of Mathematics, Faculty of Education, Sana'a University, Yemen

nsweilam@sci.cu.edu.eg[1,*], sih.almikhlafi@su.edu.ye[2]

Abstract: A novel crossover model for monkeypox disease that incorporates Ψ-Caputo fractional derivatives is presented here, where we use a simple nonstandard kernel function Ψ. We can be obtained have the Caputo and Caputo-Katugampola derivatives as special cases from the proposed derivative. Four different models of variable-order, fractional order, fractal fractional, and fractional stochastic derivatives driven by fractional Brownian motion (FBM) are defined in four-time intervals for the crossover dynamics model. Ψ-nonstandard finite difference method (Ψ-NFDM) is constructed to solve the mathematical models of variable order, fractional order, and fractal fractional order. Also, the nonstandard modified Euler Maruyama method (NMEMM) is used to study the fractional stochastic model. Numerous numerical tests and comparisons with real data were conducted to validate the methods' efficacy and support the theoretical conclusions.

keywords: Crossover model for monkeypox disease; Ψ-Caputo fractional derivative; Nonstandard modified Euler Maruyama method.

MSC2020: 65B10; 34F5; 65Q10.

1 Introduction

The mathematical model of monkeypox disease [1] was extended to Ψ-Caputo piecewise fractional-variable-order-fractal-fractional-fractional stochastic monkeypox disease in the following by employing the concept of a piecewise differential equation system. The deterministic model is extended fractional using Ψ-Caputo operator in the range $0 < t \leq t_1$ and using Ψ-Caputo variable order operator in the range $t_1 < t \leq t_2$, and fractal-fractional order in $t_2 < t \leq t_3$, the fractional stochastic differential equation (FSDE) is extended in the range $t_3 < t \leq T_f$. In order to be compatible with the physical model problem, a new parameter ζ is given. Additionally, by adding an auxiliary parameter called ζ to the variable order fractional model, we prevent

dimensional incompatibilities [2]. The resulting system can be written as follows:

$$\begin{cases} \zeta^{\mu-1C}D^{\mu,\Psi}S_H &= A_H - \frac{(b_1+b_2)I_H(t)S_H(t)}{N_H} + vQ_H - m_H S_H, \\ \zeta^{\mu-1C}D^{\mu,\Psi}E_H &= \frac{(b_1+b_2)I_H(t)S_H(t)}{N_H} - (a_1+a_2+m_H)E_H, \qquad 0 < t \le t_1, \\ \zeta^{\mu-1C}D^{\mu,\Psi}I_H &= a_1E_H - (m_H+d_H+r)I_H, \\ \zeta^{\mu-1C}D^{\mu,\Psi}Q_H &= a_2E_H - (v+u+m_H+d_H)Q_H, \\ \zeta^{\mu-1C}D^{\mu,\Psi}R_H &= rI_H + uQ_H - m_H R_H, \\ \zeta^{\mu-1C}D^{\mu,\Psi}S_R &= A_R - \frac{b_3S_RI_R}{N_R} - m_R S_R, \\ \zeta^{\mu-1C}D^{\mu,\Psi}E_R &= \frac{b_3S_RI_R}{N_R} - (a_3+m_R)E_R, \\ \zeta^{\mu-1C}D^{\mu,\Psi}I_R &= a_3E_H - (d_R+m_R)I_R, \end{cases} \tag{1}$$

with initial conditions

$$\begin{aligned} &I_H(t_0) = i_{H_0} \ge 0, S_H(t_0) = s_{H_0} \ge 0, E_H(t_0) = e_{H_0} \ge 0, \\ &R_H(t_0) = r_{H_0} \ge 0, S_R(t_0) = s_{r_0} \ge 0, E_R(t_0) = e_{R_0} \ge 0, \\ &I_R(t_0) = i_{R_0} \ge 0, Q_H(t_0) = q_{H_0} \ge 0. \end{aligned} \tag{2}$$

In $t_2 \ge t > t_1$, the model can be represented in the following way:

$$\begin{cases} \zeta^{\mu(t)-1C}D^{\mu(t),\Psi}S_H &= A_H - \frac{(b_1+b_2)I_H(t)S_H(t)}{N_H} + vQ_H - m_H S_H, \\ \zeta^{\mu(t)-1C}D^{\mu(t),\Psi}E_H &= \frac{(b_1+b_2)I_H(t)S_H(t)}{N_H} - (a_1+a_2+m_H)E_H, \qquad t_2 \ge t > t_1, \\ \zeta^{\mu(t)-1C}D^{\mu(t),\Psi}I_H &= a_1E_H - (m_H+d_H+r)I_H, \\ \zeta^{\mu(t)-1C}D^{\mu(t),\Psi}Q_H &= a_2E_H - (v+u+m_H+d_H)Q_H, \\ \zeta^{\mu(t)-1C}D^{\mu(t),\Psi}R_H &= rI_H + uQ_H - m_H R_H, \\ \zeta^{\mu(t)-1C}D^{\mu(t),\Psi}S_R &= A_R - \frac{b_3S_RI_R}{N_R} - m_R S_R, \\ \zeta^{\mu(t)-1C}D^{\mu(t),\Psi}E_R &= \frac{b_3S_RI_R}{N_R} - (a_3+m_R)E_R, \\ \zeta^{\mu(t)-1C}D^{\mu(t),\Psi}I_R &= a_3E_H - (d_R+m_R)I_R, \end{cases} \tag{3}$$

$$\begin{aligned} &S_H(t_1) = s_{H_1} \ge 0, E_H(t_1) = e_{H_1} \ge 0, I_H(t_1) = i_{H_1} \ge 0, Q_H(t_1) = q_{H_1} \ge 0, \\ &R_H(t_1) = r_{H_1} \ge 0, S_R(t_1) = s_{r_1} \ge 0, E_R(t_1) = e_{R_1} \ge 0, I_R(t_1) = i_{R_1} \ge 0. \end{aligned} \tag{4}$$

In $t_3 \ge t > t_2$‘, the model can be represented in the following way:

$$\begin{cases} \zeta^{\mu-1C}D^{\mu,\nu,\Psi}S_H &= A_H - \frac{(b_1+b_2)I_H(t)S_H(t)}{N_H} + vQ_H - m_H S_H, \\ \zeta^{\mu-1C}D^{\mu,\nu,\Psi}E_H &= \frac{(b_1+b_2)I_H(t)S_H(t)}{N_H} - (a_1+a_2+m_H)E_H, \qquad t_3 \ge t > t_2, \\ \zeta^{\mu-1C}D^{\mu,\nu,\Psi}I_H &= a_1E_H - (m_H+d_H+r)I_H, \\ \zeta^{\mu-1C}D^{\mu,\nu,\Psi}Q_H &= a_2E_H - (v+u+m_H+d_H)Q_H, \\ \zeta^{\mu-1C}D^{\mu,\nu,\Psi}R_H &= rI_H + uQ_H - m_H R_H, \\ \zeta^{\mu-1C}D^{\mu,\nu,\Psi}S_R &= A_R - \frac{b_3S_RI_R}{N_R} - m_R S_R, \\ \zeta^{\mu-1C}D^{\mu,\nu,\Psi}E_R &= \frac{b_3S_RI_R}{N_R} - (a_3+m_R)E_R, \\ \zeta^{\mu-1C}D^{\mu,\nu,\Psi}I_R &= a_3E_H - (d_R+m_R)I_R, \end{cases} \tag{5}$$

with

$$\begin{aligned} &S_H(t_2) = s_{H_2} \ge 0, E_H(t_2) = e_{H_2} \ge 0, I_H(t_2) = i_{H_2} \ge 0, Q_H(t_2) = q_{H_2} \ge 0, \\ &R_H(t_2) = r_{H_2} \ge 0, S_R(t_2) = s_{r_2} \ge 0, E_R(t_2) = e_{R_2} \ge 0, I_R(t_2) = i_{R_2} \ge 0, \end{aligned} \tag{6}$$

In $T_f \geq t > t_3$, the model can be represented in the following way:

$$\begin{cases} dS_H &= (A_H - \frac{(b_1+b_2)I_H(t)S_H}{(}t)N_H + vQ_H - m_H S_H)dt + \sigma_1 S_H(t)dB_1^{H^*}, \\ dE_H &= (\frac{(b_1+b_2)I_H(t)S_H(t)}{N_H} - (a_1+a_2+m_H)E_H)dt + \sigma_2 E_H(t)dB_2^{H^*}, \qquad T_f \geq t > t_3, \\ dI_H &= (a_1 E_H - (m_H + d_H + r)I_H)dt + \sigma_3 I_H(t)dB_3^{H^*}, \\ dQ_H &= (a_2 E_H - (v+u+m_H+d_H)Q_H)dt + \sigma_4 Q_H(t)dB_4^{H^*}, \\ dR_H &= (rI_H + uQ_H - m_H R_H)dt + \sigma_5 E_H(t)dB_5^{H^*}, \\ dS_R &= (A_R - \frac{b_3 S_R I_R}{N_R} - m_R S_R)dt + \sigma_6 S_R(t)dB_6^{H^*}, \\ dE_R &= (\frac{b_3 S_R I_R}{N_R} - (a_3+m_R)E_R)dt + \sigma_7 E_R(t)dB_7^{H^*}, \\ dI_R &= (a_3 E_H - (d_R+m_R)I_R)dt + \sigma_8 I_R(t)dB_8^{H^*}, \end{cases} \tag{7}$$

$$\begin{aligned} S_H(t_3) = s_{H_3} \geq 0, E_H(t_3) = e_{H_3} \geq 0, I_H(t_3) = i_{H_3} \geq 0, Q_H(t_3) = q_{H_3} \geq 0, \\ R_H(t_3) = r_{H_3} \geq 0, S_R(t_3) = s_{r_3} \geq 0, E_R(t_3) = e_{R_3} \geq 0, I_R(t_3) = i_{R_3} \geq 0, \end{aligned} \tag{8}$$

2 Results and discussion

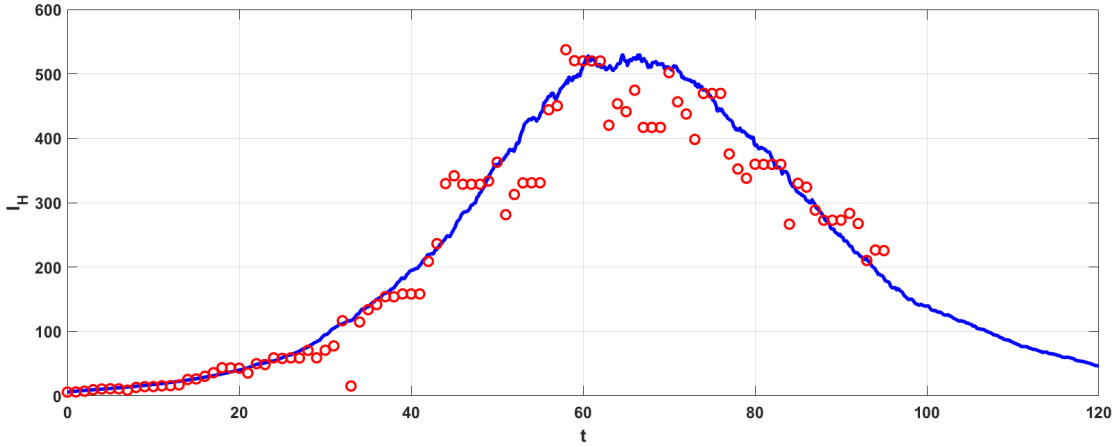

Figure 1: Monkeypox data from the United States (June 13 to September 16, 2022), with a 7-day moving average fitted compared with the obtained results when $\epsilon = 1, \varrho = 0, \eta = 1, H^* = 0.5, \mu = 0.98, \nu = 0.98, \mu(t) = 0.99 - 0.001t$.

3 Conclusions and Future Work

This study focuses on studying a novel crossover models for monkeypox disease that incorporates Ψ-Caputo fractional derivatives. Four different models of variable-order, fractional order, fractal fractional, and fractional stochastic derivatives are defined in four-time subintervals. Two simple numerical methods were constructed to solve the proposed models. These methods are Ψ-NSFD to solve the deterministic models and NMEMM to solve the fractional stochastic differential equations driven by FBM. The selection of this generalized-Caputo operator in our work is grounded in several merits that make it a suitable choice for our study due to its versatility, suitability for modeling fractional order systems, and its ability to capture complex dynamics. Overall, our Ψ-fractional system can be reduced to a classical Caputo system using $\Psi(t) = t, \eta = 1, \epsilon = 1, \varrho = 0$, and Caputo-Katugampola derivative when $\Psi(t) = t^{\epsilon}, \eta = 1, \varrho = 0$.

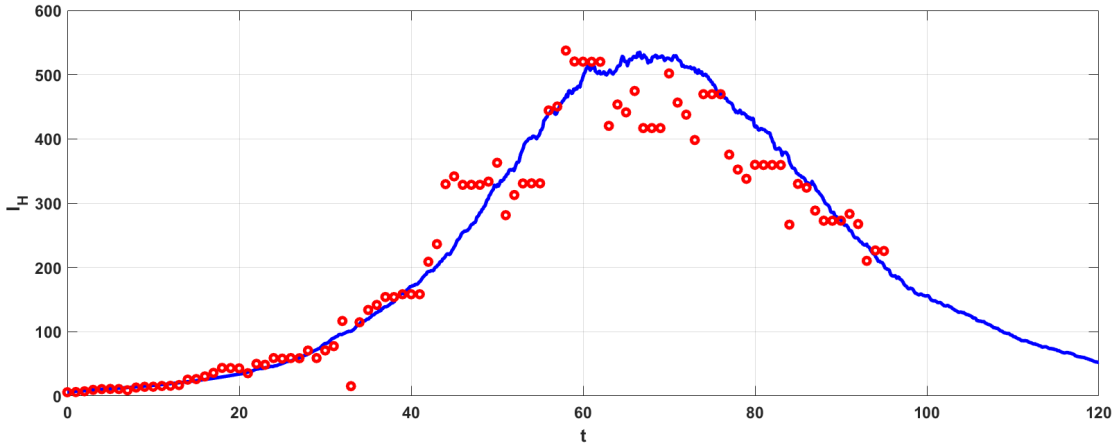

Figure 2: Monkeypox data from the United States (June 13 to September 16, 2022), with a 7-day moving average fitted compared with the obtained results when $\epsilon = 0.97, \varrho = 0.95, \eta = 0.98, H^* = 0.98, \mu = 0.97, \nu = 0.95, \mu(t) = 0.99 - 0.001t$.

We demonstrated from comparing our result with real data that it is not necessary to use nontrivial functions Ψ to advance the state of the art. Indeed, we outperform existing classical and fractional models in the literature by using a simple nonstandard kernel function. In future work, we will extend this work to control the proposed model problem with time delay.

References

[1] O. J. Peter, S. Kumar, N. Kumari, F. A. Oguntolu, K. Oshinubi, & R. Musa, Transmission dynamics of Monkeypox virus: a mathematical modelling approach. *Modeling Earth Systems and Environment,* 8(3), 3423-3434, (2022).

[2] J.F.Gómez-Aguilar, J. J.Rosales-García, J.J. Bernal-Alvarado,T. Córdova-Fraga, R. Guzmàn-Cabrera, Fractional mechanical oscillators.*RevisaMex Fis.* 58, 348-352, (2012).

[3] N. H. Sweilam, S. M. Al-Mekhlafi, S. M. Hassan,, N. R. Alsunaideh, A. E. Radwan, A novel hybrid crossover dynamics of monkeypox disease mathematical model with time delay: Numerical Treatments, Fractal Fractional, 8(4), 185, (2024) https://doi.org/10.3390/fractalfract8040185

International Conference on Mathematical Analysis and Applications in Science and Engineering ICMA²SC'24

ISEP **Porto-Portugal, June 20 - 22, 2024**

Numerical Investigation of a Fractional order Wolbachia Invasive Model using Stochastic Bayesian Neural Network

Zeshan Faiz[1] **Shumaila Javeed**[2 *]

[1] COMSATS University Islamabad, Pakistan

[2*] Shumaila_javeed@comsats.edu.pk

Abstract: The major goal of this research study is to solve the fractional order Wolbachia invasive model (FWIM) by developing a computational framework based on the Bayesian regularization backpropagation neural network (BRB-NN) approach. The dynamics of the Wolbachia model categorized into four classes, namely Wolbachia-uninfected aquatic mosquitoes (A_n), Wolbachia-uninfected adult female mosquitoes (F_n), Wolbachia-infected aquatic mosquitoes (A_w), and Wolbachia-infected adult female mosquitoes (F_w). We incorporate incomplete cytoplasmic incompatibility and imperfect maternal transmission. We investigate the three different cases of the fractional order derivative ($\alpha = 0.5,0.7,0.9$), and reproduction rate of Wolbachia-infected mosquitoes ($\phi_w = 1.0,1.5,2.0$) on the dynamics of mosquitoes. The proposed Bayesian regularization backpropagation scheme is applied to three distinct cases using 80% and 20% of the created dataset for training and testing, respectively, with 15 hidden neurons. Comparisons of the results are presented to verify the validity of the proposed technique for solving the model. The Bayesian regularization approach is used to minimize the mean square error (MSE) for the fractional order Wolbachia invasive model. The achieved results are based on MSE, correlation, state transitions, error histograms, and regression analysis to confirm the effectiveness of the suggested approach. Additionally, the absolute error value modifies the designed approach's accuracy.

keywords: Biological problem; Mathematical modeling; Neural networks

MSC2020: 92-08; 92-10; 92B20.

References

[1] Bhatt, Samir, Peter W. Gething, Oliver J. Brady, Jane P. Messina, Andrew W. Farlow, Catherine L. Moyes, John M. Drake, The global distribution and burden of dengue, Nature 496, (2013), 504-507.

[2] Adekunle, Adeshina I., Michael T. Meehan, Emma S. McBryde, Mathematical analysis of a Wolbachia invasive model with imperfect maternal transmission and loss of Wolbachia infection, Infectious Disease Modelling, 4 (2019), 265-285.

[3] Baleanu, Dumitru, Amin Jajarmi, Ebenezer Bonyah, Mojtaba Hajipour, New aspects of poor nutrition in the life cycle within the fractional calculus, Advances in Difference Equations, 1(2018), 1-14.

[4] Lee, Keun Young, Namil Chung, Suntae Hwang, Application of an artificial neural network (ANN) model for predicting mosquito abundances in urban areas, Ecological informatics, 36 (2016), 172-180.

[5] Faiz, Zeshan, Iftikhar Ahmed, Dumitru Baleanu, and Shumaila Javeed, A Novel Fractional Dengue Transmission Model in the Presence of Wolbachia Using Stochastic Based Artificial Neural Network, 139(2024), 1217-1238.

International Conference on Mathematical Analysis and Applications in Science and Engineering
ICMA²SC'24
ISEP Porto-Portugal, June 20 - 22, 2024

Identifying fractional order transfer functions from frequency responses

Duarte Valério[1⋆]

[1] IDMEC, Instituto Superior Técnico, Universidade de Lisboa, Lisboa, Portugal

[1⋆]duarte.valerio@tecnico.ulisboa.pt

Abstract: This paper explores simple methods to identify fractional order models from a frequency response. The models addressed are explicit and commensurate, with one or two pseudo-poles. Such identification methods complement Levy's identification method.

keywords: Fractional calculus; Identification; Transfer functions; Frequency response.

MSC2020: 26A33; 34A08; 93B30.

1 Introduction

This paper is concerned with the identification of explicit commensurate fractional order models with one or two poles from frequency responses, often referred to as first and second species transfer functions. They are, with $\nu > 0$ and $\omega_0 > 0$,

$$F_{c1}(s) = \frac{1}{1 + \left(\frac{s}{\omega_0}\right)^\nu} \tag{1}$$

$$F_{c2}(s) = \frac{K}{1 + 2\zeta \left(\frac{1}{\omega_0}\right)^\nu + \left(\frac{s}{\omega_0}\right)^{2\nu}} \tag{2}$$

Identification from a frequency response can always be carried out using the Levy method [4], but it requires knowing in advance the orders of both numerator and denominator and the fractional order. Here, we present simple methods to estimate the parameters of (1)–(2).

2 One pseudo-pole

Making $\Omega = \frac{\omega}{\omega_0}$, the frequency response of (1) is

$$F_{i1}(j\omega) = \frac{1}{1 + \left(\frac{j\omega}{\omega_0}\right)^\nu} = \frac{1}{1 + \cos\frac{\nu\pi}{2}\left(\frac{\omega}{\omega_0}\right)^\nu + j\sin\frac{\nu\pi}{2}\left(\frac{\omega}{\omega_0}\right)^\nu} \tag{3}$$

$$\begin{aligned} 20\log_{10}|F_{i1}(\Omega)| &= -20\log_{10}\left|1 + \cos\frac{\nu\pi}{2}\Omega^\nu + j\sin\frac{\nu\pi}{2}\Omega^\nu\right| \\ &= -10\log_{10}\left(1 + 2\cos\frac{\nu\pi}{2}\Omega^\nu + \cos^2\frac{\nu\pi}{2}\Omega^{2\nu} + \sin^2\frac{\nu\pi}{2}\Omega^{2\nu}\right) \\ &= -10\log_{10}\left(1 + 2\cos\frac{\nu\pi}{2}\Omega^\nu + \Omega^{2\nu}\right) \end{aligned} \tag{4}$$

$$\angle F_{i1}(\Omega) = \angle 1 - \angle\left(1 + \cos\frac{\nu\pi}{2}\Omega^{\nu} + j\sin\frac{\nu\pi}{2}\Omega^{\nu}\right)$$
$$= -\arctan\frac{\sin\frac{\nu\pi}{2}\Omega^{\nu}}{1+\cos\frac{\nu\pi}{2}\Omega^{\nu}} \tag{5}$$

To identify a model given by (1), the order ν can be found from the from the behaviour at high frequencies, where the phase is constant and equal to $-\nu 90°$, and the gain varies linearly with the logarithm of the frequency, with a -20ν dB/decade. This is the only practical method if there is no resonance peak, which appears [5] when $\nu > 1$, at frequency

$$\left(\frac{\omega}{\omega_0}\right)^{\nu} = -\cos\frac{\nu\pi}{2} \Leftrightarrow \omega = \omega_0\left(-\cos\frac{\nu\pi}{2}\right)^{\frac{1}{\nu}} \tag{6}$$

and with an amplitude given by (4) evaluated at (6):

$$\max 20\log_{10}|F_{i1}(\Omega)| = -10\log_{10}\left(1 + 2\cos\frac{\nu\pi}{2}\left(-\cos\frac{\nu\pi}{2}\right) + \left(-\cos\frac{\nu\pi}{2}\right)^2\right)$$
$$= -10\log_{10}\left(\left(\sin\frac{\nu\pi}{2}\right)^2\right) = -20\log_{10}\left|\sin\frac{\nu\pi}{2}\right| \tag{7}$$

Then, we can find the order from the peak value inverting (7), $\nu = \frac{2}{\pi}\arcsin\frac{1}{\max|F_{i1}(\Omega)|}$, and the value of ω_0 can then be found from the peak frequency using (6):

$$\omega_0 = \omega_{\text{peak}}\left(-\cos\frac{\nu\pi}{2}\right)^{-\frac{1}{\nu}} \tag{8}$$

3 Two pseudo-poles

Making again $\Omega = \frac{\omega}{\omega_0}$, the frequency response of (2) is [2]

$$F_{i2}(j\omega) = \frac{1}{1 + 2\zeta\left(\frac{j\omega}{\omega_0}\right)^{\nu} + \left(\frac{j\omega}{\omega_0}\right)^{2\nu}}$$
$$= \frac{1}{1 + 2\zeta\cos\frac{\nu\pi}{2}\left(\frac{\omega}{\omega_0}\right)^{\nu} + \cos(\nu\pi)\left(\frac{\omega}{\omega_0}\right)^{2\nu} + j2\zeta\sin\frac{\nu\pi}{2}\left(\frac{\omega}{\omega_0}\right)^{\nu} + j\sin(\nu\pi)\left(\frac{\omega}{\omega_0}\right)^{2\nu}} \tag{9}$$

$$20\log_{10}|F_{i2}(\Omega)| = -20\log_{10}\left|1 + 2\zeta\cos\frac{\nu\pi}{2}\Omega^{\nu} + \cos(\nu\pi)\Omega^{2\nu} + j2\zeta\sin\frac{\nu\pi}{2}\Omega^{\nu} + j\sin(\nu\pi)\Omega^{2\nu}\right|$$
$$= -10\log_{10}(1 + 4\zeta^2\cos^2\frac{\nu\pi}{2}\Omega^{2\nu} + \cos^2(\nu\pi)\Omega^{4\nu} + 4\zeta\cos\frac{\nu\pi}{2}\Omega^{\nu} + 2\cos(\nu\pi)\Omega^{2\nu} + 4\zeta\cos\frac{\nu\pi}{2}\cos(\nu\pi)\Omega^{3\nu} + \ldots$$
$$\ldots + 4\zeta^2\sin^2\frac{\nu\pi}{2}\Omega^{2\nu} + 4\zeta\sin\frac{\nu\pi}{2}\sin(\nu\pi)\Omega^{3\nu} + \sin^2(\nu\pi)\Omega^{4\nu})$$
$$= -10\log_{10}\left(1 + 4\zeta^2\Omega^{2\nu} + \Omega^{4\nu} + 4\zeta\cos\frac{\nu\pi}{2}\Omega^{\nu} + 2\cos(\nu\pi)\Omega^{2\nu} + 4\zeta\cos\frac{\nu\pi}{2}\Omega^{3\nu}\right) \tag{10}$$

$$\angle F_{i1}(\Omega) = \angle 1 - \angle\left(1 + 2\zeta\cos\frac{\nu\pi}{2}\Omega^{\nu} + \cos(\nu\pi)\Omega^{2\nu} + j2\zeta\sin\frac{\nu\pi}{2}\Omega^{\nu} + j\sin(\nu\pi)\Omega^{2\nu}\right)$$
$$= -\arctan\frac{2\zeta\sin\frac{\nu\pi}{2}\Omega^{\nu} + \sin(\nu\pi)\Omega^{2\nu}}{1 + 2\zeta\cos\frac{\nu\pi}{2}\Omega^{\nu} + \cos(\nu\pi)\Omega^{2\nu}} \tag{11}$$

It can be shown [5] (from the Matignon theorem [3]) that, for $\nu < 2$, the limit between stability and unstability is given by $\zeta = -\cos\frac{\nu\pi}{2}$, and that [2, 1] when the system is stable there are four possibilities, as seen in Figure 1:

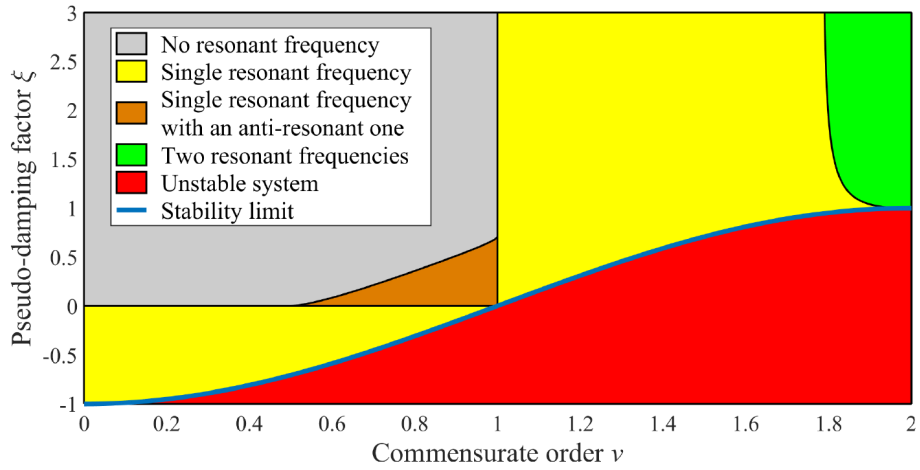

Figure 1: Zones of the (ν, ζ) plane where there are zero or one resonance peaks for (2). Extracted from [1].

(a) There may be no resonant frequencies. In this case, the slope of the gain in always negative.

(b) There may be one resonant frequency, if the slope of the gain is positive for low frequencies, and negative after the resonance.

(c) There may be one resonant frequency, if the slope of the gain is negative for both low and high frequencies, but positive in-between.

(d) There may be two resonant frequencies. In this case,(2) can be written as the product of two transfer functions with one root (1), having the same fractional order ν (otherwise their product would be non-commensurable), and having one resonant peak each.

In this last case, the maximum value of the gain is found at the first peak, since the two peaks result from the superposition of two systems with one root, both with a maximum value of the gain given by (7). Consequently, the peak value can be approximated by (7):

$$\max 20 \log_{10} |F_{i2}(\Omega)| > -20 \log_{10} \left| \sin \frac{\nu\pi}{2} \right| \tag{12}$$

The actual value is always larger, since the contribution of the other pole is being neglected. A better approximation can be found using the exact expression of the gain (10) with an approximation of the frequency peak. Combining denominator roots

$$\left(\frac{s}{\omega_0}\right)^{\nu} = \frac{-2\zeta \pm \sqrt{4\zeta^2 - 4}}{2} \Leftrightarrow s^{\nu} = \omega_0^{\nu} \left(-\zeta \pm \sqrt{\zeta^2 - 1}\right) \tag{13}$$

with peak frequency (6) results in

$$\omega_1 \approx \omega_0 \left(-\zeta - \sqrt{\zeta^2 - 1}\right)^{\frac{1}{\nu}} \left(-\cos \frac{\nu\pi}{2}\right)^{\frac{1}{\nu}} \tag{14}$$

$$\omega_2 \approx \omega_0 \left(-\zeta + \sqrt{\zeta^2 - 1}\right)^{\frac{1}{\nu}} \left(-\cos \frac{\nu\pi}{2}\right)^{\frac{1}{\nu}} \tag{15}$$

The actual values will be below ω_1 and above ω_2, since the contribution of each pole on the other's is being neglected. They are separated by

$$\log_{10} \Delta\omega = \log_{10} \frac{\omega_0 \left(-\zeta + \sqrt{\zeta^2 - 1}\right)^{\frac{1}{\nu}} \left(-\cos \frac{\nu\pi}{2}\right)^{\frac{1}{\nu}}}{\omega_0 \left(-\zeta - \sqrt{\zeta^2 - 1}\right)^{\frac{1}{\nu}} \left(-\cos \frac{\nu\pi}{2}\right)^{\frac{1}{\nu}}} = \frac{1}{\nu} \log_{10} \frac{-\zeta + \sqrt{\zeta^2 - 1}}{-\zeta - \sqrt{\zeta^2 - 1}} \text{ decades} \tag{16}$$

If $\log_{10} \Delta\omega$ is one decade or more, it is reasonable to approximate the second peak from the gain slope of the first, which is -20ν dB/decade:

$$|G(j\omega_2)| \approx -20 \log 10 \frac{-\zeta + \sqrt{\zeta^2 - 1}}{-\zeta - \sqrt{\zeta^2 - 1}} - 20 \log_{10} \left| \sin \frac{\nu\pi}{2} \right| \tag{17}$$

Expressions (12)–(14) can be used when there is only one resonance peak, and $\zeta > 1$. When $\zeta < 1$, different approximations are needed, which can be found numerically, and will be established and shown during this paper's presentation.

To identify a model given by (2), the order ν can be found from the from the behaviour at high frequencies, where the phase is constant and equal to $-\nu 180°$, and the gain varies linearly with the logarithm of the frequency, with a -40ν dB/decade. This is the only practical method if there is no resonance peak. If there are one or two resonance peaks, the order $\nu > 1$ can be found from (12), and then ζ can be found from (14). If there are two resonance peaks, these values can be confirmed from (16)–(17). If, however, $\nu < 1$, then it is necessary to invert the numerical expressions mentioned above that apply in that case.

4 Conclusions and Future work

Similar expressions and methods would be useful for non-commensurable systems as well.

Acknowledgments

The authors acknowledge Fundação para a Cieência e a Tecnologia (FCT) for its financial support via the project LAETA Base Funding (DOI: 10.54499/UIDB/50022/2020).

References

[1] Assia Boubidi, Sihem Kechida, and Hicham Tebbikh. Analytical study of resonance regions for second kind commensurate fractional systems. *Discrete and Continuous Dynamical Systems - B*, 26(7):3579–3594, 2021.

[2] Rachid Malti, Xavier Moreau, and Firas Khemane. Resonance of fractional transfer functions of the second kind. In *Fractional Differentiation and its Applications*, Ankara, 2008. IFAC.

[3] Denis Matignon. Stability results on fractional differential equations to control processing. In *Proceedings of the Computational Engineering in Syatems and Application Multiconference*, volume 2, pages 963–968, Lille, 1996.

[4] Duarte Valério, Manuel Duarte Ortigueira, and José Sá da Costa. Identifying a transfer function from a frequency response. *ASME Journal of Computational and Nonlinear Dynamics*, 3(2):021207, 2008.

[5] Duarte Valério and José Sá da Costa. *An Introduction to Fractional Control*. IET, Stevenage, 2013. ISBN 978-1-84919-545-4.

Brief recording - Photos

Opening Ceremony


INTERNATIONAL
CONFERENCE
Mathematical
Analysis and
Applications in
Science and
Engineering


JUNE 20–22, 2024
ISEP · PORTO, PORTUGAL
INTERNATIONAL

Releasing stress.....

Starting the plenary sessions 1 and 2 and .... and chairs...

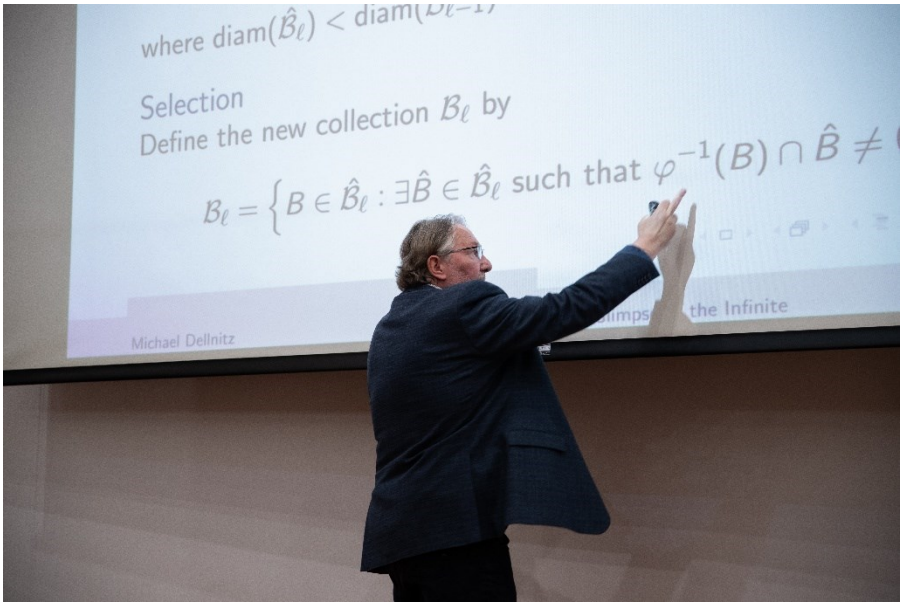

CLOSING CEREMONY AND PORTO OF HONOR


INTERNATIONAL CONFERENCE
BEST POSTER


INTERNATIONAL CONFERENCE
Mathematical Analysis
and Applications
in Science and Engineering
BEST POSTER


INTERNATIONAL
CONFERENCE


INTERNATIONAL
CONFERENCE
EST POSTER


INTERNATIONAL
CONFERENCE


BEST POSTER


BEST STUDENT PAPER


JUNE 20–22, 2024
ISEP · PORTO, PORTUGAL
INTERNATIONAL
CONFERENCE

Gala Dinner

Boat Trip

https://www2.isep.ipp.pt/icmasc/

2024